ABSTRACT

Title of dissertation: VARIABLE QUBIT-QUBIT COUPLING VIA A TUNABLE LUMPED-ELEMENT RESONATOR

Cody J. Ballard, Doctor of Philosophy, 2018

Dissertation directed by: Professor Frederick C. Wellstood
Department of Physics

Professor Christopher J. Lobb
Department of Physics

This dissertation examines the design, fabrication, and characterization of a superconducting lumped-element tunable LC resonator that is used to vary the coupling between two superconducting qubits. Some level of qubit-qubit coupling is needed to perform gating operations. However, with fixed coupling, single qubit operations become considerably more difficult due to dispersive shifts in their energy levels transitions that depend on the state of the other qubit. Ideally, one wants a system in which the qubit-qubit coupling can be turned off to allow for single qubit operations, and then turned back on to allow for multi-qubit gate operations.

I present results on a device that has two fixed-frequency transmon qubits capacitively coupled to a tunable thin-film LC resonator. The resonator can be tuned *in situ* over a range of 4.14 GHz to 4.94 GHz by applying an external magnetic flux to two single-Josephson junction loops, which are incorporated into the resonator's inductance.

The qubits have 0-to-1 transition frequencies of 5.10 GHz and 4.74 GHz. To isolate the system and provide a means for reading out the state of the qubit readout, the device was mounted in a 3D Al microwave cavity with a TE_{101} mode resonance frequency of about 6.1 GHz. The flux-dependent transition frequencies of the system were measured and fit to results from a coupled Hamiltonian model.

With the LC resonator tuned to its minimum resonance frequency, I observed a qubit-qubit dispersive shift of $2\chi_{qq} \approx 0.1$ MHz, which was less than the linewidth of the qubit transitions. This dispersive shift was sufficiently small to consider the coupling "off", allowing single qubit operations. The qubit-qubit dispersive shift varied with the applied flux up to a maximum dispersive shift of $2\chi_{qq} \approx 6$ MHz. As a proof-of-principle, I present preliminary results on performing a CNOT gate operation on the qubits when the coupling was "on" with $2\chi_{qq} \approx 4$ MHz.

This dissertation also includes observations of the temperature dependence of the relaxation time T_1 of three $Al/AlO_x/Al$ transmons. We found that, in some cases, T_1 increased by almost a factor of two as the temperature increased from 30 mK to 100 mK. We found that this anomalous behavior was consistent with loss due to non-equilibrium quasiparticles in a transmon where one electrode in the tunnel junction had a smaller volume and slightly smaller superconducting energy gap than the other electrode. At sufficiently low temperatures, non-equilibrium quasiparticles accumulate in the electrode with a smaller gap, leading to an increased density of quasiparticles at the junction and a corresponding decrease in the relaxation time. I present a model of this effect, use the model to extract the density of non-equilibrium quasiparticles in the device, and find the values of the two superconducting energy gaps.

VARIABLE QUBIT-QUBIT COUPLING VIA A TUNABLE LUMPED-ELEMENT RESONATOR

by

Cody James Ballard

Dissertation submitted to the Faculty of the Graduate School of the
University of Maryland, College Park, in partial fulfillment
of the requirements for the degree of
Doctor of Philosophy
2018

Advisory Committee:
Professor Frederick C. Wellstood, Advisor/Chair
Professor Christopher J. Lobb, Advisor
Dr. Kevin D. Osborn
Dr. Benjamin S. Palmer
Professor Ichiro Takeuchi

For my wife, Allison,
and daughter, Aurelie

Acknowledgements

I would first like to thank the Lord God because I would not have been able to accomplish any of this without Him.

I would like to give a special thanks to my wife, Allison. I've lost count of the number of times that her love and support helped me through tough times and setbacks in the course of this research. This was certainly not an easy road, and I know I wouldn't have gotten this far without her. Allison, if you end up reading this, you should know that you are the best wife I could ever have imagined.

I would also like to especially thank my parents, Jim and Vanessa. I believe their dedication to my education was the key element that eventually landed me here. As a child, being asked often what I learned at school that day forced me to pay attention and make sure I had an answer. On top of that, whenever I had a question about math or science, you both always took the time to sit down and help me, or to look up the answer with me whenever it was particularly tough. I learned a lot from y'all, and I am incredibly grateful for everything. I hope that I show that gratitude as much as or even more than I say it.

I would like to thank my in-laws, Doug and Ann, as well. Having them in my corner has been incredible, especially during the birth of our daughter, Aurelie. I was a mess, and they picked up the pieces.

I can't neglect to mention my best friend, Andrew. I know he doesn't care for acknowledgement, but he is like a brother to me. Without a doubt, Allison and I wouldn't be at this point in life without him.

I could never put something like this acknowledgement section together without recognizing my high school math teacher Mrs. Beverly Martin. Before I had her as a teacher, math was just another school subject. After only a few short weeks, she awoke in me a passion that led me here and, I hope, will never die down. As a teenager, only my parents could rival the level of confidence in me that she held.

I definitely want to thank my undergrad advisor Dr. Fred Cawthorne. In my very first conversation with him, he convinced me to major in physics. Then, over the course of my undergrad career, getting to work so close to him showed me that I wanted to go to grad school. The confidence and physics knowledge he instilled in me helped me make it here to Maryland.

Thank you very much to my advisor, Dr. Fred Wellstood. I am extremely thankful for him allowing me onto this project and then allowing me to stay on it over all the years. I didn't always share the faith he seemed to have in me, but knowing he had it helped immensely. I would like to especially thank him for taking the time to explain all sorts of difficult concepts whenever I needed it. Without fail, he would take the time to help me.

Another big thanks has to go to my co-advisor, Dr. Chris Lobb. Every time I talked to Chris about difficult research or life issues, I would come away less overwhelmed. I believe that making it through all this without him involved would have been close to impossible

I don't know what I would have done without Sudeep Dutta joining the group as a Post Doc these past three years. I got severely lost in the doldrums of fabrication, and he was there to make sure practically everything else in lab kept going. Taking point on

data taking allowed me to also have time in my day to see my wife and daughter. I will be forever grateful. Also, I will always remember to "never stop learning." However, I failed miserably on following through with "don't go to grad school." In my defense, though, that ship had already sailed.

I would also like to thank Rangga Budoyo and Ben Cooper. In my early years in the group, they both were there to mentor me and help me grow into a functioning member of the lab. Shadowing them set me on the path that culminated in this dissertation.

I would like to thank Ben Palmer and members of his superconducting group at LPS, including Shavindra Premaratne, Jen-Hao Yeh, Rui Zhang, Sergey Novikov, and Baladitya Suri. In my earliest days of fabrication, I headed over to LPS a lot to use their JEOL system, and they were consistently there to help me get set up and fix any issues I encountered. The collaboration with this group was a significant source of growth for me, and I am thankful I was even a little involved. Also, I would like to thank Dr. Palmer for allowing us to use a spare sheet of Cryoperm. This was an imporant addition to the magnetic shielding on the dilution refrigerator.

I would also like to thank Dr. Kevin Osborn and his group for guiding us through the process of coating the inside of our dilution refrigerator can and for allowing us to use some extra Silicon Carbide crystals for the coating. This helped to reduce background noise we had been experiencing in our data and improved the performance of our devices.

I couldn't have performed any measurements without being able to cool down my devices; so, I would like to thank the Joint Quantum Institute (JQI) for the funding to

purchase our Oxford Triton 200 dilution refrigerator. Also, a majority of the time-resolved measurements I show in Chapter 9 were conducted using a Tektronix arbitrary waveform generator (AWG). I would like to thank the Physics Frontier Center (PFC) for the funding to purchase the AWG.

I'd like to also acknowledge staff members here that helped along the way and made all this possible. First, I would like to thank Mary Sutton. You were a constant bright light in my day, and I've never enjoyed filling out TARs more than when you needed one from me. Second, I would like to thank Doug Bensen and Brian Straughn. I'm convinced that nothing would work around here without you two, and this place would be a lot less interesting without getting to talk to you both. Other important staff members that made this all possible were: Al Godinez, Jesse Anderson, Paulina Alejandro, and Pauline Rirksopa in Physics; Tom Loughran, John Abrahams, and John Hummel at Fablab.

I know I've missed people. With the amount of effort and time that goes into doctoral research, it is impossible to remember everyone, especially "on the spot" writing such a personal part of my dissertation. To anyone I have thus far forgotten, thank you.

Table of Contents

List of Figures

List of Tables

Chapter 1

Introduction

1.1 Quantum Computing

For classical computers, information is encoded and manipulated in the form of bits. A Boolean or "classical" bit can only be in a state of 0 or 1, there is no third option. On the other hand, information in a quantum computer, is encoded and manipulated in qubits (quantum bits). A qubit may be in quantum states $|0\rangle$, $|1\rangle$, or in any coherent quantum superposition of $|0\rangle$ and $|1\rangle$.

The first discussion of how quantum states could be used for computation was by Feynman [1] in the 1980s. The idea was to use a quantum computer in order to efficiently simulate quantum systems. Using classical computers to simulate many-particle quantum systems requires computing power that grows exponentially with the number of particles. Feynman realized that a quantum computer would require only a polynomial increase in the number of qubits to simulate an N particle system. Since then, it has been found that some other important problems could be solved faster on a quantum computer than a classical computer. One example is Grover's algorithm [2], which is a proposed method used to search an unsorted list. Another well-known example is Shor's algorithm [3], which is a proposed method for using a quantum computer to find the prime factors of numbers. The best known classical algorithms for factoring numbers are exponential in the size of the number. On the other hand, Shor's algorithm would be able to find the factors in a time that scaled as a polynomial in the size of the number [4]. This algorithm is of particular importance due to the reliance of

RSA encryption on the difficulty of factoring large numbers [5]. The potential to rapidly break RSA encryption stimulated wide-ranging theoretical and experimental research in quantum computing.

In order for a quantum system to be useful as a quantum bit, it must satisfy the DiVincenzo criteria [6], which includes the requirements that the system can be initialized in a well-defined quantum state and that the coherence time is much longer than the gate time. Over the last two decades a wide range of systems have been proposed and investigated for use as qubits. Some examples of such systems include photons [7], trapped ions [8], trapped neutral atoms [9], nitrogen vacancy (NV) centers in diamond [10], nuclear spins in silicon [11], and a wide variety of superconducting circuits [12]-[20].

Each of these systems and others too numerous to mention have certain advantages and disadvantages for use as a qubit. My research was focused on qubits formed from superconducting circuits that utilize Josephson junctions [21] as a non-linear element. These circuits are macroscopic in size and patterned onto substrates by standard lithography techniques. Some advantages that come along with this includes a high level of control over the design, ease of fabrication, and an ease in coupling to external systems. Due to their size and the high level of control over the pattern, it is quite simple to couple to superconducting qubits. On the other hand, a few disadvantages are an ease in coupling to external systems and issues in scalability. The ease with which superconducting qubits can couple to their surroundings can often be a negative attribute as the qubits will couple to unintended systems such as resonances in microwave lines or

two-level systems (TLSs) [22]-[24]. This can lead to a serious degradation in performance and coherence time, and extra effort must be taken to mitigate this.

1.2 Superconducting Qubits

Superconducting qubits can be classified into a few broad categories. Each category uses a different sharply defined quantum operator as its computational basis states. In 1999, Nakamura *et. al.* reported the first coherent measurement of a superconducting qubit with an experiment on a Cooper pair box (CPB) [12]. In this charge qubit, the number of Cooper pairs on a small superconducting island is the sharply defined quantum operator. The phase qubit, which was initially developed here at Maryland [13], uses resonances in states with a relatively well-defined phase in the tilted-washboard potential of a current-biased Josephson junction [25, 26]. As another example, the flux qubit uses trapped flux states in a SQUID style circuit as the basis states [14].

The parameters that most determine which category a certain qubit is in are the Josephson energy E_J, the charging energy E_C, and the inductive energy E_L, which are defined as

$$E_J \equiv \frac{\Phi_0 I_0}{2\pi}, \tag{1.1}$$

$$E_C \equiv \frac{e^2}{2C}, \tag{1.2}$$

and

$$E_L \equiv \frac{\Phi_0^2}{2L}, \tag{1.3}$$

where Φ_0 is the magnetic flux quantum, I_0 is the critical current of the junction in the circuit, C is the capacitance shunting the junction, and L is the characteristic inductance of the device. For charge qubits, typically $E_J/E_C \lesssim 1$. On the other side of the spectrum, phase qubits typically have $E_J/E_C \gg 1$. Finally, flux qubits usually are in the regime $E_J/E_C \approx E_L/E_C \gtrsim 1$.

Achieving a long coherence time is only possible if the qubit is well-isolated from the environment. The development of the transmon qubit [18] showed how an existing qubit design could be tweaked in order to greatly improve the coherence. This style of qubit drew on the design of the phase qubit and Cooper pair boxes. The modification came in the form of adding a shunt capacitance across the junction in order to decrease the charging energy and set the energy ratio in the range $50 \leq E_J/E_c \leq 200$ where the phase across the junction was well-defined. This capacitive shunting exponentially suppressed charge noise and produced a circuit that behaves much like a phase qubit. However, by restricting E_J/E_C to be in this range, the device retained enough anharmonicity that it did not need to be current-biased. With no external bias lines and by coupling it to a resonant cavity, this design was well-isolated from noise and showed marked improvements in the coherence times over both phase qubits and the CPB [17].

Another remarkable development was the advent of circuit quantum electrodynamics (cQED) [28]. In this architecture, the qubit is coupled to a resonator that not only helps to decouple the qubit from the surrounding environment but also provides natural readout techniques [29]. cQED is based on the AMO field of quantum electrodynamics (QED) where single atoms are coupled to the electromagnetic field in a resonant optical cavity [30].

A key development in cQED came when Paik *et. al.* redesigned the transmon and replaced the 2D coplanar resonator with a 3D microwave cavity [18]. This new design led to large increases in the qubit coherence time and qubit lifetime by reducing the participation ratio of the dielectric volume and by further isolating the qubit from the electromagnetic environment. Many other groups, including our own took notice and soon adopted this approach. The work I describe in this dissertation is one such example.

1.3 Coupled Systems

Among other requirements, the DiVincenzo criteria [6] states that a quantum computer needs to have a universal set of quantum gates. In classical computing the NAND gate is a universal gate because it can be used to construct any logical operation. In quantum computing, a set of gates that has the controlled NOT (CNOT) gate and single-qubit operations forms a universal set [31]. The CNOT is an entangling two-qubit gate in which one qubit is the "control" and the other is the "target". In operation, the CNOT gate inverts the state of the target qubit when the control qubit is in $|1\rangle$ but leaves the state unchanged if the control qubit is in $|0\rangle$.

The key to producing an entangling two-qubit gate such as the CNOT is that there must be coupling between the two qubits. The simplest way to achieve this is with a fixed level of coupling between the two qubits [32]. For example, S. Premaratne *et. al*. recently demonstrated a SWIPHT gate [33] on two 3D transmons in a 3D cavity [34, 35]. The capacitive coupling between the two qubits was fixed by their physical separation in the cavity and the detuning from the cavity resonance.

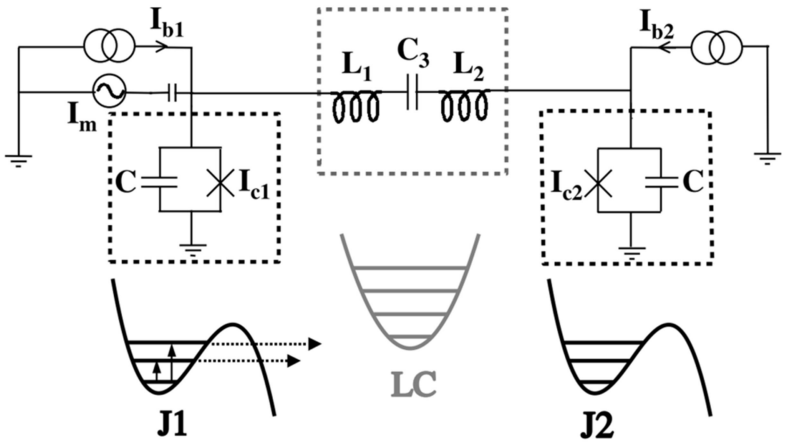

Fig. 1.1: Circuit schematic of two phase qubits coupled via a fixed LC resonator reproduced from ref. [32].

The main drawback to a system with fixed qubit-qubit coupling arises when performing single qubit operations. When the coupling is constantly present, the transition frequency of the qubit one is intending to manipulate is dependent on the state of the other qubit. For a set of universal quantum gates one must be able to control the state of individual qubits, and this becomes harder to implement with fixed coupling.

One alternative to the use of fixed coupling is to vary the qubit-qubit coupling strength in such a way that it can be effectively turned off when performing single-qubit operations and turned on for two-qubit gating. One way this can be achieved is by using qubits with tunable energy levels. This was the original approach devised by Strauch *et. al*. for phase qubits [32]. Figure 1.1 shows a circuit schematic from this experiment for two phase qubits coupled via a fixed-frequency resonator, reproduced from ref. [32]. In the figure, the dashed boxes indicate the two phase qubits (black) and the LC resonator (gray). The bias current into each phase qubit tilts its washboard potential, which sets the

transition frequency. When the two qubits need to be coupled, they can simply be brought close together in frequency space. Since the dispersive frequency shift is inversely dependent on the detuning between them, tuning the qubits to the same frequency leads to strong coupling. To turn the coupling off, one simply detunes them. Another example is the Xmon qubit from the Martinis group [20]. This qubit, which borrows ideas from transmons and phase qubits, uses a dc SQUID to produce a tunable transition frequency.

A major drawback to tunable qubits is their susceptibility to noise in the tuning bias lines. Any noise that causes variations in the qubit frequency will lead directly to inhomogenous broadening and a degradation of the qubit's coherence time. With proper care taken on filtering and isolation, this can be mitigated, but the issue remains. Another problem is that sweeping the energy levels can cause loss of fidelity due to the presence of unintended avoided level crossing from coupling to two-level systems (TLSs) [34].

The work I describe in this dissertation was focused on variably coupling two fixed-frequency transmons via a tunable thin-film resonator. The idea was to take advantage of the long lifetimes typically seen in fixed frequency transmons and vary the coupling between them by tuning the frequency of a resonator coupled to both qubits. To decouple the qubits and resonator from the environment, I mounted the device in a single 3D microwave cavity, which was also used to read out the state of the qubits. In Fig. 1.2 I show a photo of device TRES_092917, where I have placed dashed boxes around the fixed-frequency qubits (red boxes) and the tunable resonator (blue box). In principle, this design could readily be scaled up to include additional qubits by simply replicating additional tunable resonators and transmons to the left and right.

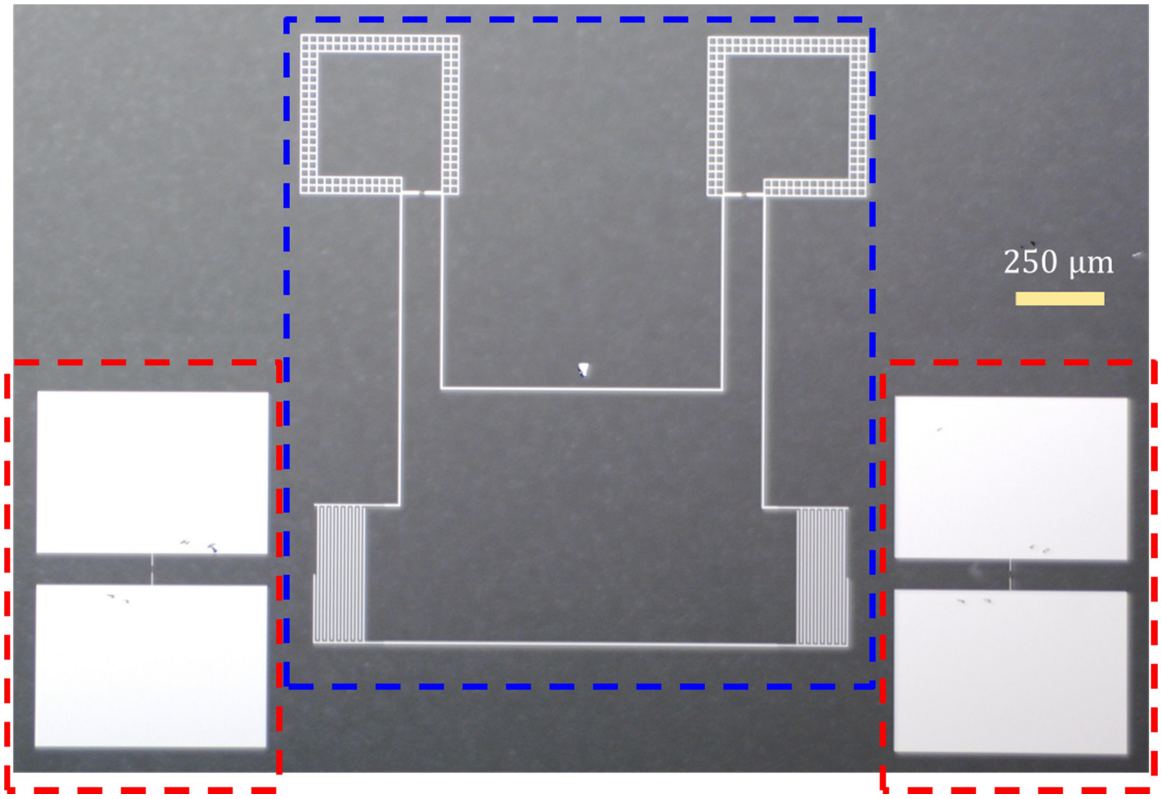

Fig. 1.2: Photograph of device TRES_092917. The red boxes are around the two transmon qubits, and the blue box is around the tunable, lumped element resonator.

1.4 Overview of Dissertation

The overarching aim of this work was to demonstrate coupling between two qubits that could be turned on and off. Turning off the coupling allows for single qubit operations, while turning on the coupling allows for two-qubit entangling operations. To read out the qubit state and to isolate the device from the environment, I mounted the devices in a single 3D microwave cavity.

The theory behind the individual elements of the circuit are discussed in Chapters 2 through 5. In Chapter 2, I discuss the mode structure in the 3D microwave cavity,

derive the mode frequencies, and then show simulations of the electromagnetic fields for different cavity modes. I then follow a derivation by E. U. Condon [35] to find the effective capacitance and inductance of a cavity mode.

In Chapter 3, I discuss my work on individual tunable thin-film LC resonators. I show results on an LC resonator mounted in a 3D cavity in which the temperature was varied to modulate the resonance frequency using the kinetic inductance of the Al film. I also discuss the theory of how the inclusion of an rf SQUID loop allows the resonance frequency of a resonator to be varied. Finally, I show results on one of my tunable resonators.

In Chapter 4, I discuss the theory of the transmon. I begin by deriving the Hamiltonian and finding the energy levels. I then give a brief discussion of the characteristic times measured in qubits.

In Chapter 5, I derive the Hamiltonian of two transmons coupled to a tunable resonator and cavity. I begin with a circuit model, from which I derive the classical Hamiltonian. Upon quantizing this Hamiltonian, I show that the model exhibits Jaynes-Cummings style coupling between the qubits, resonator, and cavity. I end the chapter with a discussion of how I chose the frequency and coupling parameters for the devices.

In Chapters 6 and 7, I discuss how I designed, fabricated, and measured my devices. In the design sections, I discuss how the qubits and tunable LC resonator were configured to achieve the design parameters discussed in Chapter 5. In the fabrication sections, I discuss the steps I went through to build devices. Finally, in the measurement sections, I discuss the dilution refrigerator setup and the electronics that were used to measure and characterize the devices.

In Chapters 8 and 9, I present the results on device TRES_092917, which had two transmons coupled to a tunable LC resonator. Chapter 8 discusses the spectroscopic measurement, and I also compare the spectrum to that of the model Hamiltonian derived in Chapter 5. This allowed me to extract the frequencies and coupling parameters. The key facet of this chapter is showing that the device exhibits variable coupling that produced qubit-qubit dispersive shifts from $2\chi_{qq}$= 0.1 MHz when fully off, up to $2\chi_{qq} \gtrsim$ 6 MHz when fully on. Time resolved measurements, such as measuring the relaxation time and Rabi oscillations, are discussed in Chapter 9. Also included in Chapter 9 are preliminary results on using the variable coupling to accomplish a CNOT gate.

In Chapters 10 and 11, I discuss a surprise we encountered during this research. We observed an anomalous behavior of the transmon relaxation time T_1 vs. temperature T. In Chapter 10, I present the model and theory we used to describe this phenomenon. In Chapter 11, I show measurements and comparison with our model.

Finally, in Chapter 12, I conclude with a summary of the main results from this research.

Chapter 2

3D Microwave Cavities

In this chapter I discuss the theory of our 3D microwave cavities. I include a derivation of the cavity modes and of the effective inductance and capacitance of the modes. I start with the basic behavior of EM modes in a waveguide, and then extend this result to obtain expressions for the modes in a 3d cavity.

2.1 3D Cavity Modes

2.1.1 Modes in a Uniform Cross-Section Waveguide

For this discussion, I follow the derivation in ref. [1]. Consider the uniform cross section waveguide shown in Fig. 2.1. If the space inside the cavity is empty, so that the charge density ρ and current density J are zero, and with time dependence of the electric and magnetic field given by $e^{-i\omega t}$, Maxwell's equations may be stated as:

$$\nabla \cdot \boldsymbol{E} = 0 \tag{2.1}$$

$$\nabla \cdot \boldsymbol{H} = 0 \tag{2.2}$$

$$\nabla \times \boldsymbol{E} = i\omega\mu_0 \boldsymbol{H} \tag{2.3}$$

$$\nabla \times \boldsymbol{H} = -i\omega\epsilon_0 \boldsymbol{E}, \tag{2.4}$$

where ϵ_0 and μ_0 are the permittivity and permeability of free space, respectively. By taking the curl of Eqs. (2.3) and (2.4) and then using a vector calculus relation (see Eq. (A1.11) in Appendix A.1), one finds the wave equation for freely propagating electromagnetic fields in a waveguide,

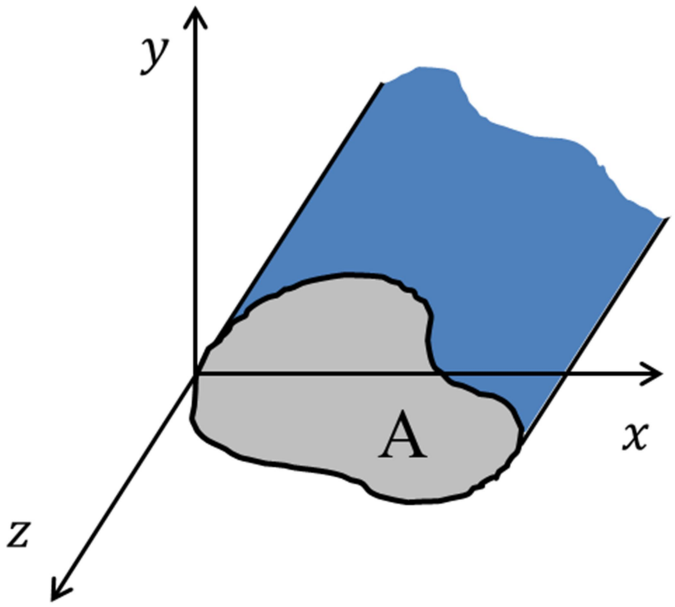

Figure 2.1. Depiction of a waveguide with a uniform cross sectional area A.

$$(\nabla^2 + \mu_0\epsilon_0\omega^2)\boldsymbol{E} = 0. \tag{2.5a}$$

$$(\nabla^2 + \mu_0\epsilon_0\omega^2)\boldsymbol{H} = 0. \tag{2.5b}$$

By orienting the axes so that these waves are propagating along the z-axis (see Fig. 2.1), one can find solutions such that the z-component of these waves has a $e^{\pm ikz}$ dependence. The Laplacian operator can now be written as $\nabla^2 = \nabla_t^2 + \frac{\partial^2}{\partial z^2}$, where ∇_t^2 accounts for contributions from the transverse directions. Equations (2.5) then become

$$\left(\nabla_t^2 + (\mu_0\epsilon_0\omega^2 - k^2)\right)\boldsymbol{E} = 0. \tag{2.6a}$$

$$\left(\nabla_t^2 + (\mu_0\epsilon_0\omega^2 - k^2)\right)\boldsymbol{H} = 0. \tag{2.6b}$$

Equations (2.6) holds for all components of the fields inside the waveguide.

Instead of solving Eqs. (2.6a) and (2.6b) for each component of the electric and magnetic fields, I will show that the transverse components of the fields are dependent on the z-components. Hence, one need only solve for the z-component. To do this, I resolve the components of the fields into their transverse and z-components,

$$\boldsymbol{E} = \boldsymbol{E}_t + \boldsymbol{E}_z \tag{2.7}$$

$$\boldsymbol{H} = \boldsymbol{H}_t + \boldsymbol{H}_z, \tag{2.8}$$

where the z-component of $\boldsymbol{E}$ is given by $\boldsymbol{E}_z = E_z\hat{\boldsymbol{z}}$ and the transverse component is given by $\boldsymbol{E}_t = (\hat{\boldsymbol{z}} \times \boldsymbol{E}) \times \hat{\boldsymbol{z}}$. Similarly, $\boldsymbol{H}_z = H_z\hat{\boldsymbol{z}}$ and $\boldsymbol{H}_t = (\hat{\boldsymbol{z}} \times \boldsymbol{H}) \times \hat{\boldsymbol{z}}$. I next write $\nabla = \nabla_t + \frac{\partial}{\partial z}\hat{\boldsymbol{z}}$ and find that Maxwell's equations may be written as (see Appendix A.2)

$$\frac{\partial \boldsymbol{E}_t}{\partial z} + i\omega\mu_0\hat{\boldsymbol{z}} \times \boldsymbol{H}_t = \nabla_t E_z \qquad \hat{\boldsymbol{z}} \cdot (\nabla_t \times \boldsymbol{E}_t) = i\omega\mu_0 H_z$$

$$\frac{\partial \boldsymbol{H}_t}{\partial z} - i\epsilon_0\omega\hat{\boldsymbol{z}} \times \boldsymbol{E}_t = \nabla_t H_z \qquad \hat{\boldsymbol{z}} \cdot (\nabla_t \times \boldsymbol{H}_t) = -i\epsilon_0\omega E_z \tag{2.9}$$

$$\nabla_t \cdot \boldsymbol{E}_t = -\frac{\partial E_z}{\partial z} \qquad \nabla_t \cdot \boldsymbol{H}_t = -\frac{\partial H_z}{\partial z}.$$

Solving Eqs. (2.9) for the transverse field components as a function of the z-components yields:

$$\boldsymbol{E}_t = \frac{i}{\mu_0\epsilon_0\omega^2 - k^2}[\pm k\nabla_t E_z - \mu_0\omega\,\hat{\boldsymbol{z}} \times \nabla_t H_z] \tag{2.10}$$

and

$$\boldsymbol{H}_t = \frac{i}{\mu_0\epsilon_0\omega^2 - k^2}[\pm k\nabla_t H_z + \epsilon_0\omega\,\hat{\boldsymbol{z}} \times \nabla_t E_z]. \tag{2.11}$$

In these expressions, the $\pm$ in front of k corresponds to waves travelling forward or backward in the waveguide, respectively, and the factor of i produces a phase shift of $\pi/2$ between the z-component and the transverse components. Given these relations, one

need only to solve Eqs. (2.6) for the z-component of the field, and then apply Eqs. (2.10) and (2.11).

I now consider the boundary conditions and type of waves that can be supported inside a waveguide or cavity. There are only two types of solutions [1]: transverse magnetic waves (TM) and transverse electric waves (TE).

For TM modes, $\boldsymbol{H}$ only has a transverse component (*i.e.* $H_z = 0$ everywhere), which means that Eqs. (2.10) and (2.11) reduce to

$$\boldsymbol{E}_t = \frac{\pm ik}{\mu_0 \epsilon_0 \omega^2 - k^2} [\nabla_t E_z] \tag{2.12}$$

and

$$\boldsymbol{H}_t = \frac{i\epsilon_0 \omega}{\mu_0 \epsilon_0 \omega^2 - k^2} [\,\hat{\boldsymbol{z}} \times \nabla_t E_z]. \tag{2.13}$$

For simplicity, I assume that the walls of the waveguide are perfectly conducting, Maxwell's equations then dictate that components of $\boldsymbol{E}$ that are tangential to the walls must vanish. Thus, $E_z = 0$ at the walls.

In the case of TE waves the electric field only has transverse components (*i.e.* $E_z = 0$ everywhere). In this case, Eqs. (2.10) and (2.11) reduce to

$$\boldsymbol{E}_t = \frac{-i\mu\omega}{\mu_0 \epsilon_0 \omega^2 - k^2} [\,\hat{\boldsymbol{z}} \times \nabla_t H_z] \tag{2.14}$$

and

$$\boldsymbol{H}_t = \frac{\pm ik}{\mu_0 \epsilon_0 \omega^2 - k^2} [\nabla_t H_z]. \tag{2.15}$$

The corresponding wall boundary condition dictates that the normal component of the magnetic field vanishes at the walls. This is accomplished by setting $\hat{\boldsymbol{n}} \cdot \nabla H_z = 0$ at the walls, where at each point on the wall $\hat{\boldsymbol{n}}$ is normal to the wall's surface.

2.1.2 Modes in a Rectangular Waveguide

I now consider the specific geometry of interest and find the modes of a uniform, rectangular waveguide (see Fig. 2.2). The length in the x dimension is a, and the length in the y dimension is b. I am most interested in is a TE mode (specifically the TE_{101}); so, here I only work through the TE modes for the waveguide and simply state the results for the TM modes for completeness.

I begin by making an ansatz that the general form of the z-component of the magnetic field is given by

$$H_z(x,y,z) = \psi(x,y)e^{\pm ikz}. \tag{2.16}$$

Substituting Eq. (2.16) into Eq. (2.5) and defining $\gamma^2 \equiv \mu_0\epsilon_0\omega^2 - k^2$, I get

$$\left(\frac{\partial^2}{\partial x^2} + \frac{\partial^2}{\partial y^2} + \gamma^2\right)\psi(x,y) = 0. \tag{2.17}$$

With the assumption that $\psi(x,y) = H_0X(x)Y(y)$, where H_0 is the magnitude of the magnetic field, and the boundary condition that $\hat{\boldsymbol{n}} \cdot \nabla H_z = 0$ at the walls, Eq. (2.17) can be solved by separation of variables to give

$$\psi_{mn}(x,y) = H_0 \cos\left(\frac{m\pi x}{a}\right)\cos\left(\frac{n\pi y}{b}\right) \tag{2.18}$$

and

$$\gamma_{mn}^2 = \pi^2\left(\frac{m^2}{a^2} + \frac{n^2}{b^2}\right), \tag{2.19}$$

where m and n are integers. Putting Eq. (2.18) back into Eq. (2.16) and including the time dependence gives

$$H_z = H_0 \cos\left(\frac{m\pi x}{a}\right)\cos\left(\frac{n\pi y}{b}\right)e^{\pm ikz - i\omega t}. \tag{2.20}$$

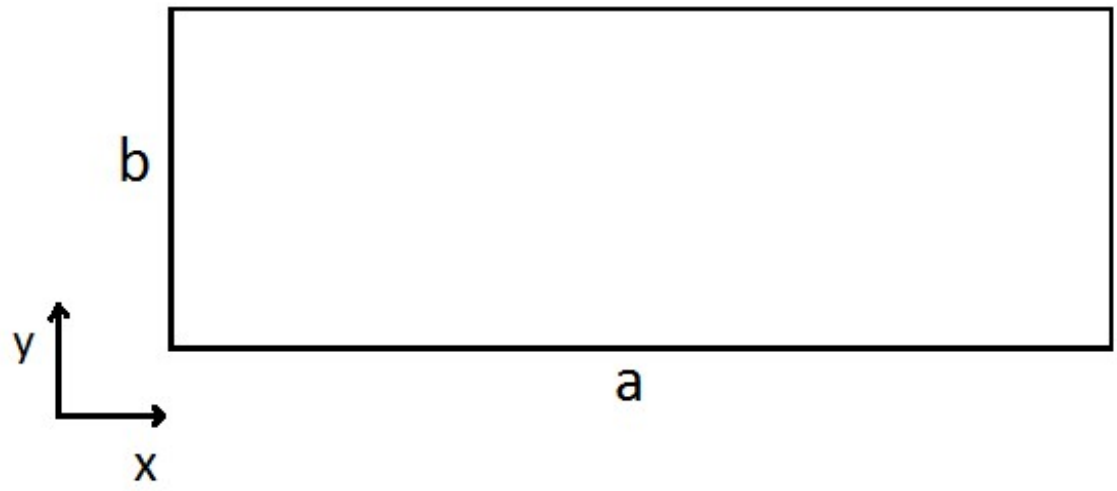

Fig. 2.2: Cross section of rectangular waveguide.

Using Eqs. (2.14) and (2.15) to solve for the transverse components of the fields then yields

$$\boldsymbol{E}_t = \frac{i\mu_0\omega H_0\pi}{\gamma^2}\left[-\frac{n}{b}\cos\left(\frac{m\pi x}{a}\right)\sin\left(\frac{n\pi y}{b}\right)\hat{\boldsymbol{x}} + \frac{m}{a}\sin\left(\frac{m\pi x}{a}\right)\cos\left(\frac{n\pi y}{b}\right)\hat{\boldsymbol{y}}\right]e^{\pm ikz - i\omega t} \tag{2.21}$$

and

$$\boldsymbol{H}_t = \frac{\mp ikH_0\pi}{\gamma^2}\left[\frac{m}{a}\sin\left(\frac{m\pi x}{a}\right)\cos\left(\frac{n\pi y}{b}\right)\hat{\boldsymbol{x}} + \frac{n}{b}\cos\left(\frac{m\pi x}{a}\right)\sin\left(\frac{n\pi y}{b}\right)\hat{\boldsymbol{y}}\right]e^{\pm ikz - i} \quad . \tag{2.22}$$

Equations (2.20), (2.21), and (2.22) specify the field components for a TE mode in a rectangular waveguide.

If, instead, I had solved for a TM mode, the solution would have begun with the z-component of the electric field

$$E_z(x,y,z) = \psi(x,y)e^{\pm ikz}. \tag{2.23}$$

In this case, Eq. (2.17), with the condition that E_z vanishes at the boundary, yields the solution

$$\psi_{mn}(x,y) = E_0 \sin\left(\frac{m\pi x}{a}\right)\sin\left(\frac{n\pi y}{b}\right) \tag{2.24}$$

and

$$\gamma_{mn}^2 = \pi^2\left(\frac{m^2}{a^2}+\frac{n^2}{b^2}\right), \tag{2.25}$$

where m and n are integers, and E_0 is the amplitude of the z-component of the electric field. Also, notice that Eqs. (2.25) and (2.19) are identical. Similarly, I find

$$E_z = E_0 \sin\left(\frac{m\pi x}{a}\right)\sin\left(\frac{n\pi y}{b}\right)e^{\pm ikz-i\omega t}, \tag{2.26}$$

and the transverse components of the fields

$$\begin{aligned}\boldsymbol{E}_t = \frac{\pm ikE_0\pi}{\gamma^2}\Big[&\frac{m}{a}\cos\left(\frac{m\pi x}{a}\right)\sin\left(\frac{n\pi y}{b}\right)\hat{\boldsymbol{x}} \\ &+\frac{n}{b}\sin\left(\frac{m\pi x}{a}\right)\cos\left(\frac{n\pi y}{b}\right)\hat{\boldsymbol{y}}\Big]e^{\pm ikz-i\omega t}\end{aligned} \tag{2.27}$$

and

$$\begin{aligned}\boldsymbol{H}_t = \frac{i\epsilon_0\omega_0E_0\pi}{\gamma^2}\Big[&\frac{n}{b}\sin\left(\frac{m\pi x}{a}\right)\cos\left(\frac{n\pi y}{b}\right)\hat{\boldsymbol{x}} \\ &-\frac{m}{a}\cos\left(\frac{m\pi x}{a}\right)\sin\left(\frac{n\pi y}{b}\right)\hat{\boldsymbol{y}}\Big]e^{\pm ikz-i\omega t}.\end{aligned} \tag{2.28}$$

Now that I have expressions for the fields of the allowed waveguide modes of this geometry, I can find the angular frequencies of the modes. Since $\gamma^2 = \mu_0\epsilon_0\omega^2 - k^2$, I can use Eq. (2.19) and solve for ω to get

$$\omega_{mn} = \frac{1}{\sqrt{\mu_0\epsilon_0}}\sqrt{\pi^2\left(\frac{m^2}{a^2}+\frac{n^2}{b^2}\right)+k^2}\,. \tag{2.29}$$

The cutoff angular frequency for a particular mode in the waveguide is defined as the angular frequency where $k = 0$, which gives

$$\omega_{mn,cutoff} = \frac{\pi}{\sqrt{\mu_0 \epsilon_0}} \sqrt{\left(\frac{m^2}{a^2} + \frac{n^2}{b^2}\right)}. \tag{2.30}$$

For $a > b$, the lowest possible angular frequency allowed in the waveguide happens when $m = 1$ and $n = 0$. This angular frequency is given by

$$\omega_{10,cutoff} = \frac{\pi}{\sqrt{\mu_0 \epsilon_0}} \frac{1}{a}. \tag{2.31}$$

For comparison, I note that Eqs. (2.26) - (2.28) imply that the components of a TM mode will all vanish if either m or n are zero. Thus, Eq. (2.31) gives the angular frequency of the lowest TE mode, which occurs when $m = n = 1$:

$$\omega_{11,cutoff} = \frac{\pi}{\sqrt{\mu_0 \epsilon_0}} \sqrt{\frac{1}{a^2} + \frac{1}{b^2}}. \tag{2.32}$$

2.1.3 Modes in a Rectangular Cavity

The results of the previous section may easily be extended to the case of a rectangular 3D cavity formed by placing conducting walls in the z dimension of the waveguide (see Fig. 2.3). I assume that the cavity has dimensions a and b in the x and y directions, respectively, and has length d in the z dimension. The boundary conditions, again, are that components of $\boldsymbol{E}$ that are tangential to the walls vanish and components of $\boldsymbol{H}$ that are normal to the walls must vanish. Whether I am considering TE or TM modes, these boundary conditions require that

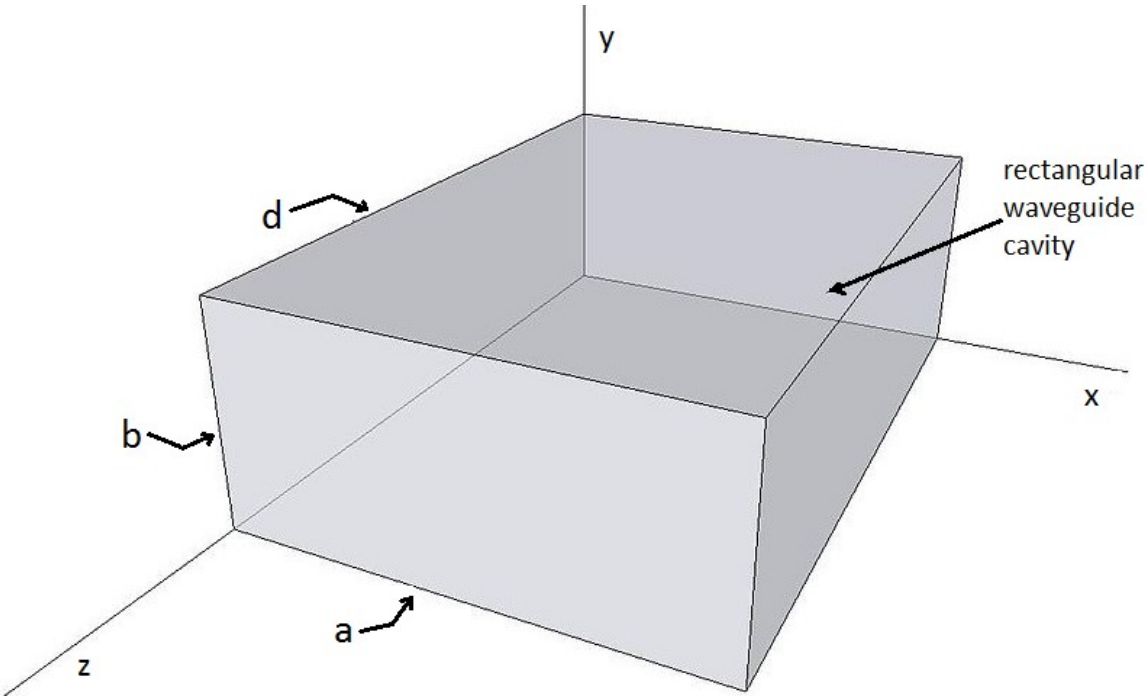

Fig. 2.3: Schematic of rectangular 3d microwave cavity, formed by taking the rectangular waveguide in Fig. 3.2 and placing conducting walls a distance d apart from each other in the z-direction.

$$k = \frac{l\pi}{d}, \tag{2.33}$$

where l is an integer. From this expression and Eq. (2.29), one finds the angular frequencies of the allowed modes in the cavity

$$\omega_{mnl} = \frac{\pi}{\sqrt{\mu_0 \epsilon_0}} \sqrt{\frac{m^2}{a^2} + \frac{n^2}{b^2} + \frac{l^2}{d^2}}, \tag{2.34}$$

or, equivalently the frequencies

$$f_{mnl} = \frac{1}{2\sqrt{\mu_0 \epsilon_0}} \sqrt{\frac{m^2}{a^2} + \frac{n^2}{b^2} + \frac{l^2}{d^2}} = \frac{c}{2} \sqrt{\frac{m^2}{a^2} + \frac{n^2}{b^2} + \frac{l^2}{d^2}}, \tag{2.35}$$

where c is the speed of light.

For the TE modes, the z-component of the $\boldsymbol{H}$ field is given by

$$H_z = H_0 \cos\left(\frac{m\pi x}{a}\right) \cos\left(\frac{n\pi y}{b}\right) \sin\left(\frac{l\pi z}{d}\right) e^{-i\omega t}. \tag{2.36}$$

The transverse components are then obtained from Eqs. (2.14) and (2.15) to give

$$\begin{aligned} \boldsymbol{E}_t = \frac{i\mu\omega H_0 \pi}{\gamma^2} \Big[& -\frac{n}{b} \cos\left(\frac{m\pi x}{a}\right) \sin\left(\frac{n\pi y}{b}\right) \hat{\boldsymbol{x}} \\ & + \frac{m}{a} \sin\left(\frac{m\pi x}{a}\right) \cos\left(\frac{n\pi y}{b}\right) \hat{\boldsymbol{y}} \Big] \sin\left(\frac{l\pi z}{d}\right) e^{-i\omega t} \end{aligned} \tag{2.37}$$

and

$$\begin{aligned} \boldsymbol{H}_t = \frac{il H_0 \pi^2}{\gamma^2 d} \Big[& \frac{m}{a} \sin\left(\frac{m\pi x}{a}\right) \cos\left(\frac{n\pi y}{b}\right) \hat{\boldsymbol{x}} \\ & + \frac{n}{b} \cos\left(\frac{m\pi x}{a}\right) \sin\left(\frac{n\pi y}{b}\right) \hat{\boldsymbol{y}} \Big] \cos\left(\frac{l\pi z}{d}\right) e^{-i\omega t}. \end{aligned} \tag{2.38}$$

In Fig. 2.4 I show two plots of the fields from the TE_{101} mode of the cavity, which I simulated using the software COMSOL Multiphysics [2]. Figure 2.4(a) shows a 3D color plot, where the color represents the magnitude of the electric field, and Fig. 2.4(b) shows a vector plot of the fields where the black arrows represent the magnetic field and the red arrows represent the electric field. Notice that in Fig. 2.4(b) the electric field only points in the y-direction and the magnetic field circulates around the perimeter. In Fig. 2.5 I show the magnitude of the electric field for a few higher modes in the cavity.

For TM modes, I find the z-component of the fields to be

$$E_z = E_0 \sin\left(\frac{m\pi x}{a}\right) \sin\left(\frac{n\pi y}{b}\right) \cos\left(\frac{l\pi z}{d}\right) e^{-i\omega t}, \tag{2.39}$$

and the transverse components are given by

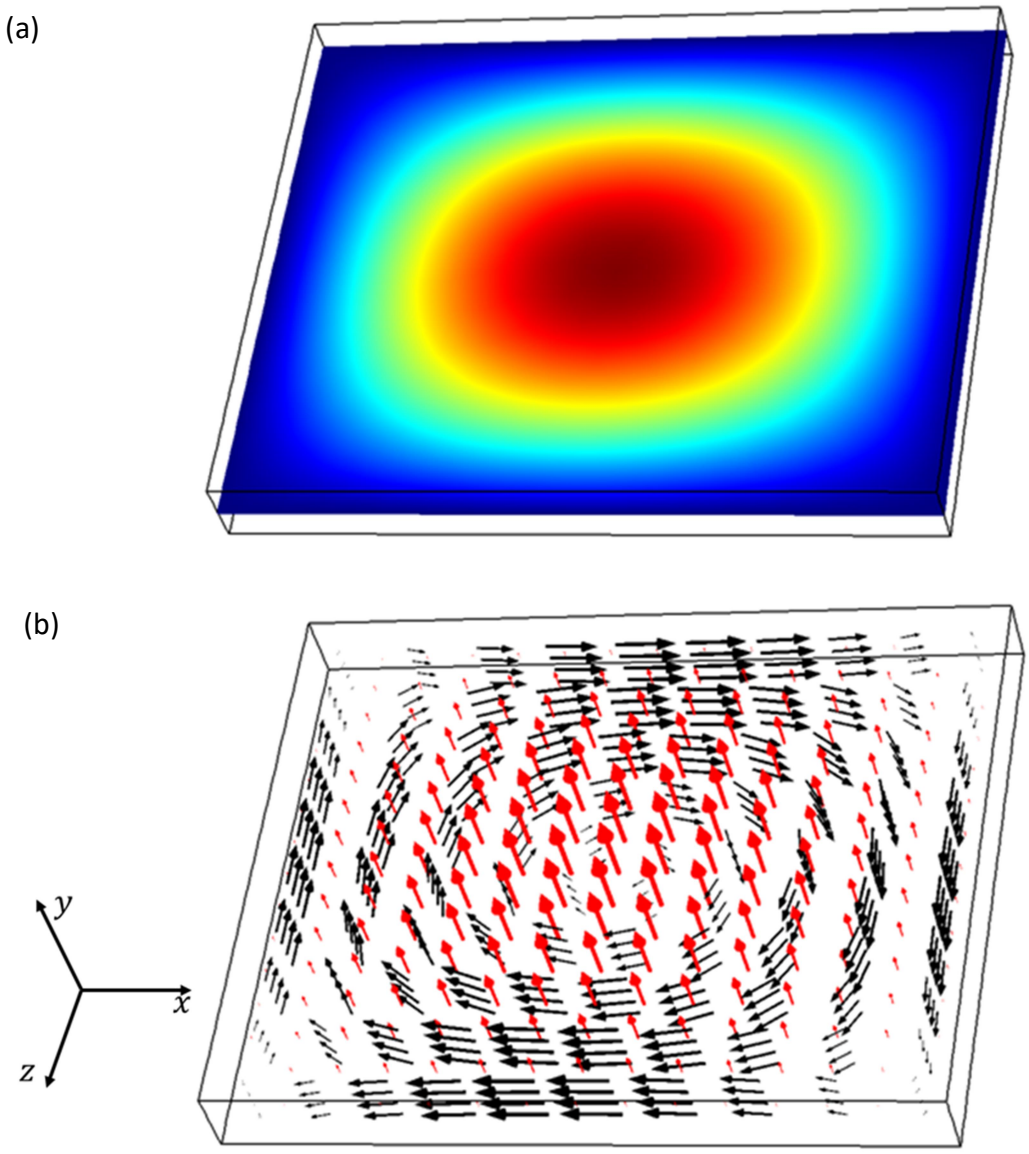

Fig. 2.4: Simulation of TE_{101} mode in microwave cavity. (a) is a color plot depicting the magnitude of the electric field for the mode. (b) is a vector plot showing the mode structure of the electric (red arrows) and magnetic (black arrows) fields.

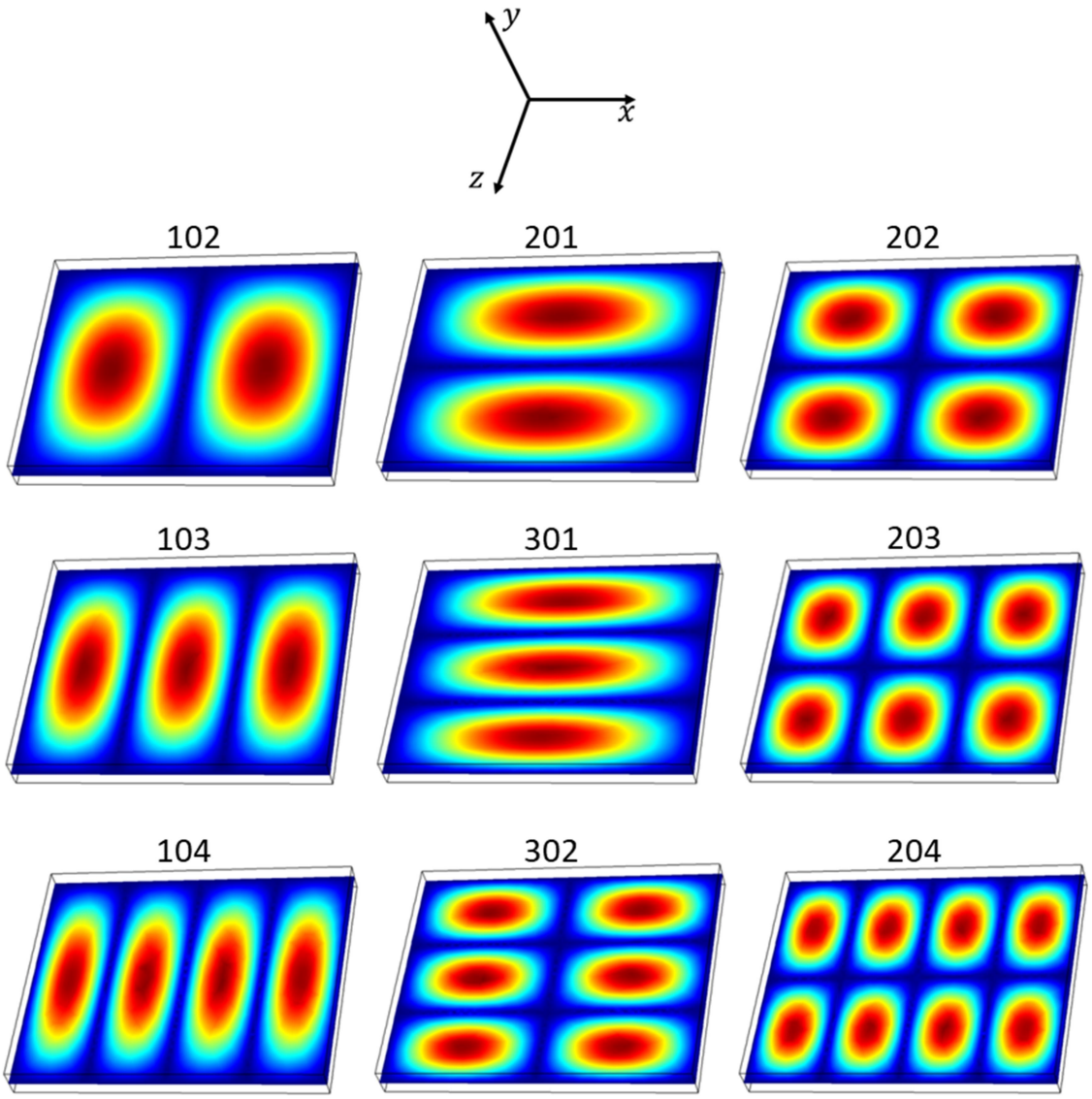

Fig. 2.5: Color plot showing the electric field magnitude for higher order modes in the cavity. Starting at the upper left, the modes shown are: TE_{102}, TE_{201}, TE_{202}, TE_{103}, TE_{301}, TE_{203}, TE_{104}, TE_{302}, and TE_{204}. The frequencies for these modes are listed below in Table 2.1.

$$\boldsymbol{E}_t = \frac{ilE_0\pi^2}{\gamma^2 d}\left[\frac{m}{a}\cos\left(\frac{m\pi x}{a}\right)\sin\left(\frac{n\pi y}{b}\right)\hat{\boldsymbol{x}} + \frac{n}{b}\sin\left(\frac{n\pi x}{a}\right)\cos\left(\frac{n\pi y}{b}\right)\hat{\boldsymbol{y}}\right]\sin\left(\frac{l\pi z}{d}\right)e^{-i\omega t} \tag{2.40}$$

and

$$\boldsymbol{H}_t = \frac{i\epsilon\omega E_0\pi}{\gamma^2}\left[\frac{n}{b}\sin\left(\frac{m\pi x}{a}\right)\cos\left(\frac{n\pi y}{b}\right)\hat{\boldsymbol{x}} - \frac{m}{a}\cos\left(\frac{m\pi x}{a}\right)\sin\left(\frac{n\pi y}{b}\right)\hat{\boldsymbol{y}}\right]\cos\left(\frac{l\pi z}{d}\right)e^{-i\omega t}. \tag{2.41}$$

It is instructive to calculate the expected frequencies of the modes in my 3D cavity. Cavities SI-2a, SI-2b, SI3, and SI-4 have dimensions a= 3.81 cm, b= 0.4 cm, and d= 3.048 cm. Since I operate these cavities only in air or vacuum, the relative permeability and permittivity are $\varepsilon_r = \mu_r = 1$. Table 2.1 shows the frequencies of the four lowest TE modes and the two lowest TM modes, all calculated using Eq. (2.34).

Table 2.1: Frequencies of the lowest ten TE modes and the lowest two TM modes of a microwave cavity with dimensions a= 3.048 cm, b= 0.4 cm, and d= 3.81 cm. These dimensions were used in cavities SI-2a, SI-2b, SI-3, and SI-4.

Mode type	m	n	l	f_{mnl} (GHz)
TE	1	0	1	6.30
TE	1	0	2	9.28
TE	2	0	1	10.6
TE	2	0	2	12.6
TE	1	0	3	12.8
TE	3	0	1	15.3
TE	2	0	3	15.4
TE	1	0	4	16.5
TE	3	0	2	16.7
TE	2	0	4	18.6
TM	1	1	0	37.68
TM	0	1	1	37.80

The mode I am interested in is the TE_{101} mode, which has a frequency of 6.298 GHz. The nearest mode frequency to this mode is the TE_{102} mode, which has a frequency of 9.279 GHz. In order to reduce coupling to higher modes, I designed my qubits and resonators to be at a frequency lower than the TE_{101} mode; typically, at least 1 GHz lower. I also note that the lowest TM mode occurs at 37.68 GHz. This is so high that I could safely ignore all TM modes.

I note that the frequencies mentioned in Table 2.1 are for a completely empty cavity. However, my devices were fabricated on a sapphire substrate, which has a relative permeability of $\mu_r = 1$ but a relative permittivity of $\epsilon_r \cong 10$. This causes the resonance frequency to be reduced relative to the empty cavity mode frequency. Since the volume of the sapphire chip was small relative to the cavity volume, perturbation theory may be used to extract the shift in frequency that we can expect. From Pozar [3], this frequency shift is approximately

$$\Delta f_{mnl} \cong -\frac{1}{2} f_{mnl}(\epsilon_r - 1)\frac{V_{chip}}{V_{cav}}, \tag{2.42}$$

where V_{chi} is the volume of the sapphire chip and V_{cav} is the cavity volume. The typical volume of my chips was 11.43 mm^3 and, for the cavities mentioned above, the volume was about 4,650 mm^3. For the TE_{101} mode (6.298 GHz), I find $\Delta f_{101} \cong -70\ MHz$.

2.2 3D Cavity Design

The main design consideration for the 3d cavity is what frequency I wanted the TE_{101} mode, which, again, is the lowest mode. Since quite a few of the microwave components I used in my experiments have a bandwidth of 4-8 GHz, I chose a frequency of $f_c \approx 6$ GHz.

I machined the cavity in two halves so that devices could be mounted inside the cavity at the center. Since the end mill I used to machine the cavity only had a 2.54 cm cut length and it is not good to overwhelm the bit, I chose to make each half of the cavity 1.524 cm in height, which corresponds to a full cavity height of 3.048 cm. For the width of the cavity, I chose 3.810 cm. Using Eq. (2.35), these dimensions give an expected TE_{101} frequency of f_c= 6.3 GHz. The depth of the cavity has no effect on the TE_{101} mode; so, I chose 4 mm in order to easily accommodate my 5 mm x 5 mm sapphire chips. In Fig. 2.6 I show a photograph of cavity SI-2b and a picture of one of the cavities being machined.

The cavities I machined for my experiments are named SI-2a, SI-2b, SI-3, and SI-4. All of these cavities were machined from Al-6063 alloy, which was chosen because this particular alloy has very few magnetic impurities. The cavities SI-2a and 2b are identical cavities with the exception that SI-2b has an off-center chip mounting shelf and a slot to pass in a flux tuning coil (see Chapter 3). Cavity SI-3 was designed to hold a chip fully off to the side of the cavity space and to have a slot for the aforementioned flux tuning coils. Finally, cavity SI-4 was designed to accommodate a tunable chip in the center of the cavity space.

In Fig. 2.7 I show photographs of the inside of both halves of cavity SI-2b showing how samples were mounted for my experiments. Since my chips were all 5 mm by 5 mm, I machined a small shelf that was slightly larger than this. One of these shelves may be seen in the very center of the cavity space on the left half of the cavity in Fig. 2.7(a). Also, since the corners of my chip are square and end mills are round, I machined

(a)

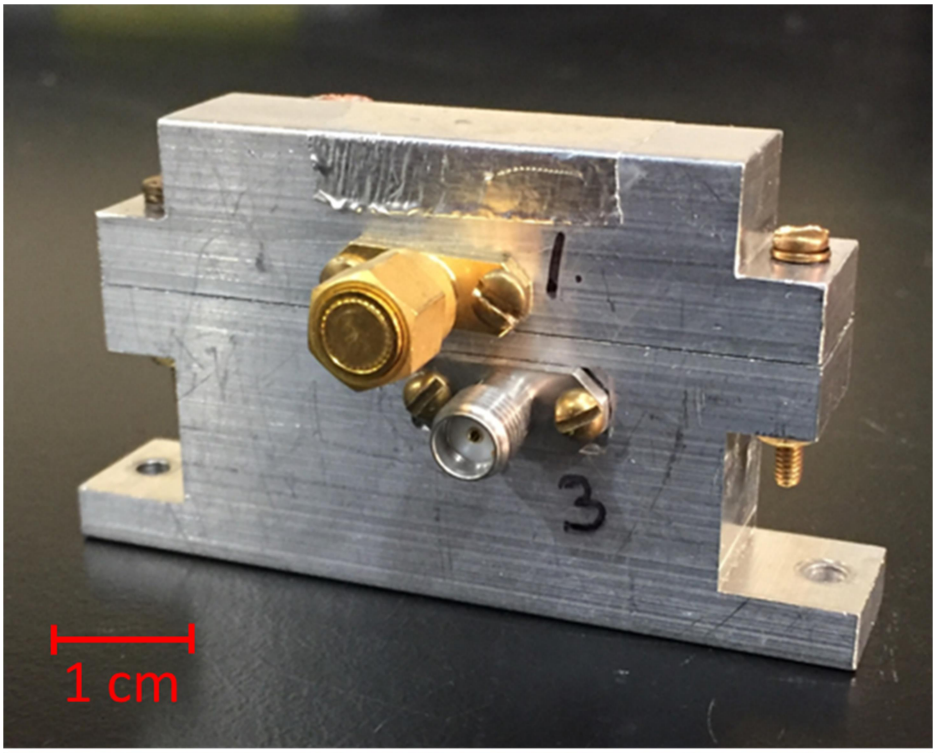

(b)

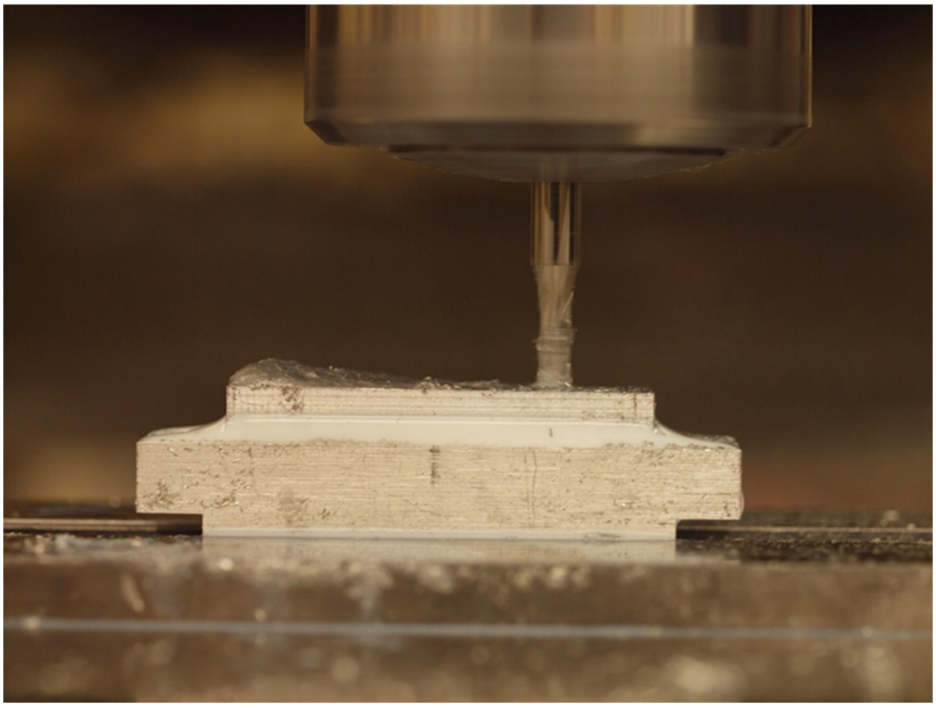

Fig. 2.6: (a) Photo of cavity SI-2b shown with microwave SMA connectors attached. (b) Photo showing this cavity being machined.

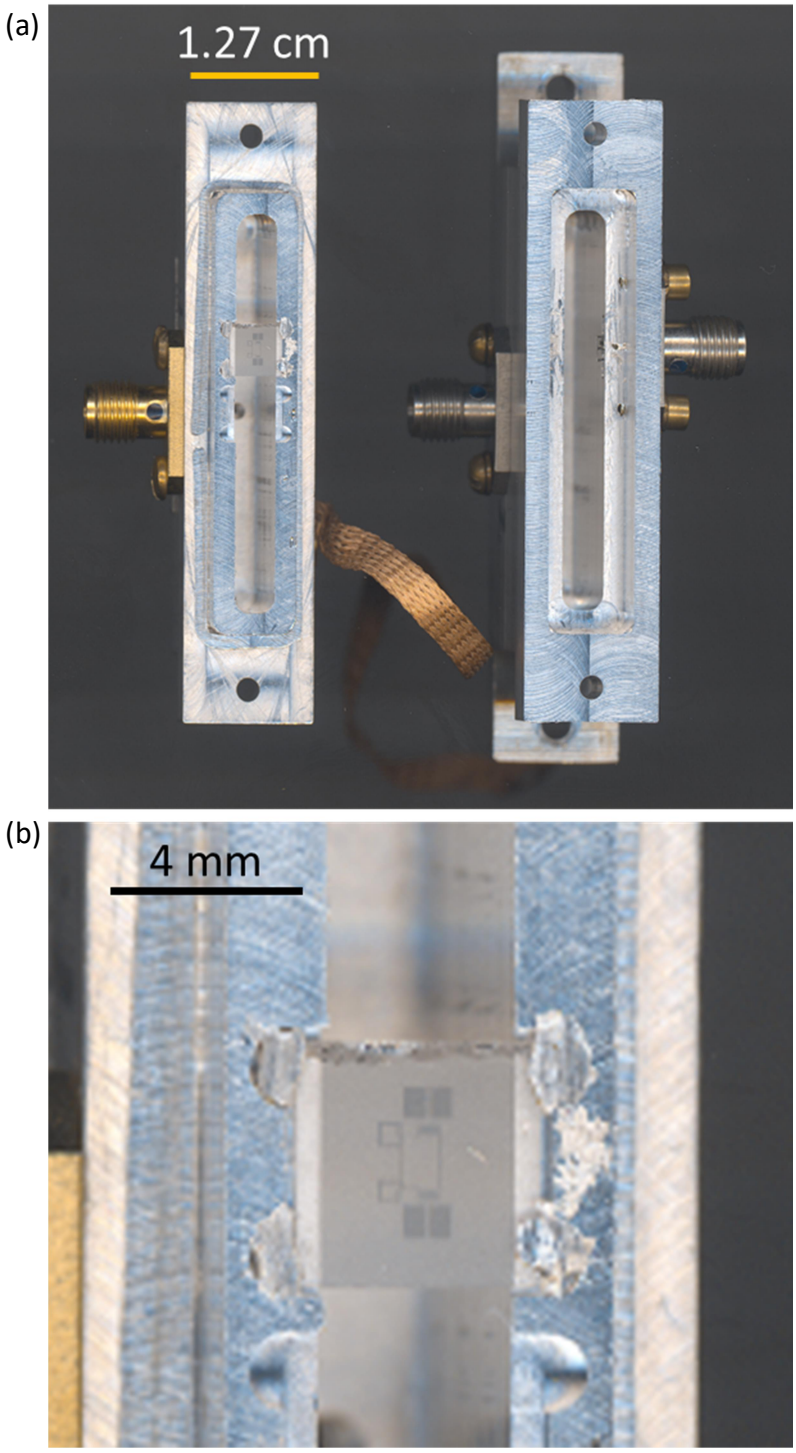

Fig. 2.7: (a) Photo showing inside both halves of cavity SI-2b. (b) Photo showing a sapphire chip mounted in cavity SI-2b using indium at the corners.

out the corners to provide extra room for mounting. To hold the chip, I placed small pieces of indium at the corners and smashed them down using the other cavity half. This method held the chips quite well. The main issue in this mounting method is that the extra space around the chip to allowed for the indium expansion sometimes led to the chip not being mounted as straight as needed to properly bias the resonator tuning loops with flux. This just meant that I had to be careful when mounting and check the positioning after pressing the indium.

Once the chip is mounted and all the SMA connectors are attached (using short 2-56 brass bolts and bronze, split-ring locking washers), the cavity halves are held together using long 2-56 brass bolts and nuts. The holes for these bolts may be seen in Fig. 2.7(a) at the outer ends of the cavity space. This particular design (specifically SI-2b) only used two bolts to hold the cavity halves together, but for later designs SI-3 and SI-4 I used four, one at each corner.

2.3 3D Cavity Results

Once I had a completed cavity, I cleaned it in Acetone and measured its properties at room temperature. To take this data I used a Keysight E5071C Vector Network Analyzer (VNA). I connected port 1 of the VNA to the input port of the cavity and port 2 of the VNA to the output port,

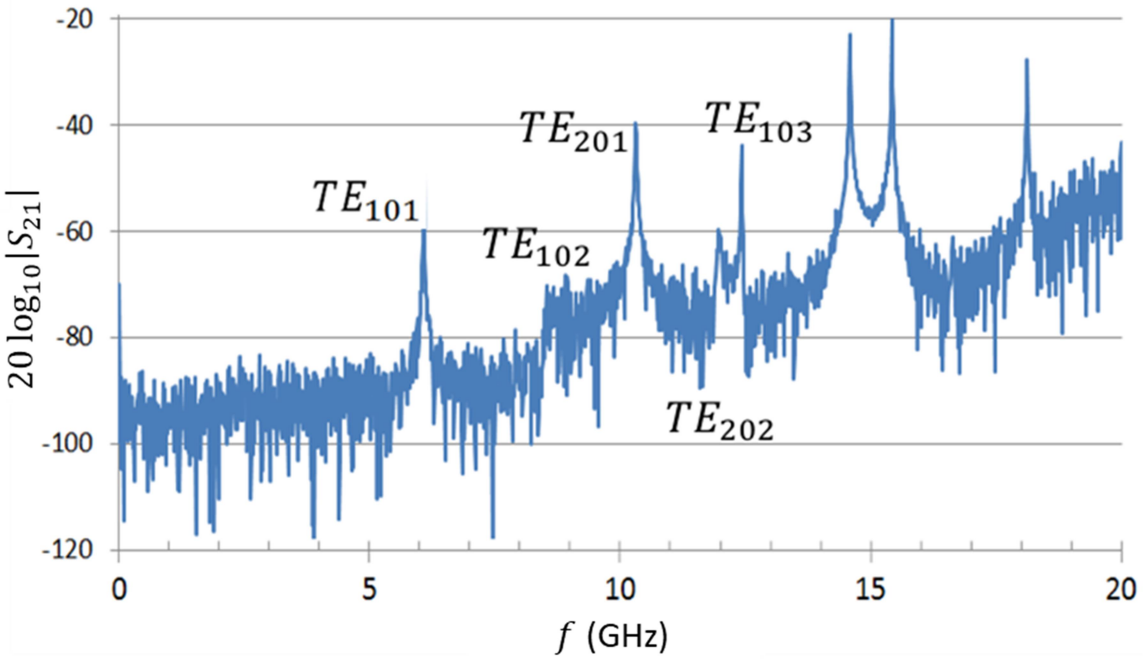

Fig. 2.8: $20\log_{10}|S_{21}|$ vs. Frequency data on cavity SI-2b measured by the Keysight E5071C VNA. I have labelled the first 5 mode frequencies.

and I then had the VNA sweep the frequency and measure the scattering parameter $|S_{21}|^2$. Shown in Fig. 2.8 is a plot of $20\log_{10}|S_{21}|$ vs. frequency on my cavity SI-2a. As seen in the plot there are quite a few mode resonances. I have labeled the first 5 modes seen in the data. The TE_{101} mode is just above 6 GHz, the TE_{102} is just below 9 GHz, the TE_{201} is around 10.5 GHz, the TE_{202} mode is at 12 GHz, and the TE_{103} is approximately 12.6 GHz. This corresponds very well to the expected values shown in Table 2.1. The only discrepancies observed show up at the higher frequency modes. I believe this is due to my cavities not being perfectly square. Since I used an end mill that has a diameter of 0.125 in, there was an appreciable amount of curvature at the corners. At higher frequencies this becomes important because more field is at those rounded edges.

I also note the observed suppression of the 102 and 202 modes. These modes appear so much smaller compared to the others due to the placement of the input and output connector pins. I chose to place them directly in the center of the cavity in the z-dimension. This places them directly on nodes in the electric field when the third index is even, which means that they do not interact very strongly with those modes. I chose this to limit the coupling of my pins to the next highest mode in the cavity. My idea was that this would limit, as much as possible, device loss through coupling to photons in that mode.

2.4 Effective Inductance and Capacitance of Cavity Modes

In this section I derive expressions for the effective inductance and capacitance of individual cavity modes. This gives some insight into modeling the cavity as a lumped element resonator. However, one must be careful in integrating the results, as I discuss below. The discussion below follows Condon [4]; although, I use SI units.

2.4.1 Scalar and Vector Potential

As described in ref. [4], it is useful to analyze the problem using scalar and vector potentials. Since the divergence of the magnetic field is zero, I can express the magnetic field as the curl of a vector potential $\boldsymbol{A}$:

$$\boldsymbol{H} = \nabla \times \boldsymbol{A}. \tag{2.43}$$

By inserting Eq. (2.43) into Maxwell's equations (specifically, $\nabla \times \boldsymbol{E} = -\mu_0 \frac{\partial \boldsymbol{H}}{\partial t}$), rearranging, and commuting the curl operator with the time derivative, I get

$$\nabla \times \left(\boldsymbol{E} + \mu \frac{\partial \boldsymbol{A}}{\partial t} \right) = 0. \tag{2.44}$$

Since the curl of $\boldsymbol{E} + \frac{\partial \boldsymbol{A}}{\partial t}$ is zero, it may be written as the negative gradient of a scalar potential φ, which yields

$$\boldsymbol{E} = -\mu \frac{\partial \boldsymbol{A}}{\partial t} - \nabla \varphi. \tag{2.45}$$

Equations (2.43) and (2.45) are well-known relations that show how the electric and magnetic fields may be written in terms of vector and scalar potentials.

The next step is to find the wave equation in terms of these potentials. As detailed in Appendix A.3, inserting Eqs. (2.43) and (2.45) into Maxwell's equations yields

$$-\nabla^2 \boldsymbol{A} + \mu_0 \epsilon_0 \frac{\partial^2 \boldsymbol{A}}{\partial t^2} + \nabla \left(\nabla \cdot \mathbf{A} + \epsilon_0 \frac{\partial \varphi}{\partial \mathrm{t}} \right) = \boldsymbol{J} \tag{2.46}$$

and

$$-\nabla^2 \varphi + \mu_0 \epsilon_0 \frac{\partial^2 \varphi}{\partial t^2} - \frac{\partial}{\partial \mathrm{t}} \left(\nabla \cdot \mathbf{A} + \epsilon_0 \frac{\partial \varphi}{\partial \mathrm{t}} \right) = \frac{\rho}{\epsilon_0}. \tag{2.47}$$

By choosing the gauge $\nabla \cdot \mathbf{A} = -\epsilon_0 \frac{\partial \varphi}{\partial \mathrm{t}}$, I obtain

$$-\nabla^2 \boldsymbol{A} + \mu_0 \epsilon_0 \frac{\partial^2 \boldsymbol{A}}{\partial t^2} = \boldsymbol{J} \tag{2.48}$$

and

$$-\nabla^2 \varphi + \mu_0 \epsilon_0 \frac{\partial^2 \varphi}{\partial t^2} = \frac{\rho}{\epsilon_0}. \tag{2.49}$$

I next assume that there are no currents or charge in the system, and set $\varphi = 0$ everywhere because $\rho = 0$. Thus, I arrive at a wave equation for the vector potential

$$\nabla^2 \boldsymbol{A} + \mu_0 \epsilon_0 \omega^2 \boldsymbol{A} = 0 \tag{2.50}$$

with the added bonus that

$$\nabla \cdot \boldsymbol{A} = 0. \tag{2.51}$$

Note that I have again put in a time dependence of $e^{-i\omega t}$. From the definition of $\boldsymbol{A}$, the components of $\boldsymbol{A}$ must vanish at the walls or must be perfectly normal to the walls, depending on which mode being considered. Equations (2.50) and (2.51) along with this boundary condition, are equivalent to the problem I solved in section 2.1.3.

2.4.2 Eigenfunction Representation of Excitation

From Section 2.1, I know the eigenvalues κ_1^2, κ_2^2, κ_3^2, *etc*., corresponding to eigenfunctions $\boldsymbol{A}_1$, $\boldsymbol{A}_2$, $\boldsymbol{A}_3$, *etc*. Using Eq. (2.50), it is simple to show that the eigenvalues for a particular mode are identical to those obtained by simply solving Eq. (2.6) for the fields themselves. As an example, for the rectangular cavity the eigenvalues are given by Eq. (2.34), which yields

$$\kappa_a^2 = \mu_0 \epsilon_0 \omega_{mnl}^2 = \pi^2 \left(\frac{m^2}{a^2} + \frac{n^2}{b^2} + \frac{l^2}{d^2} \right). \tag{2.52}$$

The next step in this derivation involves an orthogonality condition I will need for a Sturm-Liouville analysis. As shown in Appendix A.4, by integrating the expression

$$\boldsymbol{A}_b^* \cdot \left(\nabla \times (\nabla \times \boldsymbol{A}_a) \right) - \boldsymbol{A}_a \cdot \left(\nabla \times (\nabla \times \boldsymbol{A}_b^*) \right) \tag{2.53}$$

one can show that the eigenfunctions of different modes are orthogonal. Since I am free to choose the normalization of these orthogonal functions, I can set

$$\int\int\int \boldsymbol{A}_a \cdot \boldsymbol{A}_b^* dV = \begin{cases} 0 & \text{for } a \neq b \\ V & \text{for } a = b, \end{cases} \tag{2.54}$$

where V is the total volume of the cavity. I note that this orthogonality condition yields eigenfunctions that are dimensionless.

The general solution $\boldsymbol{A}$ for the vector potential in the cavity for any excitation is then given by a linear combination of these eigenfunctions

$$\boldsymbol{A} = \sum_a \zeta_a(t)\boldsymbol{A}_a(x,y,z), \tag{2.55}$$

where the coefficient $\zeta_a(t)$ for each mode a is the time-dependent amplitude of the mode excitation. Since the eigenfunctions $\boldsymbol{A}_a$ are dimensionless but $\boldsymbol{A}$ is the fully dimensional vector potential these coefficients have units of the magnetic vector potential, which happens to be amps (A).

2.4.3 Energy Integral

In this section I use Eq. (2.55) to derive an effective inductance for the cavity modes. The energy stored in the magnetic field can be written as

$$W_{mag} = \frac{\mu_0}{2}\int\int\int (\boldsymbol{H}\cdot\boldsymbol{H}^*)dV. \tag{2.56}$$

Using Eqs. (2.42) and (2.54), this may be rewritten as

$$W_{mag} = \frac{\mu_0}{2}\int\int\int \left(\nabla\times\sum_a \zeta_a(t)\boldsymbol{A}_a\right)\cdot\left(\nabla\times\sum_b \zeta_b^*(t)\boldsymbol{A}_b^*\right)dV. \tag{2.57}$$

Transposing the sums with both the integrals and derivatives, which I am free to do since both operations are linear, simplifies the expression to

$$W_{mag} = \frac{\mu_0}{2}\sum_a\sum_b \zeta_a(t)\zeta_b^*(t)\int\int\int (\nabla\times\boldsymbol{A}_a)\cdot(\nabla\times\boldsymbol{A}_b^*)dV. \tag{2.58}$$

As shown in Appendix A.5, this integral reduces to

$$\int\int\int (\nabla\times\boldsymbol{A}_a)\cdot(\nabla\times\boldsymbol{A}_b^*)dV = \kappa_a^2 V\delta_{ab}. \tag{2.59}$$

Substituting into Eq. (2.58) collapses one of the sums, which gives

$$W_{mag} = \frac{V\mu}{2}\sum_a \kappa_a^2 |\zeta_a|^2. \tag{2.60}$$

As described earlier, this sum is over all the possible cavity modes. Hence, for a particular mode, say the p^{th} mode, the energy stored in the magnetic field is

$$\frac{1}{2}V\mu_0\kappa_p^2\left|\zeta_p\right|^2. \tag{2.61}$$

Comparing this expression to the energy stored in an inductor ($\frac{1}{2}LI^2$), it is easy to see that this fits the general form for an inductance $L = V\mu_0\kappa_p^2$ and a current squared with $I = \left|\zeta_p\right|$. However, it remains to be seen what this current corresponds to.

To find an expression for $\left|\zeta_p\right|$ in a special case, I will consider again my rectangular cavity, and, specifically, I will restrict myself to modes of the form TE_{m0l}. This is the only mode type until 37.68 GHz and will insure that I only have a $\hat{y}$ component in the electric field. Using Eq. (2.45), for a particular mode I have

$$\boldsymbol{E}_{m0l}(\boldsymbol{r}) = -\mu_0\frac{\partial\zeta_{m0l}(t)}{\partial t}\boldsymbol{A}_{m0l}(\boldsymbol{r}) = i\omega\mu_0\zeta_{m0l}(t)\boldsymbol{A}_{m0l}(\boldsymbol{r}), \tag{2.62}$$

where I have used the fact that the only time dependence is from $e^{-i\omega t}$. From Eq. (2.37), I have

$$\boldsymbol{E}_{m0l}(\boldsymbol{r}) = i\omega\mu_0\frac{H_0\pi m}{\gamma_{m0}^2 a}e^{-i\omega t}\sin\left(\frac{m\pi x}{a}\right)\sin\left(\frac{l\pi z}{d}\right)\hat{y}\ . \tag{2.63}$$

Comparing Eqs. (2.62) and (2.63) I get expressions for $\zeta_{m0l}(t)$ and $\boldsymbol{A}_{m0l}(\boldsymbol{r})$ given by

$$\zeta_{m0l}(t) = \frac{H_0\pi m}{\gamma_{m0}^2 aN}e^{-i\omega t} \tag{2.64}$$

and

$$\boldsymbol{A}_{m0l}(\boldsymbol{r}) = N\sin\left(\frac{m\pi x}{a}\right)\sin\left(\frac{l\pi z}{d}\right)\hat{y}\ , \tag{2.65}$$

where I have included a normalization factor N to insure the condition in Eq. (2.54).

To find this normalization factor, taking the integral in Eq. (2.54) yields

$$\int\int\int \boldsymbol{A}_{m0l} \cdot \boldsymbol{A}^*_{m0l} dV = \frac{N^2 V}{4} \ . \tag{2.66}$$

Setting Eq. (2.66) equal to the volume V of the cavity gives $N = 2$. So, Eqs. (2.64) and (2.65) are then

$$\zeta_{m0l}(t) = \frac{H_0 \pi m}{2\gamma_{m0}^2 a} e^{-i\omega t} \tag{2.67}$$

and

$$\boldsymbol{A}_{m0l}(\boldsymbol{r}) = 2 \sin\left(\frac{m\pi x}{a}\right) \sin\left(\frac{l\pi z}{d}\right) \hat{y} \ . \tag{2.68}$$

Finally, from Eq. (2.67) I get

$$|\zeta_{m0l}| = \sqrt{\zeta^*_{m0l}(t)\zeta_{m0l}(t)} = \frac{H_0 \pi m}{2\gamma_{m0}^2 a} = \frac{H_0 a}{2}, \tag{2.69}$$

where I have used Eq. (2.19) for γ_{m0}^2. So, for this specific example, this current is simply half the amplitude of the z-component of the magnetic field times a.

2.4.3.1 Condon Defined Current

Going back to Eq. (2.61), by following Condon and using $|\zeta_p|$ as the current, I have that the inductance of this particular mode is given by

$$L_p = V\mu_0\kappa_p^2 = 4\pi^2 V \mu_0^2 \epsilon_0 f_p^2 \ . \tag{2.70}$$

where I have used the dispersion relation $\kappa_m^2 = \mu_0\epsilon_0\omega_m^2 = 4\pi^2\mu_0\epsilon_0 f_m^2$. Since the frequency of a simple LC resonator is

$$f_p = \frac{1}{2\pi\sqrt{L_p C_p}} \ . \tag{2.71}$$

Solving (2.71) for C_m yields

$$C_p = \frac{\epsilon}{V\kappa_p^4} = \frac{1}{16\pi^4 V\mu_0^2\epsilon_0 f_p^4}. \tag{2.72}$$

Equations (2.70) and (2.72) represent the effective inductance and capacitance of any particular cavity mode. Also, these expressions match those found in Dicke [5], which were derived by using a Lagrangian approach to the cavity modes. Finally, I can also define an effective impedance. Again, assuming the mode acts like a simple LC circuit, I can define

$$Z_p = \sqrt{\frac{L_p}{C_p}} = 8\pi^3 V\mu_0^2\epsilon_0 f_p^3 \ . \tag{2.73}$$

I note that this analysis was done for an arbitrary cavity shape, and is valid if one knows the volume of the cavity and the frequency of the mode being considered.

Care must be used in interpreting these expressions. In particular, Eq. (2.73) presents an effective mode impedance that is not dependent on the position in the cavity. However, these effective L and C parameters do not correspond to the position-dependent effective circuit parameters that the cavity presents to a device such as a transmon qubit (see Chapter 4). Instead, this can be obtained by taking the ratio of the electric field to the magnetic field at the transmon's position [1].

2.4.3.2 Displacement Current Magnitude

Instead of just using $|\zeta_p|$ as the current, it is interesting to check what these parameters would be if I used the magnitude of the displacement current $|I_d|$ from Ampere's law. This is analogous to W. W. Hansen's method of finding the effective

mode inductance and capacitance [6]. Since, I am considering a system with no free currents (*i.e.* $\boldsymbol{J} = 0$), I have that the displacement current density is given by

$$\boldsymbol{J}_d = -\varepsilon_0 \frac{\partial \boldsymbol{E}}{\partial t} \tag{2.74}$$

or, equivalently

$$\boldsymbol{J}_d = \nabla \times \boldsymbol{H} \,. \tag{2.75}$$

By inserting Eq. (2.75) and using A1.11, I get

$$\boldsymbol{J}_d = \nabla \times (\nabla \times \boldsymbol{A}) = -\nabla^2 \boldsymbol{A} \;, \tag{2.76}$$

where I have used Eq. (2.51) to remove the divergence of $\boldsymbol{A}$. Inserting Eq. (2.55) into this expression yields

$$\boldsymbol{J}_d = \sum_a \kappa_a^2 \zeta_a(t) \boldsymbol{A}_a \,, \tag{2.77}$$

where I have operated the Laplacian operator on the eigenfunctions (i.e. $\nabla^2 \boldsymbol{A}_a = -\kappa_a^2$). So, for a particular mode p this gives

$$\boldsymbol{J}_{d,p} = \kappa_p^2 \zeta_p(t) \boldsymbol{A}_p \,. \tag{2.78}$$

Since, I am actually looking for $|\zeta_p|$, taking the norm of Eq. (2.78) yields

$$|J_{d,p}|\hat{e} = \sqrt{J_{d,p}^* J_{d,p}}\hat{e} = \kappa_p^2 \sqrt{\zeta_p^*(t)\zeta_p(t)} \sqrt{A_p^* A_p}\hat{e} = \kappa_p^2 |\zeta_p(t)||A_p|\hat{e} \,. \tag{2.79}$$

To find the displacement current for a particular mode, all that is left is to integrate Eq. (2.79). However, the questions remain of what area to integrate over and what the functional form of $\boldsymbol{A}_p$ is. To find these, a specific cavity and mode type must be chosen.

Returning to the example of a rectangular cavity with modes of the form TE_{m0l}, which means that $\boldsymbol{A}_{m0l}$ only has a $\hat{y}$ component by Eq. (2.68), I need simply to integrate over the x-z plane

$$\left|I_{d,m0l}\right| = \kappa_{m0l}^2 |\zeta_{m0l}| \iint \sqrt{A_{m0l}^* A_{m0l}}\, dxdz\,, \tag{2.80}$$

which goes to

$$\left|I_{d,m0l}\right| = 2\kappa_{m0l}^2 |\zeta_{m0l}| \int_0^a \left|\sin\left(\frac{m\pi x}{a}\right)\right| dx \int_0^d \left|\sin\left(\frac{l\pi z}{d}\right)\right| dz\,. \tag{2.81}$$

For the first integral in Eq. (2.81), for whatever integer m I have, I know that after the range $x = 0$ to $x = a/m$, the integrand repeats itself for a total of m iterations. So, the first integral in Eq. (2.81) then becomes

$$\int_0^a \left|\sin\left(\frac{m\pi x}{a}\right)\right| dx = m \int_0^{a/m} \sin\left(\frac{m\pi x}{a}\right) dx = \frac{2a}{\pi}\,. \tag{2.82}$$

Repeating this for the second integral and putting the results into Eq. (2.81) yields

Table 2.2: Summary of the inductance, capacitance, and impedance results using the two definitions of currents. Note that the results for the displacement current were found for the specific choice of a rectangular cavity with modes of the form TE_{m0l}, while the Condon results are for an arbitrary cavity and mode choice.

Description	Current	Inductance	Capacitance	Impedance
Condon	$\left\|\zeta_p\right\|$	$4\pi^2 V\mu^2\epsilon f_p^2$	$\frac{1}{16\pi^4 V\mu^2\epsilon f_p^4}$	$8\pi^3 V\mu^2\epsilon f_p^3$
Displacement	$\left\|I_{d,m0l}\right\|$	$\frac{b}{ad}\frac{\pi^2}{256\epsilon f_{m0l}^2}$	$\frac{64}{\pi^4}\frac{ad}{b}\epsilon$	$\frac{b}{ad}\frac{\pi^3}{128\epsilon f_{m0l}}$

$$\left|I_{d,m0l}\right| = 8\kappa_{m0l}^2 |\zeta_{m0l}| \frac{ad}{\pi^2} \ . \tag{2.83}$$

Substituting this into Eq. (2.61) gives

$$\frac{1}{2}\left[\frac{b}{ad}\frac{\pi^4\mu_0}{64k_{m0l}^2}\right]\left|I_{d,m0l}\right|^2 = \frac{1}{2}\left[\frac{b}{ad}\frac{\pi^2}{256\epsilon_0 f_{m0l}^2}\right]\left|I_{d,m0l}\right|^2. \tag{2.84}$$

Comparing Eq. (2.84) to $\frac{1}{2}LI^2$ with the current now given by $I = \left|I_{d,m0l}\right|$ gives the inductance of the particular $m0l$ mode

$$L_{d,m0l} = \frac{b}{ad}\frac{\pi^2}{256\epsilon_0 f_{m0l}^2}. \tag{2.85}$$

From $f = 1/2\pi\sqrt{LC}$, I can find the mode capacitance

$$C_{d,m0l} = \frac{64}{\pi^4}\frac{ad}{b}\epsilon_0. \tag{2.86}$$

Table 2.3: Values for the inductance, capacitance, and impedance from Table 2.2 for the first few modes of my cavities SI-2a, SI-2b, SI-3, and SI-4. Again, the dimensions of this cavity are a= 3.048 cm, b= 0.4 cm, and d= 3.81 cm.

Mode index			Condon Expressions			Displacement Current Expressions		
m	n	l	L (nH)	C (fF)	Z (kΩ)	L (pH)	C (pF)	Z (Ω)
1	0	1	102	6.28	4.02	378	1.69	15.0
1	0	2	221	1.33	12.9	174	1.69	10.2
2	0	1	288	0.78	19.2	134	1.69	8.90
2	0	2	407	0.39	32.2	94.5	1.69	7.48
1	0	3	419	0.37	33.7	91.7	1.69	7.37
3	0	1	598	0.18	57.4	64.3	1.69	6.17

I note that Eq. (2.86) is interesting in that it has the form of a parallel plate capacitor ($C = \frac{A}{d}\epsilon_0$). The area of the cavity face is given by ad, the height by b; however, there is a prefactor of $64/\pi^4$. In this view, the cavity faces are acting like a parallel plate capacitor with a scaling factor due to the conducting walls at the sides. The impedance is then given by

$$Z_{d,m0l} = \sqrt{\frac{L_{d,m0l}}{C_{d,m0l}}} = \frac{b}{ad}\frac{\pi^3}{128\epsilon f_{m0l}} \tag{2.87}$$

I note that, while in section 2.2.3.1 I left the cavity and choice of modes arbitrary, in this section I chose a rectangular cavity with modes of the form TE_{m0l}. So, Eqs. (2.85)-(2.87) should only be applied in this particular case. However, in this case the impedance presented in Eq. (2.87) is no longer dependent on one's position in the cavity space.

In Table 2.2 I summarize the results of this section. One interesting thing in comparing these two views of current is the fact that the mode impedances have a very different frequency dependence. When using the Condon definition of current, the impedance increases with a f_p^3 dependence. On the other hand, when using the displacement current magnitude, the impedance decreases with a $1/f_p$ dependence. In Table 2.3 I give the values of these expressions for the first six modes of my cavities.

More importantly, neither of these effective mode impedances, inductances, or capacitors, are those which would be experienced by a transmon placed in the cavity. The underlying reason for this discrepancy is the assumption that there is a single impedance for a cavity mode, where in fact the impedance will vary depending on the

location in the cavity. A more accurate value for the impedance seen by a transmon is found by simulating the field in the cavity as discussed in ref. [7].

Chapter 3

Tunable LC Resonators

In this chapter I discuss the theory behind my tunable LC resonators. I begin with a discussion of LC resonator modes. Then I describe an initial experiment where I used the kinetic inductance of a thin-film resonator to tune the frequency. Finally, I discuss my flux-tunable resonators. I begin with a discussion of the theory behind the design, and then I show results on device tunres_112115.

3.1 Fixed Frequency LC Resonators

Most of the experiments I discuss in this dissertation involved modulating the resonance frequency of a planar LC resonator. However, the basic building block to this and, subsequently, where I began, is the fixed-frequency LC resonator formed by connecting together a capacitor and inductor. An optical microscope picture of one such resonators is shown in Fig. 3.1(a). This particular device is named JH_1 and was made by Dr. Jared Hertzberg for a hybrid quantum experiment involving trapping atoms onto optical fibers and coupling them to cavities, resonators, and qubits [1]. As shown in the figure, this design used an interdigitated capacitor and a long wire for the inductor.

3.1.1 Resonance Frequency and Energy Levels

In Fig. 2.1(b) I show a lumped element model of an LC resonator. Using Kirchhoff's voltage law, we can write

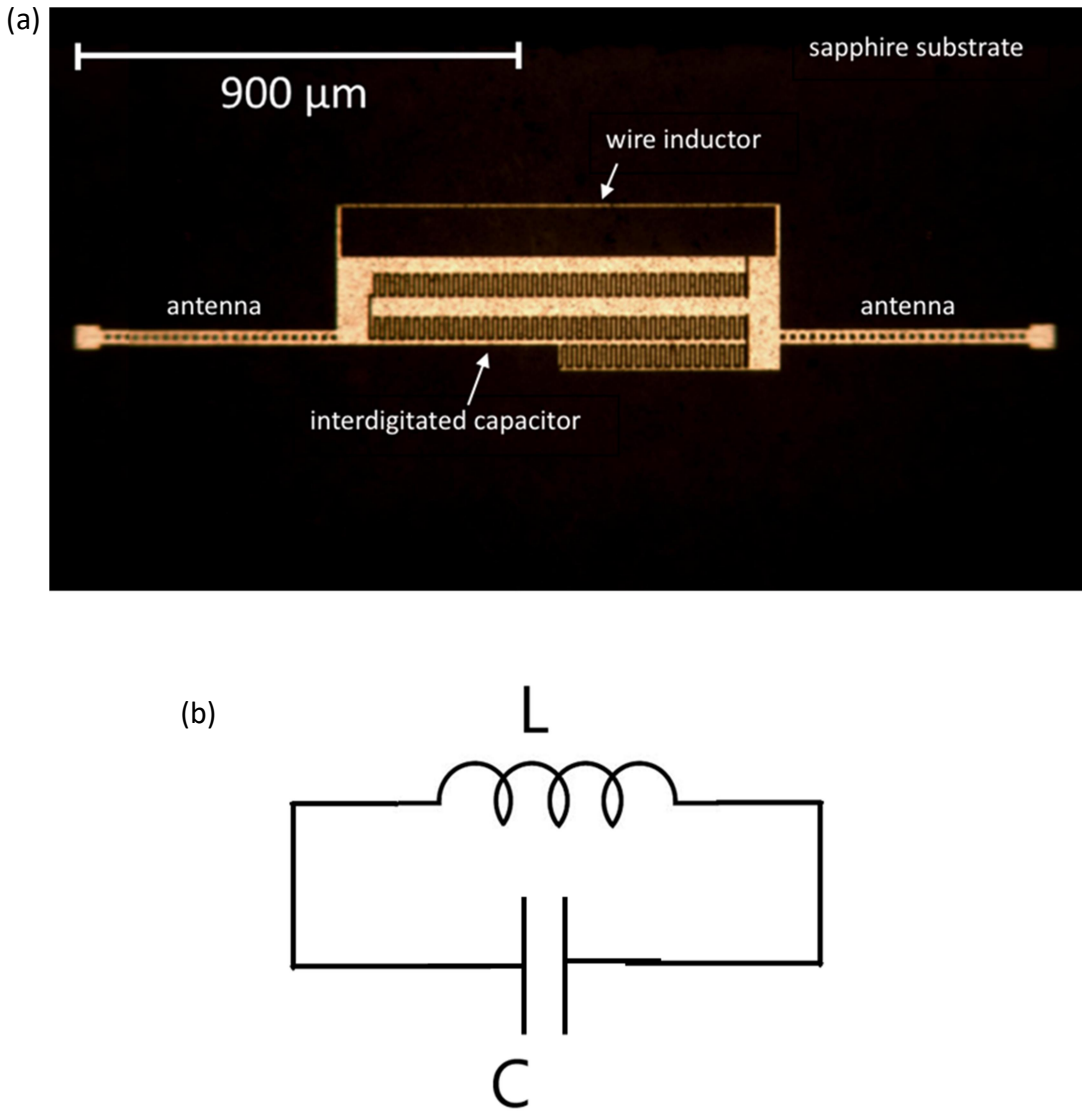

Fig. 3.1: (a) Optical microscope picture of a fixed frequency resonator device JH_1. (b) Lumped element model of the resonator.

$$\frac{q}{C} + L\frac{dI}{dt} = 0, \tag{3.1}$$

where q is the charge on one plate of the capacitor and I is the current flowing out of this plate and through the inductor. The current is given by the negative time derivative of the charge on the capacitor; so, Eq. (3.1) may be rewritten as

$$\ddot{q} + \frac{q}{LC} = 0. \tag{3.2}$$

Equation (3.2) is the equation of motion of a simple harmonic oscillator, with resonance frequency given by

$$f_r = \frac{\omega_r}{2\pi} = \frac{1}{2\pi\sqrt{LC}}. \tag{3.3}$$

In quantum mechanics, this system behaves as a quantum harmonic oscillator with energy levels

$$E_n = \hbar\omega_r\left(n + \frac{1}{2}\right), \tag{3.4}$$

where n is a positive integer or zero. The nth energy level corresponds n photons in the resonator. Notice that each energy level is separated from the next by energy $\hbar\omega_r$, *i.e.* $\left|E_n - E_{n\pm1}\right| = \hbar\omega_r$. This equal spacing means that the system is harmonic and the application of an external classical drive field will place the system into a superposition of multiple eigenstates. Thus, no two eigenstates may be isolated, which implies that this type of system is not viable as a qubit. Never-the-less, resonators are useful for coupling signals to qubits, for coupling qubits together, for coupling to other systems, and for qubit state readout [2-4].

3.1.2 Resonance Shape and Quality Factors

I primarily used microwave spectroscopy to measure the response of my resoantors. In order to extract information from spectroscopic data, a model of the system was needed in order to understand the factors that determine the resonance shape. The model and results I present below are from refs. [5,6], which contain many additional details.

In Fig. 3.2 I show the lumped element circuit of an LC resonator coupled to input and output lines. In the following analysis, I find an analytic expression for

$$S_{21} = \frac{V_{out}}{V_{in}}, \tag{3.5}$$

where S_{21} is the scattering parameter, V_{out} is the voltage measured on the output side of the circuit, and V_{in} is the voltage put into the circuit. This is accomplished by finding the admittances the input line, the output line, and the resonator itself and then using these expressions to find the Thevenin equivalent source voltage, impedances, and transmission

$$S_{21} = \frac{2Z_0(i\omega C_{in} + \omega^2 C_{in}^2 Z_0)(i\omega C_{out} + \omega^2 C_{out}^2 Z_0)}{\frac{1}{R} + \omega^2 C_{in}^2 Z_0 + \omega^2 C_{out}^2 Z_0 + i\left[\omega(C + C_{in} + C_{out}) - \frac{1}{\omega L}\right]}, \tag{3.6}$$

where C_{in} is the input capacitance, C_{out} is the output capacitance, Z_0 is the characteristic impedance of the microwave lines, R is the resistance of the resonator, L is the inductance of the resonator, and C is the capacitance of the resonator.

Although Eq. (3.6) is an analytic result, there are many parameters and the expression is not transparent. A more useful and intuitive form can be found by first defining the internal quality factor Q_i, input coupling factor Q_{in}, and output coupling factor Q_{out} as

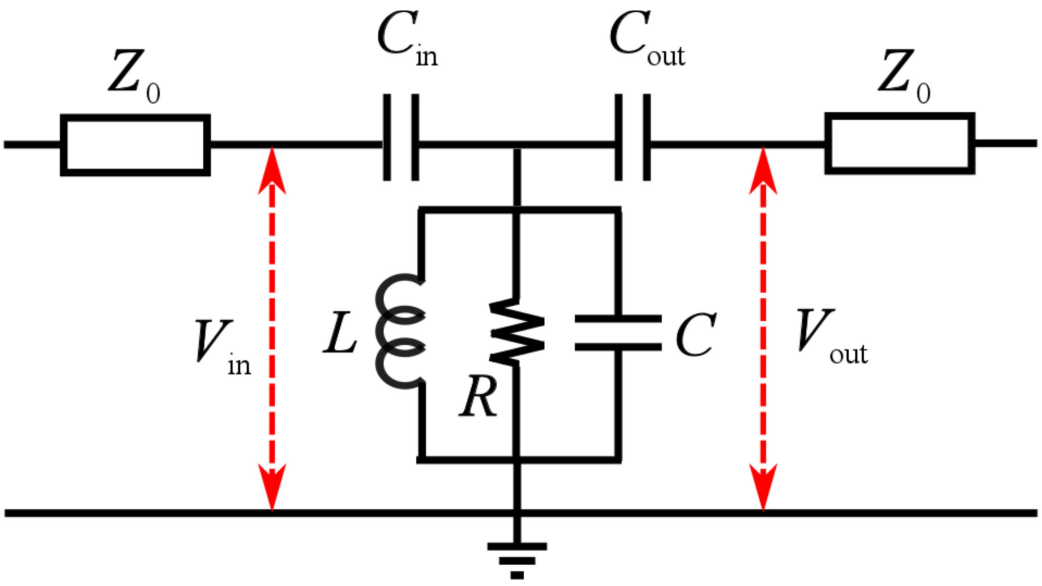

Fig. 3.2: Lumped element model of a fixed frequency resonator capacitively coupled to input and output lines. In refs. [5, 6] this model was used to derive Eq. (3.12).

$$\frac{1}{Q_i} \equiv \frac{\omega_0 L}{R}, \tag{3.7}$$

$$\frac{1}{Q_{in}} \equiv \omega_0^3 C_{in}^2 L Z_0 , \tag{3.8}$$

and

$$\frac{1}{Q_{out}} \equiv \omega_0^3 C_{out}^2 L Z_0 , \tag{3.9}$$

where $\omega_0 = 1/\sqrt{LC}$ is the bare angular resonance frequency of the resonator. The external quality factor Q_e and overall quality factor Q may then be defined as

$$\frac{1}{Q_e} \equiv \frac{1}{Q_{in}} + \frac{1}{Q_{out}} \tag{3.10}$$

$$\frac{1}{Q} \equiv \frac{1}{Q_i} + \frac{1}{Q_e}. \tag{3.11}$$

Using these definitions, S_{21} from Eq. (3.6) may be rewritten as

$$S_{21} = -\frac{2Q\left(\frac{1}{\sqrt{Q_{in}Q_{out}}}\right)}{1 + \frac{2iQ(\omega - \omega_0)}{\omega_0}}. \tag{3.12}$$

Equation (3.12) is what I used to fit my spectroscopic data on my resonators. I note that more general expressions have been obtained by Khalil *et. al.* [31] to account for the effects of mismatched input and output lines and the resulting asymmetric line shapes.

3.2 Resonator Coupled to a 3D Cavity

As discussed in Chapter 2, a resonant microwave cavity may be approximately modelled as a lumped element LC resonator. Here, I ignore all modes except the lowest cavity mode and I treat the cavity as a lumped element circuit.

In Fig. 3.3(a) I show a circuit schematic of two lumped element LC resonator circuits capacitively coupled through capacitor C_c. Resonator 1 has inductance L_1 and capacitance C_1 while resonator 2 has values L_2 and C_2. Without loss of generality, I will consider resonator 1 to be the LC resonator and resonator 2 to be the cavity.

Before writing down the equations of motion, I first define three charge variables in terms of the time integral of the three currents shown in Fig. 3.3(b):

$$q_1 \equiv \int I_1 dt\,, \tag{3.13}$$

$$q_2 \equiv \int I_2 dt\,, \tag{3.14}$$

and

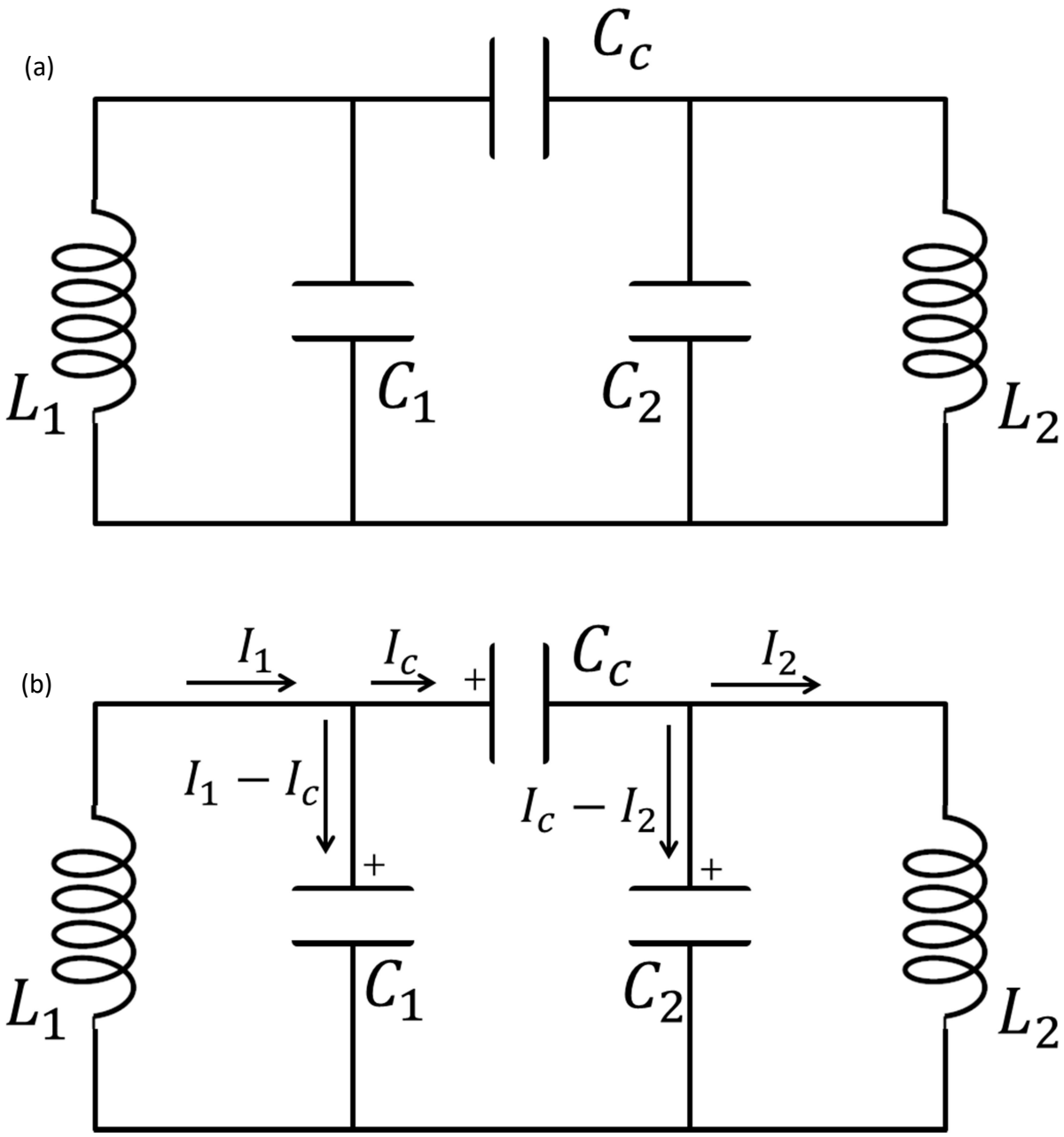

Figure 3.3: Lumped element circuit model for LC resonator capacitively coupled to microwave cavity resonator. Depicted in (a) is just the circuit. In part (b), however, I show the loop currents used to derive the equations of motion for the system.

$$q_c \equiv \int I_c dt\,. \tag{3.15}$$

Going around the two outer loops, I can write the equations

$$L_1 \frac{dI_1}{dt} = -\frac{q_1 - q_c}{C_1} \tag{3.16}$$

and

$$L_2 \frac{dI_2}{dt} = -\frac{q_2 - q_c}{C_2}. \tag{3.17}$$

Going around the center loop yields

$$\frac{q_c}{C_c} + \frac{q_c}{C_2} - \frac{q_2}{C_2} + \frac{q_c}{C_1} - \frac{q_1}{C_1} = 0. \tag{3.18}$$

Solving for q_c gives

$$q_c = \frac{C_S}{C_1} q_1 + \frac{C_S}{C_2} q_2\,, \tag{3.19}$$

where I have defined

$$\frac{1}{C_S} \equiv \frac{1}{C_1} + \frac{1}{C_2} + \frac{1}{C_c}. \tag{3.20}$$

By inserting Eq. (3.20) into Eqs. (3.16) and (3.17) I get

$$L_1 \frac{d^2 q_1}{dt^2} = \frac{C_S - C_1}{C_1^2} q_1 + \frac{C_S}{C_1 C_2} q_2 \tag{3.21}$$

and

$$L_2 \frac{d^2 q_2}{dt^2} = \frac{C_S}{C_1 C_2} q_1 + \frac{C_S - C_2}{C_2^2} q_2\,. \tag{3.22}$$

For this coupled LC system, by making the definitions

$$\omega_1^2 \equiv \frac{C_1 - C_S}{C_1^2 L_1} \tag{3.23}$$

$$\omega_2^2 \equiv \frac{C_2 - C_S}{C_2^2 L_2}$$

$$\gamma_1 \equiv \frac{C_S}{C_1 C_2 L_1}$$

$$\gamma_2 \equiv \frac{C_S}{C_1 C_2 L_2},$$

and by assuming that the charge variables have an $e^{-i\omega t}$ dependence, I can write Eqs. (3.21) and (3.22) as

$$-\omega^2 q_1 = -\omega_1^2 q_1 + \gamma_1 q_2 \tag{3.24}$$

and

$$-\omega^2 q_2 = \gamma_2 q_1 - \omega_2^2 q_2 \,. \tag{3.25}$$

In matrix form, this gives

$$\begin{pmatrix} \omega_1^2 - \omega^2 & -\gamma_1 \\ -\gamma_2 & \omega_2^2 - \omega^2 \end{pmatrix} \begin{pmatrix} q_1 \\ q_2 \end{pmatrix} = \mathbf{0}\,, \tag{3.26}$$

which is simply an eigenvalue problem with characteristic equation

$$\omega^4 - (\omega_1^2 + \omega_2^2)\omega^2 + \omega_1^2 \omega_2^2 - \gamma_1 \gamma_2 = 0\,. \tag{3.27}$$

By solving Eq. (3.27) I arrive at the two angular eigenfrequencies of the system

$$\omega_+ = \sqrt{\frac{(\omega_1^2 + \omega_2^2) + \sqrt{(\omega_1^2 - \omega_2^2)^2 + 4w^2}}{2}} \tag{3.28}$$

and

$$\omega_- = \sqrt{\frac{(\omega_1^2 + \omega_2^2) - \sqrt{(\omega_1^2 - \omega_2^2)^2 + 4w^2}}{2}}\,, \tag{3.29}$$

where $w^2 \equiv C_S^2 / C_1^2 C_2^2 L_1 L_2$. In terms of frequency this gives

$$f_+ = \sqrt{\frac{(f_1^2 + f_2^2) + \sqrt{(f_1^2 - f_2^2)^2 + 4W^2}}{2}} \tag{3.30}$$

and

$$f_- = \sqrt{\frac{(f_1^2 + f_2^2) - \sqrt{(f_1^2 - f_2^2)^2 + 4W^2}}{2}}\ , \tag{3.31}$$

where $f_+ = \omega_+/2\pi$, $f_- = \omega_-/2\pi$, $f_1 = \omega_1/2\pi$, $f_2 = \omega_2/2\pi$ and $W^2 = w^2/16\pi^4$.

The main importance of Eqs. (3.30) and (3.31) is that I can fit them to the measured LC resonator and cavity frequencies when I vary the frequency of the LC resonator (see Section 3.3). The fit will allow me to extract the bare frequency of the LC resonator, the bare frequency of the microwave cavity, and the coupling strength between them.

3.3 Proof of Principle: Kinetic Inductance Tuning

While there was never any doubt that a resonator could be coupled to a 3D cavity, it was unclear how difficult it would be to measure exactly how big the coupling would be. The simplest test case was to build a "fixed frequency" resonator and observe changes in frequency due to changes in the film's kinetic inductance as I varied the resonator's temperature. Here I describe kinetic inductance and how I used it to modulate the resonance frequency of my resonator.

3.3.1 Kinetic Inductance

Kinetic inductance is an effective series inductance that arises from the fact that charge carriers have mass and, consequently, carry kinetic energy when moving. In order

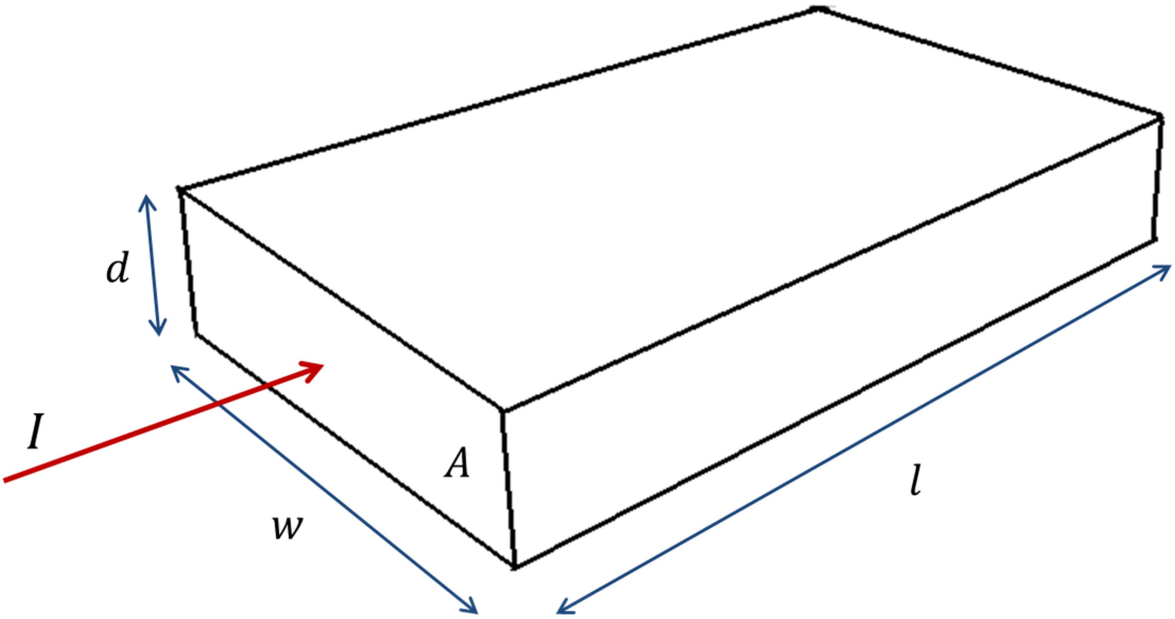

Fig. 3.4: Schematic of a small portion of a superconducting film. The film thickness d and the film width w combine to give a cross-sectional area of A. The length of the film is l. A current I is flowing into the section.

to derive an expression for this inductance, I consider the total kinetic energy of charge carriers in a section of a thin-film superconducting line. I will assume that the length of the section is l and the area of the face is $A = wd$, where w is the width of the strip and d is the thickness of the strip (see Fig. 3.5). The total current flowing through this strip is I. I also assume that the film is thin enough that the current density is uniformly distributed throughout the height of the strip, *i.e.* $d \ll 2\lambda$, where λ is the London penetration depth [7].

The total kinetic energy is given by

$$K = \frac{1}{2} m_t v_s^2 \,, \tag{3.32}$$

where m_t is the total mass of all the charge carriers in this strip and v_s is the average velocity of each charge carrier. The total mass may be written as

$$m_t = m_s n_s A l \,, \tag{3.33}$$

where m_s is the mass of an individual charge carrier and n_s is the density of the charge carriers. Since I am considering a superconducting strip, m_s is the mass of a Cooper pair, which I can set to twice the mass m_e of an electron. The current density may be written as

$$J = \frac{I}{A} = n_s q_s v_s \,, \tag{3.34}$$

where $q_s = 2e$ is the charge of the carriers. Solving for the drift velocity v_s gives

$$v_s = \frac{I}{n_s q_s A} \,. \tag{3.35}$$

Putting Eqs. (3.33) and (3.36) back into Eq. (3.32) yields

$$K = \frac{1}{2} \left(\frac{m_s l}{n_s q_s^2 A} \right) I^2 \,. \tag{3.36}$$

Equating this to $\frac{1}{2} L I^2$ gives an expression for the kinetic inductance,

$$L_K = \frac{m_e l}{n_s e^2 A} \,. \tag{3.37}$$

The mass m_e, charge e, and dimensions l and A are fixed for a given device. However, the density of cooper pairs n_s is temperature dependent and dramatically decreases as the temperature T approaches the critical temperature T_c of the superconducting film from below.

3.3.2 Temperature Dependence of Kinetic Inductance

From Eq. (3.38), one sees that the kinetic inductance the kinetic inductance is inversely proportional to the density of Cooper pairs n_s. As the temperature T is increased from absolute zero, fewer Cooper pairs occupy the volume due to thermal excitations. In general I can write,

$$n_s(T) = n_s(0) - \frac{n_{qp}(T)}{2} \tag{3.38}$$

where $n_s(T)$ is the temperature dependent pair density and $n_{qp}(T)$ is the density of quasiparticles at temperature T. For this derivation I assume that I only have thermal quasiparticles. For $T \ll T_c$, we have $n_{qp}(T) \ll n_s(T)$. Thus, I can write

$$L_K(T) = \frac{n_e l}{2e^2 A\left(n_s(0) - \frac{n_{qp}(T)}{2}\right)} \approx L_K(0)\left(1 + \frac{n_{qp}(T)}{2n_s(0)}\right), \tag{3.39}$$

For a superconductor with gap Δ and $T < T_c$, the total density of quasiparticles is [7]

$$n_T = 4N(0)\int_{\Delta}^{\infty} \frac{E}{\sqrt{E^2 - \Delta^2}}\, f(E,\mu)dE\,, \tag{3.40}$$

where μ is the chemical potential, $N(0) = 3n_e/4\varepsilon_F$ is the density of states of electrons with spin up when the superconductor is in the normal state, n_e is the density of electrons in the normal state, ε_F is the Fermi energy, and $f(E,\mu)$ is the Fermi-Dirac distribution and is given by

$$f(E,\mu) = \frac{1}{1 + e^{(E-\mu)/k_B T}}\ . \tag{3.41}$$

Since I am only concerned with the equilibrium thermal quasiparticle density, I set $\mu = 0$, which reduces Eq. (3.40) to

$$n_{qp}(T) = 4N(0)\int_{\Delta}^{\infty} \frac{E}{\sqrt{E^2-\Delta^2}}\,\frac{1}{1+e^{E/k_BT}}\,dE\,. \tag{3.42}$$

Equation (3.42) may be evaluated numerically. However, it is often more convenient to have an analytic expression. To do this, I first pull out a factor of e^{E/k_BT} from the denominator and rewrite the integrand to get

$$n_{th} = 4N(0)\int_{\Delta}^{\infty} \frac{Ee^{-E/k_BT}}{\sqrt{E^2-\Delta^2}}\left(\frac{1}{1+e^{-E/k_BT}}\right)dE\,. \tag{3.43}$$

Since $E \geq \Delta \gg k_BT$, I can make a Taylor expand the expression in parenthesis and arrive at

$$n_{qp}(T) = 4N(0)\sum_{n=1}^{\infty}(-1)^{n+1}\int_{\Delta}^{\infty} \frac{E}{\sqrt{E^2-\Delta^2}}\,e^{-nE/k_BT}\,dE\,. \tag{3.44}$$

Considering the integral in Eq. (3.44), making the substitution $t = E/\Delta$ yields

$$\int_{\Delta}^{\infty} \frac{E}{\sqrt{E^2-\Delta^2}}\,e^{-nE/k_BT}\,dE = \Delta\int_{1}^{\infty} \frac{t}{\sqrt{t^2-1}}\,e^{-n\Delta t/k_BT}\,dt\,. \tag{3.45}$$

This integral is simply Δ times the Laplace transform of the function F(t) given by

$$F(t) = \begin{cases} 0 & for\ t = 0\ to\ 1 \\ \dfrac{t}{\sqrt{t^2-1}} & for\ t = 1\ to\ \infty \end{cases} \tag{3.46}$$

with the variable $s = n\Delta/k_BT$. This transform yields [8]

$$\Delta\int_{1}^{\infty} \frac{t}{\sqrt{t^2-1}}\,e^{-n\Delta t/k_BT}\,dt = \Delta\,K_1\left(\frac{n\Delta}{k_BT}\right), \tag{3.47}$$

where K_1 is the modified Bessel function of the second kind with $\nu = 1$. Putting this all back into Eq. (3.44) gives the simplified and analytic expression

$$n_{qp}(T) = 4N(0)\Delta\sum_{n=1}^{\infty}(-1)^{n+1}K_1\left(\frac{n\Delta}{k_BT}\right). \tag{3.48}$$

One question remaining is how many terms in Eq. (3.48) are necessary to insure good convergence to the integral in Eq. (3.44). Figure 3.5(a) shows a plot of $n_{th}/4N(0)\Delta$ vs. k_BT/Δ for the full integral in Eq. (3.42) evaluated numerically and for Eq. (3.48) with one, two, and three terms in the expansion. Figure 3.5(b) shows the sum of the squared difference between the integral expression and the Bessel function expansion as a function of the number of n terms over the range $k_BT/\Delta = 0$ to $k_BT/\Delta = 1$. From the figure, one sees that the expansion in Eq. (3.50) converges to the full expression exponentially with the number of terms. Having three or four terms is plenty for going up to temperatures of $k_BT \approx 0.9\Delta$, and for temperatures $k_BT \leq 0.5\Delta$, two terms give $n_{qp}(T)$ to better than 0.013%.

With $n_{qp}(T)$ determined, I can now write a general form for the temperature dependence of the kinetic inductance. From Eq. (3.39) I have

$$\delta L_K(T) \equiv L_K(T) - L_K(0) \approx L_K(0)\frac{n_{qp}(T)}{2n_s(0)} \tag{3.49}$$

One complication hiding in Eq. (3.49) is that the superconducting gap Δ is dependent on temperature. $\Delta(T)$ can be found by solving the transcendental equation [7]

$$\frac{1}{N(0)V} = \int_0^{\hbar\omega_c} \frac{\tanh\left(\frac{1}{2}\beta\left(\zeta^2 + \Delta^2(T)\right)\right)}{\zeta^2 + \Delta^2(T)}\, d\zeta \tag{3.50}$$

However, for $T \lesssim T_c$, Tinkham gives the following approximate expression

$$\Delta(T) = \Delta(0) \cdot 1.74 \cdot \sqrt{1 - T/T_c}\,, \tag{3.51}$$

where T_c is the critical temperature of the superconductor and [7]

$$\Delta(0) = 1.764\, k_B\, T_c\,. \tag{3.52}$$

For Eq. (3.49) this gives

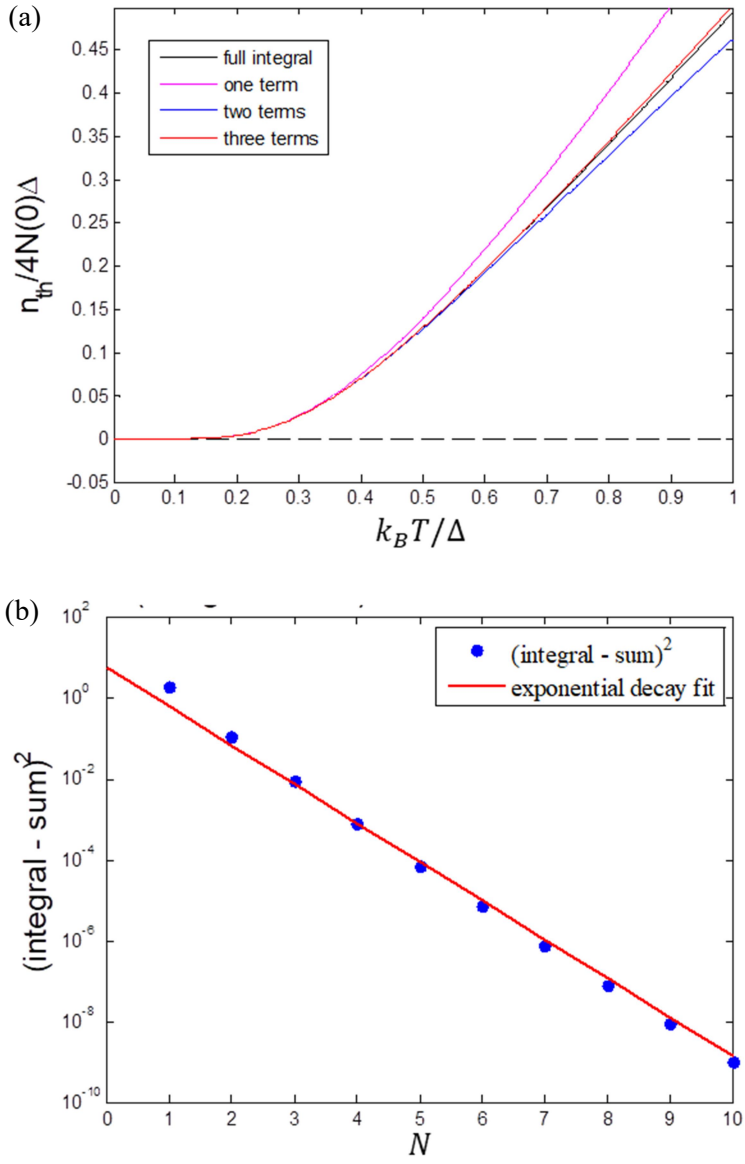

Figure 3.5: (a) Plot of the equilibrium thermal quasiparticle density for the integral in Eq. (3.43), shown in black, and one, two, and three terms of the Bessel function expansion in Eq. (3.48) shown in magenta, blue, and red, respectively. (b) Shows the value of the squared difference between Eqs. (3.43) and (3.48) over the range k_BT/Δ= 0 to 1 as a function of the number of terms in the expansion on a log scale. The red line is a fit to a decaying exponential.

$$\delta L_K(T) \approx L_K(0)\frac{4N(0)\Delta(T)\sum_{n=1}^{\infty}(-1)^{n+1}K_1\left(\frac{n\Delta(\mathrm{T})}{k_BT}\right)}{2n_s(0)}. \tag{3.53}$$

The frequency of the resonator is then given by

$$f_{res}(T) = \frac{1}{2\pi\sqrt{C\left(L_g + L_K(0) + \delta L_K(T)\right)}} = \frac{f_0}{\sqrt{1 + \frac{\delta L_K(T)}{L_g + L_K(0)}}} \tag{3.54}$$

where f_0 is the resonance frequency of the resonator at very low temperatures and L_g is the geometric inductance of the film. In the regime my devices occupy, the limit $L_g \gg \delta L_K(T)$ applies, which gives

$$f_{res}(T) \approx f_0\left(1 - \frac{\delta L_K(T)}{2L_g}\right). \tag{3.55}$$

Equation (3.55) is the model I use to fit the data in the following section.

3.3.3 Kinetic Inductance Tuning Results

To determine the coupling strength of the qubit-cavity interaction, I mounted the fixed-frequency LC resonator shown in Fig. 3.1(a), device JH_1, in the center of my 3D Al microwave cavity SI-2a (see Fig. 3.7) and cooled them on the mixing plate stage of an Oxford Triton 200 dilution refrigerator. To couple microwave signals into and out of the cavity, I used SMA pin connectors that extended into the cavity space. For more details on the 3D cavity see Chapter 2, and for more details on the dilution refrigerator see Chapter 7. The idea was to couple the resonance frequency of the resonator to the lowest mode of the microwave cavity, the TE_{101} mode (see Chapter 2). By then varying the base temperature T of the refrigerator, I could vary the density of equilibrium thermal quasiparticles density $n_{qp}(T)$ enough to change the kinetic inductance and, subsequently,

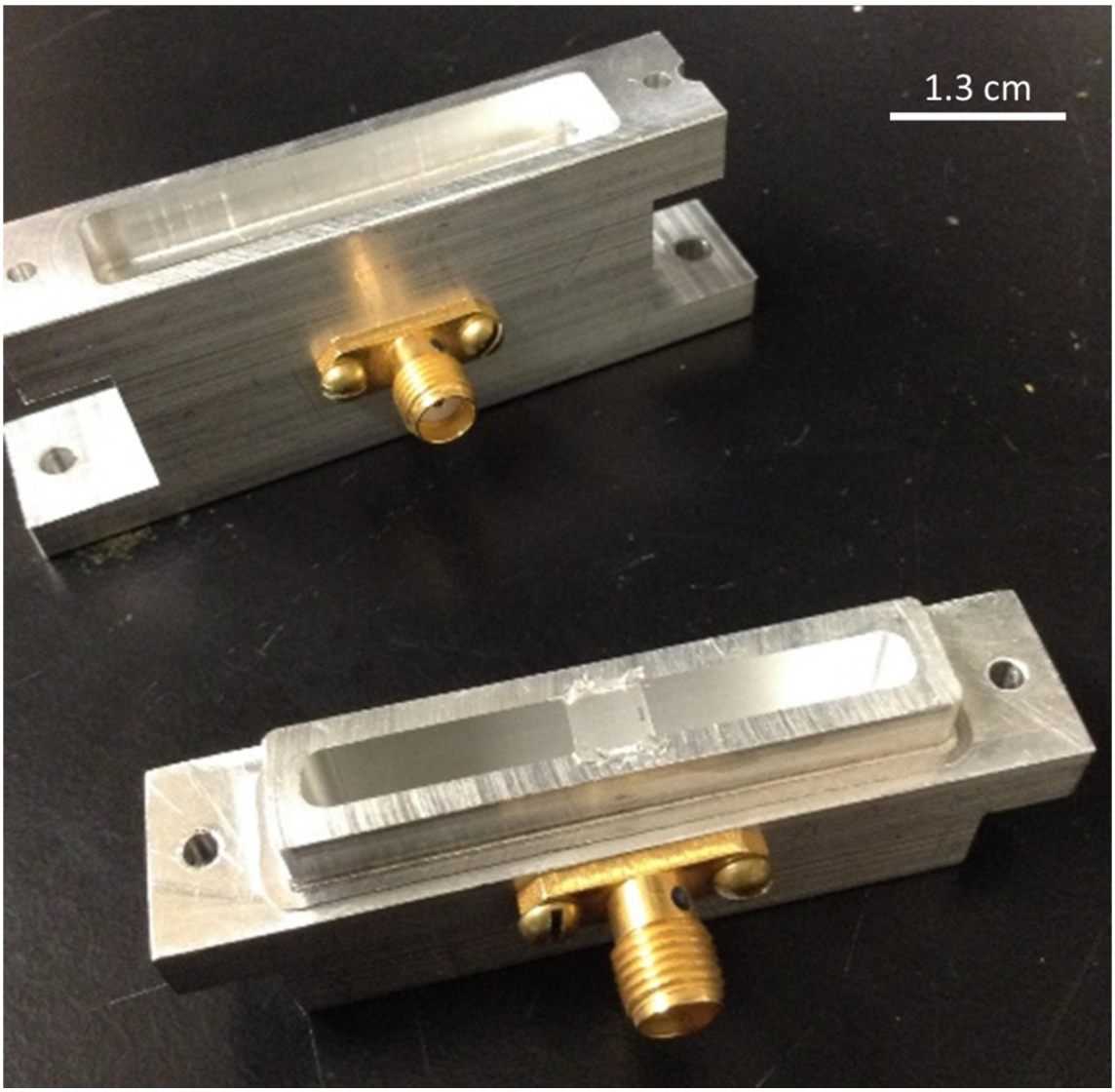

Fig. 3.6: Photo of microwave cavity SI-2a. The fixed frequency resonator chip JH_1 is also shown mounted in the cavity space.

the resonance frequency of the resonator. By fitting the observed dependence of the cavity and LC mode frequencies to Eqs. (3.30) and (3.31) with the temperature dependence of the resonator's frequency given by Eq. (3.55), I could determine the coupling strength.

This was the first device run on this refrigerator, which had just been obtained with support from the Joint Quantum Institute (JQI). There was still not much filtering or and the HEMT amplifier, cryoperm magnetic shield, and Cu 15 mK thermal shield had yet to be installed. To measure the cavity and LC resonance frequencies of this system, I used an Agilent E5071C Vector Network Analyzer (VNA) to sweep over a range of frequencies and measure the magnitude of $|S_{21}|^2$. Figure 3.7(a) shows typical VNA data that I collected from this experiment. The x-axis of the plot is frequency and the y-axis is the magnitude of $20\log_{10}|S_{21}|$. As seen in the figure, there are two sharp peaks, which are the normal mode frequencies of the coupled cavity-LC system.

I don't show the data here, but the VNA also records the phase of S_{21} so that the full complex value of S_{21} is determined. In Figs. 3.7(b) and 3.7(c) I show fits of Eq. (3.12) in a narrow range around each peak. From the fit, I find the center frequency and the various quality factors. The main piece of information I needed was the location of the two peaks. Once this was found, I changed the base temperature of the refrigerator, took a new S_{21} spectrum with the VNA, and, fit the new data to find the new location of the resonances.

Figure 3.8 shows plots of the measured resonance frequencies f_+ and f_- versus temperature T. The temperature range I covered was 16 mK (base temperature) to 700 mK. Figure 3.10(a) shows f_+, and Fig. 3.10(b) shows f_-. Note that both the resonance

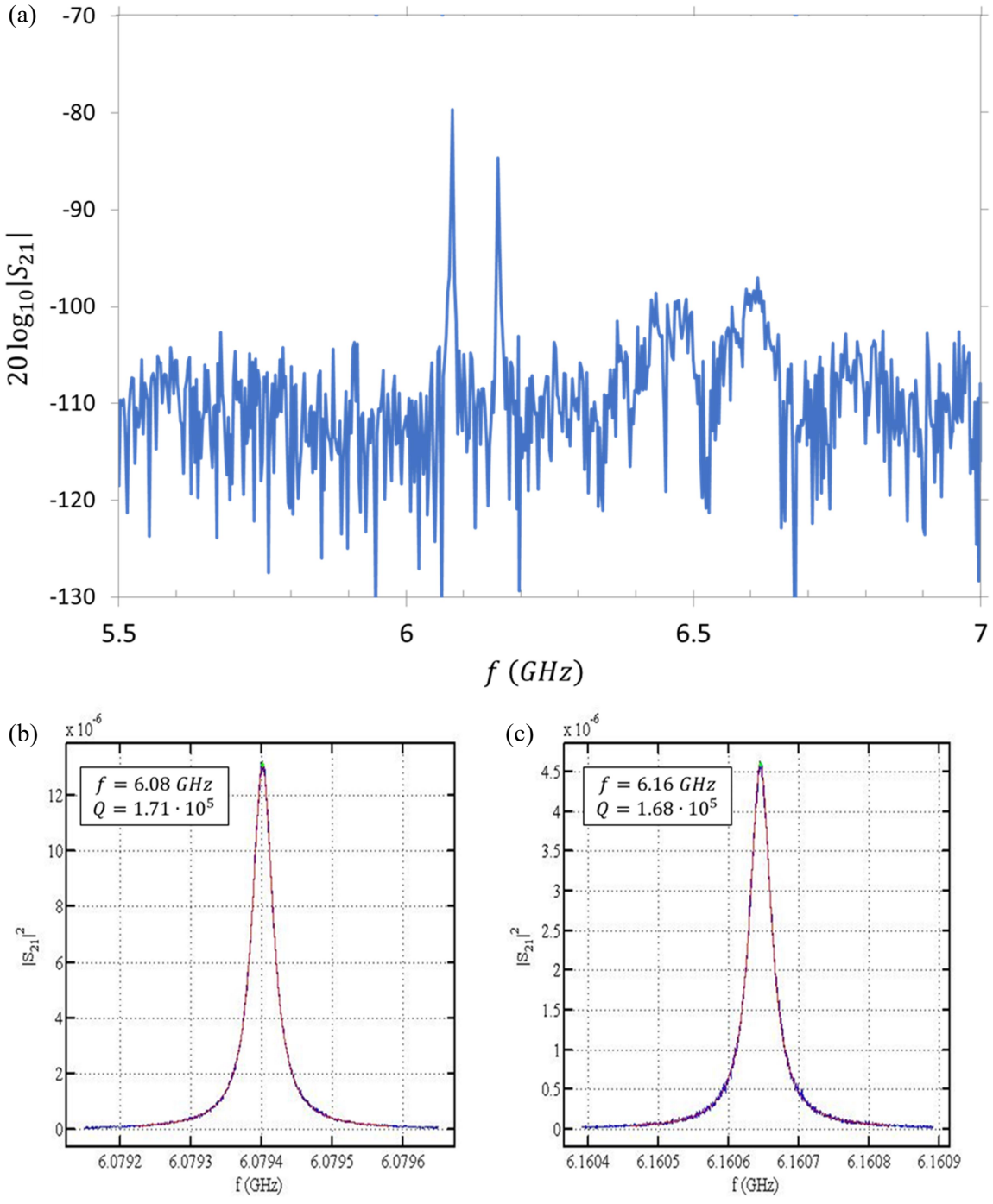

Fig. 3.7: (a) Measured $|S_{21}|$ vs. frequency f on the kinetic inductance tuning device JH_1 measured at 15 mK. The two peaks are the coupled resonator and cavity normal mode frequencies. (b) Plot of the left peak with fit to Eq. (3.12) shown as the solid red line. (c) Plot fo the right peak with fit to Eq. (3.12) shown as the solid red line.

frequencies drop as T increases. The f_+ resonance drops by approximately 40 MHz over the temperature range, and the f_- resonance drops by about 25 MHz. Since f_+ decreased by much more than f_-, this strongly suggested that the f_+ normal mode resonance contained much more of the LC resonance than f_-.

The solid curves in Fig. 3.8 are fits of $f_+(T)$ and $f_-(T)$ from Eqs. (3.30) and (3.31) with the temperature dependence on the LC resonator given by equation (3.55) to the data points, where I let f_1 be the cavity resonance and f_2 be the resonance of the resonator. Since the variation in the kinetic inductance had only a very slight effect on the cavity resonance, due to it being made from bulk Al with wall thickness much greater than the London penetration depth, I assumed the cavity resonance was fixed over the temperature range in question. For the kinetic inductance expression in the resonator's frequency, I used three terms in the expansion of $n_{qp}(T)$ in Eq. (3.53). The fitting parameters were the resonance frequency of the cavity TE_{101} cavity mode $f_{0,cav}$, the

Table 3.1: Fit parameters for device JH_1 kinetic inductance tuning experiment.

Parameter	Value
f_{0cav}	6.106 GHz
f_{0res}	6.134 GHz
T_c	0.85 K
W	342 MHz
L_{K0}	4.37e-6

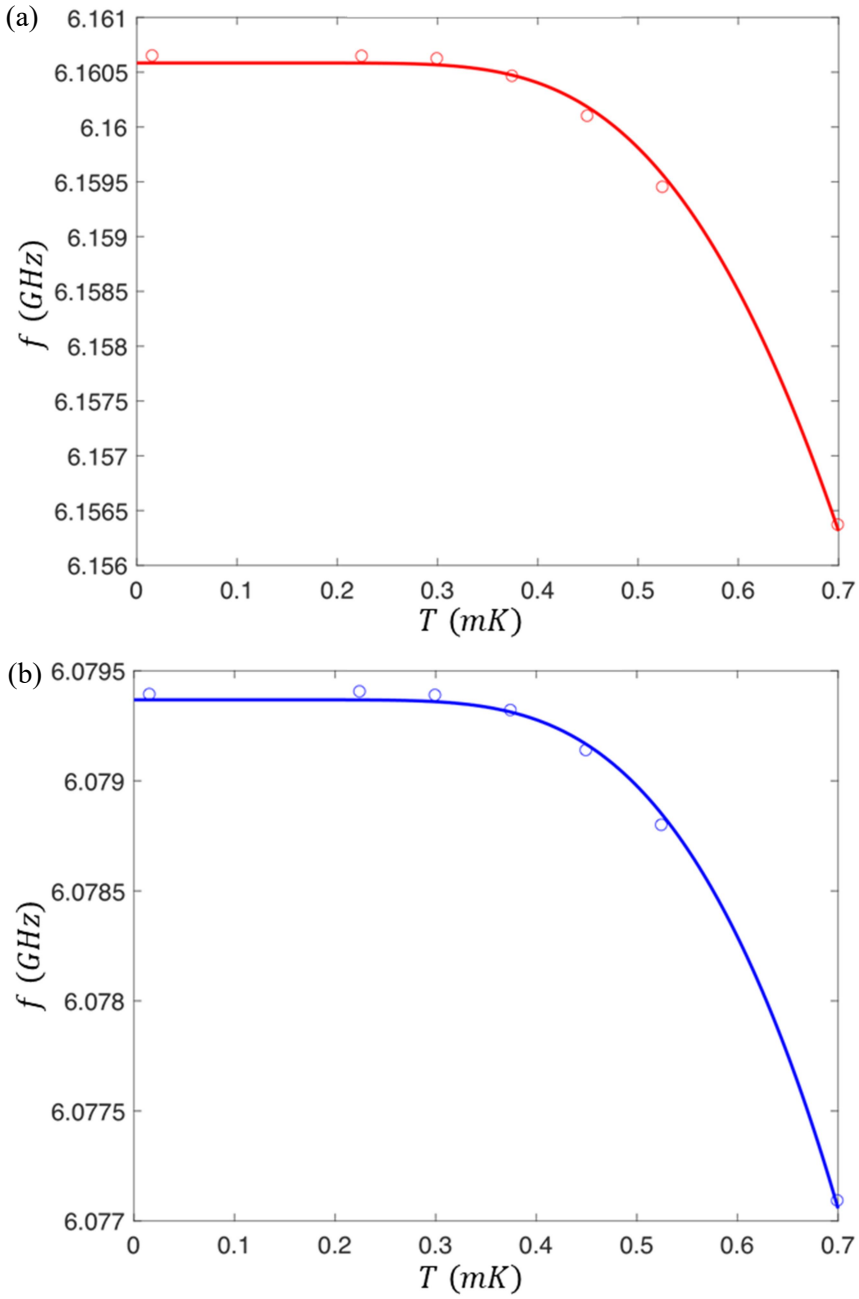

Fig. 3.8: (a) Plot showing the frequency f_+ vs. temperature T. Measured values are open circles and the solid curve is a fit to the coupled resonator model in Eq. (3.30). (b) Plot showing the frequency f_- vs. temperature T. Measured values are open circles and the solid curve is a simultaneous fit to the coupled resonator model in Eq. (3.31).

geometric resonance of the resonator $f_{0,res}$, the critical temperature of the Al film T_c, coupling strength W, and the scale factor L_{K0} defined as

$$L_{K0} \equiv L_K(0)\frac{4N(0)}{2n_s(0)}. \tag{3.56}$$

The extracted parameters are shown below in Table 3.1.

The fit curves in Fig. 3.8 are in good agreement with the data. The parameter I was most interested in was the coupling strength W= 342 MHz. This coupling was so strong due to the fact that this resonator had 1 mm antennas attached to it (see Fig. 3.1(a)) that increased its dipole moment. Since it was placed very close to the center of the cavity and it was aligned in the direction of the electric field, this led to a relatively strongly coupled system. I note also that $T_c \approx 0.85$ K was much lower than expected, but this may be due to the use of Eq. (3.51), which is not valid for $T \ll T_c$.

As expected, this experiment showed that it was easy to couple a resonator to a cavity. Of course, this method of tuning the resonator was not good for a system with a qubit because the temperature increases the thermal excitations would destroy the coherence. Also, the tuning range of the resonator was only about 40 MHz, which is too small to be useful. Hence, I had to use another technique to tune the resonator.

3.4 Josephson Junction Tuning

In this section I describe an LC resonator that achieves tuning by incorporating a variable Josephson inductance. I first describe the Josephson effect and how I used it for tuning purposes. Then, I next present a simple model of a tunable LC circuit and derive the expected tuning range and other relevant behavior. Finally, I discuss the full circuit model for my tunable LC resonators.

3.4.1 The Josephson Effect and Non-Linear Inductance

The essential component that allowed tuning of my LC resonators was a Josephson junction. I exclusively used S-I-S junctions fromed by Al superconducting leads sandwiching an AlOx barrier (see Fig. 3.9). In Fig. 3.9 the barrier is represented in red. From Ginzburg-Landau theory [7] I can write the wave function for pair condensation on the left as

$$\psi_L = \sqrt{\rho_L} e^{i\phi_L} \tag{3.57}$$

and on the right as

$$\psi_R = \sqrt{\rho_R} e^{i\phi_R}, \tag{3.58}$$

where ρ_L and ρ_R are the densities of the superconducting Cooper pairs and ϕ_L and ϕ_r are the phase of the wave functions on the left and right electrodes, respectively. The physicially important parameter is the phase difference

$$\phi = \phi_L - \phi_R \,. \tag{3.59}$$

The dc Josephson effect gives the current I through a junction as

$$I = I_0 \sin(\phi) \,, \tag{3.60}$$

where I_0 is the critical current of the junction, and the AC Josephson effect relates the voltage difference V across the junction to the rate at which the phase difference is changing as

$$V = \frac{\Phi_0}{2\pi} \frac{d\phi}{dt} \,, \tag{3.61}$$

where $\Phi_0 = h/2e$ is the magnetic flux quantum. The critical current is dependent on the attributes of the tunnel barrier such as the area, the superconducting gap, and the barrier thickness. For my devices, I adjusted the critical current by setting the junction area and

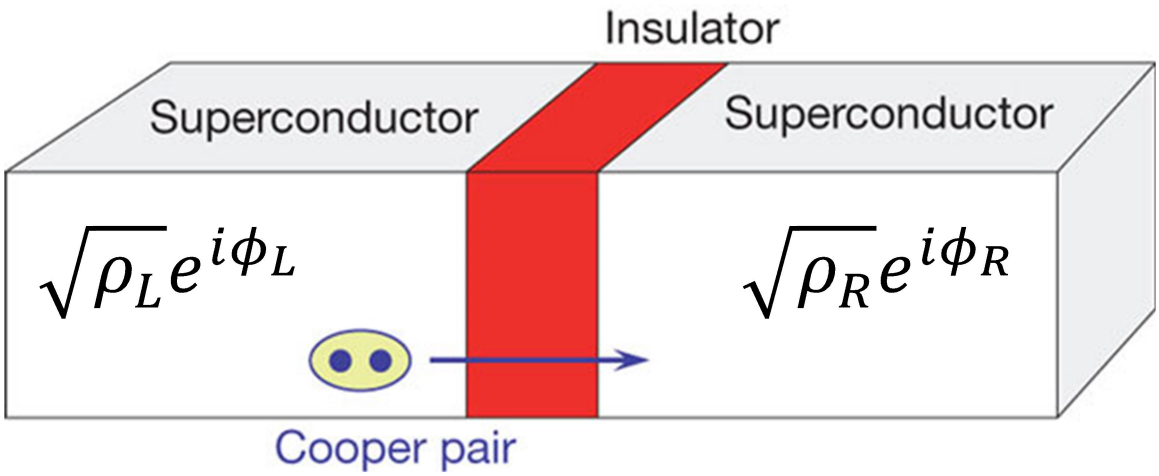

Figure 3.9: Schematic of an S-I-S Josephson junction formed by sandwiching a thin layer of insulation between two superconducting leads. A Cooper pair is depicted tunneling from the left superconductor to the right.

by varying the barrier thickness by varying the oxidation pressure and time on the first aluminum layer.

One implication of the Josephson relations is that if $I < I_0$, then by Eq. (3.60) there will be a constant phase difference $\phi = \sin^{-1}\left(\frac{I}{I_0}\right)$, and from Eq. (3.61) this constant phase difference produces zero voltage. This means that dc currents may flow with no voltage drop across the junction. Another implication is that a constant voltage V_0 across the junction produces a time-dependent phase difference of $\phi(t) = 2\pi V_0 t/\Phi_0$. Plugging this result into Eq. (3.60) gives a current of $I = I_0 \sin(2\pi V_0 t/\Phi_0)$, which is an alternating current at frequency $f = \omega/2\pi = V_0/\Phi_0$. Thus, a dc voltage produces an ac current.

Another implication of Eqs. (3.60) and (3.61) is essential to my method of tuning the resonators. Taking the derivative of Eq. (3.60) with respect to time produces

$$\frac{dI}{dt} = I_0 \cos(\phi) \frac{d\phi}{dt} \ . \tag{3.62}$$

Comparing Eqs. (3.61) and (3.62) I can write

$$V = \frac{\Phi_0}{2\pi I_0 \cos(\phi)} \frac{dI}{dt} \ . \tag{3.63}$$

Now, recall that the voltage across an inductor is given by $V = L\frac{dI}{dt}$; thus, Eq. (3.63) gives the effective, non-linear inductance of a Josephson junction

$$L_j = \frac{\Phi_0}{2\pi I_0 \cos(\phi)} . \tag{3.64}$$

Notice that this is inductance varies inversely with the cosine of ϕ. Since this phase difference is a little difficult to visualize, I can instead write this inductance in terms of current. Since $\sin^2\phi + \cos^2\phi = 1$, I have that

$$L_j = \pm \frac{\Phi_0}{2\pi I_0 \sqrt{1 - \sin^2(\phi)}} . \tag{3.65}$$

Using Eq. (3.60), this can also be written as

$$L_j = \pm \frac{\Phi_0}{2\pi \sqrt{I_0^2 - I^2}} . \tag{3.66}$$

From (3.66), one sees the Josephson inductance depends on the current and diverges as I approaches the critical current I_0. Note also that the Josephson inductance can be negative. Equation (3.64) makes this clear because $\cos(\phi)$ can be positive or negative. One must be careful when using Eq. (3.66) to select the correct sign. This variable Josephson inductance is what I use to tune my resonators.

3.4.2 Single-Loop Resonator Tuning Range

Figure 3.10(a) depicts the circuit schematic of a resonator where a portion of the inductance in the circuit can be varied. As discussed in the previous section, I used a Josephson junction as this variable inductance by varying the current through the junction. Current can be driven through the junction by placing it in a loop (see Fig. 3.12(b)) and applying external magnetic flux Φ_{ext}. This will vary the junciton inductance and the total inductance of the circuit, thereby changing the resonance frequency.

With the basic idea in hand, I now derive the expected tuning range. Figure 3.10(b) shows the labeling of the model parameters L_0, L_1, L_{1x}, L_J, and Φ_{ext}. The resonance frequency is given by

$$f_{LC} = \frac{1}{2\pi\sqrt{L_t(\phi)C}}, \tag{3.67}$$

where the total inductance is

$$L_t(\phi) = L_0 + \frac{L_1\left(L_{1x} + L_j(\phi)\right)}{L_1 + L_{1x} + L_j(\phi)}, \tag{3.68}$$

which can be put in the form

$$L_t(\phi) = L_0\left(1 + \frac{L_1\left(L_{1x} + L_j(\phi)\right)}{L_0\left(L_1 + L_{1x} + L_j(\phi)\right)}\right). \tag{3.69}$$

I now define

$$\gamma^2(\phi) \equiv 1 + \frac{L_1\left(L_{1x} + L_j(\phi)\right)}{L_0\left(L_1 + L_{1x} + L_j(\phi)\right)}, \tag{3.70}$$

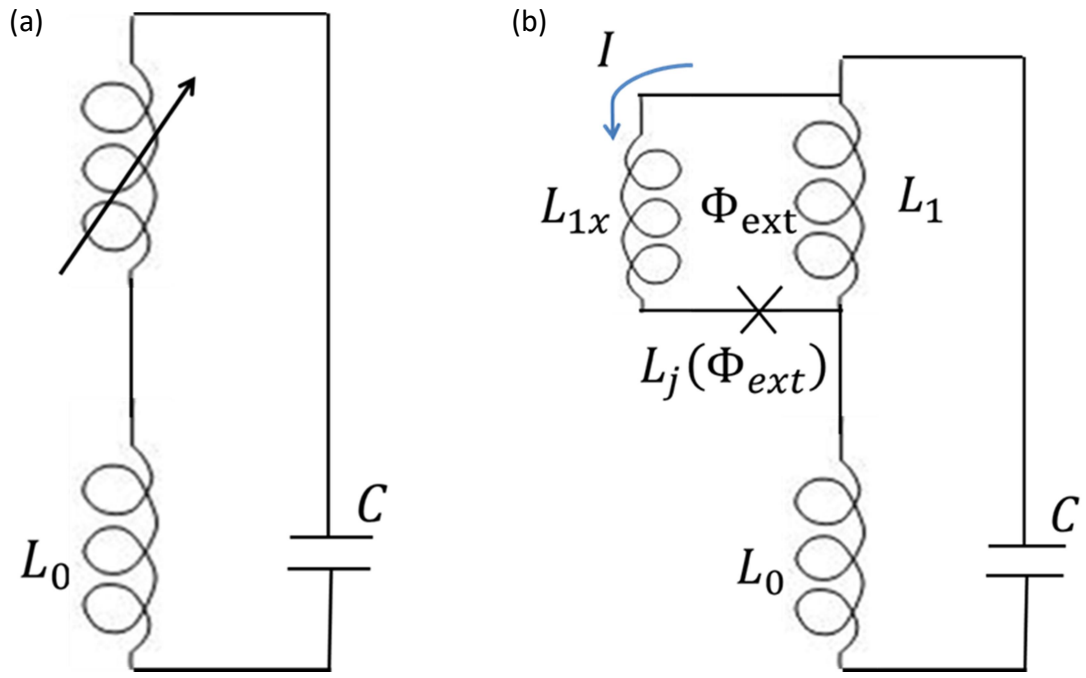

Figure 3.10: (a) Lumped element model for a tunable resonator with geometric inductance L_0 shunted by a tunable inductor. (b) Simplified circuit model for flux-tunable resonators. As DC magnetic flux Φ_{ext} is coupled into the loop, a current I is induced. This current modulates the Josephson inductance L_J and, subsequently, the overall inductance of the circuit, tuning the resonance frequency.

which is simply the term in parenthesis in Eq. (3.69). Putting this back into Eq. (3.67) yields

$$f_{LC} = \frac{1}{2\pi\sqrt{C L_0 \gamma^2(\phi)}} = \frac{f_0}{\gamma(\phi)}, \tag{3.71}$$

where $f_0 = 1/2\pi\sqrt{L_0 C}$ is the bare resonance frequency that would occur if $L_J \to \infty$ and $L_1 \to 0$.

From Eq. (3.71), one sees that f_{LC} is at a maximum when $\gamma(\phi)$ is at a minimum and vice versa. The tuning range may be then be written as

$$\Delta f_{LC} = f_{LC}^{max} - f_{LC}^{min} = f_0 \left(\frac{1}{\gamma_{min}} - \frac{1}{\gamma_{max}}\right), \tag{3.72}$$

and the fractional tuning range is then

$$\frac{\Delta f_{LC}}{f_0} = \frac{\gamma_{max} - \gamma_{min}}{\gamma_{max}\gamma_{min}}. \tag{3.73}$$

I now examine the function $\gamma(\phi)$ to determine its behavior and find the maximum and minimum values. I now define the total geometric inductance going around the loop

$$L_{loop} \equiv L_1 + L_{1x}, \tag{3.74}$$

the ratio of the geometric inductance of the non-junction loop branch to the geometric inductance of the junction branch

$$\alpha \equiv \frac{L_1}{L_{1x}}, \tag{3.75}$$

the ratio of the total loop inductance to the bare inductance of the LC resonator

$$\rho \equiv \frac{L_{loop}}{L_0}, \tag{3.76}$$

and the modulation parameter

$$\beta_\pi \equiv \frac{2\pi L_{loop} I_0}{\Phi_0} \tag{3.77}$$

From Eqs. (3.74) and (3.75) I can write

$$L_{1x} = \frac{L_{loop}}{\alpha + 1} \tag{3.78}$$

and

$$L_1 = \frac{\alpha L_{loop}}{\alpha + 1}. \tag{3.79}$$

With Eqs. (3.74) – (3.79), $\gamma^2(\phi)$ may be written as

$$\gamma^2(\phi) = 1 + \frac{\alpha\rho}{(\alpha+1)^2} \cdot \frac{\beta_\pi \cos(\phi) + \alpha + 1}{\beta_\pi \cos(\phi) + 1}. \tag{3.80}$$

An important consequence of Eq. (3.80) is that if $\beta_\pi \geq 1$, certain values of ϕ will cause the denominator to be zero, which causes $\gamma(\phi)$ to diverge. As I show below, this situation results in the loop having multiple allowed trapped flux states. To avoid this situation, one needs to enforce the constraint

$$\beta_\pi < 1\,. \tag{3.81}$$

Figure 3.12 shows plots of $\gamma(\phi)$ for different α, ρ, and β_π values. In Fig. 3.11(a), β_π= 0.9 and α= 0.1 are kept fixed and $\gamma(\phi)$ is plotted for 4 different values of ρ. As can be seen from this plot, increasing ρ both increases the tuning depth and reduces the minimum value of $\gamma(\phi)$. Note that since L_0 and L_{loop} are fixed by the geometry of the device, and the tuning range is not strongly dependent on ρ. Since I typically wanted a 10% to 20% tuning range, I chose values of $\rho < 1$; in my first tunable resonators I chose $\rho \approx 0.9$ and then $\rho \approx 0.3$ for later designs.

In Fig. 3.11(b), I set β_π= 0.9 and ρ= 0.3 and plotted $\gamma(\phi)$ for four different values of α. Note that α has a relatively strong effect on the tuning range compared to ρ. For my earliest tunable resonator designs I put the junction on the larger of the two loop branches, which gave α= 0.1. In my later devices I dramatically increased the tuning range by flipping the position of the junction to the small branch to achieve $\alpha \approx 10$.

In Fig. 3.11(c), I show $\gamma(\phi)$ for four different values of β_π leaving α= 0.1 and ρ= 0.3 fixed. From this plot, one sees that the tuning range depends strongly on β_π. Since β_π is directly proportional to the critical current of the junction, this varied the most from

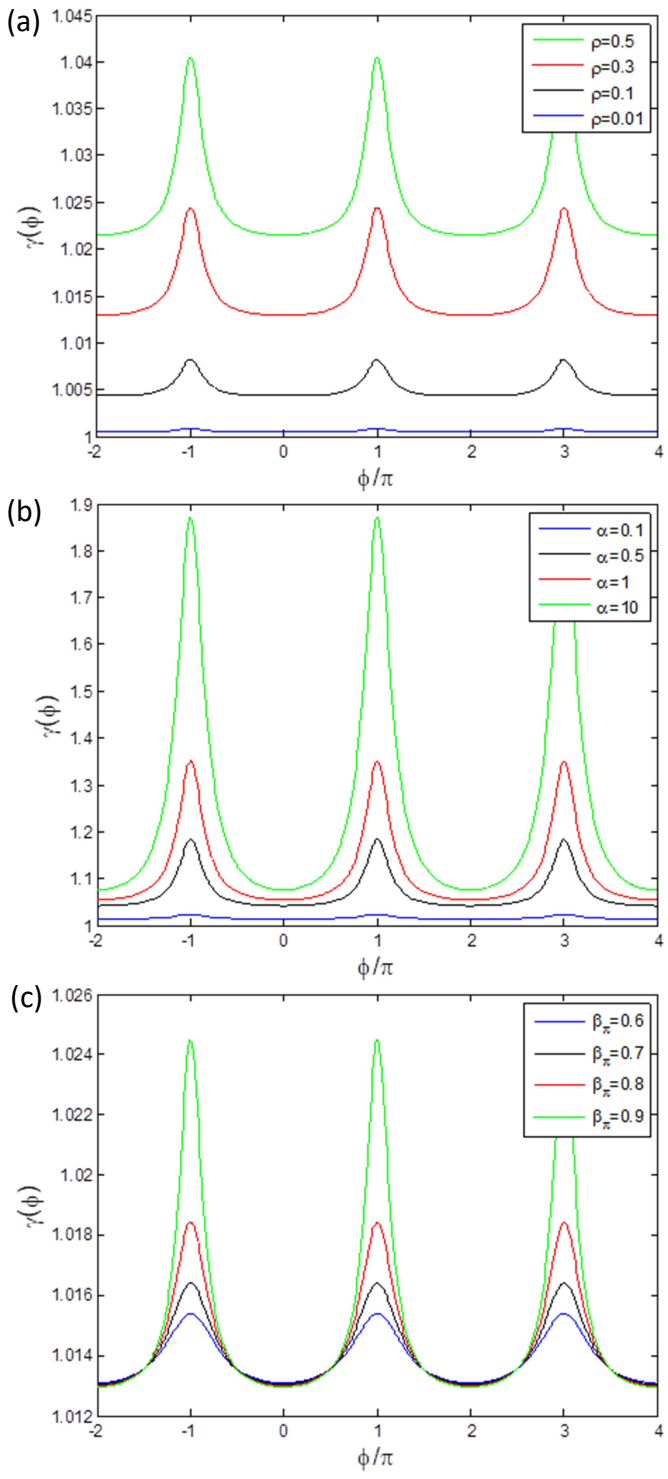

Figure 3.11: (a) Plot of $\gamma(\phi)$ for four different values of ρ with β_π= 0.9 and α= 0.1. (b) Plot of $\gamma(\phi)$ for four different values of α with β_π= 0.9 and ρ= 0.3. (c) Plot of $\gamma(\phi)$ for four different values of β_π with α= 0.1 and ρ= 0.3

one device oxidation run to the next. In order to achieve a tuning of 1 GHz (20% tuning range), while staying in the limit of $\beta_\pi < 1$, I typically aimed for a value of $\beta_\pi = 0.9$.

From the plots in Fig. 3.12, one sees that γ_{max} occurs at odd multiples of π (*i.e.* at $\phi = \cdots -3\pi, -\pi, \pi, 3\pi, 5\pi \cdots$) and γ_{min} occurs at even multiples of π (*i.e.* at $\phi = \cdots -4\pi, -2\pi, 0, 2\pi, 4\pi \cdots$). This can be checked by taking a derivative. Thus,

$$\gamma_{max}^2 = \gamma^2(\pi) = 1 + \frac{\alpha\rho}{(\alpha+1)^2} \cdot \frac{-\beta_\pi + \alpha + 1}{-\beta_\pi + 1} \tag{3.82}$$

and

$$\gamma_{min}^2 = \gamma^2(0) = 1 + \frac{\alpha\rho}{(\alpha+1)^2} \cdot \frac{\beta_\pi + \alpha + 1}{\beta_\pi + 1}. \tag{3.83}$$

Equation (3.73) then yields

$$\frac{\Delta f_{LC}}{f_0} = \frac{\sqrt{1 + \frac{\alpha\rho}{(\alpha+1)^2} \cdot \frac{-\beta_\pi + \alpha + 1}{-\beta_\pi + 1}} - \sqrt{1 + \frac{\alpha\rho}{(\alpha+1)^2} \cdot \frac{\beta_\pi + \alpha + 1}{\beta_\pi + 1}}}{\sqrt{\left(1 + \frac{\alpha\rho}{(\alpha+1)^2} \cdot \frac{-\beta_\pi + \alpha + 1}{-\beta_\pi + 1}\right) \cdot \left(1 + \frac{\alpha\rho}{(\alpha+1)^2} \cdot \frac{\beta_\pi + \alpha + 1}{\beta_\pi + 1}\right)}}, \tag{3.84}$$

For $\alpha = 0.1$, $\rho = 0.3$, $\beta_\pi = 0.9$ this gives a fractional tuning range of approximately 1%, which is too small to be useful. On the other hand, for $\alpha = 10$, $\rho = 0.3$, $\beta_\pi = 0.9$, I find $\delta f / f_0$= 20%, which is what I was aiming for.

3.4.3 Single-Loop Resonator Tuning as a Function of Applied Current

So far I have only shown the resonator's response as a function of the phase difference across the loop junction. However, for direct comparison with data it is useful to express the resonance frequency as a function of the tuning current I apply to the flux coil (see Section 3.4). Figure 3.12 shows a simplified, lumped-element circuit schematic of my tunable resonator including the input drive coil that couples magnetic flux into a single tuning loop. This imput flux coil carries a current I_f and couples to the tunable

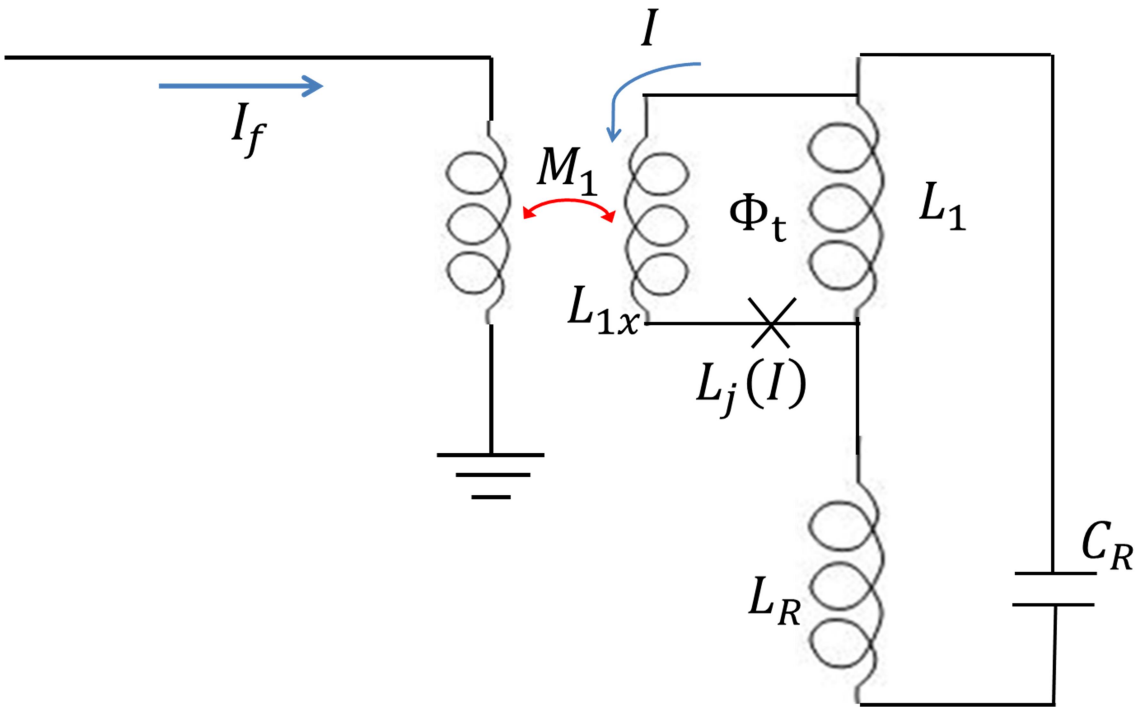

Figure 3.12: Schematic of a flux tunable resonator coupled to input flux coil. A dc current I_f is passed through the coil and couples flux Φ_x into the tuning loop of the resonator through mutual inductance M. This induces a circulating current in the tuning loop I which then modulates the overall inductance of the circuit and tunes the resonator.

resonator through a mutual inductance M. The flux from this coil induces a circulating current I_{loop} in the loop.

From (3.60) the current through the loop may be written as

$$I_{loop} = I_0 \sin(\phi)\,. \tag{3.85}$$

However, using the fact that the superconducting condensate wave function must be single-valued [12-14], one finds that $\phi = -2\pi\Phi_T/\Phi_0$ and Eq. (3.75) may be recast as

$$I_{loop} = -I_0 \sin\left(2\pi \frac{\Phi_T}{\Phi_0}\right), \tag{3.86}$$

where Φ_T is the total flux linked into the loop. This total flux is made up of the externally applied flux Φ_{ext} and the flux created by the circulating current I_{loop}

$$\Phi_t = \Phi_x + L_{loop} I_{loop} . \tag{3.87}$$

The external flux term is the flux MI_f applied from the flux coil to the tuning loop through the mutual inductance plus whatever background flux Φ_{x0} is present (*i.e.* from the screened earth's magnetic field, from trapped vortices, *etc.*) so that

$$\Phi_x = MI_f + \varphi . \tag{3.88}$$

Thus, I can write

$$I_{loop} = -I_0 \sin\left(\frac{2\pi}{\Phi_0}\left[L_{loop} I_{loop} + MI_f + \Phi_{x0}\right]\right). \tag{3.89}$$

Using Eq. (3.77), this expression becomes

$$I_{loop} = -I_0 \sin\left(\frac{\beta_\pi}{I_0}\left[I_{loop} + \frac{MI_f + \varphi}{L_{loop}}\right]\right). \tag{3.90}$$

For a given I_f and Φ_{x0}, the transcendental Eq. (3.91) may be solved to obtain the current I_{loop} in the loop. To get a better understanding of the parameters involved in this, I now define

$$z \equiv \frac{\beta_\pi}{I_0}\left[I_{loop} + \frac{MI_f + \Phi_{x0}}{L_{loop}}\right]. \tag{3.91}$$

Applying this to Eq. (3.91) gives

$$-\frac{z}{\beta_\pi} + \frac{MI_f + \varphi}{I_0 L_{loop}} = \sin(z) . \tag{3.92}$$

Plots of both sides of (3.93) as a function of z with $\varphi = 0$ are shown below in Fig. 3.13. The solutions are where the curves intersect.

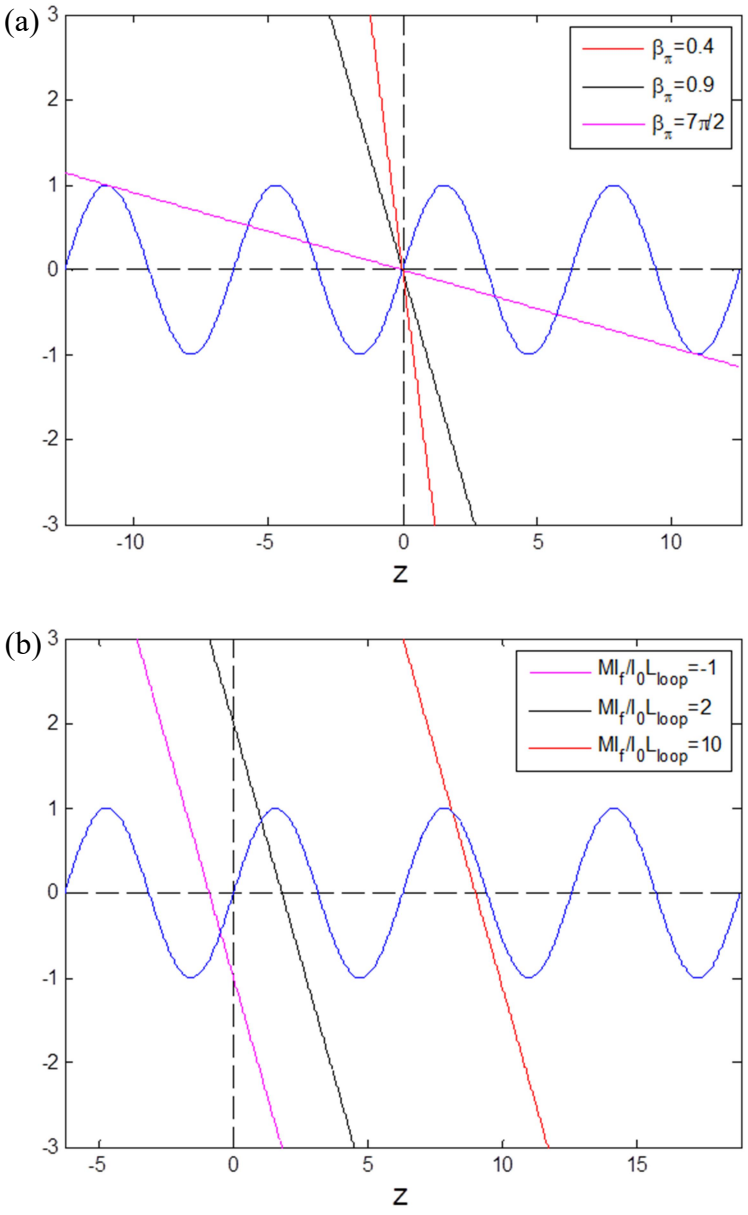

Figure 3.13: Plots of both sides of the transcendental equation shown in (3.49). Plot (a) shows the effect of varying the β_π parameter, and plot (b) shows how the solution as I_f is varied while keeping β_π at the nominal value of 0.9.

With Fig. 3.13 in hand, one can better understand the behavior of the tunable resonators. For example, in Fig. 3.13(a) a larger β_π corresponds to a less steep line. Once β_π reaches a critical value, there are multiple solutions (intersections) corresponding to multiple possible trapped magnetic flux values in the loop. The behavior of the tuning would then be hysteretic, which would not be desirable for my purpose of building a consistent, variable coupling element. The critical value of β_π occurs at the point where the slope of the linear line $(-1/\beta_\pi)$ is greater than the slope of the sine function at its most negative point. This point occurs when z is at odd multiples of π (i.e. $z = \cdots -3\pi, -\pi, \pi, 3\pi \cdots$), and the slope at these points is -1. Putting this together gives

$$-\frac{1}{\beta_\pi} \geq -1\,, \tag{3.93}$$

or,

$$\beta_\pi \geq 1\,. \tag{3.94}$$

So, $\beta_\pi > 1$ is the limit where multiple solutions exist and the tuning loop could trap different flux states. I chose $\beta_\pi < 1$ specifically to avoid this limit because of the hysteresis introduced.

The other thing in Fig. 3.13 I can comment on is how the solution changes as a function of I_f. When the slope of $\sin(z)$ is positive, the solution changes gradually, while, when the slope is negative, the solution changes rapidly. This is the explanation for the sharp changes in $\gamma(\phi)$ near the maximum value and the much more gentle variation near the minimum. This corresponds to a more gentle variation of the resonator

frequency with flux near the maximum tuning frequency and a much more rapid variation near the minimum frequency.

Finally, I need to address the sign (positive or negative) of the inductance as a function of current. The sign of the Josephson inductance is determined by $\cos(\phi)$. Following as above, the cosine of the phase difference is given by

$$\cos(\phi) = \cos\left(\frac{\beta_\pi}{I_0}\left[I_{loop} + \frac{MI_f + \varphi}{L_{loop}}\right]\right). \tag{3.95}$$

So, once a solution is found to the transcendental equation in (3.90), I can find the sign of the inductance by calculating

$$sgn\left(\cos\left(\frac{\beta_\pi}{I_0}\left[I_{loop} + \frac{MI_f + \Phi_{x0}}{L_{loop}}\right]\right)\right). \tag{3.96}$$

Another option for finding the Josephson inductance, and what I used in analyzing my data, is to solve for the phase difference directly. Putting Eq. (3.60) into Eq. (3.90) gives

$$I_0 \sin(\phi) = -I_0 \sin\left(\frac{\beta_\pi}{I_0}\left[I_0 \sin(\phi) + \frac{MI_f + \varphi}{L_{loop}}\right]\right). \tag{3.97}$$

Equating the terms inside the sine functions yields

$$\phi = -\beta_\pi \sin(\phi) - \frac{2\pi M}{\Phi_0} I_f + \phi_0\,, \tag{3.98}$$

where $\phi_0 = -2\pi\varphi/\Phi_0$. Solving this transcendental equation for ϕ as a function of I_f is nice because, when used in conjunction with Eq. (3.64), the sign of the inductance is already taken care of.

3.4.4 Full Model

As I discuss in a later section of this chapter, and in Chapter 6, my tunable resonator designs always had two tuning loops rather than the single loop mentioned in the previous section. There are several potential advantages to two loops, including an increased tuning range and isolation of the flux coil from from the cavity RF frequencies. To couple flux into these two loops, I used a "split" input coil. A circuit schematic of this system is shown in Fig. 3.14. The total flux bias current is split between two branches of the coil. I call the current down each branch I_f and assume the magnitude of the split currents in each arm are equal. Note that Fig. 3.14 is very similar to Fig. 3.12, except there are two tuning loops.

With two tuning loops, the function $\gamma_2^2(\phi)$ can be defined as

$$\gamma_2^2(\phi) \equiv 1 + \frac{\alpha_1\rho_1}{(\alpha_1+1)^2}\cdot\frac{\beta_{\pi1}\cos(\phi_1)+\alpha_1+1}{\beta_{\pi1}\cos(\phi_1)+1} + \frac{\alpha_2\rho_2}{(\alpha_2+1)^2} \cdot\frac{\beta_{\pi2}\cos(\phi_2)+\alpha_2+1}{\beta_{\pi2}\cos(\phi_2)+1}. \tag{3.99}$$

From Eq. (3.99) it is clear that the second and third terms may add or subtract from each other. If both loops are in their strong tuning regime the effect adds together. As an example consider the case with $\alpha_1 = \alpha_2 = 0.1$, $\rho_1 = \rho_2 = 0.3$, and $\beta_{\pi1} = \beta_{\pi2} = 0.9$. With only one loop, the fractional tuning range was approximately 1.1%; with two loops, the tuning range increases to 2.1%.

For the circuit in Fig. 3.14, we also have the following flux-phase relations

$$\phi_1 = -\beta_{\pi1}\sin(\phi_1) - \frac{2\pi M_1}{\Phi_0}I_f + 2\pi\frac{\Phi_{x1}}{\Phi_0} \tag{3.100}$$

and

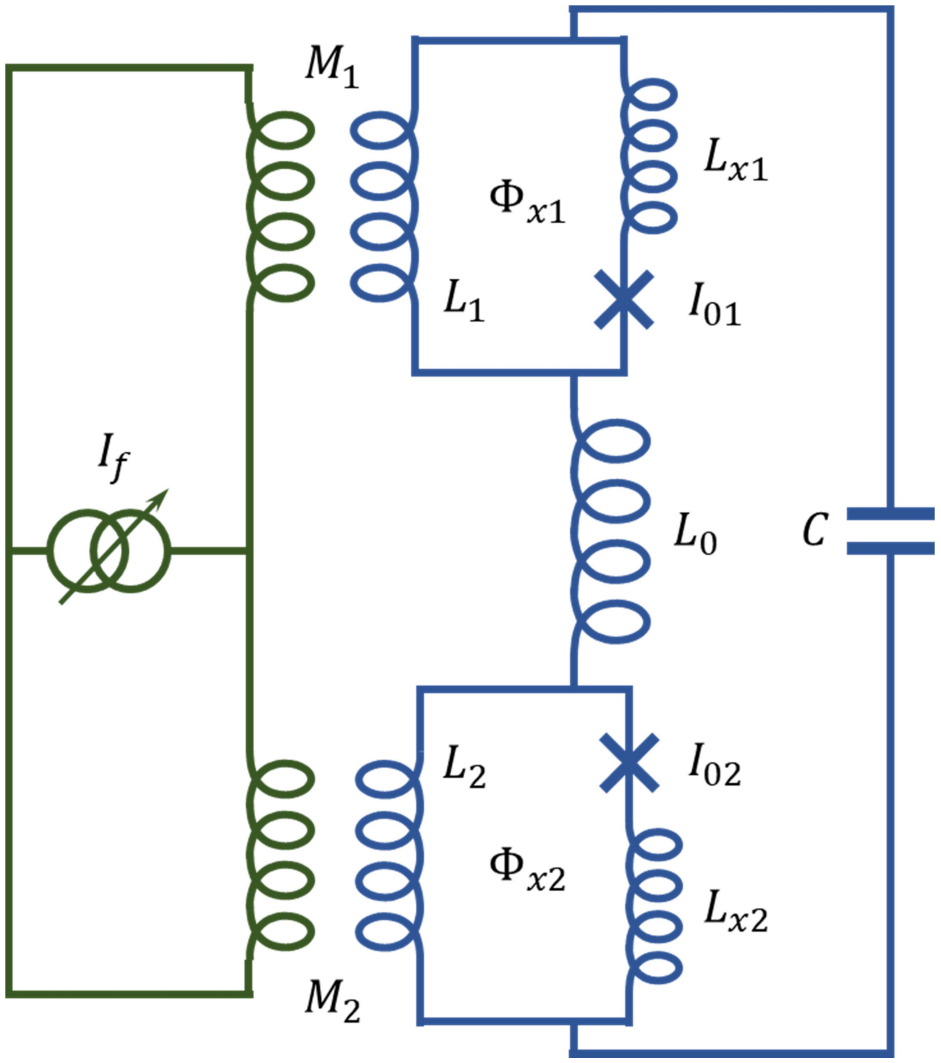

Fig. 3.14: Full model of my tunable resonators. As in the actual devices there are two tuning loops.

$$\phi_2 = -\beta_{\pi 2}\sin(\phi_2) - \frac{2\pi M_2}{\Phi_0} I_f + 2\pi \frac{\Phi_{x2}}{\Phi_{x0}} \tag{3.101}$$

for the phase differences across each of the junctions, where $\beta_{\pi 1} = 2\pi L_{loop} I_{01}/\Phi_0$, $\beta_{\pi 2} = 2\pi L_{loop2} I_{02}/\Phi_0$, M_1 and M_2 are the mutual inductances between the tuning coil and loops 1 and 2, respectively, and Φ_{x1} and Φ_{x2} are the offset flux values for loops 1 and 2, respectively. The total inductance of the circuit is then given by

$$L_t(I_f) = L_0 + \frac{L_1\left(L_{1x} + L_{j1}(\phi_1)\right)}{L_1 + L_{1x} + L_{j1}(\phi_1)} + \frac{L_2\left(L_{2x} + L_{j2}(\phi_2)\right)}{L_2 + L_{2x} + L_{j2}(\phi_2)}, \tag{3.102}$$

where $L_{j1}(\phi_1) = \Phi_0/2\pi I_{01}\cos(\phi_1)$, $L_{j2}(\phi_2) = \Phi_0/2\pi I_{02}\cos(\phi_2)$, L_0 is the geometric inductance of the resonator, L_1 and L_2 are the geometric inductances of the tuning loop branches without a junction in loops 1 and 2, respectively, and L_{1x} and L_{2x} are the geometric inductances of the tuning loop branches with the junction in loops 1 and 2, respectively. Finally, the resonance frequency is then given by

$$f = \frac{1}{2\pi\sqrt{C L_t(I_f)}}. \tag{3.103}$$

The capacitance of the resonator was usually found using a formula for the capacitance of an interdigitated capacitor, which I describe in Section 3.5. Preliminary estimates for all the inductances are taken from FastHenry, but they were ultimately fit parameters. For more details on my characterization of these devices see Chapters 6-9.

3.5 Flux Bias Coils

Since my cavities were made from Al and were superconducting at the measurement temperature external magnetic fields were heavily screened. So, to couple

(a) 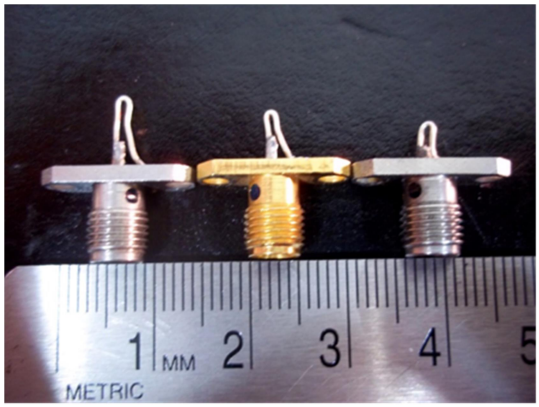

(b) 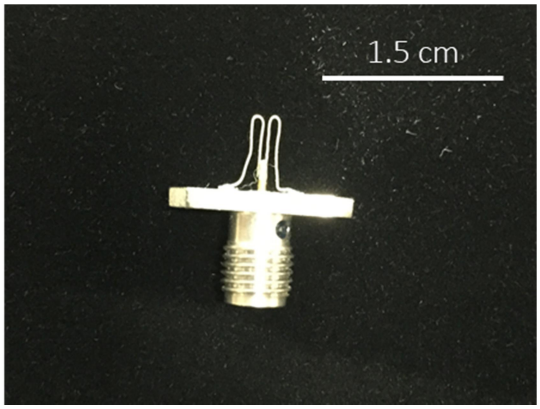

Fig. 3.15: (a) Photo of handmade single loop flux coils. (b) Photo of my first handmade split flux coil.

flux into the tuning loops of the tunable resonators, I added a flux coil inside the cavity. I first tried making single coils from a fine wire that went from the input pin of an SMA bulkhead connector to the body of the connector (see Fig. 3.15(a)). The main drawback to this coil was that it strongly coupled to the cavity mode, which severely limited the overall quality factor of the cavity. In my initial tunable resonator experiments I placed the device entirely over to a side of the cavity space. As I describe in Chapter 2, in that location the field of the TE_{101} cavity mode is uniform across the short dimension and is almost entirely magnetic.

In order to decouple the flux tuning coil from the cavity, I switched to a gradiometric design with two coils that produced flux in opposite directions. I refer to this as a "split" coil design. Figure 3.15(b) shows a photograph of the first version I made, which had two coils formed from two wires soldered to the SMA connector The use of this gradiometric design dramatically reduced the coupling of the flux coil to the

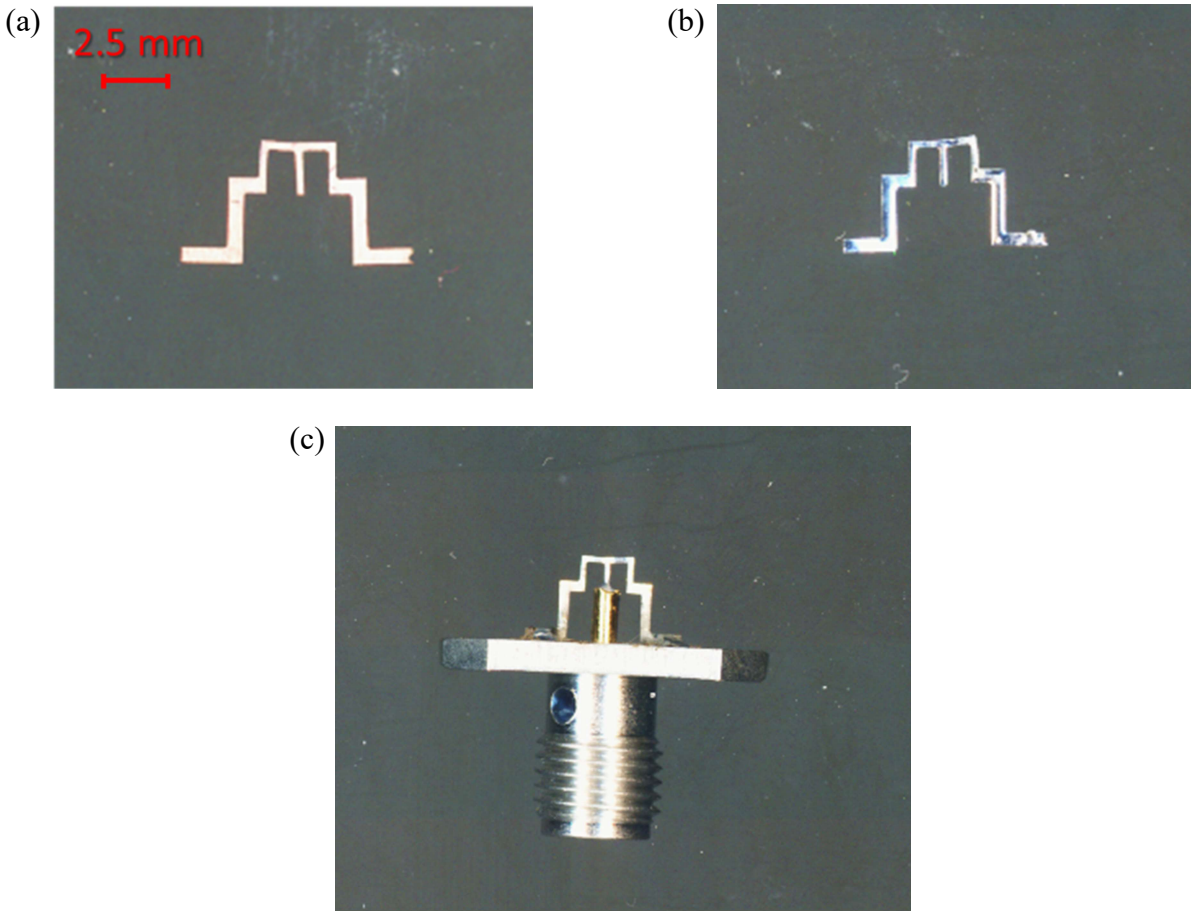

Fig. 3.16: (a) Photo of a machined split coil. (b) Photo of a machined split coil after being tinned with solder. (c) Photo of the completed split flux coil.

cavity. The coupling quality factor was roughly equal to 1000 with the single coils and this increased to ~10^6 with the split coil design mounted at the end of the cavity.

While I ran an experiment with the handmade version of these coils, it was difficult to make the two coils equal in size. To get equal sized coils, I had the Physics Machine Shop cut coils out of very thin copper foil using wire electrical discharge machining (EDM) (see Fig. 3.16(a). This allowed for consistent control over the length and size of the coils.

Once I had the machined flux loops, I first tinned them with 63:37 Pb:Sn rosin free solder to make sure that they would be superconducting at the measurement temperature. I usually dipped them in Super Safe no. 30 flux [15] before dipping them into the solder I had melted in a small pyrex container on top of a hot plate. Figure 3.16(b) shows a freshly tinned coil.

To complete assembling a split coil, I soldered the tinned coil to a Fairview Microwave SC3778 [16] half-moon connector. The overall length of the pin was a little too long; so, I used cutters remove some of the pin before soldering. This particular model of SMA pin connector has a passivated stainless steel body that was a little difficult to solder to. To overcome this, I used the much stronger LA-CO, N-3 all-purpose flux [16] and tinned the locations I would be soldering to on the body. I then held the coil in place on the pin and completed the solder joints. I would then typically use more of the Super Safe flux to get nice connections. Figure 3.17(c) shows a photo of a completed split coil.

Putting one of these split-coil connectors into a cavity affects the cavity's quality factor. In my experiments where I coupled two transmon qubits to a tunable resonator

(see Chapters 5-9), the chip and split-coil connector were placed in the middle of the cavity. In this position, the drive voltage coupling to the coil reduced the overall quality factor of the cavity to around 2000-3000; the coils acted somewhat like a large voltage pin coupler. While the low Q was unfortunate, I was able to take advantage of this by using the split coil connector both as the dc flux bias line and as the microwave signal output line (see Chapter 7).

3.6 Tunable Resonator Experiment

In this section I discuss my "mad Mickey" tunable resonator design. I start with a discussion of the design of the resonator. I then summarize the fabrication and the experimental setup. These topics are covered in greater detail in Chapters 6 and 7. Finally, I show results of measurements on device tunres_112115.

3.6.1 Device Design

The "mad mickey" tunable resonator looks like an angry Mickey Mouse. This design is based on a fixed-frequency resonator designed by Jared Hertzberg and developed by Kristen Voigt for an experiment involving coupling optically trapped atoms to superconducting resonators [18]. In fact, I used one of these resonators in my kinetic inductance tuning experiment discussed in Section 3.2 (see Fig. 3.1(a)). These resonators were designed with antennas attached to produce strong coupling to the cavity mode. Also, they were designed to have a relatively large superconducting volume to allow optically generated quasiparticles to diffuse away from the inductor and recombine.

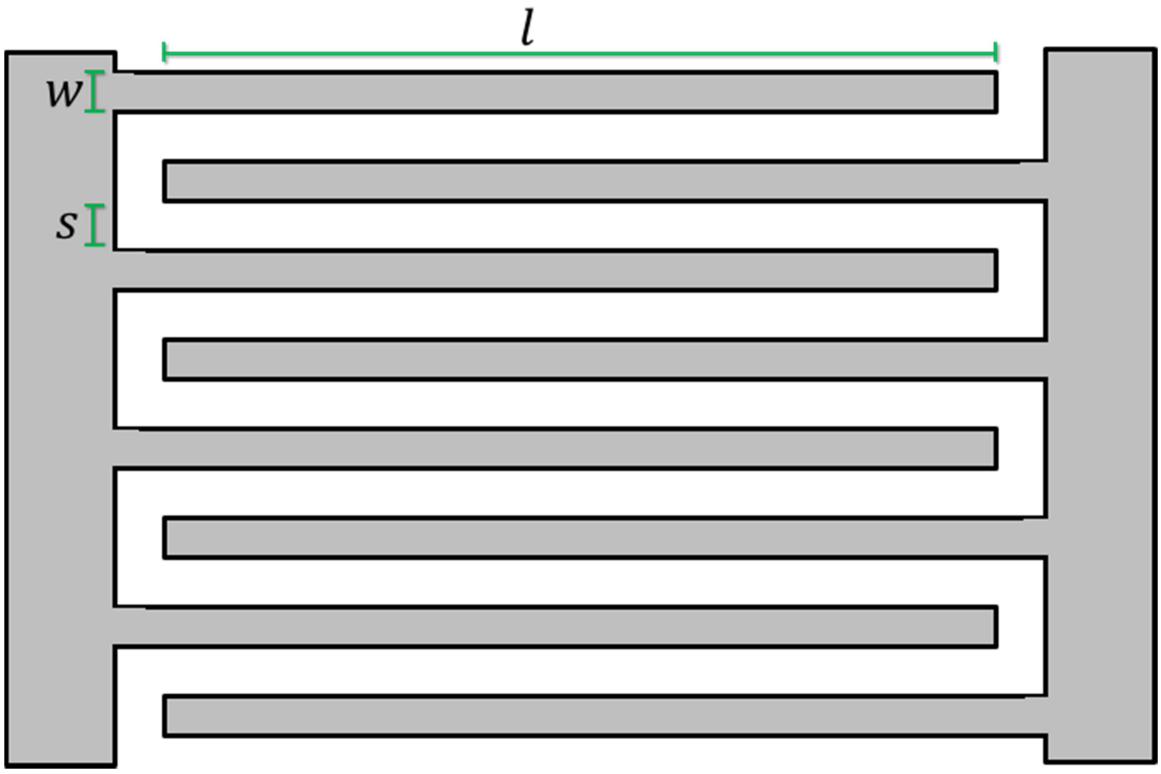

Fig. 3.17: Schematic of interdigital capacitor showing dimensions l, w, and s.

Using FastHenry, the expected inductance of the inductor in Fig. 3.1(a) was found to be approximately 2 nH. To estimate the capacitance of the IDC I used a formula for an interdigitated capacitor from ref. [19],

$$C = \varepsilon_c \frac{10^{-9}}{18\pi} \frac{K(k)}{K'(k)} (n-1) l \,, \tag{3.104}$$

In Fig. 3.18 I labelled the capacitor finger length l, the width w, and the spacing between the fingers s. Also, in Eq. (3.104), n is the total number of fingers (both electrodes combined), and the quantity ε_c is the effective permittivity

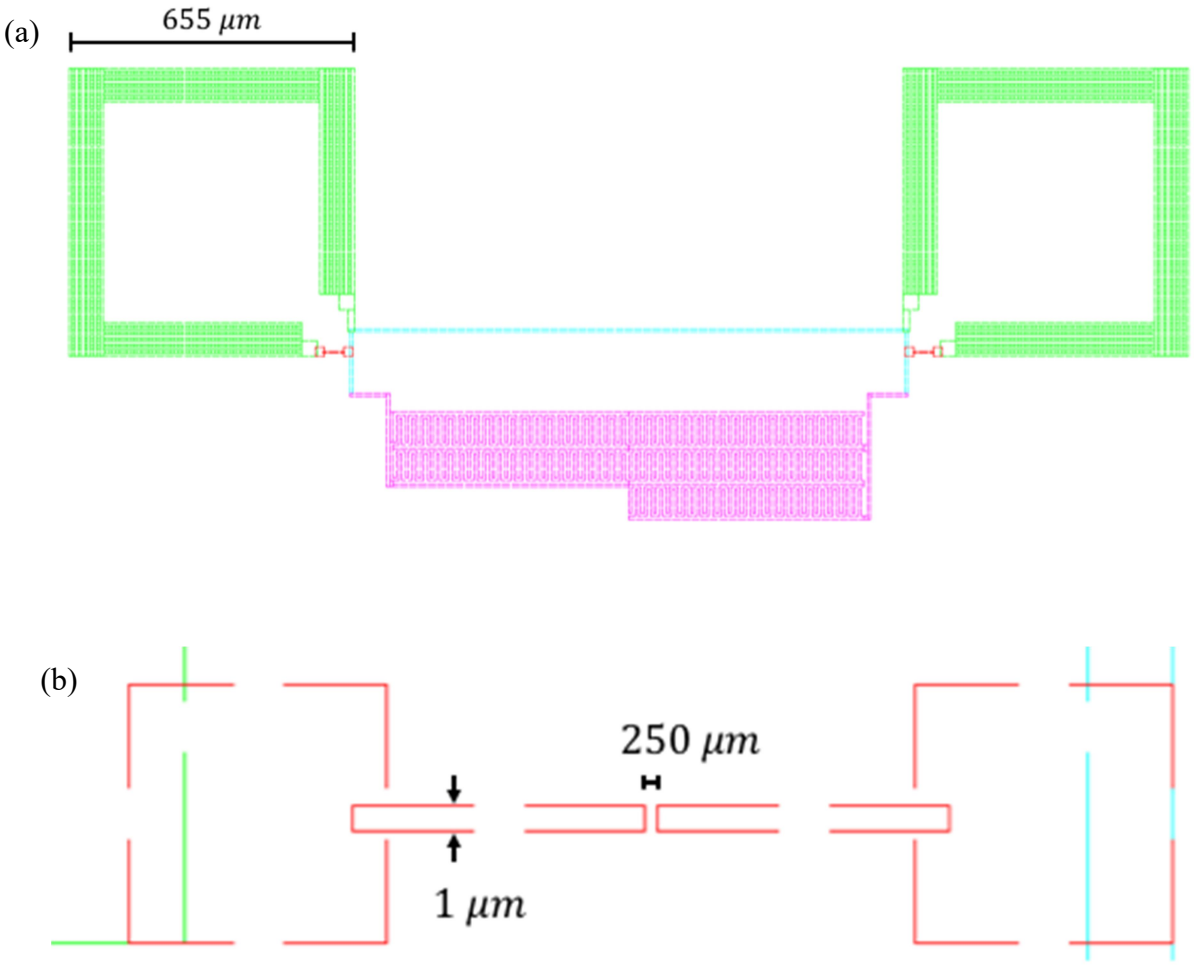

Fig. 3.18: (a) CAD rendering of the "mad Mickey" tunable resonator design. The green sections are the tuning loops, the red areas are the junctions, the light blue is the inductor line, and the purple is the interdigitated capacitor. (b) Detailed view of the junction pattern.

$$\varepsilon_c = \frac{\varepsilon_d + 1}{2} + \frac{\varepsilon_d - 1}{2\sqrt{1 + \frac{12h}{w}}}, \tag{3.105}$$

where h is the height of the fingers above the ground plane, w is the width of the fingers, and ε_d is the relative permittivity of the substrate. The second term in Eq. (3.105) arises naturally from the method of images. For an IDC on a sapphire chip in a cavity, I take $h \to \infty$, which gives $\varepsilon_c \approx (\varepsilon_d + 1)/2 = 5.5$ for sapphire with $\varepsilon_d = 10$. Finally, $K(k)$ and $K'(k)$ are the complete elliptical integral of the first kind and its complement [Arfken], respectively, where $k = \tan^2(\pi a/4b)$, $a = w/2$, and $b = (w + s)/2$. From the properties of the elliptic integral, one has $K'(k) = K\left(\sqrt{1 - k^2}\right)$.

For all my devices (including the TRES design discussed in Chapter 6) I used $w = s = 5$ μm, which gives $k = \tan^2(\pi/8)$. Equation (3.104) then yields

$$C = (4.57135 \cdot 10^{-11})(n - 1)l\,. \tag{3.106}$$

Table 3.2: Design parameters for resonator device tunres_112115.

Parameter	Value
L_0	2 nH
C_0	367 fF
f_0	5.8 GHz
L_1	50 pF
L_{1x}	850 pF
β_π	0.9
Δf	30 MHz

The "mad Mickey" design used a length of $l = 42.5\,\mu m$ and $n = 190$ fingers. So, I estimate the capacitance should be $C \approx (4.57135 \cdot 10^{-5})(189)(42.5) = 367\,fF$. This, combined with the inductance estimate yields a resonance frequency of $f_0 \approx 5.87\,GHz$.

A CAD layout of my this resonator design is shown in Fig. 3.18(a). Comparing Fig. 3.1(a) and Fig. 3.18, one sees that several modification were made. First, I removed the dipole antennas. This device was designed to couple to the magnetic field of the mode instead of the electric field; the antennas were for coupling to the electric field. Second, I removed the extra superconducting volume that was present in the original design. In my experiments there was no light intentionally involved; so, I did not need to include the additional volume for quasiparticle recombination. Finally, I added two rf-SQUID loops to the inductor to allow the resonant frequency to be tuned.

As noted above, the β_π parameters of the loops were important for setting the tuning range. As I described in section 3.3, I required $\beta_\pi < 1$ to prevent multiple trapped flux states for a given applied flux. However, if β_π was too small, the device would have a tuning range too small to be useful. A value of $\beta_{\pi 1} = \beta_{\pi 2} = 0.9$ was a good compromise for this design.

For the loops, I wanted loop size to be large enough that they would easily be able to couple to the flux tuning coils but not so large that they would take up too much room. I decided on a size of 460 μm x 460 μm. However, loops this size have a relatively large geometric inductance if I were to use 5 to 7 μm wire widths. To lower the geometric inductance I made the loop wires considerably wider [20]. After simulating different values of loop widths with FastModel's FastHenry, I decided on a 55 μm wire width,

which gives a loop inductance of L_{loop}= 0.9 nH. This means that I will need a critical current of roughly $I_0 \approx 0.3\ \mu A$.

For ease of fabrication, I chose the junction area to be 1 μm^2. The junction pattern was formed by two 1 μm wires coming together to a 250 nm x 1μm bridge (see Fig. 3.19(b)). I didn't want to make the junction much bigger than this because large bridges tend to collapse and large area junctions would contribute an appreciable amount of capacitance ($\approx 90\ fF/\mu m^2$) and dielectric loss.

I then used Eqs. (3.99) and (3.72) to estimate the tuning range,. The FastHenry estimates for the parameters L_1= 50 pH and L_{1x}= 850 pH. This gives $\alpha = L_1/L_{1x} = 0.05$ and $\rho = L_{loop}/L_0 = 0.45$, which lead to an estimate of $\Delta f/f_0 \approx 0.5\%$. So, for f_0=5.8 GHz, I expected a tuning range of about 30 MHz. This was quite small compared to my later tunable resonator designs, but it served quite well as a proof-of-principle. I have summarized all these estimates and design parameters into Table 3.2.

3.6.2 Device Fabrication

In Fig. 3.19 I show an optical photo of device tunres_112115. I used e-beam lithography and double-angle evaporation to fabricate this device, both of which are described in detail in Chapter 6. Here, I discuss the main differences in the fabrication process for these early devices.

For this early series of devices, I only used one anti-charging layer: a 15 nm thick layer of evaporated Al. Unfortunately, this was insufficient to prevent charging effects on my sapphire substrates. For example, I found that after a few seconds of trying to focus the beam, the whole screen would wash out. This only gave me brief moments of

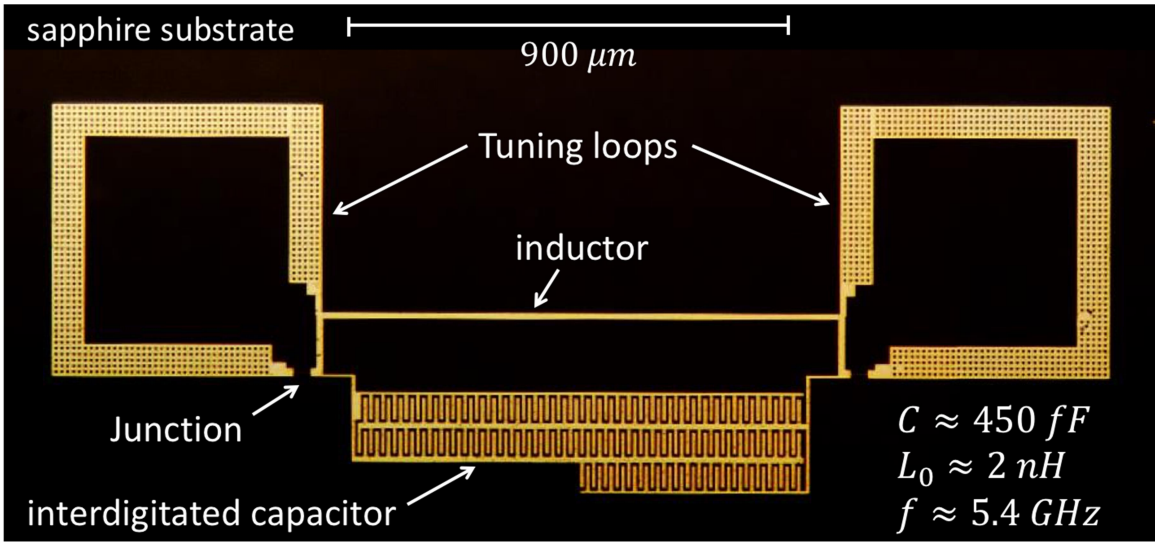

Fig 3.19: Optical photo of tunable resonator device tunres_112115. In the photo I have labeled important pieces of the design.

focus time. Due to this, I was never able to properly focus the beam, which meant I had to keep the junction sizes relatively large. This charging issue also meant that I had to run at higher e- beam dose values, leading to an increased spot dwell time and an increased overall writing time.

As I discuss in Chapter 6, I eventually started using aquaSAVE conducting polymer [21] as a second anti-charging layer in addition to the Al layer. This completely removed the charging issue, and I had no further issues in my later devices with focusing the beam.

3.6.3 Experimental Setup

As in the previous section, here I discuss the main differences between the setup

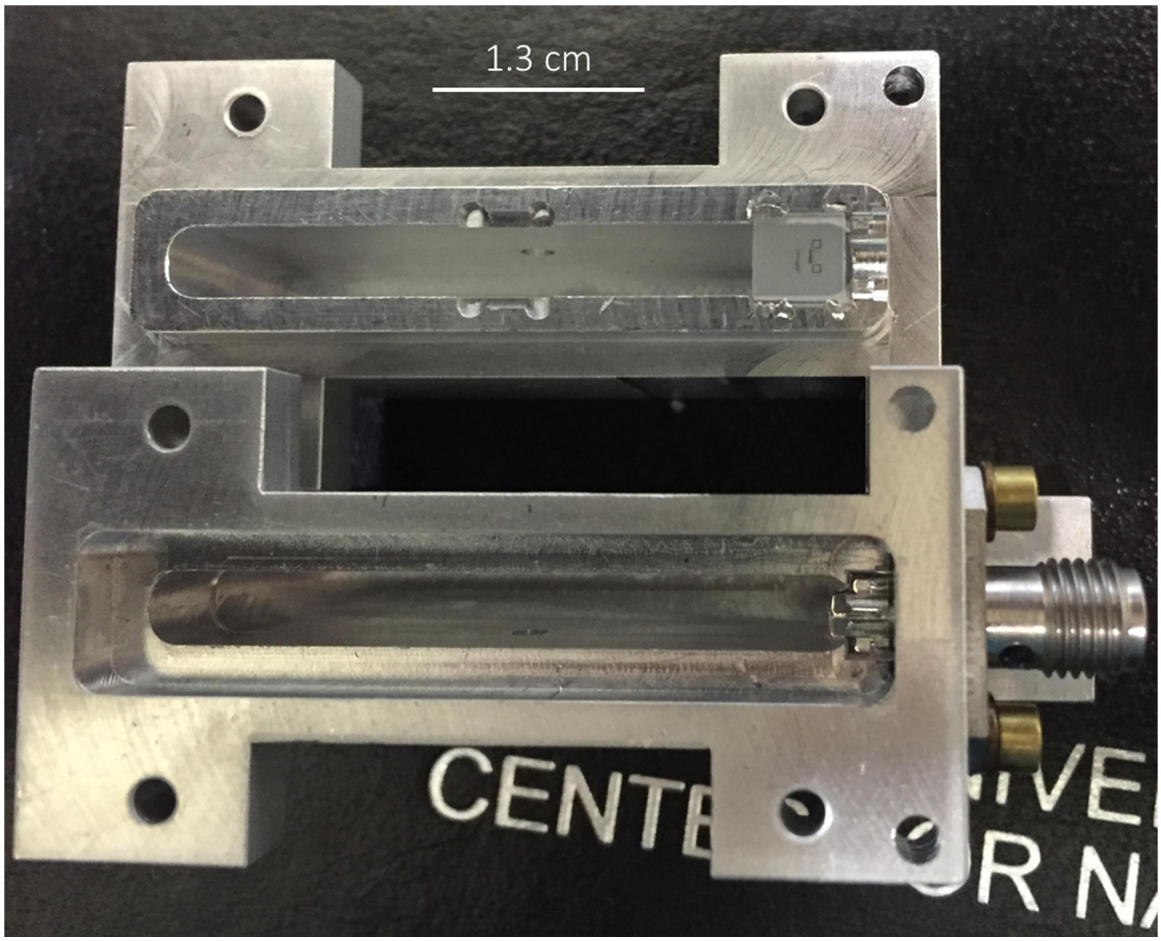

Fig. 3.20: Photo of cavity SI-3 before assembly. Mounted in this cavity is device tunres_112115.

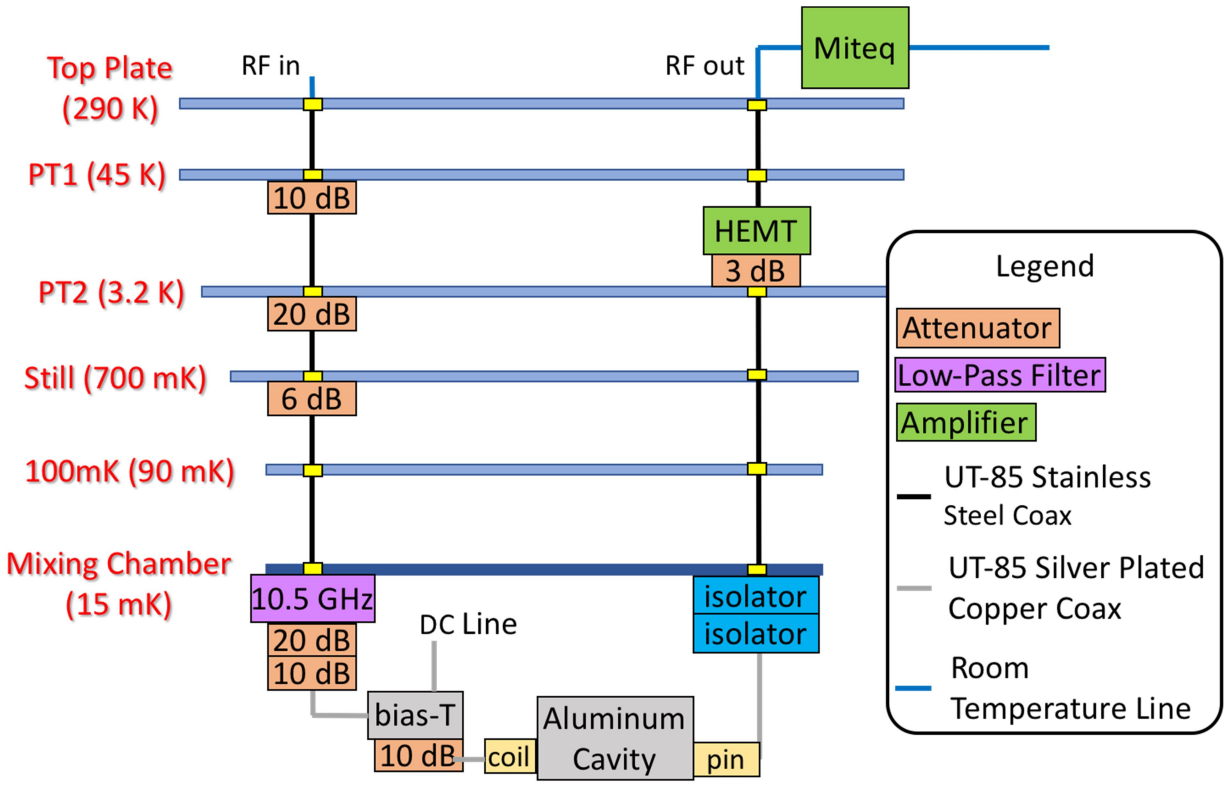

Fig. 3.22: Microwave line setup for tunable resonator measurements.

for measuring device tunres_112115 vs. the setup I used on my later TRES devices. I used Al cavity SI-3 for this tuning experiment (see Fig. 3.20). As Fig. 3.21 shows, the tunable resonator was mounted near the end of the cavity space, where the fundamental TE_{101} mode is magnetic at its maximum. In the figure I show a tunable resonator device mounted. As seen in the photo, the chip is mounted near the end of the cavity space where the mode field is entirely magnetic. In the photo I have labeled the device and the SMA split-coil flux loop, which is discussed in section 3.4.

I measured device tunres_112115 in the Oxford Triton 200 dilution refrigerator [22] I discuss in chapter 7 for measuring device TRES_092917. However, this

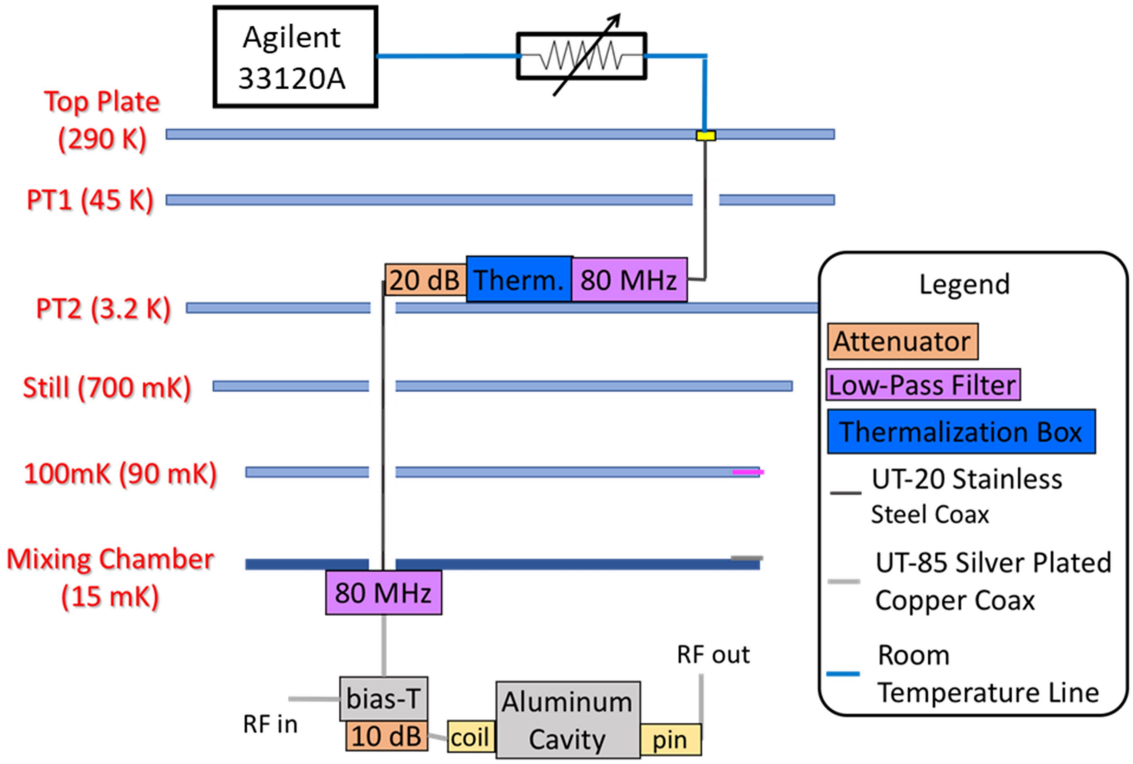

Fig. 3.23: DC bias line setup for applying flux to the tunable resonators.

experiment was done before I installed the Cu thermal shield and CryoPerm magnetic shield on the mixing chamber (see chapter 7). Also, at this time the microwave components were not properly thermalized. To take microwave spectroscopic measurements on the resonator, I used the same VNA setup I show in chapter 7. Other important differences occur in the microwave input/output lines and on the DC flux bias line. In Fig. 3.22, I show the microwave line setup used in this experiment. As seen in Fig. 3.22, the microwave input signal first passes through a K&L 10.5 GHz low-pass filter [23]. It then goes through a 20 dB attenuator and a 10 dB attenuator before arriving at the Anritsu K250 biase-tee [24]. The input signal is then combined with the DC bias

current. Finally, this combined input signal/DC bias current passes through a 10 dB attenuator before arriving at the cavity through one of the split loop flux bias coil connectors I describe in section 3.4.

The output signal from the cavity passes through two Pamtech CTH1365KS cryogenic isolators [25] at the mixing chamber. It then goes through a 3 dB attenuator right before the cold HEMT amplifier [hemt] on the PT2 stage (see Fig. 3.22). The signal was then amplified through a Miteq AMF-3F-04000800[26] low-noise amplifier at room temperature.

The DC flux bias line setup is shown in Fig. 3.23. When compared to the DC bias line I show in Fig. 7.9, many differences become apparent. I used an Agilent 33120A arbitrary waveform generator [27] as the voltage source. I turned this into a current source by driving this voltage through a large resistor chosen so that the overall resistance of the bias line was 1 kΩ. From room temperature to the PT2 stage, the DC current was carried by a 38 cm long UT-20 SMA coaxial cable [27] with stainless steel inner and outer conductor. This material was chosen to reduce the heat load on the PT2 stage. At the PT2 stage, the current passed through a Mini-Circuits 80 MHz low-pass filter [28] that was connected to a breakout thermalization box that thermally grounded the inner conductor of the line. The current then went into an XMA 20 dB attenuator [XMA attenuator]. I was worried about attenuation; so, I used attenuators just like I would on a microwave line. However, this attenuator acted as a current divider. The remaining current was carried to the mixing chamber via a 50 cm section of the same stainless steel UT-20 SMA cable. At the mixing chamber I used another Mini-Circuits 80 MHz low-pass filter right before the DC input of the Anritsu K250 bias-tee [24]. From the bias-tee,

I passed the current through an XMA 10 dB attenuator right before the SMA flux bias coil attached to the cavity.

While this DC line configuration I describe worked for this particular experiment, there were several issues that needed to be addressed. First, when supplying a 1 mA current into the line at room temperature, I measured only 0.1 μA of current at the split coil. This reduction by a factor of 10,000 due to the attenuation made it extremely difficult to put many flux quanta in the tuning loops due to the limited range of the voltage source. Another big issue was that there was obvious heating observed when biasing the tuning coils. The heating was from the attenuators dissipating current and from dissipation in the high-resistance UT-20 stainless steel lines. I estimated that the device could have been seeing a noise temperature in excess of 100 K. Fortunately, this did not affect the resonator too much, but as soon as qubits were involved things quickly fell apart. In Chapter 7 I discuss improvements I made to be able to tune the resonator without the current dissipation or heating.

3.7 Tunable Resonator Results

3.7.1 Resonator Spectroscopy

The Keysight E5071C VNA measured the complex scattering parameter S_{21} over a range of frequencies. To view the resonances I typically plotted the magnitude of S_{21} vs. frequency f. In order to fit to the complex expression in Eq. (3.12), I also recorded the phase of the signal.

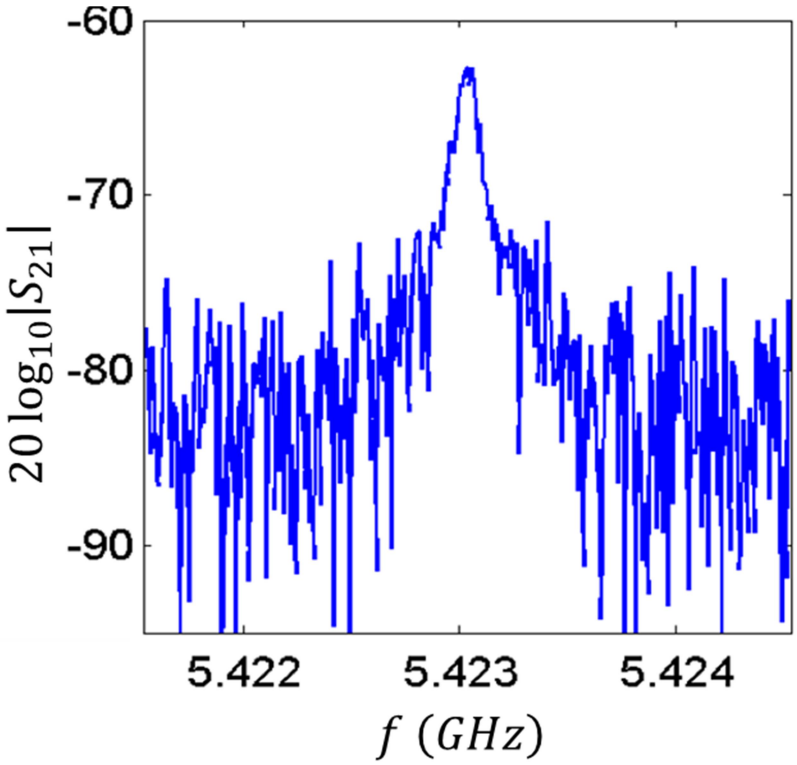

Fig. 3.24: VNA measurement of $|S_{21}|$ vs. frequency f of the resonance in device tunres_112115.

In Fig. 3.24 I show a typical VNA S_{21} spectrum for device tunres_112115. The x-axis is the frequency range swept over by the VNA and the y-axis is a log scale plotting $20\log_{10}|S_{21}|$. The flux maps involved setting the flux bias current I_f and measuring the $S_{21}(f)$ spectrum repeated over the number of flux bias points chosen.

Figure 3.25(a) shows a false color map of the magnitude of S_{21} vs. I_f for device tunres_112115. The x-axis of this plot is the current I_f applied at room temperature into the DC bias flux line. I took into account the current division from the attenuators when doing fits to the data, but here I show the current applied. The resonance frequency of

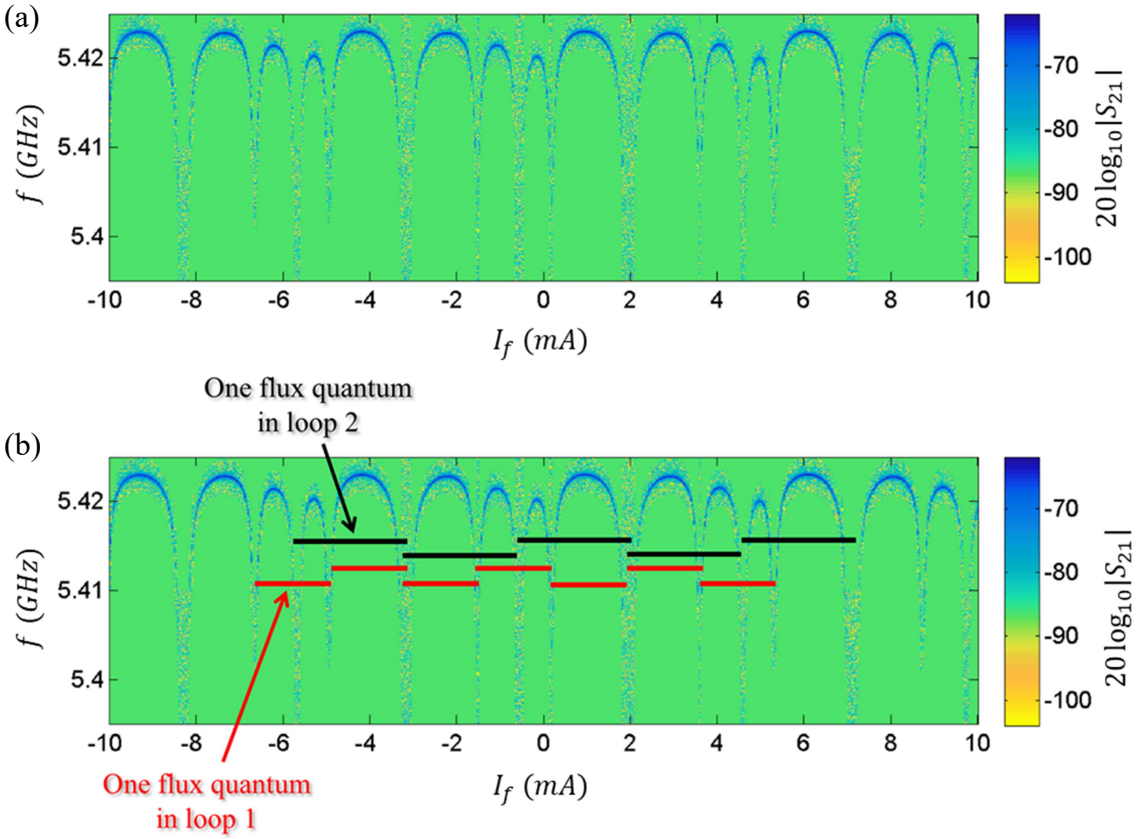

Fig. 3.25: (a) False color plot of a spectroscopic measurement on the tunable resonator device tunres_112115 as a function of applied current I_f. The color corresponds to the magnitude of $|S_{21}|$. (b) Same plot as (a), but with bars that correspond to the addition of a single quantum of flux in loop 1 (red bars) and in loop 2 (black bars).

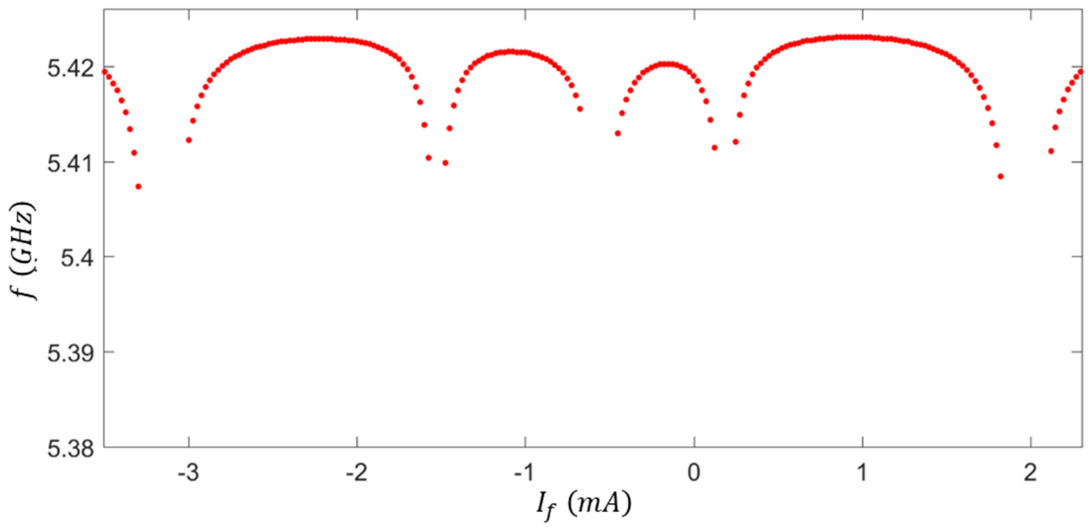

Fig. 3.26: Observed resonance frequency f_r vs. bias flux current I_f in device tunres_112115.

the resonator clearly changes as a function of the applied current. The sharp dips are where one or more of the tuning loops are in their strong tuning regime. Note that there appears to be at least three different sizes of tuning dips. The smallest dips correspond to one tuning loop, which I'll call loop 1. The slightly larger dips are when loop 2 is being tuned through a half integer flux quantum bias. Finally, the largest dips are when both loops have half-integer flux (see section 3.3.4 for a discussion on this behavior).

As discussed in section 3.3, the tuning in each loop is periodic over a flux quantum. Thus, the ΔI_f distance between dips associated with a given loop is set by the mutual inductance between the loop and the flux bias coil. In Fig. 3.25(b) I show the same plot as in Fig. 3.25(a); except, I have drawn bars onto the plot that correspond to the addition of a single flux quantum in a loop. The red bars are for loop 1 and the black are

for loop 2. Since the red bars are shorter than the black bars, it must be that the mutual inductance for loop 1 is greater than the mutual inductance to the flux coil seen by loop 2.

The reason the loops produce tuning dips of different depths is due to the β_π parameters. Since the tuning dips corresponding to loop 1 are smaller than that of loop 2, it should be that $\beta_{\pi 1} < \beta_{\pi 2}$.

One key question that Fig. 3.25 cannot quite answer is what tuning range is actually being achieved. To find this out, I fit the $|S_{21}|$ peaks at each bias current to find the center frequency. In Fig. 3.26, I plot the resulting resonance frequencies f_R vs. the bias current I_f. Note that there are no red points for frequencies less than 5.405 GHz. It turns out that the resonance became unobservable by direct means in these areas. The peaks broaden out and get lost in the noise. Since the tuning range is heavily influenced by the β_π parameters, any fits run on this data would be insufficient for extracting all the parameters. To actually find out the tuning range, we had to measure the effect the resonator had on the cavity.

3.7.2 Cavity Spectroscopy and Coupling Strength

In addition to directly observing the resonator, I also measured the cavity TE_{101} mode frequency as a function of bias current (see Fig. 3.27). For an uncoupled 3D cavity mode, there should be no variation in the resonance frequency f_c as a function of the bias current I_f. However, as is clearly seen in the plot, the cavity clearly has a small but distinct dependence on the flux bias current. Comparing Fig. 3.27 with either Fig. 3.25(a) or Fig. 3.26, one sees that the cavity response was very similar to that of the

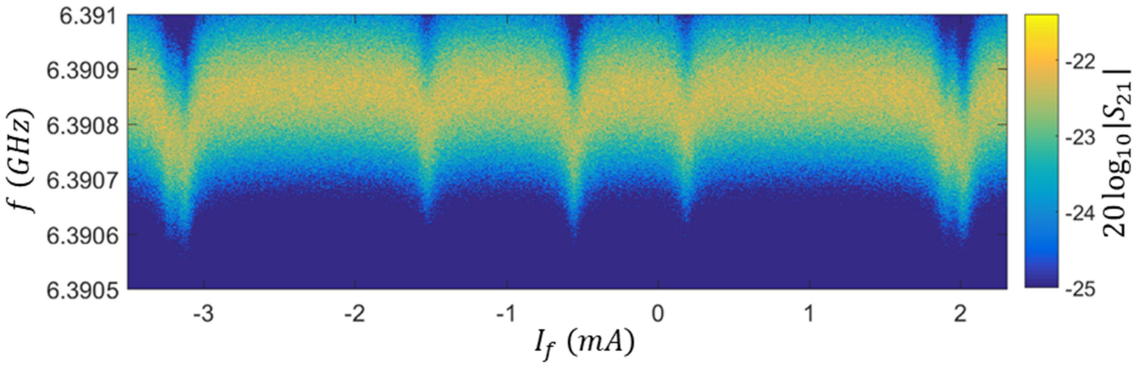

Fig. 3.27: Spectroscopic VNA data of the cavity as a function of applied current into the DC lines. The x-axis is the current into the DC lines in mA and the y-axis is frequency in GHz. The color represents the measured magnitude of S_{21}.

tunable LC resonator. This variation of the cavity frequency with flux demonstrated that the cavity was coupled to the LC resonator.

In Fig. 3.28 I show three different data sets from device tunres_112115. The left column (plots (a)-(c)) are resonator flux maps, and the right column (plots (d)-(f)) are cavity flux maps. The rows were taken on different dates and clearly show shifts due to different levels of trapped flux in the loops. The upper row is the data I have been showing so far for the cavity and resonator. The middle row was taken after a sudden, unexpected jump in the offset flux in one of the tuning loops. This can be seen by comparing the plots in this row to the top row. The tuning dips from loop 2 are unchanged, but the tuning dips from loop 1 have shifted over. Unfortunately, though, the chilled water system failed while the resonator spectroscopy was being taken, and only half the data set was taken before the refrigerator warmed up above the T_c of the device.

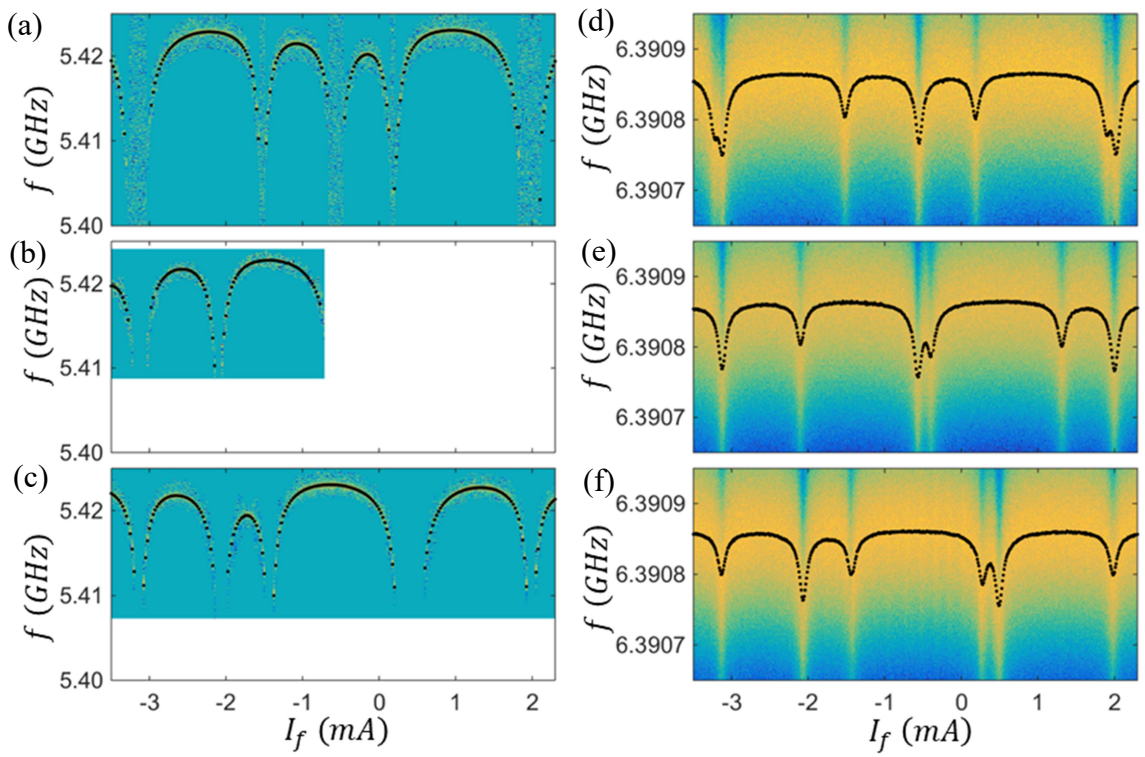

Fig. 3.28: (a)-(c) False color plot of LC resonator $|S_{21}|$ vs. flux bias current I_f on device tunres_112115. (d)-(f) Corresponding false color plot of cavity $|S_{21}|$ vs. flux bias current I_f. (a) and (d) were taken right after the system was cooled. (b) and (e) were taken after a "jump" in the offset flux in one of the tuning loops. (c) and (f) were taken after thermally cycling the system to $T > 10$ K leading to different offset flux values in each loop.

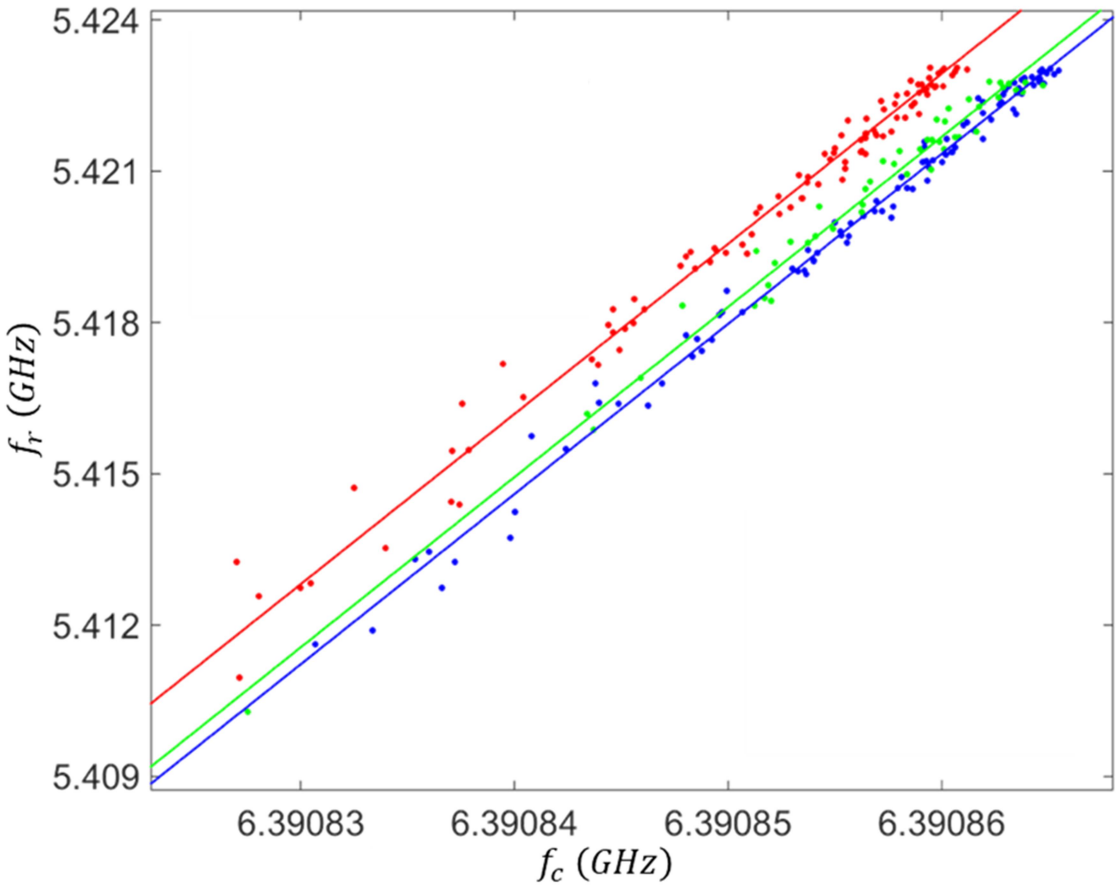

Fig. 3.29: Scatter plot of tunable resonator tunres_112115 frequency f_r vs. cavity resonance frequency f_c. The points are from the data sets shown in Fig. 3.26. The solid lines are fits to Eq. (3.108) with $g^2/\Delta^2 = 1/337$, $\Delta = 968$ MHz, and $g = 53$ MHz.

The bottom row was taken after cooling the system back down to base temperature. During this unplanned thermal cycling, the trapped offset flux was shifted in both loops.

The black points in Fig. 3.28 are the extracted frequencies from fits to Eq. (3.12). In Fig. 3.29 I show a scatter plot of the measured resonator frequency f_R vs. measured cavity frequency f_c where each point on the plot was from a single flux setting in the data shown in Fig. 3.28. The red points are from the top row in Fig. 3.27, the green for the middle row, and the blue points for the bottom row. As is clearly seen in this scatter plot, there is a linear relationship between the frequency of the cavity and the resonator. Fitting to a straight line given by the expression

$$f_{c0} - f_c = \frac{g^2}{\Delta^2}(f_{r0} - f_r) \tag{3.107}$$

yields a slope of $g^2/\Delta^2 = 1/337$, where g is the coupling strength and $\Delta = 968$ MHz is the detuning between the bare resonances of the cavity and resonator, f_{c0} and f_{r0}, which gives g= 53 MHz. I note that the bare resonator frequency stayed consistent between each run; however, the cavity bare resonance shifted by ≈4 kHz from the first data set to the last. Since the device was mounted all the way over to one side of the cavity space, it is most strongly coupled via the magnetic field. So, this coupling strength g is a measure of how strongly the magnetic field can couple energy into the resonator and vice versa.

With all the parameters in hand, Eq. (3.108) can be solved to find the perturbed resonant frequency f_r as a function of the perturbed cavity frequency f_c to obtain

$$f_r = f_{r0} - \frac{\Delta^2}{g^2}(f_{c0} - f_c)\,. \tag{3.108}$$

A key implication of this result is that we can use Eq. (3.109) to find the LC resonance frequency f_r by measuring the cavity frequency f_c. In Fig. 3.30 I show the resulting LC

resonance frequency from a cavity measurement. The red points are the scaled cavity frequencies from Fig. 3.27(d). From this plot my device tunres_112115 had a tuning range of 39 MHz.

3.7.3 Fit to Model

The blue curve in Fig. 3.30 shows a fit of the scaled cavity data to the tunable LC model discussed in section 3.3. From the figure it is clear that this is a very good fit. The 11 fit parameters in the model are shown in Table 3.3. Since some of the parameters only had a slight effect on the fit, it was important to have good estimates of as much as possible in order to make sure the fit values made sense.

As discussed above, for these fits I fixed the capacitance C at a value of 367 fF as determined by Eq. (3.106); it was not a fit parameter. All of the inductances were allowed to vary, though. I used FastModel's FastHenry to estimate all the geometric inductances. To estimate the critical current and the β_π parameter, I measured the room temperature resistance R_n of test pattern junctions on the same chip and found the critical current I_0 using the Ambegaokar-Baratoff [7] relation.

$$I_0 R_n = \frac{\pi \Delta}{2}, \tag{3.109}$$

where I_0 is the junction critical current, R_n is the room temperature resistance, and this Δ is the superconducting energy gap (measured in eV). The mutual inductance was harder to estimate, but I calculated it would be on the order of pH.

All the parameters I show in Table 3.3 line up quite well with these estimates and calculations. Altogether, this gives confidence that, not only is tuning a resonator this way possible, but understanding the model and extracting parameters is achievable. I

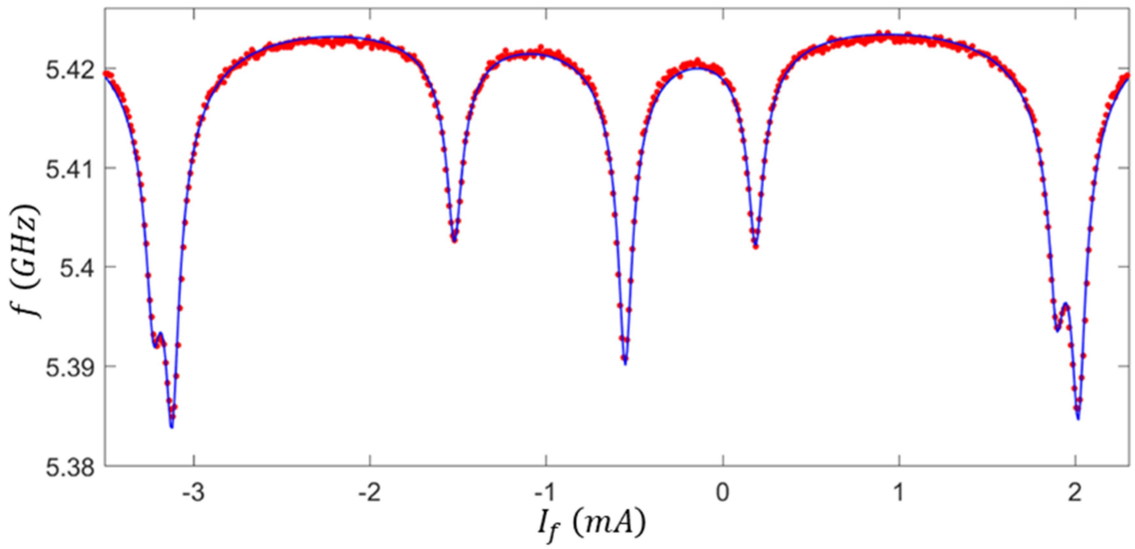

Fig. 3.30: Scaled cavity resonance data vs. applied flux. The x-axis of this plot is the applied flux current into the DC lines in mA and the y-axis is frequency in GHz. The red points on this plot are the scaled cavity frequencies from using the linear fit results from section 3.6.2. The blue line is a fit to the model presented in section 3.4.

Table 3.3: List of parameters from fit in Fig. 3.30. The unshaded cell is the capacitance, which was set by a interdigital capacitance formula discussed in section 3.5.1. The light-green shaded cells were the fit parameters. Finally, the light-red shaded cells are extracted parameters using the definition of β_π

L_0	2.5 nH		C	347 fF
M_1	1.21 pH		M_2	0.804 pH
$\beta_{\pi 1}$	0.743		$\beta_{\pi 2}$	0.811
L_1	90.9 pH		L_2	93.0 pH
L_{1x}	895 pH		L_{2x}	822 pH
ϕ_{01}	-0.610		ϕ_{02}	-0.286
I_{01}	248 nA		I_{02}	292 nA

would just add that this tuning range of 40 MHz is nowhere near large enough for the main experiment I describe in this dissertation. In chapter 6 I discuss how I took this "mad Mickey" design and modified it to couple to two qubits and a cavity and how I modified the tuning loop structure to achieve a tuning range of 700 MHz.

Chapter 4

Transmon Theory

In this chapter I review the quantum theory of transmons. I present the Hamiltonian, find the energy levels, and discuss the anharmonicity. I conclude by discussing energy relaxation, dephasing, and the associated characteristic times including T_1, T', T_ϕ, and T_2.

4.1 Transmon Hamiltonian

In Section 3.1.1, I described the behavior of a quantum harmonic oscillator formed by connecting a capacitor to an inductor. The energy levels are given by

$$E_n = \hbar\omega(n + 1/2)\,, \tag{4.1}$$

where $\omega = 1/\sqrt{LC}$ and n is a non-negative integer that can be thought of as being the number of photonic excitations in the resonator. Since the energy levels are harmonic (hence the name), they are equally spaced. This means that if the system is driven using a classical external field, it will be driven into a coherent state that is a superposition of more than just two energy levels. If steady power is applied on resonance, the system will climb the energy ladder and go into a coherent state that is a superposition of all the energy levels. For a qubit, one must prevent this and be able to selectively address the two lowest levels. This requires anharmonicity.

The standard way to introduce a non-linearity in a superconducting device is to include a Josephson junction in the circuit. As discussed in Section 3.4.1, a Josephson junction may be thought of as a non-linear inductor with inductance

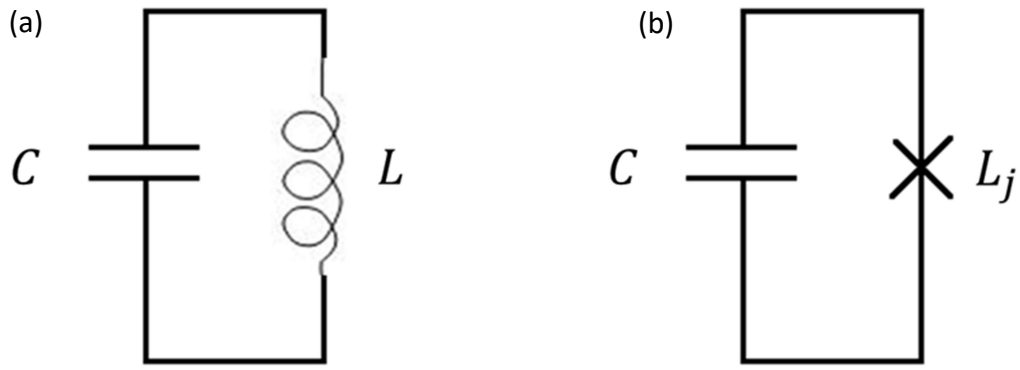

Fig. 4.1: Schematic of a harmonic LC resonator (left) and a transmon (right) where the inductor has been replaced by a Josephson junction.

$$L_j = \frac{\Phi_0}{2\pi I_0 \cos(\gamma)}, \tag{4.2}$$

where I_0 is the critical current of the junction, γ is the gauge-invariant phase difference across the junction, and $\Phi_0 = h/2e$ is the magnetic flux quantum. A transmon is formed by simply connecting a capacitor in parallel with a Josephson junction [1]. The result is an anharmonic oscillator with individually addressable energy states. In a transmon, the anharmonicity is set by the charging energy

$$E_C = \frac{e^2}{2C_T}, \tag{4.3}$$

where C_T is the total capacitance shunting the transmon junction. The other characteristic energy associated with a transmon is the Josephson energy, which is given by

$$E_J = \frac{\Phi_0 I_0}{2\pi}. \tag{4.4}$$

The ratio E_J/E_C is important in determining whether the quantum operator for the phase $\hat{\gamma}$ is sharply defined or whether the quantum operator $\hat{n}$ for the number of Cooper

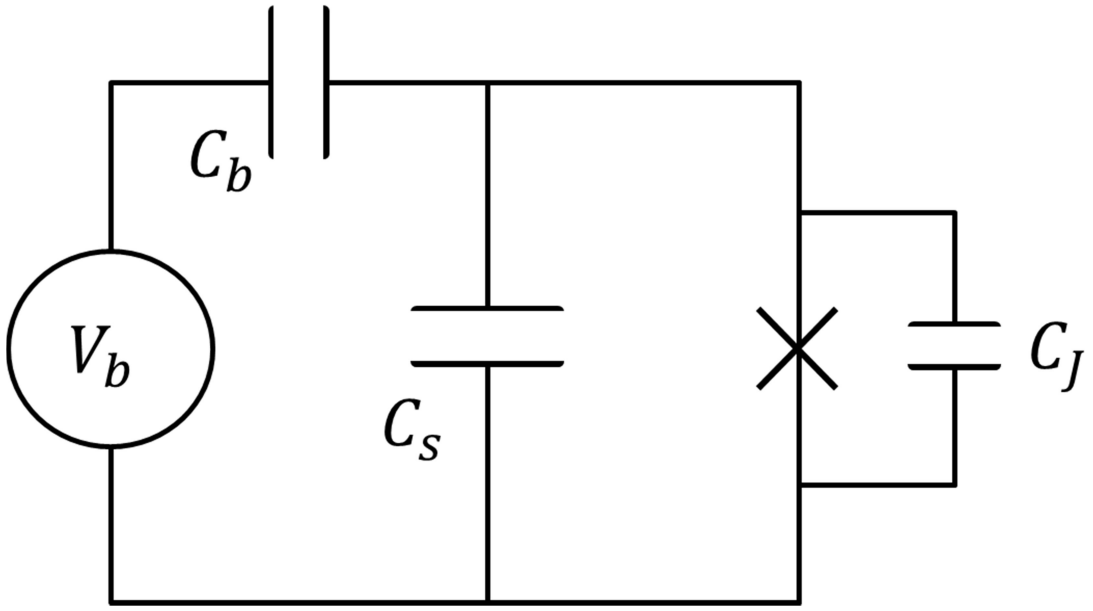

Fig. 4.2: Circuit schematic depicting a transmon coupled to a voltage source V_b via capacitance C_b. Here the transmon has shunt capacitance C_s in parallel with the junction capacitance C_J.

pairs transferred across the junction is sharply defined. In a phase qubit [2], which is simply a Josephson junction that is biased by a current source, $E_J/E_C \gg 1$, and the phase difference γ is relatively well-defined. In contrast, charge qubits [3] have $E_J/E_C \lesssim 1$ and the number of Cooper pairs on a small superconducting island $\hat{n}$ is the well-defined quantity rather than the phase. The transmon qubit is a hybrid (of sorts) between these two designs. It may simply be thought of as an unbiased phase qubit operated with E_J/E_C in the range of 50 to 150. This means that the phase is relatively well-defined and makes the device relatively isolated from charge fluctuations or static applied voltage.

Figure 4.2 shows a circuit schematic of a transmon that is connected to a voltage source V_b. There are three main sources of capacitance for the transmon. First, there is the junction capacitance C_J formed by the two electrodes of the Josephson junction. Second, a shunt capacitance C_s is connected across the junction. Third, the bias voltage source is connected to the transmon by a coupling capacitor C_b. For this circuit, the total capacitance is

$$C_T = C_J + C_s + C_b \tag{4.5}$$

and the charging energy is then given by

$$E_C = \frac{e^2}{2\left(C_J + C_s + C_b\right)} \ . \tag{4.6}$$

The Hamiltonian for the circuit in Fig. 4.2 may then be written as [1, 4]

$$\mathcal{H}_T = 4E_C(\hat{n} - n_b)^2 - E_J \cos(\hat{\gamma}) \ , \tag{4.7}$$

where $n_b = C_b V_b / 2e$ is the offset charge number, $\hat{n}$ is the operator for the number of Cooper pairs that have tunneled across the junction, and $\hat{\gamma}$ is the operator corresponding to the gauge invariant phase difference across the junction.

Much like the operators for momentum and position, $\hat{n}$ and $\hat{\delta}$ are conjugate variables, and they satisfy the commutation relation [5]

$$[\hat{n}, \hat{\gamma}] = i. \tag{4.8}$$

I note that the commutation relation between these two variables has some subtleties that do not arise in the more familiar case of position and momentum. For a discussion see ref. [5]. For this conjugate relationship, the number operator may be expressed in the phase basis as

$$\hat{n} = i\frac{\partial}{\partial\gamma}. \tag{4.9}$$

Equation (4.7) may then be written as

$$\mathcal{H} = 4E_C\left(i\frac{\partial}{\partial\gamma} - n_b\right)^2 - E_J\cos(\gamma). \tag{4.10}$$

For energy eigenstates $\psi_m(\gamma)$, the time-independent Schrodinger equation gives

$$\mathcal{H}_T\psi_m(\gamma) = E_m\psi_m(\gamma). \tag{4.11}$$

Combining Eqs. (4.10) and (4.11) yields

$$4E_C\left(i\frac{\partial}{\partial\gamma} - n_b\right)^2\psi_m(\gamma) - E_J\cos(\gamma)\ \psi_m(\delta) = E_m\psi_m(\gamma). \tag{4.12}$$

By using Mathieu functions [6], Eq. (4.12) may be solved analytically to yield eigenenergies [1]

$$E_m = E_C A_{2(n_b+k(m,n_b))}\left(-\frac{E_J}{2E_C}\right), \tag{4.13}$$

where m is an integer representing the energy levels of the transmon, $A_\nu(q)$ is the characteristic value for Mathieu functions with exponent ν and argument q, and $k(m,n_b)$ is an integer valued function for sorting the eigenvalues that is given by

$$\begin{aligned} k(m,n_b) = \sum_{l=\pm1}&\big((Round[2n_b + l/2])mod\ 2\big) \\ &\times\big(Round[n_b] + l(-1)^m(Quotient[m+1,2])\big), \end{aligned} \tag{4.14}$$

where the function $Round$ rounds its argument to the nearest integer and the function $Quotient$ gives the integer quotient of its two arguments [1].

Figure 4.3 shows a plot of the eigenenergies using Eq. (4.13) as a function of n_b for E_J/E_C values 1, 10, 50, and 1000. When $E_J/E_C = 1$, which is in the charge qubit regime, there is a very strong dependence on n_b (see Fig. 4.3(a)). Charge qubits are best

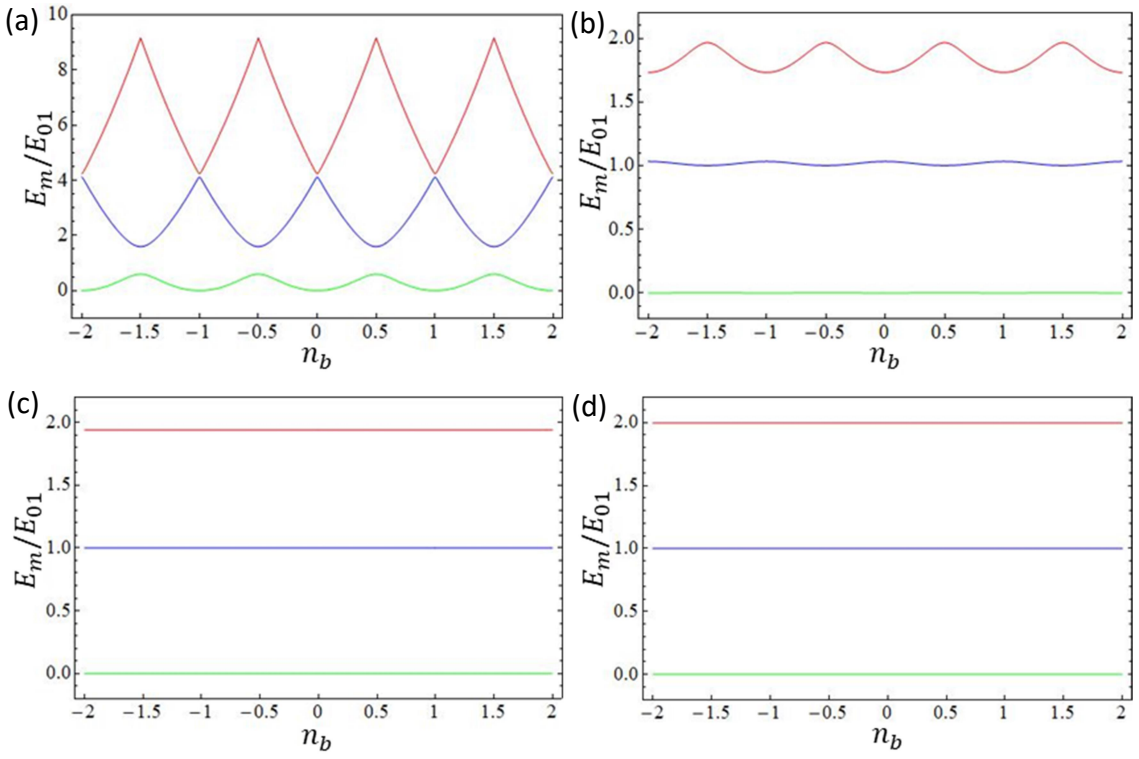

Fig. 4.3: Ground state (green), first excited state (blue), and second excited state (red) transmon energy levels, scaled by the lowest transtition energy E_{01}, as a function of bias charge number n_b for different values of E_J/E_C. (a)-(d) are for E_J/E_C = 1, 10, 50, and 10000, respectively.

operated at "sweet spots" such as $n_b = \pm 1/2$ where they are insensitive to charge noise to first order. However, even when biased at a sweet spot, it turns out that charge noise is typically so large that the dephasing seen from second-order contributions is large. At $E_J/E_C = 10$, it is clear from Fig. 4.3(b) that the modulation of the energy levels as a function of n_b is heavily suppressed, although not enough to completely eliminate charge noise desphasing issues. At $E_J/E_C = 50$, Fig. 4.3(c) shows that the modulation is no longer visible. This is the regime in which transmons operate. At this ratio, transmon qubits are quite insensitive to charge noise. This comes at the cost of reduced anharmonicity. However, examination of Fig. 4.3(c) shows that there is still ≈5% anharmonicity in the energy levels, which is sufficient to allow its use as a qubit.

Finally, at $E_J/E_C = 10000$, Fig. 4.3(d) shows that not only is the charge modulation gone, but the anharmonicity is also heavily suppressed. This ratio was typically where phase qubits were operated, but anharmonicity was achieved in these qubits by applying a bias current [2].

Since a transmon is not sensitive to n_b or to V_b, they may be removed from the circuit diagram and Hamiltonian. Figure 4.4 shows the resulting circuit diagram of a typical

transmon. It consists simply of a junction and a shunt capacitance. The transmon Hamiltonian then reduces to

$$\mathcal{H}_T = 4E_C\hat{n}^2 - E_J\cos(\hat{\gamma}), \tag{4.15}$$

which is identical to that of an unbiased phase qubit.

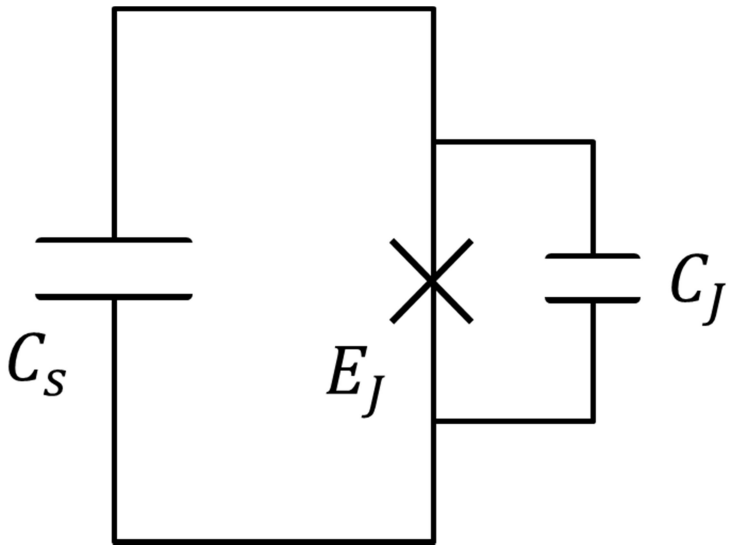

Fig. 4.4: Circuit schematic of an undriven transmon.

4.2 Energy Levels and Anharmonicity

The exact expressions for the energy levels and eigenfunction solutions to Eq. (4.15) are not very transparent or easy to use. Much understanding may be gained by approximating the $\cos(\hat{\gamma})$ potential and considering small oscillations about a minimum of potential energy at $\gamma = 0$. Expanding the potential about this minimum to fourth order in $\hat{\gamma}$ yields

$$-E_J \cos(\hat{\delta}) \approx -E_J + \frac{1}{2} E_J \hat{\gamma}^2 - \frac{1}{24} E_J \hat{\gamma}^4 . \tag{4.16}$$

The first term represents a shift in the overall energy of the system, and I will ignore it, although there are situations where this term may produce observable effects. The second term is a quadratic potential and acts as a harmonic oscillator potential. Finally, the third term introduces a small anharmonicity that I treat as a perturbation. The Hamiltonian in Eq. (4.15) then becomes

$$\mathcal{H}_T = 4E_C\hat{n}^2 + \frac{1}{2}E_J\hat{\gamma}^2 - \frac{1}{24}E_J\hat{\gamma}^4 \,. \tag{4.17}$$

As with a harmonic oscillator, it is convenient to define creation and annihilation operators [7]

$$\hat{b}^\dagger \equiv \left(\frac{E_J}{32E_C}\right)^{\frac{1}{4}}\left(\hat{\gamma} - i\sqrt{\frac{8E_C}{E_J}}\hat{n}\right) \tag{4.18}$$

and

$$\hat{b} \equiv \left(\frac{E_J}{32E_C}\right)^{\frac{1}{4}}\left(\hat{\gamma} + i\sqrt{\frac{8E_C}{E_J}}\hat{n}\right). \tag{4.19}$$

The Hamiltonian may then be written as

$$\mathcal{H}_T = \sqrt{8E_JE_C}\left(\hat{b}^\dagger\hat{b} + \frac{1}{2}\right) - \frac{E_C}{12}\left(\hat{b}^\dagger + \hat{b}\right)^4 . \tag{4.20}$$

Note that the first term in this Hamiltonian is that of a harmonic oscillator with an energy spacing of $\sqrt{8E_JE_C}$.

The second term in Eq. (4.18) may now be treated as a perturbation. The first order perturbation $E_n^{(1)}$ on the energy $E_n^{(0)}$ of the unperturbed state $|n\rangle$ is then

$$E_n^{(1)} = -\frac{E_C}{12}\left\langle n\left|\left(\hat{b}^\dagger + \hat{b}\right)^4\right|n\right\rangle = -\frac{E_C}{6}(2n^2 + 2n + 1)\,. \tag{4.21}$$

Thus, the nth energy level has energy

$$E_n = \sqrt{8E_JE_C}\left(n + \frac{1}{2}\right) - \frac{E_C}{6}(2n^2 + 2n + 1). \tag{4.22}$$

The transition energy to go from the n to the n+1 state is then

$$E_{n\to n+1} \equiv E_{n+1} - E_n = \sqrt{8E_JE_C} - E_C(n+1). \tag{4.23}$$

For qubits, the most important transition is that between the ground state with n= 0 and the first excited state with n= 1, which corresponds to a frequency of

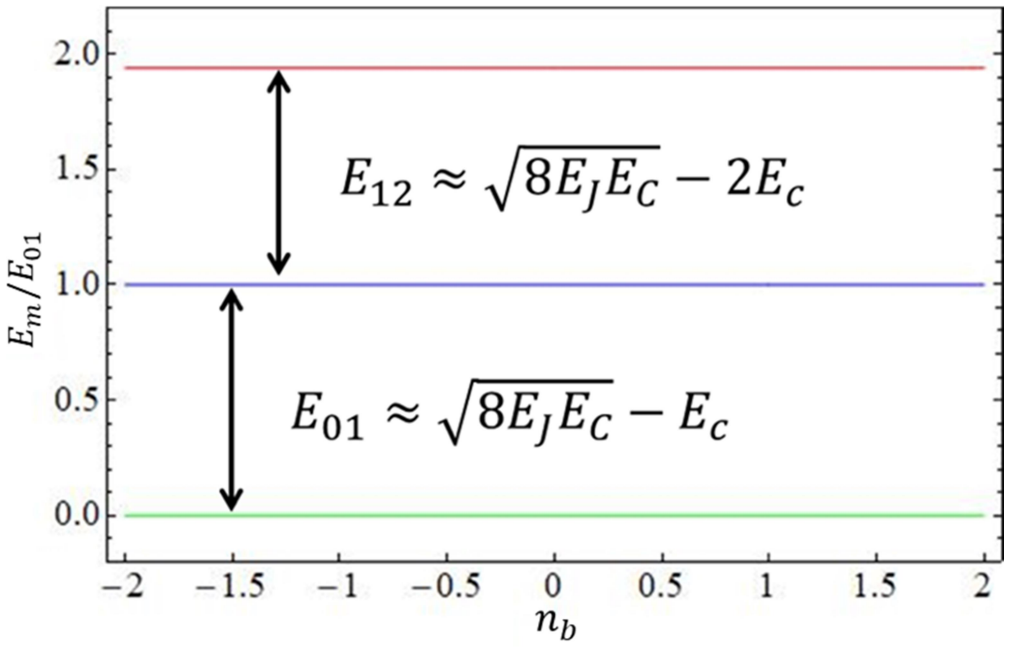

Figure 4.5: Energy levels of a transmon with $E_J/E_C = 50$.

$$f_{01} = \frac{E_{0\to1}}{h} = \frac{\sqrt{8E_JE_C} - E_C}{h}. \tag{4.24}$$

To be used as a qubit there must be enough anharmonicity in the system so that transitions from level 0 to 1 don't excite higher energy levels. The anharmonicity of the transmon to first order is simply

$$\alpha \equiv E_{n+1\to n+2} - E_{n\to n+1} = -E_C\,, \tag{4.25}$$

where the negative sign indicates that $E_{n+1\to n+2}$ is less than $E_{n\to n+1}$. For a typical transmon, the anharmonicity is a few percent of the lowest transition frequency. In Fig. 4.5 I show a plot of the resulting three lowest energy levels for a transmon.

Typically, my qubits had f_{01} frequencies in the range of 4 to 5.5 GHz, anharmonicities of $E_C/h \approx 200$ MHz, and E_J/E_C ratios somewhere between 65 and 125.

See Chapter 8 for a summary of the measured device parameters in my two-qubit variable coupling device TRES_092917.

4.3 Relaxation Time T_1

In this section I present a simple model of qubit energy loss and show how that gives rise to the relaxation time T_1, which quantifies the time it takes for the qubit to relax back to its equilibrium thermal state after it has been excited. Assuming the qubit's thermal equilibrium state is its ground state $|g\rangle$ and that it has been excited into its excited state $|e\rangle$, it will relax to the ground state following an exponential decay. Thus, the probability of finding the qubit in its excited state at time t is given by

$$P_e(t) = P_e(0)e^{-t/T_1}\,, \tag{4.26}$$

In Chapters 10 and 11, I discuss the case where this relaxation is caused by non-equilibrium quasiparticles. Here, I consider loss that is due to a general, dissipative impedance being coupled to the qubit.

4.3.1 Circuit Model

Figure 4.5 shows two simple circuit models of a transmon with a dissipative channel. In Fig. 4.5(a) the dissipative impedance Z is directly coupled to the qubit, and Fig. 4.5(b) depicts the impedance Z onnected to the transmon via coupling capacitance C_c. Initially, if the transmon capacitor is charged at $t = 0$, then the charge will decay exponentially through Z, and T_1 will be given by the RC time constant of the circuit

$$T_1 = \frac{C_T}{Re[Y(\omega)]}\,, \tag{4.27}$$

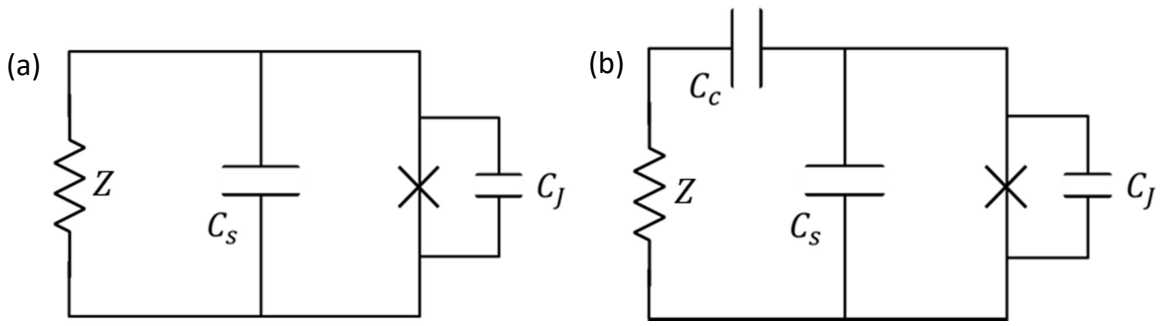

Figure 4.6: Simple circuit models showing channels for energy loss in the transmon. (a) depicts a loss channel directly coupled to the qubit, and (b) shows the same impedance connected through a coupling capacitance.

where $Y(\omega)$ is the total admittance of the dissipative channel [8]. For the directly coupled circuit in Fig. 4.5(a), $Y(\omega) = 1/Z$ and I have that

$$T_{10} = \frac{C_T}{Re[1/Z]} \tag{4.28}$$

If $Z = Z_0 = 50\ \Omega$ and a typical value of $C_T = 100$ fF is assumed, this gives $T_{10} = 5$ ps, which would render the qubit useless for practical purposes.

On the other hand, for the circuit in Fig. 4.5(b), if Z is real (*i.e.* resistive), the admittance of the dissipative channel seen by the qubit is

$$Y(\omega) = \frac{\omega^2 C_c^2 Z + j\omega C_c}{1 + \omega^2 C_c^2 Z^2}\ . \tag{4.29}$$

In the limit $Z_0 \ll 1/\omega C_c$, this gives

$$Re[Y(\omega)] \approx \omega^2 C_c^2 Z_0\ . \tag{4.30}$$

Equation (4.27) then yields

$$T_1 \approx \frac{C_T}{\omega_{01}^2 C_c^2 Z} = T_{10} \cdot \frac{1}{\omega_{10}^2 C_c^2 Z^2}, \tag{4.31}$$

which is a factor of $1/\omega_{01}^2 C_c^2 Z^2$ larger than the directly coupled case of Eq. (4.28). For sufficiently small C_c, T_1 can exceed 100 μs.

4.3.2 Multiple Dissipation Channels

In general there can be multiple mechanisms causing dissipation to occur. Well-known examples include: coupling to a bath of two-level systems [9-11], the Purcell effect [12, 13], and quasiparticles [14, 15]. In Chapters 10 and 11 I give the details on an anomalous effect on relaxation time we observed that was due to quasiparticle tunneling.

When there are multiple channels of dissipation, the overall relaxation rate $1/T_1$ can be found from

$$\frac{1}{T_1} = \sum_i \frac{1}{T_{1,i}}. \tag{4.32}$$

where $1/T_{1,i}$ is the relaxation rate due to the ith dissipation mechanism. If one source of dissipation produces large relaxation effects, it will tend to dominate T_1. Understanding and reducing all possible channels of dissipation is important for qubits because T_1 sets a bound on the time available for coherently manipulating the qubit state.

4.4 Dephasing Time T_ϕ

The dephasing time T_ϕ, which is a characteristic time that quantifies the loss of phase coherence, can be thought of as arriving from low-frequency noise in the system. In this section I present a brief overview of how noise leads to dephasing. For more

details and discussions on how particular types of noise affects qubit systems, see refs. [16-21].

Any pure state of a two-level quantum system may be written as

$$|\psi(0)\rangle = \cos\left(\frac{\theta}{2}\right)|g\rangle + \sin\left(\frac{\theta}{2}\right)e^{i\phi_0}|e\rangle\,, \tag{4.33}$$

where $|g\rangle$ and $|e\rangle$ are the ground and excited states of the qubit, respectively, and where θ_0 and ϕ_0 can be thought of as polar and azimuthal angles on the Bloch sphere. Now, with the assumption that relaxation can be ignored, the time evolution of the state can be found by applying the unitary operator

$$U(t) = e^{-i\mathcal{H}t/\hbar} \tag{4.34}$$

on $|\psi(0)\rangle$. Here, $\mathcal{H}$ is the Hamiltonian of the system. With the further assumption that the Hamiltonian is time independent, applying $U(t)$ to Eq. (4.33) then gives

$$\begin{aligned} |\psi(t)\rangle &= e^{\frac{-i\mathcal{H}t}{\hbar}}|\psi(0)\rangle \\ &= \cos\left(\frac{\theta}{2}\right)e^{-\frac{iE_0t}{\hbar}}|g\rangle + \sin\left(\frac{\theta}{2}\right)e^{i\left(\phi_0-\frac{E_1t}{\hbar}\right)}|e\rangle. \end{aligned} \tag{4.35}$$

Since the overall phase of $|\psi(t)\rangle$ has no physical relevance, I am free to remove an overall complex factor and obtain the physically equivalent state

$$|\psi(t)\rangle = \cos\left(\frac{\theta}{2}\right)|g\rangle + \sin\left(\frac{\theta}{2}\right)e^{i\left(\phi_0-\frac{(E_1-E_0)}{\hbar}t\right)}|e\rangle. \tag{4.36}$$

I now define the 0-to-1 transition angular frequency as

$$\omega_{01} \equiv \frac{E_1 - E_0}{\hbar} = \frac{E_{01}}{\hbar}\,, \tag{4.37}$$

and Eq. (4.36) then becomes

$$|\psi(t)\rangle = \cos\left(\frac{\theta}{2}\right)|g\rangle + \sin\left(\frac{\theta}{2}\right)e^{i(\phi_0-\omega_{01}t)}|e\rangle. \tag{4.38}$$

Equation (4.38) shows that the phase $\phi = \phi_0 - \omega_{01}t$ progresses steadily in time at angular frequency ω_{01}. On the Bloch sphere, this corresponds to a precession about the z-axis. Dephasing occurs when random fluctuations in E_{01} cause the precession frequency to evolve unpredictably, which leads to an exponential decay in phase information.

Some common sources of noise that lead to these fluctuations and to dephasing are Gaussian white noise, $1/f$ noise, and fluctuations in the critical current of the qubit's Josephson junction [16]. Another source of dephasing that is of particular interest in my experiment is from fluctuations in the number of photons in a cavity that is coupled to the qubit, as my device TRES_092917 had two transmons that were strongly coupled to both a 3D microwave cavity and a 2D tunable LC resonator (see Chapters 5 to 9).

Photon induced dephasing has a non-trivial dependence on the coupling between the qubit and cavity. In the weak-dispersive limit ($2\chi \ll \kappa$) Bertet *et al.* found that the dephasing time is given by [22]

$$T_\phi = \frac{1}{4\langle n_{cav}\rangle(\langle n_{cav}\rangle + 1)\chi^2 T_{cav}}, \tag{4.39}$$

where $\langle n_{cav}\rangle$ is the average thermal population of photons in the cavity, χ is the dispersive shift of the coupled cavity-qubit system (see Chapter 5), and T_{cav} is the characteristic relaxation time of the cavity. In the strong dispersive regime ($2\chi \gg \kappa$), which is where my device TRES_092917 operated, Sears *et al.* found that the dephasing time is given by [23]

$$T_\phi = \frac{T_{cav}}{N(\langle n_{cav}\rangle + 1) + \langle n_{cav}\rangle(N+1)}, \tag{4.40}$$

where N denotes which photon number peak you are considering. Of most interest for qubit systems is the result for $N = 0$, for which Eq. (4.40) reduces to

$$T_\phi = \frac{T_{cav}}{\langle n \rangle}. \tag{4.41}$$

I note that an interesting result of Eq. (4.40) is that, if one has a measure of T_ϕ, the average cavity photon number may be found. This is of particular importance due to the fact that the effective temperature of the cavity-qubit system is directly related to this photon number. This technique was recently used by J. Yeh *et. al.* to characterize a novel microwave attenuator design where extra care was taken to dissipate heat and reduce the noise temperature seen by the qubit [24].

4.5 Rabi Decay Time T'

The relaxation time T_1 and dephasing time T_ϕ are just two examples of characteristic time scales that arise in the dynamics of two-level systems. Driving the system will produce a trajectory on the Bloch sphere and the resulting time decay of the coherent response will depend on the trajectory. Perhaps the most important example is when a qubit is driven in a Rabi oscillation. If the drive frequency is to the qubit's g-to-e transition frequency, the qubit responds by oscillating between $|g\rangle$ and $|e\rangle$. These oscillations are called Rabi oscillations. For more details see refs. [17], [25-28].

For simplicity, I restrict the system to only the ground and first excited states of the qubit. Applying an external classical microwave drive to the qubit introduces an additional term in the qubit Hamiltonian, which may be written as [28]

$$\mathcal{H}_{dr,2} = \frac{\hbar\Omega_q(t)}{2}\left(\sigma^+ e^{-i\omega_d t} + \sigma^- e^{i\omega_d t}\right), \tag{4.42}$$

where $\Omega_q(t)$ is the drive strength that scales with the amplitude of the drive and with the coupling strength between the qubit and drive, σ^+ and σ^- are the raising and lowering operators, respectively, for the qubit, and ω_d is the frequency of the drive. In this discussion I will consider only a constant drive strength; hence, $\Omega_q(t) = \Omega_{q0}$ is constant. The Hamiltonian of the driven qubit can then be written as

$$\mathcal{H} = \mathcal{H}_0 + \mathcal{H}_{dr,2} = \frac{\hbar\omega_{01}}{2}\sigma_z + \frac{\hbar\Omega_{q0}}{2}\left(\sigma^+ e^{-i\omega_d t} + \sigma^- e^{i\omega_d t}\right), \tag{4.43}$$

where σ_z is the z Pauli matrix.

Since $\mathcal{H}_0$ is time independent and we can readily obtain its eigenvalues and eigenstates, it is useful at this point to switch to the interaction picture and consider $\mathcal{H}_{dr,2}$ as a time-dependent perturbation on the system. In the interaction picture I can define the time evolution operator

$$\mathcal{U} \equiv e^{i\mathcal{H}_0 t/\hbar}, \tag{4.44}$$

which in matrix form is given by

$$\mathcal{U} = \begin{pmatrix} e^{i\omega_{01}t/2} & 0 \\ 0 & e^{-i\omega_{01}t/2} \end{pmatrix}. \tag{4.45}$$

The drive Hamiltonian $\mathcal{H}_{dr,2}$ in the interaction picture is then given by

$$\begin{aligned} \mathcal{H}_{dr,2,I} &= \mathcal{U}\mathcal{H}_{dr,2}\mathcal{U}^\dagger \\ &= \frac{\hbar\Omega_{q0}}{2}\begin{pmatrix} e^{i\omega_{01}t/2} & 0 \\ 0 & e^{-i\omega_{01}t/2} \end{pmatrix}\begin{pmatrix} 0 & e^{-i\omega_d t} \\ e^{i\omega_d t} & 0 \end{pmatrix}\begin{pmatrix} e^{-i\omega_{01}t/2} & 0 \\ 0 & e^{i\omega_{01}t/2} \end{pmatrix}. \end{aligned} \tag{4.46}$$

Simplifying Eq. (4.46) yields

$$\mathcal{H}_{dr,2,I} = \frac{\hbar\Omega_{q0}}{2}\begin{pmatrix} 0 & e^{i(\omega_{01}-\omega_d)\,t} \\ e^{-i(\omega_{01}-\omega_d)\,t} & 0 \end{pmatrix}. \tag{4.47}$$

In the interaction picture [29] the time evolution of the interaction basis states evolves according to the Schrödinger equation

$$i\hbar\frac{\partial}{\partial t}|\psi(t)\rangle_I = \mathcal{H}_{dr,2,I}|\psi(t)\rangle_I. \tag{4.48}$$

Now consider a generic state of the system $|\psi(t)\rangle_I = \rho_0(t)|g\rangle + \rho_1(t)|e\rangle$. Plugging this into Eq. (4.48) gives two coupled differential equations

$$i\frac{\partial\rho_0(t)}{\partial t} = \frac{\Omega_{q0}}{2}\rho_1(t)e^{-i(\omega_{01}-\omega_d)t} \tag{4.49}$$

and

$$i\frac{\partial\rho_1(t)}{\partial t} = \frac{\Omega_{q0}}{2}\rho_0(t)e^{i(\omega_{01}-\omega_d)t}. \tag{4.50}$$

With the assumption that the system is initially in its ground state, I can solve Eqs. (4.49) and (4.50) to obtain the solution [28]

$$\begin{aligned}|\psi(t)\rangle_I = e^{i\omega_{01}t}&\left[\cos\left(\frac{t}{2}\sqrt{\delta\omega^2+\Omega_{q0}^2}\right)+\frac{i\delta\omega}{\sqrt{\delta\omega^2+\Omega_{q0}^2}}\sin\left(\frac{t}{2}\sqrt{\delta\omega^2+\Omega_{q0}^2}\right)\right]|0\rangle\\ &-e^{-i\omega_{01}t}\frac{i\Omega_{q0}}{\sqrt{\delta\omega^2+\Omega_{q0}^2}}\sin\left(\frac{t}{2}\sqrt{\delta\omega^2+\Omega_{q0}^2}\right)|1\rangle\,,\end{aligned} \tag{4.51}$$

Then by transforming back into the Schroedinger picture with

$$|\psi(t)\rangle_S = \mathcal{U}^\dagger|\psi(t)\rangle_I\,, \tag{4.52}$$

I get

$$|\psi(t)\rangle_S = \left[\cos\left(\frac{t}{2}\sqrt{\delta\omega^2+\Omega_{q0}^2}\right)+\frac{i\delta\omega}{\sqrt{\delta\omega^2+\Omega_{q0}^2}}\sin\left(\frac{t}{2}\sqrt{\delta\omega^2+\Omega_{q0}^2}\right)\right]|0\rangle - \frac{i\Omega_{q0}}{\sqrt{\delta\omega^2+\Omega_{q0}^2}}\sin\left(\frac{t}{2}\sqrt{\delta\omega^2+\Omega_{q0}^2}\right)|1\rangle\,, \tag{4.53}$$

where $\delta\omega = \omega_{01} - \omega_d$ is the detuning of the drive frequency from the qubit transition frequency.

With (4.53) in hand, I can then find the probability of finding the system in the excited state as a function of time, which is given by

$$P_e(t) = |\langle 1|\psi(t)\rangle_S|^2 = \frac{\Omega_{q0}^2}{2\left[\delta\omega^2+\Omega_{q0}^2\right]}\left[1-\cos\left(t\sqrt{\delta\omega^2+\Omega_{q0}^2}\right)\right]. \tag{4.54}$$

Equation (4.54) gives a sinusoidal oscillation at the Rabi frequency

$$\Omega_R = \sqrt{\delta\omega^2+\Omega_{q0}^2}\,, \tag{4.55}$$

and these oscillations in $P_e(t)$ are called Rabi oscillations.

On resonance $\delta\omega = 0$ and the Rabi frequency is at a minimum given by

$$\Omega_R = \Omega_{q0}\,, \tag{4.56}$$

and the amplitude of the oscillation is at a maximum, corresponding to the state continually evolving between the ground and excited state. On the Bloch sphere, the state vector is initially pointing up (the ground state, see Fig. 4.7). After the drive is turned on, the state evolves around the sphere on a great circle and, at time $t = 1/2\Omega_R$ is in the excited state (South pole on the Bloch sphere). As t progresses further, the state continues its journey and begins to head back to the ground state, and this process repeats until the drive is turned off. Note that if the drive is stopped at $t = 1/2\Omega_R$, the state vector will have completed a rotation with $\theta = \pi$. If the qubit state is initially in $|g\rangle$, this

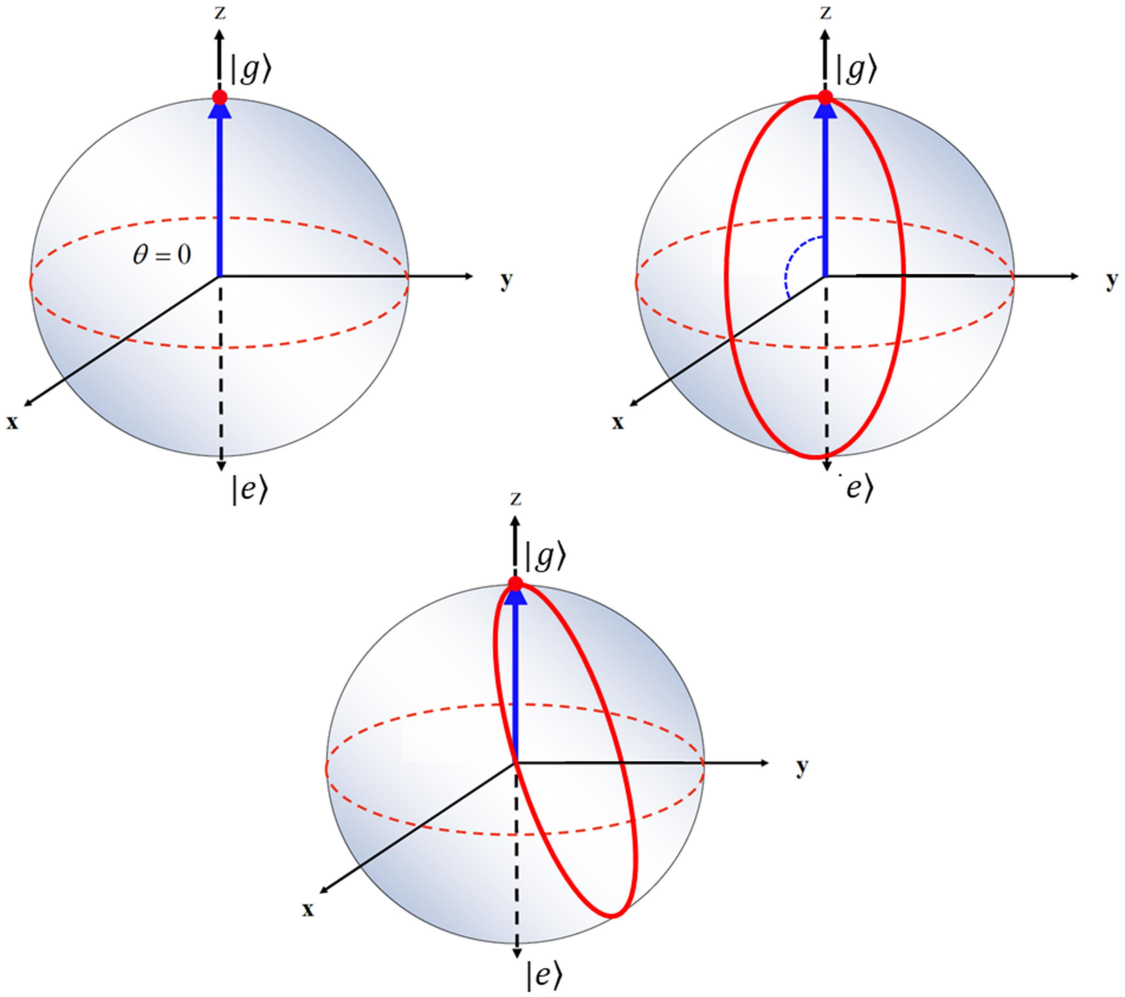

Fig. 4.7: (a) Bloch sphere representation of qubit in ground state. (b) On-resonance Rabi oscillations. (c) Off-resonance Rabi oscillations.

rotation will leave the system in $|e\rangle$, completely "inverting" the population of the qubit. This π-pulse is a useful qubit operation, the NOT, and is also useful in measuring quantities such as T_1.

When $\delta\omega \neq 0$, the drive is off resonance, and the behavior is slightly different. From Eq. (4.55) it is clear that the Rabi frequency increases as the detuning increases. For small detunings, the Rabi frequency may be expanded to give

$$\Omega_R \approx \Omega_{\mathrm{q0}} + \frac{1}{2}\frac{\delta\omega^2}{\Omega_{q0}}. \tag{4.57}$$

This shows that the initial response of the frequency is to increase quadratically. In the limit of large detuning, the Rabi frequency approaches the detuning $|\delta\omega|$. In addition, Eq. (4.68) shows that the amplitude of the oscillations decreases with increasing detuning, which means that the qubit is not driven completely into the excited state. On the Bloch sphere, if the system starts in $|g\rangle$ it will no longer be driven through the south pole, but instead along a small circle on the sphere (see Fig. 4.7(b)).

One serious short-coming of the above discussion is that it neglects relaxation and dephasing, which will cause the Rabi oscillations to decay. Including dephasing, relaxation, and detuning seriously complicates the analysis, and, in general, there is no analytical solution for the state evolution [25]. For simplicity, I use an approximate expression

$$P_e(t) = |\langle 1|\psi(t)\rangle_S|^2 \approx \frac{\Omega_{q0}^2}{2\left[\delta\omega^2 + \Omega_{q0}^2\right]}\left[1 - e^{-t/T'}\cos\left(t\sqrt{\delta\omega^2 + \Omega_{q0}^2}\right)\right]. \tag{4.58}$$

Here T' is the Rabi decay, and for dephasing characterized by T_ϕ it is given by [29, 30]

$$\frac{1}{T'} = \frac{1}{2T_1} + \frac{1}{2T_2} = \frac{3}{4T_1} + \frac{1}{2T_\phi}, \tag{4.59}$$

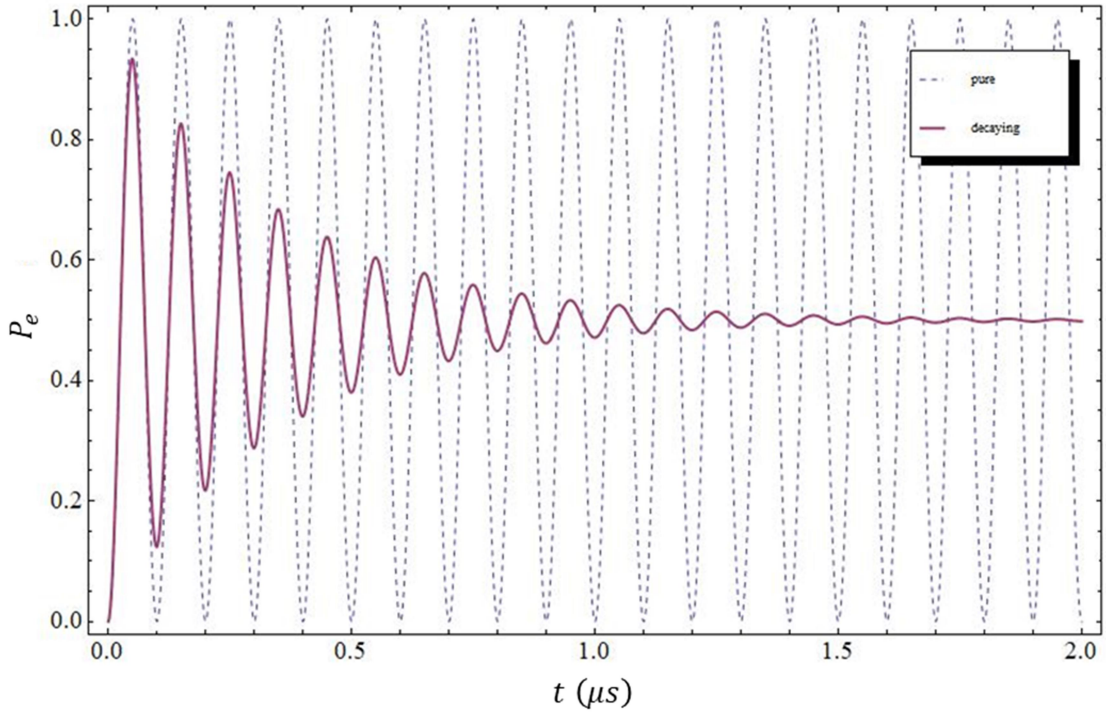

Figure 4.8: Plot of excited state probability P_e versus time t showing Rabi oscillations with and without decay. The dashed curve shows Rabi oscillations in the limit where $T' \to \infty$. The solid curve shows Rabi oscillations for $T' = 0.5$ μs.

where $T_2 = \left(1/2T_1 + 1/T_\phi\right)^{-1}$ is the coherence time (see Section 4.5). In the limit of very small dephasing rate $T_\phi \to \infty$, $T_2 = 2T_1$ and the maximum value for $T' = 4T_1/3$. Any added dephasing will decrease T'.

Figure 4.8 shows a plot of a decaying Rabi oscillation from Eq. (4.58) and a non-decaying oscillation with the same frequency. Notice that at long times P_e approaches a steady state value of $1/2$. This corresponds to a mixed state with the system equally likely to be found in the ground state $|g\rangle$ or the excited state $|e\rangle$.

4.6 Coherence Time T_2

The coherence time T_2 is another important characteristic time of a qubit. This is also called the spin-echo time [32] or Hahn-echo time and is well-known from NMR. This characteristic time quantifies the overall decoherence from both relaxation and dephasing processes.

The spin-echo measurement process involves three steps [19]. First, with the qubit initially in the ground state, a $\pi/2$-pulse is applied to place the system into a superposition state on the equator of the Bloch sphere. Second, after a time $\Delta t/2$, a π-pulse is applied. Finally, after another time delay of $\Delta t/2$ (equal to the first time delay), another $\pi/2$-pulse is applied to bring the qubit to the excited state, and the probability of being in the excited state P_e is measured. One finds that P_e decays exponentially as a function of time with characteristic time T_2. For a system in which dephasing is exclusively from a white-noise source, T_2 is related to T_1 and T_ϕ by [31]

$$\frac{1}{T_2} = \frac{1}{2T_1} + \frac{1}{T_\phi} \tag{4.60}$$

I note that a spin-echo measurement is insensitive to first order to inhomogenous broadening, *i.e.* spin-echo decay measurements are insensitive to small shot-to-shot variations in the energy level transition frequencies.

4.7 Ramsey Coherence Time T_2^*

The Ramsey coherence time, or spectroscopic coherence time T_2^* is yet another important characteristic time for qubits. While the spin-echo decay T_2 is not sensitive to inhomogenous broadening, the Ramsey decay time T_2^* is. Instead of removing low

frequency noise sources inherent in the measurement, Ramsey spectroscopy includes everything. This typically leads to $T_2^* < T_2$. Since the qubit is experiencing this low-frequency noise, this characteristic time may be important for understanding the properties of the particular system being measured.

The Ramsey decay measurement sequence is very similar to the spin-echo measurement [19]. The main difference lies in not inverting the state with a π-pulse midway through the measurement. After the initial $\pi/2$-pulse at frequency $\omega_d/2\pi$, putting the qubit on the equator of the Bloch sphere, the state is allowed to precess freely for a set amount of time. At the end of the delay, another $\pi/2$-pulse is then applied to rotate the state to the excited state, where it is projected onto the z-axis and the probability of being found in the excited state P_e is measured. When measured, P_e will oscillate at frequency $f_{01} = (\omega_{01} - \omega_d)/2\pi$. Since there is dephasing and inhomogenous broadening, the state vector will spread out over the Bloch sphere as the decay increases and these Ramsey oscillations will decay with characteristic time T_2^*.

Chapter 5

TRES Device Hamiltonian

In earlier chapters I considered resonators, cavities, and qubits separately; except in Chapter 2 where I discussed a resonator coupled to a cavity. The experiment I describe in Chapters 5-9 involved device TRES_092917, which had two qubits coupled to a tunable LC resonator and a 3D microwave cavity. Here, I begin with a description of a Jaynes-Cummings approach to a single transmon coupled to a cavity. Next, I discuss the model Hamiltonian for my TRES devices. Finally, I discuss the design choices for the frequency and coupling strength for my qubits and resonators.

5.1 Single Qubit Coupled to Cavity

The basic idea of circuit quantum electrodynamics (cQED) [1] is to treat a superconducting qubit as an artificial atom and adapt ideas originally developed in atomic physics and quantum optics. I begin by discussing the Jaynes-Cummings Hamiltonian [2] and how it can be applied to a transmon coupled to a cavity. I then use this Hamiltonian to show how the behavior of a transmon in a microwave cavity is affected by the coupling between them.

5.1.1 Two-Level Qubit Jaynes-Cummings Hamiltonian

The Hamiltonian of a two-level qubit that is coupled to the electric field in a resonator can be described by the Jaynes-Cummings Hamiltonian [2]

$$\mathcal{H} = \hbar\omega_r a^\dagger a + \frac{1}{2}\hbar\omega_{ge}\sigma_z + \hbar g(a^\dagger\sigma_- + a\sigma_+), \tag{5.1}$$

where I have ingnored the zero-point energy of the resonator. In Eq. (5.1) $\omega_r/2\pi$ is the resonator resonance frequency, $\omega_{ge}/2\pi$ is the qubit $g \to e$ transition frequency, a and $a^\dagger$ are the annihilation and creation operators for the resonator, σ_z is the z Pauli matrix, g is the coupling strength between the qubit and resonator, and σ_- and σ_+ are the lowering and raising operators, respectively, for the qubit, which can be written as

$$\sigma_\pm = \frac{\sigma_x \pm i\sigma_y}{2}. \tag{5.2}$$

The first term in Eq. (5.1) describes the energy stored in the resonator. The operator $n = a^\dagger a$ is the number operator and gives the number of photons stored in the resonator. The second term describes the energy in the qubit. When the qubit is in its ground state $|g\rangle$ the operator σ_z returns $-|g\rangle$, while it returns $+|e\rangle$ when the qubit is in its excited state $|e\rangle$. Finally, the third term in Eq. (5.1) is the coupling term, which describes the two systems exchanging a single photon. For instance, if the system is in the state $|e, n\rangle$, then the first term in parenthesis will lower the qubit state and raise the resonator state to give $\sqrt{n+1}|g, n+1\rangle$. The coupling term is of a very special form and only connects energy levels of the system that have the same total number of excitations. Figure 5.1(a) shows the uncoupled ($g = 0$) energy levels of the system with arrows connecting levels that are coupled when $g \neq 0$.

Writing the Hamiltonian in matrix form yields a block diagonal matrix (see Fig. 5.2). Since the eigenvalues of a block diagonal matrix are simply the eigenvalues of the individual blocks that comprise the matrix, I need only consider the individual 2x2 blocks.

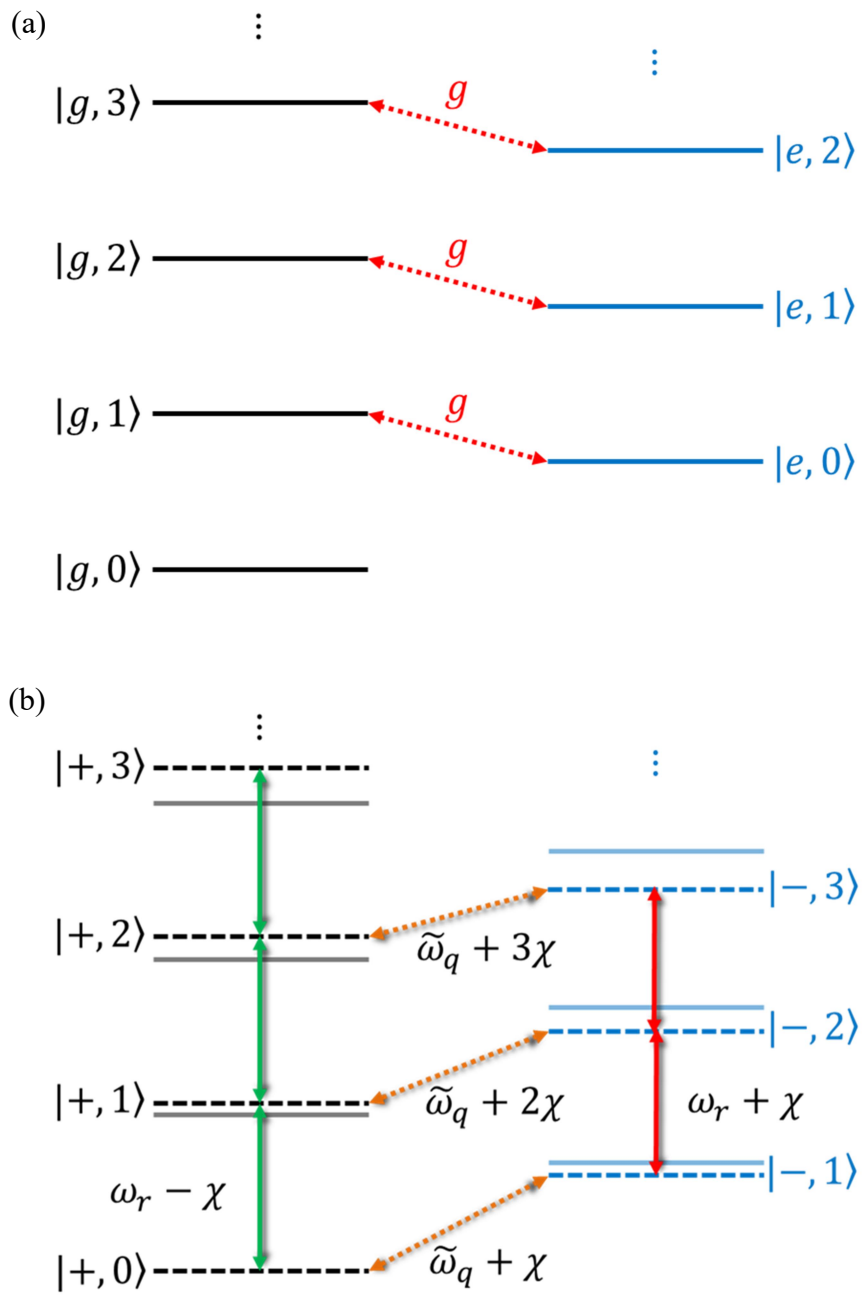

Fig. 5.1: (a) Uncoupled energy levels of a cavity and two level system (qubit). The coupling term, with strength g, is depicted as the red, dashed lines. (b) Energy levels and frequency shifts in the dispersive limit. Solid lines are the uncoupled states and dashed lines represent the dressed states. Dispersively shifted transition frequencies are depicted by the solid, arrowed lines.

$$H = \hbar \begin{pmatrix} -\frac{1}{2}\omega_{ge} & 0 & 0 & 0 & 0 & & 0 & 0 & \\ 0 & \frac{1}{2}\omega_{ge} & g & 0 & 0 & & 0 & 0 & \\ 0 & g & \omega_r - \frac{1}{2}\omega_{ge} & 0 & 0 & \cdots & 0 & 0 & \\ 0 & 0 & 0 & \omega_r + \frac{1}{2}\omega_{ge} & g\sqrt{2} & & 0 & 0 & \cdots \\ 0 & 0 & 0 & g\sqrt{2} & 2\omega_r - \frac{1}{2}\omega_{ge} & & 0 & 0 & \\ & & \vdots & & & \ddots & 0 & 0 & \\ 0 & 0 & 0 & 0 & 0 & 0 & (n-1)\omega_r + \frac{1}{2}\omega_{ge} & g\sqrt{n} & \\ 0 & 0 & 0 & 0 & 0 & 0 & g\sqrt{n} & n\omega_r - \frac{1}{2}\omega_{ge} & \\ & & & \vdots & & & & & \end{pmatrix}$$

Fig. 5.2: Matrix representation of Jaynes-Cummings Hamiltonian Eq. (5.1).

For $n = 0$, one finds a block with only one entry and we have that $E_{g,0} = -\hbar\omega_{ge}/2$. The block for $n > 0$ total excitations is given by

$$\begin{pmatrix} (n-1)\omega_r + \frac{\omega_{ge}}{2} & g\sqrt{n} \\ g\sqrt{n} & n\omega_r - \frac{\omega_{ge}}{2} \end{pmatrix}. \tag{5.3}$$

The eigenvalues of this block are

$$E_{n,+} = \hbar\omega_r(n - 1/2) + \frac{\hbar\Delta}{2}\sqrt{1 + \frac{4g^2 n}{\Delta^2}}, \tag{5.4a}$$

and

$$E_{n,-} = \hbar\omega_r(n - 1/2) - \frac{\hbar\Delta}{2}\sqrt{1 + \frac{4g^2 n}{\Delta^2}}, \tag{5.4b}$$

where here $\Delta \equiv \omega_{ge} - \omega_r$ is the detuning between the qubit transition frequency and the cavity frequency (not to be confused with the superconducting gap Δ). The normalized eigenvectors corresponding to the eigenvalues in Eq. (5.4) are [1]

$$|+,n\rangle = \cos(\theta_n)\,|e,n-1\rangle - \sin(\theta_n)\,|g,n\rangle \tag{5.5}$$

and

$$|-,n\rangle = \sin(\theta_n)\,|e,n-1\rangle + \cos(\theta_n)\,|g,n\rangle. \tag{5.6}$$

where

$$\theta_n = \frac{1}{2}\arctan\left(\frac{2g\sqrt{n}}{\Delta}\right) \tag{5.7}$$

These energy eigenvalues give the energy of each state. From these, one can obtain the transition frequency between different states. For $g \ll \Delta$, one finds that θ_n is small and the $|+,n\rangle$ ladder of states corresponds to the qubit being mainly in the ground state. On this ladder, the energy to add a photon in the cavity is given by

$$E_{+,n+1} - E_{+,n} = \hbar\omega_r + \frac{\hbar\Delta}{2}\left[\sqrt{1+\frac{4g^2(n+1)}{\Delta^2}} - \sqrt{1+\frac{4g^2n}{\Delta^2}}\right]. \tag{5.8}$$

Similarly, if the system is in the $|-,n\rangle$ ladder of states, the qubit is predominately in the excited state, and the energy to add a photon in the cavity is given by

$$E_{-,n+1} - E_{-,n} = \hbar\omega_r - \frac{\hbar\Delta}{2}\left[\sqrt{1+\frac{4g^2(n+1)}{\Delta^2}} - \sqrt{1+\frac{4g^2n}{\Delta^2}}\right]. \tag{5.9}$$

On the other hand, the energy needed to excite the qubit from the ground to its excited state (*i.e.* to go from the $+$ ladder to the $-$ ladder while keeping the number of photons in the cavity fixed) is given by

$$E_{-,n+1} - E_{+,n} = \hbar\omega_r - \frac{\hbar\Delta}{2}\left[\sqrt{1 + \frac{4g^2(n+1)}{\Delta^2}} + \sqrt{1 + \frac{4g^2 n}{\Delta^2}}\right]. \qquad (5.10)$$

Note that n is the total number of excitations in the system.

Figure 5.3(a) shows plots of the cavity transition frequency from Eqs. (5.8) (green points) and (5.9) (blue points) for increasing photon number n on the y-axis. All were plotted using $\omega_r/2\pi$ = 6.3 GHz, $\omega_q/2\pi$ = 4.5 GHz, and $g/2\pi$ = 130 MHz. At low resonator photon number, these equations predict that the cavity frequency will depend on the qubit state. Assuming that $\omega_r > \omega_q$ so $\Delta < 0$, when the qubit is in the ground state, the cavity frequency will be pushed up by $-\chi > 0$ from its uncoupled (bare) value to a new "dressed" value. Similarly, the cavity frequency will be shifted down by χ if the qubit is in its excited state. However, at high enough occupation, the resonator transition frequency recovers to the bare value.

I note that, at low cavity powers, the qubit state may be probed by observing the location of the cavity frequency. It is important to realize that, when a transmon is coupled to a cavity, the situation is not exactly the same as when a cavity is coupled to a Two-Level system (TLS). For a transmon, it turns out that the cavity resonance does not split equally above and below the bare cavity frequency. Instead, one typically observes multiple dressed peaks of the cavity, which are all on the same side of the bare resonance. This is due to a transmon having more than just two states and a relatively low anharmonicity. As I discuss in a later section, it is necessary to include more than two states to predict the behavior of these "dressed" cavity resonance peaks in the presence of a transmon.

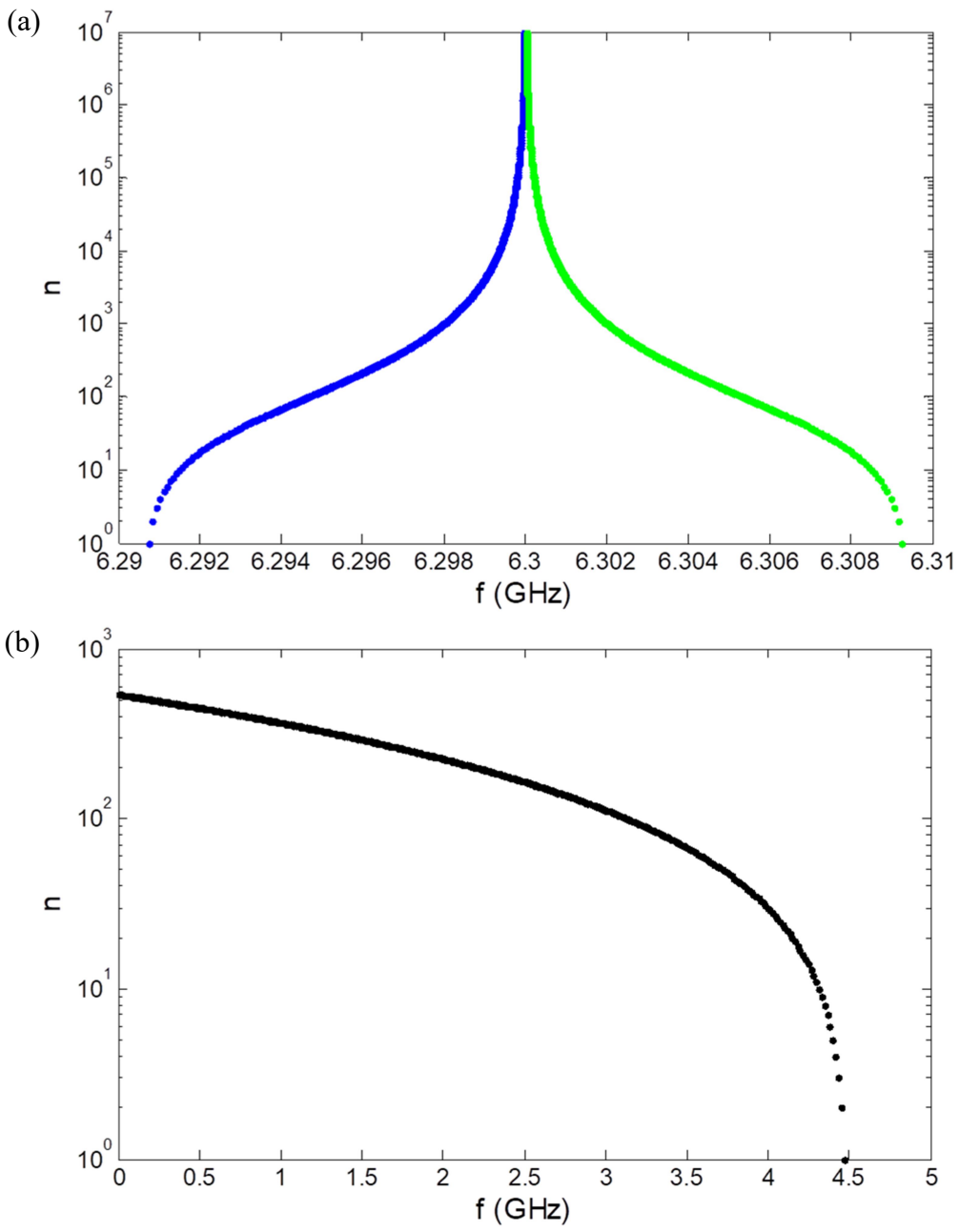

Fig. 5.3: (a) Plot of cavity transition frequency f (x-axis) as a function of photon number n (y-axis) for a cavity coupled to a two-level system. (b) Corresponding plot showing how the qubit transition frequency f (x-axis) depends on photon number n (y-axis). The parameters used were $\omega_r/2\pi = 6.3\ GHz$, $\omega_q/2\pi = 4.5\ GHz$, and $g/2\pi = 130\ MHz$.

In Fig. 5.3(b) I show a plot of the qubit transition frequency from Eq. (5.10) as a function of photon number. One sees that the TLS transition frequency decreases as the number of excitations increases. This behavior gives photon number peaks in the qubit's spectrum, *i.e.* peaks corresponding to different numbers of photons in the cavity. One can get a measure of the cavity-qubit coupling strength by adding photons to the resonator and observing the dispersive shift on the qubit. Also, if there is insufficient shielding or filtering in the system, leading to thermal noise and excitations in the system, fluctuations in the number of cavity photons will cause a broadening of the qubit's resonance. The qubit's performance can be degraded due to this shifting transition frequency.

5.1.2 Dispersive Regime

Continuing with the two-level approximation, it is useful to examine the behavior of the dressed peak at low cavity photon numbers. The key parameter is the critical photon number

$$n_c \equiv \frac{\Delta^2}{4g^2}. \tag{5.11}$$

The dressed energy levels in Eqs. (5.8) and (5.9) may then be written as

$$E_{+,n} = \hbar\omega_r(n - 1/2) + \frac{\hbar}{2}\Delta\sqrt{1 + n/n_c}\ . \tag{5.12}$$

and

$$E_{-,n} = \hbar\omega_r(n - 1/2) - \frac{\hbar}{2}\Delta\sqrt{1 + n/n_c}\ . \tag{5.13}$$

The weak-coupling limit occurs when $n \ll n_c$. In the single-photon limit this can be achieved by designing the system to have $|\Delta| \gg g$, which is the dispersive limit. In this dispersive limit, Eqs. (5.12) and (5.13) reduce to

$$\begin{aligned} E_{+,n} &\approx \hbar\omega_r\left(n-\frac{1}{2}\right)+\frac{\hbar}{2}\Delta\left(1+\frac{n}{2n_c}\right) \\ &= \hbar\omega_r\left(n-\frac{1}{2}\right)-\frac{\hbar}{2}\Delta\left(1+\frac{2\mathrm{g}^2 n}{\Delta^2}\right). \end{aligned} \tag{5.14}$$

and

$$E_{-,n} \approx \hbar\omega_r\left(n-\frac{1}{2}\right)-\frac{\hbar}{2}\Delta\left(1+\frac{2\mathrm{g}^2 n}{\Delta^2}\right). \tag{5.15}$$

To understand the eigenstates in the dispersive limit, I now consider how $\sin(2\theta_n)$ and $\cos(2\theta_n)$ depend on n and n_c. Starting from Eq. (5.7), I find

$$\theta_n = \frac{1}{2}\arctan\left(\sqrt{\frac{n}{n_c}}\right) \approx \frac{1}{2}\sqrt{\frac{n}{n_c}}. \tag{5.16}$$

Thus, I have

$$\sin(\theta_n) \approx \theta_n = \frac{1}{2}\sqrt{\frac{n}{n_c}} = \frac{g\sqrt{n}}{\Delta} \ll 1 \tag{5.17}$$

and

$$\cos(\theta_n) \approx 1. \tag{5.18}$$

The eigenstates to first order are then given by

$$|-,n\rangle = |e,n-1\rangle - \frac{g\sqrt{n}}{\Delta}|g,n\rangle \tag{5.19}$$

and

$$|+,n\rangle = \frac{g\sqrt{n}}{\Delta}|e,n-1\rangle + |g,n\rangle. \tag{5.20}$$

Since transmons are typically operated in the dispersive limit, it is useful to examine the energy levels in detail for this limit. For the $|+\rangle$ branch, which corresponds to the qubit being in the ground state (see Fig. 5.1(b)) I get

$$E_{+,n+1} - E_{+,n} = \hbar\left(\omega_r - \frac{g^2}{\Delta}\right) = \hbar(\omega_r - \chi), \tag{5.21}$$

where the dispersive shift is $\chi \equiv g^2/\Delta$. Equation (5.21) describes a resonator with a frequency given by $\omega_r - \chi$. Similarly, for the $|-\rangle$ branch I get

$$E_{-,n+1} - E_{-,n} = \hbar(\omega_r + \chi)\,. \tag{5.22}$$

Thus, when the qubit is in its excited state, the cavity operates as a resonator with frequency $\omega_r + \chi$. So, for $|\chi| > 0$, the spacing between the rungs on the $+$ ladder are larger by 2χ than the spacing of the rungs on the – ladder shift (see Fig. 5.1(b)).

Next, note that going from one ladder to the other, while keeping the photons in the cavity fixed, corresponds to exciting the qubit. In this case I can find

$$E_{-,n+1} - E_{+,n} = \hbar(\omega_q + \chi) + \hbar 2\chi n\,. \tag{5.23}$$

For $\chi < 0$, the first term on the right-hand-side in Eq. (5.23) gives an overall downward shift of its transition frequency by $|\chi|$, even at zero photon occupation number. However, the last term causes the qubit transition frequency to shift down by an additional 2χ for each photon in the cavity (see Fig. 5.3(b)).

As a side note, this sensitivity of the qubit's transition frequency to the number of photons in the cavity can lead to decoherence in the qubit if the number of photons in the cavity is randomly fluctuating. To avoid dephasing from photon noise, the microwave lines must be heavily filtered, and the filters must be thermally grounded to the refrigerator's mixing chamber plate [3]. On the other hand, this sensitivity to photon

number was useful in characterizing our qubits. By purposefully pumping photons into the cavity while monitoring the qubit transition frequency, accurate measurements of 2χ were extracted, and this is related to the coupling strength and Δ. Although, Eq. (5.23) is only valid for a two-level system, and I discuss the case of a transmon coupled to a qubit in the next section.

Using the above results, I can write an effective Hamiltonian for a TLS coupled to a cavity in the dispersive limit:

$$\mathcal{H}_d \approx \hbar(\omega_r + \chi\sigma_z)a^\dagger a + \frac{\hbar}{2}\Big((\omega_q + \chi) + 2\chi a^\dagger a\Big)\sigma_z. \tag{5.24}$$

The first term in Eq. (5.21) represents the cavity and shows that the bare frequency $\omega_r/2\pi$ is shifted by $\chi/2\pi$ either down or up depending on the qubit's state. The second term shows that the qubit frequency $\omega_q/2\pi$ is shifted by χ and then an additional 2χ for each photon in the cavity. For more details on the system's behavior in the dispersive limit, see refs. [4, 5, 6].

5.1.3 Theory of a Multi-Leveled Qubit Coupled to Resonator

To accurately capture the behavior of a transmon that is coupled to a resonator, it is necessary to include more than two levels. This situation can be handled by using a generalized Jaynes-Cummings Hamiltonian [7]

$$\begin{aligned}\mathcal{H} = \hbar\omega_r a^\dagger a + \hbar\sum_m \omega_m |m\rangle\langle m| \\ + \hbar\sum_m g\sqrt{m+1}(|m\rangle\langle m+1|a^\dagger + |m+1\rangle\langle m|a)\,,\end{aligned} \tag{5.25}$$

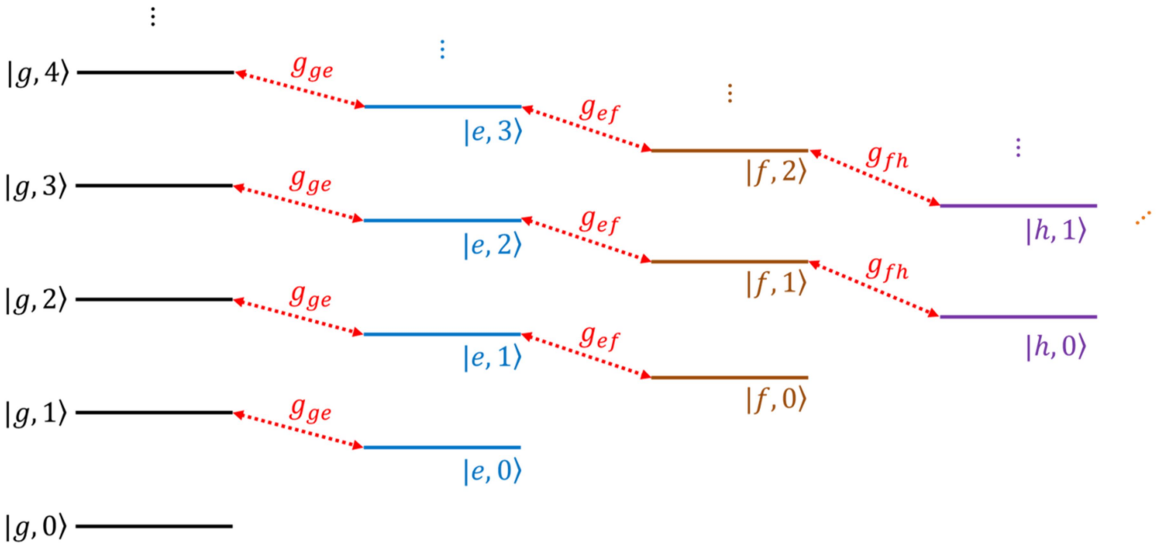

Fig. 5.4: Energy levels of multi-level qubit coupled to a resonator. The red, dashed lines indicate the Jaynes-Cummings type coupling between the states.

where the index m is for the states of the transmon, $\hbar\omega_m$ is the energy corresponding to the mth qubit state (see Chapter 4), and $g\sqrt{m+1}$ is the coupling strength between the cavity and transmon when the qubit is in state m and there is one photon in the cavity. The bare, uncoupled energy levels are shown schematically in Fig. 5.4, and the coupling between the states (from the third term in Eq. (5.25)) is indicated by the red, dashed lines.

In section 5.1.1, I wrote out the matrix form for the two-level Jaynes-Cummings Hamiltonian, showed that it has a block diagonal form, and then diagonalized each block corresponding to a fixed total number of excitations in the system. This treatment may also be done for Eq. (5.25). For m total qubit levels, each block of the Hamiltonian corresponding to n excitations is spanned by the set of states $\{|m,n-m\rangle, |m-1,n-m+1\rangle, \ldots, |f,n-2\rangle, |e,n-1\rangle, |g,n\rangle\}$. For a 3-level qubit, this gives blocks of size 3x3, and for an n-level qubit this gives nxn blocks.

(a)

	$\lvert f, n-2\rangle$	$\lvert e, n-1\rangle$	$\lvert g, n\rangle$
$\langle f, n-2\rvert$	$\omega_r(n-2)+\omega_{gf}$	$g\sqrt{2}\sqrt{n-1}$	0
$\langle e, n-1\rvert$	$g\sqrt{2}\sqrt{n-1}$	$\omega_r(n-1)+\omega_{ge}$	$g\sqrt{n}$
$\langle g, n\rvert$	0	$g\sqrt{n}$	$\omega_r n$

(b)

	$\lvert k, n-4\rangle$	$\lvert h, n-3\rangle$	$\lvert f, n-2\rangle$	$\lvert e, n-1\rangle$	$\lvert g, n\rangle$
$\langle k, n-4\rvert$	$\omega_r(n-4)+\omega_{gk}$	$g\sqrt{4}\sqrt{n-3}$	0	0	0
$\langle h, n-3\rvert$	$g\sqrt{4}\sqrt{n-3}$	$\omega_r(n-3)+\omega_{gh}$	$g\sqrt{3}\sqrt{n-2}$	0	0
$\langle f, n-2\rvert$	0	$g\sqrt{3}\sqrt{n-2}$	$\omega_r(n-2)+\omega_{gf}$	$g\sqrt{2}\sqrt{n-1}$	0
$\langle e, n-1\rvert$	0	0	$g\sqrt{2}\sqrt{n-1}$	$\omega_r(n-1)+\omega_{ge}$	$g\sqrt{n}$
$\langle g, n\rvert$	0	0	0	$g\sqrt{n}$	$\omega_r n$

Fig. 5.5: (a) Block of the generalized Jaynes-Cummings Hamiltonian for three-level qubit and a fixed excitation number n. (a) Block for a five-level qubit with n excitations.

As an example, I show the blocks for a 3-level qubit and 5-level qubit in Fig. 5.5. In these blocks there are a few important things to consider. For the diagonal terms, I have subtracted the ground state energy of the qubit $\hbar\omega_g$ and defined terms such as $\omega_{gf} \equiv \omega_f - \omega_g$, where the energy levels $\hbar\omega_g$, $\hbar\omega_e$, *etc.* are given in section 4.1. Second, I have assumed that the coupling constant g is the same for each qubit transition. Finally, a big mistake I made initially was not scaling the coupling with the square root of the excitation number of the qubit, as well as the cavity, when lowering or raising its state (*e.g.* the $\sqrt{2}$ in the term $\langle f, n-2|\,\mathcal{H}\,|e, n-1\rangle = g\sqrt{2}\sqrt{n-1}$).

Figure 5.6 shows a numerical example from diagonalizing the blocks using the representative parameters $\omega_r/2\pi$ =6.3 GHz, $\omega_{ge}/2\pi$ =4.5 GHz, $g/2\pi$ =130 MHz, and

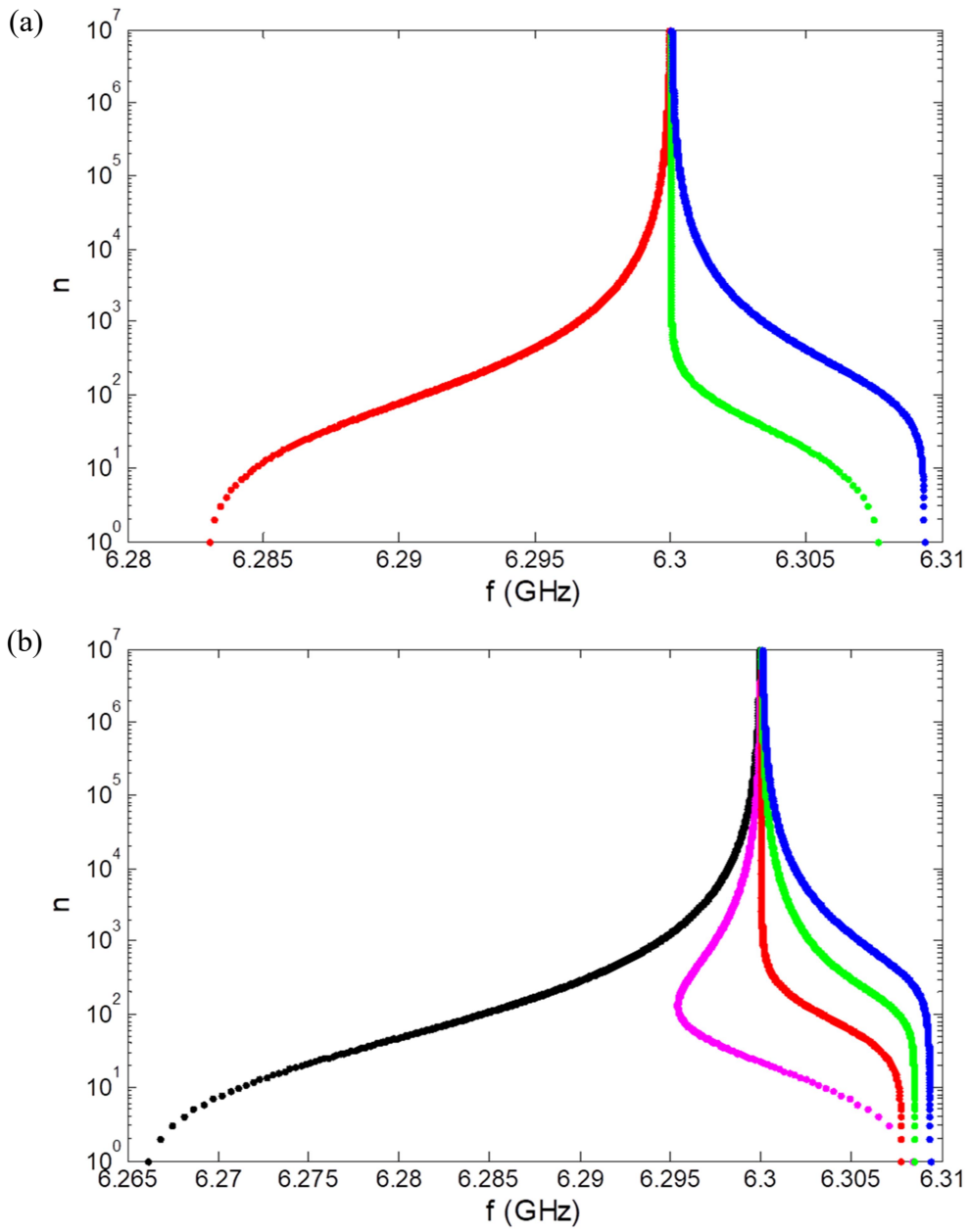

Figure 5.6: Numerical simulation results of resonator dispersive shift (x-axis) vs. excitation number n from Eq. (5.25) for (a) a three-level transmon when it is in its ground (blue), first excited (green), and second excited states (red) and for (b) a five-level transmon when it is in its ground (blue), first excited (green), second excited (red), third excited (magenta), and fourth excited states (black). The parameters were $\omega_r/2\pi = 6.3$ GHz, $\omega_{ge}/2\pi =$ 4.5 GHz, $g/2\pi = 130$ MHz, and $E_c/h = 180$ MHz.

E_c/h =180 MHz. In Fig. 5.6(a), I plot the dressed cavity frequency vs. photon number in the resonator for three qubit levels. The blue points correspond to when the qubit is in the ground state, the green to when the qubit is in the first excited state, and the red to when the qubit is in its second excited state. Even with just three qubit levels, this recovers the qualitative behavior of the dressed cavity resonance of a transmon in its $|e\rangle$ or $|g\rangle$ states. Note, in particular, at low photon occupation number there is a dressed peak when the qubit is in the ground state and a dressed peak when the qubit is in its first excited state, and for these parameters they are both at a frequency greater than the bare resonator frequency. However, the highest level is below the bare resonance.

In Fig. 5.6(b) I used five qubit levels with the same representative parameters as the simulation shown in Fig. 5.6(a) and plotted the cavity eigenfrequencies corresponding to the qubit in each of its available states: ground state $|g\rangle$ (blue points), first excited $|e\rangle$ (green points), second excited $|f\rangle$ (red points), third excited $|h\rangle$ (magenta points), and fourth excited $|j\rangle$ (black points). As seen in this figure there are now four dressed peaks above the bare cavity resonance (for all states except the highest level). One of the big takeaways from numerically simulating this Hamiltonian is that you need to include at least two more levels in the numerical simulation than you intend to consider to obtain accurate results for the remaining levels. For example, comparing the green curves in Figs. 5.6(a) and 5.6(b), one sees that the qualitative behavior is similar, but the curves differ quantitatively. Note also that the dressed cavity peak for the highest qubit level is always shifted from the bare cavity resonance in the opposite direction from that of the ground state.

5.1.4 Brief Qubit Readout Discussion

As Fig. 5.6 shows, at low cavity photon numbers, the dressed peak of the resonator depends on the state of the qubit. This suggests that the qubit state may be measured by probing the cavity at low powers to find its resonance. This is a relatively benign measurement which may not greatly affect the qubit state. In fact, Murch *et. al.* [8] have shown that this technique may be used to continuously monitor the state of a qubit during manipulations.

However, a disadvantage of this measurement is that it requires very low measurement powers. This need for extremely low powers requires very low-noise amplification such as a Josephson bifurcation amplifier [9] to boost the signal-to-noise ratio, and it often necessitates long averaging times. This is the main reason I did not pursue using this measurement scheme.

At high photon occupation the resonator resonance is located at the bare resonance frequency independent of the state of the qubit. Notice, however, that when the qubit is in the excited state, the system has a "head start" and reaches this bare cavity frequency at a lower power than when the qubit is in the ground state. So, by choosing a power where the cavity has its bare frequency when the qubit is in its excited state but the cavity has a significantly different frequency when the qubit is in the ground state, the qubit state may be measured (see Chapter 7 for more details). This high-power Jaynes-Cummings readout measurement scheme [10] can be very fast and can easily achieve a good signal-to-noise ratio.

This high-power scheme has one main drawback: driving the cavity hard will leave it in a highly excited state that will lead to additional qubit transitions and possibly

heating. This effectively destroys the quantum state of the qubit. To mitigate this, enough time must pass between individual measurements to allow the system to settle back down into the ground state.

5.1.5 Dispersive Regime Again

To understand what happens in the transmon-cavity system at low photon number, it is instructive to again consider the dispersive limit. For the multi-level system, this limit is achieved for the mth level when $g_{m,m+1} \ll \Delta_{m,m+1}$, where the detuning is given by $\Delta_{m,m+1} = \omega_{m,m+1} - \omega_r$. The dispersive shift for the mth qubit state transition can be defined as

$$\chi_{m,m+1} = \frac{g_{m,m+1}^2}{\Delta_{m,m+1}} \,. \tag{5.26}$$

As shown in ref. [11], by limiting the system to only allow three qubit levels, the effective Hamiltonian may in general be written as

$$\mathcal{H}_{eff} \approx \hbar\tilde{\omega}_r a^\dagger a + \frac{\hbar}{2}\tilde{\omega}_q \sigma_z - \hbar\chi_{eff} a^\dagger a \sigma_z \,, \tag{5.27}$$

where $\tilde{\omega}_r \approx \omega_r + \chi_{ef}/2$ is the dressed cavity frequency, $\tilde{\omega}_q \approx \omega_q - \chi_{ge}$ is the dressed qubit frequency, and $\chi_{eff} = \chi_{ge} - \chi_{ef}/2$ is the effective dispersive shift.

The situation represented by Eq. (5.27) is very similar to the two-level case (see Eq. (5.24)). By grouping the last two terms, one can see that the qubit transition frequency decreases by $2|\chi_{eff}|$ for every photon in the cavity, which is the same as in Eq. (5.24). It is also instructive to consider the first and last terms together, which yields

$$\hbar\left(\tilde{\omega}_r - \chi_{eff}\sigma_z\right)a^\dagger a \,. \tag{5.28}$$

When the qubit is in the ground state, this gives a cavity frequency of

$$\widetilde{\omega}_r + \chi_{eff} = \omega_r + \chi_{ge}\,, \tag{5.29}$$

as in the two-level case. On the other hand, when the qubit is in its first excited state the cavity frequency is given by

$$\widetilde{\omega}_r - \chi_{eff} = \omega_r - \left(\chi_{ge} - \chi_{ef}\right). \tag{5.30}$$

For typical transmon parameters, this gives a dressed cavity peak for the $|e\rangle$ state on the same side as the dressed cavity peak for the qubit ground state $|g\rangle$.

5.2 Two Qubits and a Tunable Resonator Walk into a Cavity…

In this section I derive the Hamiltonian for my TRES devices, which coupled together two transmons, a tunable resonator, and a 3D microwave cavity. Due to the complexities involved in coupling these systems together, I first consider a tunable resonator capacitively coupled to two transmons. I then expand the analysis, albeit in an *ad hoc* manner, to include the cavity.

5.2.1 Circuit Schematic and Equations of Motion

Figure 5.7(a) shows a circuit schematic for a tunable LC resonator that is capacitively coupled to two transmons. The resonator is in the center and has inductance L_r and two capacitances C_{r1} and C_{r2}. The tunability of this resonator is provided by the adjustable value of L_r (see Chapter 3). The resonator is coupled through the coupling capacitors C_{c1} and C_{c2} to the two transmons, which each have a Josephson junction and shunting capacitor C_{q1} for qubit 1 and C_{q2} for qubit 2.

Using current conservation at the four nodes shown in Fig. 5.9(b), I can write

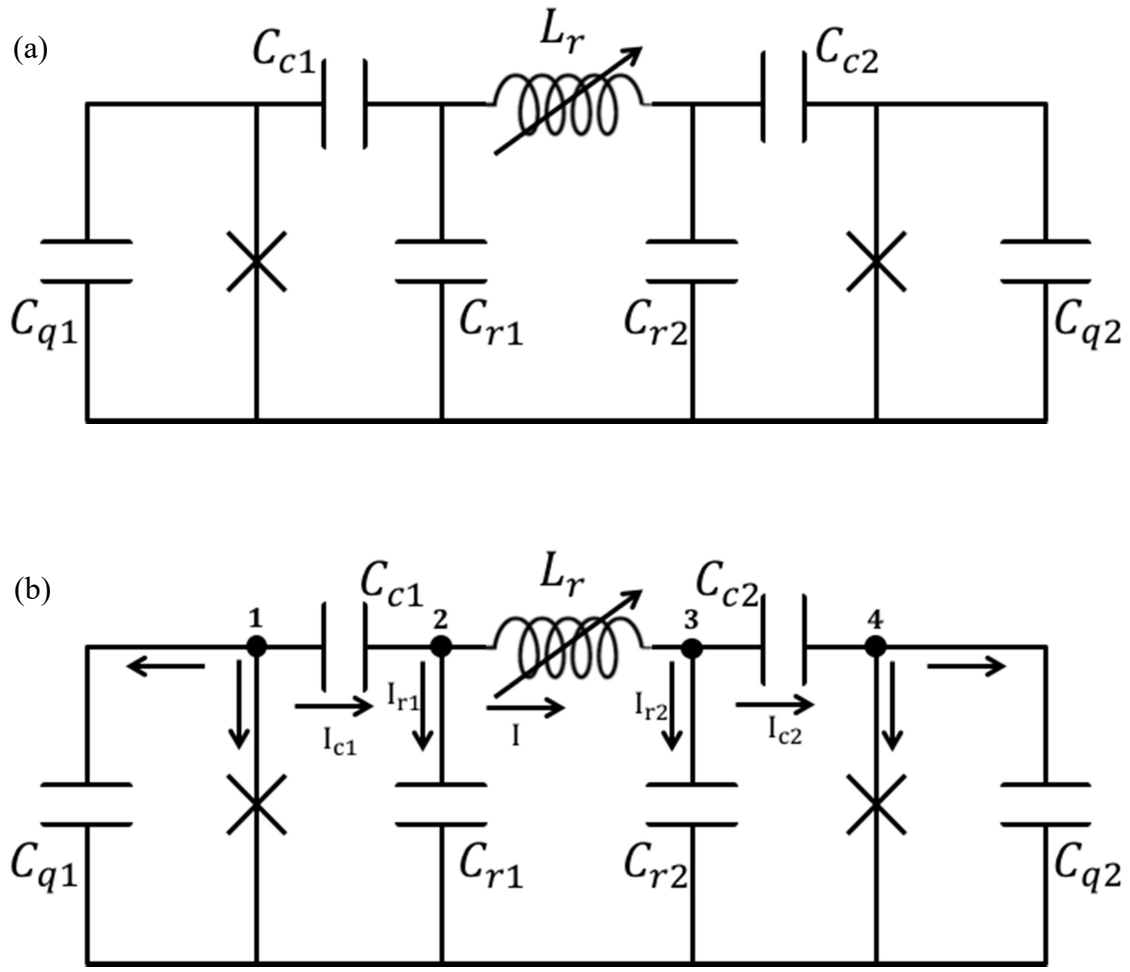

Figure 5.7: (a) Circuit schematic of a tunable resonator that is capacitivley coupled to two transmons. (b) Labeled nodes and currents used in the analysis.

$$
\begin{aligned}
-I_{c1} - I_{01}\sin(\gamma_1) - \frac{\Phi_0}{2\pi} C_{q1}\ddot{\gamma}_1 = 0 \\
I_{c1} - I_{r1} - I = 0 \\
I - I_{r2} - I_{c2} = 0 \\
I_{c2} - I_{02}\sin(\gamma_2) - \frac{\Phi_0}{2\pi} C_{q2}\ddot{\gamma}_2 = 0,
\end{aligned}
\tag{5.31}
$$

where I_{01} and I_{02} are the critical currents of the transmon 1 and 2 junctions, respectively, γ_1 and γ_2 are the gauge-invariant phase differences across junction 1 and junction 2, respectively, I_{c1} and I_{c2} are the currents through coupling capacitors C_{c1} and C_{c2}, respectively, and I_{r1} and I_{r2} are the currents through the resonator capacitors C_{r1} and C_{r2}, respectively.

The voltages across each capacitive element, can be expressed in terms of the time derivative of a phase difference across the capacitor [12]. For example, for capacitor C_{r1} I can define phase γ_{r1}, and write.

$$
V_{r1} = \frac{\Phi_0}{2\pi}\dot{\gamma}_{r1} \tag{5.32}
$$

I next apply Kirchoff's voltage law to the central loop and find

$$
-L_r\dot{I} + \frac{\Phi_0}{2\pi}\dot{\gamma}_{r1} - \frac{\Phi_0}{2\pi}\dot{\gamma}_{r2} = 0. \tag{5.33}
$$

Integrating this with respect to time gives

$$
I = \frac{\Phi_0}{2\pi L_r}(\gamma_{r1} - \gamma_{r2}). \tag{5.34}
$$

Next, notice that the voltage across capacitor C_{c1} is simply the difference in voltage between nodes 1 and 2, and thus

$$
I_{c1} = C_{c1}\frac{\Phi_0}{2\pi}\ddot{\gamma}_{c1} = C_{c1}\left(\dot{V}_{q1} - \dot{V}_{r1}\right) = C_{c1}\frac{\Phi_0}{2\pi}(\ddot{\gamma}_1 - \ddot{\gamma}_{r1}), \tag{5.35}
$$

which then gives

$$\gamma_{c1} = \gamma_1 - \gamma_{r1}. \tag{5.36}$$

Similarly, I find

$$\gamma_{c2} = \gamma_{r2} - \gamma_2. \tag{5.37}$$

By combining Eqs. (5.31) with Eqs. (5.33), (5.36), and (5.37) I can eliminate γ_{c1} and γ_{c2} and arrive at the four coupled equations

$$\begin{aligned}
&\frac{\Phi_0}{2\pi}\left(C_{c1} + C_{q1}\right)\ddot{\gamma}_1 + I_{01}\sin(\gamma_1) - \frac{\Phi_0}{2\pi}C_{c1}\ddot{\gamma}_{r1} = 0 \\
&\frac{\Phi_0}{2\pi}\left(C_{c2} + C_{q2}\right)\ddot{\gamma}_2 + I_{02}\sin(\gamma_2) - \frac{\Phi_0}{2\pi}C_{c2}\ddot{\gamma}_{r2} = 0 \\
&\frac{\Phi_0}{2\pi}(C_{c1} + C_{r1})\ddot{\gamma}_{r1} + \frac{\Phi_0}{2\pi L_r}(\gamma_{r1} - \gamma_{r2}) - \frac{\Phi_0}{2\pi}C_{c1}\ddot{\gamma}_1 = 0 \\
&\frac{\Phi_0}{2\pi}(C_{c2} + C_{r2})\ddot{\gamma}_{r2} - \frac{\Phi_0}{2\pi L_r}(\gamma_{r1} - \gamma_{r2}) - \frac{\Phi_0}{2\pi}C_{c2}\ddot{\gamma}_2 = 0.
\end{aligned} \tag{5.38}$$

For simplicity, I now assume that $C_c = C_{c1} = C_{c2}$ and $C_r = C_{r1} = C_{r2}$. Equations (5.38) then reduce to

$$\frac{\Phi_0}{2\pi}\left(C_c + C_{q1}\right)\ddot{\gamma}_1 + I_{01}\sin(\gamma_1) - \frac{\Phi_0}{2\pi}C_c\ddot{\gamma}_{r1} = 0 \tag{5.39a}$$

$$\frac{\Phi_0}{2\pi}\left(C_c + C_{q2}\right)\ddot{\gamma}_2 + I_{02}\sin(\gamma_2) - \frac{\Phi_0}{2\pi}C_c\ddot{\gamma}_{r2} = 0 \tag{5.39b}$$

$$\frac{\Phi_0}{2\pi}(C_c + C_r)\ddot{\gamma}_{r1} + \frac{\Phi_0}{2\pi L_r}(\gamma_{r1} - \gamma_{r2}) - \frac{\Phi_0}{2\pi}C_c\ddot{\gamma}_1 = 0 \tag{5.39c}$$

$$\frac{\Phi_0}{2\pi}(C_c + C_r)\ddot{\gamma}_{r2} - \frac{\Phi_0}{2\pi L_r}(\gamma_{r1} - \gamma_{r2}) - \frac{\Phi_0}{2\pi}C_c\ddot{\gamma}_2 = 0. \tag{5.39d}$$

I now define the phase

$$\gamma_d \equiv \gamma_{r1} - \gamma_{r2}, \tag{5.40}$$

which is simply the difference in the phases γ_{r1} and γ_{r2}. With this definition, solving for $\ddot{\gamma}_{r1}$ and $\ddot{\gamma}_{r2}$ in Eqs. (5.39c) and (5.39d) gives

$$\ddot{\gamma}_{r1} = \frac{C_c}{C_c + C_r}\ddot{\gamma}_1 - \frac{1}{L_r(C_c + C_r)}\gamma_d \tag{5.41}$$

and

$$\ddot{\gamma}_{r2} = \frac{C_c}{C_c + C_r}\ddot{\gamma}_2 + \frac{1}{L_r(C_c + C_r)}\gamma_d\,. \tag{5.42}$$

By inserting Eqs. (5.41) and (5.42) into Eqs. (5.39a) and (5.39b), I then arrive at the three coupled equations

$$\begin{gathered}
\frac{\Phi_0}{2\pi}\left(C_1 + \frac{C_c C_r}{C_c + C_r}\right)\ddot{\gamma}_1 + I_{01}\sin(\gamma_1) + \frac{\Phi_0}{2\pi}\frac{C_c}{L_r(C_c + C_r)}\gamma_d = 0 \\
\frac{\Phi_0}{2\pi}\left(C_2 + \frac{C_c C_r}{C_c + C_r}\right)\ddot{\gamma}_2 + I_{02}\sin(\gamma_2) - \frac{\Phi_0}{2\pi}\frac{C_c}{L_r(C_c + C_r)}\gamma_d = 0 \\
\ddot{\gamma}_d + \frac{2}{L_r(C_c + C_r)}\gamma_d - \frac{C_c}{C_c + C_r}(\ddot{\gamma}_1 - \ddot{\gamma}_2) = 0,
\end{gathered} \tag{5.43}$$

which constitute the equations of motion for the system.

I now introduce the following definitions:

$$C_1' \equiv C_1 + \frac{C_c C_r}{C_c + C_r} \tag{5.44a}$$

$$C_2' \equiv C_2 + \frac{C_c C_r}{C_c + C_r} \tag{5.44b}$$

$$C_3 \equiv \frac{C_c^2}{2(C_c + C_r)} \tag{5.44c}$$

$$L_3 \equiv \frac{L_r(C_c + C_r)^2}{C_c^2} \tag{5.44d}$$

$$\gamma_3 \equiv \frac{C_c + C_r}{C_c}\gamma_d\,. \tag{5.44e}$$

Equations (5.43) can then be rewritten as

$$\frac{\Phi_0}{2\pi}C_1'\ddot{\gamma}_1 - \frac{\Phi_0}{2\pi}C_3(\ddot{\gamma}_3 + \ddot{\gamma}_2 - \ddot{\gamma}_1) + I_{01}\sin(\gamma_1) = 0$$

$$\frac{\Phi_0}{2\pi}C_2'\ddot{\gamma}_2 + \frac{\Phi_0}{2\pi}C_3(\ddot{\gamma}_3 + \ddot{\gamma}_2 - \ddot{\gamma}_1) + I_{02}\sin(\gamma_2) = 0 \qquad (5.45)$$

$$\frac{\Phi_0}{2\pi}C_3(\ddot{\gamma}_3 + \ddot{\gamma}_2 - \ddot{\gamma}_1) + \frac{\Phi_0}{2\pi}\frac{1}{L_3}\gamma_3 = 0.$$

The reason for writing the equations in this form is to show that they have exactly the same form as those described by Strauch *et. al.* in refs. [13, 14] for two phase qubits coupled by a fixed-frequency LC resonator. The main difference between the circuit I am describing and the one in these references is that my system has transmons while Strauch *et. al.* used phase qubits. The fact that these two circuits have practically identical Hamiltonians says a great deal about the actual differences between these devices, which amount to whether or not a current bias can be applied and the choice of the numerical value of E_J/E_C. With phase qubits, it is necessary to current bias the qubit in order to properly set the non-linearity. Since, my qubits are not current biased I can simply set the bias current terms in Strauch's dissertation to zero, and the results from refs. [13, 14] can then be applied to my coupled transmons.

5.2.2 Hamiltonian

Now that I have equations of motion for the system, the next step in deriving the Hamiltonian is to obtain the Lagrangian. It is not entirely straightforward to got from these equations of motion to the Lagrangian, but Strauch *et. al.* finds [12]

$$\mathcal{L} = \frac{1}{2}\left(\frac{\Phi_0}{2\pi}\right)^2 (C_1'\dot{\gamma}_1 + C_2'\dot{\gamma}_2) + \frac{1}{2}\left(\frac{\Phi_0}{2\pi}\right)^2 C_3(\dot{\gamma}_3 + \dot{\gamma}_2 - \dot{\gamma}_1)^2 - \frac{1}{2}\left(\frac{\Phi_0}{2\pi}\right)^2 \frac{1}{L_3}\gamma_3^2 + \frac{\Phi_0}{2\pi} I_{01}\cos(\gamma_1) + \frac{\Phi_0}{2\pi} I_{02}\cos(\gamma_2)\,. \tag{5.46}$$

The canonical momenta for the three phase coordinates are:

$$p_1 = \frac{\partial \mathcal{L}}{\partial \dot{\gamma}_1} = \left(\frac{\Phi_0}{2\pi}\right)^2 C_1'\dot{\gamma}_1 - \left(\frac{\Phi_0}{2\pi}\right)^2 C_3(\dot{\gamma}_3 + \dot{\gamma}_2 - \dot{\gamma}_1)$$

$$p_2 = \frac{\partial \mathcal{L}}{\partial \dot{\gamma}_2} = \left(\frac{\Phi_0}{2\pi}\right)^2 C_2'\dot{\gamma}_2 + \left(\frac{\Phi_0}{2\pi}\right)^2 C_3(\dot{\gamma}_3 + \dot{\gamma}_2 - \dot{\gamma}_1) \tag{5.47}$$

$$p_3 = \frac{\partial \mathcal{L}}{\partial \dot{\gamma}_3} = \left(\frac{\Phi_0}{2\pi}\right)^2 C_3(\dot{\gamma}_3 + \dot{\gamma}_2 - \dot{\gamma}_1).$$

This set of three equations is of the form $\boldsymbol{A}\vec{\dot{\gamma}} = \vec{p}$ where

$$\boldsymbol{A} = \left(\frac{\Phi_0}{2\pi}\right)^2 \begin{pmatrix} C_1' + C_3 & -C_3 & -C_3 \\ -C_3 & C_2' + C_3 & C_3 \\ -C_3 & C_3 & C_3 \end{pmatrix}. \tag{5.48}$$

This matrix is invertible and the inverse is given by

$$\boldsymbol{A}^{-1} = \left(\frac{2\pi}{\Phi_0}\right)^2 \begin{pmatrix} \frac{1}{C_1'} & 0 & \frac{1}{C_1'} \\ 0 & \frac{1}{C_2'} & -\frac{1}{C_2'} \\ \frac{1}{C_1'} & -\frac{1}{C_2'} & \left(\frac{1}{C_1'} + \frac{1}{C_2'} + \frac{1}{C_3}\right) \end{pmatrix}. \tag{5.49}$$

Taking $\vec{\dot{\gamma}} = \boldsymbol{A}^{-1}\vec{p}$, I now get

$$\dot{\gamma}_1 = \left(\frac{2\pi}{\Phi_0}\right)^2 \frac{1}{C_1'}(p_1 + p_3)$$

$$\dot{\gamma}_2 = \left(\frac{2\pi}{\Phi_0}\right)^2 \frac{1}{C_2'}(p_2 - p_3) \tag{5.50}$$

$$\dot{\gamma}_3 = \left(\frac{2\pi}{\Phi_0}\right)^2 \left(\frac{1}{C_1'} p_1 - \frac{1}{C_2'} p_2 + \left(\frac{1}{C_1'} + \frac{1}{C_2'} + \frac{1}{C_3}\right) p_3\right).$$

Since the Lagrangian in Eq. (5.46) is not explicitly time dependent, the Hamiltonian may be written as

$$\mathcal{H} = p_1\dot{\gamma}_1 + p_2\dot{\gamma}_2 + p_3\dot{\gamma}_3 - \mathcal{L}\,. \tag{5.51}$$

Inserting Eqs. (5.46) and (5.50) into Eq. (5.51) yields the Hamiltonian

$$\begin{aligned}\mathcal{H} = &\left[\frac{p_1^2}{2m_1} - \frac{\Phi_0}{2\pi} I_{01}\cos(\gamma_1)\right] + \left[\frac{p_2^2}{2m_2} - \frac{\Phi_0}{2\pi} I_{02}\cos(\gamma_2)\right] \\ &+ \left[\frac{p_3^2}{2(m_1+m_2+m_3)} + \left(\frac{\Phi_0}{2\pi}\right)^2 \frac{1}{2L_3}\gamma_3^2\right] + \left[\frac{p_1 p_3}{m_1} - \frac{p_2 p_3}{m_2}\right],\end{aligned} \tag{5.52}$$

where the effective masses are

$$\begin{aligned} m_1 &\equiv \left(\frac{\Phi_0}{2\pi}\right)^2 C_1' \\ m_2 &\equiv \left(\frac{\Phi_0}{2\pi}\right)^2 C_2' \\ m_3 &\equiv \left(\frac{\Phi_0}{2\pi}\right)^2 C_3\,. \end{aligned} \tag{5.53}$$

The first and second bracketed terms each represent a particle moving in a cosine potential. This potential was described in Chapter 4, and these terms correspond to the two transmons. The third bracketed term is a particle moving in a quadratic potential, *i.e.* a harmonic oscillator. Finally, the last bracketed term describes the coupling between the resonator and each transmon.

5.2.3 Quantization

As I just described, the Hamiltonian in Eq. (5.52) may be broken into individual pieces of the system and the coupling between them, *i.e.*

$$\mathcal{H} = \mathcal{H}_{q1} + \mathcal{H}_{q2} + \mathcal{H}_{res} + \mathcal{H}_{coupling}. \tag{5.54}$$

Using Eq. (4.20), I can then write the transmon terms as

$$\mathcal{H}_{q1} \cong \hbar\omega_{q1}\left(b_1^\dagger b_1 + \frac{1}{2}\right) - \frac{E_{C1}}{2}\left(b_1^\dagger b_1\left(b_1^\dagger b_1 + 1\right) + \frac{1}{2}\right) \tag{5.55}$$

and

$$\mathcal{H}_{q2} \cong \hbar\omega_{q2}\left(b_2^\dagger b_2 + \frac{1}{2}\right) - \frac{E_{C2}}{2}\left(b_2^\dagger b_2\left(b_2^\dagger b_2 + 1\right) + \frac{1}{2}\right), \tag{5.56}$$

where b_1 and b_2 are the lowering operators for transmons 1 and 2, respectively, and $b_1^\dagger$ and $b_2^\dagger$ are the raising operators for transmons 1 and 2, respectively. It should be emphasized here that the transmon frequencies $\omega_{q1}/2\pi$ and $\omega_{q2}/2\pi$ are the uncoupled angular transition frequencies of the transmons (see Chapter 4). However, in the coupled system the capacitance associated with transmon 1 is $C_1' = C_1 + \frac{C_c C_r}{C_c + C_r}$ (see definitions in Eq. (5.44)) instead of just C_1. Thus, the value of $E_{C1} = e^2/2C_1'$ is less than $E_{C1} = e^2/2C_1$, and the transmon transition frequency is at a lower frequency. Similarly, with $C_2' = C_2 + \frac{C_c C_r}{C_c + C_r}$, the transition frequency of transmon 2 is shifted down due to $E_{C2} = e^2/2C_2'$ being less than that of $E_{C20} = e^2/2C_2$.

Since the resonator term is simply a harmonic oscillator, the Hamiltonian may be written as

$$\mathcal{H}_{res} = \hbar\omega_r\left(a_r^\dagger a_r + \frac{1}{2}\right), \tag{5.57}$$

where a_r and $a_r^\dagger$ are the lowering and raising operators for the resonator and

$$\omega_r = \frac{1}{\sqrt{L_3(C_1' + C_2' + C_3)}} \,. \tag{5.58}$$

The coupling terms in Eq. (5.52) can be written in terms of the raising and lowering operators by using, for example [15]

$$p = i\sqrt{\frac{\hbar m\omega}{2}}(a^\dagger - a) \tag{5.59}$$

I then find

$$\mathcal{H}_{coupling} = \frac{\hbar}{2}\left(\sqrt{\frac{m_3}{m_2}\,\omega_2\omega_r}\left(b_2^\dagger a_r + b_2 a_r^\dagger\right) - \sqrt{\frac{m_3}{m_1}\,\omega_1\omega_r}\left(b_1^\dagger a_r + b_1 a_r^\dagger\right)\right). \tag{5.60}$$

Going from Eq. (5.59) to Eq. (5.60), it is important to note that I have thrown out terms such as $b_1^\dagger a_r^\dagger$ by using the rotating wave approximation. Examining Eq. (5.60), one sees that the coupling term is similar to the coupling used in the Jaynes-Cummings Hamiltonian, and I can now define the coupling strength g as

$$g_{qi\to res} = \frac{1}{2}\sqrt{\frac{m_3}{m_i}\,\omega_i\omega_r} = \frac{C_c}{2}\sqrt{\frac{\omega_i\omega_r}{2(C_iC_c + C_iC_r + C_rC_c)}}\,. \tag{5.61}$$

As in the Jaynes-Cummings Hamiltonian, this term allows the qubits to trade single photon excitations with the resonator.

Putting Eqs. (5.55), (5.56), (5.57), and (5.60) together, I find the following Hamiltonian for the circuit

$$\begin{aligned}\mathcal{H} = &\left[\hbar\omega_{q1}\left(b_1^\dagger b_1 + \frac{1}{2}\right) - \frac{E_{C1}}{2}\left(b_1^\dagger b_1\left(b_1^\dagger b_1 + 1\right) + \frac{1}{2}\right)\right] \\ &+ \left[\hbar\omega_{q2}\left(b_2^\dagger b_2 + \frac{1}{2}\right) - \frac{E_{C2}}{2}\left(b_2^\dagger b_2\left(b_2^\dagger b_2 + 1\right) + \frac{1}{2}\right)\right] \\ &+ \left[\hbar\omega_r\left(a_r^\dagger a_r + \frac{1}{2}\right)\right] \\ &+ \frac{\hbar}{2}\left(\sqrt{\frac{m_3}{m_2}\,\omega_2\omega_3}\left(b_2^\dagger a_r + b_2 a_r^\dagger\right) - \sqrt{\frac{m_3}{m_1}\,\omega_1\omega_3}\left(b_1^\dagger a_r + b_1 a_r^\dagger\right)\right).\end{aligned} \tag{5.62}$$

For low photon occupation, I will mainly be interested in the dispersive regime. In this regime the resonator transition frequency depends on the state of the qubit, and each qubits' g-to-e transition frequency is shifted down by 2χ for every photon in the resonator. Without proof, this suggests that Eq. (5.62) may be written in the form:

$$\begin{aligned}\mathcal{H}_{disp} = &\hbar\tilde{\omega}_{q1}n_{q1} - \frac{E_{C1}}{2}\left(n_{q1}\left(n_{q1}+1\right)\right) + \hbar\tilde{\omega}_{q2}n_{q2} \\ &- \frac{E_{C2}}{2}\left(n_{q2}\left(n_{q2}+1\right)\right) + \hbar\tilde{\omega}_r n_r + 2\hbar\chi_{1r}n_{q1}n_r \\ &+ 2\hbar\chi_{2r}n_{q2}n_r + 2\hbar\chi_{12}n_{q1}n_{q2}\,,\end{aligned} \tag{5.63}$$

where I have dropped constant terms and replaced all operators of the form $a^\dagger a$ or $b^\dagger b$ by the corresponding number operator. Also, in Eq. (5.63) I have explicitly used the dressed values for the frequencies $\tilde{\omega}_{q1}$, $\tilde{\omega}_{q2}$, and $\tilde{\omega}_r$. One final note about Eq. (5.63) is that I have included a final term with an explicit qubit-qubit coupling term that was not included in the derivation of Eq. (5.52); though, the term would arise from direct capacitive coupling between the qubits.

5.2.4 Including the Cavity

In my experiments, the chip with the qubits and LC resonator chips was enclosed in a 3D microwave cavity. This cavity also acted like a resonator that was capacitively coupled to both the transmons and the LC resonator. It was an integral part of the circuit and also needed to be included in this analysis. This is especially true since the cavity modes were used to perform the qubits' state readout.

A rough schematic of the full system is shown in Fig. 5.8. This is the same circuit as in Fig. 5.7, but it is now enclosed in a cavity. Based on the analysis of the previous section, I can include the cavity in an *ad hoc* fashion by writing:

$$\begin{aligned}\mathcal{H} = {} & \hbar\omega_{q1}\left(n_1+\frac{1}{2}\right)-\frac{E_{C1}}{2}n_1(n_1+1)+\hbar\omega_{q2}\left(n_2+\frac{1}{2}\right)-\frac{E_{C2}}{2}n_2(n_2+1) \\ & +\hbar\omega_r n_r+\hbar\omega_c n_c+\hbar g_{1r}\left(b_1^\dagger a_r+b_1 a_r^\dagger\right)+\hbar g_{2r}\left(b_2^\dagger a_r+b_2 a_r^\dagger\right) \\ & +\hbar g_{1c}\left(b_1^\dagger a_c+b_1 a_c^\dagger\right)+\hbar g_{2c}\left(b_2^\dagger a_c+b_2 a_c^\dagger\right) \\ & +\hbar g_{12}\left(b_1^\dagger b_2+b_1 b_2^\dagger\right)+\hbar g_{rc}\left(a_r^\dagger a_c+a_r a_c^\dagger\right),\end{aligned} \tag{5.64}$$

where $\omega_c/2\pi$ is the resonance frequency of the 3D cavity, a_c and $a_c^\dagger$ are the lowering and raising operators for the cavity, respectively, and g_{1c}, g_{2c}, and g_{rc} are the coupling strengths between the cavity and transmon 1, transmon 2, and the LC resonator, respectively.

In practice, we used Eq. (5.64) to simulate the behavior of the system. We constructed the full Hamiltonian matrix using the uncoupled basis states of the system and then diagonalized it numerically to extract the eigenvalues. As for the case of a single qubit coupled to a resonator, the coupling terms acted as a perturbation on the uncoupled system energy levels and produced dressed eigenstates. I discuss in detail in Chapter 8 how the simulations were used to extract the parameters of device TRES_092917 – essentially we compared the simulated transition frequencies to the

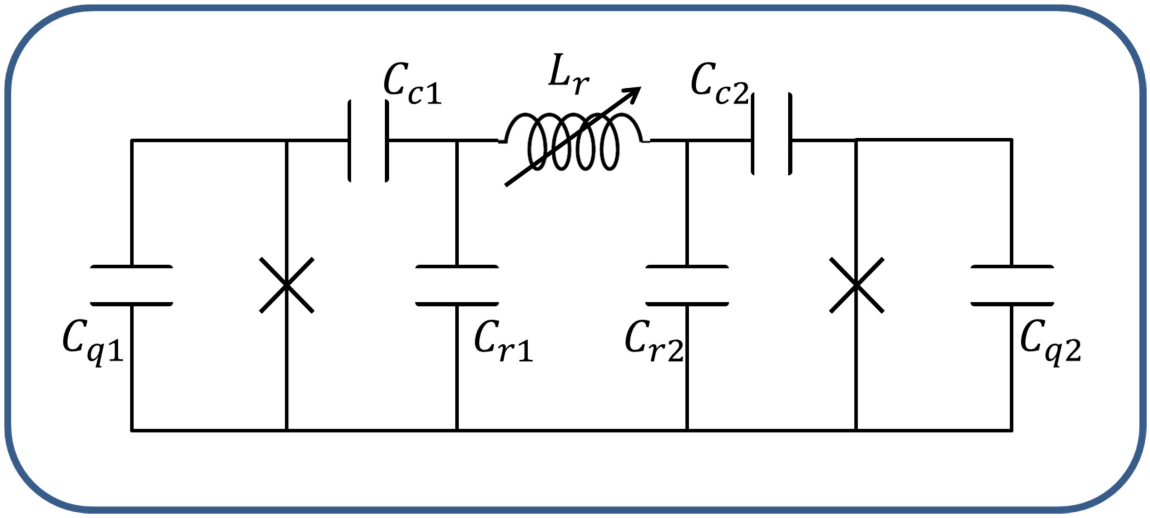

Figure 5.8: (a) Circuit schematic showing a tunable LC resonator capacitively coupled to two transmons in a 3D microwave resonant cavity (shown in dark blue).

measured frequencies and adjusted the Hamiltonian's parameters until a good agreement was obtained.

It is also useful to consider the effective system Hamiltonian at low photon occupation number in the cavity and resonator. In the low-photon number, dispersive limit I can write

$$\begin{aligned}\mathcal{H} = \hbar\tilde{\omega}_{q1}n_1 - \frac{E_{C1}}{2}n_1(n_1+1) + \hbar\tilde{\omega}_{q2}n_2 - \frac{E_{C2}}{2}n_2(n_2+1) + \hbar\tilde{\omega}_r n_r \\ + \hbar\tilde{\omega}_c n_c + 2\hbar\chi_{1r}n_1n_r + 2\hbar\chi_{2r}n_2n_r + 2\hbar\chi_{1c}n_1n_c \\ + 2\hbar\chi_{2c}n_2n_c + 2\hbar\chi_{12}n_1n_2 + 2\hbar\chi_{rc}n_rn_c.\end{aligned} \tag{5.65}$$

where the dispersive shifts χ_{1r}, χ_{2r}, χ_{1c}, χ_{2c}, χ_{12}, and χ_{rc} can be found by diagonalizing Eq. (5.64) and examining the behavior of the qubit and resonator levels for different excitation levels.

5.3 TRES Device Parameters

In this section I discuss the parameter choices for my TRES devices, which consisted of a tunable resonator and two transmon qubits inside a single 3D microwave resonant cavity. For details on how I designed the physical layout to actually achieve these parameters, see Chapter 6.

The key purpose behind this device was to produce a variable qubit-qubit coupling. In order for this to be effective, the coupling needed to produce a good on/off ratio. Here I discuss the design choices made, and I show a simulation of this device using the parameters discussed and Eq. (5.64) using 4 levels in each uncoupled subsystem.

The first choice to be made was the resonance frequency of the 3D cavity. This was an easy choice to make because I already had a cavity design from previous experiments. Every cavity I machined in the student shop or had the Physics Machine Shop make were designed to have a TE_{101} frequency at 6.3 GHz. With a sapphire chip mounted in the cavity space, the resulting frequency was shifted down to around 6.13 GHz.

The next parameters to choose were the qubit coupling strengths and frequencies. Since a system with two qubits and a tunable resonator would be complicated, I decided to keep the transmon design as simple and generic as possible by using a convential, existing 3D transmon design. In particular, I drew from references [5,16-18]. The design I settled on had two large pads that acted as the shunting capacitance of the Josephson junction (see Fig. 5.9). With this design, the qubit would be placed near the center of the cavity, and if there were no LC resonator, one

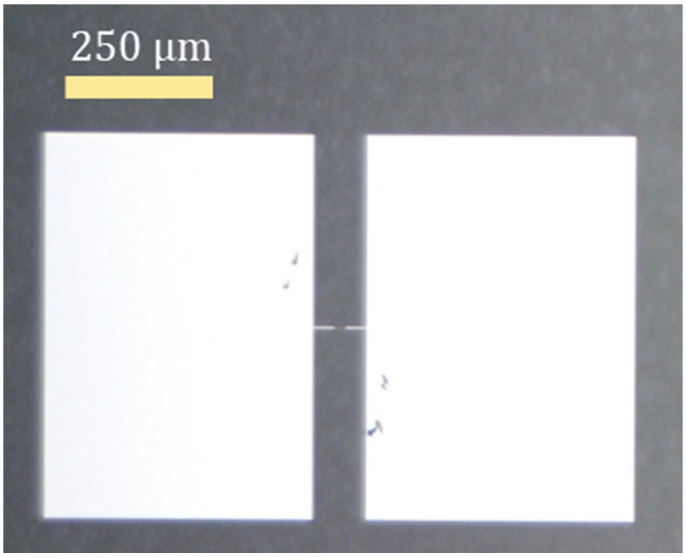

Fig. 5.9: Photograph of transmon on device TRES_092917.

would expect a coupling strength g_{qc} of approximately 150 MHz between each qubit and the cavity and an E_c of 200 MHz for each qubit [4]. In order to be in the dispersive limit (see section 5.2.2) and to reduce loss in the transmons due to the Purcell effect [19], I chose a g-to-e transition frequency of 5 GHz for qubit 1, 1.13 GHz detuned from the cavity. For qubit 2, I needed to choose a frequency close to the first qubit so that there could be a large dispersive shift and the tunable LC would be able to address both qubits, but not so close that I would have difficulty driving one and not the other. With the limits on the tuning range of the LC resonator, I chose 4.75 GHz for qubit 2.

With the frequencies of the qubits chosen, the next step was to choose the frequency range of the tunable resonator (see Fig. 5.10). To achieve a good "on" coupling between the qubits, I needed to be able to tune through both qubit transition

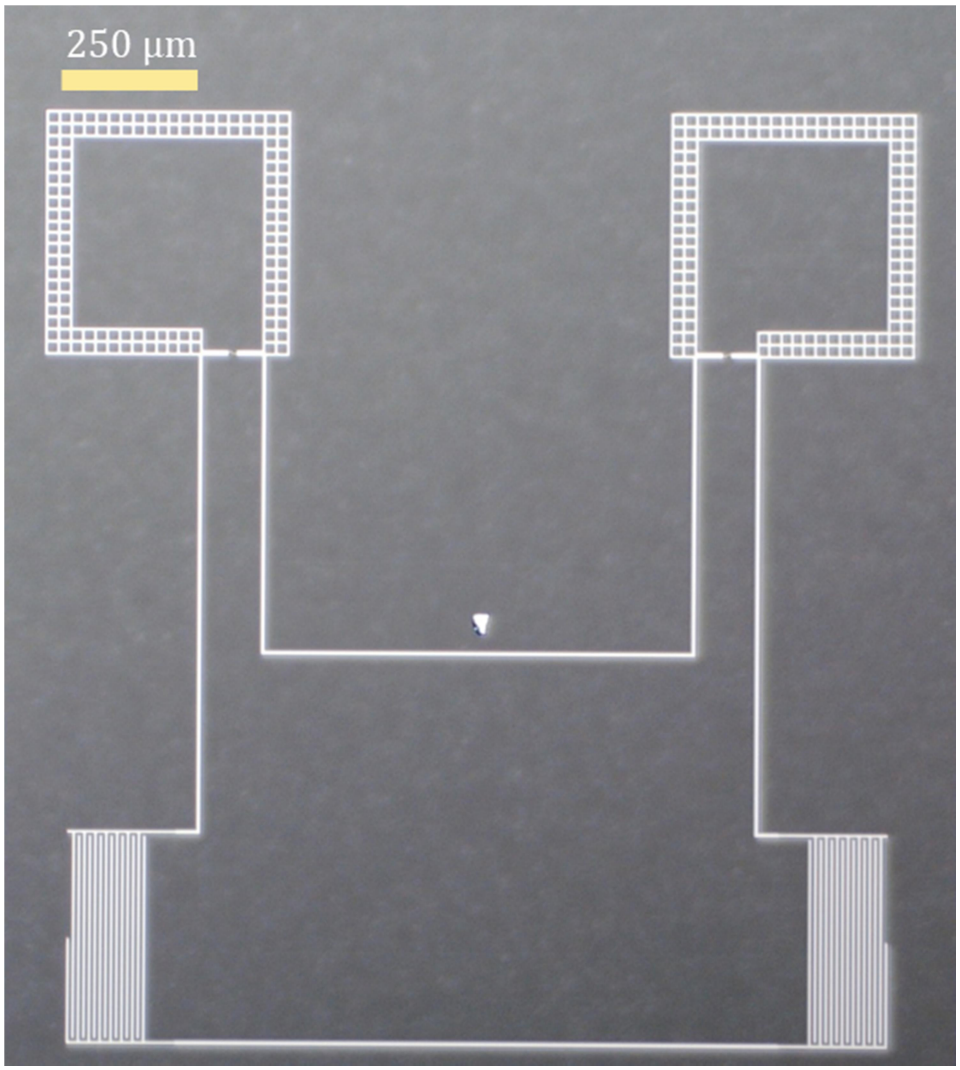

Fig. 5.10: Photograph of tunable LC resonator on device TRES_092917.

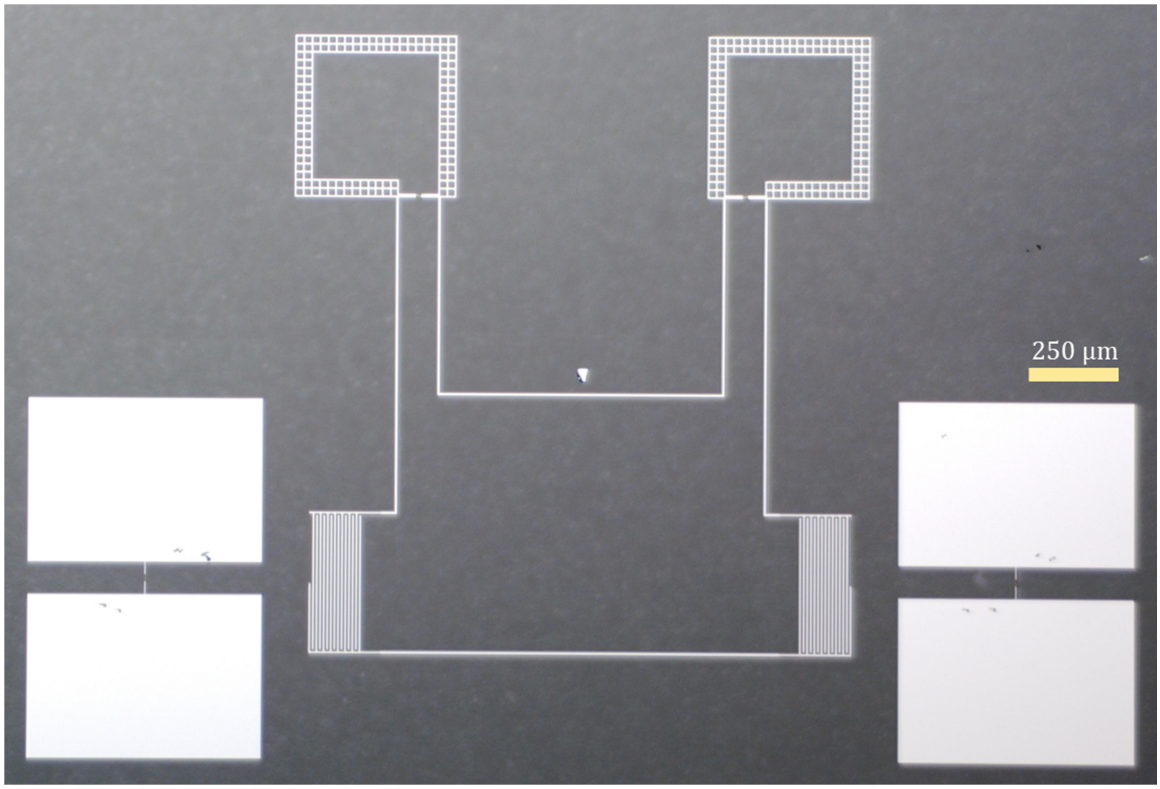

Fig. 5.11: Photograph of device TRES_092917 showing layout of transmons relative to tunable LC resonator.

frequencies. To turn the qubit-qubit coupling "off", I also needed to be able to tune low enough to be far from both qubit transitions compared to the coupling strengths g_{1r} and g_{2r}. I chose a max LC tuning frequency of 5.1 GHz and a min frequency of 4 GHz, which is a range of 1.1 GHz. Given the size of the capacitors in my TRES tunable resonator and its placement in the center of the cavity, I initially expected that this would have quite a large coupling to the cavity, of order 200 MHz. However, after some thought, it became clear that the resonant mode of the LC resonator would give the two capacitors opposite electric dipole moments (see Figs. 5.10 and 5.11), which would lead to a relatively small net coupling to the cavity mode. It was difficult to obtain a good estimate for this during the design stage, and we only used a rough number of $g_{rc} \approx 100$ MHz.

It was important to keep the coupling strength of the qubits to the tunable resonator in a reasonable range. If the coupling was too strong, the Purcell effect would dominate the lifetime; however, if the coupling is too weak, the resonator would be ineffective as a variable coupling element. The design value was set to $g_{1r} = g_{2r} = 100$ MHz. However, due to a modification of the design (see Chapter 6) this number shrank in the actual device to 60 MHz, and I used this smaller value in the simulation below.

The final important design parameter was the direct qubit-qubit coupling strength g_{12}. Since the main goal of this device was to be able to turn on and turn off the qubit-qubit coupling, this direct coupling needed to be as small as possible. In my design, the two qubits lie on either side of the tunable resonator (see Fig. 5.11). This put a relatively large amount of metal between the two qubits and helped to prevent the electric field of one qubit from reaching the other, which would lead to a fixed, direct coupling. Also, the

two qubits were separated by more than 1 mm on the chip, which should help to reduce the direct coupling. This was a difficult parameter to estimate in the design. I chose a value of 10 MHz for the simulation.

To determine the expected effective qubit-qubit dispersive shift χ_{qq} and how it depends on tuning flux, I needed to simulate the energy levels of the system. In Fig. 5.12 I show a simulation of the transition energies between key states of the system using the design parameters (see Table 5.1). For this simulation I found the eigenvalues of Eq. (5.64) truncated to 4 energy levels each for the cavity, resonator, qubit 1, and qubit 2 for a total of 256 energy levels. The plot shows the variation of the energy levels as a function of the applied tuning flux current I_f.

For comparison, in Fig. 5.12(a) I plot the resulting simulated level transitions for no coupling. The yellow and orange curves are for states $|eg00\rangle$ and $|ge00\rangle$, respectively. Since there is no coupling, their energies do not vary with flux. The blue curve represents state $|gg10\rangle$, the single-photon transitions in the tunable LC resonator. For this simulation, I used typical values for the mutual inductance and zero background flux offset in each resonator tuning loop in order to make a repeating pattern of a small tuning dips (only one tuning loop active) and then a large tuning dip (both tuning loops acting together) (see Chapter 3).

In Fig. 5.12(b), I plot the simulated energy levels including the coupling terms. It is clear that this dramatically changes the energy levels and leads to avoided level crossings. The minimum separation of the avoided levels between the LC resonator and the qubits is $2g_{1r}$ and $2g_{2r}$ for transmons 1 and 2, respectively. As the current is varied between 0 and 0.2 mA the yellow curve is mostly an excited state of the resonator while

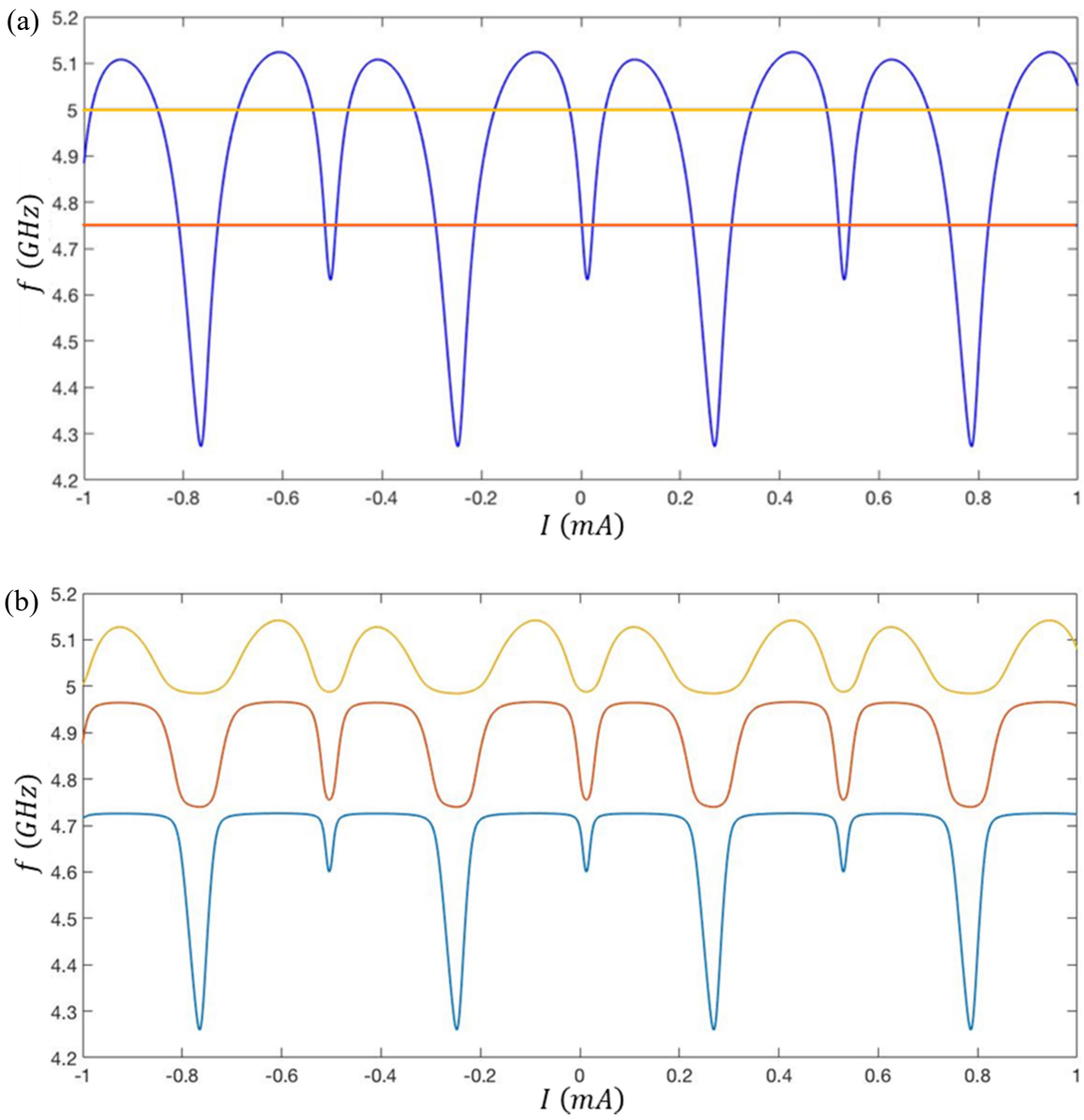

Fig. 5.12: (a) Three lowest transitions in the numerical analysis of Eq. (5.64) with each system having 4 allowed states and no coupling. The x-axis of each plot is the flux current I_f used to tune the resonator and the y-axis is the transition frequency. (b) Results with coupling.

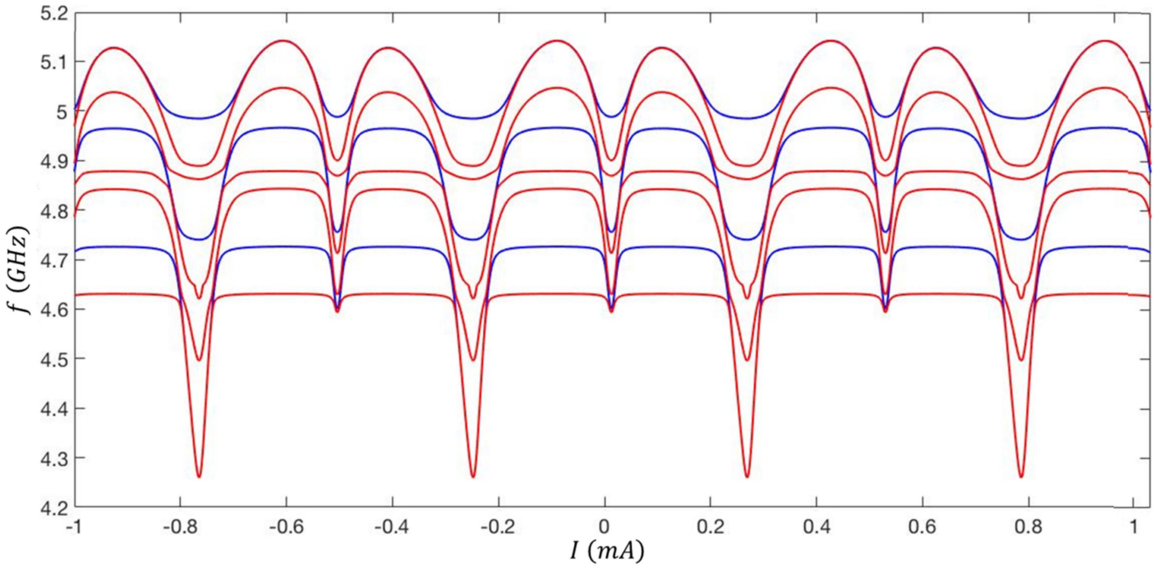

Fig. 5.13: Plot showing some of the two-photon transitions (red) predicted by the numerical analysis of Eq. (5.64). The blue curves are the single-photon transitions I show in Fig. 5.12.

the orange and blue curves are mostly excited state transitions of qubits 1 and 2 $|eg00\rangle$ and $|ge00\rangle$, respectively. However, at approximately 0.26 mA, when the resonator is tuned to a minimum, the blue curve is now mostly the resonator state $|gg10\rangle$, while the yellow and orange curves are qubits 1 and 2 states $|eg00\rangle$ and $|ge00\rangle$, respectively.

Figure 5.13 shows a plot of 6 two-photon transitions (red curves) from the ground state $|gg00\rangle$ and single-photon transitions (blue curves) between the ground state and the lowest lying states. As this figure shows, there are many possible one-photon and two-photon transitions from the ground state even in this relatively narrow frequency range. These can be very useful for extracting the many system parameters from spectroscopy (see Chapter 8).

The most important thing to take away from this device is the expected qubit-qubit dispersive shift χ_{qq} and how it depends on flux. The purpose of this device was to be able to selectively couple or decouple two or more qubits. I have defined the transition frequency of qubit 1 from state $|gg00\rangle$ to state $|eg00\rangle$ as f_1. However, in the presence of qubit-qubit coupling, the transition frequency of qubit 1 is dispersively shifted to frequency f_1' if qubit 2 is excited. Thus, $2\chi_{qq} = f_1' - f_1$. In Fig. 5.14(a) I show a plot of f_1 (blue curve) and f_1' (burnt orange curve). Near the avoided level crossings the shift is large, but the states are superpositions of the qubit-LC basis states. For a range of currents between 0.23 mA and 0.3 mA the resonator frequency is at its minimum value

Table 5.1: Design parameters for TRES devices.

Parameter	Value
$\omega_c/2\pi$	6.13 GHz
$\omega_r/2\pi$	5.1 GHz to 4 GHz
$\omega_{q1}/2\pi$	5 GHz
$\omega_{q2}/2\pi$	4.75 GHz
$g_{1c}/2\pi$	150 MHz
$g_{2c}/2\pi$	150 MHz
$g_{1r}/2\pi$	60 MHz
$g_{2r}/2\pi$	60 MHz
$g_{rc}/2\pi$	60 MHz
$g_{12}/2\pi$	10 MHz
E_{C1}/h	200 MHz
E_{C2}/h	200 MHz

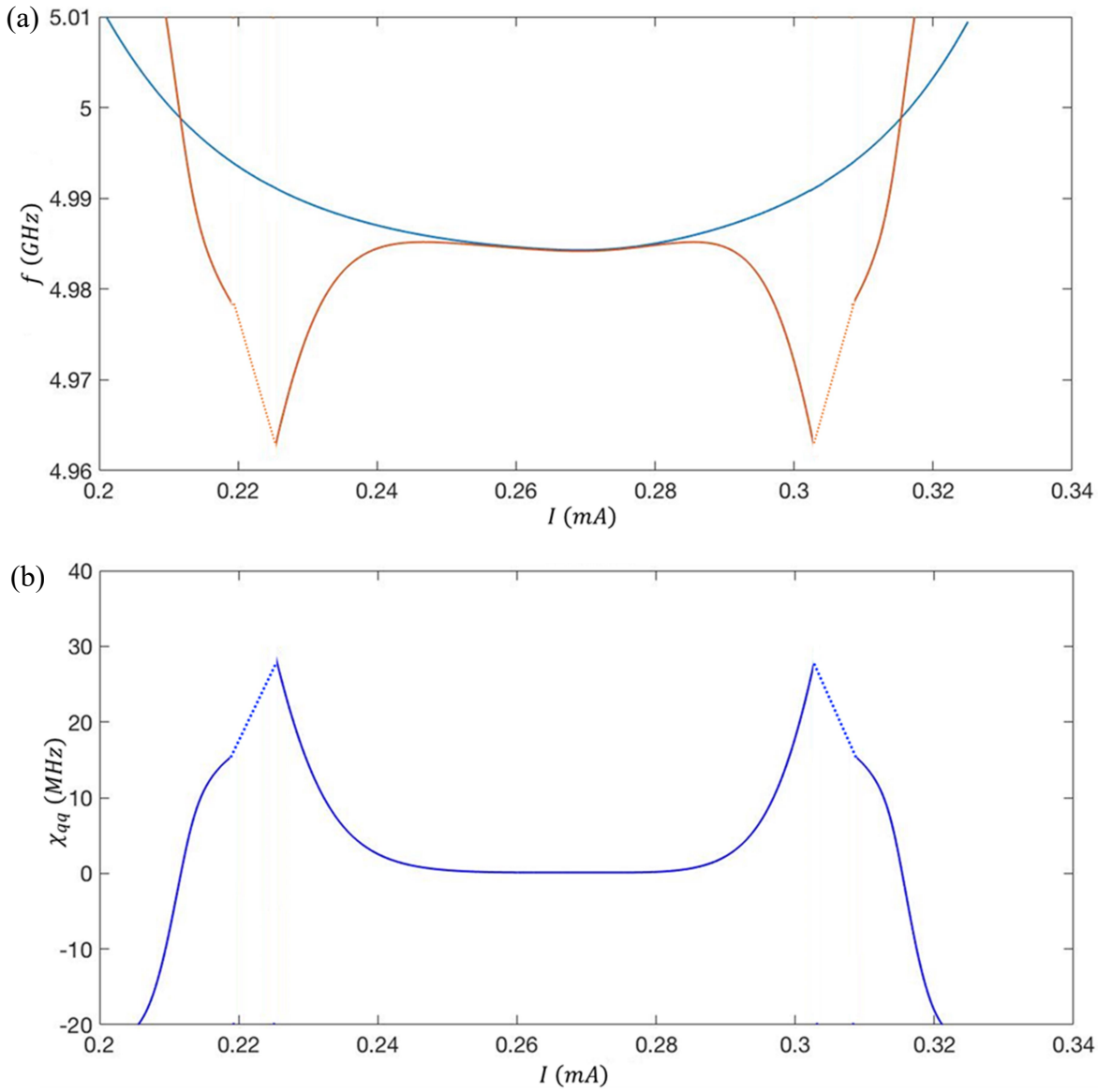

Fig. 5.14: (a) g-to-e transition frequency f_2 of qubit 2 when qubit 1 is in its ground state (blue) and when it is in its first excited state (red) vs. flux tuning bias current I. (b) Plot of the qubit-qubit dispersive shift $2\chi_{qq}$, which is the difference between the two curves in (a).

and the qubit-qubit dispersive shift is quite small with $\chi_{qq} < 0.2$ MHz. As the current approaches the edges of this range, a noticeable difference between the transition frequencies emerges to give $2\chi_{qq} = 28$ MHz before the avoided level crossing. In Fig. 5.14(b) I plotted the difference between the two curves in Fig. 5.14(a). The maximum value of $2\chi_{qq}$ is relatively large and is consistent with a CNOT gate time of about $\tau_{gate} = 25$ ns, while the minimum value of $2\chi_{qq}$ is much smaller, demonstrating that a useful tunable coupling is possible with this design.

Chapter 6

TRES_092917 Device Design and Fabrication

In this chapter I describe the design and fabrication of my device TRES_092917, which had two transmons and a tunable LC resonator. I start by discussing the main design choices I needed to make for the physical layout of the devices. I then summarize the fabrication process, including e-beam lithography, the development process, thermal evaporation, and room temperature device characterization.

6.1 Device Layout

In this section I describe how I designed the layout for my devices in order to achieve the design values for the frequencies and coupling strengths I present in Chapter 5 Table 5.1. In particular, I describe the layout and fabrication of chips that had two transmons coupled to a tunable resonator. The name for these devices, "TRES", comes from there being three (*tres* in Spanish) separate things on the chip and that the coupling component was a Tunable RESonator. Given the complexity of these devices, here I go through each piece and describe how I achieved the particular design choices. I start with the transmons, then discuss the tunable resonator, and finally end with a discussion of how the different components are coupled together.

6.1.1 Transmon Layout

As I discussed in Chapter 5, the design values for the qubit transition frequencies were $f_{q1} = 5$ GHz and $f_{q2} = 4.75$ GHz. These frequencies are set by the transmon

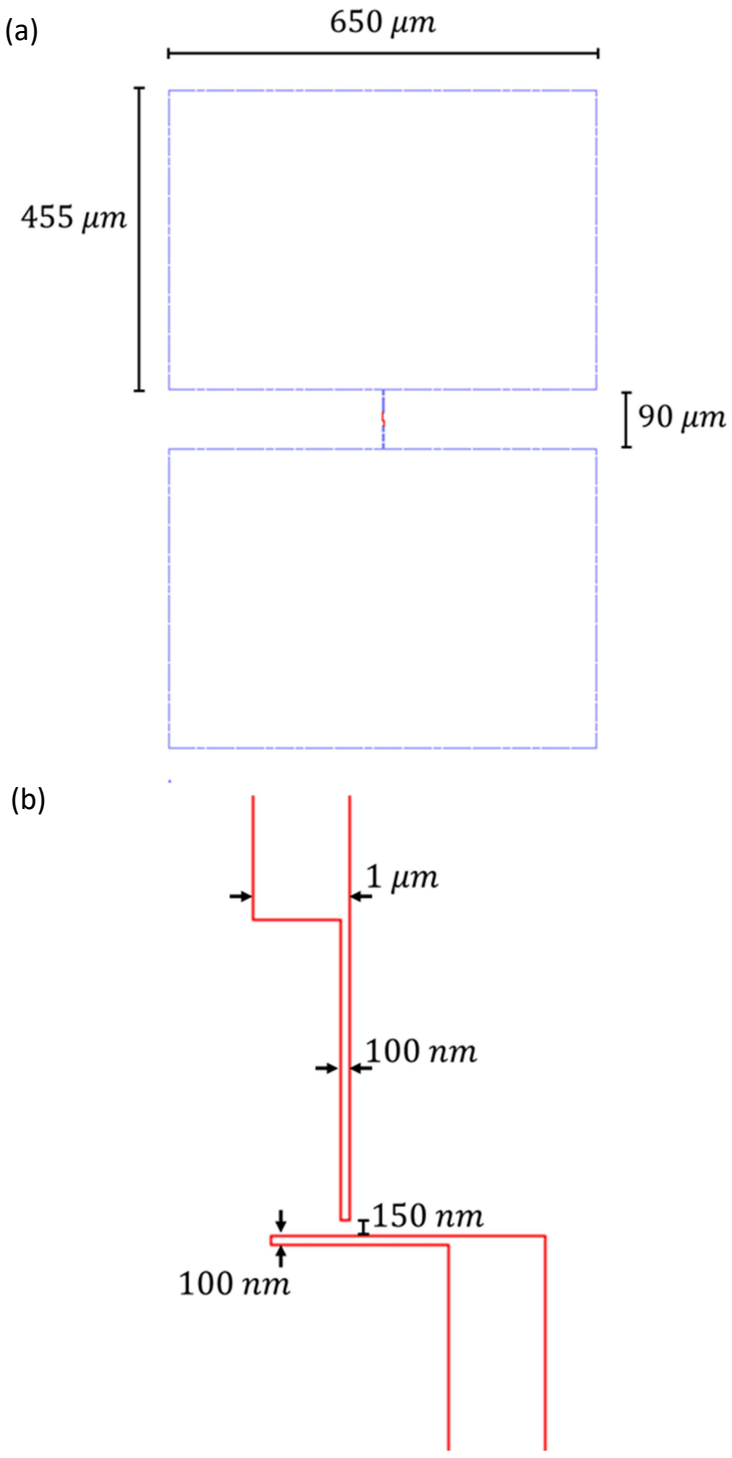

Fig. 6.1: (a) CAD rendering of transmon design used in TRES device pattern. The bluish-purple sections are the transmon pads, and the red areas are the junction. (b) CAD rendering of the transmon junction.

Josephson energy $E_J = \Phi_0 I_0/2\pi$ and the charging energy $E_C = e^2/2C$. The charging energy also sets the qubit's anharmonicity (see Chapter 4), which I wanted to be a typical value of $E_c/h = 200\ MHz$. The capacitance C is mainly controlled by the size of the transmon pads. Based on Fig. 6.3 in ref. [1], I made the pads 650 μm x 455 μm and separated them by 90 μm to produce $C_q \approx$ 100 fF and $E_C/h \approx$ 194 MHz. A CAD rendering of the resulting qubit pattern is shown in Fig. 6.1(a).

The g-to-e transition frequency of the qubit is given by (see Chapter 4)

$$f_q = \sqrt{8\left(\frac{E_J}{h}\right)\left(\frac{E_C}{h}\right)} - \left(\frac{E_C}{h}\right) \tag{6.1}$$

Given that $E_C/h \approx$ 200 MHz, the required Josephson energies are $E_{J1}/h \approx$ 16.9 GHz and $E_{J2}/h \approx$ 15.3 GHz, respectively, for qubits 1 and 2. Through the relation $E_J = \Phi_0 I_0/2\pi$, this corresponds to junction critical currents of $I_{01} \approx$ 34 nA and $I_{02} \approx$ 31 nA. Using the Ambegaokar-Baratoff relation [2]

$$I_0 R_n = \frac{\pi\Delta}{2e} \tag{6.2}$$

with a gap value of $\Delta =$ 170 μeV, the normal state resistances are estimated to be $R_{n1} \approx$ 7.9 kΩ and $R_{n2} \approx$ 8.6 kΩ (see section 6.6 for more details on the tunneling resistance).

Figure 8(b) shows a CAD drawing of the transmon junction pattern I used. In this rendering the bridge for the junction is formed by two perpendicular wires. Each wire is 100 nm wide and they are separated by a 100 nm x 150 nm bridge. Nominally, this gives a junction area $A_J =$ (100 nm)^2. With the junction area fixed, the only way to set the critical current was by varying the oxidation exposure during the double-angle evaporation process, which I discuss below. Since the two qubits were meant to have somewhat different transition frequencies, one might try to accomplish this by making

the second qubit's junction a bit bigger in order to increase the critical current. However, the on-chip variation in critical currents that I observed was so large (typically more than 20%) that such fine tuning of E_J was not going to be possible. Instead, I made the junction in each qubit the same size and relied on the spread in E_J to yield a difference between the two transmons. Achieving a sufficiently small difference was a matter of trial and error.

The qubit-cavity coupling strength was mainly set by the size of the qubit pads and the position of the chip inside the cavity space. Although the charging energy was also determined by the size and layout of the transmon pads, the coupling to the cavity depends on the effective dipole moment created by the pads, which can be varied independently by changing the pad layout, qubit location in the cavity, and the orientation of the transmon in the cavity space. Ideally, I wanted a standard design with a standard coupling strength of approximately $g_{qc} \approx 150$ MHz, which hopefully would minimize trouble that could have arisen from using atypical parameters and would let me focus on issues of constructing a system with a tunable element.

6.1.2 Designing the Tunable LC Resonator Layout

As I discussed in Chapter 5, the design of the tunable LC resonator specified a tuning range of 4 GHz to 5.1 GHz, which was an order of magnitude larger than I achieved in my earlier experiment on an isolated tunable resonator (see Chapter 3). This increase in tuning turned out to be quite simple to achieve: I just needed to move the LC resonator's junctions from the "long arm" of the tuning loops to the "short arm". This difference can be readily seen by comparing Figs. 3.18 and 6.2.

I also had to figure out how to couple two qubits to one tunable resonator. It was clear that the transmons must not be close to each other since this would produce a large fixed qubit-qubit coupling and prevent achieving a good "off" point for the total qubit-qubit coupling. With its single capacitor, the "mad Mickey" design discussed in Chapter 3 was not going to work. Instead, I split the capacitor into two series connected capacitors, one on each side of the circuit (see Fig. 6.2(a)). This new design retained the two tuning loops and the majority of the fixed inductance was provided by the relatively long wires connecting the capacitors. With two interdigitated capacitors, placed relatively far apart, each transmon could now be placed near the resonator and be capacitively coupled to a resonator capacitor without being too close to each other.

One potential issue with using two capacitors in the LC resonator was that this would give two different resonant modes. The lower frequency mode is a "circulating" mode where the voltage drop across the series connected capacitors are in phase with each other. The higher frequency mode is one in which the voltage drop across the series capacitors are 180º out of phase with each other. It turns out that for the layout I used, only the lower frequency mode is important because the second mode was at a much higher frequency, well out of the range of interest for coupling to the qubits and cavity. For the low-frequency mode, the inductances of the top and bottom lines in the device simply add, while the capacitors add in series (*i.e.* $C_r = C_1C_2/(C_1 + C_2)$).

To keep the size of the LC resonator similar to my earlier designs, I chose an overall length of 1510 μm for the resonator. FastHenry estimates of the geometric

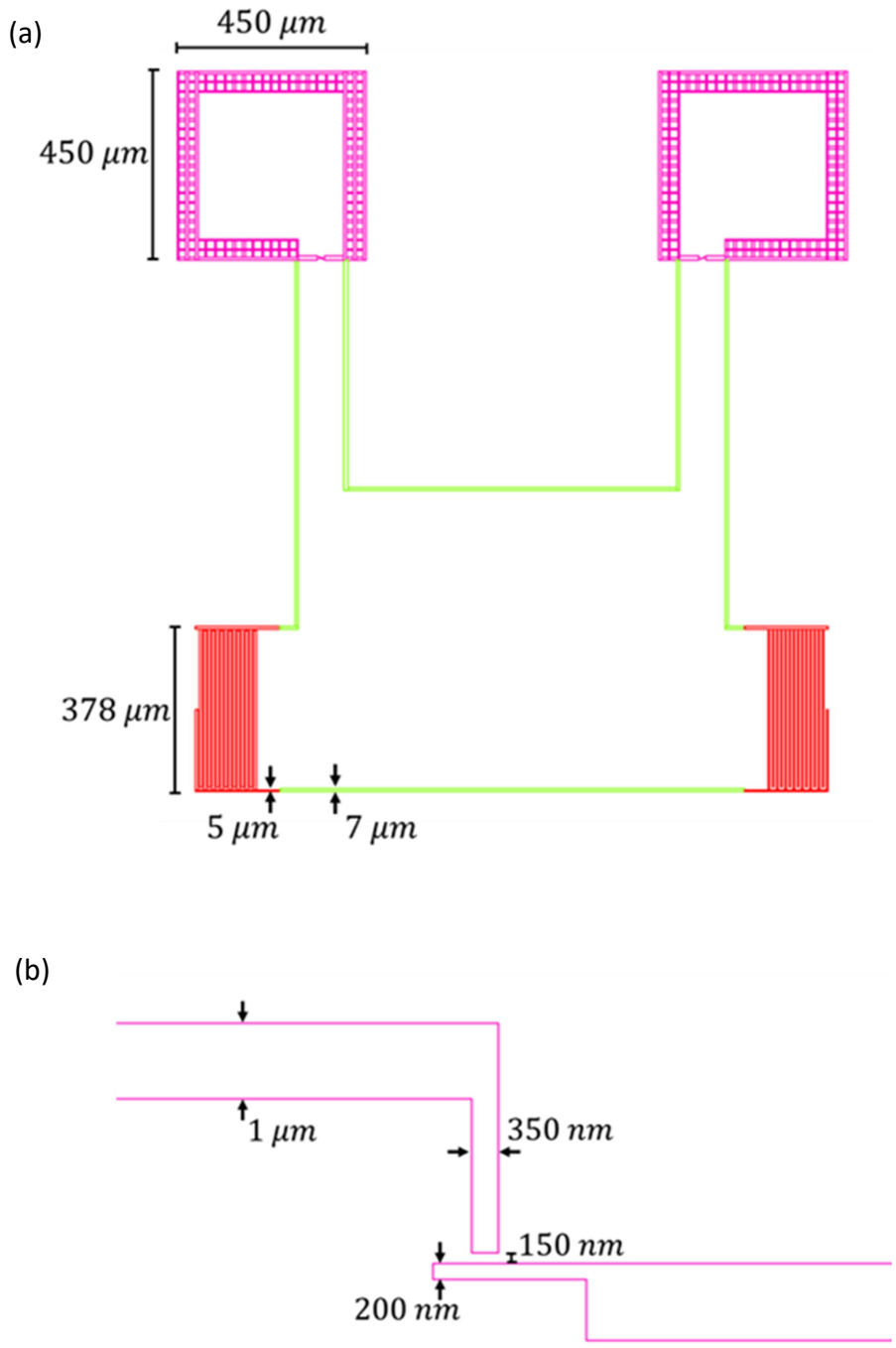

Fig. 6.2: (a) CAD rendering of TRES style tunable resonator. The magenta portions are the tuning loops, the green wires are the inductor, and the red portions are the interdigitated capacitors. (b) CAD drawing showing a detailed view of the junction bridge for a tuning loop.

inductances gave a total of $L_0 = 8.3$ nH. Ignoring the Josephson inductance of the junctions in the two SQUID tuning loops (*i.e.* setting $L_{J1} = L_{J2} = \infty$) and assuming a bare, untuned resonance frequency of $f_r = 5$ GHz, I obtained a design value for the total capacitance of $C_r = 1/4\pi^2 f_r^2 L_0 = 120$ fF. As discussed above, the total capacitance is created by two capacitors in series. For equal capacitances, this gives $C_1 = C_2 = 240$ fF. This capacitance could readily be obtained with an interdigitated capacitor (IDC), which would also produce low loss and be easy to couple to a transmon.

Figure 6.3 shows a schematic of an IDC with all the relevant geometric parameters labeled. The capacitance of an IDC is given by [3]:

$$C = \varepsilon_c \frac{10^{-9}}{18\pi} \frac{K(k)}{K'(k)} (n-1) l \,, \tag{6.3}$$

where, ε_c is the effective relative permittivity, n is the total number of fingers in the capacitor, and l is the length of the fingers. I used $\varepsilon_c = 5.5$, which was an average between the sapphire chip ($\varepsilon_r = 10$) and vacuum. The function $K(k)$ is the complete elliptic integral of the first kind, and $K'(k)$ is its complement given by $K'(k) = K\left(\sqrt{1-k^2}\right)$, where $k = \tan^2(\pi a/4b)$, $a = w/2$, and $b = (w+s)/2$, and where w is the capacitor finger width and s is the spacing between the capacitor fingers. With $w = 5$ μm and $s = 5$ μm, I obtain $k = 0.7157$, $K(k) = 1.64557$, $K'(k) = 3.50116$, and

$$C_1 = C_2 = \alpha(n-1) l \,, \tag{6.4}$$

where $\alpha = 4.57 \cdot 10^{-2}$ fF/μm. All this needs is a choice of finger length l and number of fingers n.

The process to choose values for n and l was iterative in nature. For the final values, I chose $l = 378$ μm. With $C_1 = C_2 = 240$ fF, Eq. (6.4) gives $n = 15$ for the

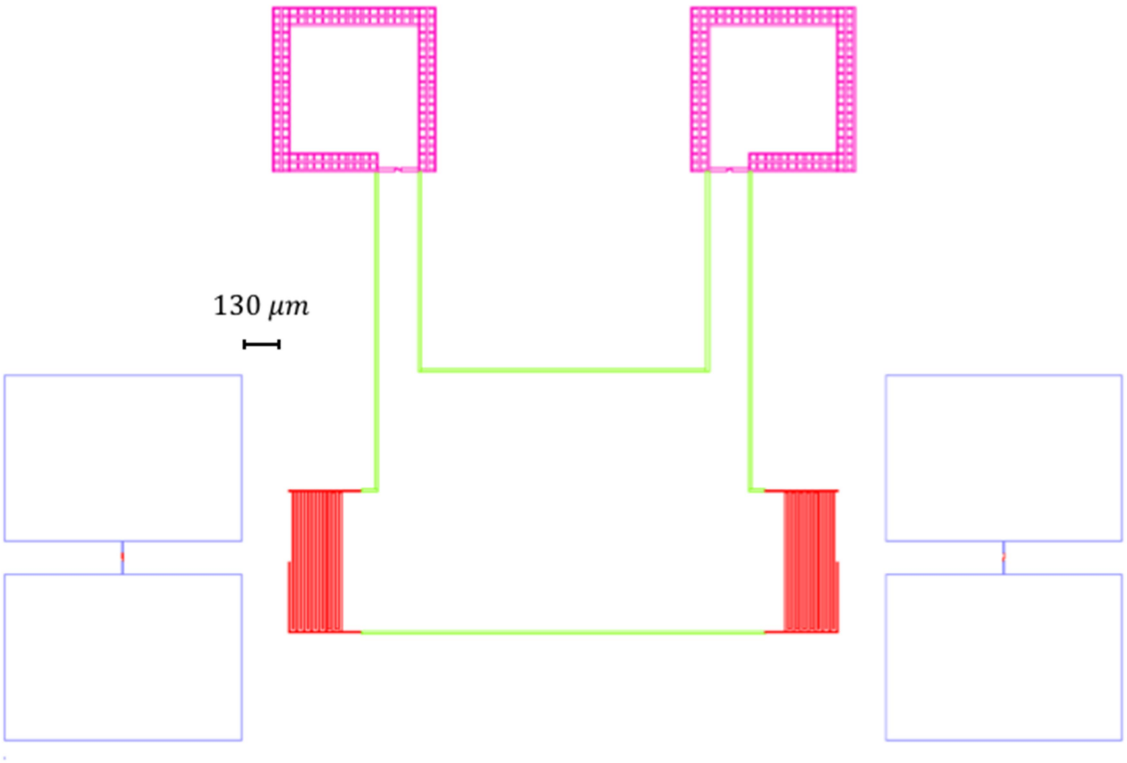

Fig. 6.3: CAD rendering of TRES device pattern. The spacing between each transmon and the capacitor in the tunable resonator is 130 µm.

number of teeth in each IDC. However, in order to ensure good coupling to each transmon, I used a half tooth as the last, outermost tooth in each IDC so that one transmon pad would couple to a 1/2-tooth on one plate of the IDC and the other transmon pad would couple equally to the 1/2-tooth on the other IDC plate. This choice of $n = 14.5$ lowered the estimated total capacitance of the series connected IDCs to about $C_r = 117$ fF.

As I mentioned above, one simple change I made was to move each junction in the LC resonator onto the short branch of the tuning loops (see Fig. 6.2(a)). This greatly

boosted the tuning range. My best FastHenry estimates gave $L_1 = L_2 = 825$ pH and $L_{1x} = L_{2x} = 86$ pH. I chose $\beta_\pi = 0.8$ as this would give a relatively large tuning range, but not too large that a small variation in the critical current would push it to the regime $\beta_\pi > 1$, which would produce multiple flux states. From Eq. (3.84) in Chapter 3, these parameters gave $\alpha = 9.59$, $\rho = 0.114$, and an estimated fractional tuning range of 15%. For a 5 GHz base frequency, this meant an expected tuning range of 750 MHz for each tuning loop, which was smaller than the 1.1 GHz range I was hoping for but still reasonable. However, at flux bias points where both loops tune together, the effect adds, almost doubling the tuning range to 1.3 GHz, which is greater than I designed for.

A β_π value of 0.8 corresponds to a critical current of $I_0 = \Phi_0\beta_\pi/2\pi(L_1 + L_{1x}) \approx$ 289 nA. Figure 6.2(b) shows a CAD drawing of the pattern for one of the loop junctions. As with the qubit junctions, this pattern defines a suspended resist bridge and is formed by two perpendicular wires. In this case the wires have widths of 350 nm and 200 nm giving a naïve overlap area of $A_{JL} =$ (350 nm) x (200 nm) = 0.07 μm^2. The bridge is 350 nm x 150 nm. This area was fixed by the e-beam lithography, and I adjusted the critical current by adjusting the oxygen exposure during the double-angle evaporation. Since both the junctions in the LC resonator and the qubit junctions were all on the same chip and in the evaporator at the same time, I had to adjust the relative areas to achieve the correct critical currents; *i.e.* all the junctions on a chip should have approximately the same critical current density, but the areas needed to be different to achieve the necessary critical current.

6.1.3 LC Resonator-Transmon Coupling Strength

Another critical design choice was to decide on the separation between each transmon and its corresponding LC resonator IDC (see Fig. 6.3). I eventually chose a separation of 130 μm. This distance sets the strength of the capacitive coupling between the resonator and the qubits and thus was a critical factor in determining the qubit-qubit dispersive shift. As I discussed in chapter 5, I chose a design value of $g_{r1}/2\pi = g_{r2}/2\pi = 100$ MHz for this coupling strength. To find the coupling capacitance between a transmon and the LC resonator I needed (and subsequently the separation), I used Eq. (5.61), which relates the coupling capacitance C_c, transmon capacitance C_t, resonator capacitance C_r, resonator frequency f_r, and the g-to-e transition frequencies f_1 and f_2 of the transmons to the coupling strengths g_{1r} and g_{2r}. The only missing piece of this is the coupling capacitance C_c.

Figure 6.4 shows a schematic of one of the resonator's capacitors and the pads of one transmon. In this schematic I have indicated the various coupling capacitances that are connecting the transmon's pads to the two plates of the left IDC in the LC resonator. For example, the capacitance C_{t1} connects the top transmon pad to the upper IDC electrode. Similarly, C_{t2} connects the top transmon pad to the lower IDC electrode, C_{b1} connects the bottom transmon pad with the upper IDC electrode, and C_{b2} connects the bottom transmon pad with the lower IDC electrode. Considering the top transmon pad, when there is a voltage difference V across the plates of the IDC, the charge induced on the upper transmon pad is

$$Q_t = C_{t1}\left(\frac{V}{2}\right) + C_{t2}\left(-\frac{V}{2}\right) = (C_{t1} - C_{t2})\left(\frac{V}{2}\right) = C_t\left(\frac{V}{2}\right), \qquad (6.5)$$

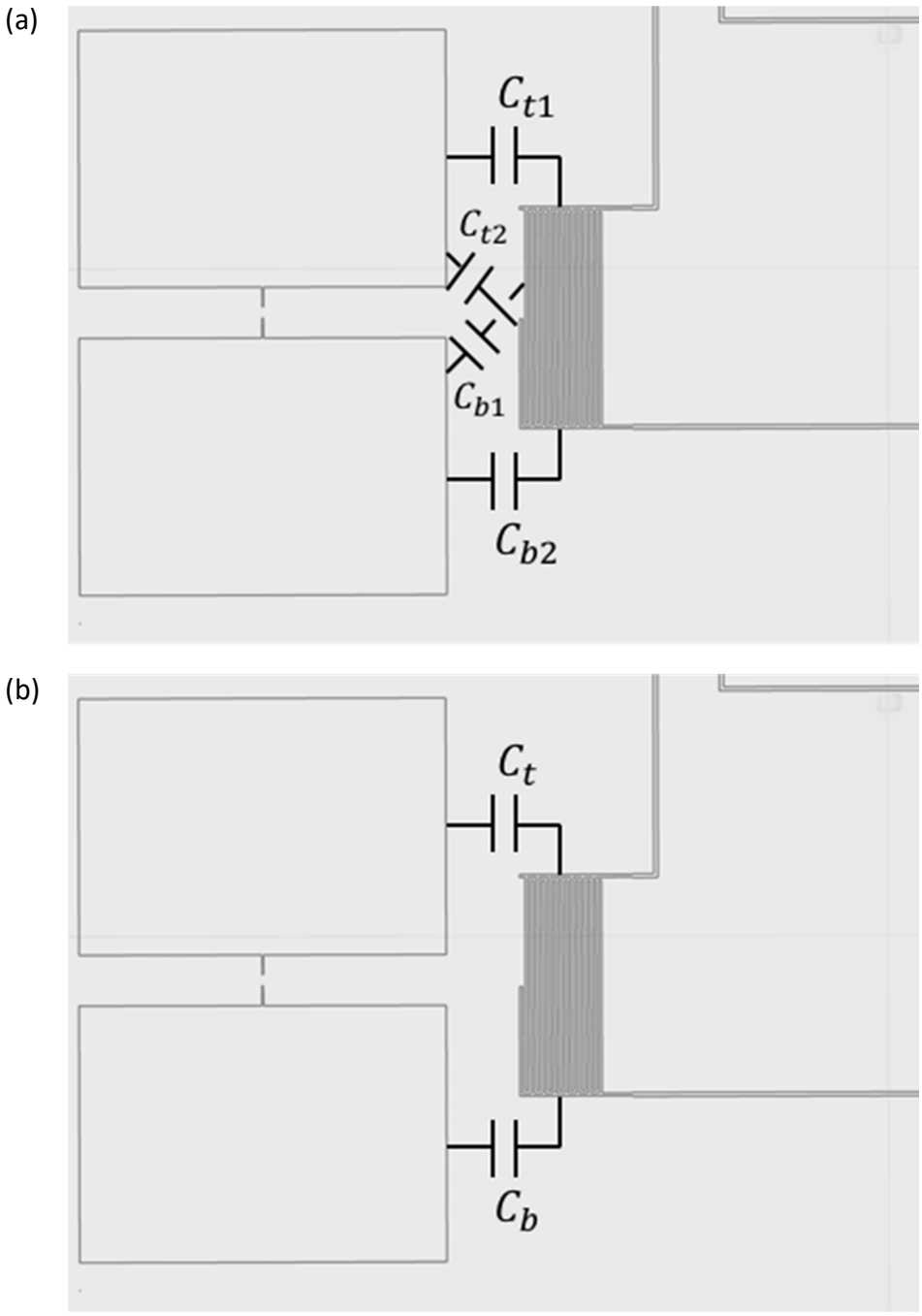

Fig. 6.4: (a) Partial schematic of TRES device showing the left transmon pads and the left resonator IDC showing all the capacitances present between the two pieces. (b) The effective coupling capacitances C_t and C_b.

where $C_t \equiv C_{t1} - C_{t2}$, which can be thought of as the effective capacitance between the top transmon pad and the upper IDC electrode. Similarly, $C_b \equiv C_{b2} - C_{b1}$ is the effective capacitance between the bottom transmon pad and the lower IDC electrode. The net coupling capacitance between the transmon and the IDC can then be written as the series combination of C_t and C_b:

$$C_c = \frac{C_t C_b}{C_t + C_b}. \tag{6.6}$$

To find C_{t1}, C_{t2}, C_{b1}, and C_{b2} I simulated the DC electric field around the device, including the cavity and input/output ports, using Comsol Multiphysics [4] modeling software. I note that I left the junctions open for this simulation. To find the expected capacitance between any two parts, I set the voltage to 1 V on the part I was interested in, such as the lower plate of the resonator, which encompassed the lower electrodes of both IDCs, and I would then set all the other parts of the device to 0 V. In the case I mentioned, this would set all four transmon pads and the upper part of the resonator to 0 V. Comsol would then compute the charge induced on each part set to 0 V and calculate the corresponding capacitance by dividing the induced charge on these pieces by 1 V.

Figure 6.5 shows two exported pictures of the simulated, from Comsol. As seen in the figure, the lower part of the LC resonator is red, indicating that it is at 1 V. In Fig. 6.5(a) I show an overview of the whole device, and in Fig. 6.5(b) I show a detailed view of the left transmon and the left IDC electrodes. Table 6.1 summarizes the resulting effective coupling capacitances I extracted from Comsol for this device design. Using Eq. (6.6), the overall coupling capacitance between a transmon and the LC resonator is $C_c = 0.79$ fF for a transmon-to-IDC separation of 130 μm.

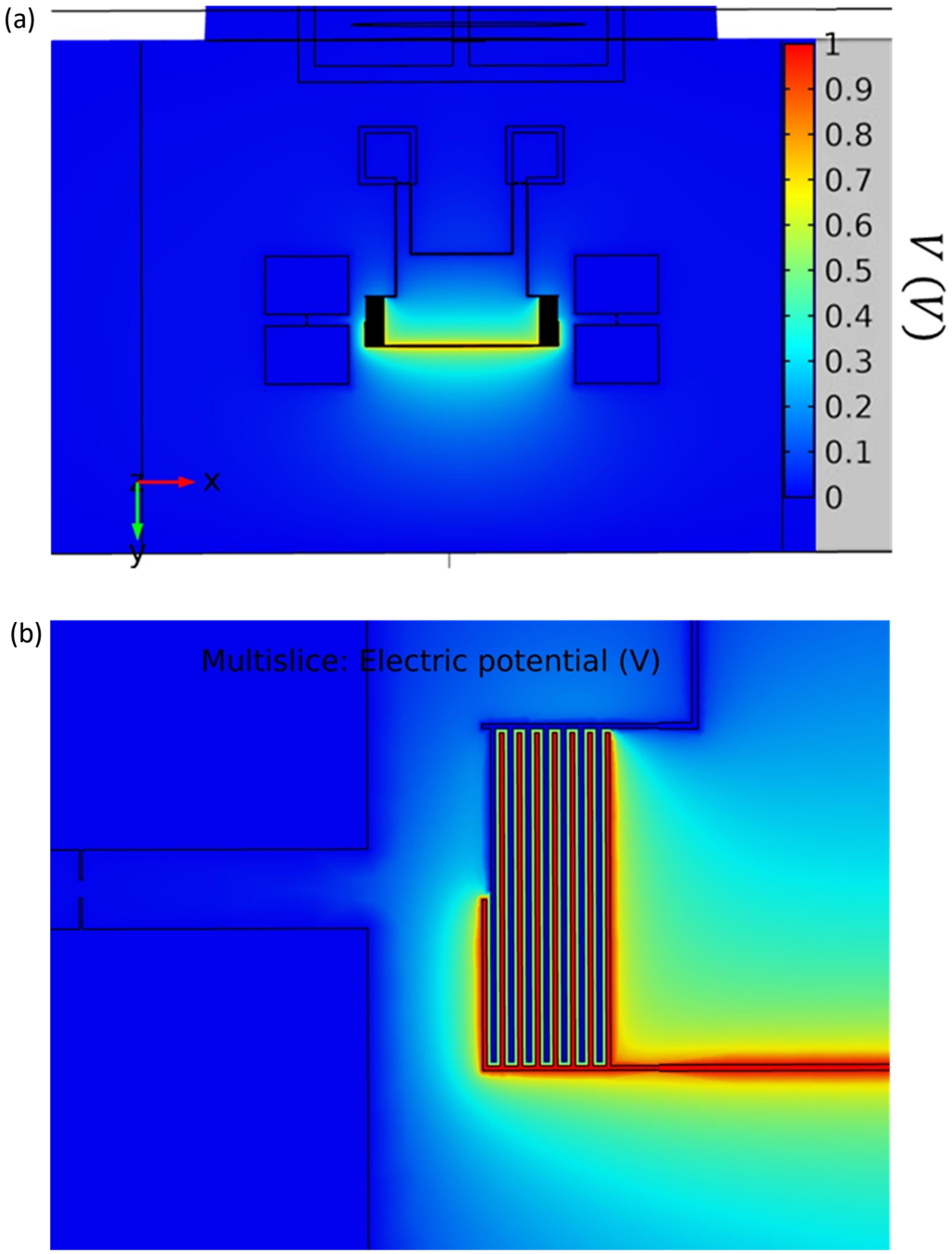

Fig. 6.5: (a) Exported image of the voltages in capacitance simulations from Comsol Multiphysics showing an overview of the entire device. (b) Detailed view of electric potential V near one interdigitated capacitor and the left transmon.

From section 5.2, I can use Eq. (5.61) to find the coupling strength between the transmons and the tunable LC resonator as

$$g_{ir} = \frac{C_c}{2}\sqrt{\frac{\omega_i \omega_r}{2(C_i C_c + C_i C_r + C_r C_c)}}. \tag{6.7}$$

With the Comsol simulated capacitance values of $C_c = 0.79$ fF, $C_r' = 328.6$ fF (Comsol treated the two IDCs as being in parallel not series), and $C_{1(2)} = 60.88$ fF and with

Table 6.1: Capacitance values from the Comsol simulations and from Eq. (6.6). The first column gives the parameter, the second column states where the value came from, and the third column gives the simulated value.

Parameter	Expression	Value
C_{t1}	(from Comsol)	36.49 fF
C_{t2}	(from Comsol)	10.77 fF
C_{b1}	(from Comsol)	16.11 fF
C_{b2}	(from Comsol)	16.92 fF
C_t	$C_{t1} - C_{t2}$	25.72 fF
C_b	$C_{b2} - C_{b1}$	0.81 fF
C_c	$C_t C_b/(C_t + C_b)$	0.79 fF
C_r'	(from Comsol)	328.6 fF
C_1	(from Comsol)	60.88 fF
C_2	(from Comsol)	60.88 fF

design values $\omega_r/2\pi = 5.1$ GHz, $\omega_1/2\pi = 5$ GHz, and $\omega_2/2\pi = 4.75$ GHz, I obtained $g_{1r}/2\pi = 61$ MHz and $g_{2r}/2\pi = 60$ MHz.

I need to comment on the discrepancy between 60 MHz coupling values and my initial design value of 100 MHz. When I first began making these devices, the original LC resonator pattern was 500 μm shorter than my final design (see Fig. 6.3), and there were more teeth in the original IDCs because the inductance of the original resonator was less. In this original design, the distance of 130 μm was chosen to make the coupling 100 MHz. However, when I changed to the final design, I kept the separation the same. This led to the reduced coupling strength seen in the final device. Naively, one might expect that this would increase the coupling strength due to C_r being less with fewer teeth in the final design. However, in moving the LC resonator's tuning loops 500 μm farther away from the transmons, the coupling capacitance C_c dropped significantly. To actually achieve a coupling strength of 100 MHz, I would need to move the transmons about 20% closer to the IDCs.

6.2 E-Beam Lithography

The pattern writing for all my devices was performed using e-beam lithography, as described in this section.

6.2.1 Application of Resist Layers

All of the resist application steps were performed in the FabLab [5] in the Kim Engineering Building by Rangga Budoyo [6] and Dr. Sudeep Dutta. We used 3 inch diameter c-axis oriented sapphire wafers [7], that were about 430 μm thick and polished

on one side. To prepare the wafers for resist application, the wafers were thoroughly rinsed with acetone, then methanol, then isopropanol, and finally DI water to remove any solvent residue. The wafers were then dried using N_2 gas. To remove any excess water, the wafers were then baked on a hot plate at 120 °C for about 5 minutes.

The first layer of resist applied to the wafers was LOR10A [8]. To apply this resist, the wafer was mounted on a Headway EC101 wafer spinner [9], and the wafer was spun at 1000 rpm as LOR10A resist was applied. The spin speed was then increased to 4000 rpm and spun at that speed for a total of 45 s. According to the manufacturer, this speed and time results in a 1000 nm thick layer. The wafer was then baked on a hot plate at 180°C to 200°C for 10 minutes.

The second layer of resist was the e-beam resist 950 PMMA C2 [10]. With the wafer stationary on the spinner, the PMMA resist was applied with an eye dropper. The wafer was then spun at 4000 rpm for 45 s, which yielded a 150 nm thick resist layer. The wafer was then baked at 230°C in an oven for 2 hours and 15 minutes.

6.2.2 Anti-Charging Layers

Since the sapphire substrates are highly insulating, I needed to apply a conductive layer that could carry away charge deposited while writing with the e-beam system. Charge build-up causes problems in focusing the beam and in writing. To provide an anti-charging layer, we thermally evaporated about 15 nm of Al on top of the LOR/PMMA bi-layer stack. This was the only type of anti-charging layer I used for the device tunres_112115 (see Chapter 3). However, as I discuss below in section 6.2.4, this Al layer alone proved to be insufficient for preventing charging during pattern writing.

6.2.3 Wafer Dicing

In order to protect the aluminum anti-charging layer and the two resist layers during dicing, 1813 photoresist [11] was applied to the wafer and spun at 4000 rpm for 45 s. It was then baked at 120 °C for 5 minutes.

To dice a wafer into individual 5 mm by 5 mm chips, we used a Microautomation Industries Model 1006 dicing saw [12] outfitted with a 200 μm wide diamond blade from Dicing Blade Technology, Inc., part number CA 008325060 H [13]. We tried out a few different types of blades, and this one produced the best results on our wafers. For mounting the wafer to the dicing saw stage, we used tape from Ultron Systems, Inc. part number 1003R-7.0 [14].

6.2.4 Chip Preparation for E-Beam Writing

To prepare an individual chip for e-beam patterning, I would first peel off the chosen chip from the dicing adhesive tape. I then placed it into a beaker of acetone for 3 minutes, swirling occasionally to remove the protective 1813 resist layer. I then dried the chip with N_2 gas. For device tunres_112115 (see Chapter 3), this step was the last one before writing.

For the TRES design and, specifically, for device TRES_092917, there were junctions smaller than 1 μm in both lateral dimensions. With junctions this small, I found that the charging was still too great to properly focus the beam. John Hummel at the FabLab [5] recommended using a conductive polymer called aquaSAVE [14] on top of

the Al anti-charging layer. Using both anti-charging layers completely removed the charging problem.

To apply aquaSAVE, I mounted the chip on a small spinner chuck, placed a drop of aquaSAVE on the chip, turned on the spinner, and then ramped it up to 4000 rpm over the course of 10-15 s. I let it spin at max speed for about 45 s. Since no baking was required for this polymer, the chips were ready for e-beam patterning after this step. In Fig. 6.7(a) I show the completed resist stack for writing.

6.2.5 E-Beam Writing

All of the TRES series of devices were patterned on a Raith eLine system [15] (see Fig. 6.6) in the FabLab [5] in the Kim Engineering Building. This system was outfitted with fixed beam moving stage (FBMS) capability and a laser interferometer for maintaining focus over a large area. However, for my chips I used only the standard writing options on the system.

I used a standard Raith universal sample holder to mount my chips. When I put chips in the clamps, I needed to ensure that there was a good electrical contact between the anti-charging layers and the metal of the clamp; so, I twisted the chip back and forth a few degrees to allow the clamp to "dig in" and make a good connection. I then loaded the sample holder into the system through the load lock. Depending on how long of a reservation I had, I would load and write up to 3 devices; on average, though, I would write 2 in a single sitting.

After the sample holder was loaded, I set the accelerating voltage to 10 kV. The Raith was optimized to operate between 10 and 20 kV, but I found it had a

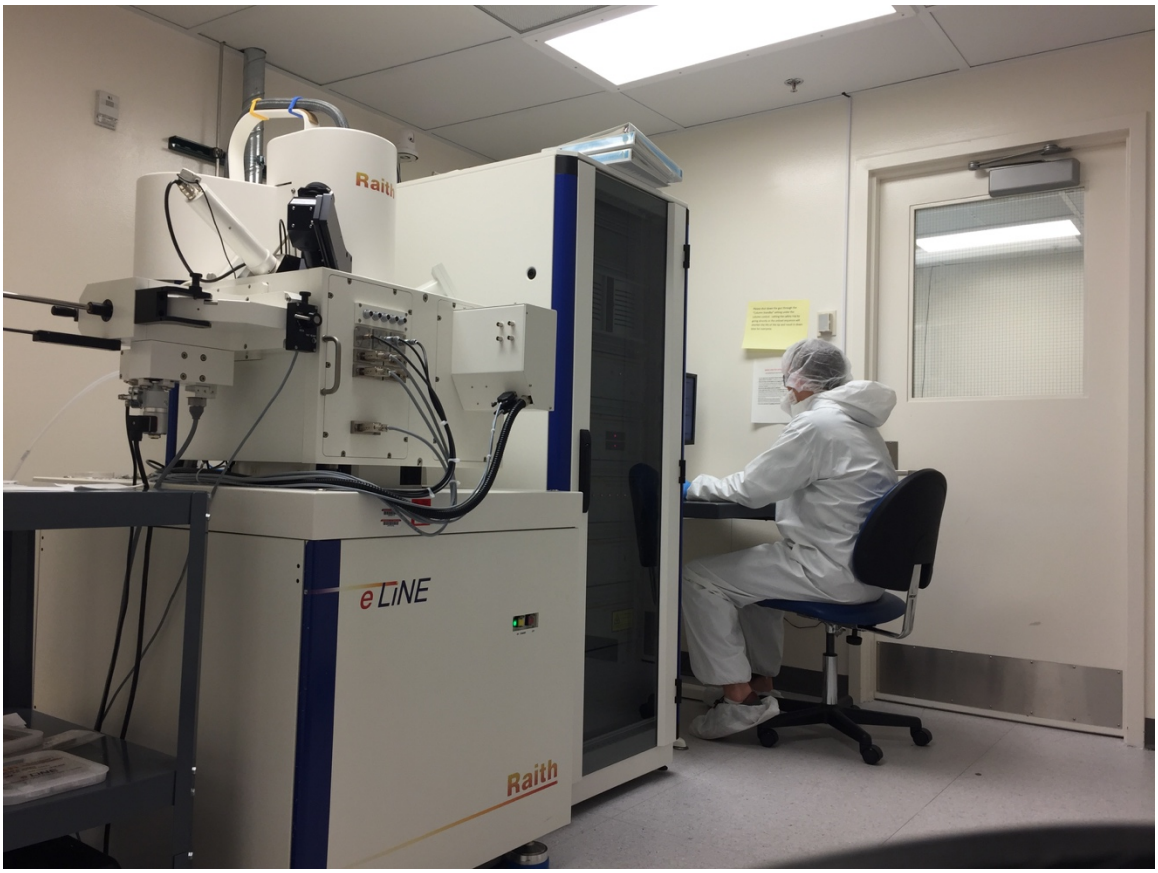

Fig. 6.6: Photograph of the Raith eLINE system in the Kim Engineering Building at the University of Maryland. I am wearing clean room attire while using the system.

longer "settling" time at higher voltages than 10 kV that dramatically increased the writing time. For device TRES_092917, I used a 60 μm aperture, which would typically give a beam current around 830 pA, and I used a dose of 180 μC/cm^2. With these settings, the typical write time for a single TRES device was about 110 minutes. I choose this dose after writing a grid of junction test patterns with a dose matrix that ranged from 100 to 300 μC/cm^2. A dose of 180 μC/cm^2 on these chips produced the best results in the least amount of time.

After measuring the beam current, I next set up the coordinate system on the chip so that the bottom-left corner was the origin. I then used the bottom-right corner of the chip as a reference to set the angle of rotation; this compensated for the chip being rotated relative to the beam.

To get a rough focus, I moved to a spot near where the pattern was going to be written and made a spot by holding the beam at the same location for about 30 s. Even though I had not performed any focusing yet, the high current would affect the resist enough to leave a mark that I could use to roughly focus the beam. After two to three iterations of this process, the beam would be focused enough for fine tuning.

The process of fine tuning the focus involved aligning the beam, adjusting the stigmation, and making small adjustments to the focus. To adjust the beam alignment, I would first turn on the focus wobble, allowing the focus to oscillate at least 40% out of focus, both above and below. If the spot I was focusing on was moving as the focus modulated, then I would adjust the beam alignment as needed to reduce this movement until to the spot was completely stationary as the focus changed. The stigmation and final focusing adjustments were done iteratively. To adjust these, I would zoom in on a spot I had made and adjust the focus until it was the best I could achieve. At this point I would adjust the stigmation in either the x or y direction until the image cleared as much as possible. I next adjusted the focus again to the best image and modulated the stigmation in the other direction, *i.e*. the x direction if I had just done the y. I repeated this process until the image was at its sharpest.

I next had to align the write fields. In the Raith, the CAD pattern is broken up into write fields that are 100 μm x 100 μm. The stages move the beam to a write field,

the system writes the pattern for that field, and then the stages move to the next write field. If the write fields are not aligned, the pattern will be misaligned and the device will be unusable. The alignment process involves a few manual steps, where the user corrects the alignment, and then an automated step where the software corrects itself. A single spot is first made, and the user tells the software where the spot is. The stages then move, and the software shows where it thinks the spot is. If the write fields are misaligned, this will be incorrect, and the user will need to move the cursor to where the spot actually is. After iterating this process a few times, at a few different magnifications, the software takes over and fine tunes the alignment. Once this alignment is complete, the device is ready to be written. The process I have described so far, including the loading, typically took 20-30 minutes to complete.

After the write fields were aligned, I loaded in the CAD drawing. All of my devices were designed and drawn using a student version of AutoCAD [16], examples of which are shown above in the design section. To import them into the Raith software, I saved the renderings as DXF format files and then simply imported them into the CAD program used by the Raith.

Everything was now ready to start writing. Upon completion, it was a simple matter to unload the written chips and place them in a sample holder for transport.

6.3 Developing the Resists

After the pattern was written, I removed the aquaSAVE anti-charging layer by rinsing the chip in water for a few seconds (see Fig. 6.7(b)). I next removed the Al anti-charging layer by placing the chip in a beaker of MF CD-26 [17] for 3 minutes (see

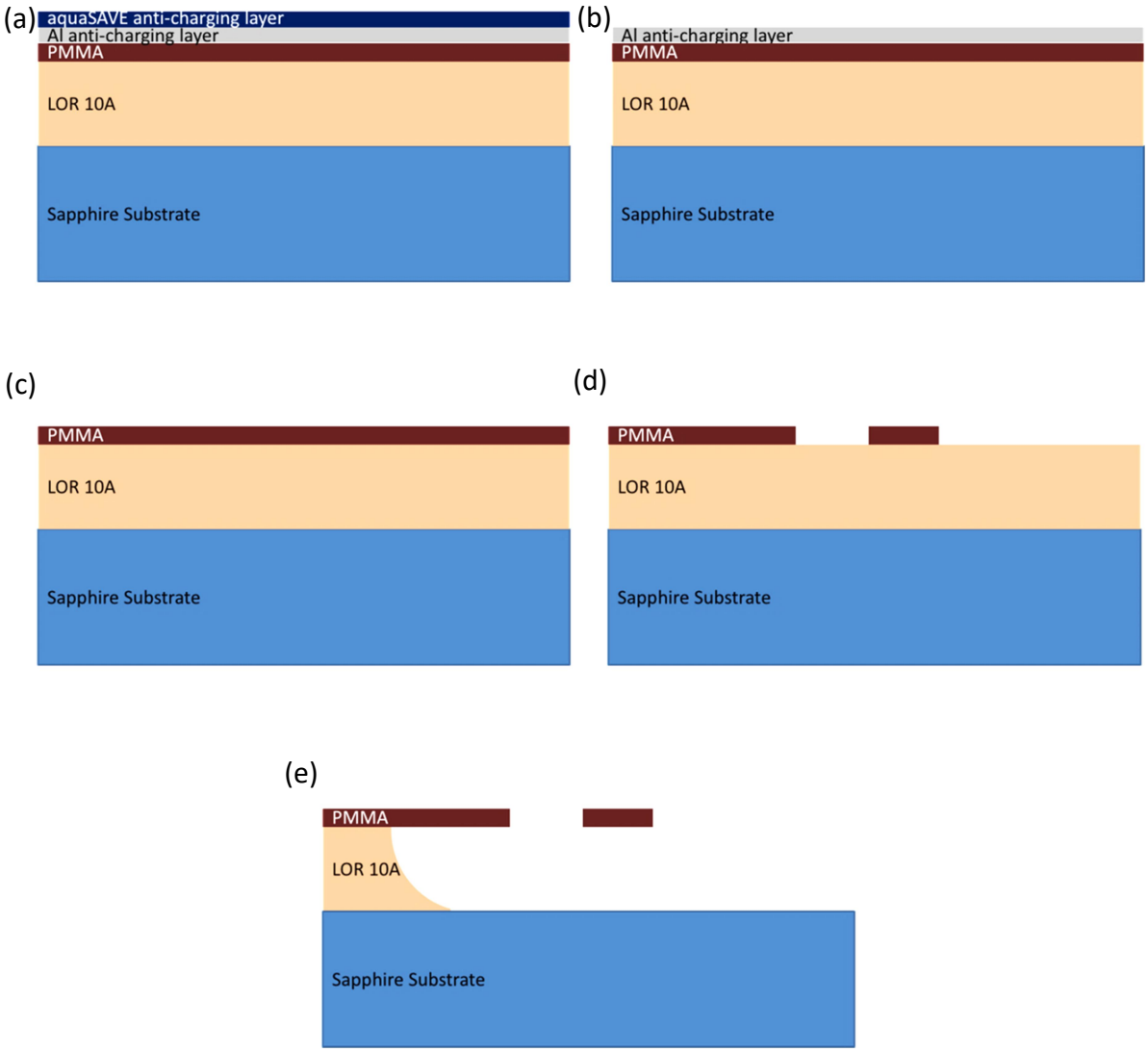

Fig 6.7: (a) Resist stack before development. (b) Resist layers after removal of aquaSAVE anti-charging layer. (c) Resist layers after removal of Al anti-charging layer. (d) Resist after developing PMMA resist exposed to e-beam in MIBK:IPA 1:3. (e) Resist after developing LOR resist in MF CD-26 showing undercut and suspended resist bridge.

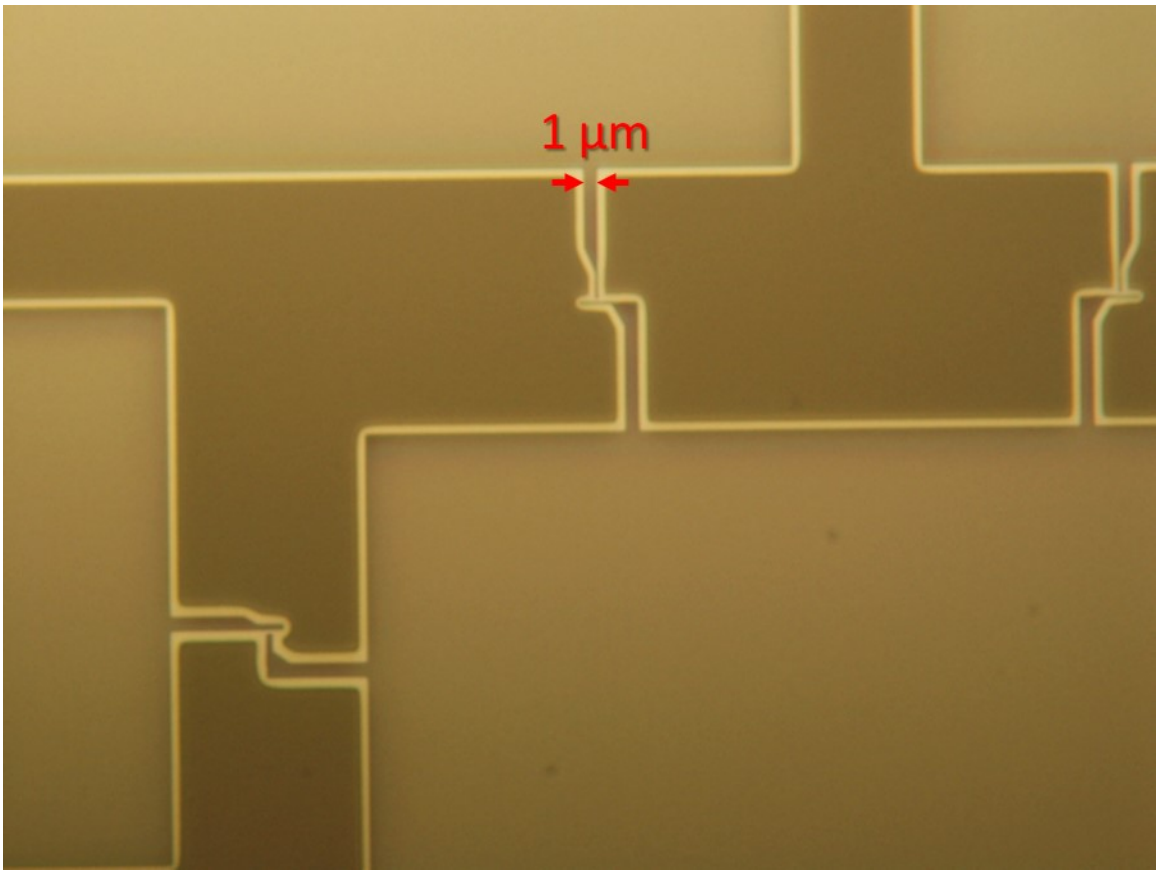

Fig. 6.8: Optical photograph of e-beam resist layers after development. The brighter areas outlining the pattern the undercut regions produced by developing the LOR10A layer.

Fig. 6.7(c)). I thenmoved the chip to a beaker of DI water for about 1 minute to rinse away the CD-26.

I next developed the PMMA e-beam resist layer by placing the chip in a beaker containing a solution of MIBK [18] and IPA (isopropyl alcohol) in a ratio of 1:3. After 120 s with almost constant swirling agitation, I moved the chip to a beaker of IPA to dilute and stop the MIBK development. This step removed all the areas that had been

exposed by the electron beam (see Fig. 6.7(d)). At this point I would typically check the device under an optical microscope to verify that the pattern had developed properly. If I had underexposed the resist with too low a dose, then remnants of the PMMA would still be there. On the other hand, if the resist was overexposed, then I would see a hardened and discolored layer of PMMA left behind after development. With the correct dose, this was not an issue.

I next removed the exposed regions of LOR and undercut the junction bridges by placing the chips back in a beaker of MF CD-26 (see Fig. 6.7(e)). After 48 s, with only occasional swirling agitation, I moved the chip into a beaker of DI water to stop the development.

Figure 6.8 shows an optical photograph of the patterned resist layers after processing. This particular pattern shown was part of a test pattern that contained 4 transmon junctions and 4 loop junctions; I used these to check the room-temperature junction resistance (see section 6.6). The undercut from the development of the LOR is visible as a bright edge around the pattern.

6.4 Thermal Evaporation

In this section, I describe the process I used for double-angle evaporation. I made many minor changes over time to the process, and here I just report the final procedure I used on device TRES_092917, while mentioning a few of the more important changes.

I performed double-angle thermal evaporation of Al and junction oxidation in the cryo-pumped thermal evaporator in Room 0219 in CNAM. Figure 6.9(a) shows a photograph of this evaporator and its various components. Figure 6.9(b) shows inside the

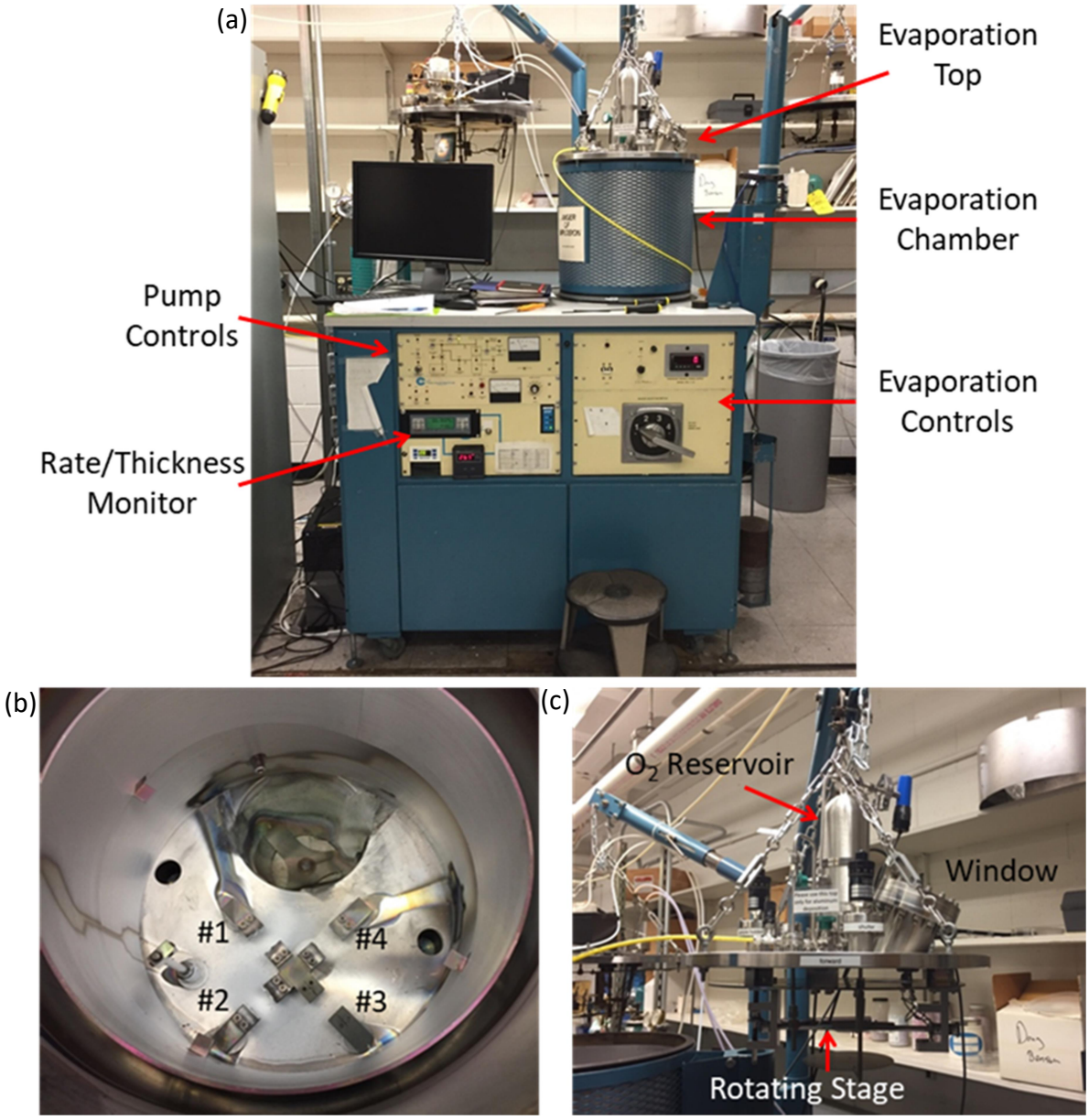

Fig. 6.9: (a) Photograph of the thermal evaporator showing the pump controls, rate/thickness monitor, evaporation controls, evaporation chamber, and evaporation top. (b) Photograph showing inside view of Al evaporation chamber with electrodes labeled. (c) Photograph of the upgraded evaporation top. The window allows a view of the angle indicator on the rotating stage.

evaporator vacuum chamber. Finally, Fig. 6.9(c) shows a photograph of the upgraded evaporation top designed and assembled by Zhongzheng Tian. There are two important features to mention about this evaporation top. First, there is a window into the evaporation space that allows one to see an angle indicator directly on the sample rotating stage. This provided a high level of accuracy in setting the evaporation angle. Second, there is a small, separate volume on the top for filling with oxygen for use during the oxidation step. This allowed for a high level of control over the exposure. The base pressure of this evaporator was about $3x10^{-7}$ Torr for the evaporation of device TRES_092917.

With the evaporation chamber vented, I first loaded in the evaporation boats and Al shot. I only used one evaporation electrode for both layers, but I would load in a second one as a backup in case the first one broke. I used tungsten evaporation boats from the R. D. Mathis Company, model number ME17-3X.025W [18]. I used Al shot of 99.999% purity and sized 4 mm from Alfa Aesar [19]. Second, I next clamped the developed chips onto a sample holder made by Dr. Sudeep Dutta. I then mounted this sample holder onto the rotating stage of the evaporation top (see Fig. 6.9(c)), placed the top back onto the vacuum chamber, and then began the process of pumping out the system.

The initial pumping was performed by an Alcatel rough pump model 2020CP1 [20]. I pumped the chamber until the pressure was ≈ 1 mTorr before purging the O_2 lines and reservoir on the evaporation top (see Fig. 6.9(c)). To purge the lines, I would first allow the reservoir to fill with O_2 until it was at a pressure between 100 mTorr and 300 mTorr. I would then open it to the evaporation chamber, allow the rough pump to empty

the reservoir, and then close the valve to allow the reservoir to fill again. I repeated this process 5 to 7 times. Once the purge step was completed I would pressurize the reservoir to 100 and 150 mTorr of O_2 and then close it off to the oxygen bottle. The O_2 stayed in the reservoir until the oxidation step and the passivation step. Finally, once the rough pump had brought the pressure down to < 200 mTorr, I would switch over to the Brooks Corporation model 8033167R cryo pump [21]. I typically cryo-pumped the chamber overnight before evaporating.

Figure 6.10 illustrates the main steps in the procedure I used to evaporate my devices. I note here that during the Al deposition steps Al is also deposited on the resist layers; however, I have neglected to reflect this in Fig. 6.10. I note that the drawings are not to scale and the ratio of the actual film thicknesses to the actual resist thicknesses is quite small.

For the first evaporation (see Fig. 6.10(a)) I set an angle of $\phi_1 = +15^{\circ}$ and used evaporator electrode #2. The typical evaporation rate on this first layer was in the range 9 Å/s to 15 Å/s. For device TRES_092917 I stopped the Al deposition at a thickness of $h_1 = 180$ Å, according to the crystal monitor. I note that this is not the actual film thickness. The crystal monitor was mounted off to the side of the rotating stage, it is at a slightly different height to the rotating stage, and it is not rotated at the same angle as the chip.

After closing the shutter, turning off the evaporation current, allowing the system about 30 s to cool, and then closing off the cryo pump from the evaporation chamber, I oxidized the first Al layer (see Fig. 6.10(b)). I used the valve in between the oxygen reservoir and the chamber to bleed in the desired amount of O_2. The amount of O_2 I used

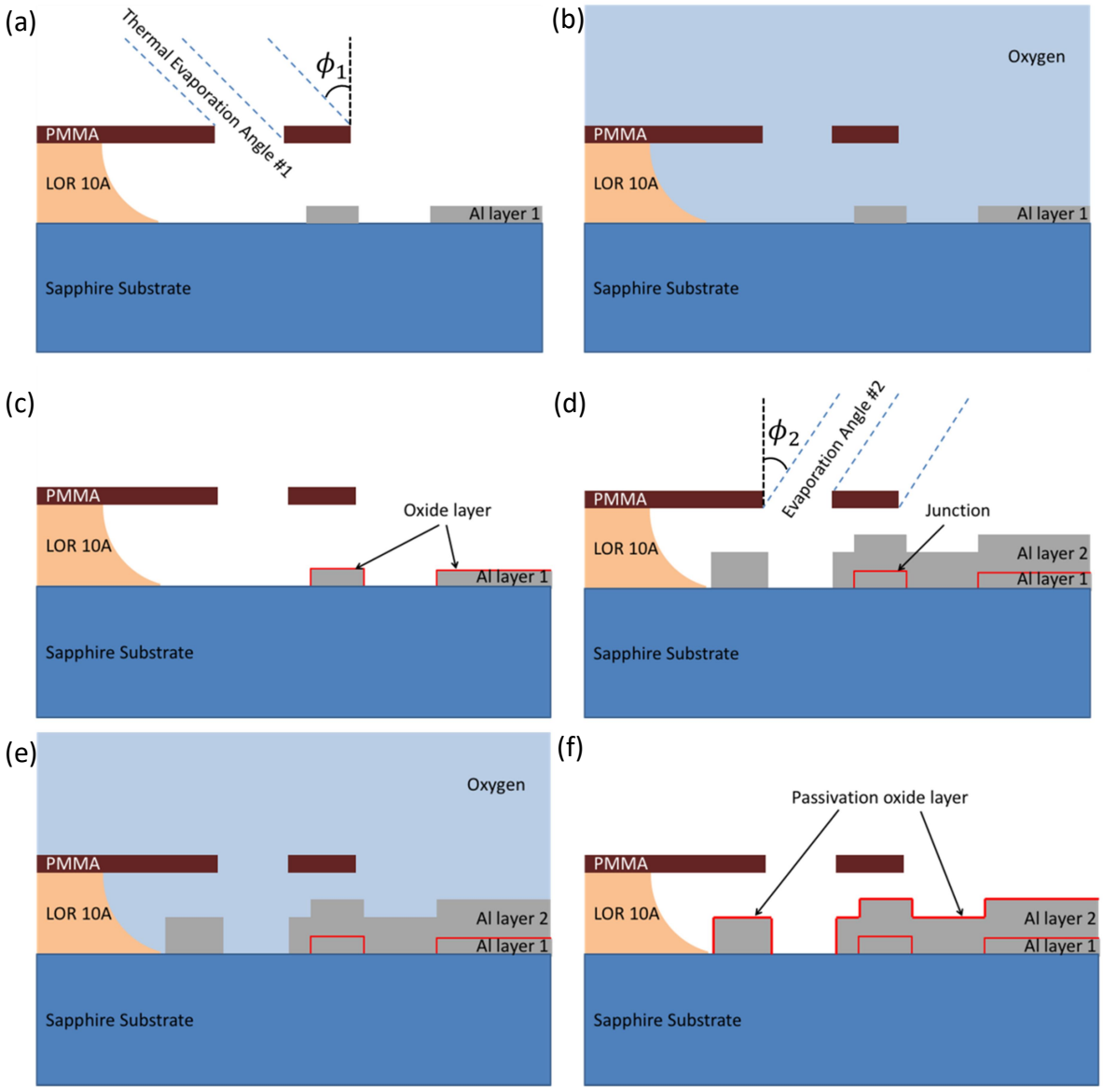

Fig. 6.10: (a) Evaporation of the first Al layer is performed at angle ϕ_1. (b) Oxygen in chamber for oxidation of layer 1. (c) After the oxidation there is a thin layer of Al_2O_x on the surface of layer 1. (d) Evaporation of the second Al layer is performed at angle ϕ_2. (e) Oxygen in chamber for passivation of device. (f) After passivation there is a protective layer of Al_2O_x on the surface of the device.

changed from evaporation-to-evaporation as I tried to obtain the correct critical current density (see section 6.6). For TRES_092917 I used 85 mTorr of O_2 for 5 min to give an oxygen exposure of 425 mTorr·min. To quickly remove the O_2 and stop the oxidation process at the end of the 5 min, I reopened the cryo pump to the chamber and allowed the system to pump for about 5 to 10 min (see Fig. 6.10(c)).

For the second evaporation, I set an angle of $\phi_2 =$ -17.5º relative to the chip surface and used evaporator electrode #2 again. Since I was using the same electrode as the first evaporation, it took less current to melt the Al again and the evaporation rate was typically in the range 4 Å/s to 8 Å/s. In order to insure good coverage, I aimed to make this layer approximately twice as thick as the first. For device TRES_092917 I closed the shutter and stopped the evaporation at a thickness of $h_2 =$ 360 Å, according to the crystal monitor.

Table 6.2: Summary of evaporation and oxidation parameters for device TRES_092917.

Parameter	Description	Value
ϕ_1	Layer 1 evaporation angle.	+15º
h_1	Layer 1 thickness.	180 Å
P	Oxidation pressure.	85 mTorr
t	Oxidation time.	5 min
ϕ_2	Layer 2 evaporation angle.	-17.5º
h_2	Layer 2 thickness.	360 Å
P'	Passivation pressure.	1.5 Torr
t'	Passivation time.	30 min

Finally, in order to try and get a clean oxide layer on the outermost part of the device from pure O_2, I ended with a passivation step. After the evaporation of the second layer, I closed off the cryo pump from the vacuum space and then opened up the O_2 reservoir to allow in a pressure of about 1.5 Torr for 15 to 30 minutes. Once this was done, I vented the chamber with N_2, placed the device in a chip holder, and moved onto the lift-off stage. In Table 6.2 I provide a summary of the evaporation and oxidation parameters used for device TRES_092917.

6.5 Lift-Off Procedure

The next step in the fabrication procedure was to lift-off the Al that does not constitute the final pattern. To perform this lift-off, I first prepared a beaker with Remover PG [22], placed it on a hot plate set to 80ºC, and covered it with a glass lid. I found out the hard way that it was important to have the Remover PG hot; it could not effectively remove the resist otherwise.

Once the remover reached 80 ºC, I placed the chip in the liquid and left it for about 15 minutes. I then removed the chip and sprayed it with isopropyl alcohol. This would usually remove most, if not all, of the excess Al. I then repeated the process with 5-15 minutes in the Remover PG followed by an IPA spray. If any Al was left after the first IPA spray, the second spray usually removed it. I then placed the chip back in the Remover PG for 30 to 45 min. I then removed it, gave it one final IPA spray, dried it using N_2 gas, and placed it in a chip carrier for transport. I note that, leaving it in the Remover PG for this last interval helped to clear away small bits of the resist stack left on the substrate.

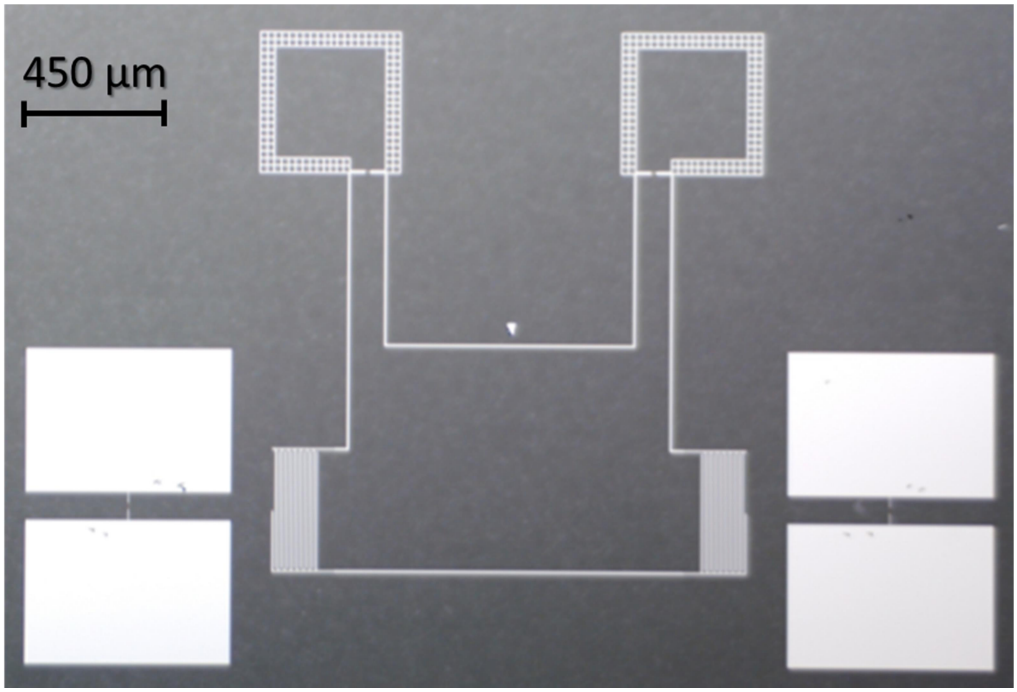

Fig. 6.11: Optical photogtraph of completed device TRES_092917. The dull, gray background is the sapphire substrate. The brightly colored areas are the leftover aluminum after the lift-off step.

Figure 6.11 shows an optical photograph of completed device TRES_092917. This is the device that I report results on in Chapters 8 and 9. I note that there is still a small piece of Al, just above the center of the upper inductive line. Luckily, this did not lead to any apparent problems with the transmons or LC resonator.

6.6 Room-Temperature Characterization

The final step in the fabrication procedure was to check the device to see if it was viable. I first did a visual inspection under an optical microscope to see if there were any major defects that would clearly affect performance. In particular, I carefully looked to

see if there was any Al left between the teeth of the LC resonator's IDCs. This would have rendered the LC resonator useless. I also checked for any signs that dust had fallen on the pattern before evaporation; this would shadow an area and stop Al from being deposited at the site. This can lead to an open in the circuit, in which case it will also not work. The narrow leads connecting the transmon's pads to its junction were particularly susceptible to this issue.

Upon passing the visual inspection, I next measured the tunneling resistance R_n of the junctions at room temperature. Ideally, the tunneling resistance R_n is related to the critical current I_0 through the Ambegaokar-Baratoff relation [2]

$$I_0 R_n = \frac{\pi \Delta}{2e}, \tag{6.8}$$

where Δ is the superconducting energy gap. When applying Eq. (6.8), I used the value $\Delta = 170$ μeV, which is close to the bulk value for Al. As I discussed in the design section, I needed $I_{01} = 34$ nA and $I_{02} = 31$ nA for the qubit junctions and $I_{0r1} = I_{0r2} = 289$ nA for the resonator junctions. Using Eq. (6.8), this corresponded to room-temperature resistances of $R_{n1} = 7.9$ kΩ, $R_{n2} = 8.6$ kΩ, and $R_{nr1} = R_{nr2} = 0.92$ kΩ, respectively.

Figure 6.12 shows a photograph of the resistance measuring station. I used a 100 kΩ resistor in series with the probes in order to protect the junctions from being blown out by spikes in current from the meter from static electricity. To measure the resistance, I used a Fluke 87 III handheld digital multimeter [23] set to a fixed range of 400 kΩ. I used a fixed range because the autoranging feature consistently blew out junctions. To further protect the junctions, I attached a grounding switch via a BNC tee in parallel with the probes. While touching the probes down, this switch was set to "ground", which

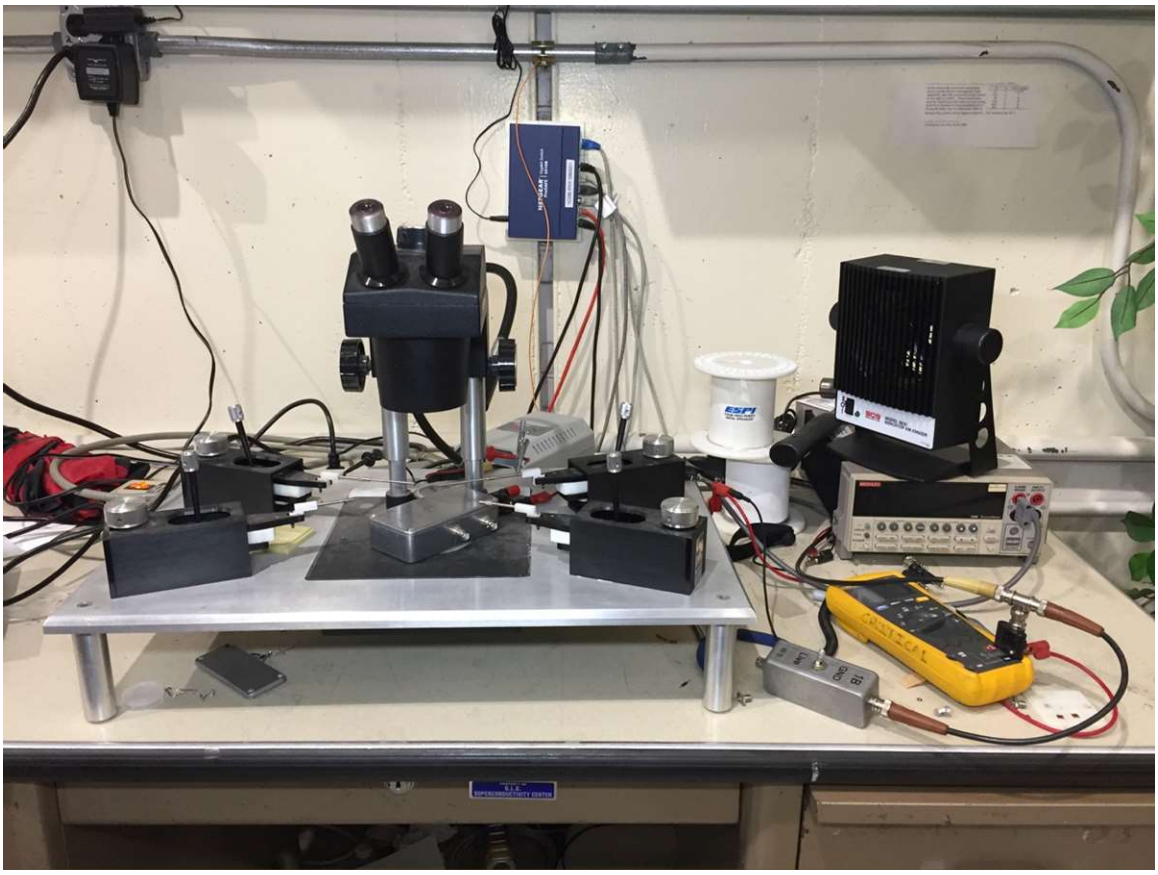

Fig. 6.12: Photograph of measurement station used to characterize junction resistance at room temperature. The probe station is located in the middle and left of the photo, the handheld Fluke digital multimeter is in the lower right hand, and the SCS model 963E benchtop ionization fan is on the right side.

grounded the probes; to take the measurement it was switched to "live", which connected the probes to the circuit. Finally, I used the probes to touch the pads of the test junctions and the transmon patterns. I used the microscope at its maximum 30x zoom in order to see what I was doing. Once I had a measurement of the total resistance, I subtracted 100 kΩ to get the junction tunneling resistance R_n.

To prevent blowing up the junctions I made sure to properly ground all the equipment. I also used an SCD model 963E benchtop air ionizer [24] (see Fig. 6.12). This fan ionized the air that passed through it, and I pointed it at the device while it was measured. Ideally, the ionized air would discharge static electric charge, reducing electrostatic damage.

In fact, I learned about the potential damage from electrostatic discharge by seeing it in action. I initially measured junction resistance using a 4-wire resistance bridge measurement setup. I would connect the probes, use a Keithley 2400 digital multimeter [25] (seen in right side of Fig. 6.12) to source a current and measure the voltage drop across the probes. Dividing the voltage by the current gave the resistance. This method was fairly accurate; however, it often blew out the junctions. The problem seemed to worsen after some electrical work was done in the lab, which may have contributed to an existing grounding problem in the circuit. This led to all the junctions I measured being either open or shorted. I eventually went to the setup shown in Fig. 6.12, and this resolved the issue. Although the handheld meter had less precision than the Keithley, it was much less destructive to the junctions.

As I briefly mentioned in the evaporation procedure section, I observed a large run-to-run variability in the critical current, and this made it difficult to get a clear

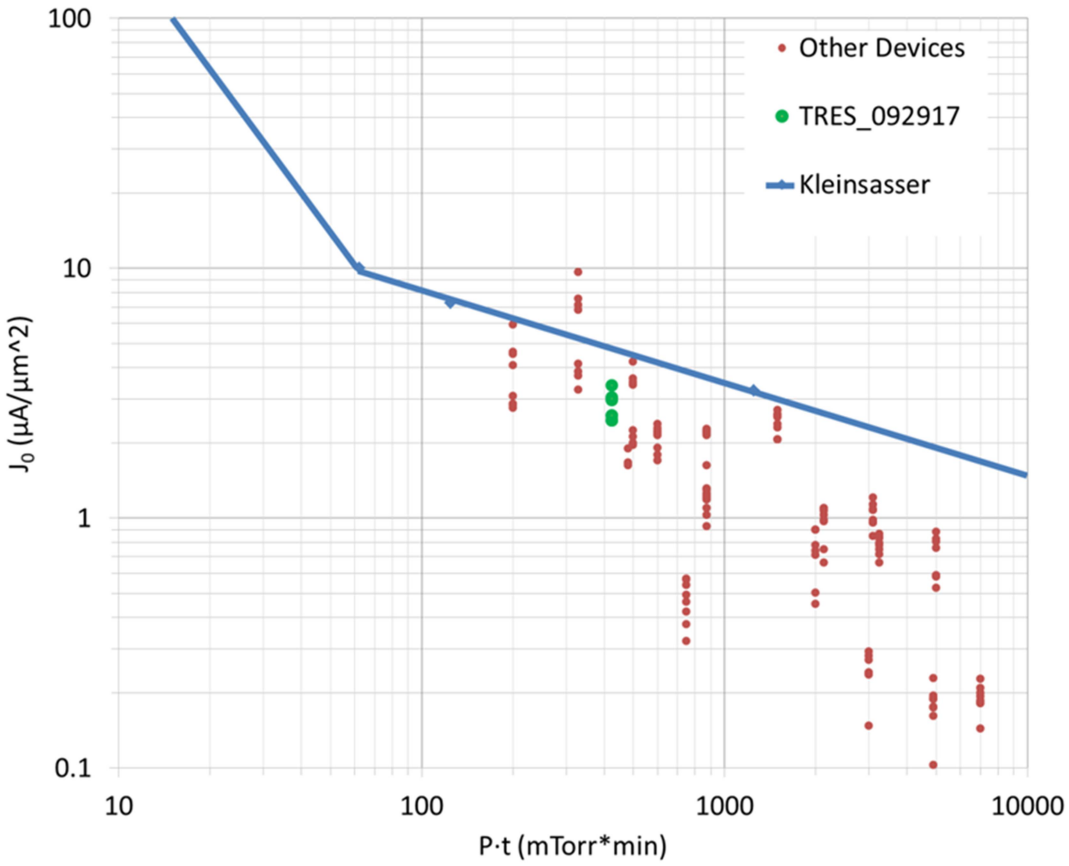

Fig. 6.13: Scatter plot of my critical current density J_0 vs. O_2 exposure $P \cdot t$. These values were measured over the course of my work. The green points are from device TRES_092917, and the red points are from other devices I built. The blue line is from Kleinsasser [26], modified for the superconducting gap Δ of Al.

dependence on O_2. Figure 6.13 shows a plot of the estimated critical current density (extracted from the resistance measurements using Eq. (6.8) and assuming an Al gap of $\Delta = 170$ μeV) vs. oxygen exposure. The solid blue curve on the plot is a scaled version of data from measurements by Kleinsasser [26] on Nb-AlOx-Nb junctions. In my figure I scaled the Kleinsasser results to match my units of exposure and to account for the difference of the gap in Nb vs. my Al junctions. The overall behavior should be very similar since the barrier was also formed from thermally grown Al_2O_x.

Examining Fig. 6.13, one sees my results only roughly follow Kleinsasser and there were large variations in the critical current density for the same exposure. I suspect some of this variability was due to poor climate control in Room 0219. This might possibly explain the variation I observed from run-to-run and the dramatic change in oxidation parameters observed over the course of weeks. However, since the chamber was pumped overnight and there were often large variations in devices made on the same chip, this was likely not the sole source of the variations. In order to mitigate humidity effects, I would only vent the chamber and go ahead with an evaporation if the humidity in the room was less than 50%.

The final thing I'll note is how my final device, TRES_092917, came to be measured. As I remarked above, aside from run-to-run variations, I also tended to see large differences between junctions on the same chip. Typically, I only measured test junctions on my chips in the hope that the junctions on the device itself followed suit. However, this was not very reliable, and I often found that the actual device had parameters quite different from the average from the test patterns. For this reason, I started directly measuring the transmon junctions by connecting the probe station to the

two transmon pads. When I first measured device TRES_092917 right after it was made, I found that the two qubit resistance values matched each other; however, the junction resistances were $R_{n1} = 3.5$ kΩ and $R_{n2} = 4.2$ kΩ, which were approximately half of what I was looking for. This meant that the parameters were unsuitable.

Since the device appeared to be unusable, I did not bother storing this in a dry box for safe keeping; instead, I just kept fabricating devices and left this device, for all intents and purposes, exposed to the elements. About one week later, I was measuring device TRES_100417, which ended up having a large difference in resistance of the two qubit junctions. Feeling somewhat desperate, I decided to remeasure TRES_092917 and found, to my surprise, that the qubit junction resistance measurements had increased to $R_{n1} = 8.0$ kΩ and $R_{n2} = 8.7$ kΩ, which was close to what I was aiming for. It was so close, that I immediately swapped this device into the refrigerator, and started measuring it. It turned out to be the major focal points of this dissertation.

Chapter 7

Experiment Setup

In this chapter I describe the experimental apparatus and procedures that were used to measure my devices. I first discuss the dilution refrigerator, including the radiation and magnetic shields, and the the microwave wiring, including filtering, the cryogenic amplifier, and room-temperature microwave equipment. I conclude with descriptions of the various types of data and the measurement procedure.

7.1 Cryogenic Setup

All measurements were conducted inside an Oxford Triton 200 series dry dilution refrigerator [1], which was operated in a shielded room in the sub-basement of the Toll Physics Building. Figure 7.1 shows photos of the refrigerator. Figure 7.1(a) shows the overall setup, including the outer vacuum can, the top plate, and the frame. In Fig. 7.1(b) I show the control panel and pump station, which is located just outside the screen room. In this section I give details on the inside of the refrigerator, including the thermal and the magnetic shielding.

7.1.1 Refrigerator Plates

The inside of the refrigerator is shown in Fig. 7.2. Going from warmest to coldest, the main refrigerator stages or plates are the room-temparature or “top” plate, pulse tube 1 (PT1), pulse tube 2 (PT2), Still, 100 mK, and Mixing Chamber (MXC).

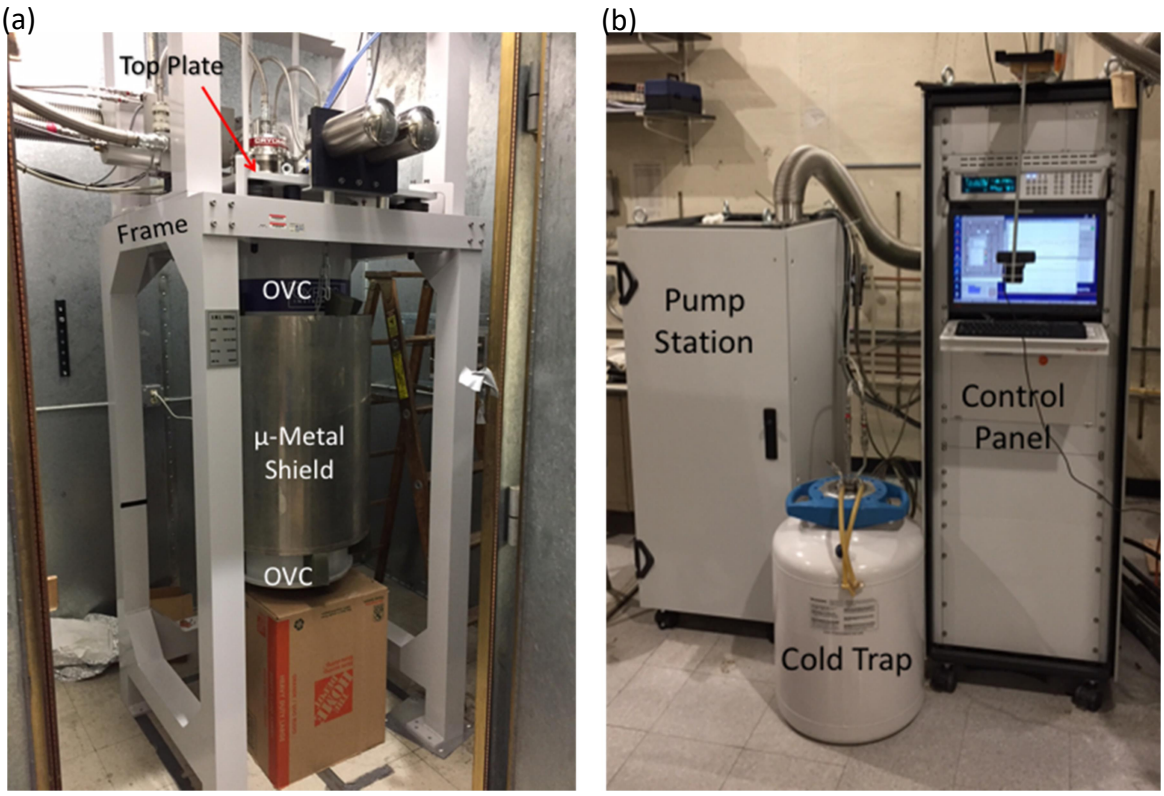

Fig. 1: Photos of the exterior of the Triton 200 refrigerator. (a) View of the setup inside the shielded room. (b) Control panel and pumping station, which are located outside the shielded room.

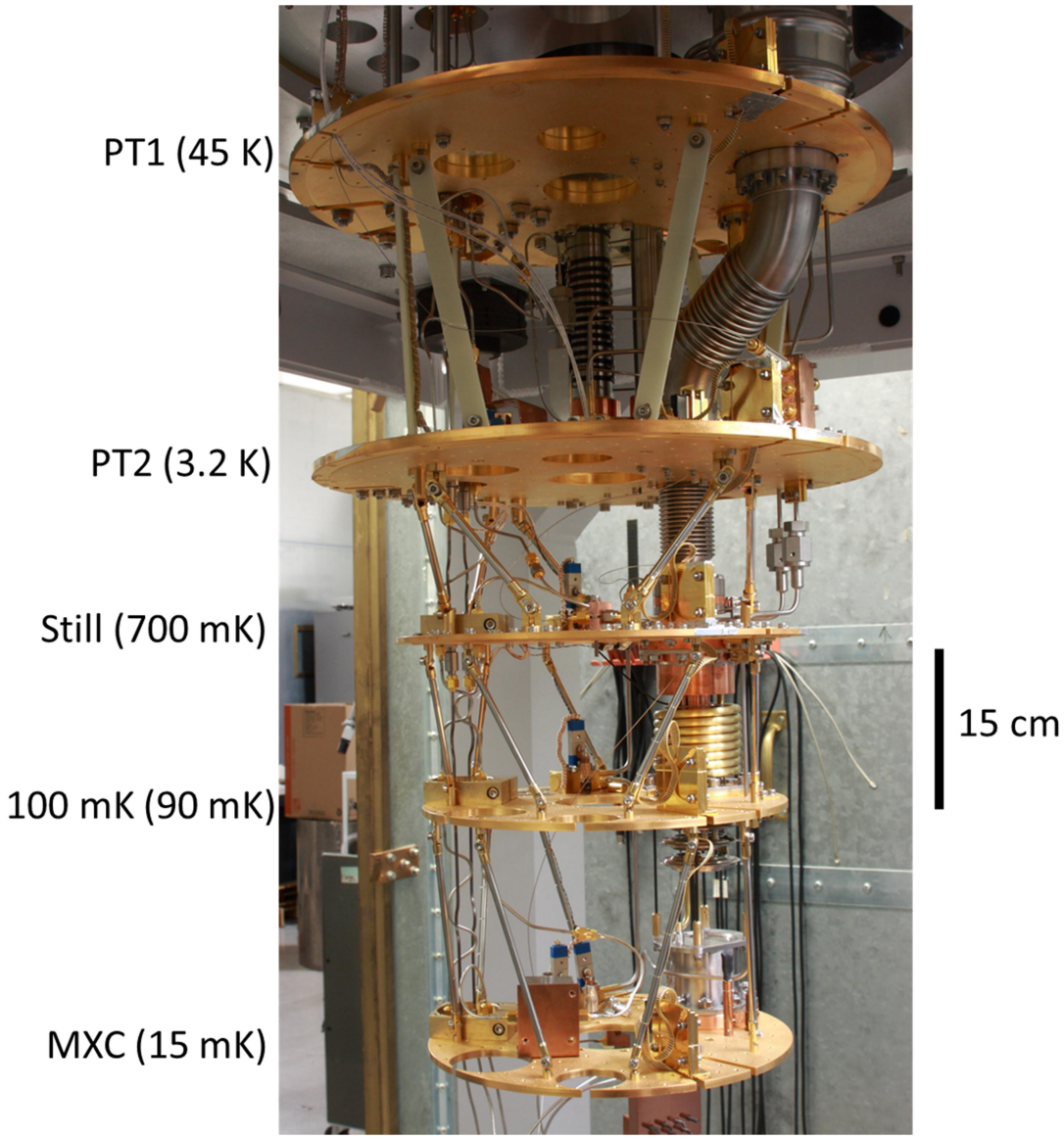

Fig. 7.2: Photograph of Triton 200 dilution refrigerator plates. Each plate is labeled with its name and typical operating temperature.

When the refrigerator is cold, these stages typically operate at temperatures of 45 K, 3.2 K, 700 mK, 90 mK, and 15 mK, respectively.

7.1.2 Refrigerator Heat Shields

In order to achieve mK temperatures, extensive heat shielding is needed in the refrigerator. In Fig. 7.3, I show a schematic of the thermal shields used in the Oxford system. The outermost shield, which is anchored at room temperature, is the Al outer vacuum can (OVC). Vacuum seals (at the top plate and in-between the three pieces of the can) are provided by O-rings. Moving inwards, the next shield is a closed Al cylinder that is anchored to the PT1 stage, which operates at 45 K. The next shield is a closed cylinder made of Al on the upper half and Cu on the bottom. It is anchored to the PT2 stage, which operates at 3.2 K. The next shield is a closed Cu cylinder that is anchored to the Still stage, which operates at 700 mK. In my runs with this system prior to June 2017, this set of stock shielding was the only thermal shielding present. However, in June 2017, to reduce the 700 mK thermal radiation from the Still stage to the sample, I installed a new thermal shield at the MXC at 15 mK. This was a Cu cylinder that enclosed the 3D cavity and device (see Fig. 7.4(a)).

The 15 mK thermal shield was made of a thin sheet of 101 alloy OFHC Cu rolled into a cylinder by the Physics Machine Shop. I had the Machine Shop cap the bottom with 101 OFHC Cu and braze all the seams with AgSn hard solder. After adding this shield we saw a large improvement in the behavior of the transmons, and we went on to coat the inside of this shield with SiC and epoxy [2] based on recommendations from other groups, including Kevin Osborn's group at the Laboratory for Physical Sciences (LPS).

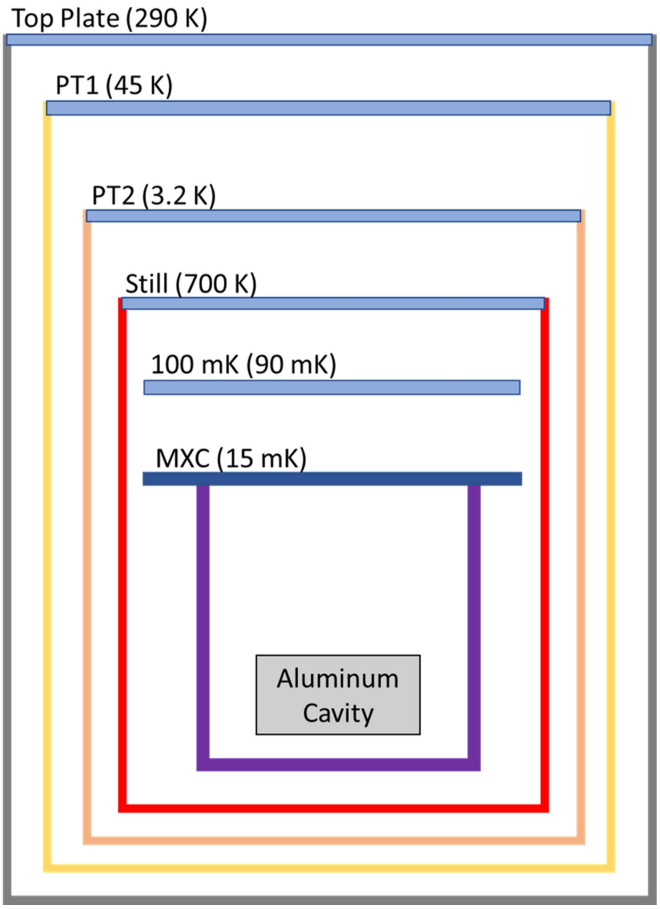

Fig. 7.3: Schematic of thermal shields on the dilution refrigerator. The outer shield (gray) is the outer vacuum can (OVC). The inner refrigerator shields are anchored to the PT1 (45 K) (yellow), PT2 (3.2 K) (orange), and Still (700 mK) (red) shields. The final custom-made Cu shield (purple) is attached to the Mixing Chamber plate at 15 mK.

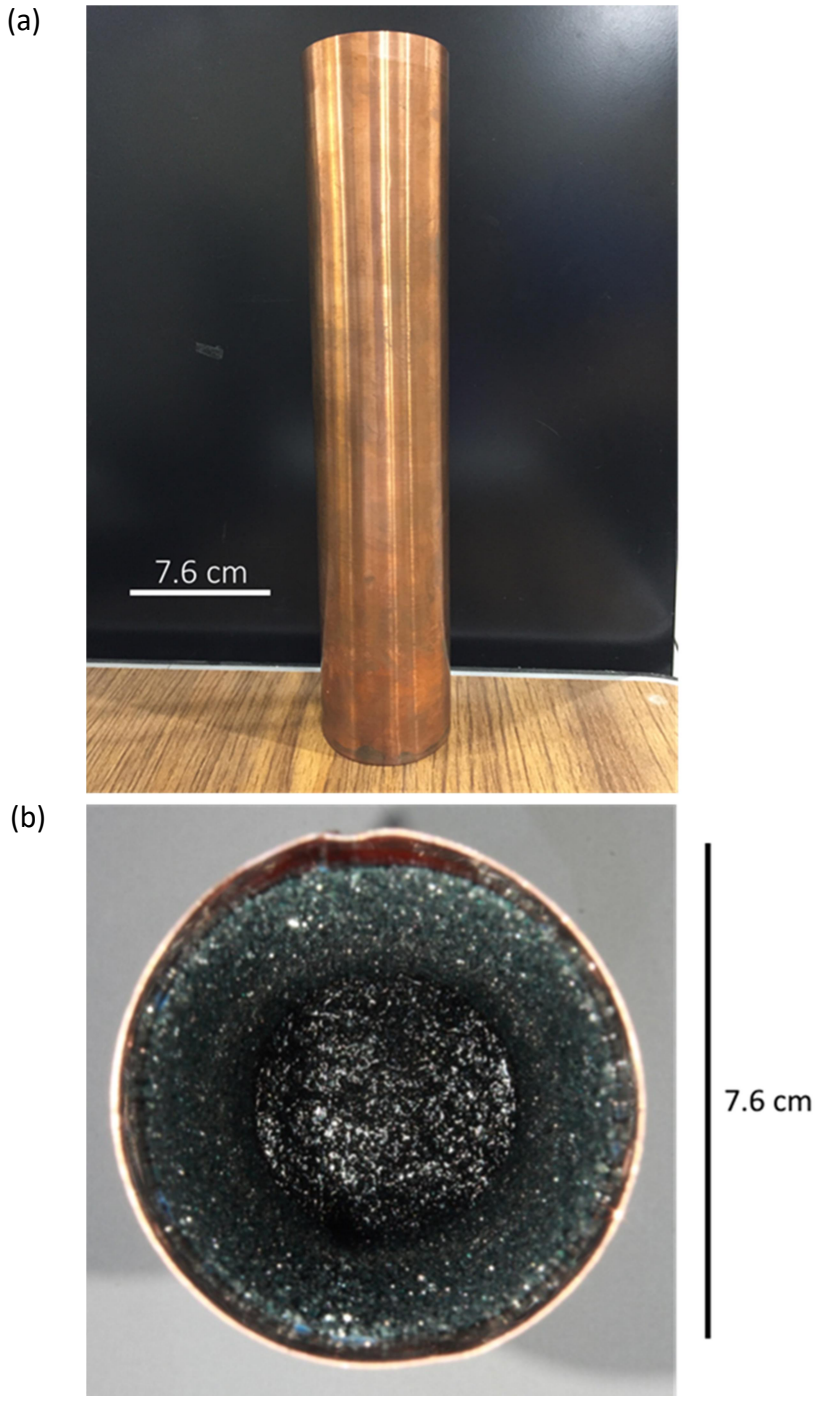

Fig. 7.4: (a) Photograph of the 15 mK Cu thermal shield. (b) Photograph showing the inside of the can with Stycast epoxy and silicon carbide coating.

Chris Lobb did the actual coating, covering the inside with black Stycast 2850 FT epoxy mixed with catalyst 24 LV CL [3] to get a roughly even, relatively thick layer. After this was applied, he poured in granules of 16 grit silicon carbide from Electro Abrasives, LLC [4], rotated the can to get an even coating, pressed in any that weren't sticking, and then poured out the excess. Figure 7.4(b) shows a view of the inside of the can after the epoxy cured. The coated shield was used starting August, 2017, and was present when all the data I discuss in Chapters 8 and 9 was acquired.

7.1.3 Magnetic Shielding

The tunable LC resonators (see Chapter 3, 8, and 9) incorporated two RF SQUID loops that made them extremely sensitive to magnetic field fluctuations. While the gradiometric design of device TRES_092917 helped to reduce field sensitivity, and the devices were mounted in a superconducting Al cavity, they were still extremely sensitive to changes in the external field. To be useful as a tunable coupling element, it was essential to further suppress variations in the external magnetic field from coupling to the device. For this reason, I also used two high-permeability magnetic shields. One shield was mounted on the outside of the OVC at room temperature and the other one was mounted on the MXC stage.

The room-temperatue magnetic shield (see Fig. 7.1(a)) was a cut-down μ-metal shield from an old Oxford wet system that had been decommissioned. Due to clearance issues, we shortened the original shield to leave a cylinder that was 30.5" tall with a diameter of about 24". At its center, this shield attenuated uniform external magnetic fields by about x100. The shield was held by two chains that attached to eye

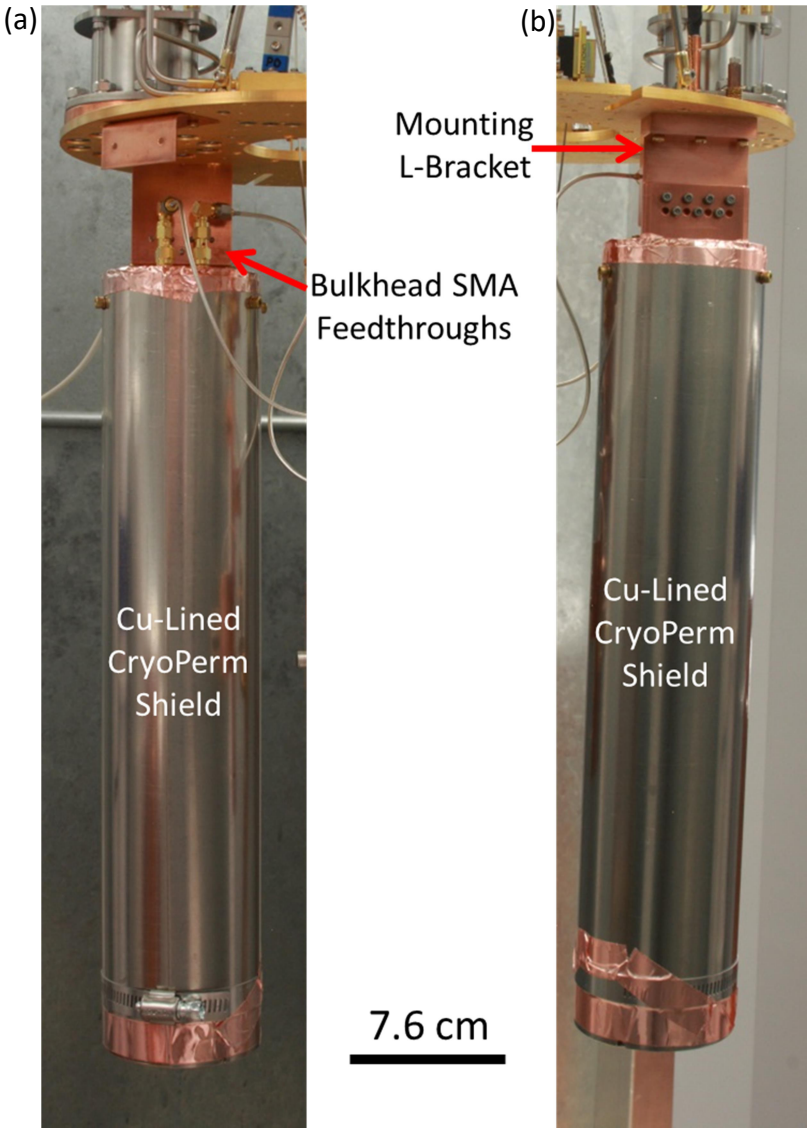

Fig. 7.5: (a) Front and (b) back views of the inner magnetic shield mounted on the 15 mK heat shield and Cu mounting post.

bolts in the refrigerator top plate. To make sure it did not sway or move too much, foam blocks were stuffed around the top and bottom to keep it in place.

The second magnetic shield was formed from a sheet of cryoperm [5] that we got from Dr. Ben Palmer. The sheet was rolled to form an open cylinder with a length of 38 cm and a diameter of 7.6 cm (see Fig. 7.5). It was mounted on the outside of the mixing chamber stage thermal shield. I note here that the seam was not welded, there was no top cap or end cap, and the shield was not annealed. Never the less, at room temperature we observed a x100 reduction in field strength using a flux-gate magnetometer. Since it is just a rolled sheet, It was secured to a mounting bracket by screws at the top of the sample mounting post. I also used a hose-clamp to prevent the rolled sheet from flaring out at the bottom (see Fig. 7.5).

7.2 Input/Output Microwave Lines

Figure 7.6 shows a schematic of the microwave lines and associated components inside the refrigerator. In the following sections I discuss the input and the output microwave lines, including how I thermalized the components and some of the issues I encountered.

7.2.1 Input Line

The input microwave drive line connects from room temperature down to the mixing chamber. To prevent thermal linkage, it is made from short lengths of rigid UT-85 coaxial cable with stainless steel inner and outer conductor [6]. The line is divided into individual sections that go from one temperature plate to the next. To thermalize the

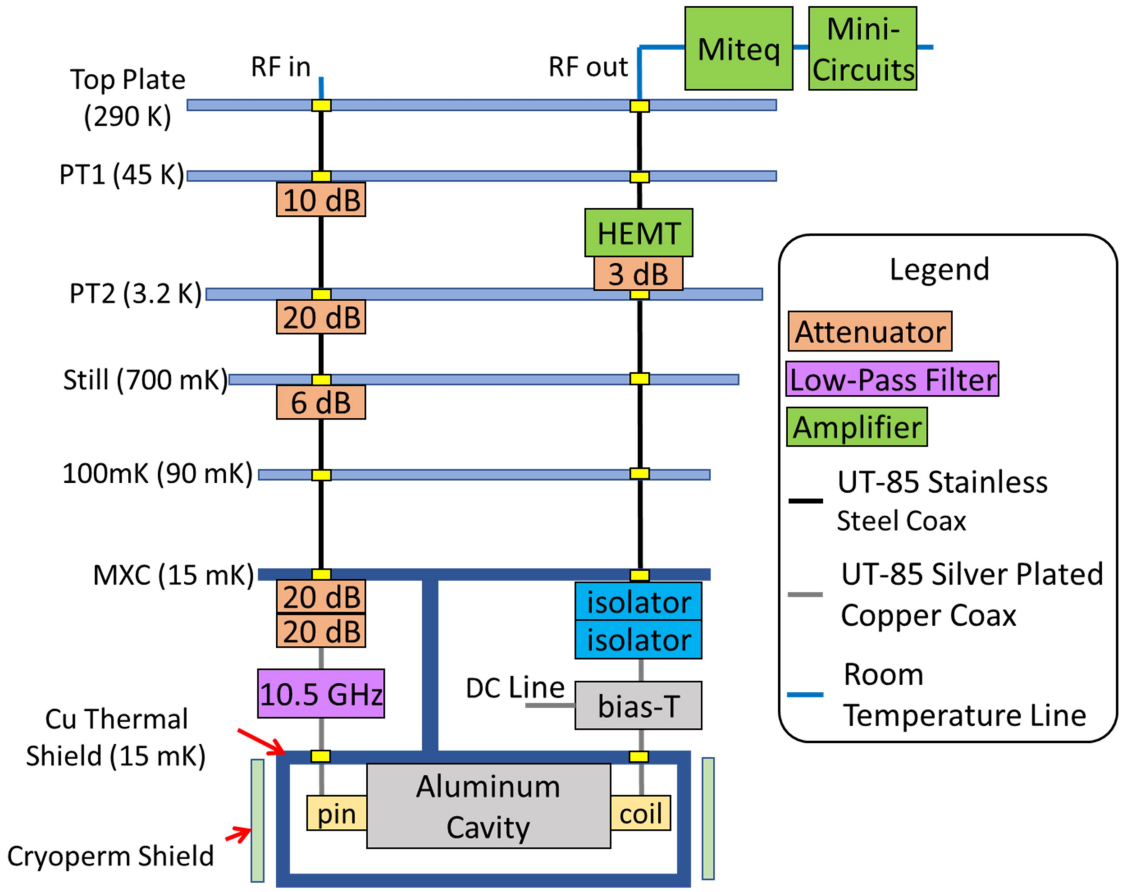

Fig. 7.6: Schematic of refrigerator plates showing details of the input and output microwave lines discussed in section 7.2.

signal on its way down and to reduce external Johnson-Nyquist noise from high-temperature stages, the lines connect to cryogenic XMA attenuators [7] that were attached to the stages. A 10 dB attenuator at the PT1 stage, a 20 dB attenuator at PT2, and a 6 dB attenuator at the Still. Combined, this gave 36 dB of attenuation between 300 K and 15 mK, not counting the SS UT-85 attenuation. This section of input line came from the factory.

At the mixing chamber stage, the input line goes to a final section that is nominally at the same temperature as the mixing chamber plate. Between each component on this plate I used flexible UT-85 coaxial cable made from Ag-plated Cu [8]. Compared to the rigid, stainless steel lines, this was a lot easier to work with, due to its flexibility, and it was a lot easier to make suitable sections of cable. This section of the input line had two 20 dB cryogenic attenuators from XMA corporation [7] (see Fig. 7.6). This resulted in a total of 76 dB of attenuation between the source and the cavity input pin, just due to the fixed attenuation. The two attenuators were followed by a 10.5 GHz low-pass filter from K&L [9]. This was chosen to block high frequency noise that might excite higher cavity modes, which would cause dephasing (see Chapter 4). I discuss the mounting and thermalization of these 15 mK components in section 7.2.3.

7.2.2 Output Line

The output microwave signal from the cavity returns to room temperature via a separate coaxial line. This line has three microwave components at the mixing chamber (see Fig. 7.6). The first component is an Anritsu K250 bias-tee [10] that combines the output signal from the cavity with the input DC flux bias current line, which I discuss in section 7.3. After the bias-tee, the microwave lines go through two Pamtek CTH1365KS cryogenic isolators [11]. These isolators limit the bandwidth of the output line with a rated range of 4 to 8 GHz. Over this bandwidth, they offer 18-19 dB of isolation from waves travelling the wrong way, *i.e.* down the lines from higher temperature stages. I discuss the mounting and thermalization of these components in the following section.

Between the mixing chamber and room temperature I built the output line from several short sections of UT-85 SMA cable with stainless steel inner and outer conductor [6]. At the PT2 stage, which is at 3.2 K, I installed a HEMT (high electron mobility transistor) amplifier from Weinreb's group at Cal Tech [12] to boost the output signal. The CITCRYO4-12A amplifier has a bandwidth of 4-12 GHz, a noise temperature of less than 5 K, and a nominal gain of 32 dB. To cut down on self-resonance from mismatched input impedance and ensure that the amplifier sees a 50 Ω line, I installed a 3 dB attenuator just before the HEMT.

After the output line exits the refrigerator (see Fig. 7.6), it goes to a room-temperature Miteq AMF-3F-04000800 low-noise amplifier [30], which has a bandwidth of 4-8 GHz and a gain of 30 dB. The output of this amplifier goes to a Mini-Circuits ZX60-14012L+ amplifier [31], which has a bandwidth of 300 kHz to 14 GHz and a gain of 11 dB. From this amplifier the signal went to whatever was currently measuring the signal as described in sections 7.5 and 7.6.

7.2.3 Thermalization of Components at the Mixing Chamber

One potential problem with the microwave components in the refrigerator was that they have stainless-steel bodies, which are relatively poor thermal conductors, and quite a bit of power may be dissipated. This makes it very important to do a good job clamping down and thermalizing each piece. This lesson took too long to learn. Since there was limited room on the mixing chamber plate, I designed and had the Physics Machine Shop make a mounting post from 101 alloy OFHC Cu. Figure 7.7 shows two

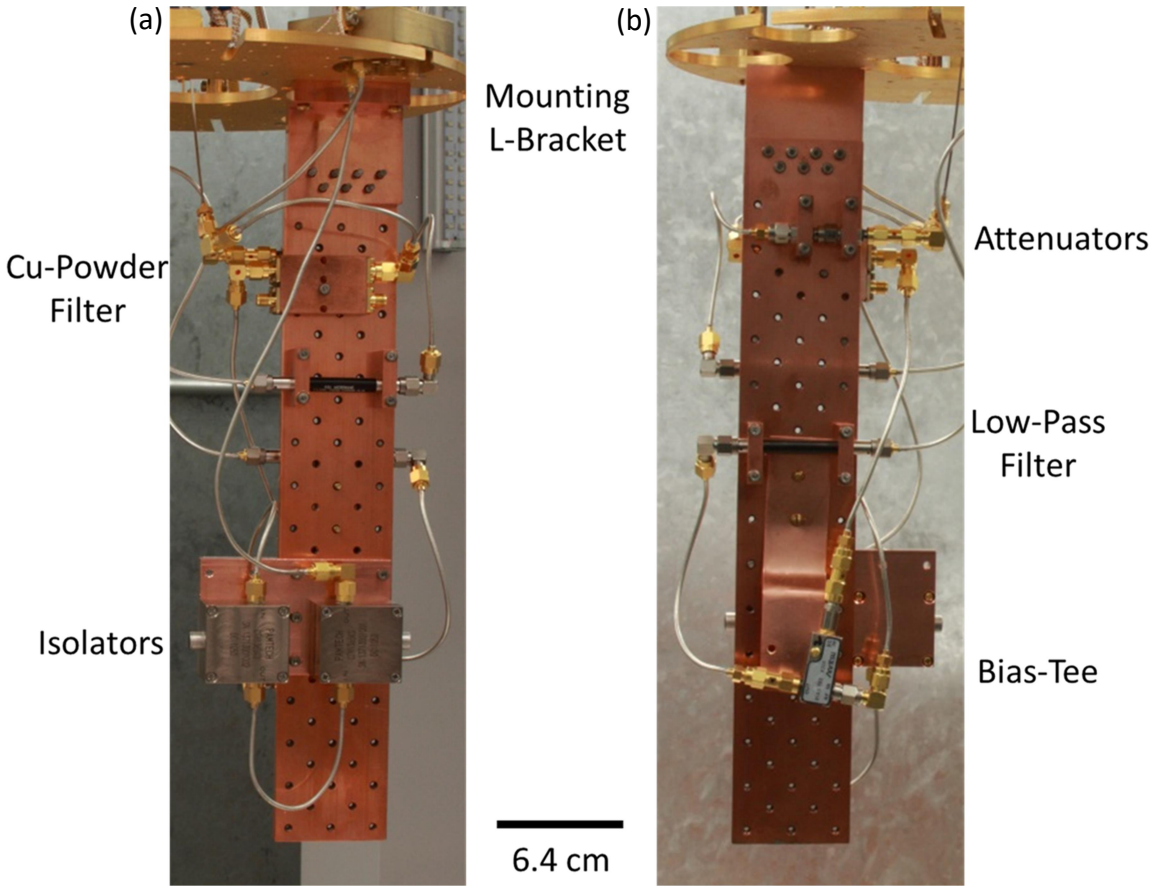

Fig. 7.7: Photographs of the (a) front and (b) back of the mixing chamber thermalization post, showing microwave and DC line components at the 15 mK mixing chamber stage.

photographs (front and back) of this post. Note the mounting screw holes, which are on a 0.75" grid and threaded for 4-40 screws. Also visible in Fig. 7.7(a) is a Cu L-bracket that attaches the post to the mixing chamber plate.

The bias-tee was the simplest component to mount. It had a single through hole, which I used to bolt it to a strip of OFHC Cu that was then attached to the mounting post. The Pamtek isolators had four tapped mounting holes. Unfortunately, these holes did not lie on the post's grid. So, I machined an adapter plate from 101 alloy OFHC Cu to let

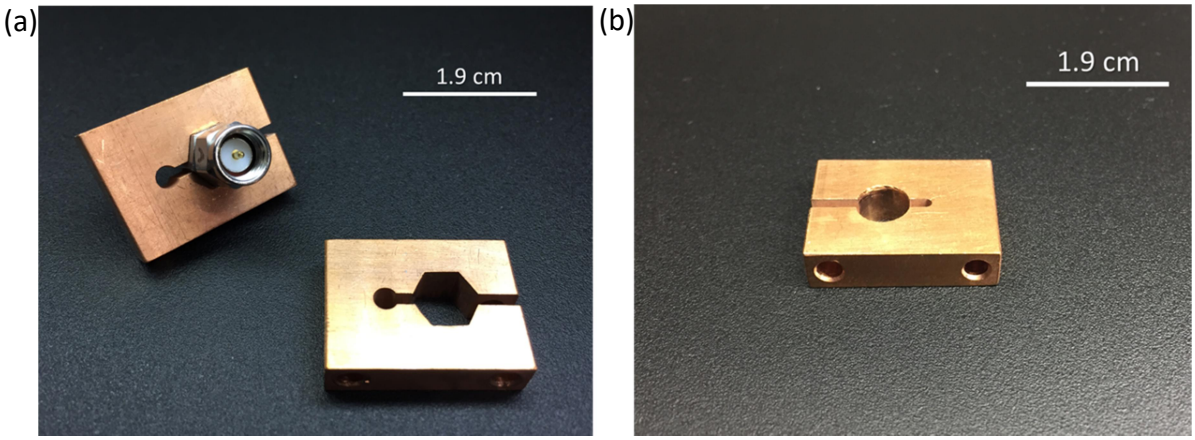

Fig 7.8: (a) Photograph of the Cu clamps used to thermally anchor the XMA attenuators to the thermalization post shown in Fig. 7.7. (b) Photograph of the Cu clamps used to thermally anchor the K&L low-pass filter to the thermalization post.

me firmly attach them to the Cu thermalization post. This block can be seen at the very bottom of the post with the two isolators in Fig. 7.7(a).

In contrast, the 20 dB XMA attenuators and the K&L low-pass filter did not have any convenient mounting holes. To mount these components, I designed and had the Physics Machine Shop build C-shaped Cu clamps that could grip them firmly. Figure 7.8 shows two of these clamps. The particular XMA cryogenic attenuators [7] we obtained had hexagonal bodies (see Fig. 7.8(a)) that made it easy to attach the attenuator to other components because the body could be held with a wrench. We tried quite a few options, but, in the end, I had the shop use wire EDM (electric discharge machining) to cut a matching hexagonal hole. This allowed for tight tolerances on the clamp, although the finish on the clamp walls appeared to be a little rough. There was some concern that this might lead to poor thermalization, but I did not notice any obvious issues. Figure 7.8(b)

shows a similar Cu clamp for the K&L low-pass filter, which had a cylindrical body, and the cutout was made to match. This clamp was machined to a high tolerance and smooth finish by using a reaming tool with the diameter of the filter.

To secure the components I used 4-40 bolts made of aluminum. This material was chosen because it had few magnetic impurities and a thermal expansion coefficient that is slightly greater than that of copper. The idea was that the clamp would hold more tightly as the system cooled.

7.2.4 Issues Encountered

As I noted above, I ran into a few issues while putting together this system. Two of the biggest headaches were associated with the attenuators and the low-pass filters.

For many years, we used attenuators from Midwest Microwave [15], and these seemed to work well. Naturally, when it came to installing new lines in the refrigerator, I ordered a new set of Midwest attenuators. However, after installation I noticed odd features in the spectroscopy: there were many peaks, none of which should have been there, and I could not see any obvious resonance from my device which was a single LC resonator. After quite a few cool downs, we finally figured that the "attenuators" were shorting at low temperature. Upon contacting a Midwest Microwave representative, it was explained to me that they had recently switched from using nichrome in their attenuators to Ta. Since Ta is superconducting with a critical temperature of roughly 4.48 K, this explained the shorting. This is why I switched to XMA brand attenuators. Their cryogenic version still has heating issues (see ref. [14]) but uses nichrome [7].

The other issue I ran into involved the K&L low-pass filters [9]. For the microwave lines, they seemed to work well. However, for the DC line, which I discuss in section 7.3, they led to a serious heating problem. It turned out that somewhere between 300 K and 15 mK, the filters developed a resistance of roughly 7 Ω at DC. This led to heating issues that were puzzling and very hard to pin down, but which disappeared after I removed the filter from the microwave output/DC input line.

7.3 Flux Bias Line

Figure 7.9 shows a schematic of the DC line that delivers bias current to the split bias coils (see Chapter 3) that I used to tune my resonators. The current is supplied by an Agilent 33120A arbitrary waveform generator (AWG) [16] set to DC mode that was attached to a resistor box. To set the resistance of the box, I measured the resistance of the lines in the refrigerator (typically $R_{dc} \approx 42$ Ω), and then adjusted the resistance until the total resistance was $R_{\Sigma} = 500$ Ω. From Ohm's law, the current was then simply the voltage V set on the source divided by R_{Σ}.

For the flux bias line, from room temperature down to the PT2 plate (3.2 K), I installed a UT-34 SMA coaxial cable with stainless steel inner and outer conductor [16]. Using stainless steel reduced the heat transmitted to the PT2 plate but led to Joule heating in the line. At the PT2 plate, the flux line went through a homemade Cu box that broke out the inner conductor and thermalized it. I salvaged this off of one of the lab's decommissioned wet dilution refrigerators. After this breakout box, the current went through semi-rigid UT-34 SMA coax to a Cu-powder filter [17] mounted on the Still stage.

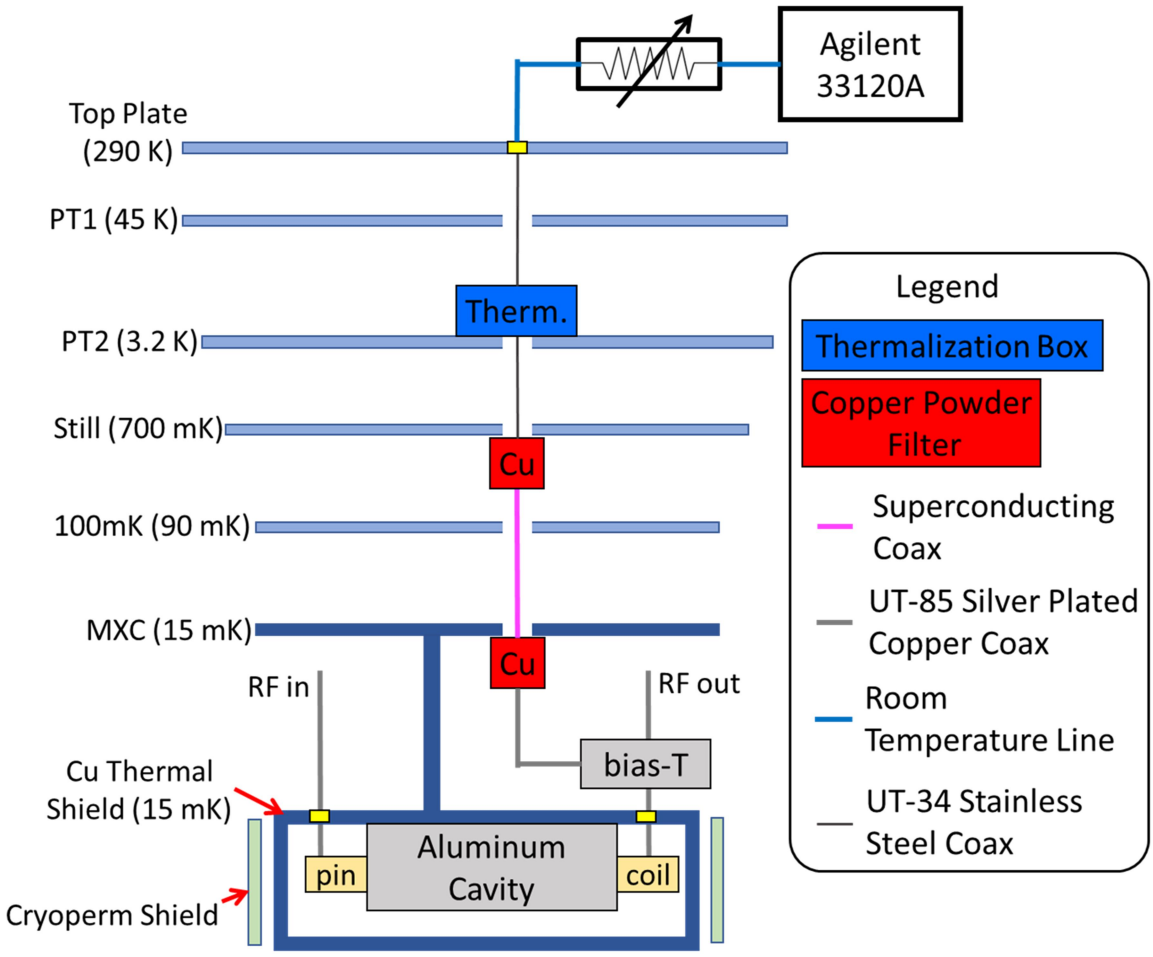

Fig. 7.9: Schematic of refrigerator plates showing details of the DC flux bias line.

From the Cu-powder filter, the flux line went to the mixing chamber via a 38 cm long piece of "superconducting" coax cable. I made this cable using CuNi (which is a normal metal) as the outer shield and Supercon brand SW-M 0.3 mm diameter NbTi superconducting wire [18] as the inner conductor. This particular wire was chosen because the NbTi superconducting wire is jacketed in CuNi, rather than Cu which is typically used, to limit the conductance of heat.

At the mixing chamber, I connected the line to another Cu-powder filter (see Fig. 7.9) that was attached to the Cu thermalization post (see section 7.2.3). From this filter, I jumpered the line over to the bias-tee via a flexible UT-85 cable [8]. Finally, the output of the bias-tee was connected to the cavity's flux tuning coil (see section 3.5) via another flexible UT-85 cable.

7.4 Cavity Mounting

The 3D Al microwave cavity was bolted to the Cu-sample post rather than directly to the mixing chamber plate. I had three reasons for not bolting cavity directly to the cold plate. First, space was at a premium, and the post let me use the volume below the mixing chamber plate. Second, I needed to properly shield the cavity from changes in magnetic field (see section 7.1.3). Finally, I needed to enclose the cavity in a Cu thermal shield at 15 mK (see section 7.1.2).

I took care these issues by adding a second Cu post, very similar to the post I used to hold the microwave components at 15 mK (see section 7.2.3). I had the Physics Machine Shop fabricate this second post out of 101 alloy OFHC copper. Figure 7.10 shows a photograph of the cavity mounting post with a 3D Al cavity attached. There are five columns of 4-40 mounting holes. Two have a 1.9 cm spacing, and three have a 2 cm spacing. The 2 cm grid is the same as on the mixing chamber plate, and all of my cavities were originally designed to mount to this grid.

The cavity mounting post was attached to the mixing chamber plate using a 101 OFHC Cu L-bracket (see Fig. 7.5). To mount the 15 mK Cu shield and the cryoperm magnetic shield (see sections 7.1.2 and 7.1.3) around the cavity post, I had the machine

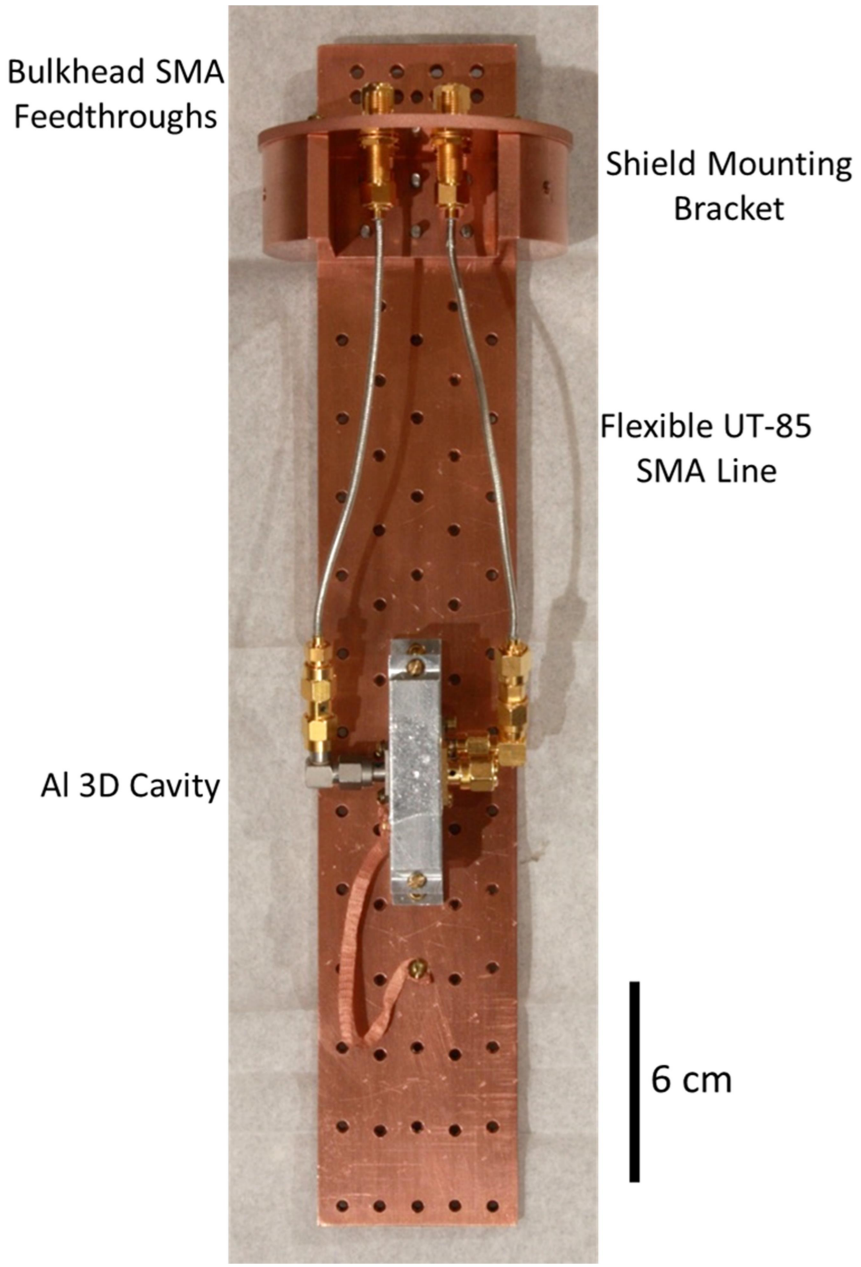

Fig. 7.10: Cavity mounting post with cavity SI-2b mounted. Flexible UT-85 coaxial cable is attached to SMA connectors that go to the microwave input pin and the flux bias coil.

shop make a cylindrical top mounting bracket with a square U-shape cut out of the middle to allow cables to be fed through. One side of the bracket was made flat to allow the cavity post to be attached. The two shields were held on by four 6-32 brass bolts that attached to tapped holes in the outer perimeter of the mounting bracket. Finally, to cap off the top of the 15 mK Cu shield, I had a round, flat piece made out of 101 alloy OFHC Cu and bolted it to the top of the cylindrical mounting bracket. The input and output microwave lines and DC flux bias lines were attached to bulkhead SMA feedthroughs in this top plate (see Fig. 7.5).

7.5 Spectroscopy Using the VNA

Figure 7.11 shows a simplified block diagram of the setup used for microwave spectroscopy. The microwave power is supplied by a Keysight E5071C Vector Network Analyzer (VNA) [19] with a frequency range of 900 kHz to 8.5 GHz and a power range of -55 dBm to 10 dBm. Output port 1 of the VNA is connected to the "RF in" port at the top plate of the refrigerator (see Figs. 7.6 and 7.11). Port 2 of the VNA is attached to the RF output from the Mini-Circuits amplifier (see Fig. 7.6). The dilution refrigerator lines, including the DC bias line, is detailed in sections 7.2 and 7.3 and shown in Figs. 7.6 and 7.9.

The VNA was controlled by a computer outfitted with a National Instruments PCI-GPIB card [20]. To automate experiments, record the data, and analyze it, I used routines written with Matlab version R2015a [21]. Dr. Sudeep Dutta wrote most of the data collection software routines.

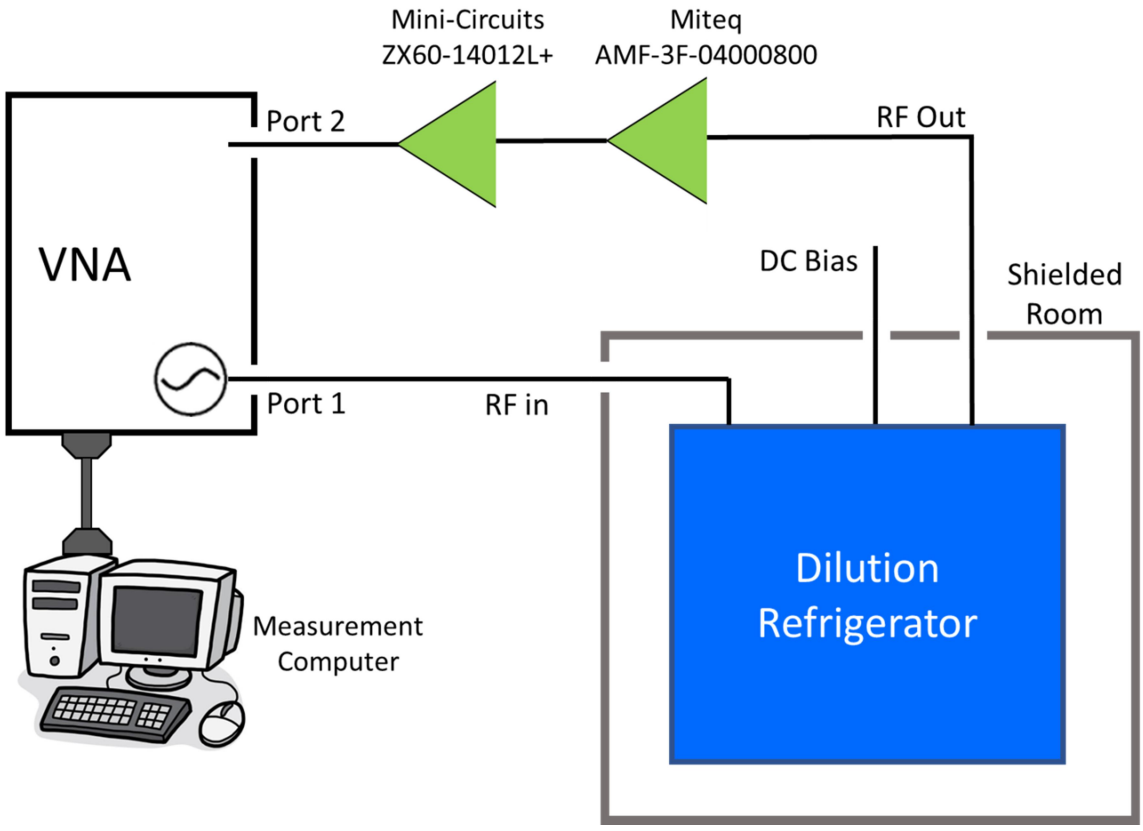

Fig. 7.11: Measurement setup for taking data with the Vector Network Analyzer (VNA). The components inside the dilution refrigerator and the DC bias setup are shown in Figs. 7.6 and 7.9.

7.6 High-Power Qubit Measurement Setup

I exclusively took qubit spectroscopic data using a high-power cavity readout technique [22]. The electronics setup for these measurements was initially put together by R. Budoyo [23]. Here I present an overview of the setup and describe the typical pulsed measurement sequence used for measurements on my devices. An in-depth discussion of this setup can be found in Budoyo's thesis [23].

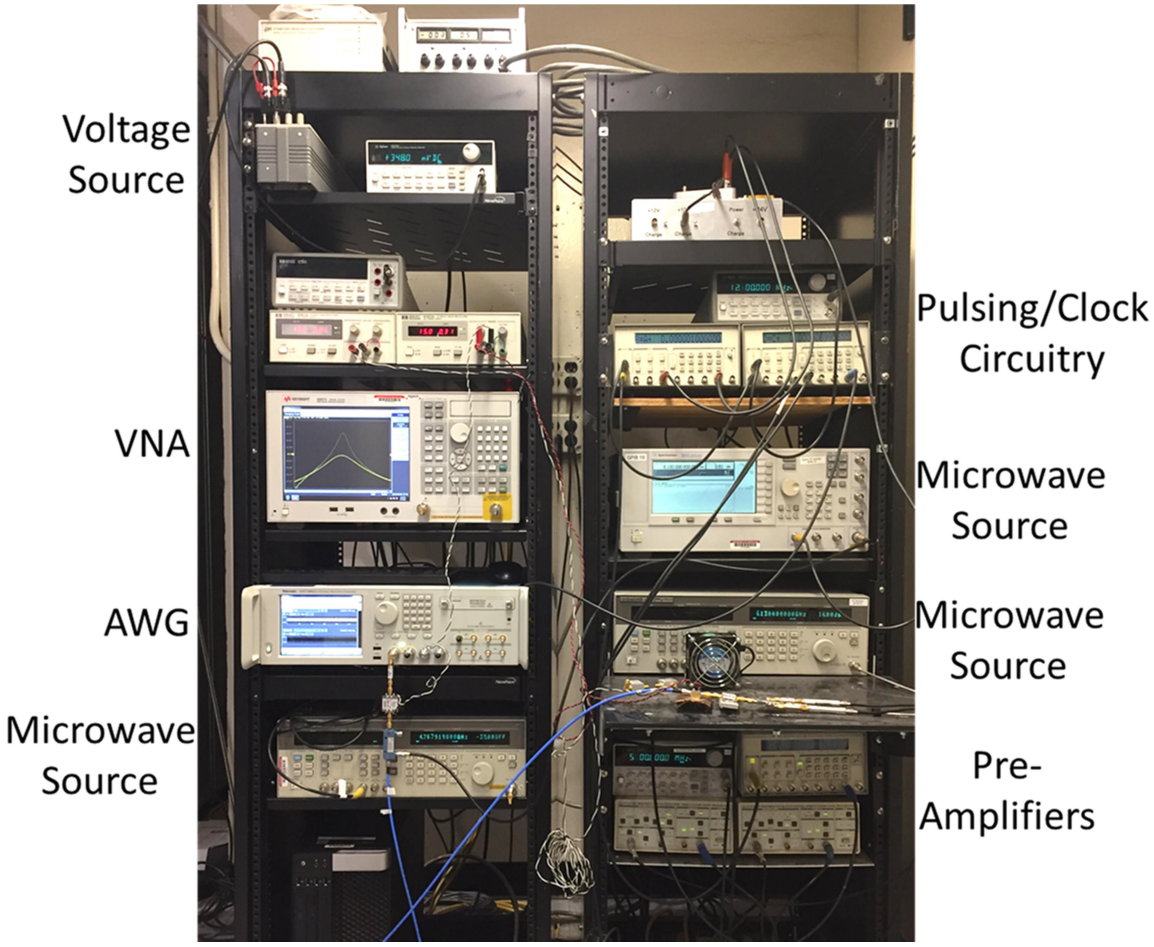

Fig. 7.12: Photograph of the electronics setup used to measure pulsed qubit spectroscopy.

7.6.1 Electronics Setup

Figure 7.12 shows a photograph of the measurement racks containing all the room-temperature components of this setup. For simplicity, Fig. 7.13 shows a block diagram of the high-power pulsed spectroscopy measurement setup, which I modified from ref. [23]. The blue, dotted lines are the timing portion of the circuit. A Stanford FS725 Rb frequency standard [24] was used to output a 10 MHz reference signal. This reference signal ensured stable frequencies and synchronized all the measurement components in time. To set the repetition rate of the measurements, this reference signal was passed to the sync input of an Agilent 33120A arbitrary waveform generator (AWG) [25], which then generated a TTL output signal that went to two Stanford DG535 pulsers [26]. These pulses gated the two measurement microwave sources and triggered the DAQ at the chosen repetition rate, which was typically in the 5 to 12 kHz range.

The pulsed microwave signals used for qubit or cavity measurements were provided by two microwave sources. An Agilent E8257D [27] was used exclusively for the cavity readout signal. For qubit drive pulses, an Agilent 83731B [28] was used. However, for qubit manipulation experiments where we needed multiple pulses and control over the phase, this source was replaced by a Tektronix AWG70002A AWG [29]. These were combined via an MAC 3205-6 6 dB directional coupler [30] and sent through a bulkhead feedthrough at the shielded room wall into the RF input line at the top plate of the dilution refrigerator. The return signal from the cavity left the output connector at the top of the refrigerator. From there it is amplified by a 30 dB Miteq amplifier [31] and by an 11 dB Mini-Circuits amplifier [32] (see section 7.2.2). The output was then fed into the RF port of a Marki IQ0318L [33] IQ Mixer. For the LO side of the mixer, an

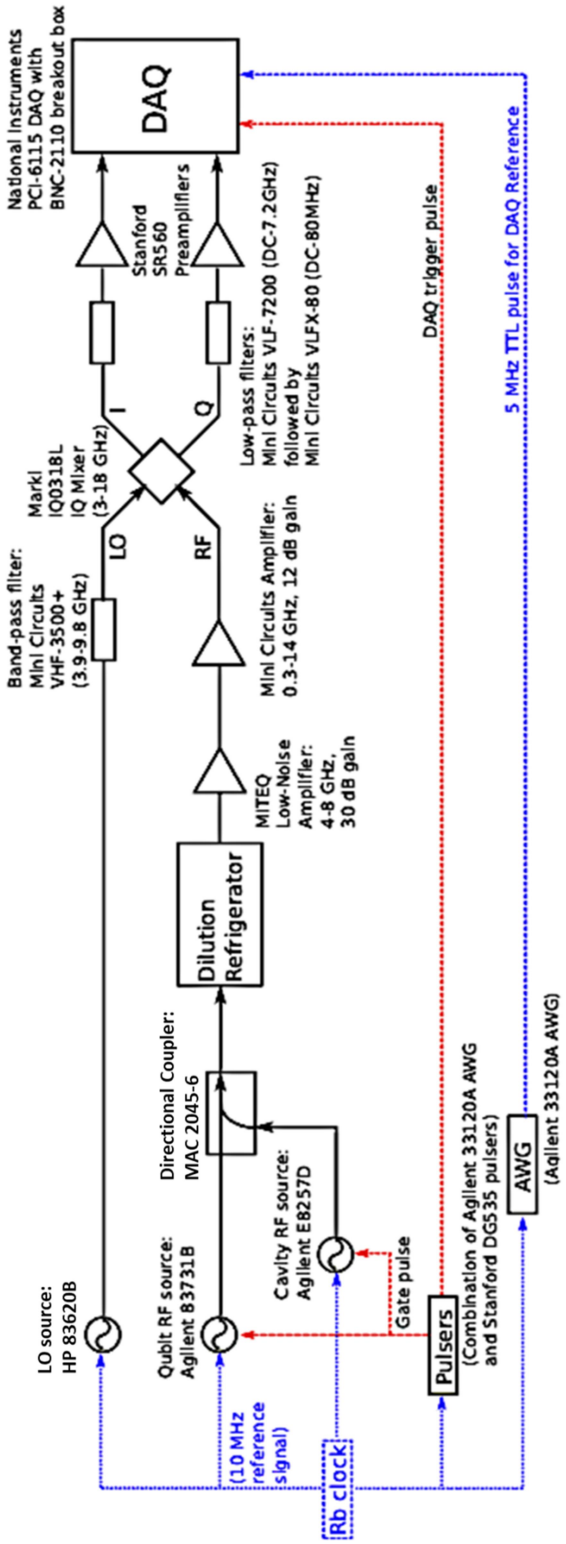

Fig. 7.13: Block diagram showing high-powr pulsed spectroscopy readout setup. This figure is a slightly modified reproduction from ref. [23].

HP 83620B [34] microwave source applied a continuous tone through a Mini-Circuits VHF-3500+ band pass filter [35] with bandwidth of 3.9-9.8 GHz. The frequency of the LO source was set to match the frequency of the cavity source. As a result, the measurements I discuss below and in Chapters 8 and 9 use homodyne detection [36].

As shown in Fig. 7.13, the mixer has two output channels, the in-phase output I and the quadrature output Q. Each output is sent to a Mini-Circuits VLF-7200 low-pass filter [37] with a frequency range of DC-7.2 GHz and then a Mini-Circuits VLFX-80 low-pass filter [38] with a frequency range of DC-80 MHz. From there, the I and the Q signals are amplified by a Stanford SR560 preamplifier [39] and the output sent to a National Instruments PCI-6115 DAQ [40] with a BNC-2110 breakout panel [41]. The DAQ converts the analog voltages to a digital signal that the computer subsequently records. The data acquisition rate was set to 5 Msamples/channel/s using a 5 MHz TTL signal from an Agilent 33120A AWG [25].

7.6.2 Typical Pulse Sequence

The setup shown in Fig. 7.13 is very versatile and can be used for a wide range of qubit measurements. The general sequence for pulsed qubit spectroscopy measurements is shown in Fig. 7.14. The first pulse is a cavity readout pulse that is done at the beginning of each measurement sequence in order to keep track of any background signal. I call this first pulse the calibration pulse. The calibration pulse was 1 μs long and was applied at the bare cavity resonance frequency. The output response from the cavity was turned into an in-phase voltage V_{I0} and a quadrature voltage V_{Q0} in the I-Q mixer (see section 7.6.1). For my measurements, we were interested in the total

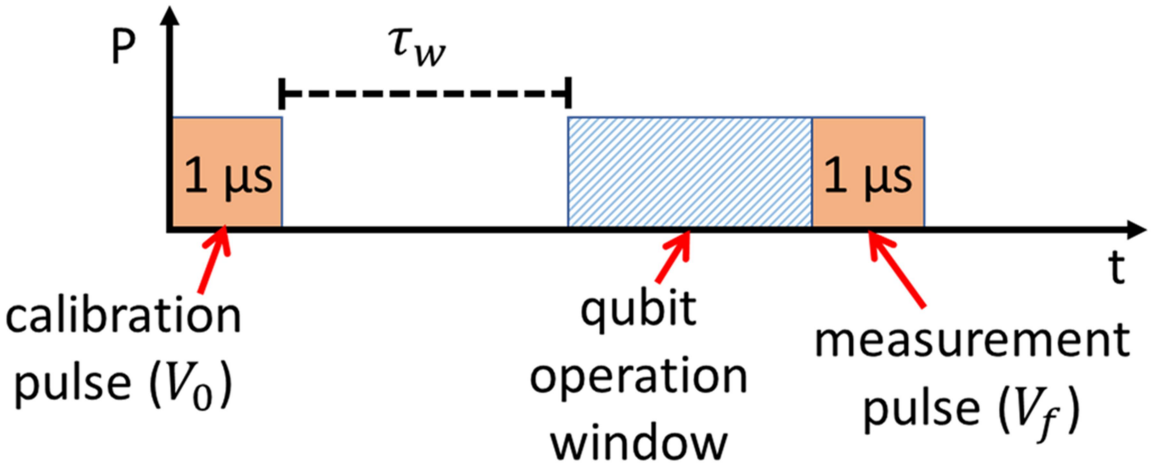

Fig. 7.14: General pulse sequence for high-power qubit spectroscopy.

magnitude of the output voltage; so, from these outputs we took

$$V_0 = \sqrt{V_{I0}^2 + V_{Q0}^2}\,. \tag{7.1}$$

In the high-power readout technique [22], the power of the pulse must be set carefully by taking S-curves (see Chapter 8).

Following the calibration pulse is a window of time τ_w in which we allowed the system to settle back down before performing any qubit manipulations. This length of this window varied depending on the particular measurement, but it was typically $\tau_w \cong 2$ µs for spectroscopic measurements and $\tau_w \geq 28$ µs for time-resolved measurements (see Chapter 9).

After the waiting interval, qubit manipulations were applied. In Fig. 7.15 I show examples of the qubit operation pulses for three types of measurements. Spectroscopy measurements are shown in Fig. 7.15(a). For this measurement, the length of the

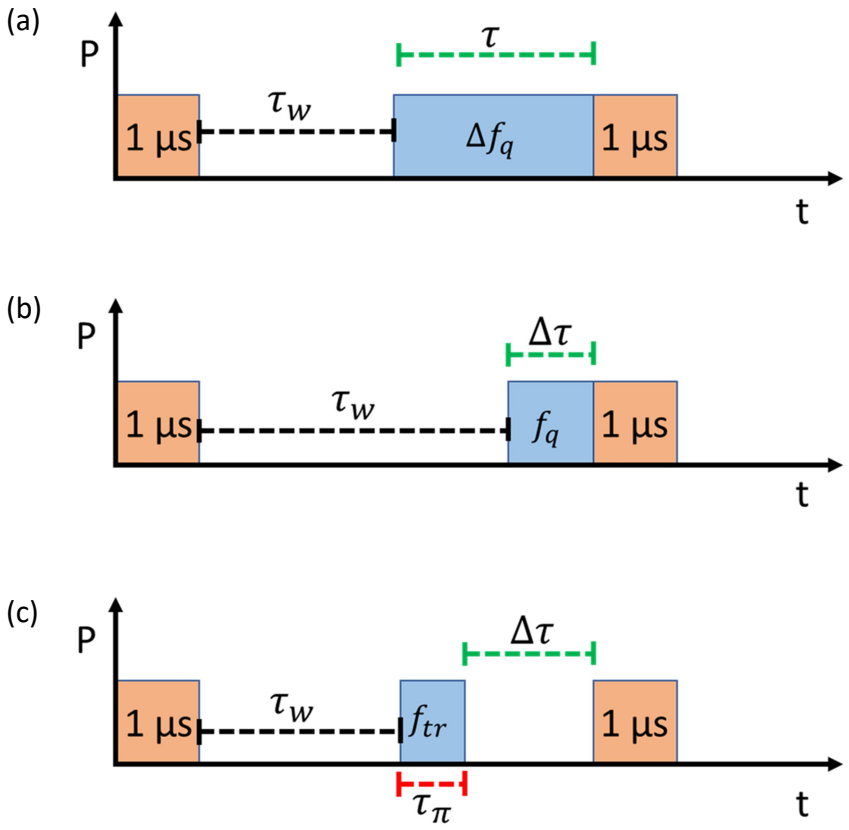

Fig. 7.15: (a) Pulse sequence for high-power qubit spectroscopy. In this sequence the frequency f_q of the pulse is varied while the duration τ is kept fixed. (b) Pulse sequence for measuring Rabi oscillations. In this sequence the frequency f_q of the pulse is kept fixed while the pulse length $\Delta\tau$ is varied. (c) Pulse sequence for measuring relaxation time. In this sequence the qubit pulse length τ_π and frequency f_q are both fixed in such a way to completely invert the qubit population (a π-pulse). The cavity throughput is measured for varying delays $\Delta\tau$.

manipulation pulse is fixed, and the frequency of the pulse is varied (see Chapter 8). Figure 7.15(b) shows the pulse sequence for measuring Rabi oscillations. In this sequence, the frequency of the manipulation pulse is fixed, and the length Δt of the pulse is varied (see Chapter 9). Finally, Fig. 7.15(c) shows the pulse sequence for measuring the relaxation time T_1 of the qubits. In this sequence, the frequency and pulse length are both fixed, and the delay Δt before the final measurement pulse is varied (see Chapter 9).

Finally, following the qubit operation pulses, a second cavity readout pulse, which I call the measurement pulse, was performed. This measurement pulse was also 1 μs long and had the same frequency and power settings as the calibration pulse. The output response of the cavity to this pulse is turned into an in-phase voltage V_{If} and a quadrature voltage V_{Qf} in the I-Q mixer (see section 7.6.1). Again for my measurements, we were interested in the total magnitude of the output voltage; so, from these outputs we formed

$$V_f = \sqrt{V_{If}^2 + V_{Qf}^2}\,. \tag{7.2}$$

Much of the data I show in Chapters 8 and 9 is presented as

$$\frac{\delta V}{V_0} = \frac{\left(V_f - V_0\right)}{V_0}\,. \tag{7.3}$$

If the cavity pulses were set up properly, this quantity is proportional to the probability P_e of the qubit being in the excited state. Typically, the resulting voltages V_0 and V_f were averaged over ≈ 6000 repetitions before calculating the quantity in Eq. (7.3).

Following the measurement pulse, there was another waiting time τ_w' to allow the system to settle back down to the ground state. This delay was set by the repetition rate, and typically was about 80 μs.

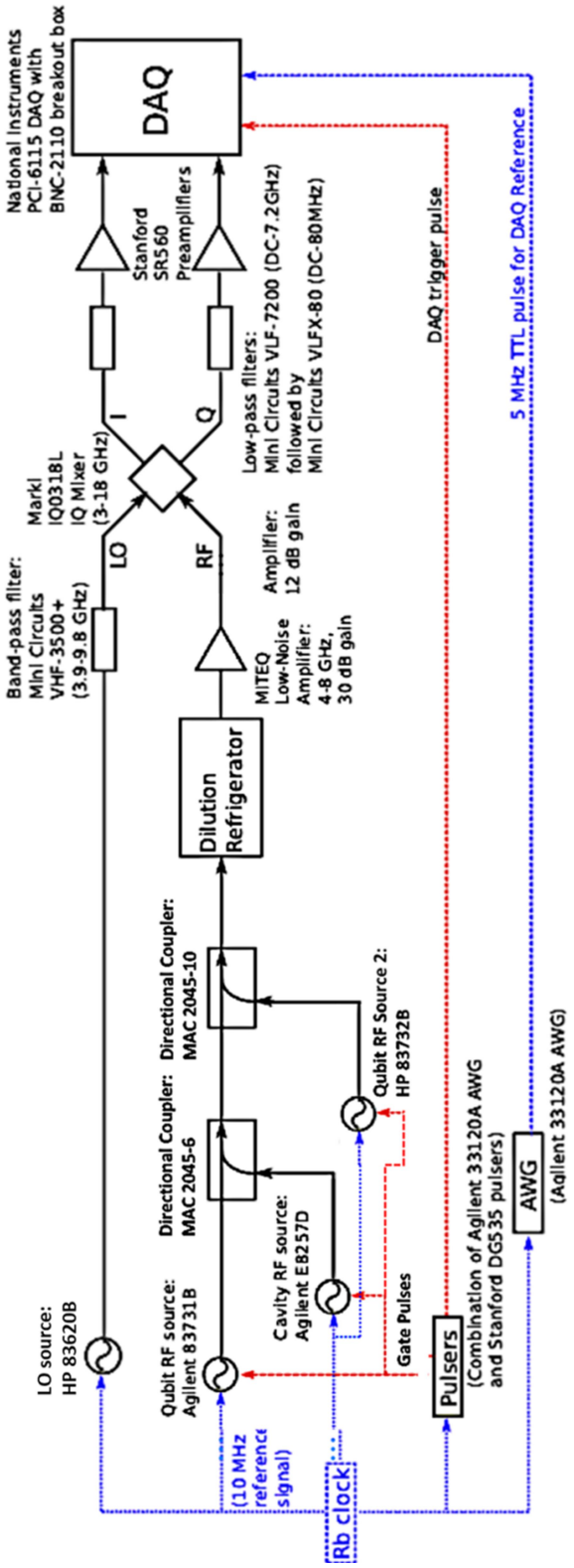

Fig. 7.16: Block diagram showing setup for two-tone qubit spectroscopy. This is a modified reproduction from ref. [22].

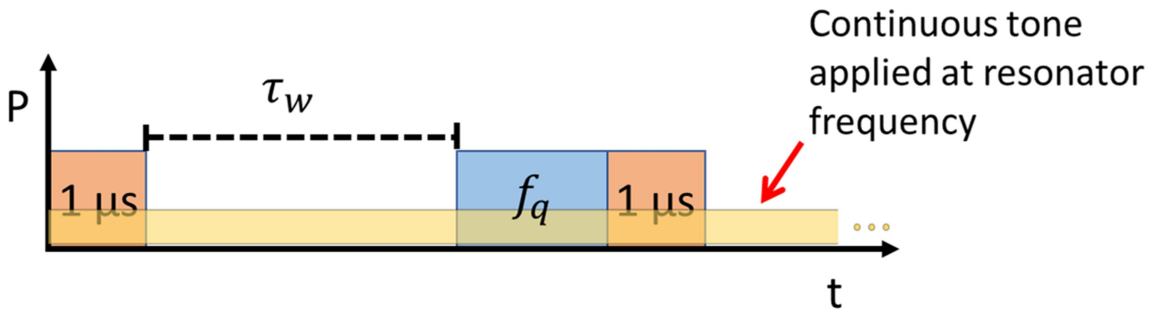

Fig. 7.17: Pulse sequence for performing two-tone qubit spectroscopy. The second tone is continuously applied during the measurement, in this case to populate the resonator with photons.

7.6.3 Two Tone Measurements

Some measurements required modifying the setup to incorporate a third microwave source. Figure 7.16 shows the modified setup, which has an added HP 83723B microwave source [41] coupled into the main input line via an MAC 2045-10 10 dB directional coupler [42].

One application of this third source was for measuring photon number peaks. As I described in Chapter 5, when the readout resonator is populated with photons, extra peaks are observed near the g-to-e transition frequency of the qubit. These peaks correspond to the qubit transition frequency when there are $n = 0, 1, 2$, *etc.* photons in the resonator. The nth peak is shifted in frequency by $2n\chi$ from the original qubit resonance, where χ is the qubit-cavity dispersive shift. χ gives a direct measure of how strongly the qubit is coupled to the resonator. Figure 7.17 shows a typical pulse sequence for this type of measurement. It is pretty much the same sequence as used in the

spectroscopy measurement shown in Fig. 7.15(a), but a continuous tone is also applied. Since two tones are applied during the qubit manipulation, this is an example of two-tone spectroscopy (the third tone for cavity readout is not counted in this total). To adjust the number of photons populating the cavity, the power and frequency of this continuous second tone can be adjusted. A similar two-tone measurement was used to find the qubit-qubit dispersive shift. Results of such measurements are discussed in Chapter 8.

Chapter 8

Spectroscopy of Variable Qubit-Qubit Coupling Device

In this chapter I discuss microwave spectroscopic measurements of my device TRES_092917. This device was sealed in 3D microwave cavity SI-4 and had two transmons capacitively coupled to a tunable resonator. The resonator was tuned by applying a DC magnetic field into two RF SQUID tuning loops (see Chapter 3).

I begin by discussing the cavity and qubit calibration measurements that were necessary for setting up high-power pulsed readout. I then show how the system behaves as the tunable resonator's frequency is varied. By fitting the transitions from the model Hamiltonian of the system (see Chapter 5) to the observed transition frequencies, we find all the coupling strengths and other parameters of the resonator, qubits, and cavity. I next show that there is a tunable qubit-qubit dispersive shift, which is essential for constructing an entangling gate such as the CNOT. Finally, I end with a brief discussion of a two-level fluctuator, which we found was coupled to one of the qubits.

8.1 Measurement Details

The data I present in this chapter on device TRES_092917 was primarily measured by Dr. Sudeep Dutta from December 2017 to June 2018. The device was initially cooled in our Oxford Triton 200 dilution refrigerator in October of 2017. However, it was subsequently warmed to room temperature twice to change cavities and to fix a heating problem on the flux bias lines. For the first warm-up, I changed cavities from SI-2b to SI-4 (see Chapter 2) in order to place the device in the center of the cavity space and to reduce the distance the flux tuning coil protruded into the cavity space (see

Chapters 3 and 6). For the second warm-up, I removed a K&L 10.5 GHz low-pass filter from the output microwave line/input DC bias line due to it producing heating when a bias current was applied (see Chapter 7). All measurements were made in the sub-basement of the physics building in room SB0331.

For the spectroscopic measurements on the qubits, the high-power readout scheme discussed in section 7.6 was used. The particular pulse sequence started with an initial cavity pulse that was used to calibrate the transmission of the system when the qubits were in their ground state. This was followed by a delay $\tau_w \cong 2$ μs that was sufficient to allow the system to relax enough for spectroscopic measurements; qubit manipulation pulses were then applied. Finally, another cavity pulse was used to measure the qubit state produced by the manipulation. For both the calibration pulse and the measurement pulse, the amplified signal from the cavity was passed to an I-Q mixer where the magnitude of the output voltages V_I and V_Q were measured by mixing it with the reference signal from the cavity drive source. V_0 is the measured voltage amplitude of the first "calibration" pulse and V_f is the measured voltage amplitude of the second "measurement" pulse. What is then plotted in spectroscopy measurements is the averaged value of

$$\frac{\delta V}{V_0} = \frac{V_f - V_0}{V_0}, \tag{8.1}$$

which is the scaled difference between the two pulse voltages, where typically on the order of 1000 to 10000 shots are averaged. This quantity is proportional to the excited state population of both qubits and is relatively insensitive to small variations in the readout.

8.2 Cavity Power Map

After cooling the device, the first step was to characterize the cavity resonance by measuring the cavity spectrum using the VNA (see Fig. 7.11). For this measurement, the VNA determined $|S_{32}|^2$ as a function of frequency and power by measuring the ratio of the microwave signal with amplitude V_{in} at the microwave input line of the dilution refrigerator to the output signal with amplitude V_{out} (*i.e.* $|S_{32}| = |V_{out}|/|V_{in}|$). I use the subscript "32" to denote the fact that the input line went to port 2 of the cavity and the output line was connected to port 3 of the cavity, which was the split coil (see Chapter 3). Cavity port 1 was unused for this experiment.

In Fig. 8.1(a), I show a false-color power map of the cavity. The x-axis of the plot is frequency, the y-axis is the power applied by the VNA, and the color represents $20\log_{10}|S_{32}|$ or $|S_{32}|$ (dB). Examining the plot at high powers, one sees there is a prominent peak centered at 6.1300 GHz. This is the bare resonance of the cavity $\omega_c/2\pi$, and I have marked it with the dashed black line. At low powers, the resonance peak shifts to just below 6.1489 GHz. This is the cavity's dressed peak and the frequency shift is due to the coupling of the cavity to both of the transmons (see Chapter 5). The frequency shift from the bare resonance is the dispersive shift χ_{eff}. We see here that $\chi_{eff}/2\pi = 18.9$ MHz. Since I was aiming for a coupling strength of $g/2\pi = 150$ MHz for each qubit, this value of χ suggests the qubits' g-to-e transition frequencies are roughly in the 5 GHz design range (see Chapters 5 and 6). This data was the first indication that this device had good parameters.

In Fig. 8.1(b) I show two line cuts through the $|S_{32}|^2$ data in Fig. 8.1(a). The first cut is at a VNA power of 10 dBm (blue curve), which is the highest power the VNA can

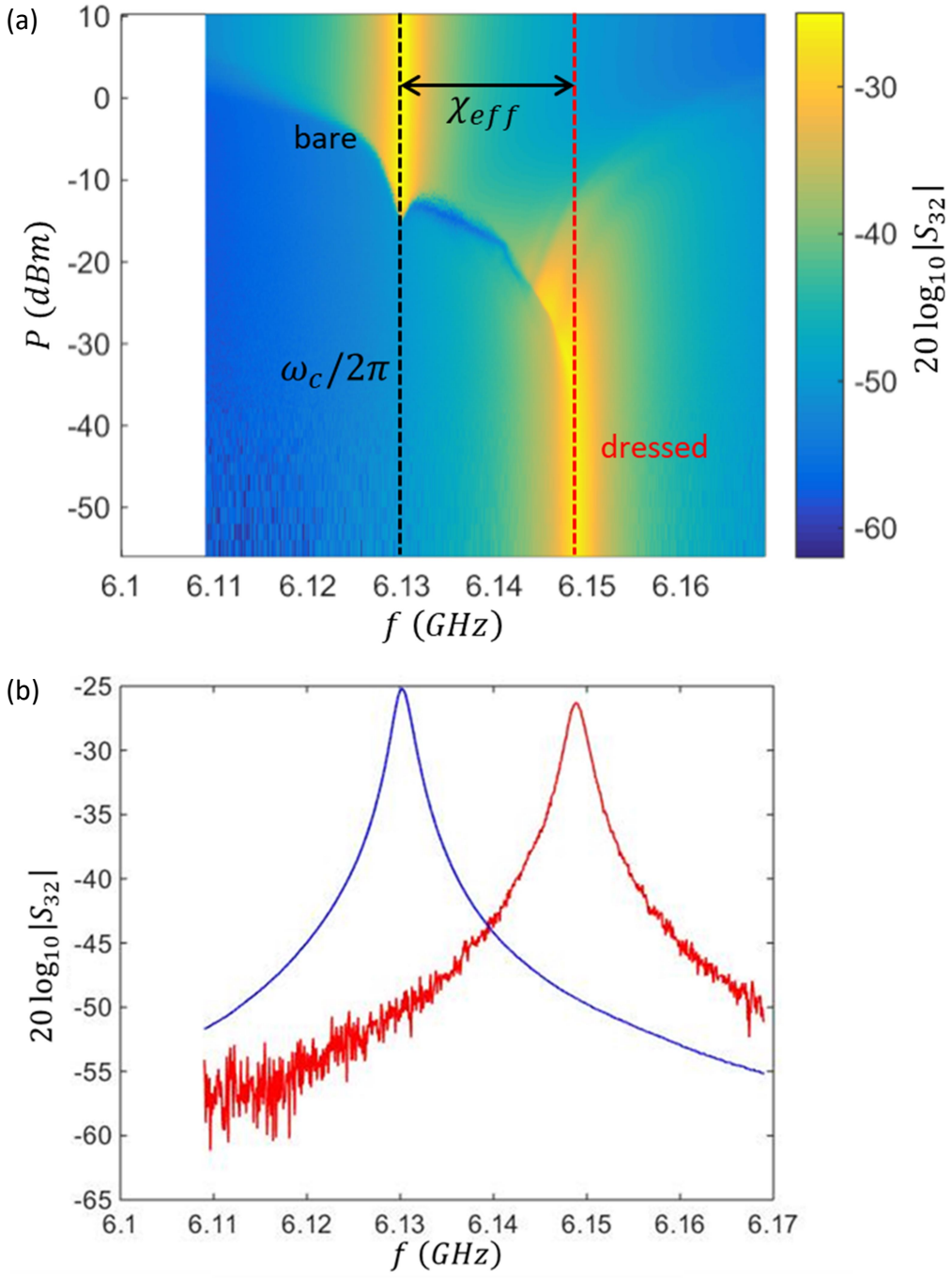

Fig. 8.1: (a) Cavity power map showing $|S_{32}|^2$ as a function of VNA frequency f and applied power P during run II-76 on device TRES_092917 with bare resonance and dispersively shifted dressed peak labelled. (b) VNA $|S_{32}|^2$ data on the cavity at 10 dBm (blue) and at -45 dBm (red).

generate, and the second cut is at a VNA power of -45 dBm (red curve), which is in the dressed peak regime. Fitting the blue peak to the Lorentzian Eq. (3.12) yields a center frequency of $\omega_c/2\pi = 6.1300$ GHz and a loaded quality factor of $Q_L = 2800$. Similarly, fitting the red peak yields a dressed frequency of $(\omega_c + \chi_{eff})/2\pi = 6.1489$ GHz and a loaded quality factor of $Q_L = 2550$. The quality factor of the dressed peak was less than that of the bare resonance. This means that there was additional loss when the cavity was in the low-power limit or there was additional dephasing present when the qubit was coupled to the cavity.

As I discussed in Chapter 5, the presence of a dressed peak is a clear indication that at least one qubit was functional. The next step was verifying that the LC resonator was tuning.

8.3 Flux Dependence of Cavity Resonance

As discussed in Chapter 3, the flux tunable resonator couples to the cavity TE_{101} mode and produces a shift in the cavity frequency as a function of the tuning. Thus, to check that the LC resonator was tuning, a simple test was to apply flux to the device and monitor the cavity's resonance frequency via $|S_{32}|^2$.

In Fig. 8.2 I show a cavity flux map taken with the VNA (see Fig. 7.11). The x-axis of this plot is the current applied to the DC flux bias line (see Fig. 7.9), the y-axis is frequency, and the color represents $20\log_{10}|S_{32}|$. This map was taken at a VNA power of -50 dBm, which is in the dressed peak regime (see Fig. 8.1). Since the cavity mode itself was not flux dependent, any modulation of this frequency was due to tuning the LC

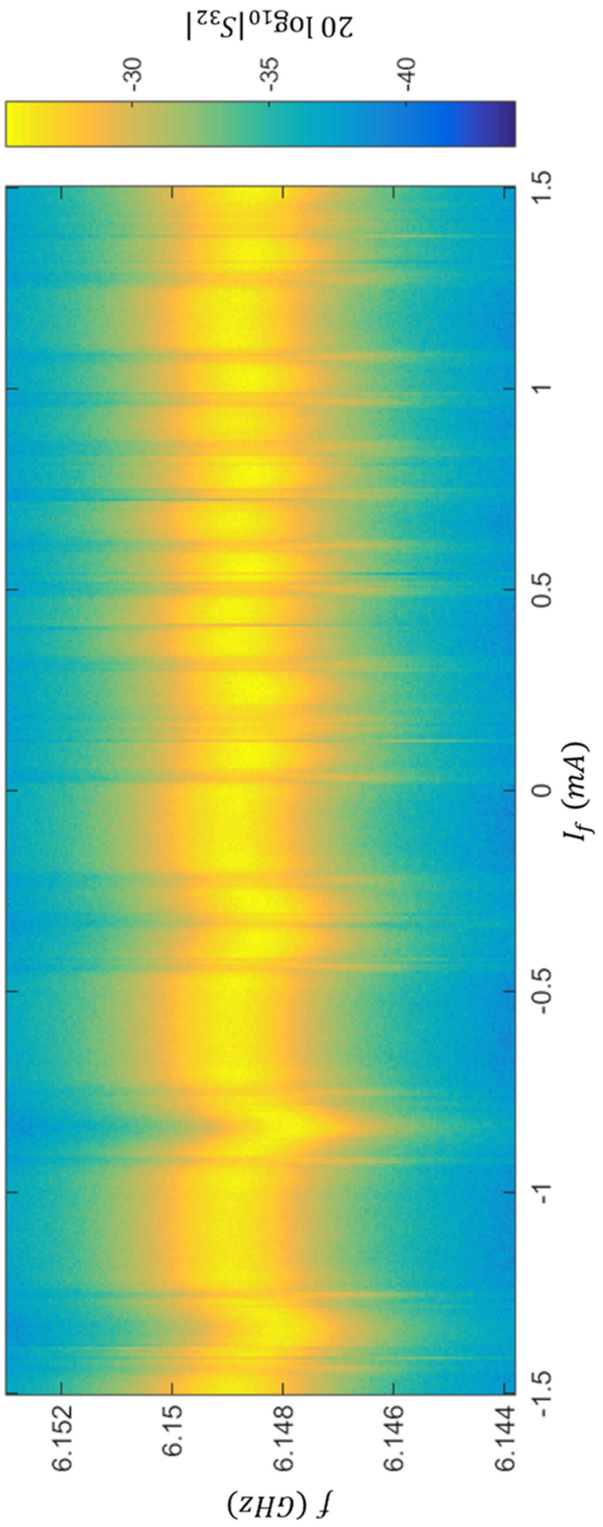

Fig. 8.2: Map of cavity $|S_{32}|^2$ vs. frequency f and bias flux current I_f taken at an applied VNA power of -50 dBm.

resonator. As is clearly seen in the plot, the cavity resonance frequency varied by about 1 MHz, showing that the resonator was working at some level.

In Chapter 3, I showed that tunable resonator device tunres_112115 had a 40 MHz tuning range, and this gave a cavity response of approximately 100 kHz. Since the expected coupling of the resonators in the two devices was similar, the 1 MHz variation of the cavity resonance in TRES_092917 suggested that the LC resonator tuning range was of order 400 MHz.

One interesting set of features visible in Fig. 8.2 are the vertical stripes that occur near the tuning dips. Further investigation showed that these were multi-photon transitions involving high levels of the LC resonator. As I show below, similar behavior is more easily seen in the spectroscopic flux maps of the qubits.

8.4 Finding the Qubit and LC Resonator Transitions

The process of identifying the qubit and resonator transitions is iterative in nature. For spectroscopic measurements the pulsed measurement setup of Fig. 7.13 was used with the pulse sequence shown in Fig. 7.15(a). Given the cavity power map in Fig. 8.1(a), the cavity microwave source power and frequency were set to a point just below where the bare cavity resonance is recovered; in this case $P_c \approx$ -18 dBm and $f_c = 6.130$ GHz. The frequency of the spectroscopic pulse was then swept and the quantity $\delta V/V_0$ (see Eq. (8.1)) was averaged and recorded at each frequency point. Peaks in the observed response correspond to excitations of the qubits or resonator.

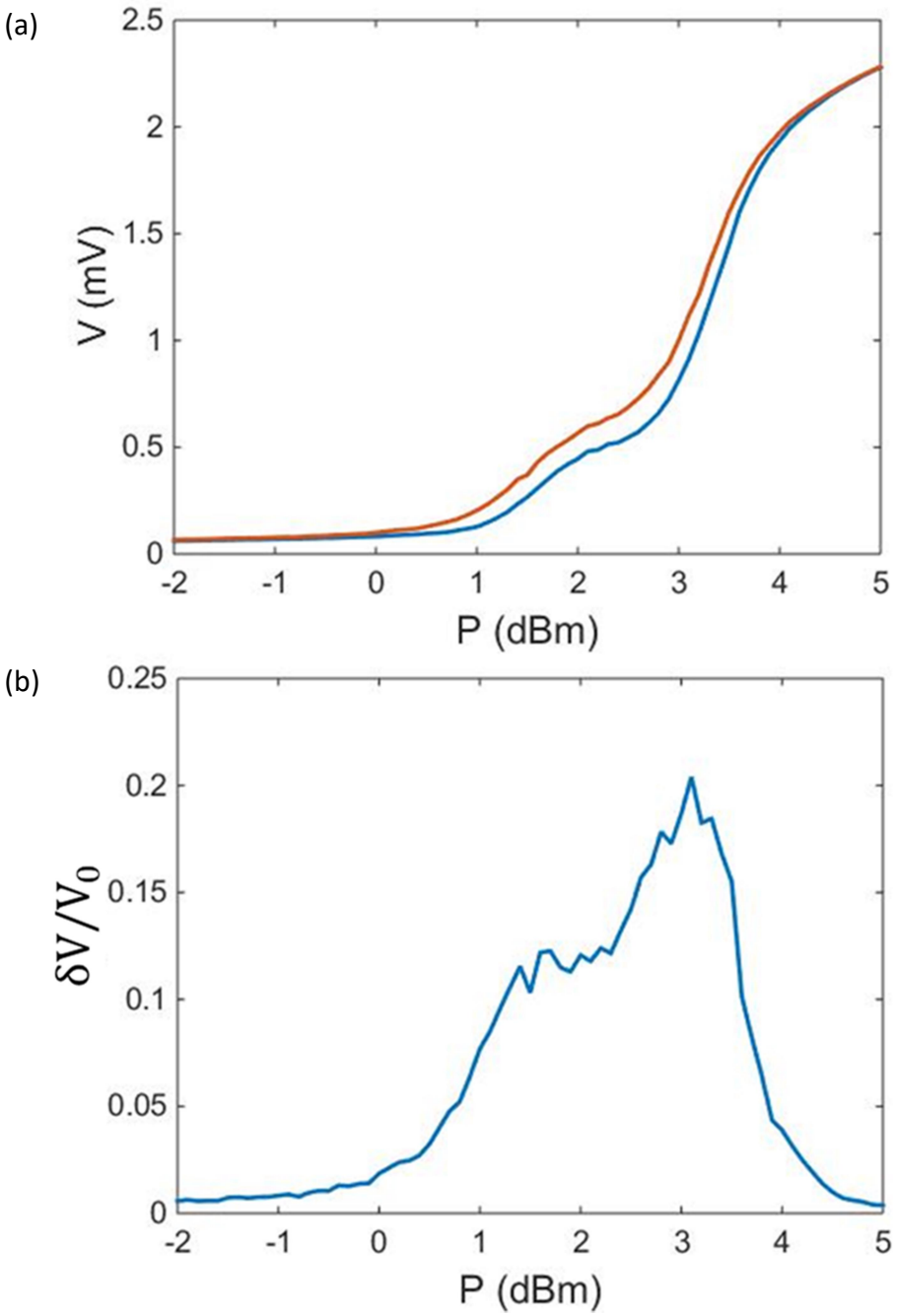

Fig. 8.3: (a) Plot of preliminary S-curves on device TRES_092917. The blue curve is the transmission through the cavity with both qubits in the ground state, and the red curve is the transmission after driving the g-to-e transition of the higher qubit Q_H. (b) Plot of the scaled difference $\delta V/V_0$ between the red and blue curves in (a), see Eq. (8.1).

A better cavity pulse power P_c and frequency f_c were then found for the cavity measurement pulses by taking S-curves while applying a spectroscopic pulse at a frequency corresponding to one of the spectroscopic peaks. In Fig. 8.3(a) I show an example. For an S-curve, the x-axis is the power P_c applied to the cavity by the microwave source and the y-axis is the magnitude of the measured output voltage V from the mixer. In the figure, the blue curve is a plot of V_0 versus P_c and the orange curve is a plot of V_f versus P_c. Comparing the blue and orange curves, one sees that driving the qubit causes the cavity to recover its bare resonance frequency at a lower power. In Fig. 8.3(b) I show the difference between these two curves. By setting the cavity pulse power P_c to the point $P_c = 3$ dBm one finds the highest contrast and the best signal-to-noise ratio (SNR) for the measurement.

Since there are two qubits in the system, it is essential in some cases to determine which qubit was excited. This requires a more sophisticated S-curve based technique such as the joint-qubit readout technique developed by Premaratne *et al.* [1]. I briefly discuss this method in section 9.7 where I discuss an initial characterization of a CNOT gate.

Once better settings were found for the cavity measurement pulse, the entire spectrum was remeasured. In Fig. 8.4 I show the pulsed spectrum over the range of 1 GHz to 11 GHz. The x-axis of the plot is the frequency of the qubit microwave source f_q, and the y-axis is the voltage enhancement $\delta V/V_0$ from the high-power cavity readout. Examining the plot, one sees just a few regions of interest. The prominent peak at 6.13 GHz is the cavity resonance frequency. The most interesting section is the closely bunched set of peaks in the 4.5 GHz to 5.2 GHz range. Since I was looking for 2

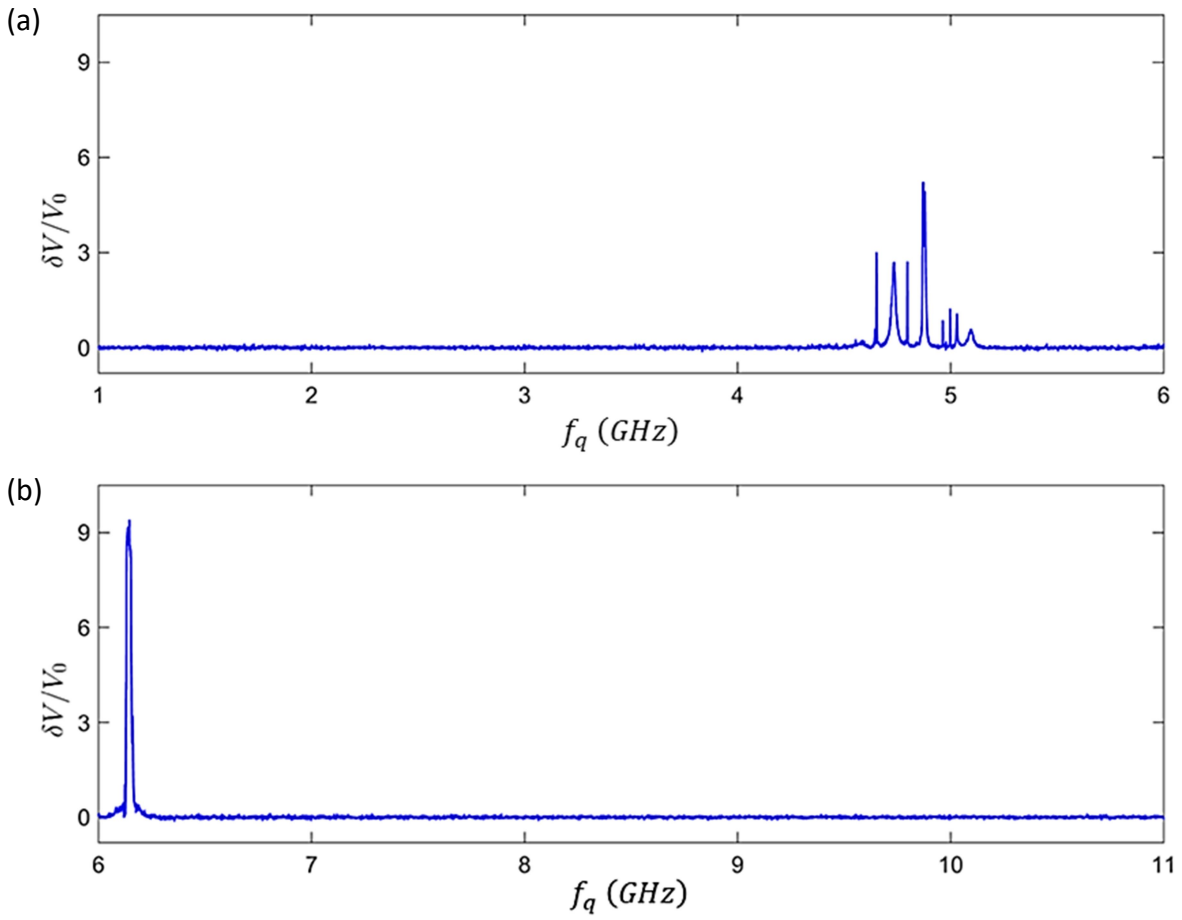

Fig. 8.4: (a) Pulsed spectroscopic measurements of the two transmons, LC resonator, and cavity in device TRES_092917 at applied power P_q = -15 dBm over the range f_q = 1 GHz to 6 GHz and (b) 6 GHz to 11 GHz.

different qubits and a resonator, all designed to be near each other in frequency, I was hoping to see at least three peaks in this range, with additional transitions visible if the device was driven hard. To figure out which peak corresponds to the LC resonator, one needed to apply flux and see how the peaks moved.

8.5 Flux Map

For this measurement I again used the high-power pulsed readout setup. In Fig. 8.5, I show the flux-dependent response of the system over the frequency range 4.1 GHz to 5.25 GHz taken at a qubit microwave source pulse power P_q of 0 dBm, which is quite high. In this false-color map, the x-axis is the current applied to the DC flux bias line, the y-axis is the frequency f_q of the qubit manipulation pulse, and the color corresponds to the voltage enhancement $\delta V/V_0$ with the dark regions corresponding to larger enhancement. Examining Fig. 8.5, the first thing one sees is that there are a lot of peaks present. This data was taken at a qubit pulse power P_q of 0 dBm, which was strong enough to drive one, two, three and even four-photon transitions. Comparing this spectroscopy to the expected behavior I showed in Fig. 5.13, it is clear that many more peaks are present in the data, but this is because Fig. 5.13 only shows single and two-photon transitions.

To track the flux-dependence of the various transition peaks, this spectrum was measured for several powers of the qubit drive P_q. In Fig. 8.6, I show a finer scan of the map for I_f values between -1.15 and -0.53 mA at a qubit drive power of P_q = -25 dBm (a relatively low power). In this figure, the single-photon transitions are quite clear, although there are still some multi-photon transitions between higher levels of the LC resonator cutting through. In Fig. 8.7, I show the same region with the qubit drive set to P_q = -15 dBm (a medium power). Finally, in Fig. 8.8(a), I show the spectrum in the same flux range but taken at P_q = -5 dBm (a high power). At this power, we were able to observe the LC transition over its full range. As seen in the plot, the tuning range was roughly 800 MHz, with a maximum frequency of about f_{LC} = 4.95 GHz and a minimum

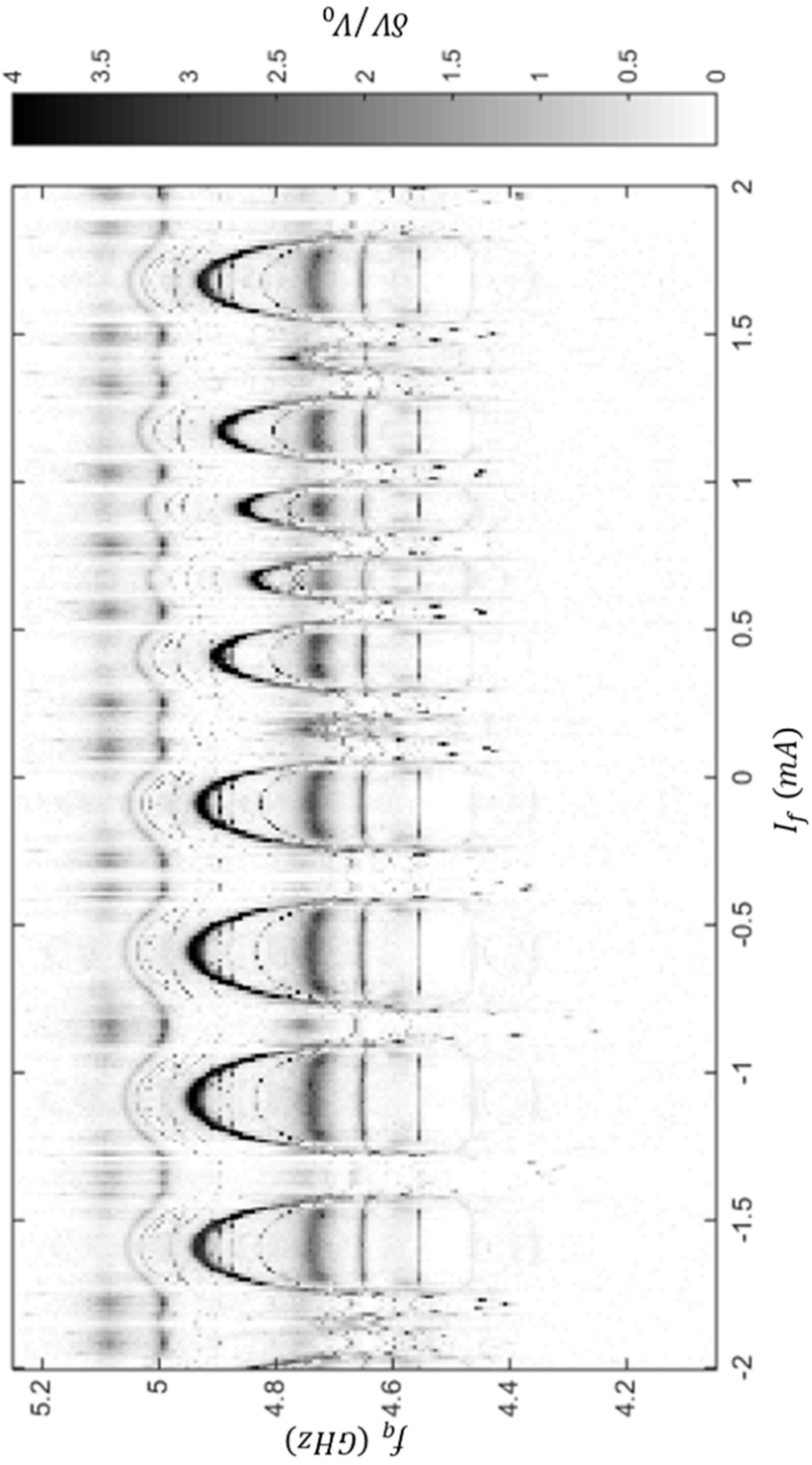

Fig. 8.5: Pulsed spectroscopy flux map of device TRES_092917 taken at qubit pulse power P_q= 0 dBm. The darkest regions on the plot correspond to an increase in transmission through the cavity and represents a spectroscopic transition.

frequency of $f_{LC} < 4.3$ GHz.

The next priority was to figure out what each transition corresponded to so that the spectrum could be compared to the transition frequencies of the model Hamiltonian discussed in Chapter 5:

$$\begin{aligned}\mathcal{H} = {} & \hbar\omega_H\left(n_H + \frac{1}{2}\right) - \frac{E_{CH}}{2}n_H(n_H+1) + \hbar\omega_L\left(n_L + \frac{1}{2}\right) - \frac{E_{CL}}{2}n_L(n_L+1) \\ & + \hbar\omega_r n_r + \hbar\omega_c n_c + \hbar g_{Hr}\left(b_H^\dagger a_r + b_H a_r^\dagger\right) \\ & + \hbar g_{Lr}\left(b_L^\dagger a_r + b_L a_r^\dagger\right) + \hbar g_{Hc}\left(b_H^\dagger a_c + b_H a_c^\dagger\right) \\ & + \hbar g_{Lc}\left(b_L^\dagger a_c + b_L a_c^\dagger\right) + \hbar g_{HL}\left(b_H^\dagger b_L + b_H b_L^\dagger\right) \\ & + \hbar g_{rc}\left(a_r^\dagger a_c + a_r a_c^\dagger\right),\end{aligned} \tag{8.2}$$

From this comparison, one can extract the frequencies and coupling parameters of the device. When fitting the model to the data, I restricted each subsystem (*i.e.* the two qubits, the resonator, and the cavity) to 4 levels. As I discussed in section 5.2.3, accurate modelling requires retaining $n + 2$ levels if one wants to fit transitions involving the first n levels. Since the numerical modelling of this device only used 4 levels for each system including the ground state, 16 energy level transitions were included in the comparison, but never more than three excitations in any one system. In this case only the single-photon and two-photon transitions were accurately captured.

Examining the spectrum in Fig. 8.8(a), an obvious feature is the dark peak that has a strong dependence on the tuning current. This peak frequency modulates over an 800 MHz range and is obviously the tunable LC resonator. Similar to the behavior observed in the tunable resonator device tunres_112115 (see Chapter 3), the peak

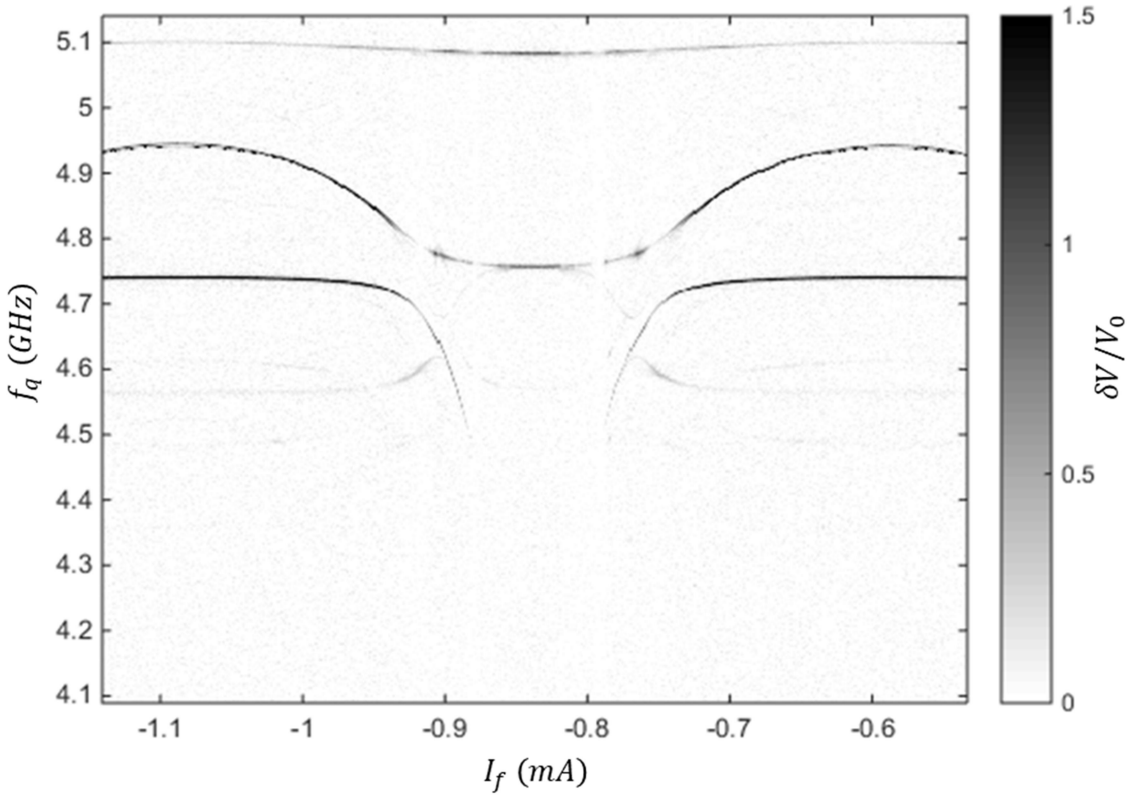

Fig. 8.6: Pulsed spectroscopic data taken at qubit pulse power P_q= -25 dBm.

becomes difficult to observe if the LC resonator was tuned too close to its minimum frequency. However, the effect of the tuning of the LC was still seen in the behavior of the other spectroscopic peaks.

The single-photon g-to-e transitions for the two qubits were also easy to identify. The transition frequency of the higher of the two qubits Q_H is readily visible in Fig. 8.8(a) at about 5.1 GHz. The evidence is as follows: First, the anharmonicity of the transmons is ≈200 MHz, with the higher level transition frequencies being less than that of the g-to-e transition. Thus, the highest frequency in a qubit's spectrum is the g-to-e transition. The set of peaks near 5.1 GHz matches the expected qualitative behavior for

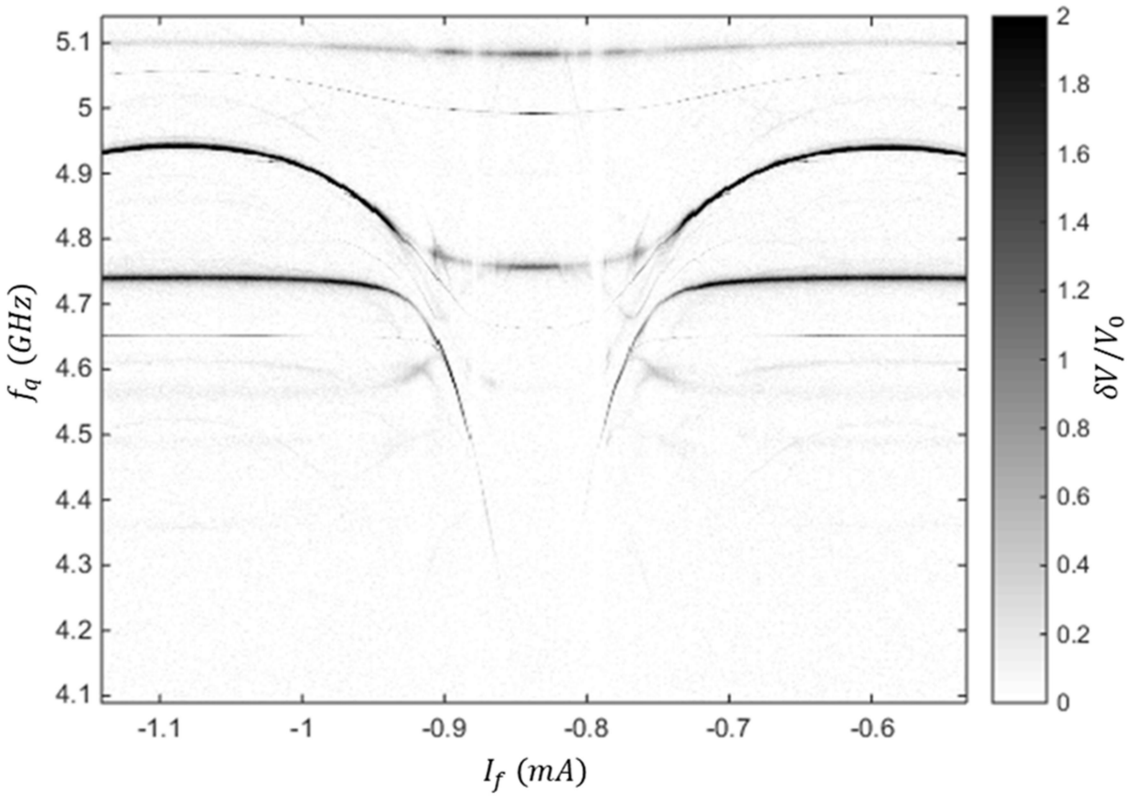

Fig. 8.7: Pulsed spectroscopic data taken at qubit pulse power P_q= -15 dBm.

a series of transitions to higher transmon levels, and in this case the highest frequency transition is the g-to-e transition. Second, the peak width increases with applied power, as expected for a single-photon transition with the applied power well above the onset of saturation. Third, at low enough power, the system should start in the ground state and the only single-photon transition observed should be the g-to-e. The corresponding two-photon g-to-f transition peak is the sharp, dark line just below the single-photon transition at about 5.05 GHz in Fig. 8.8(a).

The lower frequency qubit Q_L has a g-to-e transition frequency that is visible in Fig. 8.8(a) at about 4.75 GHz. This is in the same range as the LC resonator, but unlike

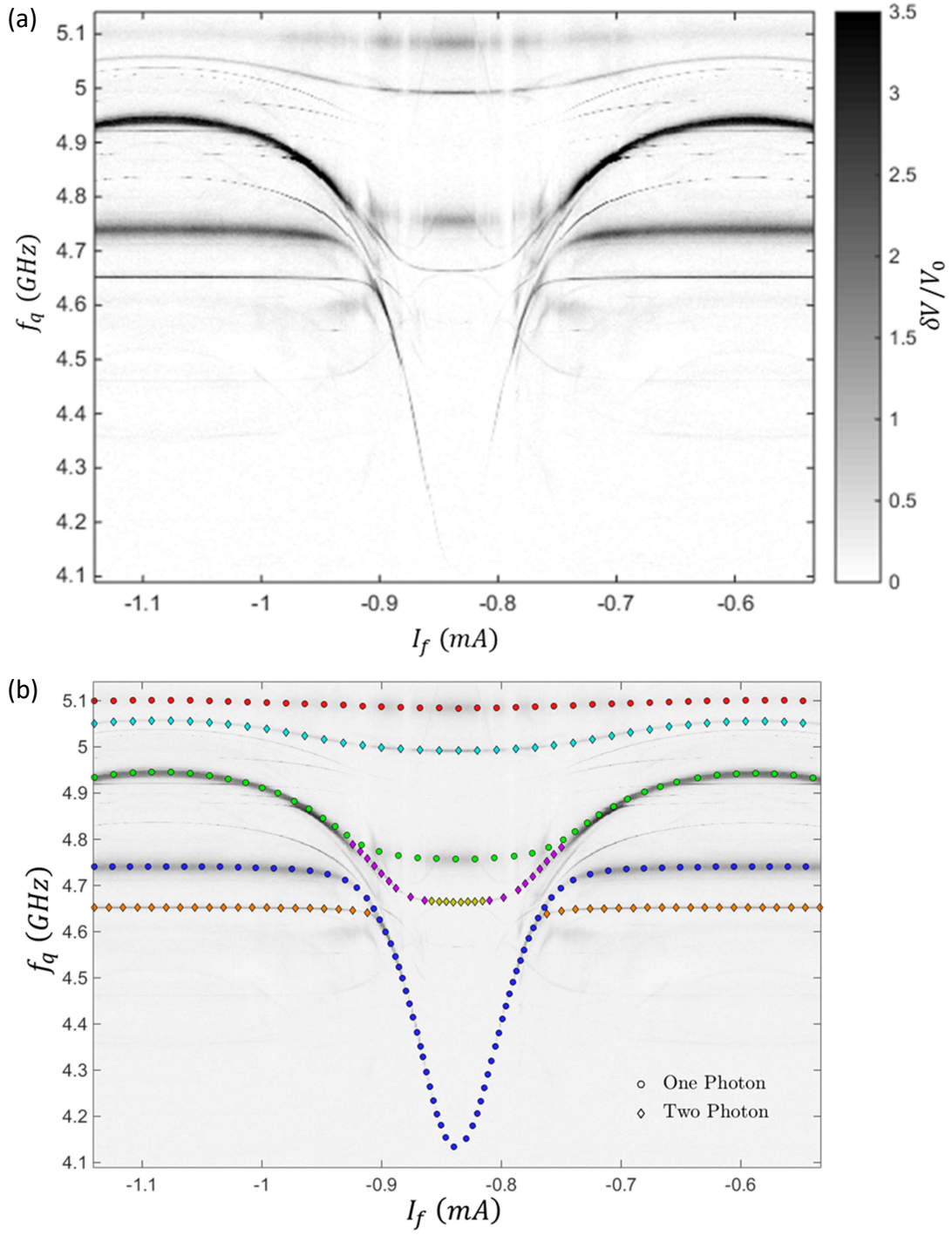

Fig. 8.8: (a) Pulsed Spectroscopic data taken at qubit pulse power P_q= -5 dBm. (b) Extracted frequencies from the spectroscopic data in Fig. 8.8(a). The circles represent single-photon transitions and the diamonds represent two-photon transitions.

the LC resonance, it broadens with increasing power. The other transition peaks just below 4.75 GHz then correspond to higher level photon transitions, mostly of Q_L. Specifically, the two-photon g-to-f transition is the sharp, dark line located at about 4.65 GHz, just below the single photon peak in Fig. 8.8(a).

In Fig. 8.8(b), I show the same spectrum as in Fig. 8.8(a) with the extracted transition frequencies superimposed. The circles correspond to single-photon transitions and the diamonds correspond to two-photon transitions. Another detail not captured in this figure is the state composition as a function of the flux current. At a current of $I_f =$ -1.1 mA the LC resonator's resonance frequency is close to its maximum of about $f_{LC} =$ 4.94 GHz. At this point, the transition represented by the green circles is predominantly due to the LC resonator, the blue circles are for the g-to-e transition of Q_L, and the orange diamonds are for the g-to-f two-photon transition of Q_L. On the other hand, at $I_f =$ -0.85 mA, the LC resonator is at its minimum tuning frequency of about $f_{LC} = 4.14$ GHz. In this region, the blue circles show the resonance frequency of the LC resonator, the green circles are now the g-to-e transition of Q_L, and the two-photon g-to-f transition frequency of Q_L are the purple and yellow diamonds.

The transitions in Fig. 8.8 carry a lot of information about the underlying energies of the states of the coupled system, including the coupling strength between the qubits and LC resonator. However, this is not enough to find the coupling parameters between the cavity and the qubits or between the cavity and the LC resonator. Similarly, additional spectroscopic data is needed to find the direct qubit-qubit. In the next two sections, I discuss these measurements.

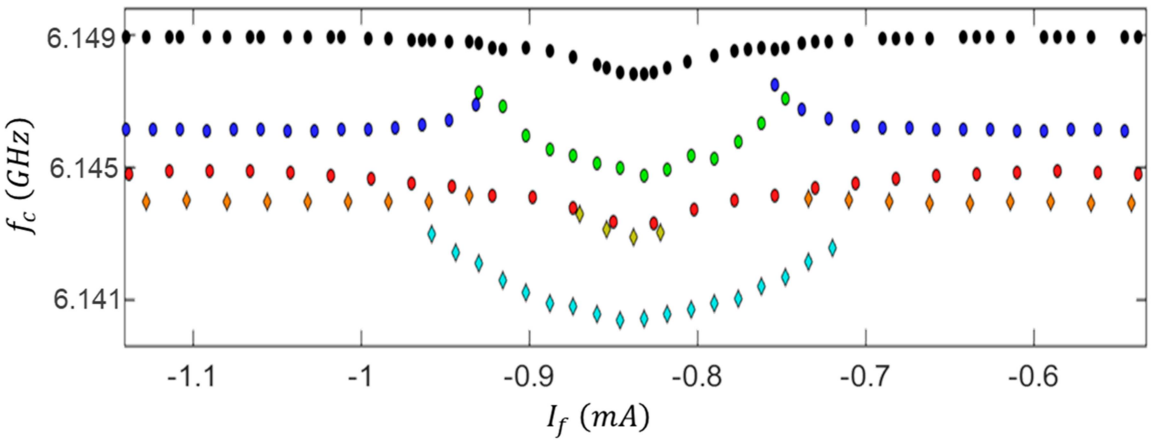

Fig. 8.9: The flux dependence of the main cavity transition at 6.144 GHz is shown as black points. The other colors are the cavity frequency when dispersively shifted by simultaneously exciting the transitions shown in Fig. 8.8(b). The color and shape of the points on this plot are color coded to match the points in Fig. 8.8(b), *i.e.* driving at the blue circles in Fig. 8.8(b) produced the blue circle points here.

8.6 Dispersively Shifted Cavity Transitions

In order to determine the coupling strength between the cavity and the other systems a relatively low-power CW (continuous waveform) microwave signal was applied to excite specific qubit or resonator transitions, and the $|S_{32}|^2$ spectrum of the cavity was then measured with the VNA using the setup described in section 7.5. In Fig. 8.9 the x-axis is the current I_f applied to the DC flux bias line (see section 7.3), and the y-axis is the frequency of the resulting cavity transition frequency. Note that the y-axis only covers a range of 8 MHz; *i.e.* the resulting shifts were relatively small. The black points are the cavity dressed peak measured at a VNA power of -50 dBm. This is the extracted cavity resonance frequency from the spectroscopy data in Fig. 8.2. The other

points in the plot correspond to the cavity transition frequency when a CW signal is used to excite the qubits or LC resonator. The color and shape of the points are coded to match the transitions shown in Fig. 8.8(b). For instance, the red circles in Fig. 8.9 are the cavity dressed peak frequency when a CW signal is applied at the g-to-e transition of Q_H. Similarly, the orange diamonds are the cavity dressed peak frequency when the two-photon g-to-f transition of Q_L is driven. Note that these dispersive shifts are typically $2\chi = 2$ MHz to 8 MHz. Since the detuning of the cavity resonance from the LC resonator and the qubits is of order 1 GHz, this suggests that the cavity is coupling to the other systems with a strength of about $g = \sqrt{2\chi\Delta} \approx 45$ MHz to 90 MHz.

8.7 The $|ee\rangle$ State

In order to accurately extract the direct qubit-qubit coupling strength g_{LH}, one needs to determine the qubit-qubit dispersive shift $2\chi_{qq}$. To observe this, the two-tone measurement setup discussed in section 7.6.3 was used with the pulse sequence shown in Fig. 7.17. A flux-map of the transition spectrum of one transmon was taken and then another map was taken with a CW signal set to the g-to-e transition of the other transmon. For this measurement, we needed to keep track of the variation of the flux-dependence of the transition frequency of the transmon that the CW signal was applied to. This was accomplished using the spectrum in Fig. 8.8(a).

Figure 8.10 shows the resulting two-tone spectroscopic data on transmon Q_H. In particular, Fig. 8.10(a) shows the flux-dependence of the g-to-e transition of transmon Q_H when transmon Q_L was in its ground state. In this gray-scale image, the gray represents the voltage enhancement $\delta V/V_0$ (see Eq. (8.1)). For comparison, Fig. 8.10(b) shows the

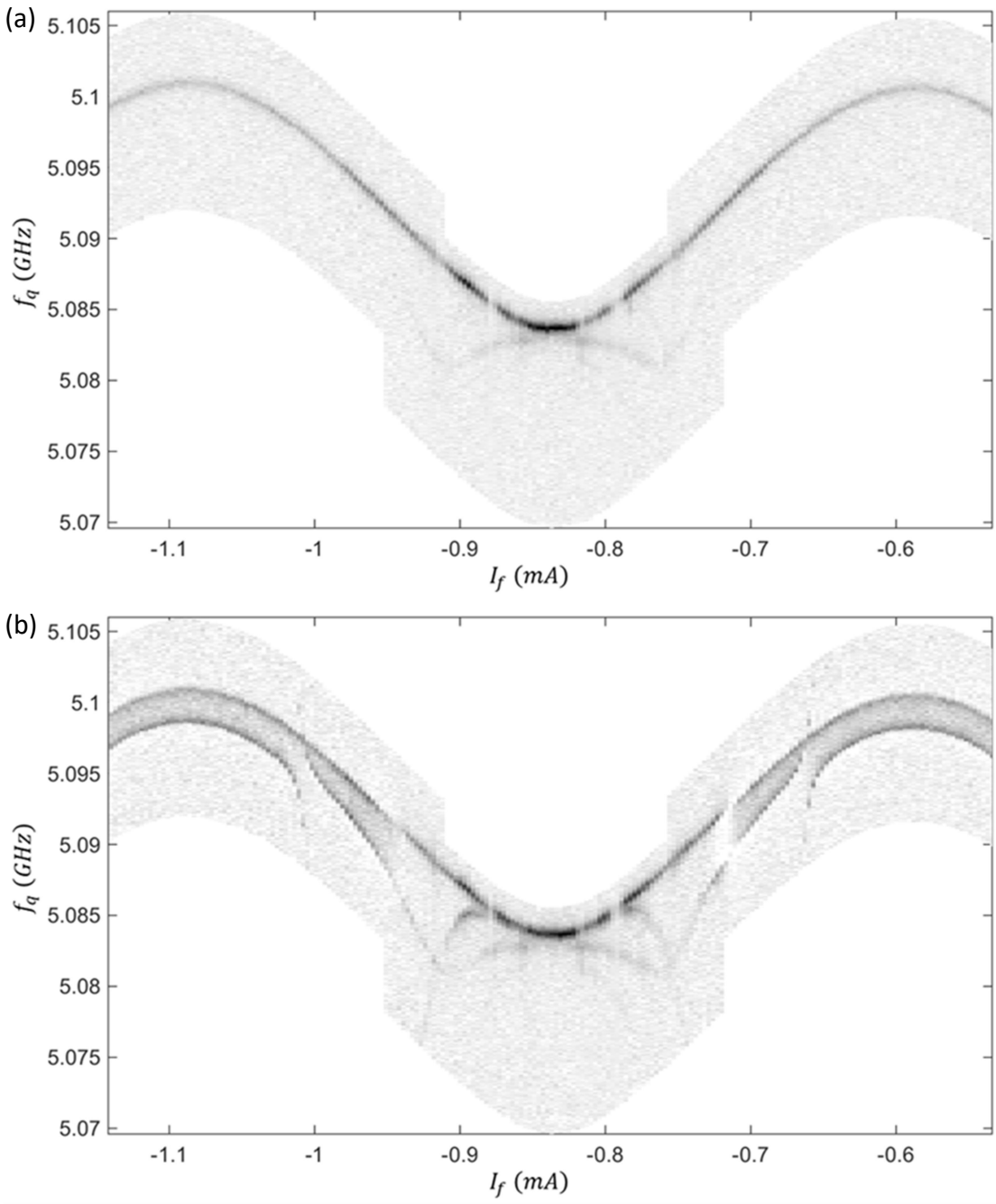

Fig. 8.10: (a) Gray scale map of pulsed spectroscopic measurement of $\delta V/V_0$ enhancement vs. bias current I_f for device TRES_092917 on Q_H when Q_L is initially in its ground state. (b) Pulsed spectroscopic data on Q_H when Q_L is saturated into a mixed state or classical superposition of its ground and excited states.

spectrum of Q_H when Q_L was driven into a superposition of its ground and first excited states by the CW signal. Since in this case there was ≈50% population in the ground state of Q_L, the $|gg\rangle$ to $|ge\rangle$ transition from Fig. 8.10(a) is still visible. However, there is now a new transition due to the $|eg\rangle$ to $|ee\rangle$ transition. The difference between this new transition frequency and the original, unperturbed transition frequency is the qubit-qubit dispersive shift $2\chi_{qq} = 2\chi_{LH} = 2\chi_{HL}$. Since $2\chi_{qq}$ depends on flux, Fig. 8.10(b) is a clear indication that the coupling between the two qubits was tunable.

8.8 Extracting TRES_092917 Device Parameters

As I discuss in Chapter 5, I used the following model Hamiltonian to describe the system:

$$\begin{aligned}\mathcal{H} = {} & \hbar\omega_L\left(n_L + \frac{1}{2}\right) - \frac{E_{CL}}{2}n_L(n_L+1) + \hbar\omega_H\left(n_H + \frac{1}{2}\right) - \frac{E_{CH}}{2}n_H(n_H+1) \\ & + \hbar\omega_r n_r + \hbar\omega_c n_c + \hbar g_{Lr}\left(b_L^\dagger a_r + b_L a_r^\dagger\right) \\ & + \hbar g_{Hr}\left(b_H^\dagger a_r + b_H a_r^\dagger\right) + \hbar g_{Lc}\left(b_L^\dagger a_c + b_L a_c^\dagger\right) \\ & + \hbar g_{Hc}\left(b_H^\dagger a_c + b_H a_c^\dagger\right) + \hbar g_{LH}\left(b_L^\dagger b_H + b_L b_H^\dagger\right) \\ & + \hbar g_{rc}\left(a_r^\dagger a_c + a_r a_c^\dagger\right).\end{aligned} \tag{8.3}$$

Table 8.1 summarizes all of the parameters in the model. For simulations, each sub-system retained 4 levels. There are 12 parameters visible in the Hamiltonian in Eq. (8.3). However, the LC resonator's frequency $\omega_r/2\pi$ is a function of the flux and there are 11 circuit parameters that must be determined to fit the frequency dependence of the tunable resonator. The model used to fit the resonator is described in detail in chapter 3, and the fit parameters from this model are also included in Table 8.1. This results in 22 total fit

Table 8.1: All the fit parameters used in the model Hamiltonian Eq. (8.3).

Fit Parameter	Description	Fit Parameter	Description
$\omega_L/2\pi$	Qubit q_L g-to-e transition frequency.	L_r	Geometric inductance of tunable resonator.
$\omega_H/2\pi$	Qubit q_H g-to-e transition frequency.	M_1	Effective mutual inductance between flux coil and loop 1.
$\omega_c/2\pi$	Cavity TE_{101} mode frequency.	M_2	Effective mutual inductance between flux coil and loop 2.
$g_{LH}/2\pi$	Qubit-qubit coupling strength.	I_{01}	Critical current of junction in loop 1.
$g_{Lr}/2\pi$	Qubit Q_L-resonator coupling strength.	I_{02}	Critical current of junction in loop 2.
$g_{Lc}/2\pi$	Qubit Q_L-cavity coupling strength.	L_1	Geometric inductance of arm of loop 1 without junction.
$g_{Hr}/2\pi$	Qubit Q_H-resonator coupling strength.	L_2	Geometric inductance of arm of loop 2 without junction.
$g_{Hc}/2\pi$	Qubit Q_H-cavity coupling strength.	L_{x1}	Geometric inductance of arm of loop 1 with junction.
$g_{rc}/2\pi$	Cavity-resonator coupling strength.	L_{x2}	Geometric inductance of arm of loop 2 with junction.
E_{CL}	Qubit Q_L charging energy.	Φ_{e1}	External flux in loop 1.
E_{CH}	Qubit Q_H charging energy.	Φ_{e2}	External flux in loop 2.

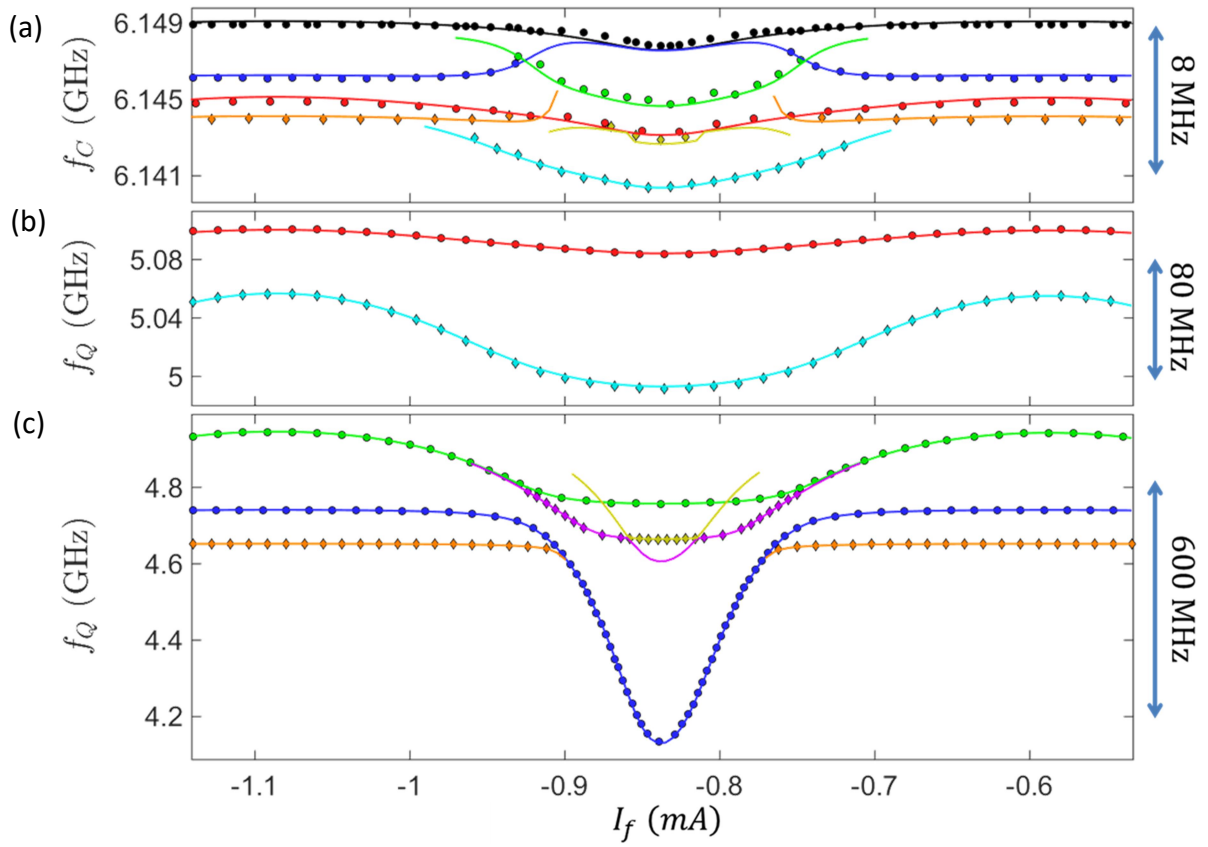

Fig. 8.11: (a) Curves are fits of the model Eq. (8.3) to spectroscopic data (points) for cavity transitions, (b) qubit Q_H transitions, and (c) qubit Q_L and LC resonator transitions.

parameters in the system model. I also note that the LC resonator capacitance was fixed at $C_r = C_1/2 = C_2/2 = 117$ fF via calculation (see Chapter 6).

Altogether, 16 different transition branches were fit simultaneously to the model Hamiltonian using a least squares method in Matlab. This includes all the transitions I discussed in sections 8.5, 8.6, and 8.7. In Fig. 8.11, transitions from the fit are the curves and they are superimposed on the measured transition frequencies (points). Examining the figure, one sees that the fit shows very good agreement with the data. In Figs 8.11(b)

and (c), I show the qubit and resonator transitions; the fits are within 2 MHz of the data. In Fig. 8.11(a), I show the cavity dispersive shifts; the fit curves here differ by no more than 0.1 MHz from the data.

In Fig. 8.12(a), I show the fit on the $|gg\rangle$ to $|ge\rangle$ transition (blue) and the $|eg\rangle$ to $|ee\rangle$ transition (red). The blue curve is the fit to the blue data points, and the red curve is the fit to on the red data points. Figure 8.12(b) shows the resulting qubit-qubit dispersive shift $2\chi_{qq}$. The green squares are $2\chi_{LH} = (E_{ge} - E_{gg})/h - (E_{ee} - E_{eg})h$, and the purple circles are $2\chi_{HL} = (E_{eg} - E_{gg})/h - (E_{ee} - E_{ge})/h$, and the black line is $2\chi_{qq}$ from the fit transitions. In the center of this window, when the LC resonator is tuned to its lowest point, the qubit-qubit dispersive shift $2\chi_{qq}$ is at a local minimum of $\chi_{qq} = 0.1$ MHz. However, as the resonator is tuned away from that point, this dispersive shift increases to $\chi_{LH} \geq 6$ MHz near an avoided level crossing. Hence, this device exhibits a tunable coupling between the two qubits that can be modulated from an "off" position ($I_f \approx$ -0.83 mA) when the resonator is at its lowest point, to an "on" position ($I_f \approx$ -0.91 mA). Achieving a variable coupling and using it to construct two-qubit gates was the main focus of my research.

In Table 8.2 I list the best fit values of the system parameters and the design values. The parameters in the table with a green background were not fit parameters but were derived from fit parameters. Most of the fit parameters are reasonably close to the design values (within $\pm$ 30%). However, there are a few that are quite a bit off. First and foremost, the parameters that are the most different are L_{1x} and L_{2x}. These parameters have quite a strong effect on the tuning range; so, this difference appears to be real. One

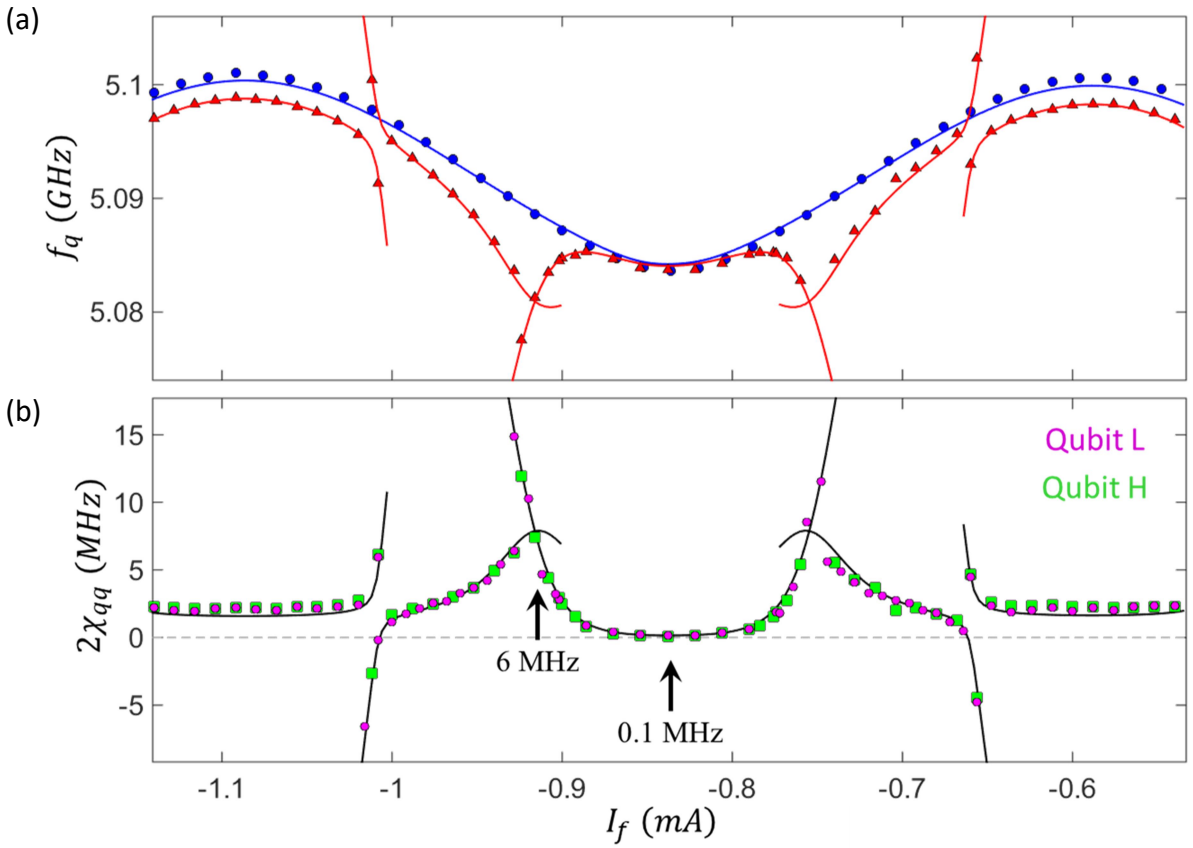

Fig. 8.12: (a) Data and fit to model for the qubit-qubit dispersive shift of qubit Q_H. The blue points are when Q_L is in its ground state and the red points are from when Q_L is in its excited state. The lines are fits on these data points to the model. (b) Plot of qubit-qubit shift $2\chi_{qq}$ as a function of the flux bias current I_f. The green squares are from data on Q_H, the purple circles are from data on Q_L, and the black line is the predicted value from the simultaneous fit to the model Hamiltonian.

Table 8.2: Fit and design values of all the parameters used in the model. The β_π parameters shaded in green were not fit parameters, but were derived from the values of the critical currents and loop inductances.

Fit Parameter	Design Value	Fit Value	% Diff.	Fit Parameter	Design Value	Fit Value	% Diff.
$\omega_L/2\pi$	4.75 GHz	4.766 GHz	0.3%	L_r	3.5 nH	3.35 nH	-4.3%
$\omega_H/2\pi$	5 GHz	5.096 GHz	1.9%	M_1	5 pH	4.42 nH	-11.7%
$\omega_c/2\pi$	6.13 GHz	6.119 GHz	-0.2%	M_2	5 pH	3.84 nH	-23.2%
$g_{LH}/2\pi$	–	11.8 MHz	–	I_{01}	289 nA	174 nA	-39.8%
$g_{Lr}/2\pi$	60 MHz	55.9 MHz	-6.8%	I_{02}	289 nA	173 nA	-39.8%
$g_{Lc}/2\pi$	150 MHz	128.2 MHz	-14.5%	L_1	825 pH	822 pH	-0.4%
$g_{Hr}/2\pi$	60 MHz	59.1 MHz	-1.5%	L_2	825 pH	831 pH	0.7%
$g_{Hc}/2\pi$	150 MHz	123.5 MHz	-17.7%	L_{x1}	86 pH	276 pH	221%
$g_{rc}/2\pi$	100 MHz	54.9 MHz	-45.1%	L_{x2}	86 pH	273 pH	217%
E_{CL}/h	200 MHz	191.9 MHz	-4.1%	Φ_{e1}	–	0.312 Φ_0	–
E_{CH}/h	200 MHz	188.3 MHz	-5.9%	Φ_{e2}	–	0.032 Φ_0	–
E_{JL}/h	16.9 GHz	15.8 GHz	-6.5%	$\beta_{\pi1}$	0.8	0.581	-27.4%
E_{JH}/h	17.4 GHz	17.2 GHz	-1.1%	$\beta_{\pi2}$	0.8	0.580	-27.5%
I_{0L}	32 nA	31.8 nA	-0.6%				
I_{0H}	35 nA	34.6 nA	-1.1%				
E_{JL}/E_{CL}	84.5	82.3	-2.6%				
E_{JH}/E_{CH}	87	91.3	4.9%				

possibility is that FastHenry [2] did not accurately simulating the geometric inductance of these sections of the loop. To find the inductance for this small (≈ 100 μm long) section of line, I naturally only included this small section. However, the effective inductance also depends on the mutual inductance between this section and the rest of the loop. This should have produced a relatively small correction to the estimate, and certainly should not have yielded an inductance that was about three times larger. Another possibility is that there is another Josephson junction in this section of the loop due to the double-angle evaporation; this would add an effective inductance to this section.

The other parameters that strongly affected the tuning range were the critical currents I_{01} and I_{02}. Although the critical currents I_{01} and I_{02} were the actual fit parameters in the model, they set the β_π parameters. As I discussed in Chapter 6, I was aiming for β_π= 0.8 for each loop, which would have given approximately 750 MHz of tuning from each loop individually. Instead I ended up with $\beta_{\pi 1}$= 0.581 and $\beta_{\pi 2}$= 0.580. This difference, combined with the difference in the loop inductance, produced loops that individually only tuned approximately 400 MHz. One reason this device still worked quite well is because when both loops tuned together the overall range added to give a tuning range of about 800 MHz, which was reasonably close to the 1 GHz design range.

8.9 Anomalous Two-Level System

Dr. Sudeep Dutta acquired a wide range of spectroscopic data on the TRES_092917 device. We only found three transitions in the spectroscopy that were not apparently explainable by the model Hamiltonian (Eq. (8.3)). In Fig. 8.13(a), I show pulsed spectroscopic data on transmon Q_L that was taken at low power and fairly high

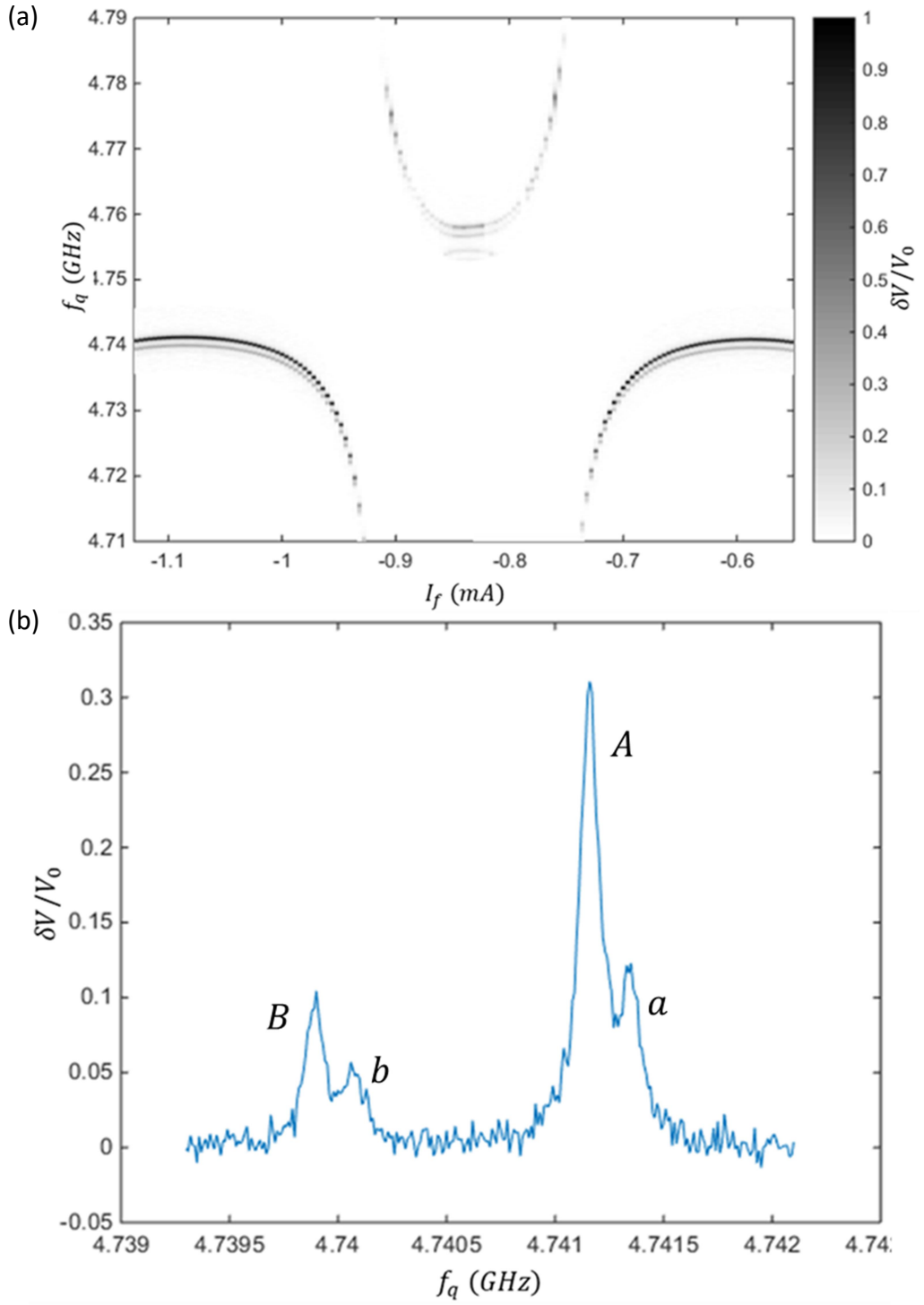

Fig. 8.13: (a) Pulsed spectroscopy of qubit Q_L showing small peak splitting. (b) Pulsed spectroscopy of Q_L at I_f = -0.6 mA and P_q = -58 dBm with the dispersively shifted peaks labelled.

resolution. In this plot, the x-axis is the current into the DC bias lines, the y-axis is the frequency of the qubit manipulation pulse, and the color represents the voltage enhancement $\delta V/V_0$. This data was taken using the high-power pulsed readout setup discussed in section 7.6 with a fairly low qubit drive power. Upon close examination, one sees a small peak just below the manin $|gg\rangle$ to $|eg\rangle$ transition peak. In Fig. 8.13(b) I show a line cut of the spectroscopic data at I_f = -0.6 mA and P_q = -58 dBm. Examining this figure, one sees that there are actually four closely spaced peaks with the two largest peaks separated by about 1 MHz.

The highest peak in Fig. 8.13(b) is the main g-to-e transition peak for transmon Q_L. Given that the transmon Q_L is coupled to two harmonic oscillators and another qubit, it is not surprising that there could be dispersively shifted peaks created when one of the other systems is excited. However, the model Hamiltonian does not produce a dispersive peak in any of these locations. A potential culprit for this dispersively shifted peak is some materials-based two-level system, such as a charge dipole, coupled only to transmon Q_L [6]. Typically, these atomic-configuration TLSs are observed via the presence of an avoided level crossing and would only produce an observable dispersively shifted qubit transition when the qubit is close to resonance with the TLS (*i.e.* when the TLS-qubit coupling g is not too small compared to the detuning Δ). Since the dispersive shift $2\chi \approx$ 1.3 MHz is relatively constant over the ≈20 MHz frequency range that Q_L occupies (see Fig. 8.13(a)), this means that the detuning Δ between Q_L and the TLS would have to be large relative to 20 MHz. However, for a TLS with Δ∼ 4 GHz to produce such a large dispersive shift, the coupling strength g would need to of order 60 MHz. While such large TLS-qubit couplings have been observed in some phase qubits

[7], this is much larger than typically seen in transmons, suggesting that this is not due to a TLS that is coupled in the conventional way.

Another curious feature of this Q_L spectrum is the two smaller peaks that appear higher in frequency than the larger peaks they are close to (see Fig. 8.13(b)). These extra peaks appear to be from another TLS that also couples to transmon Q_L. To avoid confusion, it helps to label all the peaks (see Fig. 8.13(b)). The tallest peak is in the rightmost group of two, and I label it peak A. About 0.1 MHz to the right of peak A is the small peak I have labelled a. Similarly, about 1 MHz to the left is peak B and about 0.1 MHz to the right of B is the remaining small peak b.

In Fig. 8.14, I show a power series for these transitions when the flux bias current was set to I_f = -0.6 mA. The black curves are fits that I discuss below. Figure 8.14(a) shows low-power data, Fig. 8.14(b) shows "medium" power, and Fig. 8.14(c) shows the response at high powers. For the high and medium powers, there appears to be just two transitions – the main g-to-e transition (peak A) and the 1 MHz dispersively shifted peak (peak B). However, at low powers it is clear that the small peaks a and b appear to the right of these main transitions.

As I discussed above, peak B could, in principle, arise from a charge dipole TLS in the dielectric near transmon Q_L or in its junction. Exciting the TLS would cause the transmon resonance to be dispersively shifted lower. The ratio of the peak heights is set by the probability of finding the TLS in its excited state. Due to peak A being the highest of all transitions observed, the state producing peak A is most probable and therefore of lower energy than the others, assuming the system is in thermal equilibrium.

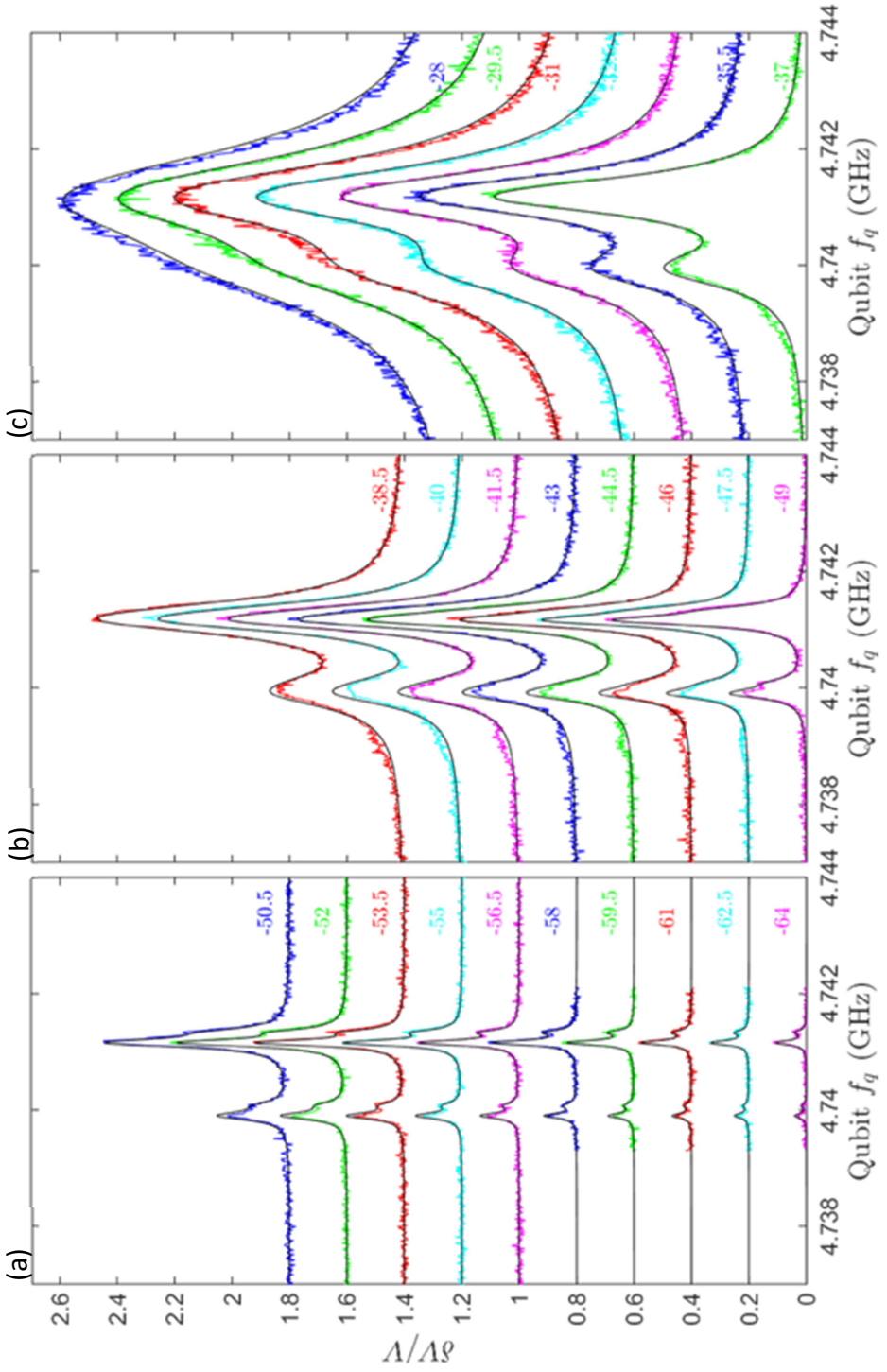

Fig. 8.14: (a) Pulsed spectroscopic power series data for qubit Q_L at low powers, (b) at medium powers, and (c) at high powers. The black curves are from a simultaneous fit to a sum of four Lorentzian peaks.

On the other hand, peak a occurs at a higher frequency than peak A. With a Jaynes-Cummings style coupling, which is how a charge dipole would couple to the electric field from a transmon, the dispersive shift (peak a) corresponding to the TLS being excited must be lower in frequency than peak A (when the TLS is not excited) [8]. Since a is shifted up in frequency, this cannot be a standard Jaynes-Cummings coupled cavity TLS system. Two possibilities are a capacitance fluctuator, which would affect the charging energy $E_C = e^2/2C$, or a critical current fluctuation, which would affect the Josephson energy $E_J = \Phi_0 I_0/2\pi$. Since the transition frequency is set by these two parameters, two-level fluctuations in them could produce either higher or lower transition frequencies, including the positive shift observed in the qubit Q_L spectrum. Pinpointing which of these two options (or neither) is occurring requires additional spectroscopy. In particular, fluctuations in E_C will cause differently spaced higher level transitions than fluctuations in E_J will produce.

Table 8.3: Summary of fit parameters used to fit Lorentzian peaks to the data in Fig. 8.14.

Fit Parameter	Value
Height ratio: A to a (P_{e1}/P_{g1})	0.33
Height ratio: A to B (P_{e2}/P_{g2})	0.39
Frequency Separation: A to a ($2\chi_{TLS1}/2\pi$)	0.172 MHz
Frequency Separation: A to B ($2\chi_{TLS2}/2\pi$)	1.256 MHz

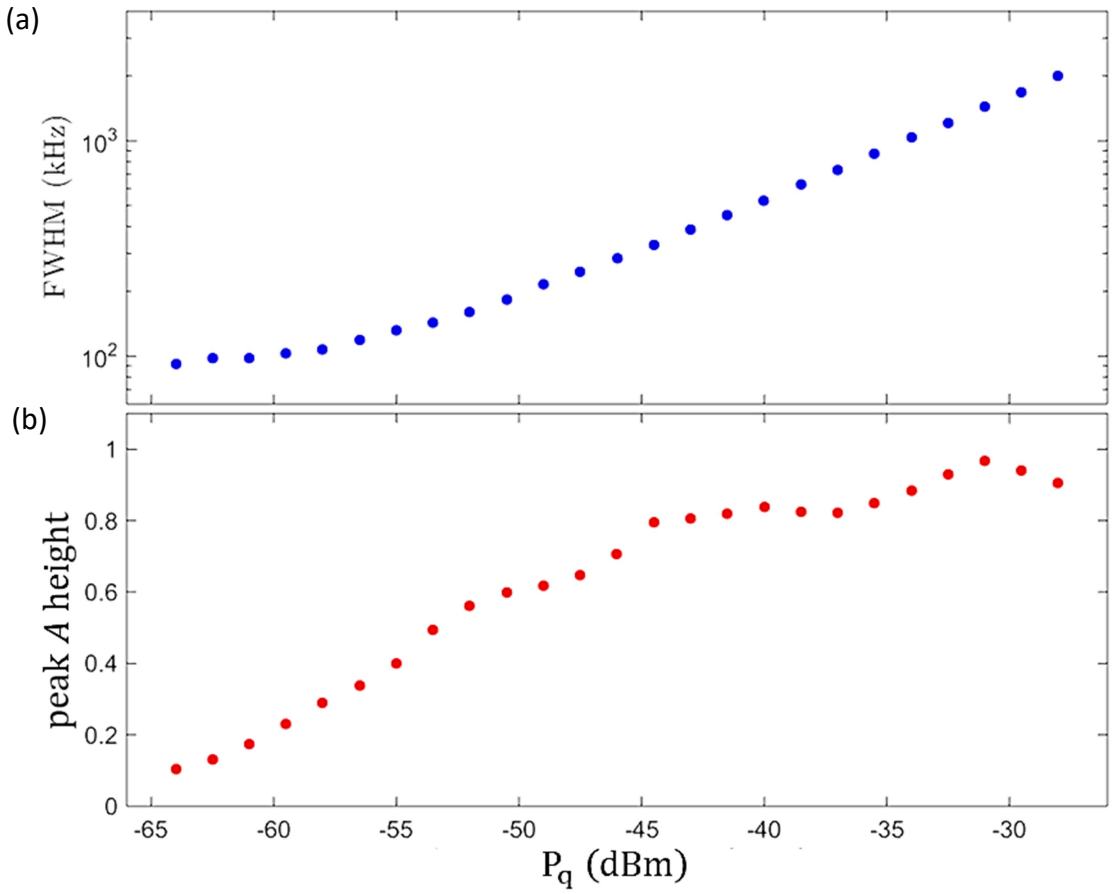

Fig. 8.15: (a) Fit value of peak A width as a function of applied power. (b) Fit value of peak A height as a function of applied power.

Also shown in Fig. 8.14 as black curves is a fit of four Lorentzian peaks to the spectrum. All the data shown in Fig. 8.14 was fit to a sum of four Lorentzian peaks. Some fit parameters were shared between each power and some that were unique to each power setting. The parameters shared over every power setting were the ratios of the heights of peak A to peak B, the height ratio of peak A to peak a, the spacing between peaks A and B, and the spacing between peaks A and a. The parameters that were unique to each power were the height, width, and position of peak A, the largest peak. This same

width was used for the other three Lorentzian peaks at each power. The height ratio and separation between peak B to peak b was set to be equal to the height ratio and separation of A to a. Table 8.3 summarizes the resulting best fit parameters shared over all the powers, and Fig. 8.15 shows a plot of the width and height of peak A as a function of microwave power. The width shows a steady rise with power, as expected for power broadening, and the height shows saturation, both consistent with the behavior of a TLS.

8.10 Conclusions

In this chapter I showed results from spectroscopic measurements on device TRES_092917, which had two qubits coupled to a tunable LC resonator and was enclosed in a 3D microwave cavity. Measurements included cavity power maps, which showed clear dressed and bare peaks. Pulsed high-power readout spectroscopic measurements on the qubits and tunable resonator showed flux-dependent features due to the LC resonator as well as transitions due to the qubits and cavity. The system parameters were extracted by fitting a 22-parameter model of system transitions to the observed spectroscopic transitions and the results compared to the design values discussed in Chapters 5 and 6. Most importantly, this device exhibited a tunable qubit-qubit dispersive shift $2\chi_{qq}$ that could be tuned from 0.1 MHz to more than 6 MHz. Finally, I showed that one of the qubits was coupled to two TLS fluctuators, one of which was either a capacitance or critical current fluctuator, rather than a conventional charge dipole coupled TLS.

Chapter 9

Time Resolved Measurements on Variable Qubit-Qubit Coupling Device

In this chapter I discuss time-resolved measurements on device TRES_092917. This device had two transmons which were each capacitively coupled to a tunable LC resonator (see Chapters 5 and 6) and the chip was mounted in a single 3D Al microwave cavity. The resonator was tuned by applying magnetic flux to two RF SQUID tuning loops (see Chapter 3).

I begin by providing details on how the time-resolved data was acquired. I then discuss Rabi oscillation measurements on the two transmons at various flux bias points of the tunable resonator. Following this, I discuss measurements of the relaxation time T_1 at various LC resonator tuning points. The following sections discuss measurements of spin-echo, Ramsey fringes, and single-qubit tomographic measurements. I conclude by discussing the initial characterization of a CNOT gate in this coupled system as well as our use of a joint-state readout scheme.

9.1 Measurement Details

As with the data presented in Chapter 8, the data in this chapter is from device TRES_092917. The data was primarily measured and analyzed by Dr. Sudeep Dutta over the course of about seven months, from December 2017 to June 2018. The device was initially cooled down in our Oxford Triton 200 dilution refrigerator in October of 2017. However, it was subsequently warmed to room temperature twice to change

cavities and to modify the microwave line to remove heating. For the first warm-up, I changed cavities from SI-2b to SI-4 (see Chapter 2) in order to move the chip to the center of the cavity and reduce the distance the flux tuning coil extended into the cavity (see Chapters 3 and 6). For the second warm-up, I removed a K&L 10.5 GHz low-pass filter [1] from the output microwave line/input DC flux bias line to eliminate heating from the flux bias current (see Fig. 7.9). The device was measured in the sub-basement of the Toll Physics Building in Room SB0331.

For the qubit characterization measurements I present in this chapter the high-power readout scheme discussed in section 7.6 was used. However, for the state tomography measurements, spin-echo decay measurements, Ramsey spectroscopy, and CNOT gate characterization the qubit microwave source was replaced with a Tektronix AWG70001 arbitrary waveform generator (AWG) [2] in order to apply multiple qubit pulses and have control over the phase of the signal.

As discussed in Chapter 7, the typical pulse sequence (see Fig. 7.14) involved an initial cavity pulse that was used to calibrate the background transmission of the system. This was followed by a waiting time τ_w, after which any qubit manipulation pulses were done. The sequence ended with an application of another cavity pulse to measure the enhancement resulting from the qubit manipulations. Each output pulse from the cavity was passed to an I-Q mixer where the magnitude of the output voltage from the I and Q ports was measured. I call the measured "calibration" voltage V_0 and the measured "measurement" voltage V_f. For the spectroscopic data in Chapter 8 and some spectroscopic data in this chapter, the quantity $\delta V/V_0$ is plotted where:

$$\frac{\delta V}{V_0} = \frac{\left(V_f - V_0\right)}{V_0}. \tag{9.1}$$

However, for many of the time-resolved measurements described in this chapter, an additional step was used to reduce relatively slow fluctuations in the readout. In addition to the V_0 and V_f measurements, we also obtained the output of the system when one or more of the qubits were pumped to its excited state. This resulted in voltages V_0' and V_f' (*i.e.* the response of the system from a π-pulse). This allowed scaling of the data to the maximum contrast possible. I call this quantity $\delta V/V_\pi$, which is given by

$$\frac{\delta V}{V_\pi} = \frac{\left(V_f - V_0\right)}{V_0} \cdot \frac{V_0'}{\left(V_f' - V_0'\right)}, \tag{9.2}$$

where again the primed voltages are the measured voltages from the π-pulse pulse calibration. Since the drift we observed happened over a larger time scale than a single measurement, this quantity normalized the data to a maximum value of 1.

9.2 Rabi Oscillation Measurements

9.2.1 Pulse Sequence

Figure 9.1 shows the pulse sequence used for the Rabi oscillation measurements. Each sequence begins with an initial 1 μs characterization pulse that measured the background transmission through the cavity. We then passed the output of this pulse to an I-Q mixer and measured the magnitude of the output voltage V_0 from the I and Q ports. Then, after waiting a time $\tau_w \geq 28$ μs for the system to settle to the ground state, a

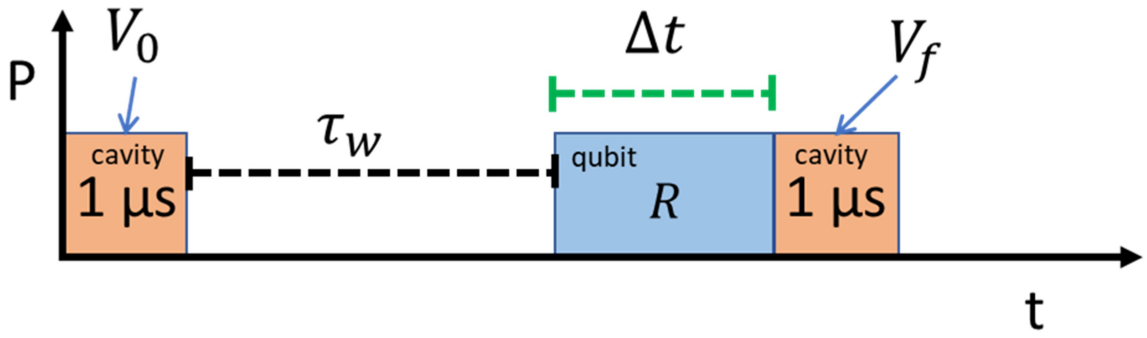

Fig. 9.1: Pulse sequence for Rabi oscillation measurement.

qubit manipulation pulse was applied. The manipulation pulse for driven Rabi oscillations has a set power P_q and frequency f_q but a variable pulse length Δt. Immediately after this manipulation pulse ends, another 1 μs cavity pulse was applied (the "measurement" pulse). The output of this pulse was passed to the I-Q mixer and we then measured the magnitude of the output voltage V_f. In order to correct for drift, we also measured the response of the system to a π-pulse at regular intervals to find the maximum possible response and then used Eq. (9.2) to find $\delta V/V_\pi$. We then plotted $\delta V/V_\pi$ vs. Δt. For each pulse length Δt this data sequence was repeated a few thousand times and the resulting measurement was averaged.

9.2.2 Measurement at LC Resonator's Maximum Tuning

As I discussed in Chapter 8, the tunable LC resonator in device TRES_092917 had a tuning range of approximately 800 MHz. Two interesting places to examine the qubits were when the resonator was tuned to its maximum frequency f_{LC}= 4.94 GHz or

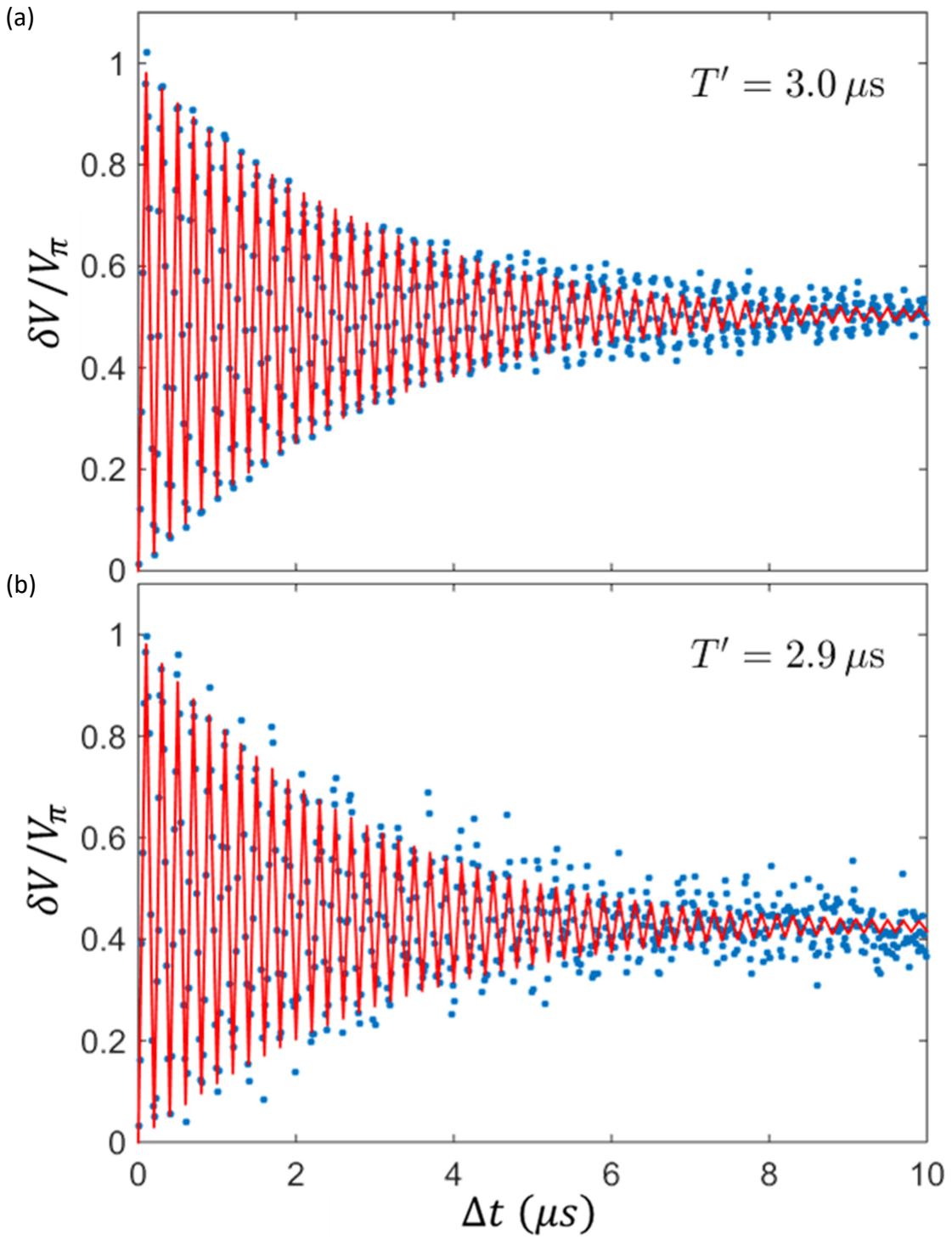

Fig. 9.2: Rabi oscillation measurements (blue points) and fit to Eq. (9.3) (red curves) for (a) qubit Q_L at $f_L = 4.741$ GHz and (b) qubit Q_H at $f_H = 5.100$ GHz when LC resonator was tuned to maximum frequency of $f_{LC} = 4.94$ GHz at I_f = -0.584 mA.

its minimum frequency f_{LC}= 4.14 GHz. In Fig. 9.2, I show measurements of Rabi oscillations in the two qubits when the resonator is tuned to its maximum frequency of f_{LC}= 4.94 GHz at bias flux current I_f = -0.589 mA. Fig. 9.2(a) shows the measurement on Q_L, which had a resonance frequency f_L = 4.741 GHz, and Fig. 9.2(b) shows the measurement on Q_H with resonance frequency f_H = 5.100 GHz. In the figure the blue points are from the measurements and the red curves are a fit to the phenomenological function

$$\frac{\delta V}{V_\pi} = A\left[1 - e^{-\Delta t/T'}\cos(\Omega \Delta t)\right], \tag{9.3}$$

where A is the amplitude of the oscillation, Ω is the Rabi frequency, which depends on the amplitude of the qubit manipulation pulse, and T' is the Rabi decay time.

With the resonator tuned to its maximum frequency, the high-power readout was not very sensitive to the state of Q_H, and the resulting Rabi curves are a little noisy. Despite the noise, the fit did not fully capture the overall amplitude of the signal. Note that some beating is obvious in the data, and this produced clear disagreements with the fit curves. However, the frequency of the oscillations and the decay time appear to be trustworthy. The extracted value of T' for Q_H was T'= 2.9 μs, and the extracted value for Q_L was T'= 3.0 μs (see Table 9.1).

9.2.3 Measurement at LC Resonator's Minimum Tuning

In Fig. 9.3 I show the Rabi oscillation measurements on the two qubits when the resonator was tuned to its minimum frequency of f_{LC}= 4.14 GHz at bias point I_f = -0.840 mA. Figure 9.3(a) shows Rabi oscillations for transmon Q_L with resonance frequency

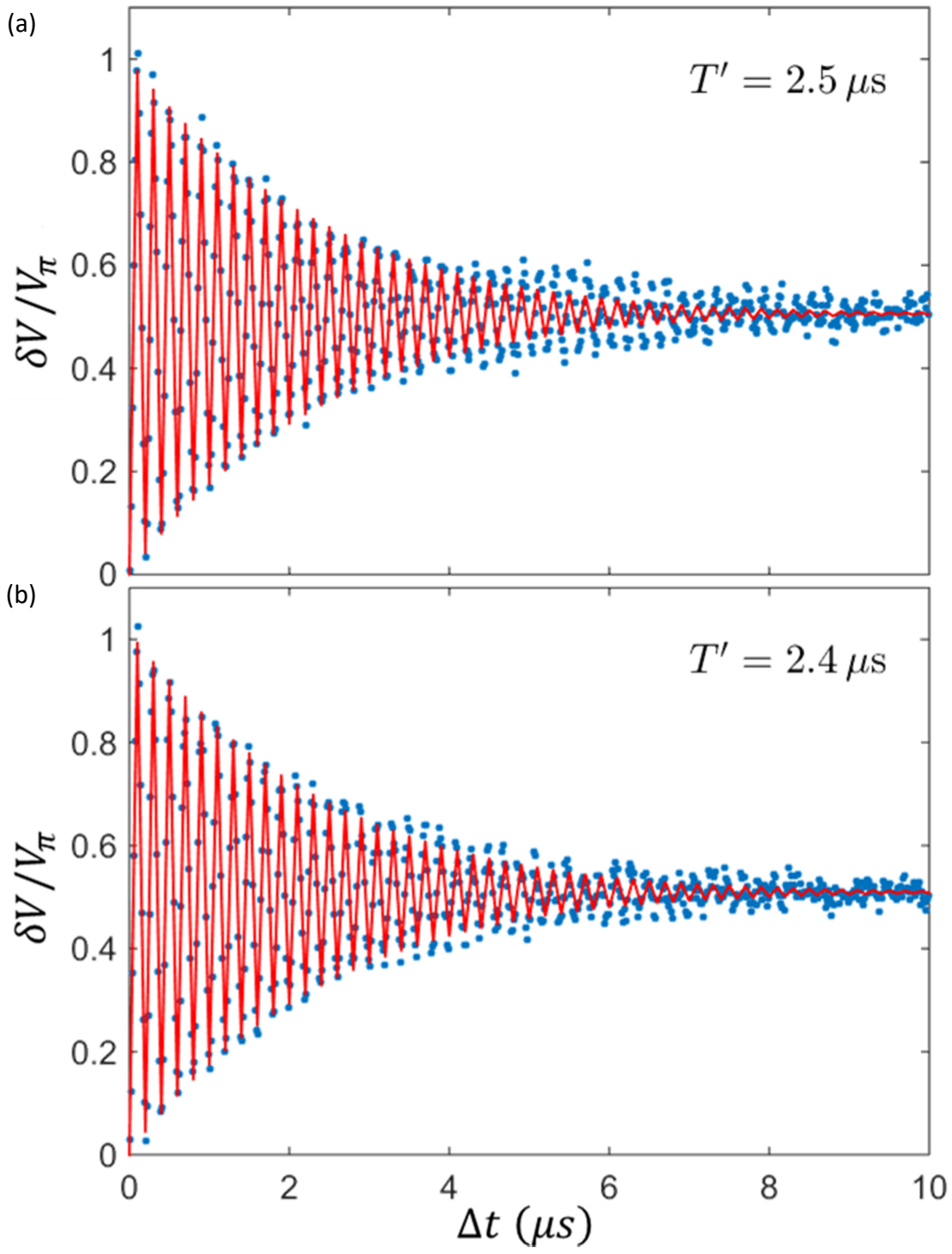

Fig. 9.3: Rabi oscillation measurements (blue points) and fit to Eq. (9.3) (red curves) on (a) qubit Q_L at $f_L = 4.758$ GHz and (b) qubit Q_H at $f_H = 5.084$ GHz when LC resonator was tuned to minimum frequency of $f_{LC} = 4.14$ GHz at I_f = -0.840 mA.

$f_L = 4.758$ GHz, and Fig. 9.3(b) shows Rabi oscillations on Q_H with resonance frequency $f_H = 5.084$ GHz. At this bias point the extracted values of the Rabi decay time were T'= 2.4 μs for Q_H and T'= 2.5 μs for Q_L (see Table 9.1).

Comparing the results at these two bias points, one sees that T' is roughly 20% shorter when the LC resonator is tuned to its minimum frequency $f_{LC} = 4.14$ GHz. This may be due to increased dephasing, dissipation, or coupling to some other mode at this drive power. Further measurements are needed to tell whether this difference is due to a difference in the relaxation time T_1 or in the dephasing time T_ϕ as they both factor into T' via the relation [3]

$$\frac{1}{T'} = \frac{3}{4T_1} + \frac{1}{2T_\phi}. \tag{9.4}$$

Note that this assumes frequency independent dephasing and loss mechanisms.

Table 9.1: Summary of Rabi decay time T' measured for both qubits at the maximum and minimum tuning point of the LC resonator.

	Resonator max: f_{LC}= 4.94 GHz, I_f = -0.584 mA	Resonator min: f_{LC}= 4.14 GHz, I_f = -0.840 mA
Qubit Q_H	T'= 2.9 μs	T'= 2.4 μs
Qubit Q_L	T'= 3.0 μs	T'= 2.5 μs

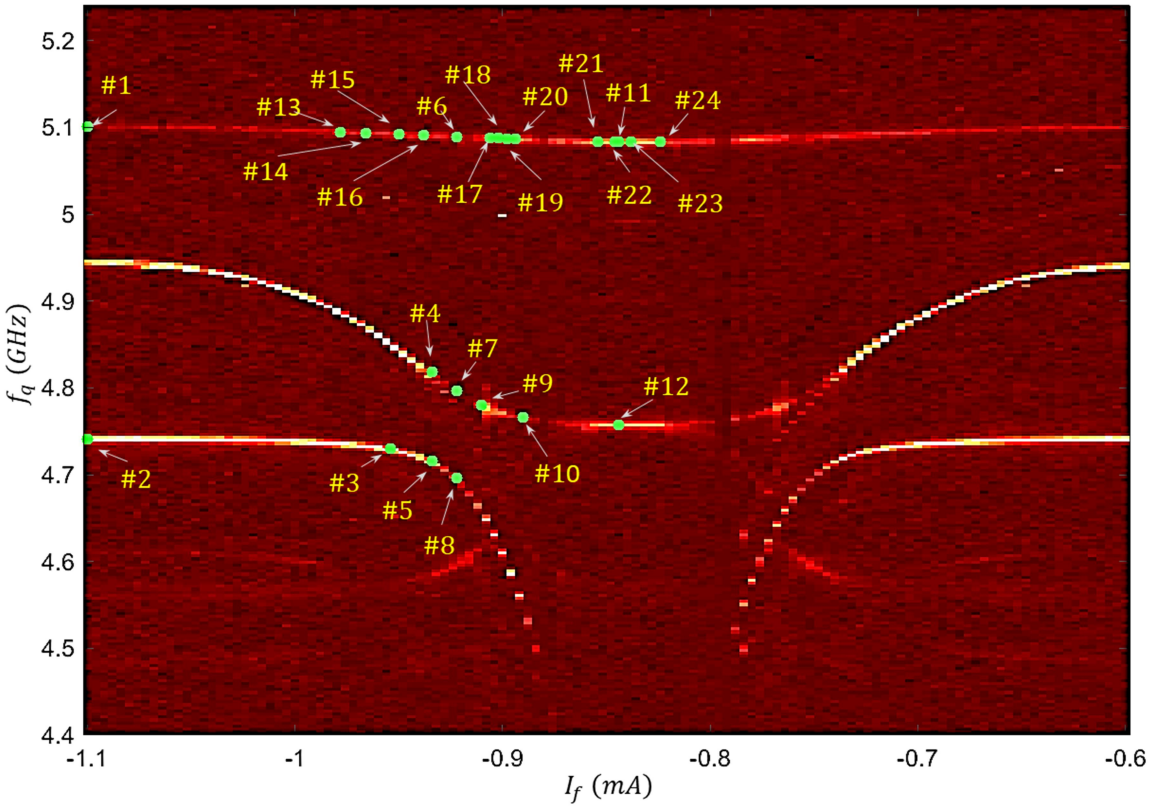

Fig. 9.4: Pulsed spectroscopy measurement on device TRES_092917 in a section near the LC resonator tuning minimum. The green circles in the figure mark bias points and frequencies at which Rabi oscillations and relaxation measurements were taken.

9.2.4 Rabi Oscillations vs. Resonator Tuning

It is interesting to see how the qubit behavior depends on the current I_f applied to the flux coils. In Fig. 9.4 I show a false-color plot of the qubit and resonator spectrum in a range of I_f = -1.1 mA to -0.6 mA. The x-axis of this plot is the bias current I_f, the y-axis is the frequency of the qubit spectroscopy pulse, and the color represents the enhancement in cavity transmission $\delta V/V_0$ due to exciting qubit states or the LC

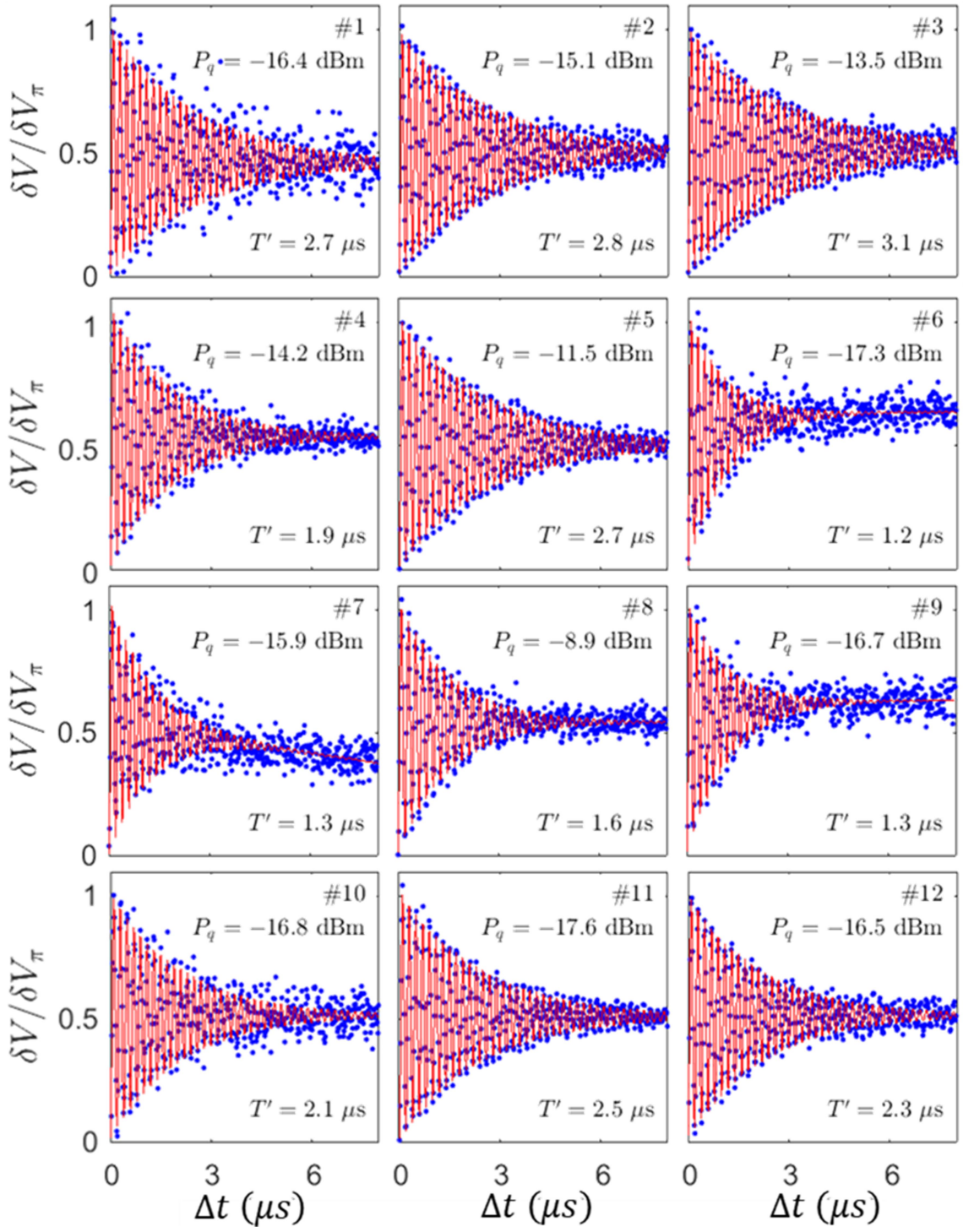

Fig. 9.5: Rabi oscillation measurements (blue points) and fits (red curves) at points 1 through 12 in Fig. 9.4. The value of P_q listed in each frame is the pulse power applied to the qubit to produce a Rabi oscillation frequency of $\Omega/2\pi = 5$ MHz.

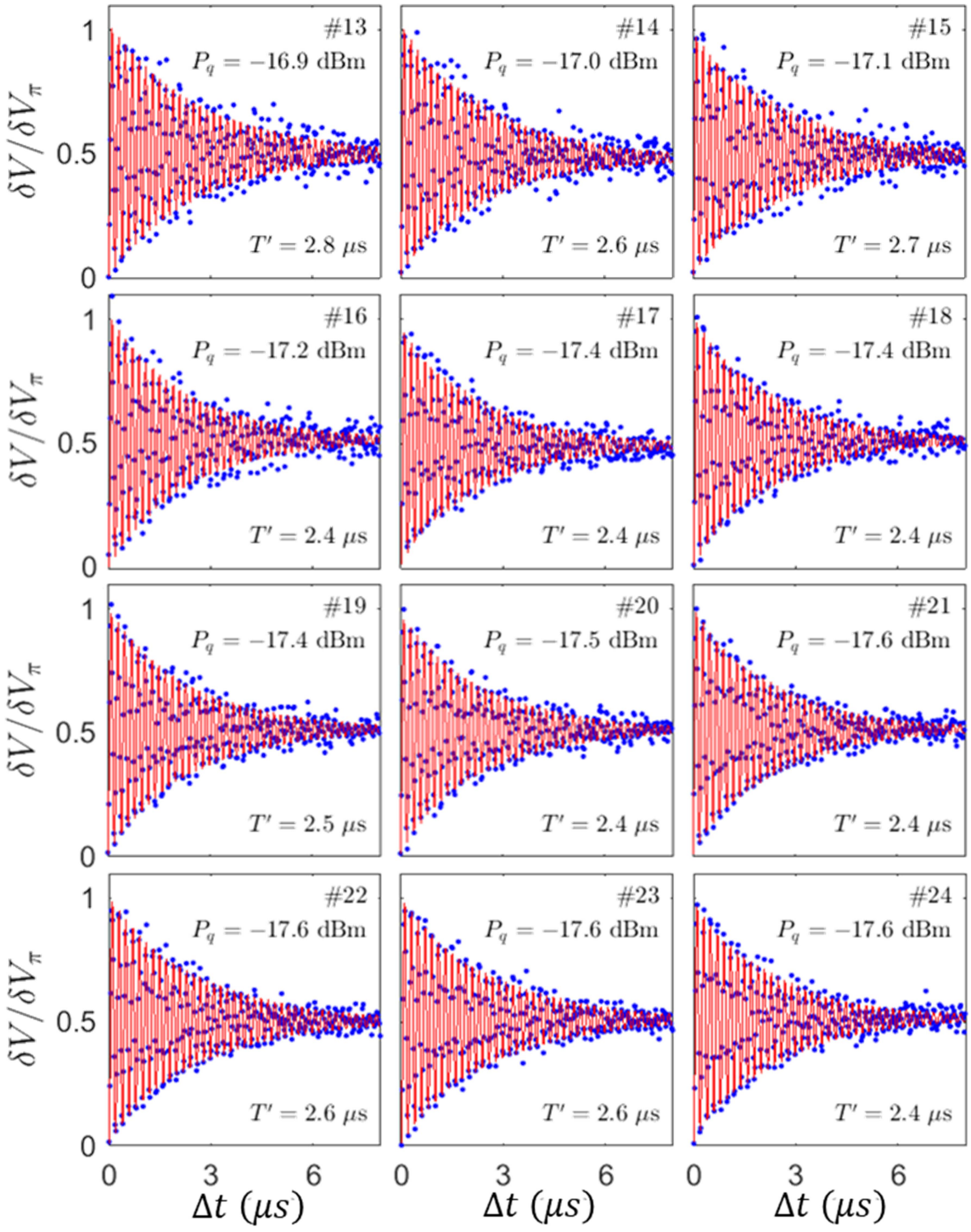

Fig. 9.6: Rabi oscillation measurements (blue points) and fits (red curves) at points 13 through 24 in Fig. 9.4. The value of P_q listed in each frame is the pulse power applied to the qubit to produce a Rabi oscillation frequency of $\Omega/2\pi = 5$ MHz.

Resonator. The 24 labelled points mark biases where both Rabi oscillations and the relaxation time T_1 were measured.

Figure 9.5 shows measurements of Rabi oscillations at points 1 through 12, and Fig. 9.6 shows Rabi oscillations at points 13 through 24. Table 9.2 summarizes the extracted T' for these measurements, which ranges from a minimum of 1.2 μs at point 6 to a maximum of 3.1 μs at point 3. Both qubits showed clear Rabi oscillations with comparable T' values. Rabi oscillations were also visible in the LC resonator. This would only be possible if the LC resonator had substantial anharmonicity from coupling to the qubits.

Table 9.2: Summary of extracted T' values at the bias points shown in Fig. 9.4.

Bias point	T' (μs)	Bias point	T' (μs)
1	2.7	13	2.8
2	2.8	14	2.6
3	3.1	15	2.7
4	1.9	16	2.4
5	2.7	17	2.4
6	1.2	18	2.4
7	1.3	19	2.5
8	1.6	20	2.4
9	1.3	21	2.4
10	2.1	22	2.6
11	2.5	23	2.6
12	2.3	24	2.4

The T' values I measured in this device were an improvement over past 3D transmons measured in this refrigerator. In 2015 R. Budoyo measured a T' value of ≈ 400 ns in device transmon05_200nm_0609A [4]. I believe a major factor in his results was that his devices suffered short dephasing times due to the lack of additional thermal shielding on the system. This produced a qubit spectrum that appeared "hot" as there were higher level qubit transitions visible in the 3D transmon's transition spectrum. Limiting the loss due to quasiparticles was one of the major motivations for adding the SiC coated Cu shield (see Chapter 7). Despite these improvements, I note that other groups typically report higher values of T'. As an example, in 2011 Paik, *et al.* achieved Rabi decay times in the range of 18 μs to 29 μs [5], where I estimate T' values from this reference using

$$\frac{1}{T'} = \frac{1}{2T_1} + \frac{1}{2T_2} \tag{9.5}$$

and their reported values of T_1 and T_2. So, while my measurements of T' in the range of 1.2 μs to 3.1 μs were an improvement over our own past results, more work needs to be done to increase this characteristic times.

9.3 Relaxation Time T_1 Measurements

9.3.1 Pulse Sequence

In Fig. 9.7, I show the pulse sequence used to measure the relaxation time T_1 of the qubits. A single measurement pulse sequence begins with an initial 1 μs long cavity pulse that measures the background transmission through the cavity. The output from

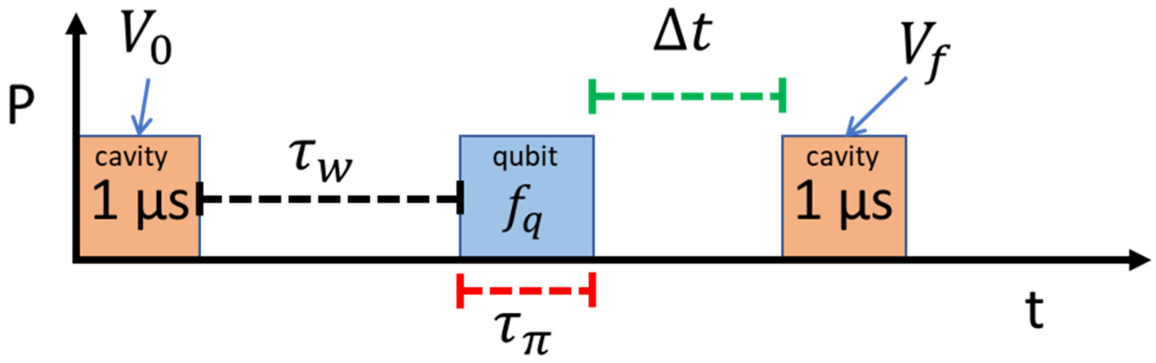

Fig. 9.7: Pulse sequence for measuring relaxation time T_1 of a qubit. In this sequence, the blue pulse is the Rabi-calibrated π-pulse that inverts the population of the qubit being measured.

this characterization pulse is passed to an I-Q mixer, from which we measured the magnitude of the output voltage V_0. After time $\tau_w \geq 20$ μs (to allow the system to settle), a qubit π-pulse is then applied with a length that was calibrated by taking a Rabi oscillation (see section 9.2). Barring background excited state population, this π-pulse puts the qubit into its excited state. After this pulse was applied, the qubit was allowed to relax for a time Δt and a measurement cavity pulse was then applied. The measurement pulse yields a voltage magnitude V_f out of the I-Q mixer. As discussed previously, these are combined to yield the quantity $\delta V/V_\pi$, which is the voltage difference scaled by the maximum response of the qubit-cavity system (see Eq. (9.2)). For each time delay Δt, this pulse sequence is repeated a few thousand times to get the average response. The resulting $\delta V/V_\pi$ is then plotted as a function of Δt.

9.3.2 Measurement at LC Resonator's Maximum Tuning

Figure 9.8 shows relaxation measurements on both transmons when the LC resonator was tuned to its maximum frequency of $f_{LC} = 4.94$ GHz at $I_f =$ -0.584 mA. The x-axis of the plots is the time delay Δt between the qubit π-pulse and the measurement pulse, and the y-axis is $\delta V/V_\pi$ (see Eq. 9.2). Figure 9.8(a) shows a relaxation measurement on Q_H, and Fig. 9.8(b) shows a relaxation measurement result on Q_L. The blue points are the measured values and the red line is a fit to an exponential decay:

$$\frac{\delta V}{V_\pi} = Ae^{-\Delta t/T_1} + C, \tag{9.6}$$

where A is the amplitude of the decay curve at $t = 0$, T_1 is the relaxation time of the qubit, and C is a background offset, which should be approximately zero. At this resonator tuning point the extracted values of T_1 for the two qubits were T_1= 2.6 μs for Q_L and T_1= 1.9 μs for Q_H.

9.3.3 Measurement at LC Resonator's Minimum Tuning

For comparison, Fig. 9.9 shows relaxation measurements on the two qubits when the resonator was tuned to its lowest point of f_{LC}= 4.14 GHz at $I_f =$ -0.840 mA. In Fig. 9.9(a) I show the relaxation measurement results for qubit Q_L, and in Fig. 9.9(b) I show relaxation measurement results for qubit Q_H. At this tuning point the extracted relaxation times are T_1= 2.4 μs for Q_L and T_1= 2.0 μs for Q_H.

In Table 9.3, I summarize the relaxation time T_1 results at the two bias points of the resonator. Transmon Q_L appears to have a relaxation time that is about 20% to 30%

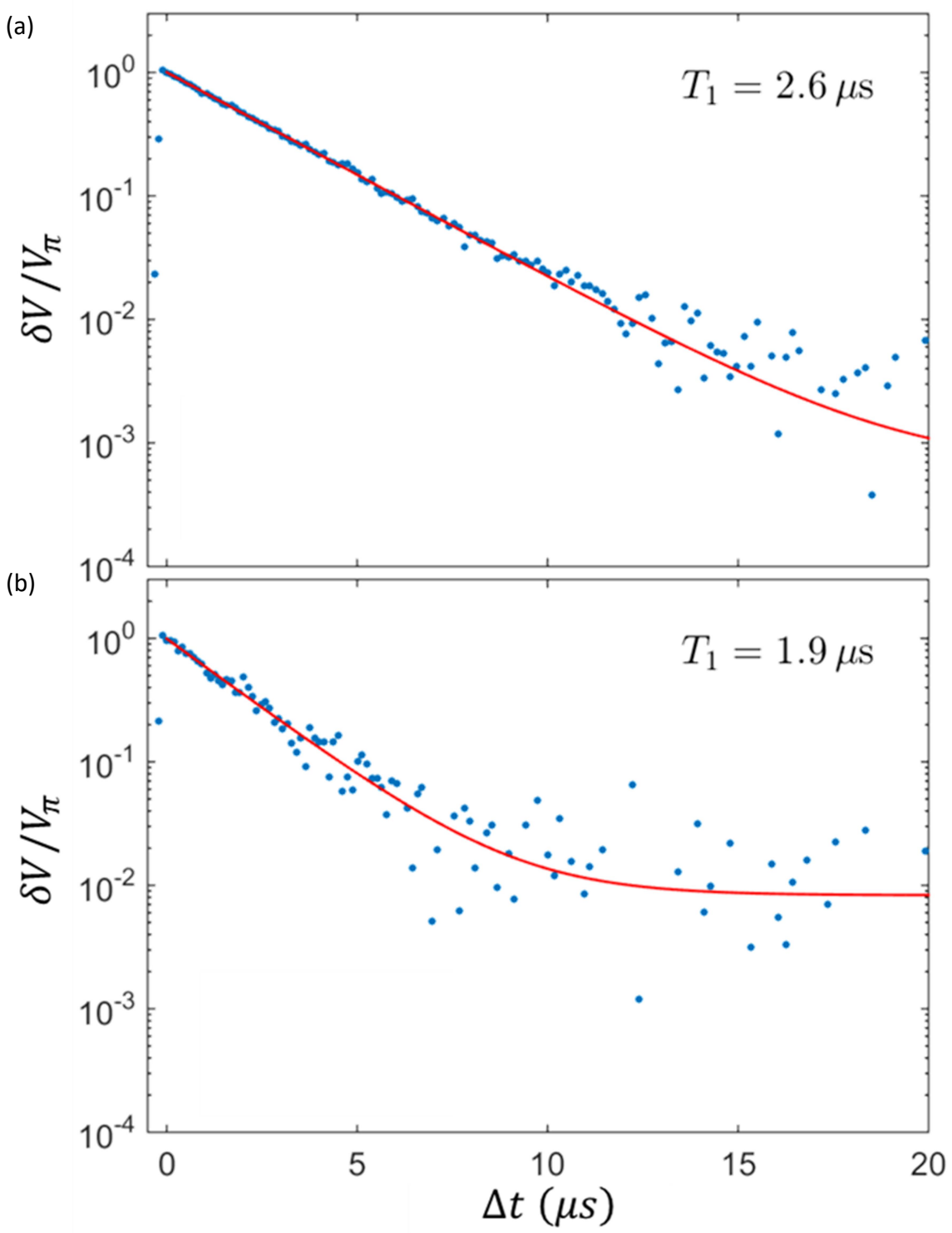

Fig. 9.8: Relaxation measurements (blue points) and fit (red curve) to Eq. (9.6) for (a) qubit Q_L at $f_L = 4.741$ GHz and (b) for qubit Q_H at $f_H = 5.100$ GHz with LC resonator tuned to max frequency $f_{LC} = 4.94$ GHz at I_f = -0.584 mA.

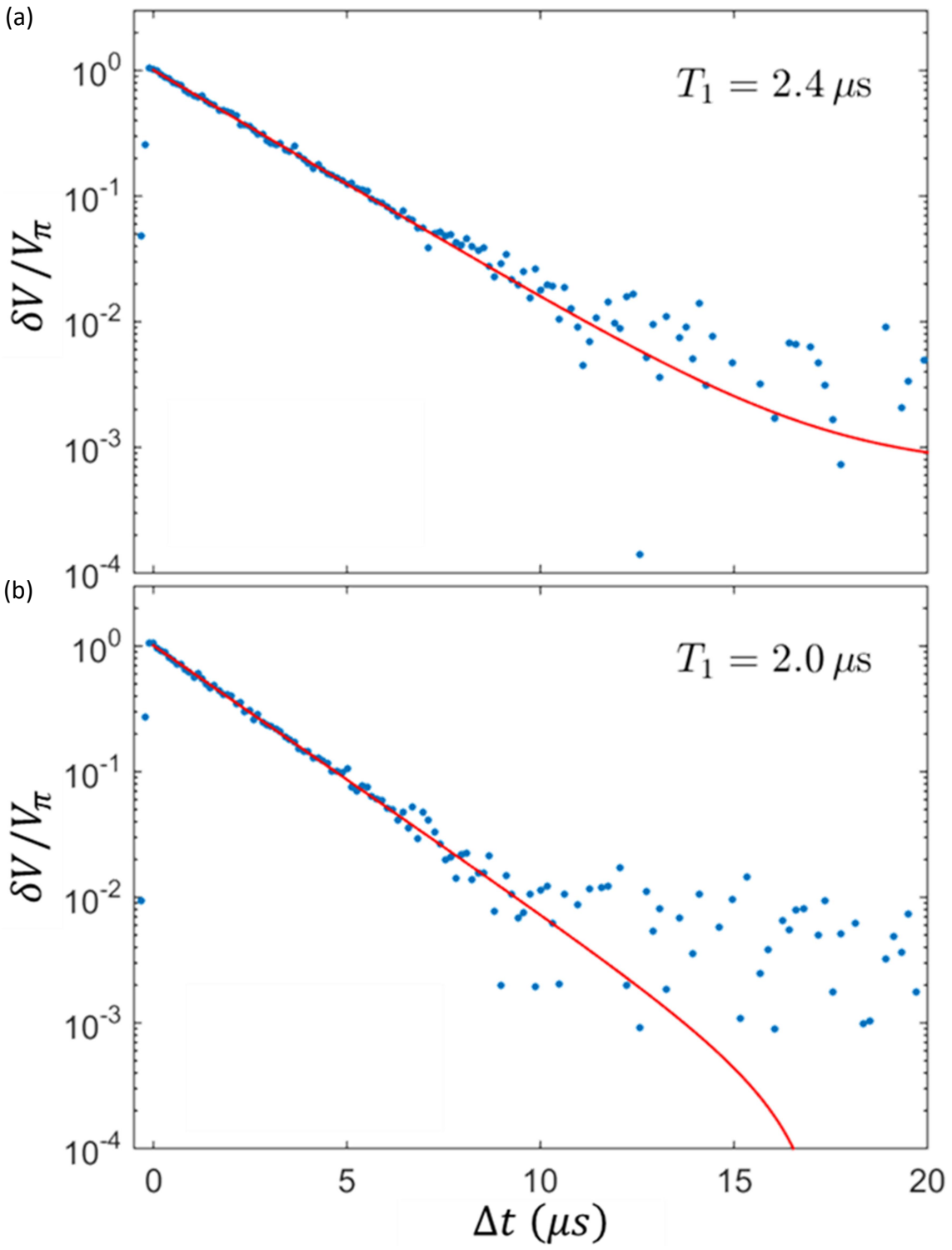

Fig. 9.9: Relaxation measurements (blue points) and fit (red curve) to Eq. (9.5) for (a) qubit Q_L at $f_L = 4.758$ GHz and (b) for qubit Q_H at $f_H = 5.084$ GHz with LC resonator tuned to min frequency $f_{LC} = 4.14$ GHz at $I_f =$ -0.840 mA.

longer than that of Q_H. Both times exceed 1 μs, but are much less than state of the art, which is greater than 100 μs. I discuss the likely cause of our relatively short T_1s in Chapters 10 and 11.

9.3.4 Relaxation Time vs. Resonator Tuning

Sudeep also acquired relaxation data at the 24 bias points shown in Fig. 9.4, *i.e.* at the same bias points where Rabi measurements were obtained. Figure 9.10 shows relaxation measurements and fits at points 1 through 12. Again, the blue points are data and the red lines are fits to Eq. (9.6). In Fig. 9.11 I show the relaxation measurements and fits at bias points 13 through 24.

In Table 9.4 I summarize all the T_1 data extracted from these fits. Note that the relaxation time ranged from 1.3 μs at point 15 to 3.0 μs at point 3. In Chapters 10 and 11 I discuss a potential explanation for why these relaxation times are so short compared to state-of-the-art values. Also included in Table 9.4 are the measured T' values from section 9.2 and the extracted T_ϕ values using Eq. (9.5). At some bias points, such as point 6

Table 9.3: Summary of T_1 results for both qubits at the maximum and minimum tuning point of the tunable resonator.

	Resonator max: f_{LC}= 4.94 GHz, I_f = -0.584 mA	Resonator min: f_{LC}= 4.14 GHz, I_f = -0.840 mA
Qubit q_H	T_1= 1.9 μs	T_1= 2.0 μs
Qubit q_L	T_1= 2.6 μs	T_1= 2.4 μs

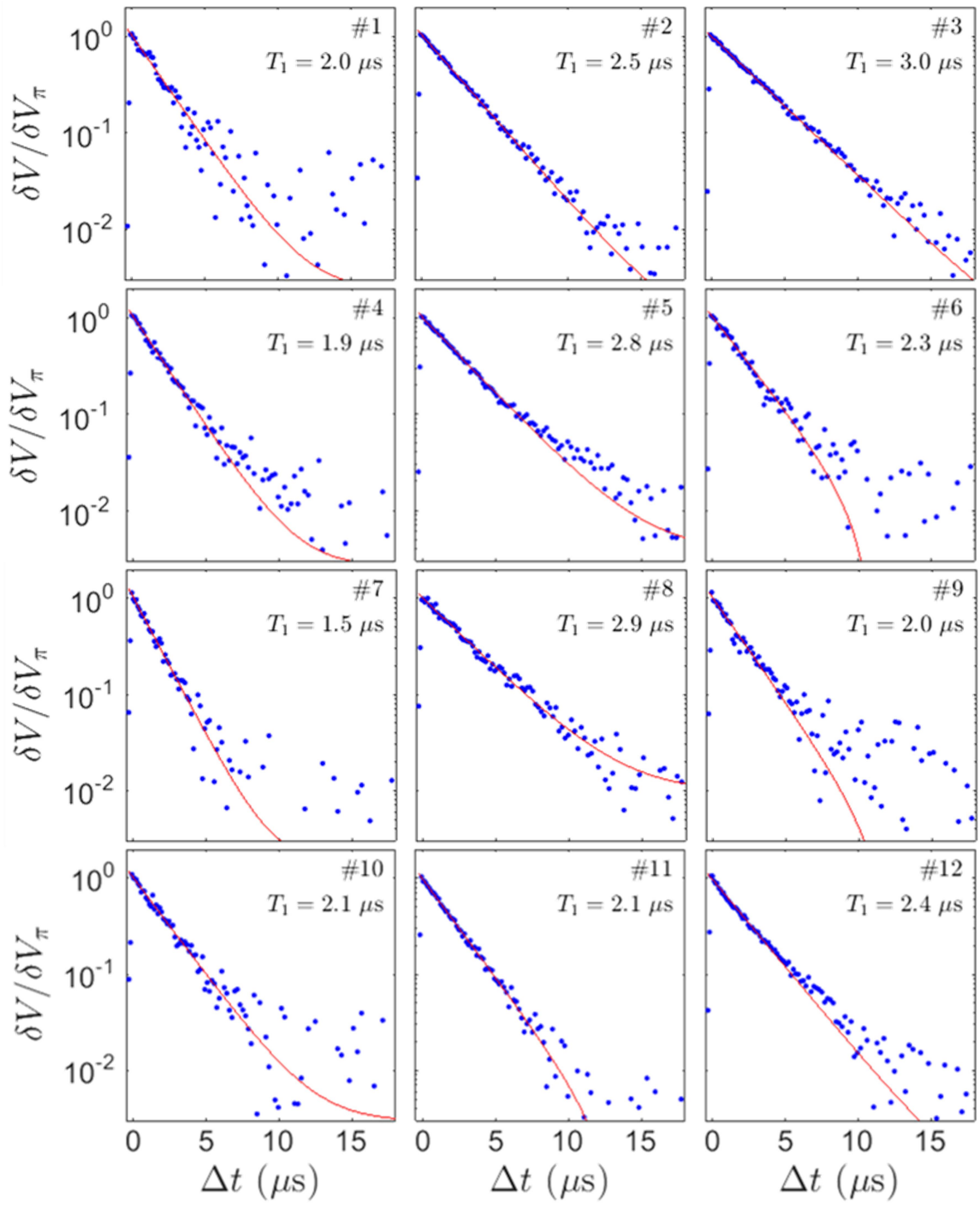

Fig. 9.10: Qubit relaxation measurements (blue points) and fits to Eq. (9.6) (red curves) at bias points 1 through 12 shown in Fig. 9.4.

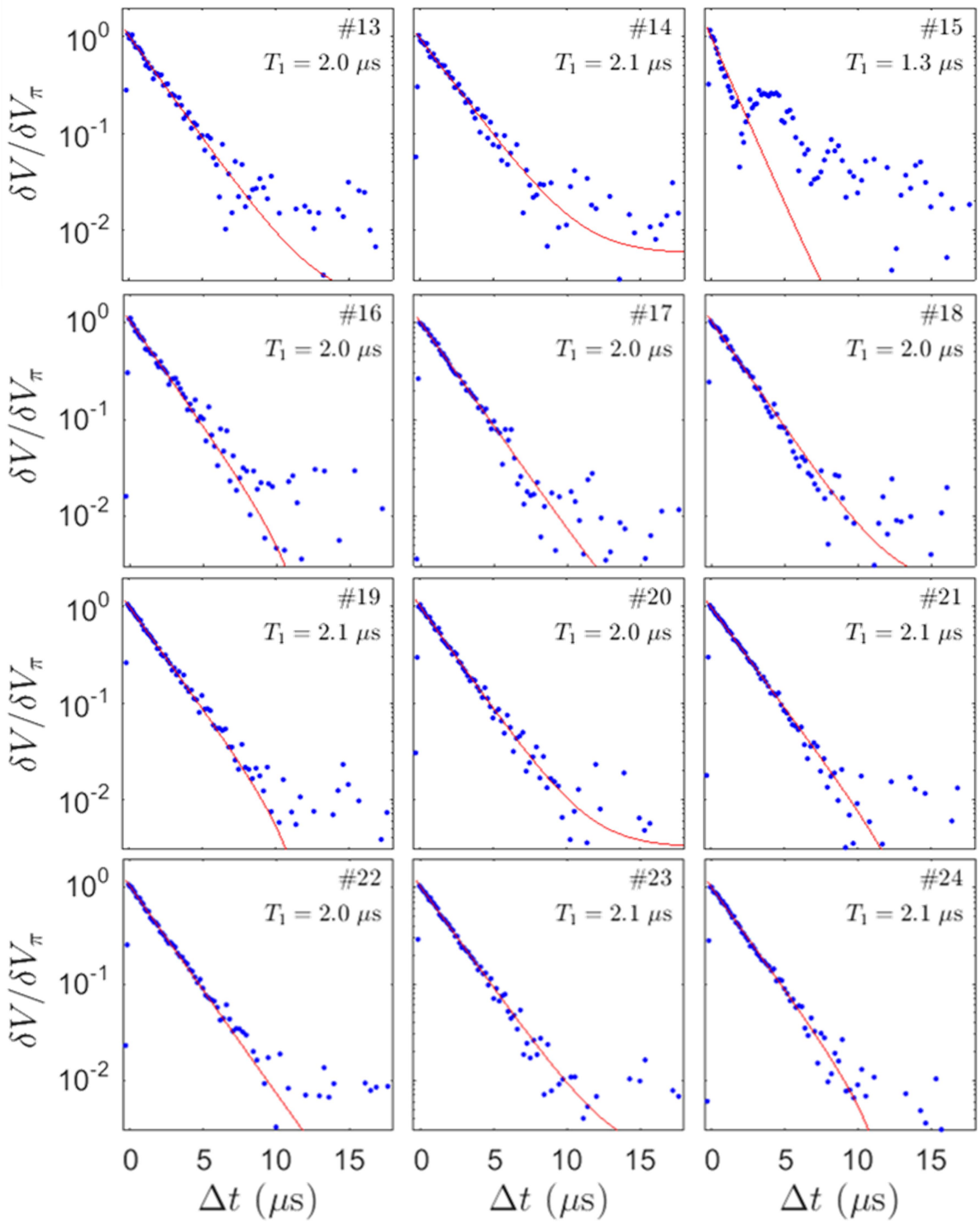

Fig. 9.11: Qubit relaxation measurements (blue points) and fits to Eq. (9.6) (red curves) at bias points 13 through 24 shown in Fig. 9.4.

Table 9.4: Summary of extracted T_1 values at the bias points shown in Fig. 9.4.

Bias point	T_1 (μs)	T' (μs)	T_ϕ (μs)	Bias point	T_1 (μs)	T' (μs)	T_ϕ (μs)
1	2.2	2.7	17	13	2.0	2.8	–
2	2.5	2.8	8.8	14	2.1	2.6	18
3	3.0	3.1	6.9	15	1.3	2.7	–
4	1.9	1.9	3.8	16	2.0	2.4	12
5	2.8	2.7	4.9	17	2.0	2.4	12
6	2.3	1.2	1.0	18	2.0	2.4	12
7	1.5	1.3	1.9	19	2.1	2.5	12
8	2.9	1.6	1.3	20	2.0	2.4	12
9	2.0	1.3	1.3	21	2.1	2.4	8.4
10	2.1	2.1	4.2	22	2.0	2.6	52
11	2.1	2.5	12	23	2.1	2.6	18
12	2.4	2.3	4.1	24	2.1	2.4	8.4

where the dephasing time was only $T_\phi = 1.0$ μs, it is clear that dephasing is dominating the loss in the system. However, for many bias points, such as point 22 where $T_\phi = 52$ μs, the relaxation time was the main limit on coherence. Recently, Yeh, *et. al.* showed that the value of T_ϕ could be used to extract the average photon number in a resonant system coupled to a cavity [6]. They then used this photon number to evaluate the effective temperature of the noise in the microwave line in order to characterize a novel design of microwave attenuators. Their measured value of T_ϕ at the base temperature of their system was approximately 200 μs, which is quite long compared to my device. As seen in Fig. 7(b) in ref. [6] at a mixing chamber temperature of about 65 mK to 70 mK their 3D transmon produced a dephasing time comparable to the point 22 $T_\phi = 52$ μs value, but to produce the point 15 value of $T_\phi = 1.0$ μs, their base temperature would need to be set to greater than 175 mK. I note that my device's dephasing times don't accurately reflect an effective temperature or photon number in their system due to the cavity decay rate being different, but this does indicate that there is a significant source of dephasing in my system, especially at bias points where the quantum state is strongly coupled to the state of the LC resonator.

9.4 Qubit State Tomography

One way to obtain a full measure of the state of an individual isolated qubit is to perform state tomography [7]. This requires good control over the phase and amplitude of the qubit manipulation pulses. As I mentioned in Section 9.1, we accomplished this by using a Tektronix AWG7000 AWG [2] Arbitrary Waveform Generator in lieu of the qubit source in Fig. 7.13.

9.4.1 Tomographic Pulse Sequence

State tomography essentially consists of preparing a state and then measureing Rabi oscillations (see Section 9.2). The key distinction with a standard Rabi oscillation is that the Rabi oscillations are driven with a different phase ϕ of the drive pulse signal. We can define the phase offset $\phi = 0^{\circ}$ to be a positive (counter-clockwise) rotation about the x-axis of the Bloch sphere, which corresponds to using the same phase as that used to prepare the state of the qubit. Using a drive with non-zero phase relative to the preparation pulses yields a Rabi oscillation along a line at angle φ with respect to the x-axis in the complex plane. For example, setting $\phi = 90^{\circ}$ would be a rotation about the y axis and setting $\phi = 180^{\circ}$ would be a negative (clockwise) rotation about the x-axis. Figure 9.13 shows a false-color representation of state tomography in the complex plane on Q_H when it was initially in its ground state (*i.e.* no state preparation pulse). In this plot, the radial distance from the center is the length Δt of the Rabi measurement, and the azimuthal angle is set by the phase offset relative with x-axis defined as $\phi = 0^{\circ}$. The color is the quantity $\delta V/V_0$ from Eq. (9.1), which corresponds to the probability that the system is found in its excited state.

The resulting tomographic maps depend on the initial state and an initial pulse is used to prepare the qubit in a particular state before taking tomographic data. Typical state preparations were $\pi/2$-pulses (putting the Bloch vector on the equator) about both the x and y axes, π-pulses (fully inverting the population to the first excited state) about both the x and y axes, and a 2π-pulse that brings the state all the way back to the ground state.

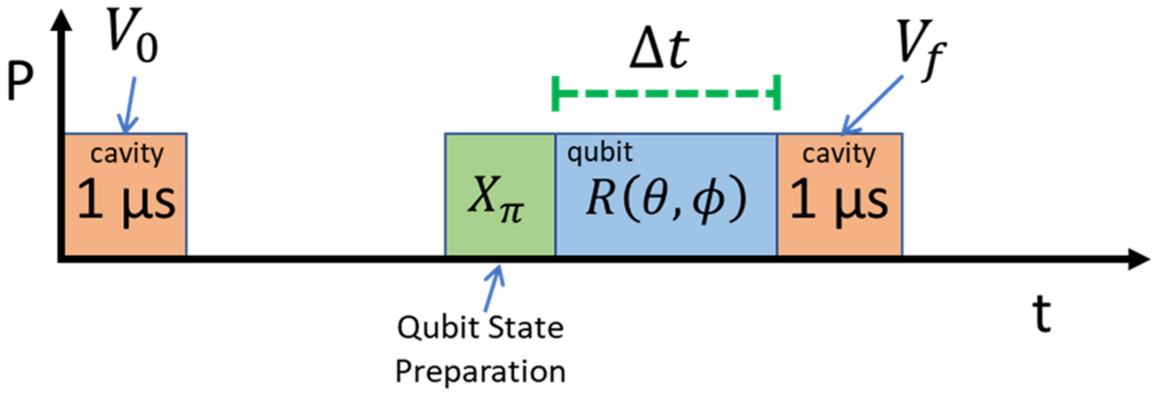

Fig. 9.12: Pulse sequence for qubit state tomography measurements. In this figure I show the particular case where the qubit is initially prepared by performing a π-pulse rotation about the x-axis.

Figure 9.12 shows the pulse control and readout sequence for constructing single-qubit tomographic maps. In this figure, I show the specific case where the initial preparation pulse was a π-pulse about the x-axis X_π, *i.e.* the measurement of $R(\theta,\phi) = R(\theta,0)$.

9.4.2 State Tomography Measurement Results

In Fig. 9.13 I show the state tomography results on qubit Q_H. For these data qubit Q_L was in its ground state and the LC resonator was tuned to its minimum frequency of f_{LC}= 4.14 GHz at I_f = -0.840 mA. In each plot the color corresponds to $\delta V/V_0$, which corresponds to the probability of finding transmon Q_H in its excited state, with blue corresponding to the ground state and red to the excited state. The upper left frame is when the qubit starts in its ground state. Notice that the point at the origin is blue,

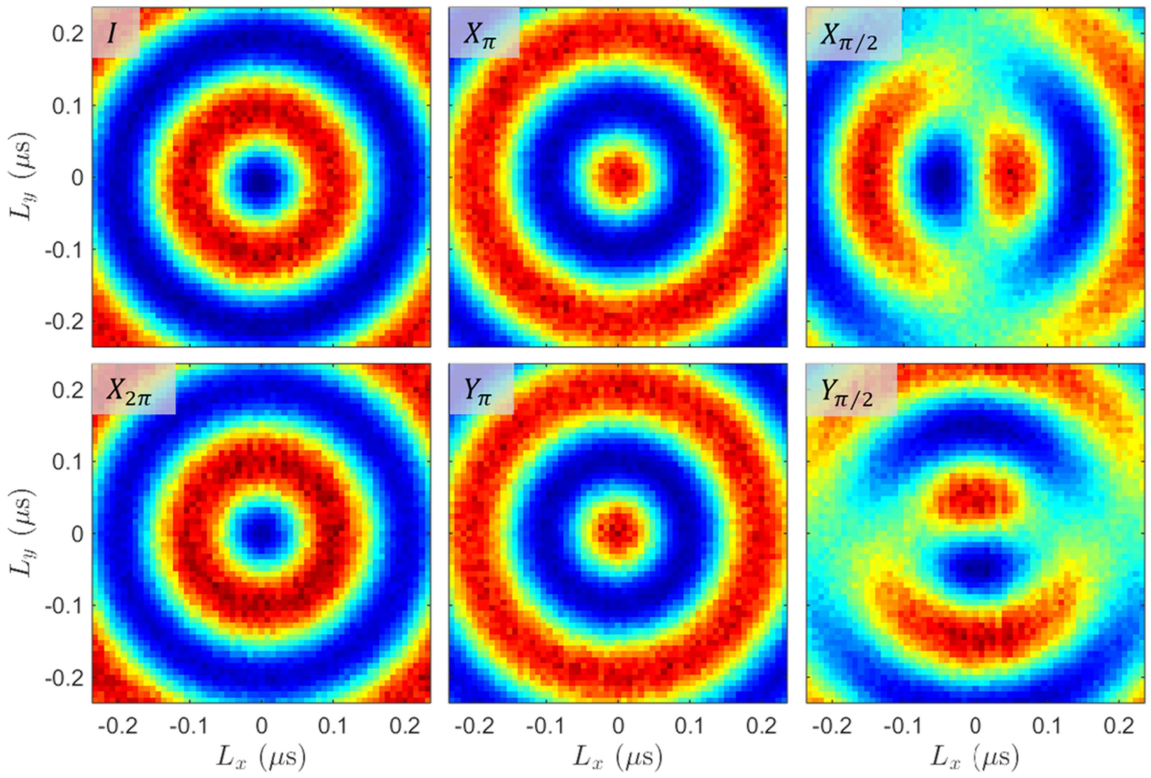

Fig. 9.13: Qubit state tomography measurement results on qubit Q_H when the resonator was tuned to its minimum frequency of f_{LC}= 4.14 GHz at I_f = -0.840 mA. The two qubits were relatively decoupled at this bias point and the resulting tomographic maps appear nearly ideal when Q_L was in the ground state, as shown here.

indicating that the qubit initially was in the ground state. Moving radially outward the population inverts to the excited state, as shown by the red ring around the center. Then, as the Rabi oscillation continues, the qubit returns to the ground state, as shown by the blue ring. For the lower left frame, the qubit was initially prepared with a 2π-pulse about the x-axis, denoted $X_{2\pi}$. Since this operation returns the qubit to its ground state, the

resulting tomographic map is virtually identical to that when the qubit was not subjected to the 2π pulse.

In the middle column, the two frames show tomographic maps when the qubit was initially prepared with a π-pulse. In the upper of these two frames the initial rotation was about the x-axis, and in the lower the initial rotation was about the y-axis, *i.e.* X_π and Y_π, respectively. In these cases, the qubit begins in its excited state; so, the point at the origin is red. Proceeding radially out from the origin, the state eventually returns to the ground state (blue ring), and this is followed by the excited state (red ring), *etc*. Since these two plots were both taken with the qubit starting in the excited state, they are virtually identical. They are also red-blue inversions of the ground state map, as expected.

Finally, in the right column I show tomographic maps when qubit Q_H was prepared with a $\pi/2$-pulse, which leaves the Bloch vector along the equator. In the upper frame the $\pi/2$ rotation was about the x-axis, *i.e.* $X_{\pi/2}$, and in the lower frame the rotation was about the y-axis, *i.e.* $Y_{\pi/2}$. The $X_{\pi/2}$ rotation leaves the qubit Bloch vector along on the equator of the Bloch sphere aligned with the y-axis on the. One sees a Rabi oscillation that starts "1/2 way" and proceeds as usual along the x-axis. On the other hand, for Rabi oscillations about the y-axis, there is no oscillation produced due to the fact that the initial state is aligned with the y-axis on the Bloch sphere. Hence, along the y-axis of the plot, the qubit state stays in the superposition state and no oscillation is evident. For the lower right frame, the original state preparation leaves the state vector aligned along the x-axis of the Bloch sphere. Hence, any rotations about the x-axis produce no oscillations.

Examination of the data in Fig. 9.13 confirms that we have full control over the state of a qubit in the Bloch sphere. With this level of control, it is possible to construct a complete set of single-qubit gates and also make many other measurements. In the following sections I show some of these other measurements. The data in Fig. 9.13 can also be analyzed quantitatively to extract the density matrix of the initial state and determine the fidelity with which the state has been prepared, although I did not attempt this analysis for my dissertation.

9.5 Measurement of Hahn Spin-Echo

The rate Γ_ϕ at which a qubit loses phase information can be quantified by the inverse of the coherence time T_2 [8, 9]. The time T_2 is also called the spin-echo time as it can be obtained via a Hahn spin-echo measurement.

9.5.1 Pulse Sequence

Figure 9.14 shows the pulse sequence used for performing a spin-echo measurement on a qubit. For this measurement there are three qubit manipulation pulses. The first pulse is a $\pi/2$-pulse about the x-axis, which induces a counter-clockwise rotation aligning the state vector with the negative y-axis. After the system evolves for a time $\Delta t/2$, a π-rotation is made about the x-axis. In the absence of decoherence and relaxation this pulse rotates the state vector so that it lies along the positive y-axis. After this pulse the system is again allowed to evolve for at time $\Delta t/2$. A $-\pi/2$ rotation (clockwise) about the x-axis is then performed. With no dechorence, this leaves the qubit in the excited state. As

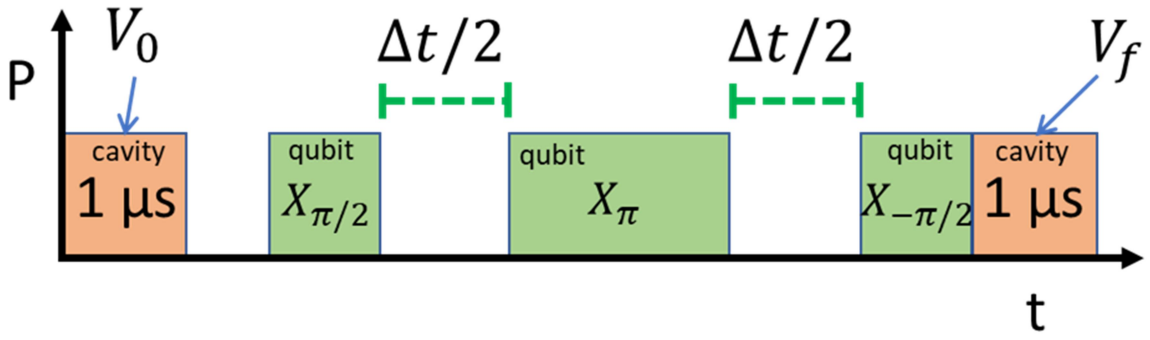

Fig. 9.14: Control and measurement pulse sequence for a Hahn spin-echo measurement.

the time delay is increased, the state will be increasingly subject to decoherence and will not necessarily end up in the excited. The final signal will decay away as

$$\delta V/V_0 = A\left(e^{-\Delta t/T_2} + 1\right), \tag{9.7}$$

where A is an overall amplitude that determines to the enhancement observed in the measurement and T_2 is the coherence time.

9.5.2 Spin-Echo Measurement

In Fig. 9.15 I show a spin-echo measurement on qubit Q_H. For this measurement, the tunable LC resonator was tuned to its minimum frequency of f_{LC}= 4.14 GHz at I_f = -0.840 mA. The x-axis is the time delay Δt, and the y-axis is the enhancement $\delta V/V_0$ given in Eq. (9.1); for this measurement, we did not correct for drift in the enhancement. The blue points on the plot are the data and the red curve is a fit to Eq. (9.6), which is an exponential decay. The fit gives T_2= 3.6 μs. At the same bias, qubit Q_H showed T_1 = 2 μs (see Fig. 9.9(b)). One expects

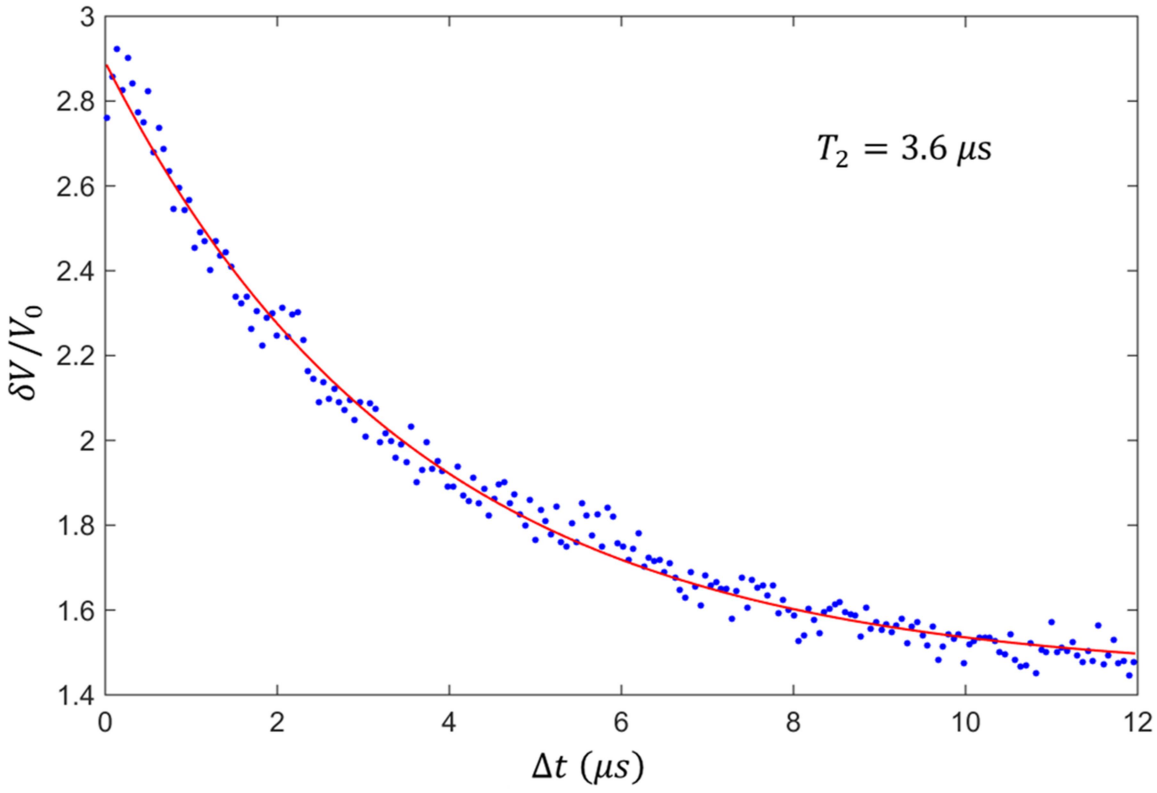

Fig. 9.15: Plot of cavity enhancement $\delta V/V_0$ vs. time delay Δt showing spin-echo relaxation in qubit Q_H. Blue points are data and red curve is a fit to Eq. (9.7). For this data the LC resonator was tuned to its minimum frequency of $f_{LC} = 4.14$ GHz at $I_f =$ -0.840 mA. The fit gives $T_2 = 3.6$ μs.

$$\frac{1}{T_2} = \frac{1}{2T_1} + \frac{1}{T_\phi}, \tag{9.8}$$

which gives $T_\phi = 36$ μs, which is at least respectable for transmons [6]. I can also compare the $T_2 = 3.6$ μs from spin-echo at this location to that expected from the Rabi decay measurements. Recall that

$$\frac{1}{T'} = \frac{1}{2T_1} + \frac{1}{2T_2}, \tag{9.9}$$

Using $T' = 2.9$ μs (see Fig. 9.2(b)) and $T_1 = 2$ μs gives $T_2 = 5.3$ μs, which is longer. Given the beating in Fig. 9.2(b), it is likely some additional levels of the qubit were involved, which may have slightly thrown off the numbers.

Sudeep also did spin-echo measurements on Q_H at the resonator was tunied to its maximum and on Q_L in both tuning places did not show a clean decay. There appeared to be beating, suggesting that other states were being excited. Additional examination of levels at this point need to be made to resolve this situation.

9.6 Ramsey Fringes

Both relaxation and dephasing decrease the coherence time of a qubit as can be seen from Eq. (9.7). Low frequency noise effects each measurement shot differently and produces the distinctly different effect called inhomogenous broadening [10]. Inhomogenous broadening, loss, and dephasing all contribute to the spectroscopic line width of the qubit, but only loos and dephasing contribute to decoherence (T_2). Thus, T_2^* can be measured via spectroscopy, but T_2^* can also be found by measuring the decay of Ramsey fringes.

9.6.1 Pulse Sequence

In Fig. 9.16 I show the pulse sequence for a single Ramsey fringe measurement. This sequence is very similar to the spin-echo measurement; however, it does not have the intermediate π-pulse. The manipulation sequence begins with a $\pi/2$-pulse about the x-axis. After this pulse, the state is allowed to evolve for a time Δt. Another $\pi/2$-pulse is then applied about the x-axis. When the time delay is $\Delta t = 0$, the final result is simply a π-pulse, *i.e.* the qubit ends up fully in the excited state. However, as the time delay is increased the qubit state vector will relax and diphase. Repeated measurements will also reveal effects from inhomogenous processes. The net result is an exponential decay in the signal with characteristic time constant T_2^*, with

$$\frac{1}{T_2^*} = \frac{1}{2T_1} + \frac{1}{T_\phi} + \frac{1}{T_2^\dagger}, \tag{9.10}$$

where $T_2^\dagger$ is the inhomogenous broadening time.

Ramsey fringes are usually produced by driving the qubit slightly off resonance. When the pulse frequency is off resonant with the qubit transition frequency, we are no longer observing the qubit in its resonant co-rotating frame. This leads to the qubit state precessing about the z-axis with the angle of precession equal to the detuning $\Delta\omega$ times the delay time Δt. When the time delay is zero, the second off-resonant $\pi/2$-pulse rotates the state farther down the Bloch sphere just as in the resonant case. However, when $\Delta t = \pi/\Delta\omega$ the state vector will have precessed 180º. At this point the second $\pi/2$-pulse rotates the qubit state vector back to its ground state. Thus, this process leads to oscillations, and the amplitude of the oscillations also with characteristic time T_2^*. The decaying oscillations were fit to

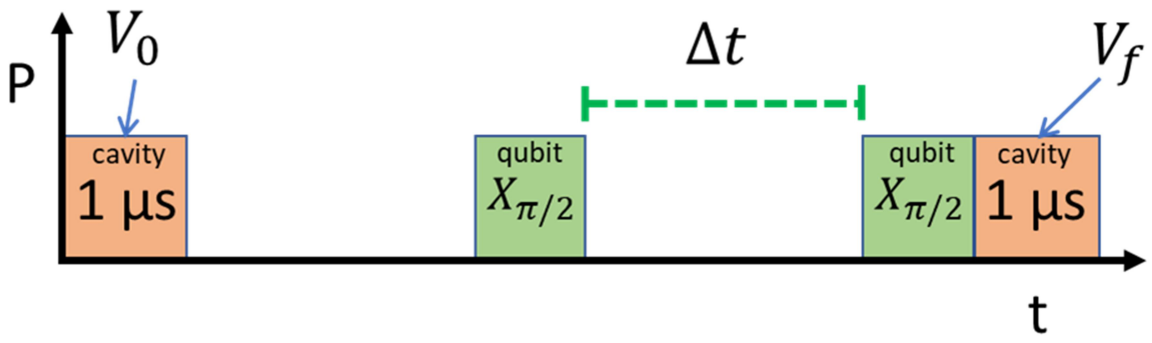

Fig. 9.16: Pulse sequence for Ramsey measurements.

$$\delta V/V_0 = A\left(1 + e^{-\Delta t/T_2^*}\sin(\Delta\omega\Delta t)\right), \tag{9.11}$$

where A is the amplitude of the oscillations and $\Delta\omega/2\pi$ is the detuning between the drive frequency and the qubit transition frequency.

Since the oscillation frequency of the fringes should be equal to the detuning, this also allows very accurate measurements of the qubit transition frequency. By extracting the oscillation frequency as a function of the drive frequency, one can identify the transition frequency as the point at which the Ramsey frequency is zero.

9.6.2 Ramsey Fringe Measurement

In Fig. 9.17 I show a Ramsey fringe measurement on qubit Q_L when the resonator was tuned to its maximum frequency of f_{LC}= 4.94 GHz at I_f = -0.584 mA. The x-axis of the plot is the length of the delay between the two $\pi/2$-pulses, the y-axis is the drive frequency of the pulses, and the color is the enhancement quantity $\delta V/V_0$ with dark blue being no enhancement (qubit in ground state) and with bright yellow being large enhancement (qubit in excited state). As discussed in Chapter 8, this qubit showed extra

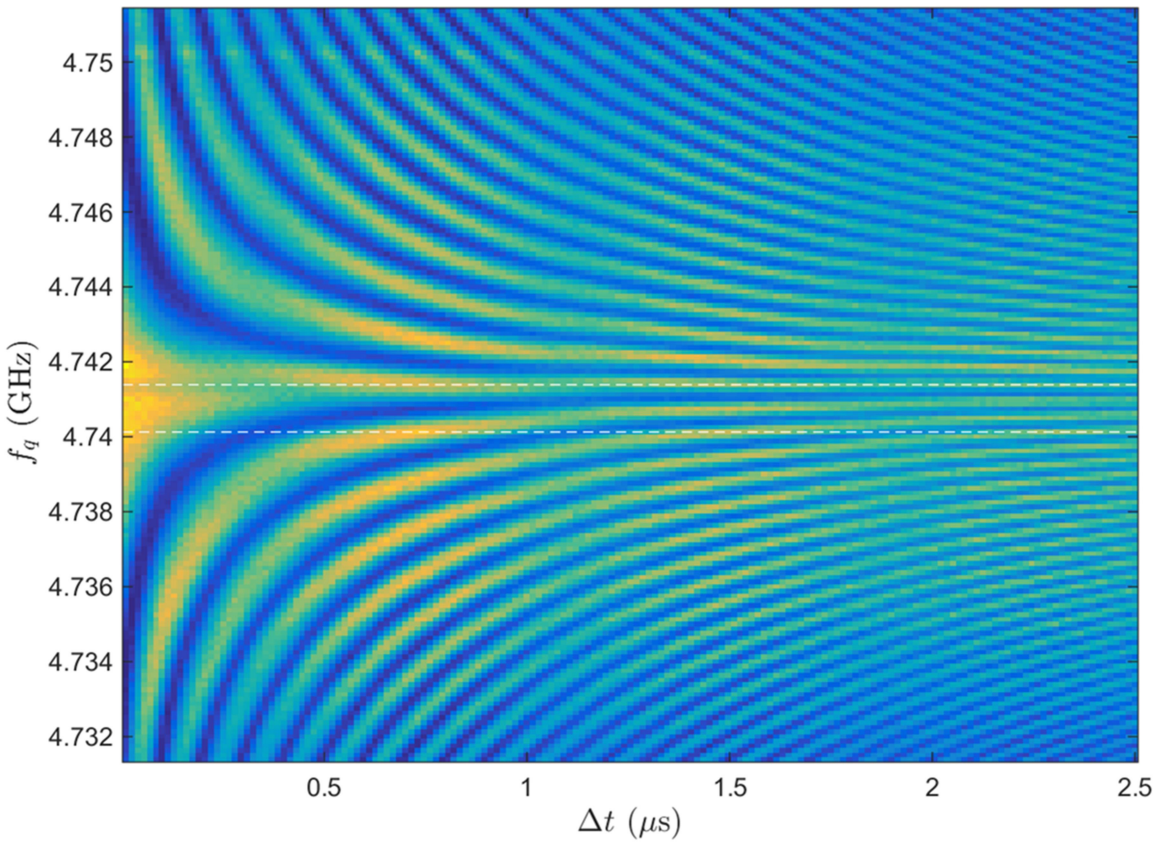

Fig. 9.17: Ramsey fringe measurement results on qubit Q_L when the resonator was tuned to its max frequency of f_{LC}= 4.94 GHz at I_f = -0.584 mA. The dashed lines show the frequency of the main g-to-e qubit transition and a dispersively shifted peak due to a TLS (see Chapter 8).

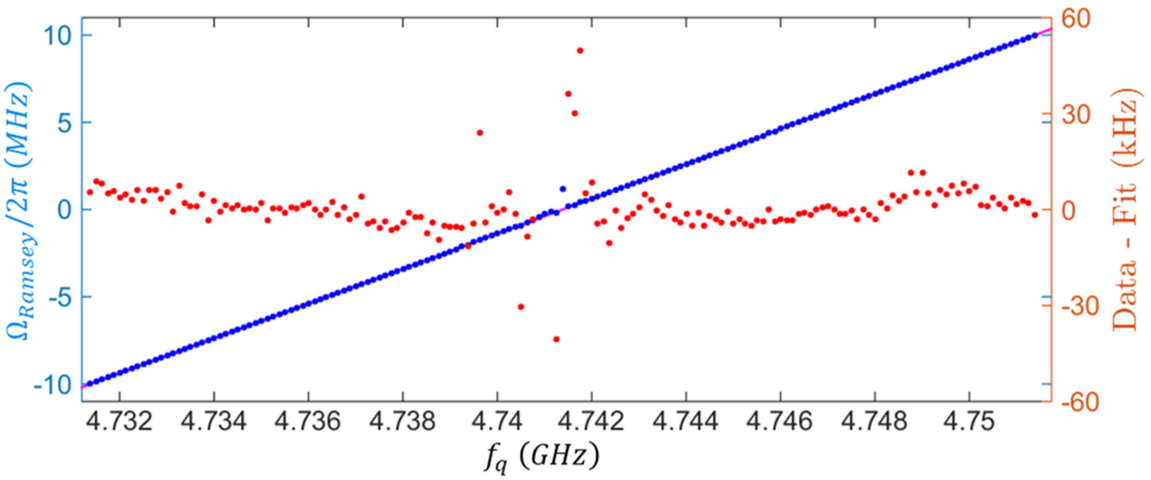

Fig. 9.18: Extracted Ramsey oscillation frequency $\Omega_{Ramsey}/2\pi$ as a function of qubit drive frequency f_q. The blue points (left y-axis) are the extracted values of the Ramsey fringe oscillation frequency from the fit to Eq. (9.8). The mostly hidden red line is a linear fit to the blue points. The red points (right y-axis) are the residues from this fit.

spectroscopic peaks due to two TLSs. As expected, careful examination of Fig. 9.17 shows additional oscillations due to the other peaks, although they are not prominent (see Chapter 8). The dashed white lines in the figure are at the transition frequency of the g-to-e transition and the ~1 MHz dispersively shifted peak. As the drive frequency was detuned from the g-to-e transition of the qubit, the oscillation frequency increased as expected.

Figure 9.18 shows extracted Ramsey frequency (blue points) versus drive frequency f_q. The frequencies we found fits to Eq. (9.11). The Ramsey oscillation frequency was chosen to be negative for negative detunings from the point where the frequency is zero. This point is consequently the transition frequency of the qubit. The

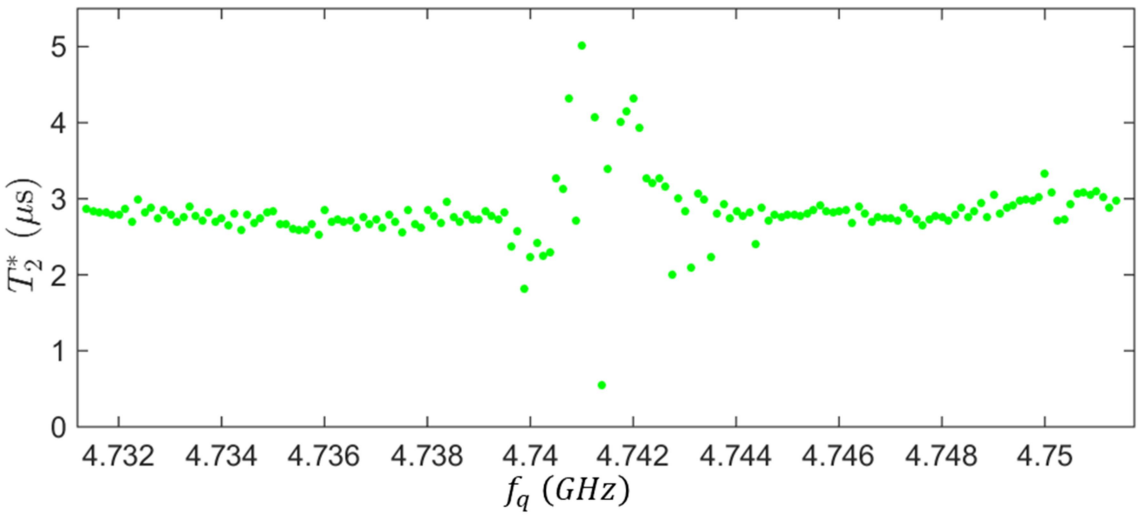

Fig. 9.19: Plot of extracted Ramsey decay time T_2^* vs. qubit drive frequency f_q from fitting the Ramsey oscillations shown in Fig. 9.17 to Eq. (9.8).

red line, mostly hidden beneath the blue points, is a linear fit to the blue points. The red points on the plot are the residues of this fit given by the data (blue points) minus the fit line. The residues are typically off by a few kHz, except near the resonance; it is difficult to accurately extract the oscillation frequency when it is slow compared to the decay rate of the oscillations. The fits are quite good when the detuning exceeded 1 MHz. The point at which the line crosses the origin in the plot is the g-to-e resonance frequency of qubit Q_L, and this measurement gives f_L= 4.741386 GHz.

Figure 9.19 shows a plot of the extracted T_2^* values as a function of the $\pi/2$-pulse frequency. T_2^* in this range is typically just below 3 μs. The green points on this plot are the extracted values from fits to Eq. (9.11). As I described above, the fits struggled near the qubit's resonance due to the decay being faster than the frequency. However, just

outside this realm, the fits clean up. The extracted value is quite consistent over the range of frequencies and is at a value just below 3 μs.

9.7 Controllable CNOT Gate

In section 8.8 I showed that by tuning the LC resonator on device TRES_092917, the qubit-qubit coupling could be varied. The range of qubit-qubit dispersive shifts available was roughly $2\chi_{qq} = 0.1$ MHz to 6 MHz. At the lowest coupling, the dispersive shift was small enough to yield an effective "off" setting for the qubit-qubit coupling. When the coupling was "on" the qubit-qubit dispersive shift was strong enough that two-qubit gates were possible. In this section I present preliminary results on a CNOT gate. Although the gate has yet to be fully characterized, for example by using quatum process tomography [11], the partial results presented below are encouraging.

9.7.1 State Readout

To verify the operation of a two-qubit gate, one must be able to determine the state of both qubits. To apply a joint qubit state readout, we took cavity S-curve enhancement data (see Chapter 8) for two-qubit state preparations. In Fig. 9.20(a) I show enhancement measurements for states $|gg\rangle$ (black curve), $|eg\rangle$ (blue curve), $|ge\rangle$ (green curve), and $|ee\rangle$ (red curve). At a cavity measurement power of P_c= 0.3 dBm, one sees that there is a clear enhancement in the signal for the $|ee\rangle$, $|ge\rangle$, and $|eg\rangle$ states compared to the ground state $|gg\rangle$. Thus, at this measurement power it is easy to distinguish when there is at least one excitation in the two-qubit system. In contrast, at cavity measurement power P_c= -3.9 dBm, there is only an enhancement the $|ee\rangle$ state.

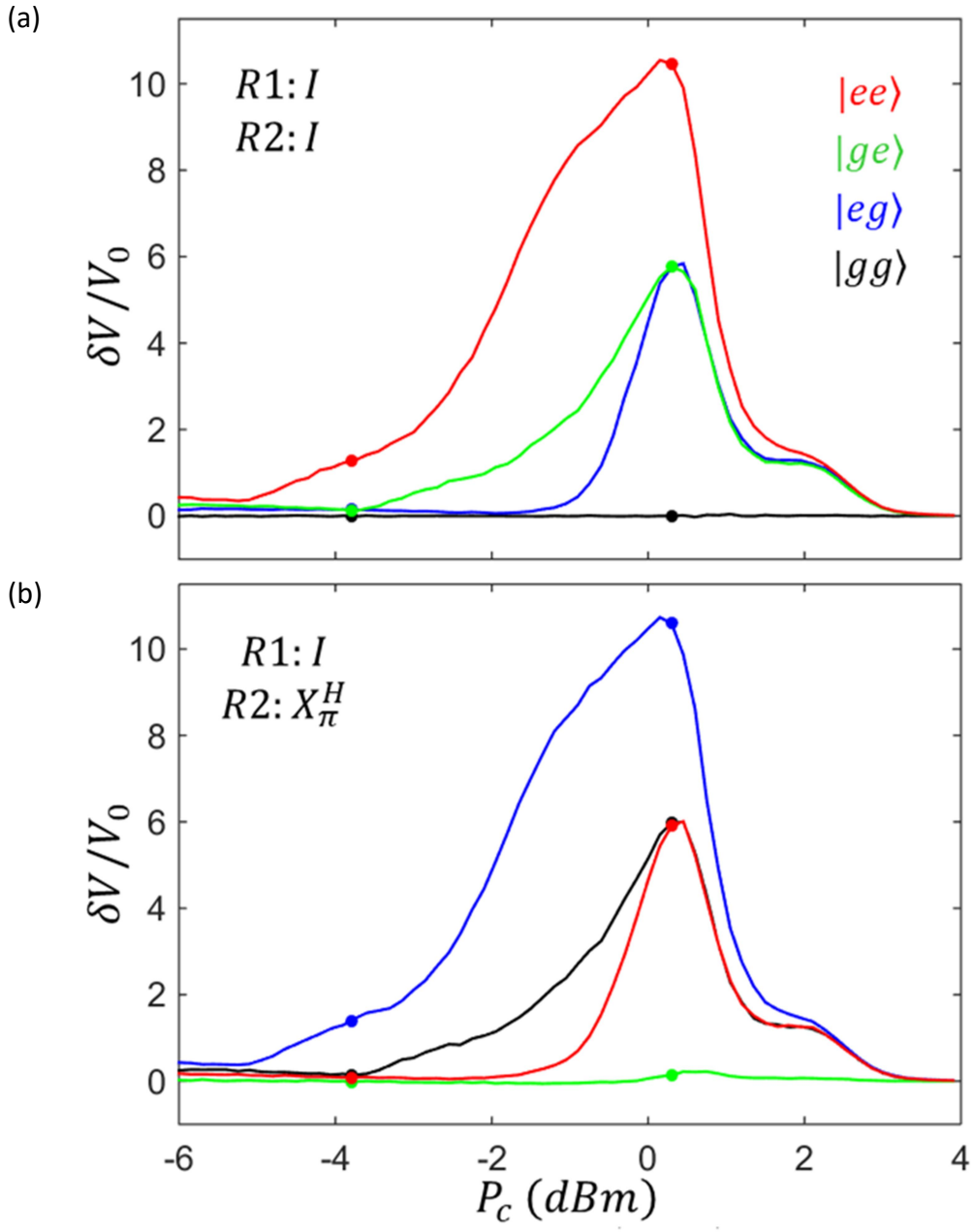

Fig. 9.20: (a) Cavity transmission enhancement measurements $\delta V/V_0$ vs. applied cavity power P_c for initial state preparations $|gg\rangle$ (black), $|eg\rangle$ (blue), $|ge\rangle$ (green), and $|ee\rangle$ (red). (b) Cavity transmission enhancement measurements for initial state preparations $|gg\rangle$ (black), $|eg\rangle$ (blue), $|ge\rangle$ (green), and $|ee\rangle$ (red) with an added π-pulse manipulation on Q_H right before measurement. Points show powers used to for extracting state probabilities for the CNOT measurements.

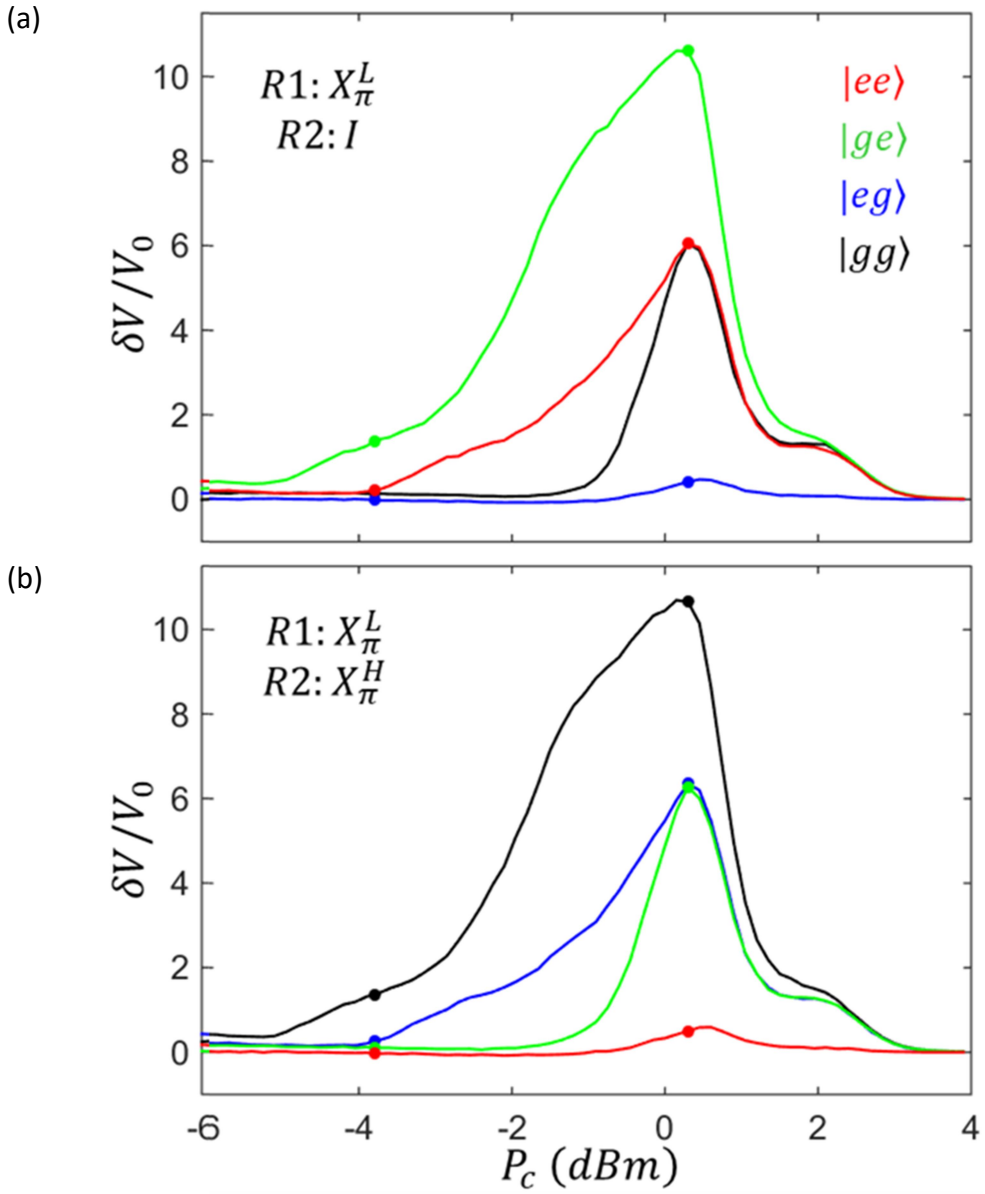

Fig. 9.21: (a) Cavity transmission enhancement measurements for initial state preparations $|gg\rangle$ (black), $|eg\rangle$ (blue), $|ge\rangle$ (green), and $|ee\rangle$ (red) with an added π-pulse manipulation on Q_L right before measurement. (b) Cavity transmission enhancement measurements for initial state preparations $|gg\rangle$ (black), $|eg\rangle$ (blue), $|ge\rangle$ (green), and $|ee\rangle$ (red) with an added π-pulse manipulation on both Q_H and Q_L right before measurement. Points show powers used to for extracting state probabilities for the CNOT measurements.

So, at this measurement power, we obtain information on whether or not both qubits were excited. Performing both these measurements allows us to discern the exact number of excitations in the system; although, it does not distinguish between the singly excited states $|ge\rangle$ and $|eg\rangle$.

Next consider Fig. 9.20(b), which shows the enhancement $\delta V/V_0$ where the system was again prepared in the states $|gg\rangle$, $|eg\rangle$, $|ge\rangle$, and $|ee\rangle$ but a π-pulse was applied to Q_H before the S-curves were measured. Examining the two measurement points P_c= 0.3 dBm and P_c= -3.9 dBm, one sees that we can now distinguish the state $|eg\rangle$. Similarly, in Fig. 9.21(a) I show enhancement measurements on the states $|gg\rangle$, $|eg\rangle$, $|ge\rangle$, and $|ee\rangle$ with a π-pulse applied to Q_L before the measurement. In this case, the measurements at $P_c = 0.3$ dBm and $P_c =$ -3.9 dBm provide a way to distinguish the state $|ge\rangle$. Finally, in Fig. 9.21(b) I show an enhancement measurement when both Q_L and Q_H were manipulated with a π-pulse after the state preparations. At the same two cavity measurement powers, this mapping provides a direct measure of the population of state $|gg\rangle$.

In general, an arbitrary state of two qubits will have some probability to be in $|gg\rangle$, $|eg\rangle$, $|ge\rangle$, and $|ee\rangle$. If we take enhancement measurements at cavity powers P_c= 0.3 dBm and P_c= -3.9 dBm for the 4 state manipulations described, we obtain 8 different measurements. From these 8 measurements, we can obtain the population in $|gg\rangle$, $|eg\rangle$, $|ge\rangle$, and $|ee\rangle$. Let the measurements be denoted by $j = 1$ to 8. Then the jth measurement will yield an average output

$$m_j = C_{1j}P_{gg} + C_{2j}P_{eg} + C_{3j}P_{ge} + C_{4j}P_{ee}\,, \tag{9.12}$$

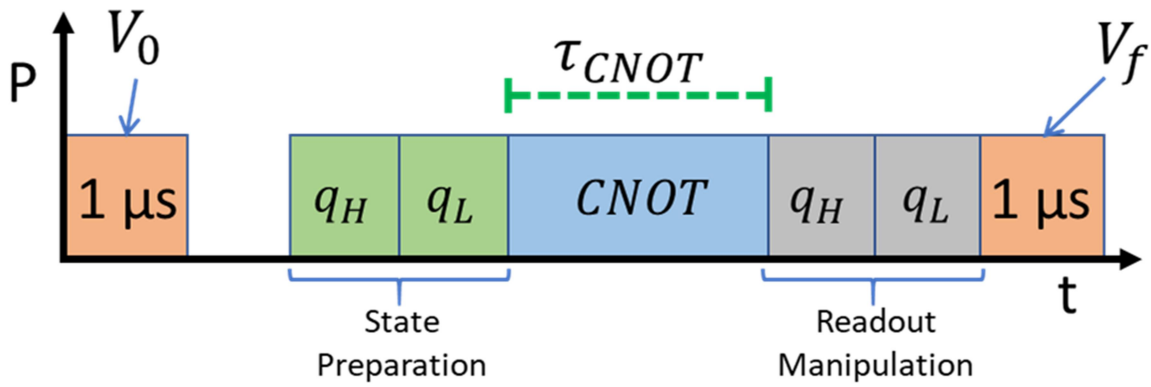

Fig. 9.22: Control and measurement pulse sequence for characterization of the CNOT gate.

where the C_{ij} is the output of the system in the ith state and measured using the jth measurement power as given by the enhancement measurements (see Figs. 9.20 and 9.21). With the 8 measurements m_j and four unknowns P_{gg}, P_{eg}, P_{ge}, and P_{ee}, we can use least squares on a χ^2-minimization to obtain best estimates for the 4 state probabilities [11].

9.7.2 CNOT Measurement Pulse Sequence

In Fig. 9.22 I show a pulse sequence used for the initial characterization of the CNOT gate. As usual, before the sequence begins, we applied a cavity characterization pulse to measure V_0. After the cavity characterization pulse there is a large time delay before the qubit state preparations to allow the system to settle. For this initial characterization we only prepared the four initial states $|gg\rangle$, $|eg\rangle$, $|ge\rangle$, and $|ee\rangle$. Immediately after state preparation, the CNOT gate pulse was applied, which involved a

careful choice of power and frequency (see below). As I show in the next section, we also measured the state populations during the CNOT pulse to see the evolution during gating; however, only at Δt= 230 ns was the full CNOT gate completed. After the CNOT pulse, we applied the state readout mappings discussed in section 9.7.1 and then the cavity measurement pulse was applied to measure the enhancement voltage V_f.

9.7.3 CNOT Gate Characterization Measurement

We chose to characterize the CNOT gate at the resonator's maximum frequency f_r= 4.94 GHz. At this bias point, the qubit-qubit dispersive shift is $2\chi_{qq}$= 4 MHz, and the device was insensitive to small variations in the bias flux current.

For this CNOT gate, we chose to use Q_L as the target qubit and Q_H as the control qubit. Unlike traditional CNOT gate configurations, we chose to make the target qubit Q_L invert when the control qubit Q_H was in its ground state (see Fig. 9.23(a)). A conventional CNOT inverts the target qubit when the control qubit is in the excited state. These choices were made because this configuration produced the cleanest results.

Another critical factor was to find an appropriate power P_q, frequency f_q, and time Δt such that a pulse would actually generate a CNOT operation. In Fig. 9.23(b) I show the results of taking Rabi spectroscopy data on Q_L at f_q= 4.74 GHz with Q_H in its ground state (blue curves) and excited state (red curves). This frequency of 4.74 GHz is on resonance with Q_L when Q_H is in its ground state (see Fig. 9.23(a)). The blue curves show the time Δt required for Q_L to complete an odd multiple of π rotations with Q_H in its ground state (*i.e* a complete inversion $|gg\rangle$ to $|eg\rangle$) as a function of the applied pulse power. The red curves, on the other, hand show the time for Q_L to complete an even

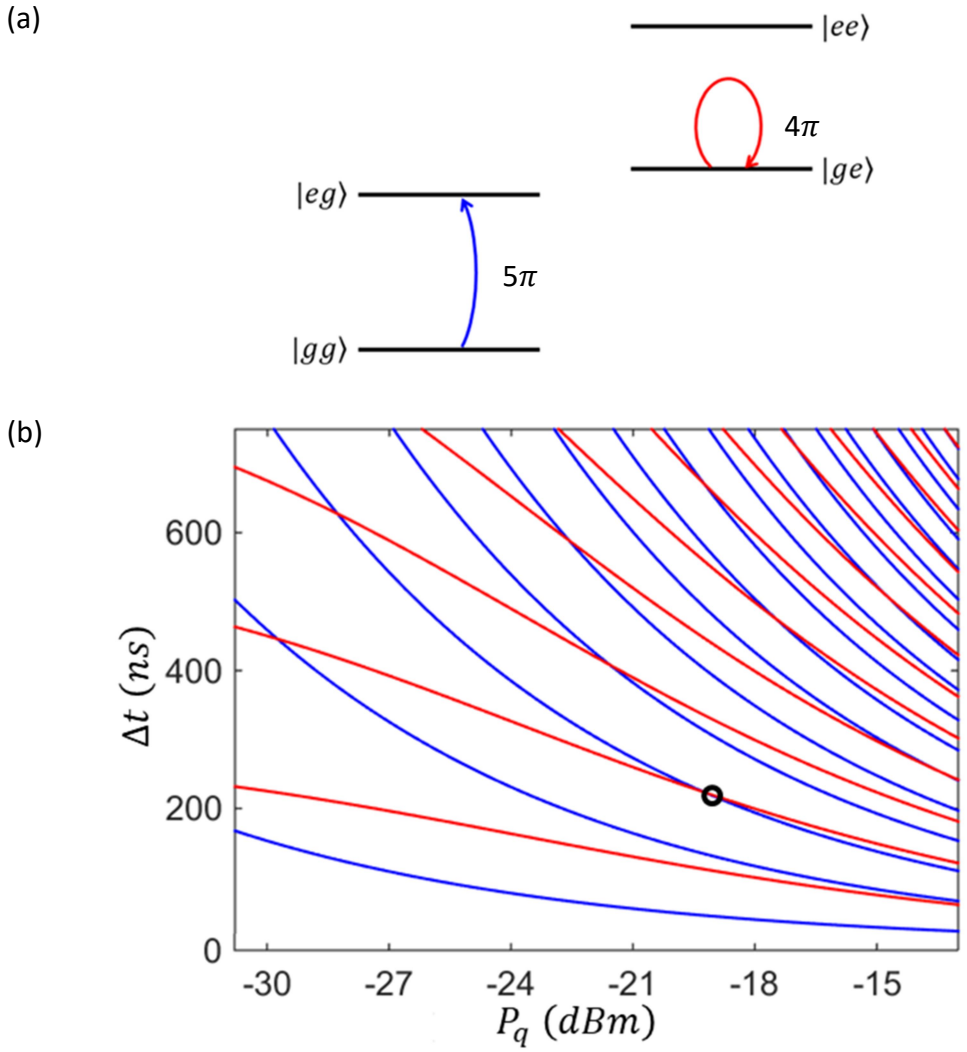

Fig. 9.23: (a) Energy level structure of Q_L and Q_H. (b) Plot used to find conditions suitable for a CNOT gate. The blue curves show gate time Δt vs. applied power for qubit Q_L to complete an odd number of π rotations with Q_H in its ground state, *i.e.* $|gg\rangle$ to $|eg\rangle$. The red curves show gate time Δt vs. applied power for qubit Q_L to complete an even multiple of π rotations with Q_H in its excited state, *i.e.* $|ge\rangle$ to $|ee\rangle$. This data was taken at $f_{gg\rightarrow eg} = 4.74$ GHz, *i.e.* on resonance with Q_L when Q_H is in its ground state. Intersections of the red and blue curves are conditions where a CNOT gate would work. The black circle shows that a CNOT can be achieved by applying ~ -19 dBm of power for ~ 230 ns.

number of π rotations (*i.e.* returning the state to $|ge\rangle$ on the $|ge\rangle$ to $|ee\rangle$ transition). To get this CNOT gate to work, we needed to find a power where a blue and red curve intersect. We chose the point P_q= -19 dBm and Δt= 230 ns (see Fig. 9.23(b)), which gave a relatively fast gate. Note that this choice actually yields a 4π rotation on Q_L in the non-inverting setting and a 5π rotation on Q_L when the CNOT gate is inverting.

In Figs. 9.24 and 9.25 I show the resulting plots of the state populations P_{gg}, P_{eg}, P_{ge}, and P_{ee} versus time Δt during the CNOT gate. Figure 9.24(a) shows the results when the initial state of the two qubits was $|gg\rangle$. Since Q_H is in its ground state, this operation should invert the population of Q_L and put the system in the state $|eg\rangle$. From the figure it is clear that the gate performed quite well; at the end of the 230 ns gate time the initial $|gg\rangle$ state population has been almost entirely translated to the state $|eg\rangle$.

In Fig. 9.24(b) I show the results of this operation on the initial state $|ge\rangle$. This time, the gate should leave the state alone because the control qubit Q_H was excited. This was not quite as effective as the operation on $|gg\rangle$. The gate produced about 88% population in the correct $|ge\rangle$ state with the remaining 12% of the state population in $|ee\rangle$. This error was most likely due to the relaxation of the $|ee\rangle$ state to the $|eg\rangle$ state during the gate operation. With the relaxation time $T_1 = 1.9$ μs measured on Q_H at this bias point (see section 9.3), one expects roughly 10% of the population to decay over the 230 ns gate time.

In Fig. 9.25(a) I show the results of the CNOT gate operating on the initial state $|eg\rangle$. Since Q_H is in its ground state, our CNOT gate should flip the state of Q_L to produce the state $|gg\rangle$. As seen in the figure, the gate did a very good job, translating

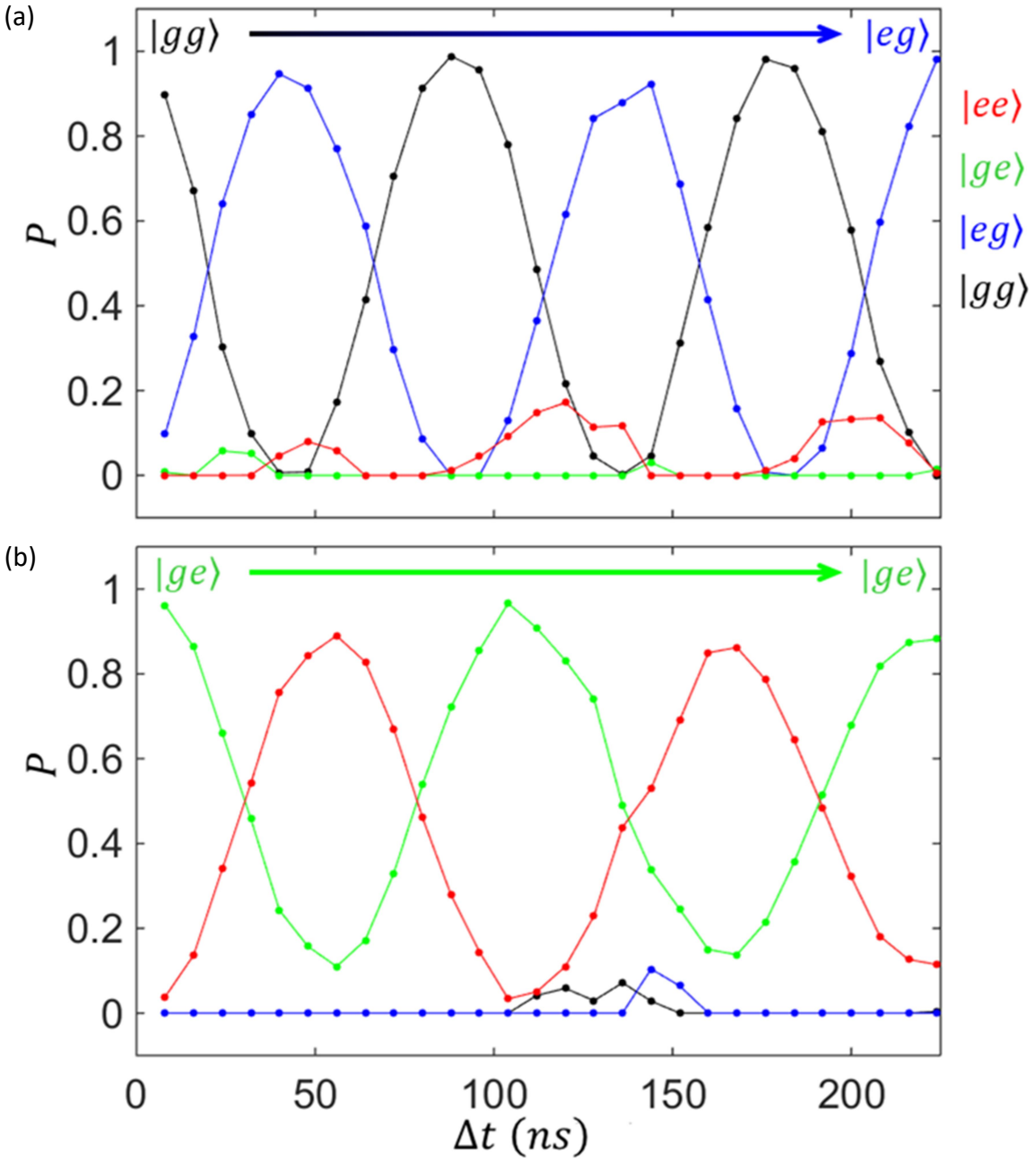

Fig. 9.24: (a) Two-qubit state populations P vs. CNOT gate pulse length Δt applied to initial state $|gg\rangle$. The system starts in $|gg\rangle$ (black) and ends in $|eg\rangle$ (blue), while the populations in $|ge\rangle$ and $|ee\rangle$ remain small as required for this version of the CNOT. (b) Two-qubit state populations P vs. CNOT gate pulse length Δt applied to initial state $|ge\rangle$.

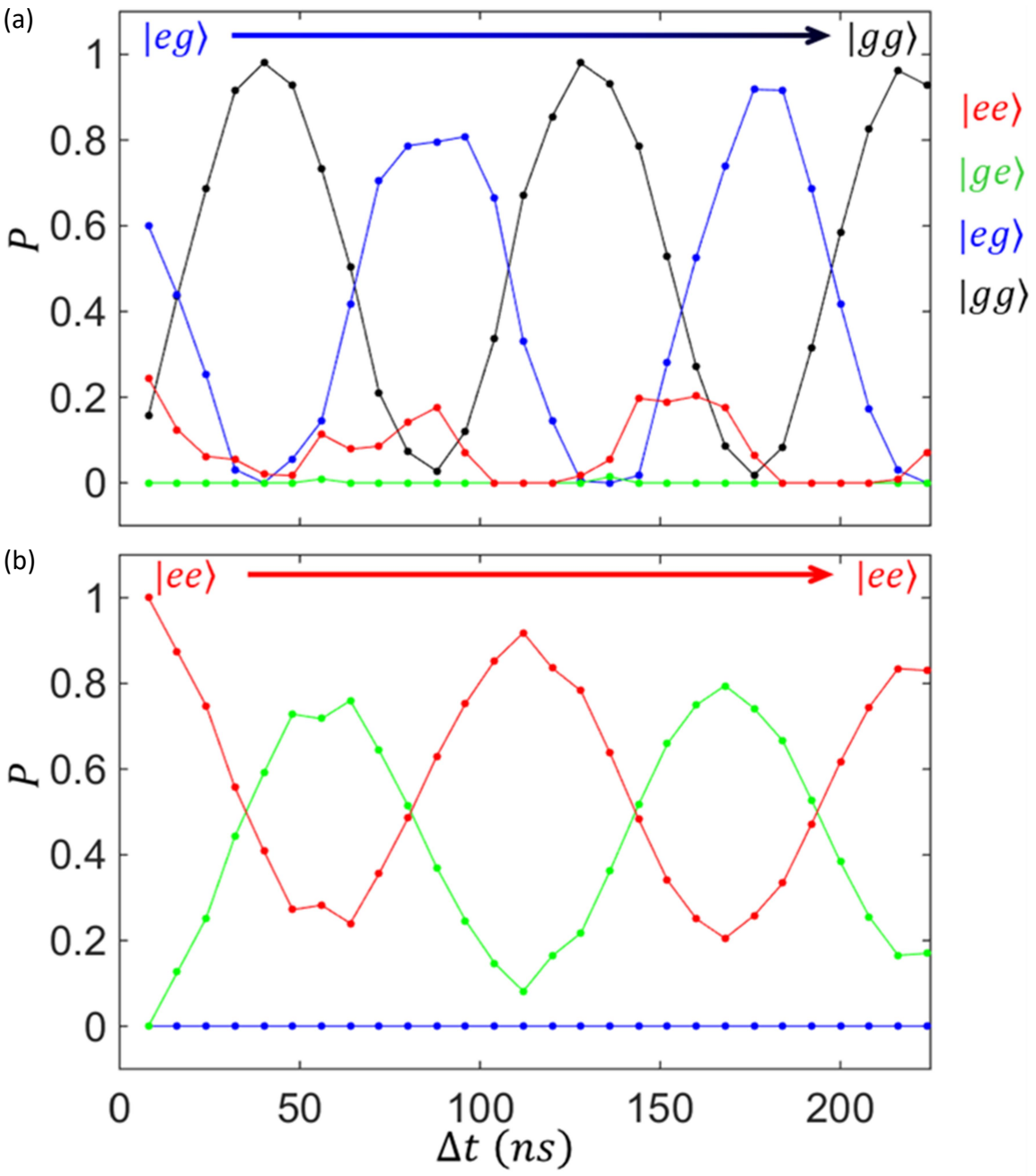

Fig. 9.25: (a) Two-qubit state populations P vs. CNOT gate pulse length Δt applied to initial state $|eg\rangle$. (b) Two-qubit state populations P vs. CNOT gate pulse length Δt applied to initial state $|ee\rangle$.

more than 90% of the population to the correct state. There was some clear noise at the end

Finally, in Fig. 9.25(b) I show the results of the CNOT gate operating on input state $|ee\rangle$. Again, with Q_H in its excited state, the CNOT operation should leave this state alone. At the end of the gate operation, the system ended with about 82% of its population in $|ee\rangle$ and about 18% in $|ge\rangle$, with the discrepancy likely due to the relaxation of the qubits. Since the qubit relaxation times at this bias point were $T_1 = 1.9$ μs and $T_1 = 2.6$ μs for Q_H and Q_L, respectively, this implies that the $|ee\rangle$ state decays with $T_1 = 1.1$ μs. Over the 230 ns gate time, one expects to lose about 19% of the population.

In Fig. 9.26 I show a histogram summarizing the results of this CNOT gate operation. The final populations for input states $|gg\rangle$ and $|eg\rangle$ were close to the expected values. However, for input states $|ge\rangle$ and $|ee\rangle$, there was obviously some population in the wrong states at the end of the operation. Overall, though, this gate performed remarkably well for an initial attempt. I note again that this is not a full characterization of this gate because it only gave us access to the diagonal terms of the density matrix. More work is needed to obtain off-diagonal terms and perform complete process tomography [11].

9.8 Conclusions

In this chapter I presented time-resolved measurements of coherent quantum behavior in my device TRES_092917. I began by showing Rabi oscillation measurements on qubits Q_H and Q_L with the LC resonator tuned to its maximum and

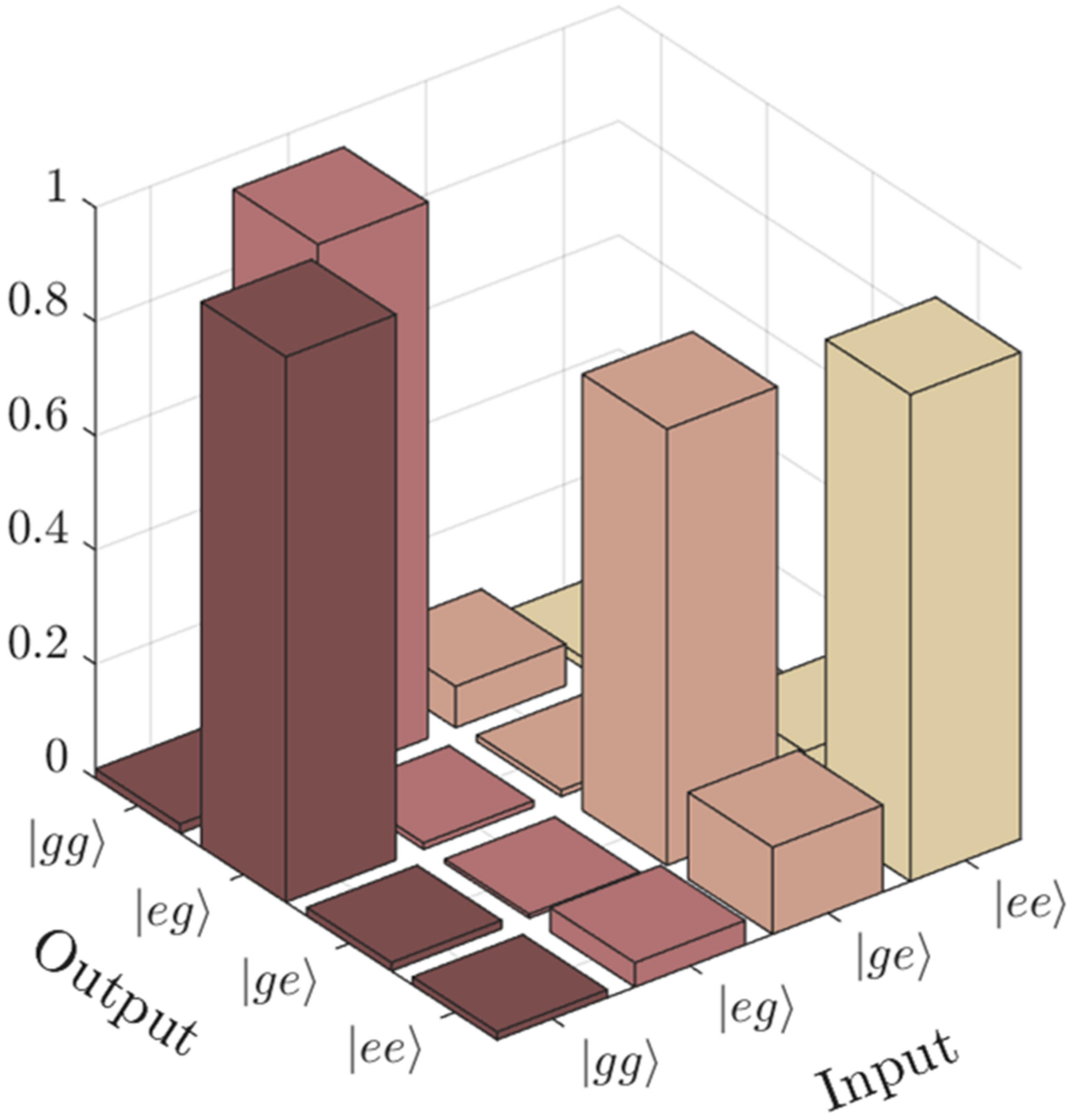

Fig. 9.26: Histogram summarizing CNOT gate final state populations vs. initial input state.

minimum resonance frequencies. This was followed by Rabi oscillation measurements taken at 24 points indicated in the spectroscopic map in Fig. 9.4. I next showed relaxation time T_1 measurements on both Q_H and Q_L at the same resonator tuning points and discussed the extraction of the qubit dephasing times at these points. I also presented state tomography measurements, spin-echo measurements, and Ramsey fringes.

The key part of this chapter was the initial characterization of a generalized CNOT gate. For these measurments, the LC resonator was tuned to its maximum frequency of $f_{LC} = 4.94$ GHz at $I_f = -0.584$ mA. Qubit Q_L was the target qubit and qubit Q_H was used as the control qubit with Q_L being inverted when Q_H was in its ground state. As I show in section 9.7, the gate performed quite well for this initial characterization with $2\chi_{qq} = 4$ MHz. While the relatively short T_1 values of the two qubits limited the fidelity at the end of the 230 ns gate time, the results were remarkably good for a first demonstration. Examination of the CNOT at other biases with qubit-qubit dispersive shifts that are greater than 4 MHz may reveal improved performance. Comparison with SWIPHT gates [11] or other two-qubit gates would be interesting.

Chapter 10

Non-Equilibrium Quasiparticle Effects on Relaxation Time

In this chapter I discuss an analysis of how non-equilibrium quasiparticles cause relaxation in transmons. In Chapter 11, I discuss experimental results on the relaxation time T_1 of three transmon qubits that were measured in our group and in Ben Palmer's group at the Laboratory for Physical Sciences (LPS). In two of the devices, T_1 increased by a factor of almost two as the temperature increased from 30 mK to 100 mK. In this chapter I present the theory that we eventually used to explain this phenomenon. The main idea is that one of the electrodes of the tunnel junction has a smaller volume and smaller superconducting energy gap than the other electrode. At sufficiently low temperatures, non-equilibrium quasiparticles accumulate in the electrode with the smaller gap, leading to an increased density of quasiparticles at the junction and a corresponding decrease in the relaxation time. At temperatures greater than the difference in the two gaps, the non-equilibrium quasiparticles are liberated from the low gap region into the whole volume of the device. This leads to a reduction in the quasiparticle density at the junction and a longer relaxation time. I note that this chapter gives further details on the T_1 vs. T model that is found in ref. [1].

10.1 Introduction and Brief Qualitative Discussion of Model

Before describing the model, I first consider the physical layout of our transmons devices. Figure 10.1(a) shows a microscope image of one of my transmons. It has two capacitor pads, which I will call left and right, that are connected via a small Josephson

(a)

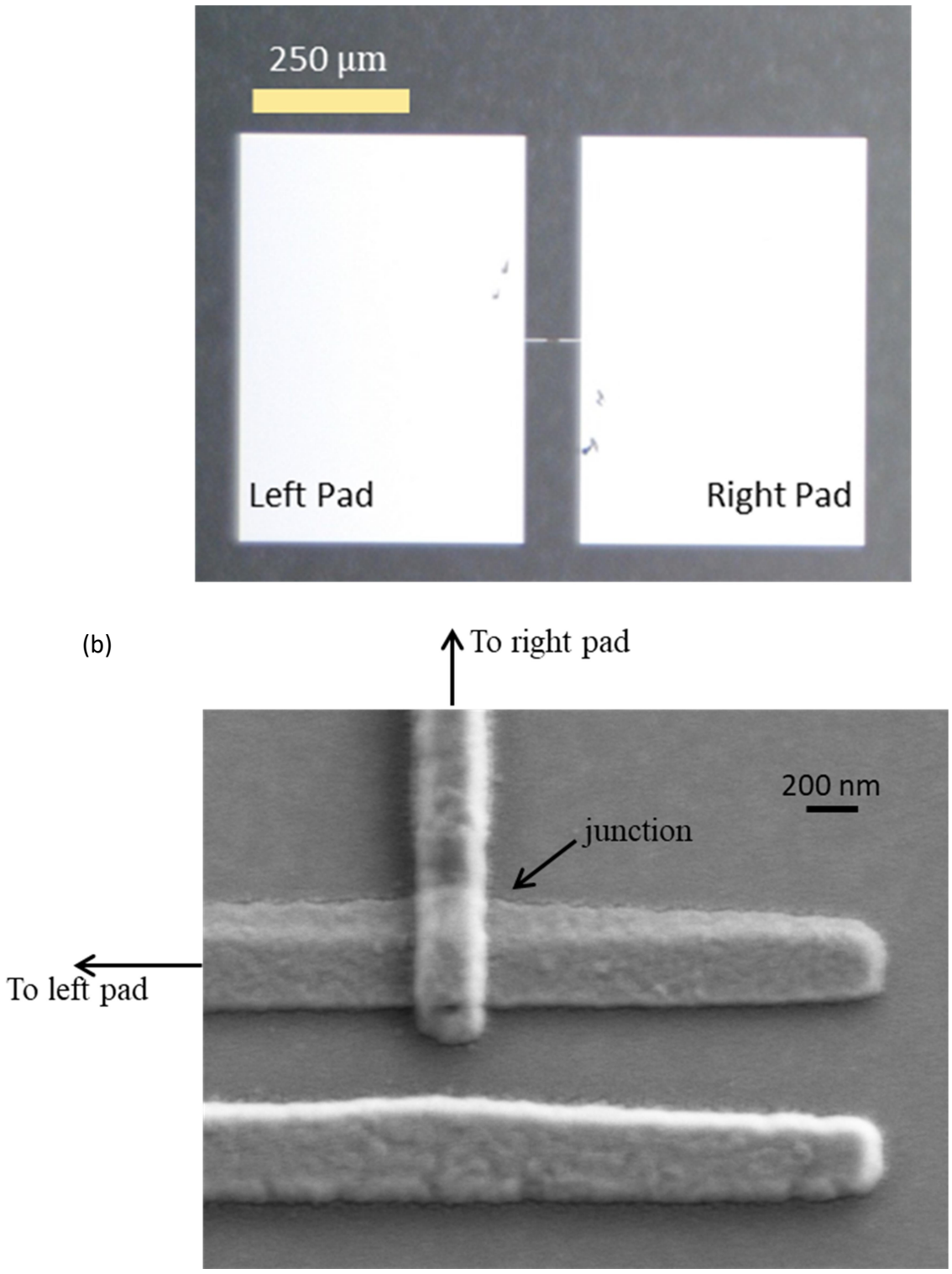

Figure 10.1: (a) Optical photograph of 3D transmon with left and right pads labelled. (b) SEM image of showing detailed view of transmon Josephson junction.

junction. Fig. 10.1(b) shows an SEM picture of a typical junction I made for my transmons.

I fabricated all my devices using double-angle evaporation of Al [2]. In this process, I first evaporated a film of Al, which I will refer to as layer 1. I then introduced O_2 into the evaporation chamber in order to grow a thin Al_2O_3 layer on the surface of the Al. I next changed the evaporation angle and evaporated a second film of Al, which I'll call layer 2, on the first (For more details on my fabrication process see Chapter 6). Rui Zhang used a similar process to build her transmons [1]. We both typically made layer 2 about twice as thick as layer 1 in order to ensure that the second layer would cover the junction. The key point here is that differences in thickness and growth conditions (presence of O_2, temperature, chamber vacuum, *etc.*) may lead to somewhat different superconducting gaps in the two layers [3-8].

I thus assume that the left junction electrode is formed from layer 1 with superconducting gap Δ_1 and that the right electrode is formed from layer 2 with gap Δ_2. For this discussion, I will also assume that $\Delta_1 < \Delta_2$. As Fig. 10.2 shows, the left electrode connects to the left pad of the transmon, which is formed from both layers 1 and 2 with volumes Ω_{1L} and Ω_{2L}, respectively. Similarly, the right electrode connects to the right transmon pad, which is also formed from both layers 1 and 2 but with volumes Ω_{1R} and Ω_{2R}, respectively. In my devices, the left and right transmon pads have the same area, and since layer 2 has roughly twice the thickness of layer 1, this implies $2\Omega_{1L} = 2\Omega_{1R} \approx \Omega_{2R} = \Omega_{2L}$.

Given this physical layout of the transmon, I can now give a brief overview of the model (see Fig. 10.3). A key assumption is that there are non-equilibrium quasiparticles

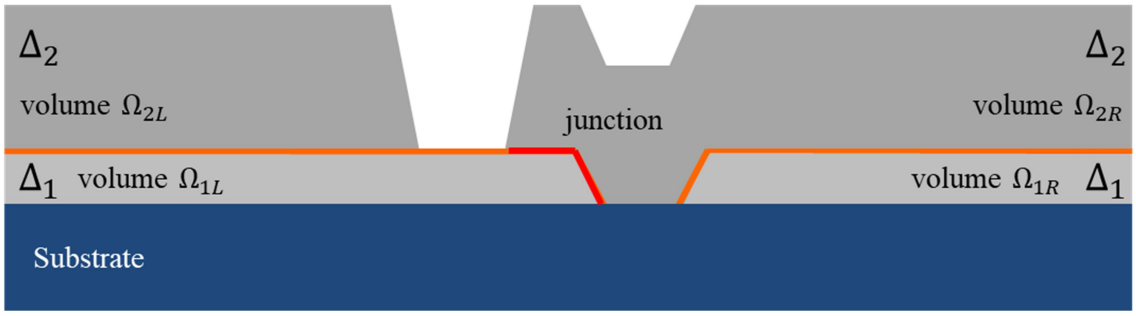

Fig. 10.2: Schematic cross-sectional view of Josephson junction formed by double-angle evaporation of Al.

present in the device. Such quasiparticles are well-known from previous work on single-electron transistors (SETs) and Cooper pair box qubits (CPBs) [9-14]. At sufficiently low temperatures $k_B T < \Delta_2 - \Delta_1$, these non-equilibrium quasiparticles will accumulate in the region with a lower gap, which is layer 1 in the model (see Fig. 10.3(a)). Since layer 1 has a smaller volume than layer 2, this leads to a relatively high density of quasiparticles at the junction. The loss is directly proportional to the density of quasiparticles at the junction [15]; so, this high density at the junction leads to an increase in dissipation.

The interesting part happens when the temperature is increased to the range $\Delta_2 - \Delta_1 < k_B T \ll \Delta_1$. In this range, there is still a negligible generation of equilibrium thermal quasiparticles. However, the background non-equilibrium quasiparticles that were trapped in the lower gap layer 1 now have enough thermal energy to occupy layer 2 as well. Since the rate of production of non-equilibrium quasiparticles is assumed to be relatively constant, this spreading into both layers leads to a noticeable reduction in

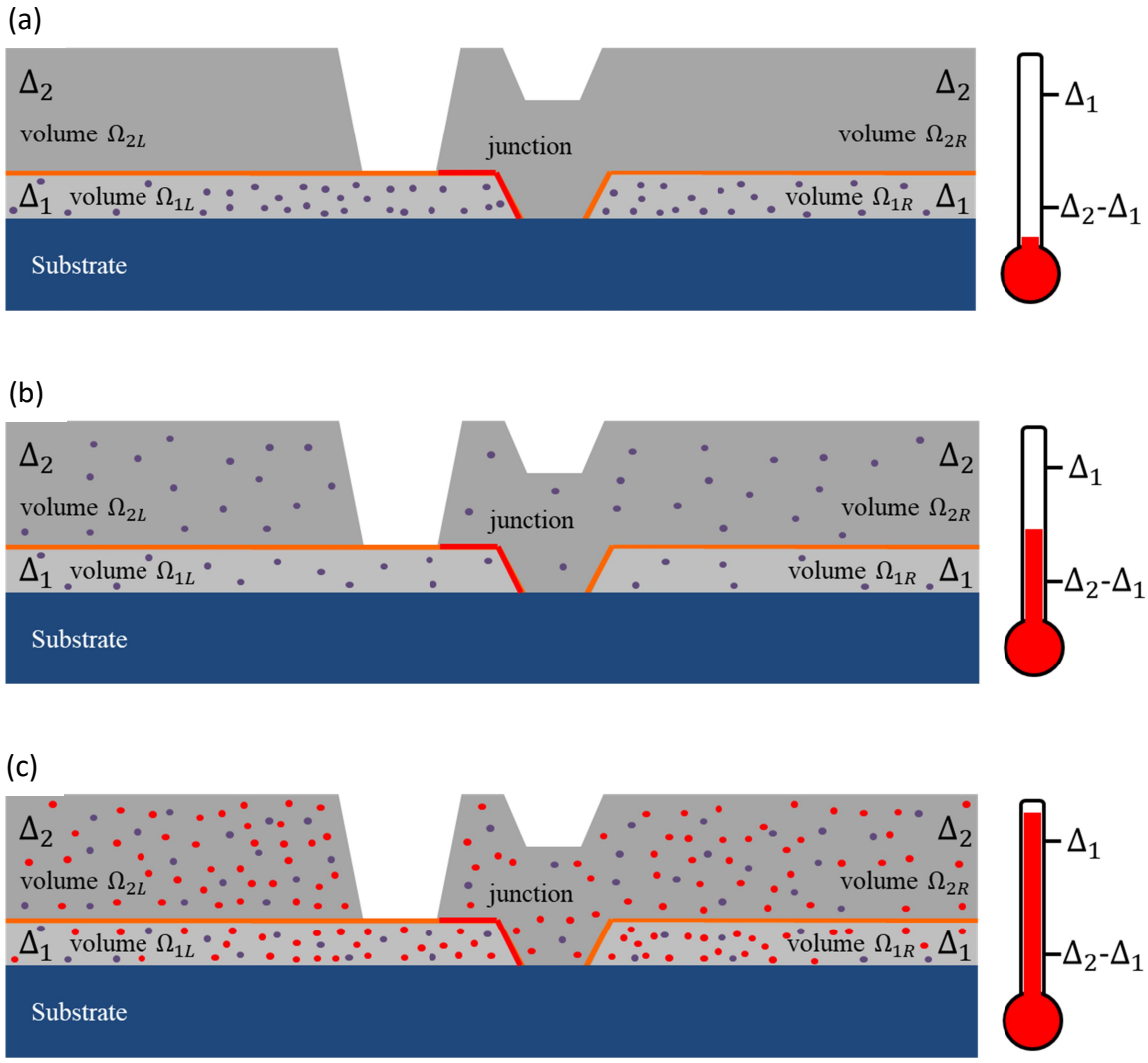

Fig. 10.3: (a) Schematic of junction showing background non-equilibrium quasiparticles (purple dots) accumulating in layer 1 at low temperatures. (b) Schematic of junction at temperatures $T > (\Delta_2 - \Delta_1)/k_B T$ showing that the non-equilibrium quasiparticles occupy both layers of the device. (c) Schematic of junction at temperature that is high enough that the density of thermal equilibrium quasiparticles (red dots) dominates.

quasiparticle density at the junction (see Fig. 10.3(b)) and a corresponding increase in the relaxation time T_1 of the transmon.

When the temperature of our Al devices is further increased to 0.15 K $\approx T_c/10$, the number of equilibrium thermal quasiparticles begins to increase to a significant level. This leads to the relaxation time rapidly declining with increasing T.

The key factors in this model are the difference $\Delta_2 - \Delta_1$ in gap values for the two layers, the volume ratio Ω_2/Ω_1 for the two layers, and the temperature-dependent re-arrangement of the non-equilibrium quasiparticles. As I discuss in Chapter 11, Rui Zhang first observed an increase of almost a factor of two in one of her devices as T increased from ~20 mK to 100 mK.

10.2 Quantum Current Noise Spectrum

In this section, I examine the effect quasiparticles have on the relaxation time T_1 of a transmon. For this analysis, I will assume that quasiparticles are the dominant relaxation mechanism. The rate at which the quasiparticles cause first excited state of the transmon to decay to the ground state can be written as [16]

$$\Gamma_{e\to g} = \frac{E_c}{h f_{ge} e^2} S_I\left(f_{ge}\right), \tag{10.1}$$

where $E_c = e^2/2C$ is the charging energy of the transmon (see chapter 4), f_{ge} is the transition frequency between the ground and first excited state, and $S_I(f)$ is the quasiparticle current noise power spectral density at frequency f [17]. This power spectral density is a double-sided quantum noise spectrum where positive frequencies correspond to downward transitions and where negative frequencies produce excitations

from the ground to the excited state of the transmon. The corresponding excitation rate due to quasiparticles is then

$$\Gamma_{g\to e} = \frac{E_c}{h|f_{ge}|e^2} S_I\left(-|f_{ge}|\right), \tag{10.2}$$

The relaxation time of the transmon, which is the time it will take the state of an undriven qubit to decay from the excited state back to its steady-state occupancy, involves both $\Gamma_{g\to e}$ and $\Gamma_{e\to g}$. Consider an un-driven transmon qubit that has probability P_e of being in the excited state and P_g of being in the ground state. Ignoring occupancy in and transitions to higher levels, the probabilities sum to unity (i.e. $P_e + P_g = 1$), and the rates at which these probabilities change are then given by

$$\frac{dP_e}{dt} = -\Gamma_{e\to g}P_e + \Gamma_{g\to e}P_g \tag{10.3}$$

$$\frac{dP_g}{dt} = \Gamma_{e\to g}P_e - \Gamma_{g\to e}P_g. \tag{10.4}$$

The solution to this system of equations for the excited state probability is given by

$$P_e(t) = P_e(\infty) + \left(P_e(0) - P_e(\infty)\right)e^{-t/T_1}, \tag{10.5}$$

where $P_1(0)$ is the initial probability of being in the excited state,

$$P_e(\infty) = \frac{\Gamma_{g\to e}}{\Gamma_{g\to e} + \Gamma_{e\to g}} \tag{10.6}$$

is the steady state solution to Eqs. (10.3) and (10.4), and

$$T_1 \equiv \frac{1}{\Gamma_{g\to e} + \Gamma_{e\to g}}. \tag{10.7}$$

Thus, to find an expression for the relaxation time T_1, I need to find both $\Gamma_{g\to e}$ and $\Gamma_{e\to g}$.

10.2.1 Noise Density for Positive Frequencies

In general, I can write $S_I(f)$ in terms of the quasiparticle current flowing through the junction from the left to right, $I_{L\to R}$, and from right to left, $I_{R\to L}$, as [18]

$$S_I(f_{ge}) = e(I_{L\to R} + I_{R\to L})\,. \tag{10.8}$$

Note that the total current flowing through the junction from $L \to R$ is $I = (I_{L\to R} - I_{R\to L})$. These currents $I_{L\to R}$ and $I_{R\to L}$ depend on the transition frequency of the qubit, the temperature, the superconducting gap for each electrode, the density of quasiparticles on each side of the junction, the height of the tunnel junction's barrier, and the junction preparation.

Here, I consider an unbiased S-I-S (superconductor-insulator-superconductor) junction with $hf_{01} \ll \Delta_1 < \Delta_2$. I am particularly interested in the case where non-equilibrium quasiparticles have been created due to a pair-breaking process, which in the semi-conductor model of a superconductor [15] produces an equal number of quasiparticles with energy $E > 0$ and $E < 0$, where the zero of energy is taken at the Fermi level. In this case, the currents in (10.8) will have contribution from electron-like quasiparticles and hole-like quasiparticles. For example, the current from the left to the right side in the junction is given by [15]

$$I_{L\to R} = \frac{1}{eR_n}\int_{-\infty}^{\infty} \frac{E\Theta(|E-\Delta_1|)}{\sqrt{E^2-\Delta_1^2}} \frac{(E+hf_{ge})\Theta(|E+hf_{ge}-\Delta_2|)}{\sqrt{(E+hf_{ge})^2-\Delta_2^2}} f_L(E,\mu_{1L})\Big(1 - f_R(E+hf_{ge},\mu_{2R})\Big)\,dE, \tag{10.9}$$

where $f(E,\mu)$ is the Fermi-Dirac distribution function given by

$$f(E,\mu) = \frac{1}{1+e^{(E-\mu)/k_BT}}\,, \tag{10.10}$$

μ_{1L} is the chemical potential in region 1 on the left, μ_{2R} is the chemical potential in region 2 on the right, R_n is the tunneling resistance of the junction in the normal state, and $\Theta(E)$ is the Heaviside step function. I would like to again emphasize that Eq. (10.9) is explicitly the current only from the left to the right and not the net current through the junction [15].

Equation (10.9) may be broken into two integrals, for the $E > 0$ and $E < 0$ cases. I can write $I_{L\to R} = I^{+}_{L\to R} + I^{-}_{L\to R}$, where the positive and negative energy integrals are given by

$$I^{+}_{L\to R} = \frac{1}{eR_n}\int_{\Delta_1}^{\infty} \frac{E}{\sqrt{E^2-\Delta_1^2}} \frac{E+hf_{ge}}{\sqrt{\left(E+hf_{ge}\right)^2-\Delta_2^2}} f_L(E,\mu_{1L})\Big(1 - f_R\left(E+hf_{ge},\mu_{2R}\right)\Big)\,dE. \tag{10.11}$$

and

$$I^{-}_{L\to R} = \frac{1}{eR_n}\int_{-\infty}^{-\Delta_2-hf_{ge}} \frac{|E|}{\sqrt{E^2-\Delta_1^2}} \frac{\left|E+hf_{ge}\right|}{\sqrt{\left(E+hf_{ge}\right)^2-\Delta_2^2}} f_L(E,-\mu_{1L})\Big(1 - f_R\left(E+hf_{ge},-\mu_{2R}\right)\Big)\,dE \tag{10.12}$$

Note that the limits of integration are set by the Heaviside function in Eq. (10.9) and the choice $\Delta_2 - \Delta_1 < hf_{ge}$. Also, since Eq. (10.12) is for hole-like quasiparticles in the semiconductor model, the chemical potential for these excitations must be taken as the negative of the chemical potential of the electron-like excitations.

Now, consider Eq. (10.12). First, I make the change of variable $E' = -\left(E+hf_{ge}\right)$, which gives

$$I_{L\to R}^{-}=\int_{\Delta_2}^{\infty}\frac{\left|E'+hf_{ge}\right|}{\sqrt{\left(E'+hf_{ge}\right)^2-\Delta_1^2}}\frac{|E'|}{\sqrt{(E')^2-\Delta_2^2}}f_L\left(-\left(E'+hf_{ge}\right),-\mu_{1L}\right)\left(1\right.$$
$$\left.-f_R(-E',-\mu_{2R})\right)dE'. \tag{10.13}$$

I now assume that the quasiparticles in different regions have thermalized and that their distributions have the same temperature T. These assumptions imply that in each region $f(-E,-\mu)=1-f(E,\mu)$, which gives

$$I_{L\to R}^{-}=\int_{\Delta_2}^{\infty}\frac{\left|E'+hf_{ge}\right|}{\sqrt{\left(E'+hf_{ge}\right)^2-\Delta_1^2}}\frac{|E'|}{\sqrt{(E')^2-\Delta_2^2}}\left(1\right.$$
$$\left.-f_L\left(\left(E'+hf_{ge}\right),\mu_{1L}\right)\right)f_R(E',\mu_{2R})dE'. \tag{10.14}$$

Altogether, this gives

$$I_{L\to R}=\frac{1}{eR_n}\left(\int_{\Delta_1}^{\infty}\frac{E}{\sqrt{E^2-\Delta_1^2}}\frac{E+hf_{ge}}{\sqrt{\left(E+hf_{ge}\right)^2-\Delta_2^2}}f_L(E,\mu_{1L})\left(1-f_R\left(E+hf_{ge},\mu_{2R}\right)\right)dE+\right.$$
$$\left.\int_{\Delta_2}^{\infty}\frac{E+hf_{ge}}{\sqrt{\left(E+hf_{ge}\right)^2-\Delta_1^2}}\frac{E}{\sqrt{E^2-\Delta_2^2}}\left(1-f_L\left(\left(E+hf_{ge}\right),\mu_{1L}\right)\right)f_R(E,\mu_{2R})dE\right). \tag{10.15}$$

For the right-to-left current, on the other hand, I have

$$I_{R\to L}=\frac{1}{eR_n}\int_{-\infty}^{\infty}\frac{\left(E+hf_{ge}\right)\Theta\left(\left|E+hf_{ge}-\Delta_1\right|\right)}{\sqrt{\left(E+hf_{ge}\right)^2-\Delta_1^2}}\frac{\Theta(|E-\Delta_2|)E}{\sqrt{E^2-\Delta_2^2}}\left(1\right.$$
$$\left.-f_L(E,\mu_{1L})\right)f_R\left(\left(E+hf_{ge}\right),\mu_{2R}\right)dE, \tag{10.16}$$

A similar analysis on this produces

$$I_{R\to L}=\frac{1}{eR_n}\left(\int_{\Delta_2}^{\infty}\frac{E+hf_{ge}}{\sqrt{\left(E+hf_{ge}\right)^2-\Delta_1^2}}\frac{E}{\sqrt{E^2-\Delta_2^2}}\left(1-f_L\left(\left(E+hf_{ge}\right),\mu_{1L}\right)\right)f(E,\mu_{2R})dE+\right.$$

$$\left.\int_{\Delta_1}^{\infty}\frac{E}{\sqrt{E^2-\Delta_1^2}}\frac{E+hf_{ge}}{\sqrt{\left(E+hf_{ge}\right)^2-\Delta_2^2}}f_L(E,\mu_{1L})\left(1-f\left(E+hf_{ge},\mu_{2R}\right)\right)dE\right). \tag{10.17}$$

Before I continue, I want to point out that the first integral in Eq. (10.15) and the second integral in Eq. (10.17) are identical. Similarly, the second integral term in Eq. (10.15) is equivalent to the first integral in Eq. (10.17). Thus, Eq. (10.8) reduces to

$$S_I\left(f_{ge}\right)=2e(I_{L\to R}^{+}+I_{R\to L}^{+})\,, \tag{10.18}$$

where

$$I_{L\to R}^{+}=\frac{1}{eR_n}\int_{\Delta_1}^{\infty}\frac{E}{\sqrt{E^2-\Delta_1^2}}\frac{E+hf_{ge}}{\sqrt{\left(E+hf_{ge}\right)^2-\Delta_2^2}}f_L(E,\mu_{1L})\left(1-f_R\left(E+hf_{ge},\mu_{2R}\right)\right)dE \tag{10.19}$$

and

$$I_{R\to L}^{+}=\frac{1}{eR_n}\int_{\Delta_2}^{\infty}\frac{E+hf_{ge}}{\sqrt{\left(E+hf_{ge}\right)^2-\Delta_1^2}}\frac{E}{\sqrt{E^2-\Delta_2^2}}\left(1-f_L\left(\left(E+hf_{ge}\right),\mu_{1L}\right)\right)f(E,\mu_{2R})dE. \tag{10.20}$$

Typically, Eqs. (10.19) and (10.20) must be evaluated numerically [15]. However, approximate expressions can be obtained in interesting limits. These are not only useful for a better understanding of the phenomenon, but can be accurate enough to allow fitting to measured results.

10.2.2 Approximate Analytical Expressions for $I_{L\to R}^{+}$ and $I_{R\to L}^{+}$

The first limit I consider is

$$\Delta_1-\mu_{1L}\gg k_BT \tag{10.21}$$

and

$$\Delta_2 - \mu_{2R} \gg k_B T \tag{10.22}$$

Since both the gaps and the chemical potential are dependent on temperature. These limits only hold if the temperature is not too small or too large. However, both of these limits are well-obeyed for the temperature range that I an interested in (0.01 K to 0.5 K) for our Al devices.

I now consider only the expression for $I^{+}_{L\to R}$ in Eq. (10.19). There are four factors in the integrand that need to be addressed. The first factor is $E/\sqrt{E^2 - \Delta_1^2}$. This piece diverges at $E = \Delta_1$, which is the lower limit of the integral and asymptotes to a value of 1 for $E \gg \Delta_1$. Due to this rapid divergence, it is important that it be handled carefully in the integration. The second factor is $\left(E + hf_{ge}\right)/\sqrt{\left(E + hf_{ge}\right)^2 - \Delta_2^2}$. In the limit $E \geq \Delta_1$, $\Delta_1 + hf > \Delta_2$, and $\Delta_2 > \Delta_1$, this term is varying with E but does not diverge. Since this term does not vary dramatically over the region of integration, the integral can be approximated by treating it as a constant, allowing it to be pulled out of the integral, albeit with the energy E set equal to some characteristic value. More formally, one could do a Taylor series expansion about a characteristic point and retain higher terms. Simply plugging in $E = \Delta_1$ is an obvious choice. However, by comparing the numerical integral of Eq. (10.19) to the final, fully simplified expression, we have found that a much better approximation is to use

$$\alpha_1 \equiv \frac{\Delta_1 + hf_{ge} + x_0 k_B T}{\sqrt{\left(\Delta_1 + hf_{ge} + x_0 k_B T\right)^2 - \Delta_2^2}}. \tag{10.23}$$

The term $x_0 k_B T$ can be thought of as the effective thermal energy of the quasiparticles that contribute to the loss. By comparing the approximated expression to the full

integrals we found that a value of $x_0 \approx 0.3$ produced good agreement with the numerical integration for typical parameters.

The third and fourth in the integrand in Eq. (10. 19) involve the two Fermi-Dirac distribution terms. By distributing the terms, I get

$$f_L(E,\mu_L) - f_L(E,\mu_L)f_R\big(E + hf_{ge},\mu_R\big). \tag{10.24}$$

As I'll show below, the first of these two terms is closely related to the density of quasiparticles, and it is important to leave in the integrand since it proved an exponential cut-off at high energies. However, the integral involving the second of these terms is a correction to the overall densities and must be considered further. For that term I have

$$f_L(E,\mu_L)f_R\big(E + hf_{ge},\mu_R\big) = \left(\frac{1}{1+e^{(E-\mu_L)/k_BT}}\right)\left(\frac{1}{1+e^{\left(E+hf_{ge}-\mu_R\right)/k_BT}}\right). \tag{10.25}$$

In the limit $hf_{ge} > \Delta_2 - \Delta_1$, this may be approximated as

$$\begin{aligned} f_L(E,\mu_L)f_R\big(E + hf_{ge},\mu_R\big) &\approx \big(e^{-(E-\mu_L)/k_BT}\big)\big(e^{-\left(E+hf_{ge}-\mu_R\right)/k_BT}\big) \\ &= e^{-\left(2E+hf_{ge}-\mu_L-\mu_R\right)/k_BT}. \end{aligned} \tag{10.26}$$

Now, putting this together, the integral in Eq. (10.19) yields the approximate expression

$$I^{+}_{L\to R} \approx \frac{\alpha_1}{eR_n}\left(\int_{\Delta_1}^{\infty}\frac{E}{\sqrt{E^2-\Delta_1^2}}f_L(E,\mu_{1L})dE - e^{\frac{-(hf_{ge}-\mu_L-\mu_R)}{k_BT}}\int_{\Delta_1}^{\infty}\frac{E}{\sqrt{E^2-\Delta_1^2}}e^{\frac{-2E}{k_BT}}dE\right). \tag{10.27}$$

What now remains are two considerably simpler integrals. The first of these can be found in ref. [15] and is given by

$$\int_{\Delta_1}^{\infty}\frac{E}{\sqrt{E^2-\Delta_1^2}}f_L(E,\mu_{1L})dE = \frac{n_{1L}(T)}{4N(0)}, \tag{10.28}$$

where $n_{1L}(T)$ is the total density of quasiparticles (both equilibrium and non-equilibrium) in region $1L$ and $N(0)$ is the density of states of electrons with up spins in the normal state. This last quantity is a material-specific constant, which I will take as

$$N(0) = \frac{3n_e}{4\varepsilon_F}, \tag{10.29}$$

where n_e is the density of electrons in the normal state and ε_F is the Fermi energy of the material.

The second integral in Eq. (10.27) is a little more involved. To start, I make the substitution $x = 2(E - \Delta_1)/k_BT$, which with a little algebra gives

$$I_2 = \int_{\Delta_1}^{\infty} \frac{E}{\sqrt{E^2 - \Delta_1^2}} e^{\frac{-2E}{k_BT}} dE = \frac{1}{2}\sqrt{k_BT}\, e^{\frac{-2\Delta_1}{k_BT}} \int_0^{\infty} \left(\frac{2\Delta_1 + xk_BT}{\sqrt{4\Delta_1 + xk_BT}}\right) \frac{e^{-x}}{\sqrt{x}} dx. \tag{10.30}$$

As in the analysis above, I again consider each factor in the integrand in Eq. (10.30) to see what can be made of it. The factor in parenthesis is relatively slowly-varying over a wide range of x values. It eventually diverges significantly for $x > \Delta_1/k_BT$, but the increase is slow as it is only proportional to $\sqrt{x}$. The other term (namely $e^{-x}/\sqrt{x}$) approaches zero exponentially fast for $x \gg 1$ and cuts off the integrand at large x values. This suggests, treating the first factor as a constant and taking it out of the integral, again with some characteristic value for x that produces a good approximation. This yields

$$I_2 \approx \frac{1}{2}\sqrt{k_BT}\, e^{\frac{-2\Delta_1}{k_BT}} \frac{2\Delta_1 + x_0k_BT}{\sqrt{4\Delta_1 + x_0k_BT}} \int_0^{\infty} \frac{e^{-x}}{\sqrt{x}} dx, \tag{10.31}$$

where I will use $x_0 = 0.3$, which is the characteristic value I introduced above for Eq. (10.23).

The integral in Eq. (10.31) is simply

$$\int_0^\infty \frac{e^{-x}}{\sqrt{x}}dx = \Gamma\left(\frac{1}{2}\right) = \sqrt{\pi}. \tag{10.32}$$

Putting this all back together into Eq. (10.27) yields

$$I^+_{L\to R} \approx \frac{\alpha_1}{eR_n}\left(\frac{n_{qp,1L}(T)}{4N(0)} - e^{\frac{\mu_L+\mu_R-hf_{ge}}{k_BT}}\frac{1}{2}\sqrt{\pi k_BT}e^{\frac{-2\Delta_1}{k_BT}}\frac{2\Delta_1 + x_0k_BT}{\sqrt{4\Delta_1 + x_0k_BT}}\right). \tag{10.33}$$

While Eq. (10.33) certainly works as a good approximation, it still involves the chemical potentials. The chemical potential is intimately connected with the density of quasiparticles via Eq. (10.28). With the limit I give in Eqs. (10.21) and (10.22), this integral may be approximated as

$$\frac{n_{1L}(T)}{4N(0)} = \int_{\Delta_1}^\infty \frac{E}{\sqrt{E^2-\Delta_1^2}}f_L(E,\mu_{1L})dE \approx e^{\frac{\mu_L}{k_BT}}\int_{\Delta_1}^\infty \frac{E}{\sqrt{E^2-\Delta_1^2}}e^{\frac{-E}{k_BT}}dE. \tag{10.34}$$

This approximation is very similar to one I used in arriving at Eq. (10.33); however, the exponential term now does not have the factor of 2. By making the substitution $x = (E-\Delta_1)/k_BT$, pulling out the slowly varying portion of the integrand with some characteristic value, and then solving for e^{μ_L/k_BT} I get

$$e^{\frac{\mu_L}{k_BT}} \approx \frac{n_{1L}(T)}{4N(0)\sqrt{\pi k_BT}}e^{\frac{\Delta_1}{k_BT}}\frac{\sqrt{2\Delta_1 + x_0k_BT}}{\Delta_1 + x_0k_BT}, \tag{10.35}$$

where, $x_0 = 0.3$ is again chosen to get a more accurate approximation. The same analysis yields

$$e^{\frac{\mu_R}{k_BT}} \approx \frac{n_{2R}(T)}{4N(0)\sqrt{\pi k_BT}}e^{\frac{\Delta_2}{k_BT}}\frac{\sqrt{2\Delta_2 + x_0k_BT}}{\Delta_2 + x_0k_BT}, \tag{10.36}$$

where $n_{2R}(T)$ is the total density of quasiparticles in region 2R.

Putting all the pieces together yields

$$I_{L\to R}^{+} \approx \frac{\alpha_1}{eR_n}\frac{n_{1L}(T)}{4N(0)}\left(1 - e^{\frac{\Delta_2-\Delta_1-hf_{ge}}{k_BT}}\gamma_1\frac{n_{2R}(T)}{8N(0)\sqrt{\pi k_BT\Delta_2}}\right), \tag{10.37}$$

where I have defined

$$\gamma_1 \equiv \frac{(2\Delta_1 + x_0k_BT)^{\frac{3}{2}}}{(\Delta_1 + x_0k_BT)}\frac{\sqrt{2\Delta_2 + x_0k_BT}}{(\Delta_2 + x_0k_BT)}\frac{\sqrt{\Delta_2}}{\sqrt{4\Delta_1 + x_0k_BT}} \approx 2\,. \tag{10.38}$$

In the limit $x_0k_BT \ll \Delta_1$, γ_1 is very nearly equal to 2.

The same analysis may be applied to the right-to-left current to obtain

$$I_{R\to L}^{+} \approx \frac{\alpha_2}{eR_n}\frac{n_{2R}(T)}{4N(0)}\left(1 - e^{\frac{\Delta_1-\Delta_2-hf_{ge}}{k_BT}}\gamma_2\frac{n_{1L}(T)}{8N(0)\sqrt{\pi k_BT\Delta_1}}\right), \tag{10.39}$$

where

$$\alpha_2 \equiv \frac{\Delta_2 + hf_{ge} + x_0k_BT}{\sqrt{\left(\Delta_2 + hf_{ge} + x_0k_BT\right)^2 - \Delta_1^2}}\,. \tag{10.40}$$

and

$$\gamma_2 \equiv \frac{(2\Delta_2 + x_0k_BT)^{\frac{3}{2}}}{\Delta_2 + x_0k_BT}\frac{(2\Delta_1 + x_0k_BT)^{\frac{1}{2}}}{\Delta_1 + x_0k_BT}\frac{\sqrt{\Delta_1}}{(4\Delta_2 + x_0k_BT)^{\frac{1}{2}}} \approx 2\,. \tag{10.41}$$

Now that I have expressions for both $I_{L\to R}^{+}$ and $I_{R\to L}^{+}$, I can put them back into Eq. (10.18) to find the current noise power spectral density for positive frequencies

$$\begin{aligned} S_I(f_{ge}) \approx \frac{1}{R_nN(0)}\Bigg[&\alpha_1 n_{1L}(T)\left(1 - e^{\frac{\Delta_2-\Delta_1-hf_{ge}}{k_BT}}\gamma_1\frac{n_{2R}(T)}{8N(0)\sqrt{\pi k_BT\Delta_2}}\right) \\ &+ \alpha_2 n_{2R}(T)\left(1 - e^{\frac{\Delta_1-\Delta_2-hf_{ge}}{k_BT}}\gamma_2\frac{n_{1L}(T)}{8N(0)\sqrt{\pi k_BT\Delta_1}}\right)\Bigg]. \end{aligned} \tag{10.42}$$

Notice in Eq. (10.42) that there are terms which are second order in quasiparticle density. Since we expect the density of quasiparticles to be very small in the temperature range to

be quite small, these second order terms should be ultimately negligible. Thus for $\Delta_2 - \Delta_1 > hf_{ge}$, Eq. (10.42) reduces to

$$S_I(f_{ge}) \approx \frac{1}{R_n N(0)} [\alpha_1 n_{1L}(T) + \alpha_2 n_{2R}(T)], \tag{10.43}$$

where I have simply discarded the second order terms.

10.2.3 Noise Density for Negative Frequencies

I still need an expression for the negative frequency part of the noise spectrum. The analysis is similar to that of the positive frequency part; the main differences are in the integration limits. For the left-to-right current expression, the negative frequency part is given by

$$I^+_{L\to R} = \frac{1}{eR_n}\int_{\Delta_2}^{\infty} \frac{E+h|f_{ge}|}{\sqrt{(E+h|f_{ge}|)^2-\Delta_1^2}} \frac{E}{\sqrt{E^2-\Delta_2^2}} f_L(E+h|f_{ge}|,\mu_{1L})(1-f_R(E,\mu_{2R}))dE. \tag{10.44}$$

Notice the lower limit of Δ_2. On the other hand, the right-to-left term is given by

$$I^+_{R\to L} = \frac{1}{eR_n}\int_{\Delta_1}^{\infty} \frac{E}{\sqrt{E^2-\Delta_1^2}} \frac{E+h|f_{ge}|}{\sqrt{(E+h|f_{ge}|)^2-\Delta_2^2}} f_R(E+h|f_{ge}|,\mu_{2R})(1-f_L(E,\mu_{1L}))dE, \tag{10.45}$$

The approximations for these integrals can be obtained using the approach in Section 6.2.3. As an example, one finds

$$I^+_{L\to R} \approx \frac{\alpha_3}{eR_n}\left(\int_{\Delta_2}^{\infty} \frac{E}{\sqrt{E^2-\Delta_2^2}} f_L(E+h|f_{ge}|,\mu_{1L})dE - e^{\frac{-(hf_{ge}-\mu_L-\mu_R)}{k_BT}} \int_{\Delta_2}^{\infty} \frac{E}{\sqrt{E^2-\Delta_2^2}} e^{\frac{-2E}{k_BT}} dE\right), \tag{10.46}$$

where

$$\alpha_3 \equiv \frac{\Delta_2 + h|f_{ge}| + x_0 k_B T}{\sqrt{\left(\Delta_2 + h|f_{ge}| + x_0 k_B T\right)^2 - \Delta_1^2}}. \tag{10.47}$$

For the first integral in (10.46) I can write

$$\int_{\Delta_2}^{\infty} \frac{E}{\sqrt{E^2 - \Delta_2^2}} f_L\left(E + h|f_{ge}|, \mu_{1L}\right) dE \approx e^{\frac{\mu_{1L} - h|f_{ge}|}{k_B t}} \int_{\Delta_2}^{\infty} \frac{E}{\sqrt{E^2 - \Delta_2^2}} e^{\frac{-E}{k_B T}} dE. \tag{10.48}$$

As in section 10.2.3, this integral may be further reduced to

$$\begin{aligned} &\int_{\Delta_2}^{\infty} \frac{E}{\sqrt{E^2 - \Delta_2^2}} f_L\left(E + h|f_{ge}|, \mu_{1L}\right) dE \\ &\qquad \approx e^{\frac{\mu_{1L} - h|f_{ge}|}{k_B t}} e^{\frac{-\Delta_2}{k_B T}} \sqrt{\pi k_B T} \frac{\Delta_2 + x_0 k_B T}{\sqrt{2\Delta_2 + x_0 k_B T}}, \end{aligned} \tag{10.49}$$

The second integral in (10.46) gives

$$\int_{\Delta_2}^{\infty} \frac{E}{\sqrt{E^2 - \Delta_2^2}} e^{\frac{-2E}{k_B T}} dE \approx e^{\frac{-2\Delta_2}{k_B T}} \frac{\sqrt{\pi k_B T}}{2} \frac{2\Delta_2 + x_0 k_B T}{\sqrt{4\Delta_2 + x_0 k_B T}}. \tag{10.50}$$

Putting these together yields

$$I_{L\to R}^{+} \approx \frac{\alpha_3}{eR_n} \sqrt{\pi k_B T} e^{\frac{\mu_{1L} - h|f_{ge}| - \Delta_2}{k_B T}} \frac{\Delta_2 + x_0 k_B T}{\sqrt{2\Delta_2 + x_0 k_B T}} \left(1 - e^{\frac{\mu_{2R} - \Delta_2}{k_B T}} \frac{1}{2} \frac{(2\Delta_2 + x_0 k_B T)^{\frac{3}{2}}}{(\Delta_2 + x_0 k_B T)\sqrt{4\Delta_2 + x_0 k_B T}}\right). \tag{10.51}$$

By again using Eqs. (10.35) and (10.36) I get

$$I_{L\to R}^{+} \approx \frac{\alpha_4}{eR_n} \frac{n_{1L}(T)}{N(0)} e^{\frac{\Delta_1 - \Delta_2 - h|f_{ge}|}{k_B T}} \left(1 - \frac{n_{2R}(T)}{8N(0)\sqrt{\pi k_B T \Delta_2}} \gamma_3\right), \tag{10.52}$$

where I have defined

$$\alpha_4 \equiv \alpha_3 \frac{\sqrt{2\Delta_1 + x_0 k_B T}}{\Delta_1 + x_0 k_B T} \frac{\Delta_2 + x_0 k_B T}{\sqrt{2\Delta_2 + x_0 k_B T}} \tag{10.53}$$

and

$$\gamma_3 \equiv \frac{(2\Delta_2 + x_0 k_B T)^2 \sqrt{\Delta_2}}{(\Delta_2 + x_0 k_B T)^2 \sqrt{4\Delta_2 + x_0 k_B T}} \approx 2. \tag{10.54}$$

Following a similar analysis of Eq. (10.45), I find

$$I^+_{R\to L} \approx \frac{\alpha_6}{eR_n} \frac{n_{2R}(T)}{N(0)}\, e^{\frac{\Delta_2 - \Delta_1 - h|f_{ge}|}{k_B T}} \left(1 - \frac{n_{1L}(T)}{8N(0)\sqrt{\pi k_B T \Delta_1}} \gamma_4\right), \tag{10.55}$$

where

$$\alpha_6 \equiv \alpha_5 \frac{\sqrt{2\Delta_2 + x_0 k_B T}}{\Delta_2 + x_0 k_B T} \frac{\Delta_1 + x_0 k_B T}{\sqrt{2\Delta_1 + x_0 k_B T}}, \tag{10.56}$$

$$\alpha_5 \equiv \frac{\Delta_1 + h|f_{ge}| + x_0 k_B T}{\sqrt{\left(\Delta_1 + h|f_{ge}| + x_0 k_B T\right)^2 - \Delta_2^2}}, \tag{10.57}$$

and

$$\gamma_4 \equiv \frac{(2\Delta_1 + x_0 k_B T)^2 \sqrt{\Delta_1}}{(\Delta_1 + x_0 k_B T)^2 \sqrt{4\Delta_1 + x_0 k_B T}} \approx 2. \tag{10.58}$$

Using Eqs. (10.52) and (10.55) I find the current noise power spectral density for negative frequencies is given by

$$\begin{aligned} S_I(-|f_{ge}|) \approx \frac{1}{R_n N(0)} \Bigg[& \alpha_4 n_{1L}(T) e^{\frac{\Delta_1 - \Delta_2 - h|f_{ge}|}{k_B T}} \left(1 - \frac{n_{2R}(T)}{8N(0)\sqrt{\pi k_B T \Delta_2}} \gamma_3\right) \\ & + \alpha_6 n_{2R}(T) e^{\frac{\Delta_2 - \Delta_1 - h|f_{ge}|}{k_B T}} \left(1 - \frac{n_{1L}(T)}{8N(0)\sqrt{\pi k_B T \Delta_1}} \gamma_4\right) \Bigg]. \end{aligned} \tag{10.59}$$

As with the positive frequency case, terms that are second order in the quasiparticle density are negligible, and this expression reduces to

$$S_I(-|f_{ge}|) \approx \frac{1}{R_n N(0)} \left[\alpha_4 n_{1L}(T) e^{\frac{\Delta_1 - \Delta_2 - h|f_{ge}|}{k_B T}} + \alpha_6 n_{2R}(T) e^{\frac{\Delta_2 - \Delta_1 - h|f_{ge}|}{k_B T}} \right]. \tag{10.60}$$

10.3 Relaxation Time Expression

With both the positive and negative frequency pieces of the noise in hand, I can plug Eq. (10.47) into Eqs. (10.1) to get

$$\Gamma_{e\to g} \approx \frac{1}{2\tau_0 n_e}\left[\alpha_1 n_{1L}(T) + \alpha_2 n_{2R}(T)\right]. \tag{10.61}$$

Similarly, plugging Eq. (10.60) into Eq. (10.2) gives

$$\Gamma_{g\to e} \approx \frac{1}{2\tau_0 n_e}\left[\alpha_4 n_{1L}(T) e^{\frac{\Delta_1-\Delta_2-h|f_{ge}|}{k_B T}} + \alpha_6 n_{2R}(T) e^{\frac{\Delta_2-\Delta_1-h|f_{ge}|}{k_B T}}\right], \tag{10.62}$$

where n_e is the density of electrons in the normal state and τ_0 is a characteristic time constant defined as

$$\tau_0 \equiv 3R_n C\left(\frac{hf_{ge}}{2\varepsilon_F}\right). \tag{10.63}$$

Thus Eq. 10.7 for the relaxation time gives

$$T_1(T) \approx \frac{2\tau_0 n_e}{n_{1L}(T)\left(\alpha_1 + \alpha_4 e^{\frac{\Delta_1-\Delta_2-h|f_{ge}|}{k_B T}}\right) + n_{2R}(T)\left(\alpha_2 + \alpha_6 e^{\frac{\Delta_2-\Delta_1-h|f_{ge}|}{k_B T}}\right)}. \tag{10.64}$$

Equation (10.64) gives a general expression for the temperature dependent relaxation time when the two junction electrodes have a different gap with $\Delta_1 < \Delta_2$ and $\Delta_2 - \Delta_1 < hf_{ge}$. It is interesting to view Eq. (10.64) in certain limits. In the low temperature range $k_B T \ll \Delta_2 - \Delta_1 < hf_{ge}$ the non-equilibrium quasiparticles will accumulate in layer 1 due to it having a lower gap than layer 2, which means that I expect $n_{2R} \ll n_{1L}$. In this limit, the expression reduces to

$$T_1(T) \approx \frac{2\tau_0 n_e}{\alpha_1 n_{1L}}, \tag{10.65}$$

which shows that the relaxation time is inversely proportional to the density of quasiparticles in layer 1 at low temperatures. Another interesting case to examine is where the gaps are equal to each other with $\Delta_1 = \Delta_2 = \Delta$. In this case it reduces to

$$T_1(T) \approx \frac{2\tau_0 n_e}{n_{1L}(T) + n_{2R}(T)} \frac{\sqrt{\left(\Delta + hf_{ge} + x_0 k_B T\right)^2 - \Delta^2}}{\left(1 + e^{\frac{-hf_{ge}}{k_B T}}\right)\left(\Delta + hf_{ge} + x_0 k_B T\right)} . \qquad (10.66)$$

For this regime, the relaxation time is inversely proportional to the average quasiparticle density in the two regions.

10.4 Quasiparticle Densities

To evaluate Eq. (10.64) and obtain T_1 as a function of temperature, I need to determine how the quasiparticle densities $n_{1L}(T)$ and $n_{2R}(T)$ depend on temperature. As I discussed above, this model must account for some constant, background source of non-equilibrium quasiparticles generated by an external source that causes pair-breaking. Some potential external sources are high-energy phonons from the substrate, high frequency microwaves, infrared photons from black-body radiation, or even optical photons [19-21]. In this section, I derive expressions for the temperature dependent quasiparticle densities $n_{1L}(T)$, $n_{2L}(T)$, $n_{1R}(T)$, and $n_{2R}(T)$. This derivation will primarily focus on the left pad of the transmon circuit; however, the right side follows in the exact manner as the left. At the end of this section I provide a summary of all the possible expressions for these densities.

To model the quasiparticle behavior, I will assume here that quasiparticle recombination can be ignored [22] but that quasiparticle traps [23] are present due to

trapped magnetic flux vortices which thread both superconducting layers of the transmon. This assumption leads to a natural explanation for some of the behavior we observed in our devices. These behaviors included run-to-run variations in T_1 and fluctuations in T_1 during the same cool-down. The run-to-run variations can be explained by different numbers of vortices trapped in the transmon pads during each run, and the mid-cooldown variations can be explained by vortex motion, driven by flux creep or changes in external field.

In addition to quasiparticle trapping, I also assume:

1. The left side of the transmon is comprised of a small-volume region and a large-volume region with volumes Ω_{1L} and Ω_{2L} and with gaps Δ_1 and Δ_2, respectively.
2. Similarly, the right side of the transmon is comprised of a small-volume and large-volume region with volumes Ω_{1R} and Ω_{2R} and with gaps Δ_1 and Δ_2, respectively.
3. $\Delta_1 < \Delta_2$
4. $\Omega_{1L} = \Omega_{1R} < \Omega_{2L} = \Omega_{2R}$
5. On each side (the left and the right) quasiparticles may be exchanged between layers 1 and 2.
6. The junction is formed between the layers 1L and 2R, and the loss in the junction will be determined by the quasiparticle density in these two layers.

With these assumptions I now write the rate equations governing the number of quasiparticles (N_{1L}, N_{2L}, N_{1R}, and N_{2R}) in the four distinct layers of the device ($1L$, $2L$, $1R$, and $2R$):

$$\frac{dN_{1L}}{dt} = \Gamma_{p1} + \Gamma_{th1} - \Gamma_{tr,1L}N_{1L} - \Gamma_{L1\to2}A\frac{N_{1L}}{\Omega_{1L}} + \Gamma_{L2\to1}A\frac{N_{2L}}{\Omega_{2L}}, \tag{10.67}$$

$$\frac{dN_{2L}}{dt} = \Gamma_{p2} + \Gamma_{th2} - \Gamma_{tr,2L}N_{1L} - \Gamma_{L2\to1}A\frac{N_{2L}}{\Omega_{2L}} + \Gamma_{L1\to2}A\frac{N_{1L}}{\Omega_{1L}}, \tag{10.68}$$

$$\frac{dN_{1R}}{dt} = \Gamma_{p1} + \Gamma_{th1} - \Gamma_{tr,1R}N_{1R} - \Gamma_{R1\to2}A\frac{N_{1R}}{\Omega_{1R}} + \Gamma_{R2\to1}A\frac{N_{2R}}{\Omega_{2R}}, \tag{10.69}$$

and

$$\frac{dN_{2R}}{dt} = \Gamma_{p2} + \Gamma_{th2} - \Gamma_{tr,2R}N_{1R} - \Gamma_{R2\to1}A\frac{N_{2R}}{\Omega_{2R}} + \Gamma_{R1\to2}A\frac{N_{1R}}{\Omega_{1R}}. \tag{10.70}$$

See Table 10.1 for a summary of all the parameters in Eqs. (10.67)-(10.70). In the steady state, all the time derivatives are zero, which yields for the left side of the transmon

$$\Gamma_{p1} + \Gamma_{th1} - \Gamma_{tr,1L}N_{1L} - \Gamma_{L1\to2}A\frac{N_{1L}}{\Omega_{1L}} + \Gamma_{L2\to1}A\frac{N_{2L}}{\Omega_{2L}} = 0 \tag{10.71}$$

and

$$\Gamma_{p2} + \Gamma_{th2} - \Gamma_{tr,2L}N_{1L} - \Gamma_{L2\to1}A\frac{N_{2L}}{\Omega_{2L}} + \Gamma_{L1\to2}A\frac{N_{1L}}{\Omega_{1L}} = 0\,. \tag{10.72}$$

By rearranging these equations I arrive at

$$N_{1L} = \frac{\Gamma_{p1} + \Gamma_{th1} + \Gamma_{L2\to1}A\frac{N_{2L}}{\Omega_{2L}}}{\Gamma_{tr,1L} + \Gamma_{L1\to2}\frac{A}{\Omega_{1L}}} \tag{10.73}$$

and

$$N_{2L} = \frac{\Gamma_{p2} + \Gamma_{th2} + \Gamma_{L1\to2}A\frac{N_{1L}}{\Omega_{1L}}}{\Gamma_{tr,2L} + \Gamma_{L2\to1}\frac{A}{\Omega_{2L}}}\,. \tag{10.74}$$

Table 10.1: Parameters used in the set of rate Eqs. (10.67)-(10.70).

Parameter	Description
N_{1L}, N_{2L}, N_{1R}, N_{2R}	Total number of quasiparticles in regions 1L, 2L, 1R, and 2R.
Γ_{p1}, Γ_{p2}	Non-equilibrium quasiparticle production rates in layers 1 and 2.
Γ_{th1}, Γ_{th2}	Thermal quasiparticle production rates in layers 1 and 2.
$\Gamma_{L1\rightarrow 2}$, $\Gamma_{L2\rightarrow 1}$	Quasiparticle transfer rates from regions 1L to 2L and from 2L to 1L.
$\Gamma_{R1\rightarrow 2}$, $\Gamma_{R2\rightarrow 1}$	Quasiparticle transfer rates from regions 1R to 2R and from 2R to 1R.
$\Gamma_{tr,1L}$, $\Gamma_{tr,2L}$, $\Gamma_{tr,1R}$, $\Gamma_{tr,2R}$	Quasiparticle trapping rates in regions 1L, 2L, 1R, and 2R.
Ω_{1L}, Ω_{2L}, Ω_{1R}, Ω_{2R}	Volumes of regions 1L, 2L, 1R, and 2R.
A_L, A_R	Top surface area of the transmon pads on the left and right side.

Substituting Eq. (10.74) into Eq. (10.73) gives (with some simplification)

$$N_{1L} = \frac{\left(\Gamma_{p1} + \Gamma_{th1}\right)\Gamma_{tr,2L} + \left(\Gamma_{p1} + \Gamma_{th1} + \Gamma_{p2} + \Gamma_{th2}\right)\Gamma_{L2\to1}\frac{A}{\Omega_{2L}}}{\Gamma_{tr,1L}\Gamma_{tr,2L} + \Gamma_{tr,1L}\Gamma_{L2\to1}\frac{A}{\Omega_{2L}} + \Gamma_{tr,2L}\Gamma_{L1\to2}\frac{A}{\Omega_{1L}}}, \qquad (10.75)$$

which is the general expression for the total number of quasiparticles in region 1L.

In order to write this in terms of the thermal and non-equilibrium quasiparticle densities, I need to establish how these densities are related to the various rates. First, consider the low-temperature limit (i.e. $k_B T < \Delta_2 - \Delta_1$). In this temperature regime there will be no thermal quasiparticles generated, which means that $\Gamma_{th1} = \Gamma_{th2} = 0$. Also, since $\Delta_1 < \Delta_2$, any quasiparticles present will accumulate in region 1, which means I can also set $\Gamma_{L1\to2} = 0$. Under this limit Eq. (10.74) becomes

$$N_{1L} = \frac{\Gamma_{p1}}{\Gamma_{tr,1L}} + \frac{\left(\frac{\Gamma_{p2}}{\Gamma_{tr,2L}}\right)\left(\frac{\Gamma_{tr,2L}}{\Gamma_{tr,1L}}\right)\left(\frac{\Gamma_{L2\to1}}{\Gamma_{tr,2L}}\frac{A}{\Omega_{2L}}\right)}{1 + \frac{\Gamma_{L2\to1}}{\Gamma_{tr,2L}}\frac{A}{\Omega_{2L}}}. \qquad (10.76)$$

Now, if there was no transfer from the second layer to the first (i.e. $\Gamma_{L2\to1} = 0$), then the second term would be zero, and I can then identify

$$N_{1L,ne} \equiv \frac{\Gamma_{p1}}{\Gamma_{tr,1L}}, \qquad (10.77)$$

where $N_{1L,ne}$ is the total number of non-equilibrium quasiparticles in region 1L in the $T = 0$ limit. This result is unsurprising as this is simply the ratio of the non-equilibrium quasiparticle generation rate to the trapping rate in region $1L$. A similar analysis for region $2L$ yields

$$N_{2L,ne} \equiv \frac{\Gamma_{p2}}{\Gamma_{tr,2L}}. \qquad (10.78)$$

To proceed further, I need to consider the quasiparticle trapping rate. Since I am considering trapping by vortices that thread both layers simultaneously, the rate at which quasiparticles are trapped in each layer will be proportional to the density of quasiparticles, the average speed v of the quasiparticles, the number of vortices N_v, and the effective surface area of the vortex $A_v = 2\pi r_v h_i$, where r_v is the effective radius of the vortex and h_i is the thickness of whichever layer is being considered (i.e. h_1 for layer 1 and h_2 for layer 2). With this assumption, I can then write

$$\Gamma_{tr,1L} = \frac{v(2\pi r_v h_1)N_v}{\Omega_{1L}} \tag{10.79}$$

and

$$\Gamma_{tr,2L} = \frac{v(2\pi r_v h_2)N_v}{\Omega_{2L}} \,. \tag{10.80}$$

The ratio of these two trapping rates yields

$$\frac{\Gamma_{tr,1L}}{\Gamma_{tr,2L}} = \frac{v(2\pi r_v h_1)N_v\Omega_{2L}}{v(2\pi r_v h_2)N_v\Omega_{1L}} = \frac{\Omega_{2L}}{h_2}\frac{h_1}{\Omega_{1L}} = \frac{A_L}{A_L} = 1\,. \tag{10.81}$$

With Eqs. (10.77), (10.78), and (10.81), the general expression Eq. (10.75) can be simplified to get

$$N_{1L} = \frac{\left(N_{1L,ne} + \frac{\Gamma_{th1}}{\Gamma_{tr,1L}}\right)\left(1 + \frac{\Gamma_{L2\to1}}{\Gamma_{tr,2L}}\frac{A}{\Omega_{2L}}\right) + \left(N_{2L,ne} + \frac{\Gamma_{th2}}{\Gamma_{tr,2L}}\right)\left(\frac{\Gamma_{L2\to1}}{\Gamma_{tr,1L}}\frac{A}{\Omega_{2L}}\right)}{1 + \frac{\Gamma_{L2\to1}}{\Gamma_{tr,2L}}\frac{A}{\Omega_{2L}} + \frac{\Gamma_{L1\to2}}{\Gamma_{tr,1L}}\frac{A}{\Omega_{1L}}}. \tag{10.82}$$

Now consider Eq. (10.82) when there are no sources of non-equilibrium quasiparticles and there is no transfer between layers. Only thermal quasiparticles will be present, and I can identify the purely thermal quasiparticle numbers as

$$N_{1L,th} \equiv \frac{\Gamma_{th1}}{\Gamma_{tr,1L}} \tag{10.83}$$

and

$$N_{2L,th} \equiv \frac{\Gamma_{th2}}{\Gamma_{tr,2L}} \ . \tag{10.84}$$

Using these definitions, I can write (10.82) as

$$N_{1L} = \frac{\left(N_{1L,ne} + N_{1L,th}\right)}{1 + \dfrac{\Gamma_{L2\to1}}{\Gamma_{tr,1L}}\dfrac{A}{\Omega_{1L}}} + \frac{\left(N_{2L,ne} + N_{2L,th}\right)}{1 + \dfrac{\Gamma_{L1\to2}}{\Gamma_{L2\to1}}\dfrac{\Omega_{2L}}{\Omega_{1L}} + \dfrac{\Gamma_{tr,1L}}{\Gamma_{L2\to1}}\dfrac{\Omega_{2L}}{A}} \ . \tag{10.85}$$

To simplify this expression I make the plausible assumption (due to the assumption that the quasiparticles accumulate in region $1L$) that the trapping in region 1L is relatively slow compared to the exchange from region $2L$ to region $1L$, which gives

$$\Gamma_{L2\to1}\frac{A}{\Omega_{1L}} > \Gamma_{L2\to1}\frac{A}{\Omega_{2L}} \gg \Gamma_{tr,1L} \ . \tag{10.86}$$

In this limit, Eq. (10.85) reduces to

$$N_{1L} = \frac{N_{1L,ne} + N_{1L,th} + N_{2L,ne} + N_{2L,th}}{1 + \dfrac{\Gamma_{L1\to2}}{\Gamma_{L2\to1}}\dfrac{\Omega_{2L}}{\Omega_{1L}}} \ . \tag{10.87}$$

To get this in terms of the density of quasiparticles in region 1L, I divide by Ω_{1L} to get

$$n_{1L} = \frac{n_{1L,ne} + n_{1L,th} + \left(n_{2L,ne} + n_{2L,th}\right)\dfrac{\Omega_{2L}}{\Omega_{1L}}}{1 + \dfrac{\Gamma_{L1\to2}}{\Gamma_{L2\to1}}\dfrac{\Omega_{2L}}{\Omega_{1L}}} \ , \tag{10.88}$$

where the lower case n denotes the density of quasiparticles in their respective regions.

The ratio $\Gamma_{L1\to2}/\Gamma_{L2\to1}$ can be found from elementary thermal considerations. In the steady state, if the two regions $1L$ and $2L$ are in thermal and diffusive equilibrium, there would be no net particle exchange between the two regions, and

$$\Gamma_{L1\to2} A \, n_{1L,th} = \Gamma_{L2\to1} A \, n_{2L,th} \ . \tag{10.89}$$

Hence, the ratio between the two transfer rates is given by the ratios of the thermal quasiparticle densities:

$$\frac{\Gamma_{L1\to 2}}{\Gamma_{L2\to 1}} = \frac{n_{2L,th}}{n_{1L,th}} \approx \frac{\sqrt{2\pi k_B T \Delta_2}\ e^{-\Delta_2/k_B T}}{\sqrt{2\pi k_B T \Delta_1}\ e^{-\Delta_1/k_B T}} = \sqrt{\frac{\Delta_2}{\Delta_1}}\ e^{-(\Delta_2-\Delta_1)/k_B T}. \tag{10.90}$$

Plugging this result back into Eq. (10.88) gives

$$n_{1L} = \frac{n_{1L,ne} + n_{1L,th} + \left(n_{2L,ne} + n_{1L,th}\sqrt{\frac{\Delta_2}{\Delta_1}}\ e^{-(\Delta_2-\Delta_1)/k_B T}\right)\frac{\Omega_{2L}}{\Omega_{1L}}}{1 + \frac{\Omega_{2L}}{\Omega_{1L}}\sqrt{\frac{\Delta_2}{\Delta_1}}\ e^{-(\Delta_2-\Delta_1)/k_B T}}, \tag{10.91}$$

which simplifies to

$$n_{1L} = n_{1L,th} + \frac{n_{1L,ne} + \frac{\Omega_{2L}}{\Omega_{1L}} n_{2L,ne}}{1 + \frac{\Omega_{2L}}{\Omega_{1L}}\sqrt{\frac{\Delta_2}{\Delta_1}}\ e^{-(\Delta_2-\Delta_1)/k_B T}}. \tag{10.92}$$

A similar analysis may be done for the rest of the layers, and one finds

$$n_{2L} = n_{2L,th} + \frac{n_{2L,ne} + \frac{\Omega_{1L}}{\Omega_{2L}} n_{1L,ne}}{1 + \frac{\Omega_{1L}}{\Omega_{2L}}\sqrt{\frac{\Delta_1}{\Delta_2}}\ e^{(\Delta_2-\Delta_1)/k_B T}}, \tag{10.93}$$

$$n_{1R} = n_{1R,th} + \frac{n_{1R,ne} + \frac{\Omega_{2R}}{\Omega_{1R}} n_{2R,ne}}{1 + \frac{\Omega_{2R}}{\Omega_{1R}}\sqrt{\frac{\Delta_2}{\Delta_1}}\ e^{-(\Delta_2-\Delta_1)/k_B T}}, \tag{10.94}$$

and

$$n_{2R} = n_{2R,th} + \frac{n_{2R,ne} + \frac{\Omega_{1R}}{\Omega_{2L}} n_{1R,ne}}{1 + \frac{\Omega_{1R}}{\Omega_{2R}}\sqrt{\frac{\Delta_1}{\Delta_2}}\ e^{(\Delta_2-\Delta_1)/k_B T}}. \tag{10.95}$$

10.4.1 Volume Dependent Generation

Equations (10.92)-(10.95) are somewhat complicated by the fact that it contains factors that account for the possibility of quasiparticle production in both layers. Here, I consider some potential sources of non-equilibrium quasiparticle generation. First, consider a source that generates non-equlibrium quasiparticles with a rate that is proportional to the volume of the region, *i.e.*

$$\frac{\Gamma_{p1}}{\Gamma_{p2}} = \frac{\Omega_{1L}}{\Omega_{2L}}. \tag{10.96}$$

From Eqs. (10.77) and (10.81) I can then write

$$\frac{n_{1L,ne}}{n_{2L,ne}} = \frac{N_{1L,ne}}{N_{2L,ne}}\frac{\Omega_{2L}}{\Omega_{1L}} = \frac{\Gamma_{p1}}{\Gamma_{tr,1L}}\frac{\Gamma_{tr,2L}}{\Gamma_{p2}}\frac{\Omega_{2L}}{\Omega_{1L}} = \frac{\Omega_{1L}}{\Omega_{2L}}\frac{\Omega_{2L}}{\Omega_{1L}} = 1. \tag{10.97}$$

Similarly, for the right side I have that $n_{1R,ne} = n_{2R,ne}$. So, for this case, Eqs. (10.92)-(10.95) give

$$n_{1L} = n_{1L,th} + \frac{n_{1L,ne}\left(1 + \frac{\Omega_{2L}}{\Omega_{1L}}\right)}{1 + \frac{\Omega_{2L}}{\Omega_{1L}}\sqrt{\frac{\Delta_2}{\Delta_1}}\, e^{-(\Delta_2 - \Delta_1)/k_B T}}, \tag{10.98}$$

$$n_{2L} = n_{2L,th} + \frac{n_{2L,ne}\left(1 + \frac{\Omega_{1L}}{\Omega_{2L}}\right)}{1 + \frac{\Omega_{1L}}{\Omega_{2L}}\sqrt{\frac{\Delta_1}{\Delta_2}}\, e^{(\Delta_2 - \Delta_1)/k_B T}}, \tag{10.99}$$

$$n_{1R} = n_{1R,th} + \frac{n_{1R,ne}\left(1 + \frac{\Omega_{2R}}{\Omega_{1R}}\right)}{1 + \frac{\Omega_{2R}}{\Omega_{1R}}\sqrt{\frac{\Delta_2}{\Delta_1}}\, e^{-(\Delta_2 - \Delta_1)/k_B T}}, \tag{10.100}$$

and

$$n_{2R} = n_{2R,th} + \frac{n_{2R,ne}\left(1+\frac{\Omega_{1R}}{\Omega_{2L}}\right)}{1+\frac{\Omega_{1R}}{\Omega_{2R}}\sqrt{\frac{\Delta_1}{\Delta_2}}\,e^{(\Delta_2-\Delta_1)/k_BT}}. \tag{10.101}$$

10.4.2 Area Dependent Generation

I next consider a case, such as infrared photon absorption, in which the non-equilibrium quasiparticle generation rate is proportional to the exposed surface areas of each pad. This gives

$$\frac{\Gamma_{p1}}{\Gamma_{p2}} = \frac{A_1}{A_2} = 1. \tag{10.102}$$

Again from Eqs. (10.77) and (10.81) I can then write

$$\frac{n_{1L,ne}}{n_{2L,ne}} = \frac{N_{1L,ne}}{N_{2L,ne}}\frac{\Omega_{2L}}{\Omega_{1L}} = \frac{\Gamma_{p1}}{\Gamma_{tr,1L}}\frac{\Gamma_{tr,2L}}{\Gamma_{p2}}\frac{\Omega_{2L}}{\Omega_{1L}} = \frac{\Omega_{2L}}{\Omega_{1L}}. \tag{10.103}$$

Similarly, for the right side I obtain

$$\frac{n_{1R,ne}}{n_{2R,ne}} = \frac{\Omega_{2R}}{\Omega_{1R}}. \tag{10.104}$$

So, for Eqs. (10.92)-(10.95) I get

$$n_{1L} = n_{1L,th} + \frac{2n_{1L,ne}}{1+\frac{\Omega_{2L}}{\Omega_{1L}}\sqrt{\frac{\Delta_2}{\Delta_1}}\,e^{-(\Delta_2-\Delta_1)/k_BT}}, \tag{10.105}$$

$$n_{2L} = n_{2L,th} + \frac{2n_{2L,ne}}{1+\frac{\Omega_{1L}}{\Omega_{2L}}\sqrt{\frac{\Delta_1}{\Delta_2}}\,e^{(\Delta_2-\Delta_1)/k_BT}}, \tag{10.106}$$

$$n_{1R} = n_{1R,th} + \frac{2n_{1R,ne}}{1+\frac{\Omega_{2R}}{\Omega_{1R}}\sqrt{\frac{\Delta_2}{\Delta_1}}\,e^{-(\Delta_2-\Delta_1)/k_BT}}, \tag{10.107}$$

and

$$n_{2R} = n_{2R,th} + \frac{2n_{2R,ne}}{1 + \frac{\Omega_{1R}}{\Omega_{2R}}\sqrt{\frac{\Delta_1}{\Delta_2}}\, e^{(\Delta_2 - \Delta_1)/k_B T}}. \tag{10.108}$$

10.4.3 Area Dependent Generation-Single Side

The final generation model I consider is one in which the quasiparticles are generated in just one layer. This situation may arise from shining optical photons directly on one side of the device [24] or from phonons in the substrate breaking pairs on the surface of layer 1, which is in direct contact with the substrate. This is the case I consider in Chapter 11, when I assume that the generation is entirely due to phonons from the substrate breaking pairs in layer 1. With this model, I have that

$$n_{2L,ne} = 0 \tag{10.109}$$

and

$$n_{2R,ne} = 0. \tag{10.110}$$

So, for Eqs. (10.92)-(10.95) I then have

$$n_{1L} = n_{1L,th} + \frac{n_{1L,ne}}{1 + \frac{\Omega_{2L}}{\Omega_{1L}}\sqrt{\frac{\Delta_2}{\Delta_1}}\, e^{-(\Delta_2 - \Delta_1)/k_B T}}, \tag{10.111}$$

$$n_{2L} = n_{2L,th} + \frac{n_{1L,ne}\left(\frac{\Omega_{1L}}{\Omega_{2L}}\right)}{1 + \frac{\Omega_{1L}}{\Omega_{2L}}\sqrt{\frac{\Delta_1}{\Delta_2}}\, e^{(\Delta_2 - \Delta_1)/k_B T}}, \tag{10.112}$$

$$n_{1R} = n_{1R,th} + \frac{n_{1R,ne}}{1 + \frac{\Omega_{2R}}{\Omega_{1R}}\sqrt{\frac{\Delta_2}{\Delta_1}}\, e^{-(\Delta_2-\Delta_1)/k_BT}}, \tag{10.113}$$

and

$$n_{2R} = n_{2R,th} + \frac{n_{1R,ne}\left(\frac{\Omega_{1R}}{\Omega_{2R}}\right)}{1 + \frac{\Omega_{1R}}{\Omega_{2R}}\sqrt{\frac{\Delta_1}{\Delta_2}}\, e^{(\Delta_2-\Delta_1)/k_BT}}. \tag{10.114}$$

Table 10.2: Summary of expressions for quasiparticle density.

Case	n_{1L}	n_{2R}
General case	$n_{1L,th} + \frac{n_{1L,ne}+\frac{\Omega_{2L}}{\Omega_{1L}}n_{2L,ne}}{1+\frac{\Omega_{2L}}{\Omega_{1L}}\sqrt{\frac{\Delta_2}{\Delta_1}}e^{-(\Delta_2-\Delta_1)/k_BT}}$	$n_{2R,th} + \frac{n_{2R,ne}+\frac{\Omega_{1R}}{\Omega_{2L}}n_{1R,ne}}{1+\frac{\Omega_{1R}}{\Omega_{2R}}\sqrt{\frac{\Delta_1}{\Delta_2}}e^{(\Delta_2-\Delta_1)/k_BT}}$
Volume dependent generation. (i.e. $n_{1L,ne} = n_{2L,ne}$)	$n_{1L,th} + \frac{n_{1L,ne}\left(1+\frac{\Omega_{2L}}{\Omega_{1L}}\right)}{1+\frac{\Omega_{2L}}{\Omega_{1L}}\sqrt{\frac{\Delta_2}{\Delta_1}}e^{-(\Delta_2-\Delta_1)/k_BT}}$	$n_{2R,th} + \frac{n_{2R,ne}\left(1+\frac{\Omega_{1R}}{\Omega_{2L}}\right)}{1+\frac{\Omega_{1R}}{\Omega_{2R}}\sqrt{\frac{\Delta_1}{\Delta_2}}e^{(\Delta_2-\Delta_1)/k_BT}}$
Area dependent generation. (i.e. $n_{1L,ne} = \left(\frac{\Omega_{2L}}{\Omega_{1L}}\right) n_{2L,ne}$)	$n_{1L,th} + \frac{2n_{1L,ne}}{1+\frac{\Omega_{2L}}{\Omega_{1L}}\sqrt{\frac{\Delta_2}{\Delta_1}}e^{-(\Delta_2-\Delta_1)/k_BT}}$	$n_{2R,th} + \frac{2n_{2R,ne}}{1+\frac{\Omega_{1R}}{\Omega_{2R}}\sqrt{\frac{\Delta_1}{\Delta_2}}e^{(\Delta_2-\Delta_1)/k_BT}}$
Generation only in layer 1. (i.e. $n_{2L,ne} = n_{2R,ne} = 0$)	$n_{1L,th} + \frac{n_{1L,ne}}{1+\frac{\Omega_{2L}}{\Omega_{1L}}\sqrt{\frac{\Delta_2}{\Delta_1}}e^{-(\Delta_2-\Delta_1)/k_BT}}$	$n_{2R,th} + \frac{n_{1R,ne}\left(\frac{\Omega_{1R}}{\Omega_{2R}}\right)}{1+\frac{\Omega_{1R}}{\Omega_{2R}}\sqrt{\frac{\Delta_1}{\Delta_2}}e^{(\Delta_2-\Delta_1)/k_BT}}$

10.5 Conclusions

In this chapter, I presented a model for qusiparticle-induced loss in transmons as a function of temperature. This model assumes that there may be a constant source of non-equilibrium quasiparticles (due to some external pair breaking process) and that the two qubit junction electrodes have slightly different superconducting gaps. At low temperatures, the non-equilibrium quasiparticles will accumulate in the lower gap layer, which is the smallest layer in this model. This accumulation leads to an increase in quasiparticle density at the junction and a corresponding reduction in relaxation time T_1. As the temperature T is increased above $(\Delta_2 - \Delta_1)/k_B T$, the non-equilibrium quasiparticles have enough energy to escape the lower-gap Δ_1 region and occupy both layers of the device. This reduction in density leads to an increase in the relaxation time of the transmon. In Chapter 11, I use this model to fit measurements of T_1 vs. T taken on three transmons.

Chapter 11

Transmon Relaxation vs. Temperature: Measurement and Results

In this chapter I discuss the measurements of relaxation time T_1 vs. temperature T taken on three different transmons. I begin by describing the different fabrication and measurement processes that were used. I then discuss the data and compare the resulting T_1 vs. T plots to the expected loss from quasiparticles. Fitting the theory from Chapter 10 to the data, I extract the key model parameters, including the density of non-equlibrium quasiparticles. Finally, I end with a conclusions section where I discuss the implications of these results. I note that this chapter gives further details on the experimental results found in ref. [1].

11.1 Fabrication and Measurement Details

The results I describe here were obtained on three transmons that were fabricated by different people using somewhat different procedures, and the devices were measured the devices in different microwave cavities in two different laboratories (see Table 11.1). Transmon #1 was fabricated by Rui Zhang in Ben Palmer's group and measured in Palmer's lab at the Laboratory for Physical Sciences (LPS). I fabricated transmons #2 and #3, and they were measured by Dr. Sudeep Dutta in our basement lab at the Toll Physics Building. Each device was fabricated on a sapphire substrate using electron-beam lithography. After the resist was exposed and developed, a thin film of Al was thermally evaporated, a thermal oxide layer was grown, and a second Al layer was deposited to create a single Al/AlO_x/Al Josephson junction [2]. Transmon 1 and 3 were deposited in the same turbo-pumped thermal evaporator at the Laboratory for Physical

Sciences (LPS), while Transmon 2 was deposited in a cryo-pumped thermal evaporator in Room 0219 in the Physics Building in the Center for Nanophysics and Advanced Materials (CNAM) at the University of Maryland. Following deposition, the remaining resist was removed, and each device was mounted in a 3D aluminum cavity [3] with a fundamental TE_{101} cavity resonance at f_c (see Table 11.2).

For measurements, the 3D cavity with its enclosed transmon was bolted to the mixing chamber stage of a cryogen-free dilution refrigerator. Transmon 1 was measured during four successive cool-downs in two different Leiden dilution refrigerators over a

Table 11.1: Fabrication details for the three transmons [1].

Device	Transmon 1	Transmon 2	Transmon 3
Made by	R. Zhang	C. Ballard	
Made at	LPS	CNAM/Kim Building	LPS
Substrate	sapphire	sapphire	sapphire
Substrate dimensions	5mm x 7mm	5mm x 5mm	5mm x 5mm
Resist stack	(1) MMA(8.5)-	(1) LOR10A	(1) LOR10A
	MMAEI.11	(2) 950 PMMA C2	(2) 950 PMMA C2
	(2) ZEP520A DR 2.3	(3) 15 nm Al anti-charging layer	(3) 15 nm Al anti-charging layer
	(3) 10 nm Al anti-		
	charging layer	(4) Aquasave [11]	(4) Aquasave [11]
Al deposition system	turbo-pumped	cryo-pumped	turbo-pumped
Base pressure	10^{-6} Torr	10^{-6} Torr	10^{-6} Torr
Al Oxidation	159 mTorr of O_2	200 mTorr of O_2	230 mTorr of O_2
	25 mins.	5 mins.	30 mins.

12-month period at LPS. Transmons 2 and 3 were measured in separate runs on an Oxford Triton 200 dilution refrigerator at CNAM.

To reduce the effects of Johnson/Nyquist noise from higher temperature stages, the input microwave line on each refrigerator had attenuators placed at different temperature stages (see Table 11.2) producing more than 70 dB of total attenuation between 300 K and the mixing chamber stage. The output signal from the cavity was fed through microwave isolators on the mixing chamber before being amplified at 3 K by a low-noise HEMT [4]. Low-pass filters with a cut-off frequency a few GHz above the cavity resonance were also mounted on the mixing chamber on the input and output lines to reduce excitations of higher modes of the cavity. Both systems had heat shields on the first pulse tube stage (≈50 K), the second pulse tube stage (≈3 K), and the still (≈700 mK). The Leiden system also had a Cu heat shield on the heat exchanger plate (≈75 mK) and two cryo-perm magnetic shields [5] surrounding the device on the mixing chamber stage. The Oxford system did not have a shield on the heat exchanger plate, but instead had a Cu heat-shield and a single, rolled cryo-perm magnetic shield [5] on the mixing chamber stage (see Fig. 7.5).

We used a high-power pulsed cavity readout technique (see Chapter 5) to measure the relaxation of the transmons [6]. With no drive signal applied to the qubit, we first applied a high-power pulse at the bare cavity frequency and measured the amplitude V_0 of the signal transmitted through the cavity for a reference measurement. We then waited enough time to allow the system to relax back to the ground state $|g\rangle$, applied a π-pulse to place the transmon in its excited state $|e\rangle$, waited for a time t, applied a second high-power cavity pulse, and measured the amplitude V_f of the signal transmitted through the

Table 11.2: Measurement details for the three transmons [1]. LPS designates a lab in the Laboratory for Physical Sciences and UMD designates a sub-basement lab in the Center for Nanophysics and Advanced Materials at the University of Maryland, College Park. Filters 1 to 4 and a low-pass filter were mounted on the input microwave line going to the cavity. A second low-pass filter was mounted on the output line between the cavity's output port and the HEMT amplifier.

Device	Transmon 1	Transmon 1	Transmon 2	Transmon 3
Run	1, 2, 3	4	1	1
Refrigerator	Leiden CF-450	Leiden CF-1400	Oxford Triton 200	Oxford Triton 200
Location	LPS	LPS	UMD	UMD
filter 1	20 dB (3 K)	20 dB (0.7 K)	10 dB (50 K)	10 dB (50 K)
filter 2	30 dB (75 mK)	30 dB (75 mK)	20 dB (3K)	20 dB (3K)
filter 3	20 dB (MXC)	20 dB (MXC)	6 dB (700 mK)	6 dB (700 mK)
filter 4	-	-	40 dB (MXC)	40 dB (MXC)
low-pass filters cut-off	10.5 GHz	10.5 GHz	12 GHz	12 GHz
shield 1	50 K	50 K	50 K	50 K
shield 2	3 K	3 K	3 K	3 K
shield 3	700 mK	-	700 mK	700 mK
shield 4	75 mK	75 mK	15 mK	15 mK
shield 5	15 mK (cryoperm)	15 mK (cryoperm)	15 mK (cryoperm)	15 mK (cryoperm)
Cavity material	Al	Al	Al	Al
Cavity frequency f_c	7.95 GHz	7.95 GHz	6.24 GHz	6.14 GHz
Cavity Q_{in}	9000	9000	2.6×10^5	2.6×10^5
Cavity Q_{out}	8.6×10^4	8.6×10^4	1.4×10^4	2.6×10^5
Loaded cavity Q	9000	9000	1.4×10^4	4.5×10^4

cavity [6]. The difference $\Delta V = V_f - V_0$ is proportional to probability $P_e(t)$ for the transmon to be in the excited state at time *t*. For each delay time *t* of interest, the measurement sequence was repeated ~6,000 times to obtain the average probability to be in the excited state at that time.

11.2 T_1 vs. Temperature Data

In Fig. 11.1(a) I show representative relaxation time measurements from the fourth cool-down of Transmon 1. The solid lines are fits to a simple exponential decay. Figure 11.1(b) shows a plot of the corresponding extracted relaxation time T_1 vs. temperature T of the mixing chamber. The red points are the data, and the solid curve is a fit to the non-equilibrium quasiparticle model discussed in Chapter 10. This plot reveals that, for this run, T_1 increased from about 18 μs at 15 mK to 32 μs at 100 mK. Above 150 mK, T_1 decreased rapidly with temperature, as expected for thermally generated quasiparticles. Since this measured T_1 is far below the estimated Purcell limit of 1.7 ms and the expected dielectric loss from the substrate, this suggests that the quasiparticle loss is the dominant source of decoherence and we assumed that we could ignore other sources of loss in the modelling of T_1. This assumption is also consistent with the T_1 vs T data not showing a "flat top" around the maximum T_1 value [1].

Figure 11.2 shows a plot of six T_1 vs. T data sets on the three devices, each measured during a different cooldown. In this plot, the points are the data and the curves are fits to the non-equilibrium quasiparticle model I discuss in Chapter 10. The purple, blue, black, and pink points are for transmon 1 in cooldowns 1, 2, 3, and 4, respectively. The green points are for transmon 2, and the gray points are for transmon 3.

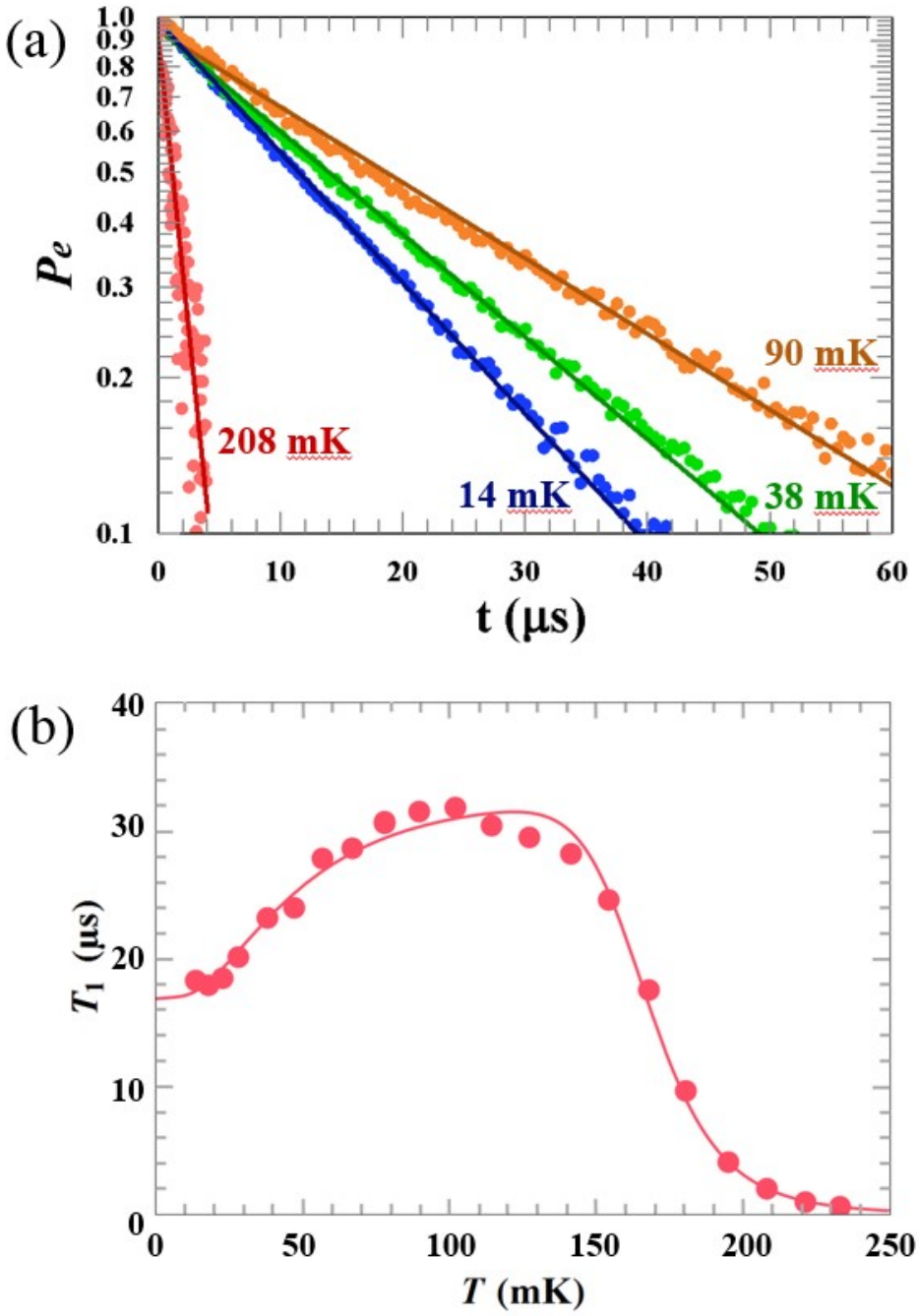

Fig. 11.1: (a) Relaxation time T_1 measurements showing probability P_e of being in the excited state vs. time t at different temperatures during cool-down 4 on transmon 1 [1]. The points are data and the lines are fits to an exponential decay. (b) Relaxation time T_1 vs. temperature T on transmon 1 during run 4 [1]. The points on the plot are the data and the solid line is a fit to the model presented in Chapter 10.

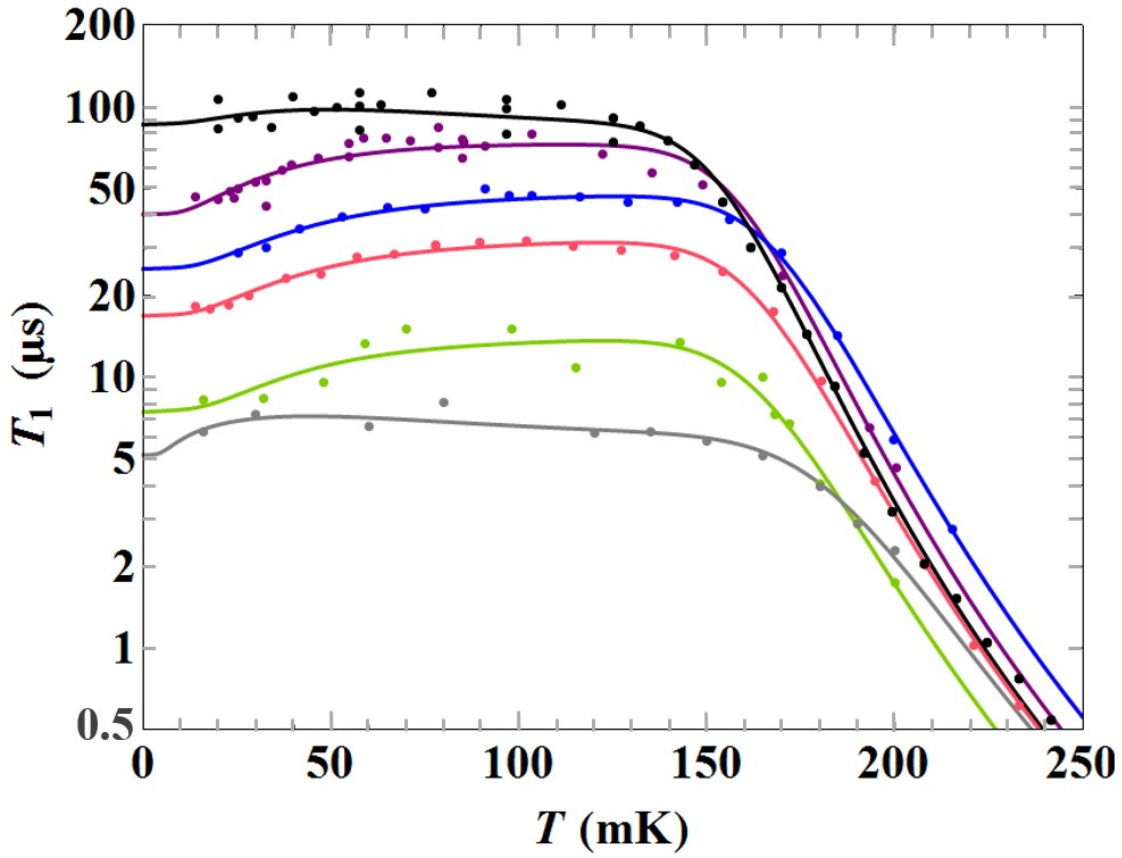

Fig. 11.2: Plot of T_1 vs. T for six different cooldowns of three transmons [1]. The points on the plot are the data and the solid lines are a fit to the model discussed in Chapter 10. Purple, blue, black, and pink are for runs 1, 2, 3, and 4 of transmon 1, respectively, green is for transmon 2, and gray is for transmon 3.

Four of the data sets show a prominent increase in T_1 as the temperature is increased from base temperature to 100 mK, while the other two show no such increase. During the first cooldown of Transmon 1 (purple points), it is clear that T_1 increased from about 40 μs at 20 mK to about 80 μs at 100 mK. Rui subsequently warmed the device to room temperature and cooled about 1 week later. During the second cool-down (blue points), the same device showed a somewhat reduced T_1 overall, but it exhibited a similar behavior with T_1 increasing from about 30 μs at 20 mK to about 50 μs at 100 mK. In contrast, for the third cool-down of Transmon 1 (black points), T_1 had a nearly temperature-independent value of 90 μs between 20 mK and 100 mK. Again, cycling Transmon 1 to room temperature and measuring T_1 for a fourth time (pink points) revealed behavior similar to that seen on the first and second cool-down but with T_1 reduced overall compared to the previous runs. For Transmon 2 (green points), T_1 increased from about 8 μs at 20 mK to about 14 μs near 100 mK. However, for Transmon 3 (gray points) T_1 had a roughly temperature independent value of about 6 μs in this temperature regime

11.3 T_1 vs. Temperature Fit Discussion

The solid curves in Figs. 11.1(b) and 11.2 are fits of Eq. (10.64) to the T_1 vs T data, with Eqs. (10.111) and (10.114) used to model the quasiparticle densities. For each data set, all of the parameters in the model were determined by independent means and set as constant with the exceptions of Δ_{1L}, $\Delta_{2R} - \Delta_{1L}$, $n_{ne,1L}$, and $n_{ne,1R}$, which are the superconducting gap in layer 1, the difference in superconducting gap between layers 1 and 2, the non-equilibrium quasiparticle density parameter in region 1L, and the non-

Table 11.3: Table of device parameters and model fitting parameters [1] for the model discussed in Chapter 10. The fit parameters are Δ_1, $\Delta_2 - \Delta_1$, $n_{ne,1L}$, and $n_{ne,1R}$. All other values in this table were either measured by other means or derived from the fit parameters.

Transmon	#1.1	#1.2	#1.3	#1.4	#2	#3
l_p (μm)	375	375	375	375	455	455
w_p (μm)	700	700	700	700	650	650
h_1 (nm)	30	30	30	30	25.1	32.5
h_2 (nm)	50	50	50	50	54	60
Ω_1 $(\mu m)^3$	7870	7870	7870	7870	7390	9610
Ω_2 $(\mu m)^3$	$1.31x10^4$	$1.31x10^4$	$1.31x10^4$	$1.31x10^4$	$1.60x10^4$	$1.77x10^4$
Ω_2/Ω_1	1.67	1.67	1.67	1.67	2.16	1.85
R_n (kΩ)	15.38	16.76	17.31	17.37	25.3	26.4
C (fF)	87	87	87	87	92.6	90.9
f_{01}(GHz)	4.00995	3.90964	3.7187	3.7071	3.07	3.10
E_c (MHz)	222	222	222	222	211	215
E_j (GHz)	10.084	9.612	8.744	8.692	5.595	5.599
E_j/E_c	45	43	39	39	27	26
τ_0 (fs)	2.86	3.04	2.98	2.98	3.81	3.94
Δ_1 (μeV)	197	204	192	191	178	189
Δ_2 (μeV)	201	209	196	196	184	190
Δ_2-Δ_1 (μeV)	4	5	4	5	6	1
$n_{ne,1L}$ $(\mu m)^{-3}$	8.8	14	4.0	20	41	92
$n_{ne,1R}$ $(\mu m)^{-3}$	2.2	2.4	6.2	3.3	16	91
$n_{ne,L}$ $(\mu m)^{-3}$	3.3	5.3	1.5	7.5	13	32
$n_{ne,R}$ $(\mu m)^{-3}$	0.8	0.9	2.3	1.2	4.9	32

equilibrium quasiparticle density parameter in region 1R, respectively. In Table 11.3 I summarize all of the model parameters, including results from the fits. l_p and w_p are the length and width of each transmon pad, respectively. For i=1,2, the parameters h_i, Ω_i and Δ_i are the thickness, volume, and gap, respectively, of Al layer i on each pad. R_n is computed from the measured value of E_J using the Ambegaokar-Baratoff formula [9]. The last two rows give overall non-equilibrium quasiparticle density in left and right transmon pads, respectively (*i.e.* total number of non-equilibrium quasiparticles in each pad divided by total volume of left or right pad). In the model, we also took the Fermi energy and density of electrons in our Al films as $\varepsilon_F = 11.63\, eV$ and $n_e = 1.81\text{x}10^{11}$ μm^{-3} [8], respectively.

To get an initial determination of the fit parameters, I note that the sharp downturn in T_1 as T is increased above about 130 mK is mainly set by the value for the smaller gap Δ_1, as this downturn is due to the production of thermal quasiparticles in the small gap layer 1. If a data set shows an increase in T_1 as the temperature is increased, the layer with the smaller volume (layer 1 in our devices) has the smaller gap and the onset of the rise occurs at a temperature that is determined by the gap difference $\Delta_2 - \Delta_1$. For the data sets that did not show this increase, the two layers have nearly equal gaps or a certain configuration of energy gaps and quasiparticle densities. Finally, the parameter $n_{ne,1L}$ sets the value of T_1 at the lowest temperatures and $n_{ne,1R}$ affects to some extent how strong the rise is in T_1.

Examining Fig. 11.2, one sees that the model did a good job of capturing the behavior of the T_1 vs. T data. However, a small but noticeable disagreement tends to occur in the 120 mK to 160 mK range, which is the "knee" region where loss from

thermally generated quasiparticles begins to contribute significantly. The model consistently tends to produce T_1 values slightly too long in this region. This discrepancy is more clearly seen in the linear plot in Fig. 11.1(b). Although the reason for this discrepancy is unclear, we can rule out a simplification we made in the model. As discussed in Chapter 10, the model includes quasiparticle trapping but not quasiparticle-quasiparticle recombination. If a recombination term is included in the model, the overall number of quasiparticles tends to be reduced, which leads to a longer T_1 as well as a distinct sharpening of the knee in the downturn region of the T_1 vs T curve, which leads to an even larger discrepancy with the data.

Examining the parameters in Table 11.3, it appears that T_1 varied from run-to-run, and between the different devices, because of differences in the density of non-equilibrium quasiparticles. For example, for the first run of Transmon 1, $n_{ne,1L}$ = 14 $(\mu m)^{-3}$ and $n_{ne,1R}$ = 2.4 $(\mu m)^{-3}$, while for the 2nd and 3rd run the densities ranged from 4.0 $(\mu m)^{-3}$ to 14 $(\mu m)^{-3}$ for these parameter. In the 4th run of Transmon 1, which was cooled down in a different Leiden refrigerator than that used for the first three runs, we found $n_{ne,1L}$ = 19.9 $(\mu m)^{-3}$ and $n_{ne,2R}$ = 3.3 $(\mu m)^{-3}$. This behavior suggests that the quasiparticle trapping rate was relatively small in the left pad during the first, second and fourth cool-down of Transmon 1. A plausible explanation is that there are different numbers of vortices trapped in each pad, and these numbers change from one run to the next [6]. Transmons 2 and 3 showed significantly higher non-equilibrium quasiparticle densities than Transmon 1. This may have been due to fewer trapped vortices (leading to a lower quasiparticle trapping rate) or to a larger rate of generation of non-equilibrium quasiparticles in the Triton refrigerator compared to the Leiden refrigerators. Examining

Table 11.2, I note that the Oxford system lacks a thermal shield on the 100 mK plate. This suggests that additional thermal radiation from the 700 mK Still plate stage in the Triton system may be a factor in the high density of non-equilibrium quasiparticles in transmons 2 and 3.

Something else that can be seen in Fig. 11.2 is that the four T_1 versus T curves for Transmon 1 showed somewhat different temperature dependence in the downturn region above 150 mK, where T_1 decreases rapidly due to thermal quasiparticles. Two possible explanations for this behavior are: (i) run-to-run ±10 mK variations in the calibration of the thermometry, or (ii) actual ±10 μeV variations in the superconducting gap Δ_1 (the smaller of the two gaps) after cycling the devices to room temperature. Additional testing would need to be done to distinguish the increase.

I note that the best fit values for the gaps in layers 1 and 2 were $\Delta_1 = 197$, 204, 192, 191, 179, and 189 μeV and $\Delta_2 = 201$, 209, 196, 196, 185, and 190 μeV. Although these values are 5-25% higher than expected for pure bulk Al, they are reasonable for thin-film Al. In particular, the superconducting gap in Al depends on size of the grains in the film [10], with smaller grains producing a larger gap. Naively, one might expect a thinner Al layer to have smaller grains and a larger gap. However, the growth conditions for the two layers are different. The first layer is grown directly on the crystalline sapphire substrate, while the second Al layer is grown on top of Al oxide that covers the first layer. This may alter the growth conditions enough so that the thicker second layer has a finer grain structure and a slightly higher gap.

It is important to note that while variations in the fit values for Δ_1 could be due to run-to-run variations in the thermometry, this cannot explain a non-zero difference in the

gaps. The two layers must have slightly different gaps to produce a T_1 that increases with T [1]. From Table 11.3, one finds that the gap difference $\Delta_2 - \Delta_1$ ranged from 4-6 μeV for the four different cool-downs of device 1. Although this range may seem quite small, it represents a significant run-to-run variation in the temperature where T_1 rises and suggests that slight changes may have occurred in the gap and morphology of the Al films when the device was cycled to room temperature [10].

11.4 Conclusions

As discussed in ref. [1], in conclusion, we have found that the relaxation time T_1 of Al/AlO_x/Al transmons may increase significantly with an increase in the temperature in the 20 mK to 100 mK range. Increasing the temperature further, above approximately 130 mK, produces a dramatic decrease in the relaxation time due to thermally generated quasiparticles. To explain the anomalous temperature dependence of T_1 below 100 mK, we analyzed the quasiparticle current noise spectrum for an unbiased junction with electrodes with different superconducting gaps, modelled the quasiparticle density in the transmon electrodes as a function of temperature when a pair-breaking mechanism was producing non-equilibrium quasiparticles, and obtained an expression for the temperature dependence of the transmon relaxation time. Fitting the model to temperature dependent T_1 data allowed us to extract the gap and density of non-equilibrium quasiparticles in each electrode.

I note that the quasiparticle model only predicts a prominent increase in T_1 with temperature if the two electrodes have different gaps and the volume of the small-gap region is sufficiently smaller than the volume of the large-gap region. In contrast, if the

difference of the gaps is larger than hf_{ge}, the result would be a rapid increase in T_1 when k_BT becomes less than the difference in the gaps. The behavior in this limit is of particular interest for applying gap engineering to increase the lifetime of transmons. Other conditions for seeing this effect are that there must be: i) a mechanism generating non-equilibrium quasiparticles, ii) a relatively low quasiparticle trapping rate to allow sufficient quasiparticle accumulation in the low gap region at low temperatures, and iii) an absence of other loss mechanisms producing substantially larger loss.

Finally, when a superconducting qubit shows either a substantial increase or decrease in T_1 as the temperature T increases for temperatures such that $k_BT \ll hf_{ge}$, it provides a distinct qualitative signature suggesting the presence of quasiparticle induced loss. Devices that show this effect could be used to perform quantitative measurements on non-equilibrium quasiparticles, find their densities, pin down accurate values for the gaps and the difference in the gaps, and perhaps be used to identify underlying sources causing the pair-breaking in experimental set-ups.

Chapter 12

Conclusions

This dissertation describes research on 3D transmon qubits and tunable superconductive LC resonators that I used as a variable coupling element.

12.1 Tunable Resonator Results

In Chapter 3, I describe the approach I used to form tunable superconductive lumped-element LC resonators. This involved shunting the resonator's inductor with a loop that contained a single Josephson junction, *i.e.* an RF SQUID loop. Applying external magnetic flux to the loop induces a circulating current I in the loop. This current biases the Josephson junction and modulates the junction's Josephson inductance

$$L_J(I) = \pm \frac{\Phi_0}{2\pi\sqrt{I_0^2 - I^2}}, \tag{12.1}$$

where I_0 is the critical current of the junction. This modulation produces a shift in the total inductance of the resonator leading to a resonance frequency that can be tuned by applying flux.

In Chapter 3 I also discuss the design, fabrication, and testing of device tunres_112115. This tunable resonator device was mounted in superconducting Al 3D cavity SI-3 and measured in our Oxford Triton 200 dilution refrigerator. By monitoring the cavity resonance frequency and using the coupling between the cavity TE_{101} mode (see Chapter 2) and the resonator, we were able to determine that the running range was $\Delta f_r \approx 39$ MHz. Although this experiment showed that the flux tuning method was viable

and that we could easily couple to the modes in the 3D cavity, the tuning range was too small for the device to be useful for coupling two transmons together.

In Chapter 6 I described how I was able to dramatically increase the tuning range of my resonators by moving the junction to the shorter arm of the tuning loop. In Chapter 8, I showed spectroscopic measurements on a tunable resonator in device TRES_092917, which had a tuning range of $\Delta f_r \approx 800$ MHz, which is about a factor of 20 time larger than in the previous design and well-suited for coupling together two transmons.

One of the biggest issues I encountered with the tunable resonators was how best to apply magnetic flux to the tuning loops. As I show in Chapter 3, I used a machined split coil that I hand-soldered to an SMA pin connector. The split coil was mounted to the cavity and extended into the cavity space. Despite reducing the size of the coils, they still coupled quite strongly to the main cavity mode. For device tunres_112115, this issue was mitigated due to the resonator and flux coil being mounted at the far edge of the cavity space, where the mode is magnetic and relatively uniform. For device TRES_092917, on the other hand, we moved the chip and flux coil to the center of the cavity, so that the qubits would be coupled to the electric field of the cavity mode. In this configuration the flux coil was strongly coupled to the electric field of the cavity with a coupling quality factor of $Q_c \approx 2000$. This coupling to the flux line was the main factor limiting the cavity Q and may have also limited the qubit lifetimes. I was able to somewhat take advantage of the situation by using the coil as the RF voltage output line in addition to the DC flux bias line.

One method for reducing the unwanted coupling of the flux coil to the cavity is to reduce the size of the flux coil even further. Much smaller coils could be produced by

patterning them onto the same substrate as the tunable resonator. The connections to the bias line could be through wire bonds to pads outside the cavity. As an added bonus, the mutual inductance between the coil and the resonator's tuning loops would be more nearly equal and much more consistent from run to run. With the existing coils, a slight rotation of the device relative to the coil or a small shift in position would produce a different mutual inductance to the loops. While this has not yet been implemented, Dr. Sudeep Dutta and Tyler Carbin worked on the preliminary design and fabrication of devices with on-chip coils.

12.2 Variable Qubit-Qubit Coupling Results

The main purpose of my research was to demonstrate tunable coupling between two qubits. In particular, we wanted a coupling element that could be turned off for single-qubit operations and then turned on for two-qubit gates. In Chapter 8, I showed that device TRES_092917 operated with variable coupling. This device consisted of two transmons that were capacitively coupled to a tunable thin-film superconductive resonator. To isolate the device and have a means of reading out the state, it was mounted in a 3D superconducting Al microwave cavity.

When two qubits are approprately coupled together, the g-to-e transition frequency of one qubit will depend on the state of the other qubit. This dispersive shift depends on the coupling strength and the detuning between the two qubits. As I show in Chapter 8, when the resonator was tuned to its minimum frequency $f_{LC} = 4.14$ GHz, the measured qubit-qubit dispersive shift was only $2\chi_{qq}$= 0.1 MHz. While the coupling at this point was not fully off, the dispersive shift makes was small enough that single qubit

operations were straight-forward to achieve. By tuning the resonator it was possible to increase the qubit-qubit coupling and produce a qubit-qubit dispersive shift of $2\chi_{qq} \approx 6$ MHz. This was large enough that two qubit gate operations were feasible. In Chapter 9, I presented results on the initial characterization of a CNOT gate.

The CNOT gate performed much as expected. However, there were a few limiting factors. One of the main limitations was the relatively short relaxation times T_1 of the two qubits. The T_1 values of the qubits changed somewhat (20%) as the resonator was tuned, with $T_1 \approx 2$ μs typically. During the 230 ns long CNOT gate, this resulted in an appreciable amount of state decay (of order 10%). Second, we could not use the resonator as a fast switch because the flux bias line had a low-pass filter cutoff below 1 Mhz. This can, in principle, be easily fixed by removing any filters in the line with this low of a bandwidth and replacing them with wider bandwidth (>10 Mhz) filters. Another issue was that the system was still somewhat sensitive to changes in the external magnetic field. Addition shielding would help.

The gate operation could be significantly improved if we could figure out why the transmons had such short relaxation times. This may be due to the qubits' coupling to the resonator, which is overcoupled to the flux coil. However, a more likely cause is loss due to non-equilibrium quasiparticles.

12.3 T_1 vs. T Results

In Chapters 10 and 11, I discussed observations of an anomalous rise in the relaxation time T_1 of some 3D transmons as the temperature T was increased from 20 mK to 100 mK. This effect was initially seen by Rui Zhang in Ben Palmer's group at LPS.

Her results prompted us to take a careful look at our own devices, and, to our surprise, we also saw this effect in one transmon.

In Chapter 10, I describe the model we used to explain this effect. A key feature of the model was that the two metal films that form the qubit's Josephson junction had different superconducting gaps. At sufficiently low temperatures, non-equilibrium quasiparticles present in the system will collect in the region with the lower gap. For our devices, this low-gap layer had about one-half the volume of the high-gap layer. When the quasiparticles accumulate in the small volume layer, the density of quasiparticles at the junction is increased, leading to a relatively short T_1. As the temperature is increased, the quasiparticles can pick up enough thermal energy to escape into the high-gap layer. If the high-gap layer has a sufficiently large volume, this reduces the density of quasiparticles at the junction, leading to a decrease in the loss and an increase in T_1. If the temperature T is increased, eventually quasiparticles will be generated thermally and T_1 will decrease rapidly with further increases in T.

This model is interesting and there are quite a few ways in which it could be applied. First, the model could be used to understand how to effectively engineer the gaps and volumes of the films in such a way that the loss due to non-equilibrium quasiparticles is negligible at low temperatures. Similarly, one could use this model to find optimum places for quasiparticle traps. For instance, in our devices a quasiparticle trap (such as a normal metal island) placed on the high gap region would produce very little effect at low temperatures, while placing a trap in the low gap region would be effective.

The model could also be applied to create a quasiparticle sensor. With such a device it would be possible to search for sources producing non-equilibrium quasiparticles and provide accurate, quantifiable measures of pair-breaking radiation in different setup. For example, as I described in Chapter 11 our group observed a much larger background density of quasiparticles than Rui did in Ben Palmer's setup. One difference between our measurement setup and hers was the thermal shielding on the dilution refrigerators. We did not have a thermal shield on the refrigerator cold plate ($\approx$ 90 mK), while the Leiden systems used by Rui did. Thus, the mixing chamber stage in our setup was bathed in 700 mK radiation from the Still stage, while for Rui's experiment the thermal radiation was presumably only at about 90 mK. While this was not the only plausible explanation for our shorter T_1s, it could be tested if we had a device that could accurately monitor the intensity of pair-breaking radiation.

Appendix A

Supplement to Chapter 2

A.1 Vector Calculus Identities

Triple Products:

$$\boldsymbol{P} \cdot (\boldsymbol{Q} \times \boldsymbol{R}) = \boldsymbol{Q} \cdot (\boldsymbol{R} \times \boldsymbol{P}) = \boldsymbol{R} \cdot (\boldsymbol{P} \times \boldsymbol{Q}) \tag{A1.1}$$

$$\boldsymbol{P} \times (\boldsymbol{Q} \times \boldsymbol{R}) = \boldsymbol{Q}(\boldsymbol{P} \cdot \boldsymbol{R}) - \boldsymbol{R}(\boldsymbol{P} \cdot \boldsymbol{Q}) \tag{A1.2}$$

Product Rules:

$$\nabla(fg) = f(\nabla g) + g(\nabla f) \tag{A1.3}$$

$$\nabla(\mathbf{P} \cdot \mathbf{Q}) = \mathbf{P} \times (\nabla \times \mathbf{Q}) + \mathbf{Q} \times (\nabla \times \mathbf{P}) + (\mathbf{P} \cdot \nabla)\mathbf{Q} + (\mathbf{Q} \cdot \nabla)\mathbf{P} \tag{A1.4}$$

$$\nabla \cdot (f\boldsymbol{P}) = f(\nabla \cdot \boldsymbol{P}) + \boldsymbol{P} \cdot (\nabla f) \tag{A1.5}$$

$$\nabla \cdot (\boldsymbol{P} \times \boldsymbol{Q}) = \boldsymbol{Q} \cdot (\nabla \times \boldsymbol{P}) - \boldsymbol{P} \cdot (\nabla \times \boldsymbol{Q}) \tag{A1.6}$$

$$\nabla \times (f\boldsymbol{P}) = f(\nabla \times \boldsymbol{P}) - \boldsymbol{P} \times (\nabla f) \tag{A1.7}$$

$$\nabla \times (\boldsymbol{P} \times \boldsymbol{Q}) = (\boldsymbol{Q} \cdot \nabla)\boldsymbol{P} - (\boldsymbol{P} \cdot \nabla)\boldsymbol{Q} + \boldsymbol{P}(\nabla \cdot \boldsymbol{Q}) - \boldsymbol{Q}(\nabla \cdot \boldsymbol{P}) \tag{A1.8}$$

Second Derivatives:

$$\nabla \cdot (\nabla \times \boldsymbol{P}) = 0 \tag{A1.9}$$

$$\nabla \times (\nabla f) = 0 \tag{A1.10}$$

$$\nabla \times (\nabla \times \boldsymbol{P}) = \nabla(\nabla \cdot \boldsymbol{P}) - \nabla^2 \boldsymbol{P} \tag{A1.11}$$

A.2 Derivation of Eqs. (2.9) – (2.11)

First, I separate the z-components of the fields and operators:

$$\boldsymbol{E} = \boldsymbol{E}_t + E_z\hat{z} \tag{A2.1a}$$

$$\boldsymbol{H} = \boldsymbol{H}_t + H_z\hat{z} \tag{A2.1b}$$

$$\nabla = \nabla_t + \nabla_z, \tag{A2.2}$$

where

$$\nabla_z = \frac{\partial}{\partial z}\hat{z}. \tag{A2.3}$$

With time dependence $e^{-i\omega t}$, Maxwell's equations may be written as

$$\nabla \cdot \boldsymbol{E} = 0 \tag{A2.4a}$$

$$\nabla \cdot \boldsymbol{H} = 0 \tag{A2.4b}$$

$$\nabla \times \boldsymbol{E} = i\omega\mu_0\boldsymbol{H} \tag{A2.4c}$$

$$\nabla \times \boldsymbol{H} = -i\omega\epsilon_0\boldsymbol{E}. \tag{A2.4d}$$

Inserting Eqs. (A2.1a) and (A2.2) into Eq. (A2.4a) gives

$$(\nabla_t + \nabla_z) \cdot (\boldsymbol{E}_t + E_z\hat{z}) = 0. \tag{A2.5}$$

Expanding Eq. (A2.5) yields

$$\nabla_t \cdot \boldsymbol{E}_t + \nabla_t \cdot (E_z\hat{z}) + \nabla_z \cdot \boldsymbol{E}_t + \nabla_z \cdot (E_z\hat{z}) = 0. \tag{A2.6}$$

Since the transverse component is orthogonal to the $\hat{z}$ direction, the second and third terms of Eq. (A2.6) are both zero. Hence, by using Eq. (A2.3) and rearranging, we arrive at

$$\nabla_t \cdot \boldsymbol{E}_t = -\frac{\partial E_z}{\partial z}. \tag{A2.7}$$

Similarly, by inserting Eqs. (A2.1b) and (A2.2) into Eq. (A2.4b) we get

$$\nabla_t \cdot \boldsymbol{H}_t = -\frac{\partial H_z}{\partial z}. \tag{A2.8}$$

Equations (A2.7) and (A2.8) are two of the six equations that comprise Eq. (2.9).

Next, consider Eq. (A2.4c). Taking the cross product of $\hat{z}$ with (A2.4c) gives

$$\hat{z} \times (\nabla \times \boldsymbol{E}) = i\omega\mu_0(\hat{z} \times \boldsymbol{H}). \tag{A2.9}$$

By applying identity (A1.4) on the left hand side of Eq. (A2.9) (with $\boldsymbol{P} = \hat{z}$ and $\boldsymbol{Q} = \boldsymbol{E}$) we get

$$\hat{z} \times (\nabla \times \boldsymbol{E}) = \nabla(\hat{z} \cdot \boldsymbol{E}) - (\hat{z} \cdot \nabla)\boldsymbol{E} - \boldsymbol{E}(\nabla \cdot \hat{z}) - \boldsymbol{E} \times (\nabla \times \hat{z}). \tag{A2.10}$$

Since any derivative acting on $\hat{z}$ is zero, the last two terms of Eq. (A2.10) vanish. By inserting Eqs. (A2.1a) and (A2.2) into Eq. (A2.10) and simplifying the scalar products involving $\hat{z}$ I get

$$\hat{z} \times (\nabla \times \boldsymbol{E}) = (\nabla_\mathrm{t} + \nabla_z)E_z - \frac{\partial}{\partial z}(\boldsymbol{E}_t + E_z\hat{z}). \tag{A2.11}$$

Expanding Eq. (A2.11) yields:

$$\hat{z} \times (\nabla \times \boldsymbol{E}) = \nabla_\mathrm{t}E_z + \frac{\partial E_z}{\partial z}\hat{z} - \frac{\partial \boldsymbol{E}_t}{\partial z} - \frac{\partial E_z}{\partial z}\hat{z}. \tag{A2.12}$$

The second and fourth terms cancel, leaving

$$\hat{z} \times (\nabla \times \boldsymbol{E}) = \nabla_\mathrm{t}E_z - \frac{\partial \boldsymbol{E}_t}{\partial z}. \tag{A2.13}$$

Now for the right hand side of Eq. (A2.9), substituting Eq. (A2.1b) gives

$$i\omega\mu_0(\hat{z} \times (\boldsymbol{H}_t + H_z\hat{z})) = i\omega\mu_0\big(\hat{z} \times \boldsymbol{H}_t + H_z(\hat{z} \times \hat{z})\big). \tag{A2.14}$$

Since $(\hat{z} \times \hat{z}) = 0$, The right hand side of Eq. (A2.9) reduces to

$$i\omega\mu_0(\hat{z} \times \boldsymbol{H}) = i\omega\mu_0(\hat{z} \times \boldsymbol{H}_t). \tag{A2.15}$$

Finally, equating Eqs. (A2.13) and (A2.15) and rearranging gives

$$\frac{\partial \boldsymbol{E}_t}{\partial z} + i\omega\mu_0(\hat{z} \times \boldsymbol{H}_t) = \nabla_t E_z. \tag{A2.16}$$

Similarly, taking the cross product of $\hat{z}$ with equation (A2.4d) and following the same steps yields

$$\frac{\partial \boldsymbol{H}_t}{\partial z} - i\omega\epsilon_0(\hat{z} \times \boldsymbol{E}_t) = \nabla_t H_z. \tag{A2.17}$$

Notice that Eqs. (A2.16) and (A2.17) are two of the expressions in Eq. (2.9).

Taking the scalar product of $\hat{z}$ with (A2.4c) yields

$$\hat{z} \cdot (\nabla \times \boldsymbol{E}) = i\omega\mu_0(\hat{z} \cdot \boldsymbol{H}). \tag{A2.18}$$

Inserting Eqs. (A2.1a) and (A2.2) into the left hand side and then expanding gives

$$\hat{z} \cdot (\nabla \times \boldsymbol{E}) = \hat{z} \cdot (\nabla_t \times \boldsymbol{E}_t + \nabla_t \times \boldsymbol{E}_z\hat{z} + \nabla_z \times \boldsymbol{E}_t + \nabla_z \times \boldsymbol{E}_z\hat{z}). \tag{A2.19}$$

The first term in the expansion is the only one that has a component in the $\hat{z}$ direction; thus, all the other terms vanish under the scalar product:

$$\hat{z} \cdot (\nabla \times \boldsymbol{E}) = \hat{z} \cdot (\nabla_t \times \boldsymbol{E}_t). \tag{A2.20}$$

With Eq. (A2.1b) the right hand side of Eq. (A2.18) reduces to

$$i\omega\mu_0(\hat{z} \cdot \boldsymbol{H}) = i\omega\mu_0 H_z. \tag{A2.21}$$

Equating Eqs. (A2.20) and (A2.21) yields

$$\hat{z} \cdot (\nabla_\mathrm{t} \times \boldsymbol{E}_t) = i\omega\mu_0 H_z. \tag{A2.22}$$

Similarly, taking the scalar product of $\hat{z}$ with (A2.4d) and following the same steps yields

$$\hat{z} \cdot (\nabla_\mathrm{t} \times \boldsymbol{H}_t) = -i\omega\epsilon_0 E_z. \tag{A2.23}$$

Equations (A2.22) and (A2.23) are the final two equations in Eq. (2.9).

The final step is to solve these equations to get the transverse components of the field as a function of the z-component (see Eqs. (2.10) and (2.11)). Taking the cross product of $\hat{z}$ with Eq. (A2.16) gives

$$\hat{z} \times \frac{\partial \boldsymbol{E}_t}{\partial z} + i\omega\mu_0\big(\hat{z} \times (\hat{z} \times \boldsymbol{H}_t)\big) = \hat{z} \times \nabla_t E_z. \tag{A2.24}$$

Consider the first term on the left hand side. Since $\partial\hat{z}/\partial z = 0$, the derivative may be commuted with the cross product to yield

$$\hat{z} \times \frac{\partial \boldsymbol{E}_t}{\partial z} = \frac{\partial}{\partial z}(\hat{z} \times \boldsymbol{E}_t). \tag{A2.25}$$

From Eq. (A2.17) I can write

$$\hat{z} \times \frac{\partial \boldsymbol{E}_t}{\partial z} = \frac{i}{\omega\epsilon_0}\frac{\partial}{\partial z}\left[\frac{\partial \boldsymbol{H}_t}{\partial z} - \nabla_t H_z\right]. \tag{A2.26}$$

With a z-dependence of $e^{\pm ikz}$, the derivatives in (A2.26) may be evaluated to yield

$$\hat{z} \times \frac{\partial \boldsymbol{E}_t}{\partial z} = \frac{i}{\omega\epsilon_0}[-k^2\boldsymbol{H}_t \mp ik\nabla_t H_z] \tag{A2.27}$$

Consider the second term in Eq. (A2.24). By applying Eq. (A1.2) on the second term of (A2.24) (with $\boldsymbol{P} = \boldsymbol{Q} = \hat{z}$ and $\boldsymbol{R} = \boldsymbol{H}_t$) I get

$$i\omega\mu_0\big(\hat{z} \times (\hat{z} \times \boldsymbol{H}_t)\big) = i\omega\mu_0[\hat{z}(\hat{z} \cdot \boldsymbol{H}_t) - \boldsymbol{H}_t(\hat{z} \cdot \hat{z})]. \tag{A2.28}$$

Since $\boldsymbol{H}_t$ has no $\hat{z}$ component, the first term vanishes, leaving

$$i\omega\mu_0\big(\hat{z} \times (\hat{z} \times \boldsymbol{H}_t)\big) = -i\omega\mu_0\boldsymbol{H}_t. \tag{A2.29}$$

Substituting Eqs. (A2.27) and (A2.29) back into Eq. (A2.24) gives

$$\frac{i}{\omega\epsilon_0}[-k^2\boldsymbol{H}_t \mp ik\nabla_t H_z] - i\omega\mu_0\boldsymbol{H}_t = \hat{z} \times \nabla_t E_z. \tag{A2.30}$$

Solving this expression for $\boldsymbol{H}_t$ yields

$$\boldsymbol{H}_t = \frac{i}{\mu_0\epsilon_0\omega^2 - k^2}[\pm k\nabla_t H_z + \epsilon_0\omega\,\hat{\boldsymbol{z}} \times \nabla_t E_z], \tag{A2.31}$$

which is Eq. (2.11).

Similarly, by taking the cross product of $\hat{z}$ with Eq. (A2.17) and following the same steps I get

$$\boldsymbol{E}_t = \frac{i}{\mu\epsilon\omega^2 - k^2}[\pm k\nabla_t E_z - \omega\mu_0\,\hat{\boldsymbol{z}} \times \nabla_t H_z], \tag{A2.32}$$

which is equation (2.10).

A.3 Wave Equation in Terms of Scalar and Vector Potentials

Maxwell's equations are

$$\nabla \cdot \boldsymbol{E} = \frac{\rho}{\epsilon_0} \tag{A3.1a}$$

$$\nabla \cdot \boldsymbol{H} = 0 \tag{A3.1b}$$

$$\nabla \times \boldsymbol{E} = -\mu_0 \frac{\partial \boldsymbol{H}}{\partial t} \tag{A3.1c}$$

$$\nabla \times \boldsymbol{H} = \boldsymbol{J} + \epsilon_0 \frac{\partial \boldsymbol{E}}{\partial t}. \tag{A3.1d}$$

The electric field and magnetic field may be written in terms of a scalar potential φ and a vector potential $\boldsymbol{A}$ as

$$\boldsymbol{E} = -\mu_0 \frac{\partial \boldsymbol{A}}{\partial t} - \nabla\varphi \tag{A3.2a}$$

$$\boldsymbol{H} = \nabla \times \boldsymbol{A}. \tag{A3.2b}$$

By inserting Eqs. (A3.2a) and (A3.2b) into Eq. (A3.1d) I get

$$\nabla \times (\nabla \times \boldsymbol{A}) = \boldsymbol{J} + \epsilon_0 \frac{\partial}{\partial t}\left[-\mu_0 \frac{\partial \boldsymbol{A}}{\partial t} - \nabla\varphi\right]. \tag{A3.3}$$

By applying Eq. (A1.11) on the left hand side of this expression, distributing the time derivative to the two terms in the square bracket, and commuting the time derivative with the gradient on φ, I get

$$\nabla(\nabla \cdot \mathbf{A}) - \nabla^2 \boldsymbol{A} = \boldsymbol{J} - \mu_0\epsilon_0 \frac{\partial^2 \boldsymbol{A}}{\partial t^2} - \nabla\left(\epsilon_0 \frac{\partial \varphi}{\partial t}\right). \tag{A3.4}$$

Rearranging these terms and grouping together the two gradient terms yields

$$-\nabla^2 \boldsymbol{A} + \mu_0 \epsilon_0 \frac{\partial^2 \boldsymbol{A}}{\partial t^2} + \nabla\left(\nabla \cdot \boldsymbol{A} + \epsilon_0 \frac{\partial \varphi}{\partial t}\right) = \boldsymbol{J}, \tag{A3.5}$$

which is Eq. (2.46).

Next, substituting Eq. (A3.2a) into Eq. (A3.1a) gives

$$\nabla \cdot \left(-\mu_0 \frac{\partial \boldsymbol{A}}{\partial t} - \nabla\varphi\right) = \frac{\rho}{\epsilon_0}. \tag{A3.6}$$

Distributing the divergence operator into the parenthesis and commuting it with the time derivative gives

$$-\nabla^2 \varphi - \mu_0 \frac{\partial}{\partial \mathrm{t}}(\nabla \cdot \boldsymbol{A}) = \frac{\rho}{\epsilon_0}. \tag{A3.7}$$

By both adding and subtracting the term $\mu\epsilon \frac{\partial^2 \varphi}{\partial t^2}$ into Eq. (A3.7) I get

$$-\nabla^2 \varphi + \mu_0 \epsilon_0 \frac{\partial^2 \varphi}{\partial t^2} - \frac{\partial}{\partial \mathrm{t}}(\nabla \cdot \boldsymbol{A}) - \epsilon_0 \frac{\partial^2 \varphi}{\partial t^2} = \frac{\rho}{\epsilon_0}. \tag{A3.8}$$

Grouping the third and fourth terms of this expression and extracting the time derivative gives

$$-\nabla^2 \varphi + \mu_0 \epsilon_0 \frac{\partial^2 \varphi}{\partial t^2} - \frac{\partial}{\partial \mathrm{t}}\left(\nabla \cdot A + \epsilon_0 \frac{\partial \varphi}{\partial t}\right) = \frac{\rho}{\epsilon_0}, \tag{A3.9}$$

which is Eq. (2.47).

A.4 Eigenfunction Orthogonality

Consider a set of eigenfunctions obtained by solving

$$\nabla^2 \boldsymbol{A} + k^2 \boldsymbol{A} = 0 \tag{A4.1}$$

under the constraint that

$$\nabla \cdot \boldsymbol{A} = 0, \tag{A4.2}$$

and with the boundary condition that $\boldsymbol{A}$ is either zero or normal to the boundary at the boundary (depending on what mode one is considering). I label the non-degenerate eigenvalues obtained from this solution as k_1, k_2, k_3, etc., with the corresponding eigenfunctions labeled as $\boldsymbol{A}_1$, $\boldsymbol{A}_2$, $\boldsymbol{A}_3$, *etc*.

To show that these eigenfunctions are orthogonal, consider the following expression with $a \neq b$:

$$F = \boldsymbol{A}_b^* \cdot \big(\nabla \times (\nabla \times \boldsymbol{A}_a)\big) - \boldsymbol{A}_a \cdot \big(\nabla \times (\nabla \times \boldsymbol{A}_b^*)\big). \tag{A4.3}$$

Applying Eq. (A1.11) to Eq. (A4.3) yields

$$F = \boldsymbol{A}_b^* \cdot [\nabla(\nabla \cdot \boldsymbol{A}_a) - \nabla^2 \boldsymbol{A}_a] - \boldsymbol{A}_a \cdot [\nabla(\nabla \cdot \boldsymbol{A}_b^*) - \nabla^2 \boldsymbol{A}_b^*]. \tag{A4.4}$$

Using Eqs. (A4.1) and (A4.2), this reduces to

$$F = k_a^2 \boldsymbol{A}_b^* \cdot \boldsymbol{A}_a - k_b^2 \boldsymbol{A}_a \cdot \boldsymbol{A}_b^*, \tag{A4.5}$$

which may be simplified to

$$F = (k_a^2 - k_b^2) \boldsymbol{A}_a \cdot \boldsymbol{A}_b^*. \tag{A4.6}$$

I now add and subtract the term $(\nabla \times \boldsymbol{A}_a) \cdot (\nabla \times \boldsymbol{A}_b^*)$ in Eq. (A4.3) to give

$$\begin{aligned} F = &\big[\boldsymbol{A}_b^* \cdot \big(\nabla \times (\nabla \times \boldsymbol{A}_a)\big) - (\nabla \times \boldsymbol{A}_a) \cdot (\nabla \times \boldsymbol{A}_b^*)\big] \\ &- \big[\boldsymbol{A}_a \cdot \big(\nabla \times (\nabla \times \boldsymbol{A}_b^*)\big) - (\nabla \times \boldsymbol{A}_b^*) \cdot (\nabla \times \boldsymbol{A}_a)\big]. \end{aligned} \tag{A4.7}$$

Note that I have reversed the order of $(\nabla \times \boldsymbol{A}_a)$ and $(\nabla \times \boldsymbol{A}_b^*)$ in the scalar product term for clarity. Applying Eq. (A1.6) separately to the first and second bracketed terms of Eq. (A4.7) (with $\boldsymbol{P} = \nabla \times \boldsymbol{A}_a$ and $\boldsymbol{Q} = \boldsymbol{A}_b^*$ for the first term and $\boldsymbol{P} = \nabla \times \boldsymbol{A}_b^*$ and $\boldsymbol{Q} = \boldsymbol{A}_a$ for the second term) gives

$$F = \nabla \cdot \big((\nabla \times \boldsymbol{A}_a) \times \boldsymbol{A}_b^*\big) - \nabla \cdot \big((\nabla \times \boldsymbol{A}_b^*) \times \boldsymbol{A}_a\big). \tag{A4.8}$$

By combining these divergences, this simplifies to

$$F = \nabla \cdot \left((\nabla \times \boldsymbol{A}_a) \times \boldsymbol{A}_b^* - (\nabla \times \boldsymbol{A}_b^*) \times \boldsymbol{A}_a\right). \tag{A4.9}$$

Equating Eqs. (A4.6) and (A4.9) gives the more useful expression

$$\nabla \cdot \left((\nabla \times \boldsymbol{A}_a) \times \boldsymbol{A}_b^* - (\nabla \times \boldsymbol{A}_b^*) \times \boldsymbol{A}_a\right) = (k_a^2 - k_b^2)\boldsymbol{A}_a \cdot \boldsymbol{A}_b^* \tag{A4.10}$$

Consider the integral of Eq. (A4.10) over the volume of the cavity:

$$I = \iiint \nabla \cdot \left((\nabla \times \boldsymbol{A}_a) \times \boldsymbol{A}_b^* - (\nabla \times \boldsymbol{A}_b^*) \times \boldsymbol{A}_a\right) dV \tag{A4.11}$$

By the divergence theorem, we have

$$I = \oiint \left((\nabla \times \boldsymbol{A}_a) \times \boldsymbol{A}_b^* - (\nabla \times \boldsymbol{A}_b^*) \times \boldsymbol{A}_a\right) \cdot \hat{n}\, dA \tag{A4.12}$$

With the boundary conditions on these basis functions (*i.e.* the $\boldsymbol{A}$ eigenfunctions are either zero or normal to the boundary at the boundary) two cases must be considered for Eq. (A4.12):

Case 1: $\boldsymbol{A}_i$ goes to zero at the boundary:

This is the trivial case. If either $\boldsymbol{A}_a$ or $\boldsymbol{A}_b^*$ go to zero at the boundary, then the integrand vanishes at the boundary and $I = 0$.

Case 2: $\boldsymbol{A}_i$ is normal to the walls at the boundary:

For this case, it is a simple matter to show that when $\boldsymbol{A}_a$ and $\boldsymbol{A}_b^*$ are normal to the walls at the boundary, then both $(\nabla \times \boldsymbol{A}_a) \times \boldsymbol{A}_b^*$ and $(\nabla \times \boldsymbol{A}_b^*) \times \boldsymbol{A}_a$ only have terms that are orthogonal to $\hat{n}$ (i.e. $\left((\nabla \times \boldsymbol{A}_a) \times \boldsymbol{A}_b^*\right) \cdot \hat{n} = \left((\nabla \times \boldsymbol{A}_b^*) \times \boldsymbol{A}_a\right) \cdot \hat{n} = 0$). Hence, the integrand vanishes and $I = 0$.

Putting this all together gives

$$I = \iiint \nabla \cdot \left((\nabla \times \boldsymbol{A}_a) \times \boldsymbol{A}_b^* - (\nabla \times \boldsymbol{A}_b^*) \times \boldsymbol{A}_a\right) dV = 0. \tag{A4.13}$$

Hence, with Eq. (A4.10) I have that

$$(k_a^2 - k_b^2) \iiint \boldsymbol{A}_a \cdot \boldsymbol{A}_b^* dV = 0. \tag{A4.14}$$

Since we have operated under the assumption that $a \neq b$ and that the eigenvalues are non-degenerate (*i.e.* $a \neq b$ implies $k_a \neq k_b$), we have

$$\iiint \boldsymbol{A}_a \cdot \boldsymbol{A}_b^* dV = 0. \tag{A4.15}$$

Hence, the eigenfunctions are orthogonal over the volume of the cavity.

A.5 Evaluation of Energy Integral

Consider the integral

$$I = \int \int \int (\nabla \times \boldsymbol{A}_a) \cdot (\nabla \times \boldsymbol{A}_b^*) dV \tag{A5.1}$$

under the conditions that, for all i, $\boldsymbol{A}_i$ is the solution to the equation

$$\nabla^2 \boldsymbol{A}_i + k_i^2 \boldsymbol{A}_i = 0, \tag{A5.2}$$

with

$$\nabla \cdot \boldsymbol{A}_i = 0, \tag{A5.3}$$

and boundary conditions such that $\boldsymbol{A}_i$ is either zero or normal at the boundary. By adding and subtracting the term $\boldsymbol{A}_a \cdot \nabla^2 \boldsymbol{A}_b^*$ from the integrand in Eq. (A5.1) along with subtracting the term $\boldsymbol{A}_a \cdot \nabla(\nabla \cdot \boldsymbol{A}_b^*)$, which is equal to zero by Eq. (A5.3), I get

$$G = (\nabla \times \boldsymbol{A}_a) \cdot (\nabla \times \boldsymbol{A}_b^*) - \boldsymbol{A}_a \cdot \nabla(\nabla \cdot \boldsymbol{A}_b^*) + \boldsymbol{A}_a \cdot \nabla^2 \boldsymbol{A}_b^* - \boldsymbol{A}_a \cdot \nabla^2 \boldsymbol{A}_b^*. \tag{A5.4}$$

Grouping the second and third terms, extracting the $\boldsymbol{A}_a$ from both of those grouped terms, and by using Eq. (A5.2) on the last term we get

$$G = (\nabla \times \boldsymbol{A}_a) \cdot (\nabla \times \boldsymbol{A}_b^*) - \boldsymbol{A}_a \cdot (\nabla(\nabla \cdot \boldsymbol{A}_b^*) - \nabla^2 \boldsymbol{A}_b^*) + k_b^2 \boldsymbol{A}_a \cdot \boldsymbol{A}_b^*. \tag{A5.5}$$

With Eq. (A1.11) Eq. (A5.5) may be simplified to

$$G = (\nabla \times \boldsymbol{A}_a) \cdot (\nabla \times \boldsymbol{A}_b^*) - \boldsymbol{A}_a \cdot \left(\nabla \times (\nabla \times \boldsymbol{A}_b^*)\right) + k_b^2 \boldsymbol{A}_a \cdot \boldsymbol{A}_b^*. \tag{A5.6}$$

Applying Eq. (A1.6) to the first two terms in Eq. (A5.6) (with $\boldsymbol{P} = \boldsymbol{A}_a$ and $\boldsymbol{Q} = \nabla \times \boldsymbol{A}_b^*$) yields

$$G = \nabla \cdot \left(\boldsymbol{A}_a \times (\nabla \times \boldsymbol{A}_b^*)\right) + k_b^2 \boldsymbol{A}_a \cdot \boldsymbol{A}_b^*. \tag{A5.7}$$

Putting Eq. (A5.7) back into Eq. (A5.1) yields two integrals we must evaluate,

$$I = \int\int\int \nabla \cdot \left(\boldsymbol{A}_a \times (\nabla \times \boldsymbol{A}_b^*)\right) dV + k_b^2 \int\int\int \boldsymbol{A}_a \cdot \boldsymbol{A}_b^* dV. \tag{A5.8}$$

The first of these integral may be evaluated by applying the divergence theorem to get

$$\int\int\int \nabla \cdot \left(\boldsymbol{A}_a \times (\nabla \times \boldsymbol{A}_b^*)\right) dV = \oiint \left(\boldsymbol{A}_a \times (\nabla \times \boldsymbol{A}_b^*)\right) \cdot \hat{n}\, dA. \tag{A5.9}$$

As shown in Appendix A.4, under our imposed boundary conditions this integral evaluates to zero. For the second integral in Eq. (A5.8), using Eq. (2.54) yields

$$I = k_b^2 \int\int\int \boldsymbol{A}_a \cdot \boldsymbol{A}_b^* dV = k_b^2 V \delta_{ab}, \tag{A5.10}$$

where V is the cavity volume. Hence, I can write

$$\int\int\int (\nabla \times \boldsymbol{A}_a) \cdot (\nabla \times \boldsymbol{A}_b^*) dV = k_b^2 V \delta_{ab}, \tag{A5.11}$$

which is Eq. (2.59).

Bibliography

Chapter 1

[1] R. P. Feynman, Int. J. Theor. Phys. 21 (6/7) 467 (1982).

[2] L. K. Grover, Phys. Rev. Lett. 79, 325 (1997)

[3] P. W. Shor, SIAM Review 41, 303 (1999)

[4] P. W. Shor, SIAM J. Comput. 26(5), 1484 (1997)

[5] Rivest, *et al.*, Communications of the ACM 21 (2): 120-126 (1978)

[6] D. P. Divincenzo, Fortschr. Phys. 48(9-11), 771 (2000)

[7] Pichler, *et al.*, PNAS 114 (43) 11362-11367 (2017)

[8] J. I. Cirac, P. Zoller, Phys. Rev. Lett. 74, 20 (1995)

[9] D. Weiss, M. Saffman, Physics Today 70, 7, 44 (2017)

[10] Childress, *et al.*, Science Vol. 314, Issue 5797 (281-285) (2006)

[11] B. E. Kane, Nature 393, 133 (1998)

[12] Y. Nakamura, *et al.*, Nature 398, 786 (1999)

[13] S. K. Dutta, *et al.*, Phys. Rev. B 78, 104510 (2008)

[14] T. P. Orlando *et al.*, Phys. Rev. B 60 15398-15413 (1999)

[15] V. E. Manucharyan *et al.*, Science 326, 5949, 113-116 (2009)

[16] M. Metcalfe *et al.*, Phys. Rev. B 76, 174516 (2007)

[17] J. Koch *et al.*, Phys. Rev. A 76, 042319 (2007)

[18] H. Paik *et al.*, Phys. Rev. Lett. 107, 240501 (2011)

[19] N. A. Masluk, Ph. D. dissertation. (Yale University, 2012)

[20] R. Barends *et al.*, Phys. Rev. Lett. 111, 080502.

[21] B. D. Josephson, Phys. Lett. 1, 7 (1962)

[22] A. M. Zagoskin *et al.*, Phys. Rev. Lett. 97, 077001 (2006)

[23] J. M. Martinis, K. D. Osborn *et al.*, Phys. Rev. Lett. 95, 210503 (2005)

[24] M. S. Khalil, Ph. D. dissertation. (University of Maryland, 2013)

[25] R. Ramos *et al.*, IEEE Trans. on App. Superc. 11, 998 (2001)

[26] B. K. Cooper, Ph. D. dissertation (University of Maryland, 2013)

[27] J. A. Schreier *et al.*, Phys. Rev. B 77, 180502(R) (2008)

[28] A. Blais *et. al*, Phys. Rev. A 69, 062320 (2004)

[29] M. D. Reed *et al.*, Phys. Rev. Lett. 105, 173601 (2010)

[30] P. A. M. Dirac, Proc. of the Royal Soc. of London A, 114 (767): 243-65 (1927)

[31] T. Sleator, H. Weinfurter, Phys. Rev. Lett. 74, 4087 (1995)

[32] F. W. Strauch, Ph. D. dissertation (University of Maryland, 2004)

[33] S. P. Premaratne, J.-H. Yeh, F. C. Wellstood, and B. S. Palmer, "Implementation of a generalized CNOT gate between fixed-frequency transmons," In review, 2018.

Chapter 2

[1] J. Jackson, "Classical Electrodynamics". Wiley, New York, NY, 3rd edition (1999)

[2] https://www.comsol.com/

[3] D. M. Pozar, "Microwave Engineering". Wiley, Hoboken, NJ, 2nd edition (2012)

[4] E. U. Condon, Rev. Mod. Phys. 14, 4 (1942)

[5] C. G. Montgomery, R. H. Dicke, E. M. Purcell, “Principles of microwave circuits”. Peter Perigrinus, Ltd. London, U. K. (1987)

[6] W. W. Hansen, J. App. Phys. 9, 654 (1938)

[7] S. E. Nigg, R. J. Schoelkopf *et al.*, Phys. Rev. Lett. 108, 240502 (2012)

Chapter 3

[1] K. D. Voigt *et al.*, IEEE Trans. on App. Supercon. 25, 3 (2015)

[2] J. Koch *et al.*, Phys. Rev. A 76, 042319 (2007)

[3] J. Majer *et al.,* Nature 449, 443-447 (2007)

[4] M. D. Reed *et al.*, Phys. Rev. Lett. 105, 173601 (2010)

[5] R. P. Budoyo, Ph. D. dissertation (University of Maryland 2016)

[6] D. I. Schuster, Ph. D. dissertation (Yale University 2007)

[7] M. Tinkham, “Introduction to Superconductivity”, McGraw-Hill Book Co. New York, NY (1975)

[8] G. Arfken, “Mathematical Methods for Physicists”, Academic Press, Orlando, FL 3rd edition (1985)

[9] https://nanoscience.oxinst.com/products/cryofree-dilution-refrigerators/triton

[10] https://www.keysight.com/en/pdx-x202270-pn-E5071C/ena-vector-network-analyzer?cc=US&lc=eng

[11] B. D. Josephson, Phys. Lett. 1, 7 (1962)

[12] A. Barone, “Physics and Applications of the Josephson Effect”, Wiley (1982)

[13] J. Clarke, “The SQUID Handbook”, Wiley, New York, NY (2004)

[14] R. Ouboter *et al.* Phys. B: Condensed Matter 205, 2 153-162 (1995)

[15] http://www.superiorflux.com/superior-no-30-supersafe-soldering-flux/

[16] https://www.fairviewmicrowave.com/sma-female-standard-stub-terminal-connector-sc3778-p.aspx

[17] http://www.laco.com/assets/1/7/N-FFluxandN-3All-PurposeFluxLiquidFastAction_CH006NA_EN_LACO1412014_v1.01.pdf

[18] K. C. Gupta *et al.* "Microstrip Lines and Slotlines", Artech, 2nd edition (1996)

[19] J. M. Jaycox, M. B. Ketchen, IEEE Trans. on Mag. MAG-17, 1 (1981)

[20] https://www.m-chemical.co.jp/en/products/departments/mcc/specialtychem/product/1201151_7976.html

[21] http://www.klmicrowave.com/

[22] http://xmacorp.com/pages/cryo

[23] https://www.anritsu.com/en-US/components-accessories/products/k250-v250

[24] https://wiki.kip.uni-heidelberg.de/KIPwiki/images/c/cb/PAMTECH_cryogenic_isolators.pdf

[25] https://www.mouser.com/new/midwest-microwave/midwest-microwave-sma-attenuators/

[26] http://www.caltechmicrowave.org/amplifiers

[27] https://nardamiteq.com/viewmodel.php?model=AMF-3F-04000800-07-10P

[28] https://www.keysight.com/en/pd-1000001289%3Aepsg%3Apro/function-arbitrary-waveform-generator-15-mhz?cc=US&lc=eng

[29] http://www.microstock-inc.com/products.htm

[30] https://www.minicircuits.com/pdfs/VLFX-80.pdf

[31] M. S. Khalil, Ph. D. dissertation. (University of Maryland, 2013)

Chapter 4

[1] J. Koch *et al.*, Phys. Rev. A 76, 042319 (2007)

[2] S. K. Dutta, *et al.*, Phys. Rev. B 78, 104510 (2008)

[3] Y. Nakamura, *et al.*, Nature 398, 786 (1999)

[4] L. Bishop, Ph. D. dissertation (Yale University 2010)

[5] R. S. Newrock, C. J. Lobb, *et al.,* Sol. State Phys. 54 (1999)

[6] G. Arfken, "Mathematical Methods for Physicists", Academic Press, Orlando, FL 3rd edition (1985)

[7] D. I. Schuster, Ph. D. dissertation (Yale University 2007)

[8] A. A. Houck *et al.,* Phys. Rev. Lett. 101 080502 (2008)

[9] J. M. Martinis, K. D. Osborn *et al.*, Phys. Rev. Lett. 95, 210503 (2005)

[10] M. S. Khalil, Ph. D. dissertation. (University of Maryland, 2013)

[11] A. L. Burin, Phys. Rev. B 92, 174201 (2015)

[12] E. M. Purcell, Phys. Rev. 69, 681 (1946)

[13] S. Haroche, D. Kleppner, Physics Today, 24-30 (1989)

[14] S. Gustavsson, Science (Dec 2016)

[15] R. P. Riwar *et al.*, Phys. Rev. B 94, 104516 (2016)

[16] A. J. Przybysz, Ph. D. dissertation (University of Maryland 2010)

[17] R. P. Budoyo, Ph. D. dissertation (University of Maryland 2016)

[18] A. P. Sears, Ph. D. dissertation (Yale University 2013)

[19] P. J. J. O'Malley, Ph. D. dissertation (UCSB 2016)

[20] J. M. Martinis *et al.*, Phys. Rev. B 67, 094510 (2003)

[21] G. Ithier *et al.,* Phys. Rev. B 72, 134519 (2005)

[22] P. Bertet, *et al.*, Phys. Rev. Lett. 95, 257002 (2005)

[23] A. P. Sears *et al.*, Phys. Rev. B 86, 180504 (2012)

[24] J. Yeh, J. of App. Phys. 121, 224501 (2017)

[25] F. W. Strauch, Ph. D. dissertation (University of Maryland, 2004)

[26] B. Suri, Ph. D. dissertation (University of Maryland 2015)

[27] S. Novikov, Ph. D. dissertation (University of Maryland 2015)

[28] J. J. Sakurai, "Modern Quantum Mechanics". Addison-Wesley, 2nd edition (2011)

[29] H. C. Torrey, Phys. Rev. 76, 1059 (1949)

[30] R. R. Ernst, "Principles of Nuclear Magnetic Resonance in One and Two Dimensions", Clarendon (1990)

[31] E. L. Hahn, Phys. Rev. 80, 4 (1950)

Chapter 5

[1] A. Blais *et. al*, Phys. Rev. A 69, 062320 (2004)

[2] B. W. Shore, P. L. Knight, Journal of Mod. Optics, 40, 7 (1993)

[3] J. Yeh, J. of App. Phys. 121, 224501 (2017)

[4] B. Suri, Ph. D. dissertation (University of Maryland 2015)

[5] A. P. Sears, Ph. D. dissertation (Yale University 2013)

[6] D. I. Schuster, Ph. D. dissertation (Yale University 2007)

[7] M. Boissonneault, J. M. Gambetta, A. Blais, Phys. Rev. Lett. 105, 100504 (2010)

[8] K. W. Murch *et al.*, Nature 502, 211-214 (2013)

[9] R. Vijayaraghavan, Ph. D. dissertation (Yale University 2008)

[10] M. D. Reed *et al.*, Phys. Rev. Lett. 105, 173601 (2010)

[11] J. Koch *et al.*, Phys. Rev. A 76, 042319 (2007)

[12] M. H. Devoret, R. J. Schoelkopf, Science 339, 1169 (2013)

[13] F. W. Strauch, Ph. D. dissertation (University of Maryland, 2004)

[14] H. Xu *et al.*, Phys. Rev. Lett. 94, 027003 (2005)

[15] J. J. Sakurai, "Modern Quantum Mechanics". Addison-Wesley, 2nd edition (2011)

[16] S. Novikov, Ph. D. dissertation (University of Maryland 2015)

[17] R. P. Budoyo, Ph. D. dissertation (University of Maryland 2016)

[18] H. Paik *et al.*, Phys. Rev. Lett. 107, 240501 (2011)

[19] E. M. Purcell, Phys. Rev. 69, 681 (1946)

Chapter 6

[1] A. P. Sears, Ph. D. dissertation (Yale University 2013)

[2] M. Tinkham, "Introduction to Superconductivity", McGraw-Hill Book Co. New York, NY (1975)

[3] K. C. Gupta *et al.* "Microstrip Lines and Slotlines", Artech, 2nd edition (1996)

[4] https://www.comsol.com/

[5] https://www.nanocenter.umd.edu/fablab/

[6] R. P. Budoyo, Ph. D. dissertation (University of Maryland 2016)

[7] https://www.msesupplies.com/collections/sapphire-wafers

[8] http://microchem.com/pdf/PMGI-Resists-data-sheetV-rhcedit-102206.pdf

[9] http://headwayresearch.com/chucks/ec_chucks.htm

[10] http://microchem.com/pdf/PMMA_Data_Sheet.pdf

[11] http://cmnst.ncku.edu.tw/ezfiles/23/1023/img/127/s1800seriesDataSheet.pdf

[12] http://www.nanophys.kth.se/nanophys/facilities/dicing-saw/Dicing_Saw_Manual.pdf

[13] http://www.dicing-blades.com/

[14] https://www.m-chemical.co.jp/en/products/departments/mcc/specialtychem/product/1201151_7976.html

[15] https://www.raith.com/products/eline-plus.html

[16] https://www.autodesk.com/

[17] http://microchem.com/products/images/uploads/MF_CD_26_Data_Sheet.pdf

[18] https://rdmathis.com/product/micro-electronic-sources-25/

[19] https://www.alfa.com/en/

[20] https://avac.com/alcatel-adixen-dry-pumps

[21] http://www.brooks.com/products/cryopumps-cryochillers/cryopumps/cryo-torr-cryopumps

[22] http://www.microchem.com/pdf/removerpg.pdf

[23] http://assets.fluke.com/manuals/8xiii___sieng0200.pdf

[24] https://www.digikey.com/catalog/en/partgroup/963e/20357?utm_adgroup=xGeneral&slid=&gclid=CjwKCAjwqarbBRBtEiwArlfEIFkLOnAMjRgI-Nf6nVqQLHuoWnWtfQSQgm08qZaZt-eROceopKnuKRoCxu8QAvD_BwE

[25] https://www.tek.com/keithley-source-measure-units/keithley-smu-2400-series-sourcemeter

[26] A. W. Kleinsasser *et al.*, IEEE Trans. on App. Supercon. 5, 1 (1995)

Chapter 7

[1] https://nanoscience.oxinst.com/products/cryofree-dilution-refrigerators/triton

[2] T. O. Klaassen *et al.*, Proc., IEEE Tenth Ann. Int. Conf. on Ter. Elec. 7503105 (2002)

[3] https://www.ellsworth.com/products/by-manufacturer/henkel-loctite/encapsulants/epoxy/henkel-loctite-stycast-2651-epoxy-encapsulant-black-1-gal-can/

[4] http://www.electroabrasives.com/Products/Black_Silicon_Carbide/

[5] https://www.cryopermshielding.com/

[6] http://www.microstock-inc.com/products.htm

[7] http://xmacorp.com/pages/cryo

[8] https://datasheet.octopart.com/UT-85-FORM-Micro-Coax-datasheet-10404415.pdf

[9] http://www.klmicrowave.com/

[10] https://www.anritsu.com/en-US/components-accessories/products/k250-v250

[11] https://wiki.kip.uni-heidelberg.de/KIPwiki/images/c/cb/PAMTECH_cryogenic_isolators.pdf

[12] http://www.caltechmicrowave.org/amplifiers

[13] https://www.mouser.com/midwest-microwave/

[14] J. Yeh, J. of App. Phys. 121, 224501 (2017)

[15] https://www.keysight.com/en/pd-1000001289%3Aepsg%3Apro/function-arbitrary-waveform-generator-15-mhz?cc=US&lc=eng

[16] http://www.microstock-inc.com/products.htm

[17] F. P. Milliken *et al.*, Rev. of Sci. Instr. 78, 024701 (2007)

[18] http://www.supercon-wire.com/content/cuni-resistive-wires

[19] https://www.keysight.com/en/pdx-x202270-pn-E5071C/ena-vector-network-analyzer?cc=US&lc=eng

[20] http://www.ni.com/en-us/support/model.pci-gpib.html

[21] https://www.mathworks.com/products/new_products/release2015a.html

[22] M. D. Reed *et al.*, Phys. Rev. Lett. 105, 173601 (2010)

[23] R. P. Budoyo, Ph. D. dissertation (University of Maryland 2016)

[24] https://www.thinksrs.com/products/fs725.html

[25] https://www.keysight.com/en/pd-1000001289%3Aepsg%3Apro/function-arbitrary-waveform-generator-15-mhz?cc=US&lc=eng

[26] https://www.thinksrs.com/products/dg535.html

[27] https://www.keysight.com/en/pdx-x202237-pn-E8257D/psg-analog-signal-generator-100-khz-to-67-ghz?cc=US&lc=eng

[28] https://www.keysight.com/en/pd-1000001883%3Aepsg%3Apro-pn-83731B/synthesized-signal-generator-1-20-ghz?cc=US&lc=eng

[29] https://www.tek.com/signal-generator/awg70002a

[30] https://www.part2go.com/rf-microwave/directional-hybrid-couplers/6-to-12-ghz/mac-c3205-06-microwave-rf-directional-coupler-4-8-ghz-06db-coupling-tested.html

[31] https://nardamiteq.com/viewmodel.php?model=AMF-3F-04000800-07-10P

[32] https://www.minicircuits.com/pdfs/ZX60-14012L.pdf

[33] https://www.markimicrowave.com/assets/datasheets/IQ-0318.pdf

[34] https://www.keysight.com/en/pd-1000001857%3Aepsg%3Apro-pn-83620B/synthesized-swept-signal-generator-001-20-ghz?cc=US&lc=eng

[35] https://www.minicircuits.com/pdfs/VHF-3500+.pdf

[36] D. C. Noll *et al.*, IEEE Trans. on Med. Imag. 10 (2): 154-163 (1991)

[37] https://www.minicircuits.com/pdfs/VLF-7200+.pdf

[38] https://www.minicircuits.com/pdfs/VLFX-80.pdf

[39] https://www.thinksrs.com/products/sr560.html

[40] http://www.ni.com/en-us/support/model.pci-6115.html

[41] https://www.keysight.com/en/pd-1000001884%3Aepsg%3Apro-pn-83732B/synthesized-signal-generator-001-20-ghz?cc=US&lc=eng

[42] https://www.part2go.com/rf-microwave/directional-hybrid-couplers/6-to-12-ghz/mac-c3205-10-microwave-rf-directional-coupler-4-8-ghz-10db-coupling-tested.html

Chapter 8

[1] S. P. Premaratne, J.-H. Yeh, F. C. Wellstood, and B. S. Palmer, "Implementation of a generalized CNOT gate between fixed-frequency transmons," In review, 2018.

[2] https://www.fastfieldsolvers.com/

[3] B. Sarabi, F. C. Wellstood, K. D. Osborn, *et al.*, Phys. Rev. Lett. 116, 167002 (2016)

[4] A. M. Holder, K. D. Osborn, C. J. Lobb, C. B. Musgrave, Phys. Rev. Lett. 111, 065901 (2013)

[5] R. P. Budoyo, Ph. D. dissertation (University of Maryland 2016)

[6] B. Sarabi, Ph. D. dissertation (University of Maryland 2014)

[7] J. M. Martinis, Quantum Information Processing, Volume 8, Issue 2-3, pp. 81-103 (2009)

[8] J. Lisenfeld *et al.*, Nat. Comm. 6, 6182 (2015)

Chapter 9

[1] http://www.klmicrowave.com/

[2] https://www.tek.com/signal-generator/awg70002a

[3] R. R. Ernst, "Principles of Nuclear Magnetic Resonance in One and Two Dimensions", Clarendon (1990)

[4] R. P. Budoyo, Ph. D. dissertation (University of Maryland 2016)

[5] H. Paik *et al.*, Phys. Rev. Lett. 107, 240501 (2011)

[6] J. Yeh, J. of App. Phys. 121, 224501 (2017)

[7] M. A. Nielsen, I. L. Chuang, "Quantum Computation and Quantum Information. 10th anniv. edn". Cambridge University Press, Cambridge, 2011.

[8] E. L. Hahn, Phys. Rev. 80, 4 (1950)

[9] P. J. J. O'Malley, Ph. D. dissertation (UCSB 2016)

[10] S. Vathyam, S. Lee, W. S. Warren, Science 272, 5258, 92-96 (1996)

[11] S. P. Premaratne, J.-H. Yeh, F. C. Wellstood, and B. S. Palmer, "Implementation of a generalized CNOT gate between fixed-frequency transmons," In review, 2018.

Chapter 10

[1] R. Zhang, C. J. Ballard, S. Premaratne, S. K. Dutta, J-H. Yeh, C. J. Lobb, B. S. Palmer, F. C. Wellstood, "Anomalous Transmon Relaxation From Non-Equilibrium Quasiparticles Accumulating in Junction Electrode", preliminary (2018)

[2] G. J. Dolan, T. A. Fulton, Ann. of Phys. 86, 1 (1974)

[3] R. W. Cohen, B. Abeles, Phys. Rev. 168, 444 (1968)

[4] M. Strongin, *et al.,* Phys. Rev. B 1, 1078 (1970)

[5] C. C. Chi, J. Clarke, Phys. Rev. B 20, 4465 (1979)

[6] C. T. Black, D. C. Ralph, M. Tinkham, Phys. Rev. Lett. 76, 688 (1996)

[7] N. A. Court, A. J. Ferguson, R. G. Clark, Superc. Sci. and Tech. 21, 1 (2007)

[8] P. Townsend, S. Gregory, R. G. Taylor, Phys. Rev. B 5, 54 (1972)

[9] P. Joyez, *et al.,* Phys. Rev. Lett. 72, 2458 (1994)

[10] A. Amar, D. Song, C. J. Lobb, F. C. Wellstood, Phys. Rev. Lett. 72, 3234 (1994)

[11] J. M. Hergenrother, *et al.*, Phys. Rev. B 51, 9407(R) (1995)

[12] P. J. de Visser, *et al.,* Phys. Rev. Lett. 106, 167004 (2011)

[13] D. J. van Woerkom, A. Geresdi, L. P. Kouwenhoven, Nature Physics 11, 547-550 (2015)

[14] J. Aumentado, M. W. Keller, J. M. Martinis, M. H. Devoret, Phys. Rev. Lett. 92, 066802 (2004)

[15] M. Tinkham, "Introduction to Superconductivity", McGraw-Hill Book Co. New York, NY (1975)

[16] A. A. Clerk, M. H. Devoret, S. M. Girvin, F. Marquardt, R. J. Schoelkopf, Rev. Mod. Phys. 82, 1155 (2010)

[17] D. Rogovin, D. J. Scalopino, Ann. Phys. 86, 1 (1974)

[18] R. J. Schoelkopf *et al.*, in Noise and Information in Nanoelectronics, Sensors, and Standards., edited by L. B. Kish, F. Green, G. Iannaccone, and J. R. Vig (Proceedings of the SPIE, 2003), vol. 5115, p. 356; condmat/0210247

[19] J. M. Martinis *et al.*, Phys. Rev. Lett. 95, 210503 (2005)

[20] H. Paik, K. D. Osborn, Appl. Phys. Lett. 96, 072505 (2010)

[21] D. Pappas *et al.* IEEE Trans. on Appl. Superc., 21, 3 (2011)

[22] C. Wang *et al.*, Nature Comm. 5, 5836 (2014)

[23] D. C. Moore *et al.*, AIP Conf. Proc. 1185, 168, (2009)

[24] R. P. Budoyo, Ph. D. dissertation (University of Maryland 2016)

Chapter 11

[1] R. Zhang, C. J. Ballard, S. Premaratne, S. K. Dutta, J-H. Yeh, C. J. Lobb, B. S. Palmer, F. C. Wellstood, "Anomalous Transmon Relaxation From Non-Equilibrium Quasiparticles Accumulating in Junction Electrode", preliminary (2018)

[2] G. J. Dolan, T. A. Fulton, Ann. of Phys. 86, 1 (1974)

[3] H. Paik *et al.*, Phys. Rev. Lett. 107, 240501 (2011)

[4] http://www.caltechmicrowave.org/amplifiers

[5] https://www.cryopermshielding.com/

[6] M. D. Reed *et al.*, Phys. Rev. Lett. 105, 173601 (2010)

[7] D. C. Moore *et al.*, AIP Conf. Proc. 1185, 168, (2009)

[8] C. Kittel, “Introduction to Solid State Physics”, 5th edition, Wiley, New York, NY (1976)

[9] M. Tinkham, “Introduction to Superconductivity”, McGraw-Hill Book Co. New York, NY (1975)

[10] B. M. McSkimming, A. Alexander, M. H. Samuels, J. of Vac. Sci. & Tech. A 35, 021401 (2017)

[11] https://www.m-chemical.co.jp/en/products/departments/mcc/specialtychem/product/1201151_7976.html